RESEARCH PAPERS

(Contents continued)

The ASME Journal of Engineering for Gas Turbines and Power is abstracted and indexed in the following:

AESIS (Australia's Geoscience, Minerals, & Petroleum Database), Applied Science & Technology Index, Aquatic Sciences and Fisheries Abstracts, Civil Engineering Abstracts, Compendex (The electronic equivalent of Engineering Index), Computer & Information Systems Abstracts, Corrosion Abstracts, Current Contents, Engineered Materials Abstracts, Engineering Index, Enviroline (The electronic equivalent of Environment Abstracts), Environment Abstracts, Environmental Science and Pollution Management, Fluidex, INSPEC, Mechanical & Transportation Engineering Abstracts, Mechanical Engineering Abstracts, METADEX (The electronic equivalent of Metals Abstracts and Alloys Index), Pollution Abstracts, Referativnyi Zhurnal, Science Citation Index, SciSearch (The electronic equivalent of Science Citation Index), Shock and Vibration Digest

(Contents continued)

Journal of Engineering for Gas Turbines and Power   **SEPTEMBER 2008**

Volume 130, Number 5

TECHNICAL BRIEFS

A Novel Low NO$_X$ Lean, Premixed, and Prevaporized Combustion System for Liquid Fuels

P. Gokulakrishnan[1]
e-mail: gokul@csefire.com

M. J. Ramotowski

G. Gaines

C. Fuller

R. Joklik

L. D. Eskin

M. S. Klassen

R. J. Roby

Combustion Science and Engineering, Inc.,
8940 Old Annapolis Road,
Suite L,
Columbia, MD 21045

Dry low emission (DLE) systems employing lean, premixed combustion have been successfully used with natural gas in combustion turbines to meet stringent emission standards. However, the burning of liquid fuels in DLE systems is still a challenging task due to the complexities of fuel vaporization and air premixing. Lean, premixed, and prevaporized (LPP) combustion has always provided the promise of obtaining low pollutant emissions while burning liquid fuels, such as kerosene and fuel oil. Because of the short ignition delay times of these fuels at elevated temperatures, the autoignition of vaporized higher hydrocarbons typical of most practical liquid fuels has been proven difficult to overcome when burning in a lean, premixed mode. To avoid this autoignition problem, developers of LPP combustion systems have focused mainly on designing premixers and combustors that permit rapid mixing and combustion of fuels before spontaneous ignition of the fuel can occur. However, none of the reported works in the literature has looked at altering fuel combustion characteristics in order to delay the onset of ignition in lean, premixed combustion systems. The work presented in this paper describes the development of a patented low NO$_x$ LPP system for combustion of liquid fuels, which modifies the fuel rather than the combustion hardware in order to achieve LPP combustion. In the initial phase of the development, laboratory-scale experiments were performed to study the combustion characteristics, such as ignition delay time and NO$_x$ formation, of the liquid fuels that were vaporized into gaseous form in the presence of nitrogen diluent. In the second phase, a LPP combustion system was commissioned to perform pilot-scale tests on commercial turbine combustor hardware. These pilot-scale tests were conducted at typical compressor discharge temperatures and at both atmospheric and high pressures. In this study, vaporization of the liquid fuel in an inert environment has been shown to be a viable method for delaying autoignition and for generating a gaseous fuel stream with characteristics similar to natural gas. Tests conducted in both atmospheric and high pressure combustor rigs utilizing swirl-stabilized burners designed for natural gas demonstrated an operation similar to that obtained when burning natural gas. Emission levels were similar for both the LPP fuels (fuel oils 1 and 2) and natural gas, with any differences ascribed to the fuel-bound nitrogen present in the liquid fuels. An extended lean operation was observed for the liquid fuels as a result of the wider lean flammability range for these fuels compared to natural gas. [DOI: 10.1115/1.2904889]

Introduction

Traditionally, spray diffusion combustors have been employed in gas turbines that operate on liquid fuels such as fuel oils 1 and 2. However, this diffusion mode of operation tends to produce unacceptable levels of NO$_x$ emissions. The current technology for burning liquid fuels in gas turbines is to use water and/or steam injection with conventional diffusion burners. Emission levels for a typical "state of the art" gas turbine, such as GE 7FA burning fuel oil 2 in diffusion mode with water/steam injection, are 42 ppm NO$_x$ and 20 ppm CO [1]. Water/steam injection has a dilution and cooling effect, lowering the combustion temperature and thus lowering NO$_x$ emissions. However, at the same time, water/steam injection is likely to increase CO emissions as a result

of local quenching effects. Thus, the "wet" diffusion type of combustion system for liquid fuels must trade off NO$_x$ emissions for CO emissions.

In recent years, stringent emission standards have made lean, premixed combustion more desirable in power generation and industrial applications than ever before since this combustion mode provides low NO$_x$ and low CO emissions without water addition. Lean, premixed combustion of natural gas avoids the problems associated with diffusion combustion and water addition. Thus, lean, premixed combustion is the foundation of modern dry low emissions (DLE) gas turbine combustion systems. When operated on natural gas, DLE combustion systems provide NO$_x$ and CO emissions of 25 ppm or less with no water addition. However, these systems cannot currently operate in a premixed mode on liquid fuels because of autoignition and flashback within the premixing section.

Plee and Mellor [2] characterized autoignition of the fuel/air mixture in the premixer as an important factor that causes flashback in practical combustion devices. Autoignition of the fuel/air mixture occurs before the main combustion zone when the ignition delay time of the fuel/air mixture is shorter than the mean residence time of the fuel in the premixer. Autoignition especially

---

occurs with the higher-order hydrocarbon fuels, such as fuel oils, which have shorter ignition delay times compared to natural gas [3]. The short ignition delay times of vaporized higher hydrocarbons have been proven difficult to overcome when burning in a lean, premixed mode.

Nevertheless, in order to overcome high NO_x levels produced by spray combustion, gas turbine designers still desire to use lean, premixed, and prevaporized (LPP) combustion. Several approaches have been reported in the literature [4–12] to overcome flashback and autoignition in the premixers of LPP combustors. These approaches attempt to achieve low NO_x emissions by designing premixers and combustors that permit rapid mixing and combustion before spontaneous ignition of the fuel can occur. In most of the work reported on LPP combustion systems in the literature, the fuel is directly sprayed into the premixer so that the liquid fuel droplets vaporize and mix with air at lean conditions. Typically, swirlers with multiport liquid fuel injection systems are employed for better fuel/air mixing [7]. However, unlike these attempts to alter hardware, there has been no reported work on altering fuel combustion characteristics in order to delay the onset of ignition in lean, premixed combustion systems.

In this study, vaporization of the liquid fuel in an inert environment has been shown to be a technically viable approach for LPP combustion. As described in this paper, a patented fuel vaporization and conditioning process [13] was developed and tested to achieve low emissions (NO_x and CO) comparable to those of natural gas while operating on liquid fuels, without water or steam addition. In this approach, liquid fuel is vaporized in an inert environment to create a fuel vapor/inert gas mixture, LPP gas, with combustion properties similar to those of natural gas. A premature autoignition of the LPP gas was controlled by the level of inert gas in the vaporization process. Tests conducted in both atmospheric and high pressure test rigs utilizing typical swirl-stabilized burners (designed for natural gas) found an operation similar to that achieved when burning natural gas. Emission levels were similar for both the LPP gas fuels (fuel oils 1 and 2) and natural gas, with any differences in NO_x emissions ascribed to fuel-bound nitrogen present in fuel oil 2. Also, tests showed that the LPP combustion system helps to reduce the NO_x emissions by facilitating stable combustion even at very lean conditions when using liquid fuels. An extended lean operation was found for the liquid fuels due to the wider lean flammability range for these fuels compared to natural gas. An added advantage of the fuel vaporization and conditioning process is the ability to achieve fuel interchangeability of a natural-gas-fired combustor with liquid fuels.

The initial phase of development of the LPP system described in this work involved laboratory-scale experiments to study combustion characteristics, such as ignition delay time and NO_x formation, of the liquid fuels that are vaporized into gaseous form in the presence of nitrogen diluent. In the second phase of this program, the LPP system [13] was commissioned to perform large-scale pilot experiments on atmospheric pressure and high pressure test rigs. Fuel oils 1 and 2 were chosen as typical liquid fuels for the tests. In this study, fuel oil 1 refers to commercially available kerosene and fuel oil 2, known as diesel fuel 2, is similar to commercially available home heating oil. Also, for a comparative study, experiments were performed with *n*-heptane, which is a widely studied liquid fuel. The chemical and physical specifications of the fuel oils are listed in Table 1. The chemical analysis shows that when compared to fuel oil 1, fuel oil 2 has a higher content of aromatics as well as fuel-bound nitrogen and sulfur.

Effect of Diluent on Ignition Delay Time

As discussed above, one of the causes of flashback in gas turbine combustors is the premature autoignition of the fuel in air during premixing. One way to avoid autoignition is to extend the induction period, known as the ignition delay time, of the fuel/air mixture by reducing the formation of combustion radicals that are

Table 1   Chemical and physical properties of fuel oils 1 and 2 used in the experiments

	Fuel oil 1	Fuel oil 2
API gravity at 60°F	45.7	37.6
Specific gravity at 60°F	0.7985	0.8373
Visocity at 40°C (cS)	1.04	2.6
Molecular weight	150	182
Paraffins (vol %)	83.6	79.3
Aromatics (vol %)	15.7	19.8
Olefins (vol %)	0.7	0.9
C (wt%)	85.78	86.83
H (wt %)	14.15	13.09
N (wt %)	0.02	0.04
S (wt %)	0.03	0.03
H/C molar ratio	1.91	1.85
Chemical formula	$C_{11}H_{21}$	$C_{13}H_{24}$

necessary for autoignition of the mixture at a given temperature. In hydrocarbon oxidation, during the induction period, the diluent plays an important role as a third-body enhancer for recombination reactions and slows down the radical formation [14]. These effects, in turn, extend the induction period so that the ignition process will be delayed. Therefore, increasing the diluent fraction of the fuel/oxidant mixture will increase the ignition delay time. In the present work, the effect of diluents on the ignition delay time was investigated for vaporized liquid fuels, such as fuel oils and *n*-heptane.

The ignition delay time experiments were performed in an atmospheric pressure flow reactor, which consists of a premixing section and a plug-flow test section. The fuel was vaporized into gaseous form in a preheated nitrogen environment before being mixed with air in the premixing section, which is located at the entrance to the reactor. Figure 1 shows the cross-sectional view of the premixing section. The premixing section opens into the plug-flow test section via an expanding duct in order to prevent the separation of flows at the entrance of the test section. The test section is a 52×2 in.^{2} alumina tube placed inside a furnace with three independently controlled zone heaters.

One of the difficulties in any flow reactor experiment is quickly mixing the fuel and oxidant at the entrance to the reactor [15,16]. In this work, the rapid mixing of the vaporized fuel with air was achieved by using a swirler followed by an expanding duct that opened into the test section. A photomultiplier coupled with a narrow band filter (centered at 430 nm) was placed at the end of the test section to detect CH* emissions. The time between the
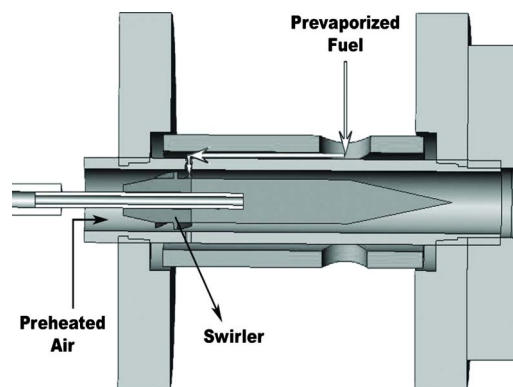
Fig. 1   Schematic of the premixing section of the flow reactor used for ignition delay time measurements
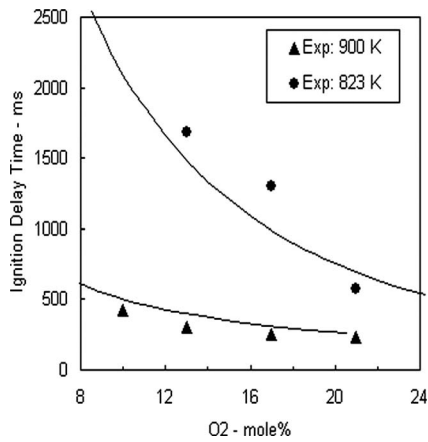
Fig. 2 Atmospheric pressure ignition delay time measurements of stoichiometric *n*-heptane/O_2/N_2, mixture as a function of the inlet O_2 composition. Key: symbols, experimental data; lines, ignition delay time model predictions using the detailed kinetic model of Curran et al. [18].

Fig. 4 Cutaway view of the bench-scale, high pressure swirl burner used to investigate NO_x emissions from the LPP combustion

injection of fuel vapor into the mixing section and the detection of the CH* emission signal was designated as the ignition delay time. The plug-flow test section was maintained at a constant initial reactor temperature. The flow reactor premixer temperature was maintained at 600 K in order to simulate the conditions in a gas turbine premixer. A detailed description of the flow reactor facility can be found in a previous publication [17].

Figure 2 shows the ignition delay time as a function of O_2 mole % in the inlet stream for *n*-heptane at 823 K and 900 K. The equivalence ratio of the fuel/oxidant mixture was maintained at stoichiometric conditions. The experimental measurements are compared to ignition delay time model predictions using the detailed kinetics mechanism of Curran et al. [18]. As can be seen in the figure, the effect of diluent on ignition delay time increases with decreasing inlet temperature. For example, for the *n*-heptane measurements shown in Fig. 2, the ignition delay time is proportional to $[X_{O_2}]^{-0.80}$ at 900 K and to $[X_{O_2}]^{-2.2}$ at 823 K, where $[X_{O_2}]$ refers to the mole % of O_2 in the inlet stream to the test section of the flow reactor.

Figure 3 compares the ignition delay time of both vaporized fuel oils with *n*-heptane as a function of O_2 mole % at the inlet to the flow reactor at 900 K. Both fuel oils 1 and 2 show ignition

Fig. 3 Comparison of ignition delay time measurements of *n*-heptane, fuel oil 1, and fuel oil 2 as a function of the inlet O_2 composition at 900 K inlet temperature, 1 atm pressure, and 1.0 equivalence ratio

delay times longer than those of *n*-heptane due to the presence of aromatic hydrocarbons in the fuel oils. Fuel oil 1 shows a similar O_2 dependency on the ignition delay time as that of *n*-heptane. However, the effect of O_2 on the ignition delay time is higher for fuel oil 2 compared to *n*-heptane. For example, for the ignition delay time measurements shown in Fig. 3, the *n*-heptane ignition delay time is proportional to $[X_{O_2}]^{-0.8}$, while the fuel oil 2 ignition delay time is proportional to $[X_{O_2}]^{-1.0}$.

Effect of Pressure on NO_x Formation

In the LPP system design, the liquid fuel is vaporized in an inert environment to create a gaseous fuel. This gaseous fuel is then premixed with air and burned in a manner similar to lean, premixed natural gas combustion. However, fuel oil, even as a gaseous fuel, is expected to produce slightly higher NO_x than natural gas fuel, as most fuel oils contain fuel-bound nitrogen. In this work, a series of experiments was performed over a range of pressures up to 10 atm in a bench-scale, high pressure swirl burner to investigate the NO_x production from the fuel oils when supplied as vaporized liquid fuels in an inert environment. To compare the formation of NO_x to the vaporized fuel oils, experiments were also performed with natural gas.

The bench-scale LPP combustion system consists of a swirl-stabilized burner where a radially injected gaseous fuel stream is mixed with primary air before the fuel/air mixture reaches the burner surface. A cutaway view of the high pressure swirl burner is shown in Fig. 4. A stand-alone vaporizing system for liquid fuels is directly connected to the fuel port of the swirler to supply the liquid fuel in gaseous form. Nitrogen was used as the diluent for vaporization. The burner was placed in a pressure vessel with a jacket cooling system along the wall. The pressure was varied from 1 atm to 10 atm. The air flow was varied from 1 g/s to 10 g/s with an input power of approximately 1 kW to 15 kW, respectively, for natural gas fuel. A water-cooled sample probe was placed just above the flame zone to draw exhaust gas samples into analyzers to measure CO, CO_2, and NO_x emissions. Measurements of CO and CO_2 were obtained using nondispersive infrared (NDIR) ray absorption analyzers, while NO_x was measured using the chemiluminescence detection method.

Experiments were performed to investigate the effect of diluent on NO_x formation by varying the N_2 to fuel molar ratio in the vaporizer in a range of 2–10. During the experiments, nitrogen was preheated to 573 K (300°C) to vaporize the liquid fuel in the vaporizer. Figure 5 shows the NO_x and CO measurements as a
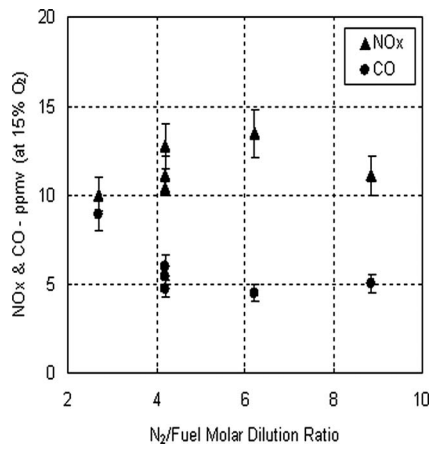
Fig. 5 The effect of N_2 to fuel dilution ratio on NO_x and CO for fuel oil 2 at 5 atm and 0.6 equivalence ratio

Fig. 7 Comparison of NO_x measurements for methane and fuel oil 2 as a function of pressure. The fuel to N_2 molar dilution ratio was 1–5.

function of diluent to fuel molar ratio for fuel oil 2 at 5 atm and at an equivalence ratio of 0.6. In Fig. 5, CO and NO_x measurements show that the diluent N_2 to fuel molar ratio does not have any significant effect on CO and NO_x emissions above a ratio of 4.

Figure 6 shows NO_x measurements as a function of equivalence ratio for methane, fuel oil 1, and fuel oil 2 at several pressures. Due to the presence of fuel-bound nitrogen, the fuel oils produce higher NO_x than methane. For methane, the NO_x measurements increased from 2 ppm to 5 ppm when the equivalence ratio was increased from 0.55 to 0.75 at 2 atm. For fuel oil 2, the NO_x increased from 5 ppm to 18 ppm when the equivalence ratio was changed from 0.5 to 0.7 at 8 atm. Fuel oils 1 and 2 have 0.02 wt % and 0.04 wt % fuel-bound nitrogen, respectively, as listed in Table 1. Thus, potentially, the fuel-bound nitrogen can produce approximately 4 ppm and 10 ppm of NO_x, respectively, for fuel oils 1 and 2 at a 0.6 equivalence ratio, assuming that all the fuel-bound nitrogen atoms are converted to NO_x. At an equivalence ratio of 0.6, methane produced approximately 2 ppm NO_x at 5 atm, as shown in Fig. 6. The measured NO_x emissions for fuel oils 1 and 2 were 6 ppm and 10 ppm, respectively, at the

Fig. 6 Comparison of NO_x measurements for methane and fuel oils 1 and 2 as a function of equivalence ratio at varying pressures. Key: methane at 2 atm (*) and 5 atm (●) pressures; fuel oil 1 at 3 atm (◇), 4 atm (□), and 5 atm (○) pressures; fuel oil 2 at 5 atm (△), 8 atm (▲), and 10 atm (+) pressures. The lines indicate the trends. The fuel to N_2 molar dilution ratio was 1–5.

same conditions. Thus, the difference in NO_x between the methane and fuel oils can entirely be accounted for by the NO_x that comes from the fuel-bound nitrogen.

The effects of pressure and equivalence ratio on the NO_x formation for fuel oil 2 are presented in Fig. 7. The results are also compared to those of methane. The effect of pressure on the NO_x formation shows a similar trend for fuel oil 2 as for methane. When the equivalence ratio was increased from 0.5 to 0.7, the formation of NO_x was increased by a multiple of approximately 2 for fuel oil 2, independent of pressure. Three factors contribute to the increase in NO_x for fuel oils as the equivalence ratio is increased: (1) the amount of fuel-bound nitrogen available for NO_x conversion is also increased; (2) the increase in flame temperature creates more thermal-NO_x formation; (3) the prompt-NO_x contribution increases as the availability of CH-like radicals increases as the mixture gets richer. The last two factors also contribute to the increase in NO_x for methane as the equivalence ratio is increased, as shown in Fig. 6. The difference in NO_x between methane and fuel oil 2 is equivalent to the NO_x produced by the fuel-bound nitrogen.

From the chemical composition analysis shown in Table 1, the contribution of fuel-bound nitrogen to NO_x would be 12 ppm for fuel oil 2 at 0.7 equivalence ratio. In Fig. 7, the measured NO_x for fuel oil 2 at 0.7 equivalence ratio is approximately equal to the NO_x produced by methane plus 12 ppm fuel NO_x. These results indicate an apparent quantitative conversion of fuel-bound nitrogen to NO_x at these lean conditions.

The results given in Fig. 7 show that NO_x formation in methane and fuel oil 2 exhibits a slight positive dependence on pressure. The effect of pressure on NO_x emissions during lean, premixed combustion is influenced by many factors [19–23]: degree of fuel-air mixing, equivalence ratio, residence time, and inlet temperature. Leonard and Stegmaier [19], Steele et al. [20], and Bhargava et al. [21] studied the influence of pressure on NO_x formation in lean, premixed systems but reached differing conclusions. Leonard and Stegmaier [19] concluded that NO_x emissions are independent of pressure for a perfectly premixed system with a flame temperature in the range from 1700 K to 1900 K. Lean, premixed combustion experiments of Bhargava et al. [21], performed from 7 atm and 27 atm, showed that the pressure effect on NO_x is negligible up to 0.50 equivalence ratio. However, equivalence ratios larger than 0.5 showed a positive pressure dependence on NO_x. Bhargava et al. [21] indicated that equivalence ratio and absolute pressure are also important factors that determine the effect of pressure on NO_x. Conversely, Steele et al. [20], who performed high pressure jet-stirred reactor experiments from
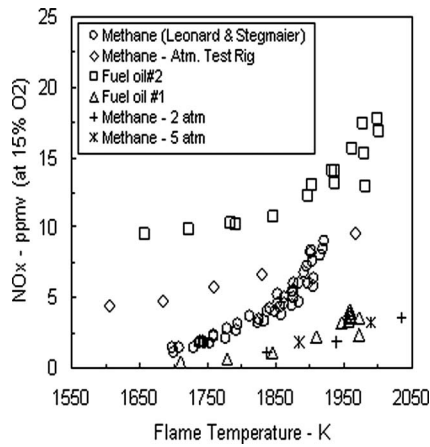
Fig. 8 NO$_x$ data obtained in the atmospheric pressure test rig for methane, fuel oil 1, and fuel oil 2. The data are compared to the methane data of Leonard and Stegmaier [19] as well as to the NO$_x$ data obtained in the high pressure swirl burner described in Fig. 6 at 2 atm and 5 atm.

1 atm to 7 atm, reported a slightly negative pressure dependence on NO$_x$. The results of Steele et al. may be due to the absence of a significant plug-flow residence time in the downstream of the jet-stirred reactor used in their experiments. Thus, based on the experimental data [19,21] reported in the literature and the experimental results discussed in this paper, it can be concluded that NO$_x$ formation in a gas turbine combustor is independent of pressure or has a slight positive pressure dependence at very lean conditions. However, NO$_x$ emissions will increase with pressure for higher equivalence ratio mixtures.

Pilot-Scale Testing

The next stage of development of the LPP system involved pilot-scale testing to study emissions and combustion characteristics, such as flame stability and lean blowout (LBO) limits, on realistic turbine hardware. A scaled-up version of the lean, premixed, swirl-stabilized burner used for the high pressure bench-scale tests was designed, built, and tested. The design of this scaled-up burner is similar to that found in modern DLE gas turbine combustion systems [1,24–27]. This large-scale test facility was able to supply up to 0.6 kg/s flow rate of air for the atmospheric pressure tests.

Atmospheric pressure tests were performed with combustion air at typical gas turbine compressor discharge temperatures of 600–620 K. Figure 8 shows NO$_x$ emission data obtained in the atmospheric pressure, swirl-stabilized burner for methane, fuel oil 1, and fuel oil 2. Figure 8 also compares the natural gas NO$_x$ measurements of Leonard and Stegmaier [19], as well as the NO$_x$ data at 2 atm and 5 atm of pressure obtained in the high pressure swirl burner described in Fig. 6. The experimental data of Leonard and Stegmaier [19] was measured between 1 atm and 30 atm. The NO$_x$ measurements shown in Fig. 8 for fuel oil 2 are approximately the same as those observed in the high pressure swirl burner experiments. The same figure also shows that fuel oil 1 produced relatively lower NO$_x$, while natural gas gave higher NO$_x$ when compared to the high pressure burner results.

Single Gas Turbine Burner Testing

The next step in the pilot-scale testing was to perform combustion tests on actual turbine hardware at both atmospheric and high pressure conditions. A Solar Turbines Centaur 50 gas turbine fuel nozzle was used for all real hardware tests. This natural gas nozzle was used for the vaporized liquid fuel (LPP gas) tests without any modifications. Tests were conducted at single nozzle, full load conditions for a Centaur 50, a Taurus 60, and a Taurus 70 gas
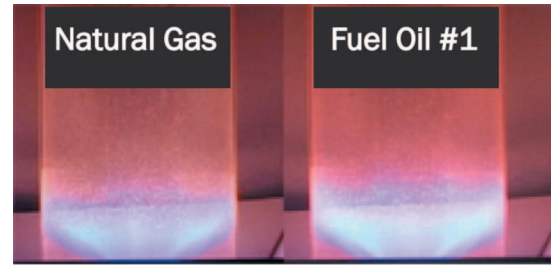
turbine [27]. During the gas turbine burner tests, the liquid fuel was supplied in gaseous form from the vaporizer.

The testing involved a study of emissions and combustion characteristics, such as flame stability and LBO limits. Both the atmospheric pressure and high pressure tests were performed at typical compressor discharge temperatures. For the high pressure tests, typical compressor discharge pressures were also used. Figure 9 shows a representative atmospheric pressure flame structure for natural gas and for fuel oil 1 from a Centaur 50 fuel nozzle at full load conditions. As can be seen in the figure, the LPP flame with fuel oil 1 exhibits a very similar flame structure and color to that of the natural gas flame.

Figures 10 and 11 show the results of atmospheric pressure testing of a single gas turbine fuel nozzle at Centaur 50 full load conditions for three fuels. Prevaporized fuel oil 1 and fuel oil 2 run as LPP gas both show low NO$_x$ and CO emissions comparable to those of DLE combustion systems fired on natural gas. The figures show that these low NO$_x$ and low CO emissions are simultaneously achieved. As discussed earlier, the primary difference between natural gas and LPP gas NO$_x$ emissions can be attributed to the fuel-bound nitrogen present in the fuel oils. Also, during the testing, no flashbacks were observed at any of the test conditions when operating on the fuel oils using the LPP system, and a stable flame was easily maintained when switching fuels from natural gas to LPP gas and back again.

Actual turbine hardware tests were conducted using a high pressure facility capable of testing a single gas turbine fuel nozzle at full compressor discharge temperature and pressure. The LPP liquid vaporizer was used to supply the liquid fuels in gaseous

Fig. 9 Comparison of natural gas and fuel oil 1 flames at atmospheric pressure for Centaur 50 fuel nozzle at full load conditions
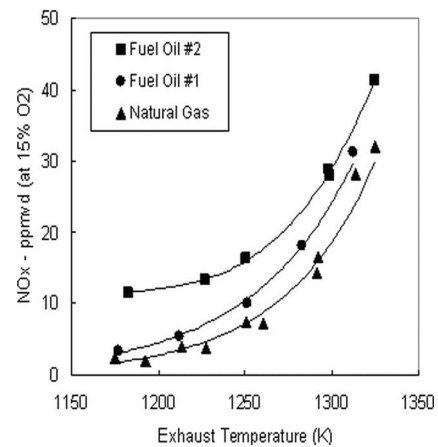
Fig. 10 Comparison of NO$_x$ emission measurements for fuel oil 2, fuel oil 1, and natural gas as a function of measured exhaust gas temperature for a single fuel nozzle at Centaur 50 full load conditions (100%). The combustion air temperature was 613 K, the combustor pressure was 1 atm, and the fuel dilution was 6:1 (molar basis).

Journal of Engineering for Gas Turbines and Power   SEPTEMBER 2008, Vol. 130 / **051501-5**
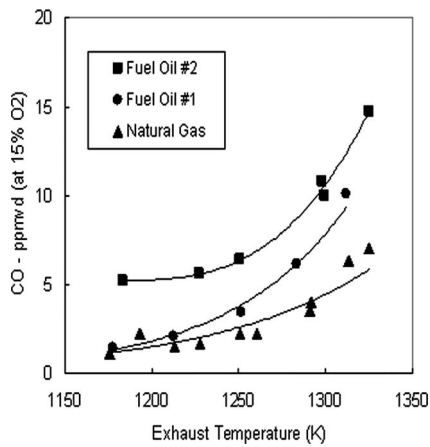
Fig. 11 Comparison of CO emission measurements for fuel oil 2, fuel oil 1, and natural gas as a function of measured exhaust gas temperature for a single fuel nozzle at Centaur 50 full load conditions (100%). The combustion air temperature was 613 K, the combustor pressure was 1 atm, and the fuel dilution was 6:1 (molar basis).

form. The same fuel nozzle used for natural gas testing was also used for liquid fuel testing on LPP gas without any modifications. Figure 12 shows NO_x and CO emissions at full load conditions for both natural gas and fuel oil 2.

During the testing, emission and dynamics data were taken over a range of lean equivalence ratios from approximately 0.75 to the LBO limit. However, the emission data are plotted against the measured exhaust gas temperature in order to provide a common temperature reference. The lowest temperature data points shown in Fig. 12 reflect the experimentally observed LBO limit. Figure 12 shows that fuel oil 2 LPP gas has an extended LBO limit compared to natural gas and can thus achieve NO_x emissions nearly as low as natural gas despite the fuel-bound nitrogen.

Figure 12 also shows that the crossover point between NO_x and CO emissions extends to lower temperatures (and therefore lower equivalence ratios) for fuel oil 2 LPP gas as compared to natural gas. As can be seen from the figure, fuel oil 2 LPP gas showed increased flame stability and an extended LBO limit at lower temperatures (equivalence ratio) compared to natural gas.
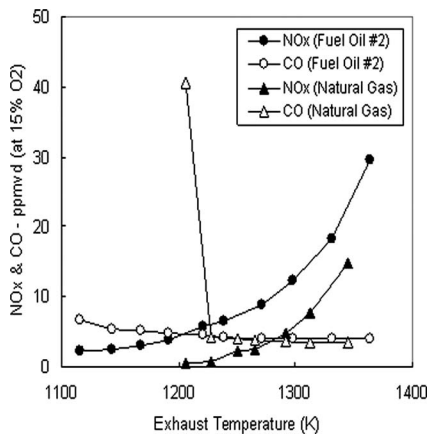
Fig. 12 Comparison of NO_x and CO emission measurements for fuel oil 2 and natural gas as a function of measured exhaust gas temperature for a single fuel nozzle at Taurus 60 full load conditions (100%). The combustion air temperature was 648 K, the combustor pressure was 12.6 atm, and the fuel dilution was 5:1 (molar basis).
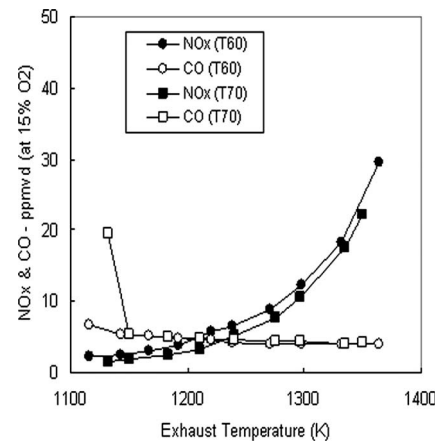
Fig. 13 Comparison of NO_x and CO emission measurements for fuel oil 2 as a function of measured exhaust gas temperature for a single fuel nozzle at Taurus 60 (T60) and Taurus 70 (T70) full load conditions (100%). The combustion air temperatures were 648 K (T60) and 706 K (T70), the combustor pressures were 12.6 atm (T60) and 16.2 atm (T70), and the fuel dilution was 5:1 (molar basis).

Figure 13 shows comparable NO_x and CO emissions for both Taurus 60 and Taurus 70 single nozzle full load conditions. The data indicate that similar emissions are achieved, even though the Taurus 70 full load conditions are at higher temperature and pressure than the Taurus 60 operating conditions. Finally, as was observed in the atmospheric pressure tests, these high pressure tests also demonstrate that a stable burner operation was easily maintained when switching fuels from natural gas to LPP gas and back again.

The significance of the data shown in Fig. 12 is that liquid fuels, such as fuel oil 2 LPP gas, are able to achieve low NO_x emission levels similar to natural gas. For an exhaust temperature (firing temperature) of 1318 K, Fig. 12 shows NO_x and CO emissions for natural gas to be 9 ppm and 3.5 ppm, respectively. The comparable fuel oil 2 LPP gas emissions at the same exhaust temperature are 16 ppm for NO_x and 4.0 ppm for CO. Because the LPP gas fuel characteristics are similar to those of natural gas, fuel oil 2 LPP gas is capable of being used in modern DLE gas turbine combustion systems without changes to the burner hardware while achieving much lower NO_x and CO emissions than fuel oils burned in conventional spray flames with water addition.

Conclusions

This paper described the development of and results from a patented low NO_x LPP combustion system for liquid fuels. In the LPP combustion system, liquid fuels were vaporized into gaseous form in an inert environment using nitrogen as diluent. The effect of nitrogen diluent on ignition delay time was measured in a laboratory-scale flow reactor. The experimental results show that diluent nitrogen increased the ignition delay time at typical air/fuel premixing conditions in gas turbines. Also, high pressure, swirl-stabilized burner experiments were performed to study NO_x formation using the LPP combustion system. The fuel oils in gaseous form were premixed with air and burned to achieve very low NO_x emissions comparable to those of natural gas in a lean, premixed combustion system. The difference in NO_x between methane and the fuel oils was attributed to the conversion of fuel-bound nitrogen into NO_x.

Finally, the test program demonstrated that the LPP combustion system described in this paper was able to produce low NO_x and low CO emissions without autoignition and flashback. These results were achieved at compressor discharge temperatures and pressures using actual full-scale turbine hardware designed for

natural gas operation without any modifications to the combustor hardware. The test data show that at equivalent exhaust (firing) temperatures, NO_x emissions for natural gas and fuel oil 2 LPP gas were 9 ppm and 16 ppm, respectively. CO emissions were 3.5 ppm and 4.0 ppm, respectively. Because the LPP gas fuel characteristics are similar to natural gas, fuel oil 2 LPP gas is capable of being used in modern DLE gas turbine combustion systems without changes to the burner hardware while achieving single digit NO_x and CO emissions levels.

Acknowledgment

References

[1] Davis, L. B., and Black, S. H., 2000, "Dry Low NO_x Combustion Systems for GE Heavy-Duty Gas Turbines," General Electric Power Systems, Report No. GER 3568G.

[2] Plee, S. L., and Mellor, A. M., 1978, "Review of Flashback Term Reported in Prevaporizing/Premixing Combustors," Combust. Flame, **32**, pp. 193–203.

[3] Oumejjoud, K., Stuttaford, P., Jennings, S., Rizkalla, H., Henriquez, J., and Chen, Y., 2005, "Emission, LBO and Combustion Characterization for Several Alternative Fuels," ASME Paper No. GT2005-68561.

[4] Maier, G., and Wiitig, S., 1999, "Fuel Preparation and Emission Characteristics of a Pressure Loaded LPP Combustor," Paper No. AIAA-99-3774.

[5] Imamura, A., Yoshida, M., Kawano, M., Aruga, N., Nagata, Y., and Kawagishi, M., 2001, "Research and Development of a LPP Combustor With Swirling Flow for Low NO_x," Paper No. AIAA-2001-3311.

[6] Ikezaki, T., Hosoi, J., and Hidemi, T., 2001, "The Performance of the Low NO_x Aero Gas Turbine Combustor Under High Pressure," ASME Paper No. 2001-GT-0084.

[7] Lin, Y., Peng, Y., and Liu, G., 2004, "Investigation on NO_x of a Low Emission Combustor Design With Multihole Premixer-Prevaporizer," ASME Paper No. GT2004-53203.

[8] Lee, C., Chun, K. S., and Locke, R. J., 1995, "Fuel-Air Mixing Effect on NO_x Emissions for a Lean Premixed-Prevaporized Combustion System," Paper No. AIAA-95-0729.

[9] Michou, Y., Chauveau, C., Gijkalp, I., and Carvalho, I. S., 1999, "Experimental Study of Lean Premixed and Prevaporized Turbulent Spray Combustion," Paper No. AIAA 99-0332.

[10] Hoffmann, S., Judith, H., and Holm, C., 1998, "Further Development of the Siemens LPP Hybrid Burner," ASME Paper No. 98-GT-552.

[11] Mansour, A., Benjamin, M., Straub, D. L., and Richards, G. A., 2001, "Application of Macrolamination Technology to Lean, Premixed Combustion," ASME J. Eng. Gas Turbines Power, **123**, pp. 796–802.

[12] Røkke, N. A., and Wilson, A. J. W., 2001, "Experimental and Theoretical Studies of a Novel Venturi Lean Premixed Prevaporized (LPP) Combustor," ASME J. Eng. Gas Turbines Power, **123**, pp. 567–573.

[13] Roby, R. J., Klassen, M. S., and Schemel, C. F., 2006, "System for Vaporization of Liquid Fuels for Combustion and Method of Use," U.S. Patent No. 7,089,745.

[14] Lifshitz, A., 2001, "Chemical and Combustion Kinetics," *Handbook of Shock Waves*, Vol. 3, Academic, New York.

[15] Yetter, R. A., Dryer, F. L., and Rabitz, H., 1991, "A Comprehensive Reaction Mechanism for Carbon Monoxide/Hydrogen/Oxygen Kinetics," Combust. Sci. Technol., **79**, pp. 129–140.

[16] Gokulakrishnan, P., Kazakov, A., and Dryer, F. L., 2003, "Comparison of Numerical and Experimental Kinetic Data for Flow Reactor Systems: Mixing Effects," *Proceedings of the Third Joint Meeting*, The Combustion Institute.

[17] Gokulakrishnan, P., Gaines, G., Currano, J., Klassen, M. S., and Roby, R. J., 2007, "Experimental and Kinetic Modeling of Kerosene-Type Fuels at Gas Turbine Operating Conditions," ASME J. Eng. Gas Turbines Power, **129**, pp. 655–663.

[18] Curran, H. J., Gaffuri, P., Pitz, W. J., and Westbrook, C. K., 1998, "A Comprehensive Modeling Study of *n*-Heptane Oxidation," Combust. Flame, **114**, pp. 149–177.

[19] Leonard, G., and Stegmaier, J., 1994, "Development of an Aeroderivative Gas Turbine Dry Low Emissions Combustion System," ASME J. Eng. Gas Turbines Power, **116**, pp. 542–546.

[20] Steele, R. C., Tonnouchi, J. H., Nicol, D. G., Horning, D. C., Malte, P. C., and Pratt, D. G., 1996, "Characterization of NO_x, N_2O and CO for Lean Premixed Combustion in High Pressure Jet-Sirred Reactor," ASME Paper No. 96-GT-128.

[21] Bhargava, A., Kendrick, D. W., Colket, M. B., Sowa, W. A., Casleton, K. H., and Maloney, D. J., 2000, "Pressure Effect on NO_x and CO Emissions in Industrial Gas Turbines," ASME Paper No. 2000-GT-97.

[22] Correa, S. M., 1992, "A Review of NO_x Formation Under Gas-Turbine Combustion Conditions," Combust. Sci. Technol., **87**, pp. 329–362.

[23] Mongia, R. K., Tomita, E., Hsu, F. K., Talbot, L., and Dibble, R. W., 1996, Sym. (Int.) Combust., [Proc.], **26**, pp. 2749–2755.

[24] Schorr, M. M., and Chalfin, J., 1999, "Gas Turbine NO_x Emissions Approaching Zero—Is It Worth the Price?," General Electric Power Generation, Report No. GER 4172.

[25] Pavri, R., and Moore, G. D., 2001, "Gas Turbine Emissions and Control," General Electric Power Systems, Report No. GER 4211.

[26] Eimers, R. A., Smith, K. O., and Cowell, L., 2001, "Developments in Low Emissions Combustion Systems for Industrial Gas Turbines," Solar Turbines, Report No. TPSOLONOX/901.

[27] Knodle, M. S., 1998, "Centaur, 40, Centaur 50 and Taurus 60 Gas Turbine Product Technology Update," Solar Turbines Turbomachinery Technology Seminar, Paper No. TTS123/398/M.

J. M. Cohen

A. Banaszuk

J. R. Hibshman

T. J. Anderson

H. A. Alholm

United Technologies Research Center,
East Hartford, CT 06108

Active Control of Pressure Oscillations in a Liquid-Fueled Sector Combustor

A system for the active control of combustor pressure oscillations in liquid-fueled, lean, premixed combustors was demonstrated in a three-nozzle sector combustor, using full-scale engine hardware. Modulation of a portion of the premixed fuel flow led to a reduction of 6.5 dB (2.1 times) in the amplitude of the dominant pressure oscillations mode. Combustor emissions were not adversely affected by the control.
[DOI: 10.1115/1.2901177]

Introduction

Emphasis on reducing the levels of pollutants created by gas turbine combustors has led to the development of lean, premixed combustor designs, especially for industrial applications. Premixing large amounts of air with the fuel prior to its injection into the combustor greatly reduces peak temperatures within the combustor and leads to lower NO_x emissions. Premixed combustors are often susceptible to thermoacoustic combustion instabilities, which can lead to large pressure oscillations in the combustor. These pressure oscillations result in increased noise and decreased durability due to the vibration and flame motion.

In a DARPA (Defense Advanced Research Projects Agency)-funded program, UTRC investigated the feasibility of attenuating combustion instability using active control techniques. Because of DARPA's interest in marine applications (which typically use liquid fuel), the focus of this research was on a liquid-fueled low-NO_X combustor. This combustor exhibited a large-amplitude pressure oscillation at a frequency near 200 Hz. The goal of the research was to develop a practical active control system, which would reduce the magnitude of the pressure fluctuations without adversely affecting NO_x levels. The effort stressed the practicality of the system and its ability to work with full-scale engine hardware at realistic operating conditions.

The initial phase of this program consisted of the development and demonstration of the technology in a 4 MW single-nozzle combustor, using a full-scale engine fuel nozzle at realistic operating conditions [1]. Results from these experiments showed that the control system was capable of achieving reductions of up to 15 dB (5.6 times) in the magnitude of the dominant pressure oscillation mode, without negatively affecting emission levels. This system used a high-speed solenoid valve to modulate a fraction of the fuel entering the premixing fuel nozzle. The fuel flow pulsations were phased relative to the combustor pressure fluctuations to give optimum performance.

This paper describes the application and scaleup of the techniques developed in the single-nozzle combustor to a three-nozzle sector combustor. The sector combustor allowed a more engine-like environment in which the effects of nozzle-to-nozzle interaction and combustor liner damping could be investigated.

Sector Combustor

A cost-effective alternative to both engine and full-annular combustor testing is to test a sector cut from the full combustor annulus containing several fuel nozzles. Sector combustor testing

offers savings over full-annular combustor testing because of the reduced hardware, and reduced compressor, and air heating capacity required. For the three-nozzle sector combustor used in this program, the outer fuel nozzles provided the center fuel nozzle with fluid dynamic boundary conditions typical of those in an engine, although it is not capable of reproducing circumferential acoustics that may be observed in full-annular engine combustors.

The combustor used for this portion of the program was a 67.5 deg sector cut from an aeroderivative gas turbine engine whose cross section is shown in Fig. 1. Three fuel nozzles at 22.5 deg spacing fed a sector of the full-annular combustor. The sector centerline was oriented horizontally, with fuel Nozzles 1, 2, and 3 positioned at 8, 9, and 10 o'clock, respectively, looking downstream on centerline. The two azimuthal boundaries (sector cutting planes) of the combustor were sealed by welding in solid plates, which were coated with a ceramic thermal barrier and convectively cooled on their outer surface by unheated air. A water cooled, simulated turbine inlet guide vane pack was installed in the exit of the combustor providing a high Mach number (~ 0.8) downstream boundary similar to that existing in the engine.

All three fuel nozzles feeding the sector combustor were identical to that used in the previous single-nozzle combustor tests [1,2]. Air from the prediffuser entered the fuel nozzles tangentially with liquid fuel injected into the airflow through six axial spokes. The premixed and prevaporized fuel/air mixture left the fuel nozzle axially with streamwise swirl induced by the air's tangential entry into the nozzle.

The sector combustor was operated at pressure-scaled conditions to accommodate the compressed air facilities. Similarity (velocity matching, in this case) between the true engine operating conditions and reduced pressure conditions could be ensured by preserving the combustor flow parameter, FP, where

$$FP = \frac{\dot{m}_{air}\sqrt{T_3}}{P_3} \qquad (1)$$

where $\dot{m}_{air}$ is the mass flow rate of air, T_3 the diffuser air total temperature, and P_3 the diffuser air total pressure.

Operating the sector combustor at a reduced pressure of 1.1 MPa and a corresponding reduced airflow of 8.2 kg/s preserved the engine operating flow parameter and fell within the operating capabilities of UTRC's compressor facilities. A nonvitiating air heater heated the air to a temperature of 730 K, typical of the engine combustor inlet temperature.

Control valves on the combustor outlet, inner diameter bleed, and outer diameter bleed controlled the balance of the airflow splits among the different flow paths (fuel nozzles, liner, bypass). Inner diameter and outer diameter bleed flows were adjusted to approximate the Mach numbers in the engine shroud. Overall airflow as well as inner and outer diameter bleed airflows were mea-

Downloaded 02 Jun 2010 to 171.66.16.107. Redistribution subject to ASME license or copyright; see http://www.asme.org/terms/Terms_Use.cfm
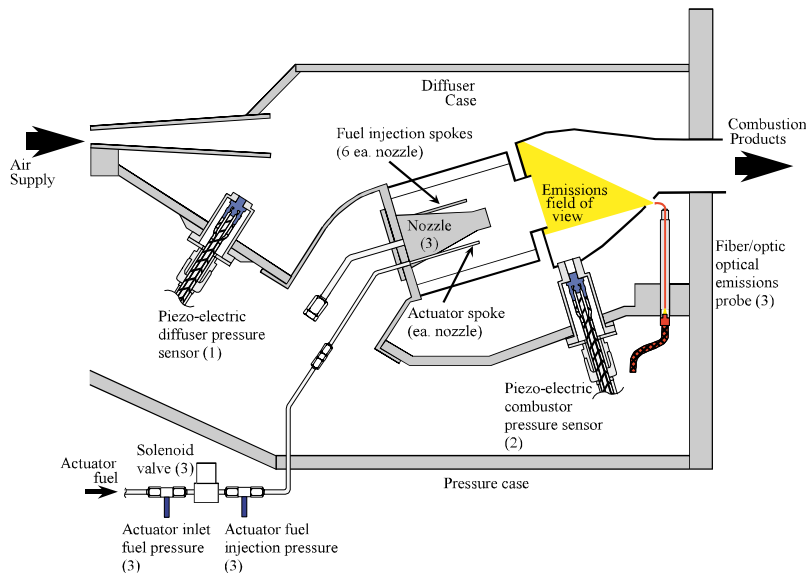
Fig. 1 Cross section of sector combustor test facility with instrumentation and actuation system

sured with choked venturis. Airflow through the combustor was calculated as the balance between the total and bleed airflows. Combustor airflow splits through the fuel nozzles and dilution holes were calculated based on nonreacting flow capacity tests. Approximately 70% of the air was delivered to the primary combustion zone. The combustor primary-zone equivalence ratios reported in this paper are based on the calculation of airflow through the fuel nozzles.

The sector combustor was fueled with No. 2 diesel, delivered to the sector combustor at a nominal flow rate of 460 kg/h. The nozzle-to-nozzle fuel flow distribution was neither controlled nor measured during combustion tests, but preliminary cold fuel flow measurements indicated that the fuel flow was evenly distributed among the three fuel nozzles.

At each fuel nozzle, the fuel flow was divided among six fuel injection spokes, where five spokes were operated steadily and the sixth spoke flow was actuated by a high-speed solenoid valve with separate feed plumbing, as shown in Fig. 2. The solenoid valves had a maximum operating frequency of approximately 250 Hz.

The average fuel flow rate to each of the three control spokes was monitored individually with turbine flow meters. The mean fuel flow through each of the actuated fuel systems was maintained at 1/6 of the fuel flow through that nozzle. Accumulators installed in the fuel system upstream of the actuating valve worked to maintain steady fuel supply pressure by adding capacitance to the system. Fuel plumbing elevations were chosen to minimize trapped air in the system that could introduce undesirable fuel system dynamics. The distance from the fuel modulating valves to the point of fuel injection through the spoke was nominally 1 m.

Instrumentation

Both time-averaged and fast-response measurements were collected during sector combustor tests. Time-averaged measurements of mean air and fuel pressures, temperatures, flow rates, and emissions concentrations were collected. Species concentrations of NO_x, CO, unburned hydrocarbons (UHC), CO_2, and O_2 concentrations were measured for each data point. Exhaust gas
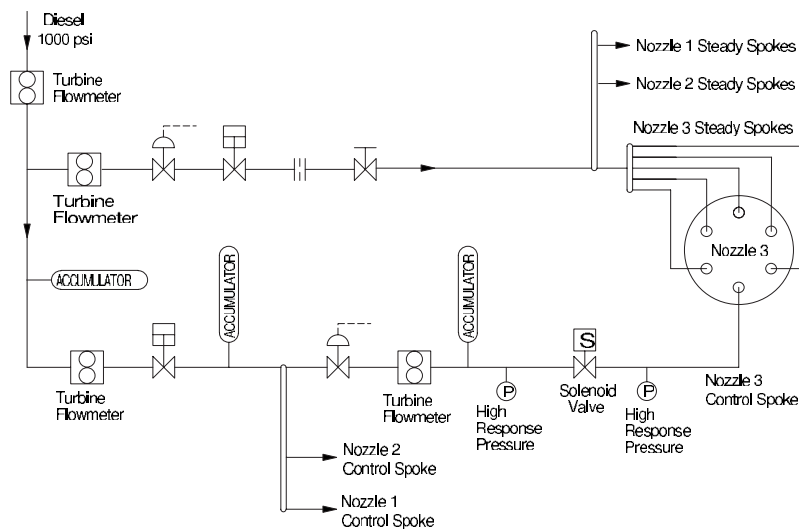
Fig. 2 Schematic of steady-state and controlled fuel systems in the sector combustor test facility
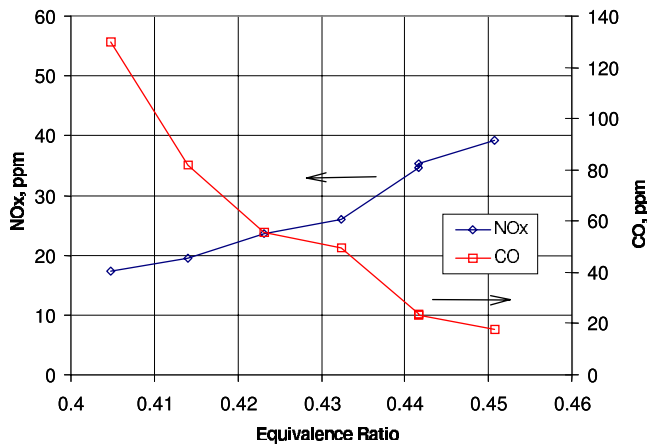
Fig. 3 Dependence of NO$_x$ and CO concentrations at combustor exit on the primary-zone equivalence ratio

Fig. 4 Dependence of combustor pressure fluctuation levels on the primary-zone equivalence ratio

was sampled from an array of locations spanning the exit of the combustor and ganged together to yield a spatially averaged sample. The sampled gas flowed to the emission analyzers through heated and insulated tubing. All emission concentrations reported in this paper have been corrected to 15% O$_2$ concentrations.

Fast-time response measurements were collected using a dSpace data acquisition system configured to sample multiple channels simultaneously at a frequency of 2 kHz with a low pass filter at 1 kHz. The sector rig instrumentation layout is shown in Fig. 1. Limited access allowed for only two combustor fluctuating pressure measurements at the same axial location just downstream of the fuel nozzle exit plane and one upstream diffuser pressure measurement. PCB pressure transducers were mounted flush to the flow path walls in special insulated and water-cooled vessels, which protected them from the surrounding containment temperature and pressure.

Photomultiplier tubes (PMT's) were used to measure the intensity of CH and CO radical emissions in the combustor. The intensity of these emissions has been shown to linearly track the rate of heat release in premixed systems [3,4]. Light was collected using fiber-optic probes "looking" upstream through the dilution air holes in the combustor liner. This orientation allowed the three PMT's to "see" the primary combustion zone downstream of each of the fuel nozzles. 200 μm diameter quartz fibers with a numerical aperture of 0.37 passed through a flange in the pressure vessel and were directly coupled to each PMT. Bandpass optical filters were installed to selectively admit only those wavelengths associated with CH and CO emissions (430 nm).

High-response pressure measurements in the actuated fuel lines were used to coordinate actuation among the three systems. These transducers were located between the valve and the fuel injector, each the same distance from the fuel injector tips, yielding a measure of the relative fuel injector phasings.

Uncontrolled Combustor Characterization

By operating the sector combustor at leaner premixed stoichiometries, and therefore lower flame temperatures, NO$_x$ emissions could be reduced from 40 ppm to less than 20 ppm, as shown in Fig. 3. The leaner stoichiometries that led to reduced NO$_x$ caused a penalty to CO emissions, increasing concentrations from less than 20 ppm to 130 ppm. A fair compromise could be achieved near a primary-zone equivalence ratio of 0.435 with NO$_x$ and CO concentrations of 30 ppm and 40 ppm, respectively. Figure 4 shows how combustor pressure oscillations increased with decreasing equivalence ratio. Controlling these pressure fluctuations would allow an engine to be operated at an equivalence ratio that optimizes the balance between NO$_x$ and CO emissions.
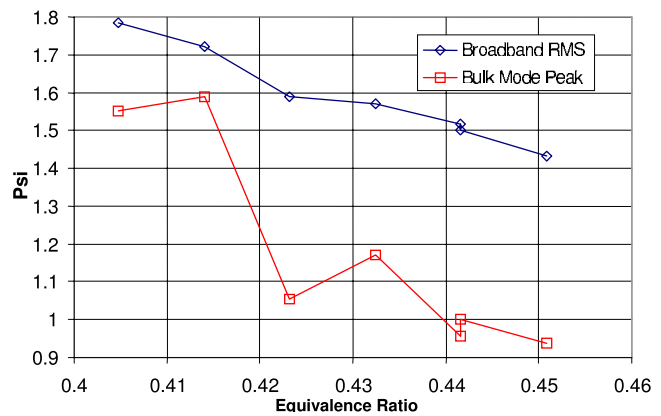
Power spectral density (PSD) plots of combustor pressure for equivalence ratios of 0.41 and 0.45 are shown in Fig. 5. Decreasing the equivalence ratio amplifies the peak and shifts it to lower frequency. PSD's of the PMT signal corresponding to fuel Nozzle 1 (Fig. 6) show heat release fluctuation spectra similar to the pressure spectra. These modes have been characterized as "bulk" modes, in which there is little spatial variation of the fluctuating pressure within the combustor [5].

Actuation System Characterization

Combustor pressure response to open-loop forcing of the control fuel flows at discrete frequencies was used as a measure of actuator authority. Figure 7 shows a combustor pressure PSD plot for a case in which the control fuel flow to Nozzle 2 was forced at 100 Hz. Subtracting the pressure spectra amplitude of the unforced case from the forced case at the open-loop forcing frequency quantified the actuator's authority at that frequency. Open-loop forcing of a single fuel nozzle could typically raise the pressure spectra at the forcing frequency from 100% to 400% of the unforced amplitude depending on the forcing frequency. Open-loop forcing experiments were not performed near the dominant pressure oscillations frequency for risk of doing damage to the combustor. In addition, the uncertainties associated with likely interaction of the forcing with the possible self-excitation
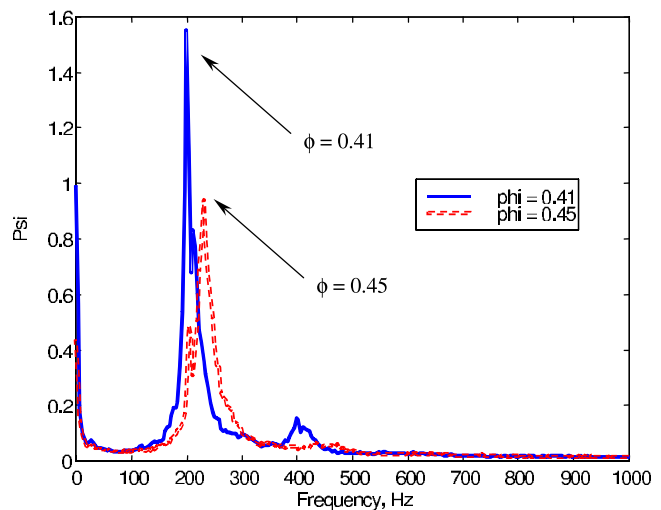
Fig. 5 Power-spectrum density plots of uncontrolled combustor pressure fluctuations at two equivalence ratios, ϕ, showing shift in amplitude and frequency of the dominant mode with equivalence ratio
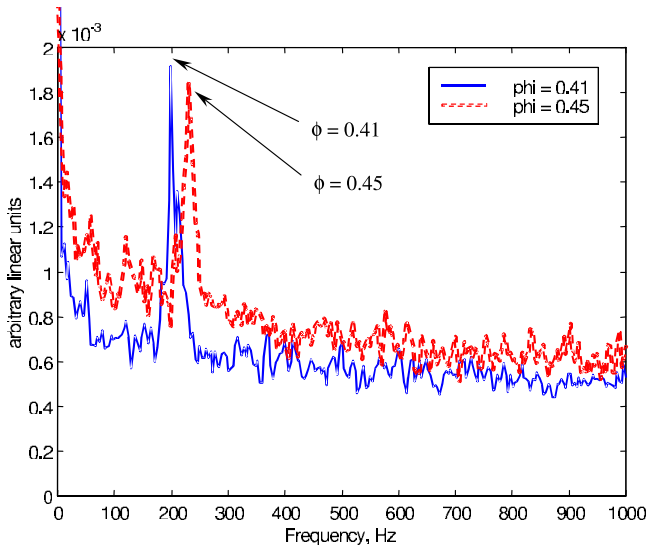
Fig. 6 Power-spectrum density plots of uncontrolled optical emissions (heat release rate) at two equivalence ratios, ϕ, showing shift in frequency and amplitude of the dominant mode similar to that seen in the pressure data

via heat release coupling would make interpretation of open-loop forcing data near the pressure oscillations frequency difficult. It was assumed that actuator authority in "quiet" regions of the spectrum was indicative of authority near the dominant frequency.

For simultaneous open-loop forcing of multiple fuel nozzles, actuator authority was dependent on the relative nozzle-to-nozzle phasing. The "diamond" curve in Fig. 8 shows combustor pressure spectral amplitudes at a 100 Hz open-loop forcing frequency for two simultaneously forced fuel nozzles versus their relative phase. A broad range of phases, $-60 \deg < (\phi 3 - \phi 2) < +60 \deg$, existed where the actuator authority was optimized and relatively insensitive to phase. Phase-optimized actuator authority increased linearly with the number of fuel nozzles actuated.

Controlled Combustor Characterization

A closed-loop control algorithm was developed to use the actuators' authority to damp combustor pressure oscillations. The algorithm chosen consisted of a frequency tracking observer

Fig. 8 Actuation authority increases linearly with the number of fuel nozzles actuated, provided the actuation is well coordinated

implemented in software, which identified the frequency and in-phase and quadrature components of the combustor pressure oscillations from a high-response pressure signal. The phase shifted pressure oscillation signal was fed back to the on/off control valve. The phase shift was selected by the user and could be specified independently for each of the three fuel nozzles.

Combustor pressure PSD plots for closed-loop control of Nozzle 2 in Fig. 9 show that depending on the controller phase chosen, the pressure oscillations in the combustor could either be damped or amplified. Figure 10 shows the combustor rms pressures for closed-loop control of individual fuel nozzles for an array of controller phases. Phase-optimized reductions in combustor rms pressure of approximately 40% (3 dB) were typical for closed-loop control of fuel Nozzle 1 or 2. It is possible that the discrepancy between the behavior of Nozzle 3 compared to Nozzles 1 and 2 was attributable to a maldistribution of air between the nozzles. This was likely caused by the artificial walls of the sector restricting the airflow to a tangential air inlet of Nozzle 3. Previous experience with this combustor indicated that Nozzle 3 operated at a slightly higher local equivalence ratio than the other two nozzles due to this effect.

Fig. 7 Effect of single-nozzle open-loop forcing at 100 Hz on combustor pressure spectrum
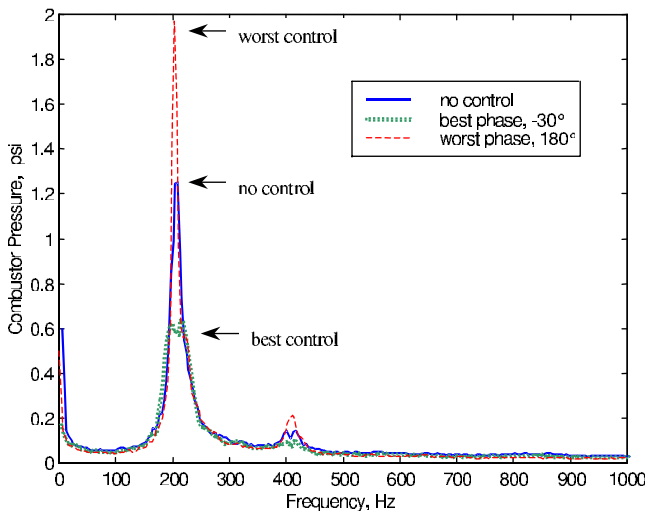
Fig. 9 Combustor pressure power spectra illustrating the ability of the control system to both amplify and attenuate the pressure oscillations (single-nozzle actuation)
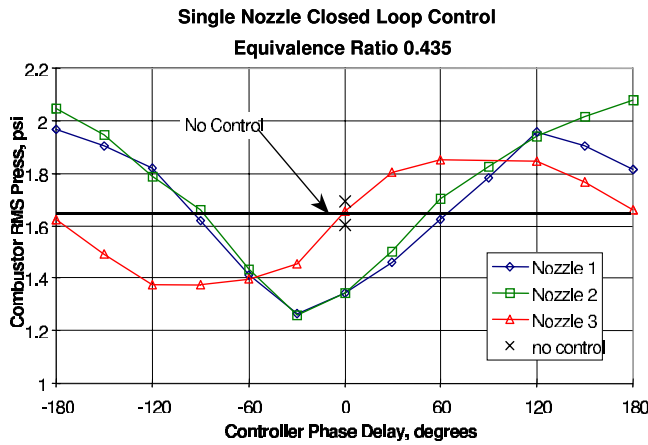
Fig. 10 Effect of controller phase on combustor pressure fluctuation levels for single-nozzle actuation

Fig. 12 Bode plot of combustor pressure over valve command signal, no control, equivalence ratio of 0.44

Speculating that the effectiveness of the controller could be increased with additional actuator authority, produced by actuating more nozzles, the control algorithm was tested using multiple simultaneously actuated fuel nozzles. Figure 11 shows the PSD plots for phase-optimized (minimum pressure oscillations) single, dual, and triple closed-loop controlled fuel nozzles. Combustor pressure oscillations were reduced by going from single to dual nozzle actuation, but no further reduction was obtained by actuating all three fuel nozzles, in spite of the open-loop forcing results. The best control was achieved with dual nozzle actuation, yielding a 6.5 dB (2.1 times or 53%) reduction in the bulk mode pressures and a 25% reduction in broadband rms pressure. These reductions in combustor pressure oscillations via active control were accompanied with no penalties to emissions compared to uncontrolled operation. The magnitude of the reduction was limited by the "splitting" of the spectral peak into two smaller peaks. This splitting behavior was evident for both two- and three-nozzle actuations, but the amplitude of the secondary peaks was larger for the three-nozzle case.

Interpretation of the Closed-Loop Results

A model-based explanation of the peak-splitting phenomenon observed during closed-loop control in the sector rig is provided

Fig. 11 Multiple-nozzle, closed-loop actuation led to relatively small incremental reductions in pressure fluctuation levels, due to "peak-splitting" phenomenon

in this section. Pressure oscillations in a combustor dominated by a narrow frequency band can be interpreted using a limit-cycling model or a stable, noise-driven model. Most references attribute pressure oscillations in combustor to self-excitation of coupled acoustics and heat release system resulting in a limit-cycling behavior. However, it will be shown that the uncontrolled sector rig combustor behavior and the splitting of the bulk mode peak observed during controlled operation of the sector combustor can be better explained using a model of the combustor as a lightly damped, linearly stable system driven by noise attributed to turbulence. Note that there are important differences between behavior observed in small laboratory combustion control experiments and full-scale industrial combustors. Laboratory combustors have typically no liner, and thus have lower damping than industrial combustors. At the same time, laboratory combustors may have lower turbulence levels than larger, more complex devices. With low damping and low noise levels, it is likely that significant pressure oscillations will *only* occur due to self-excited limit-cycle oscillations [6]. Industrial combustors can exhibit noticeable pressure oscillations in a stable, noise-driven regime and hence a self-excited model is, in many cases, not necessary. In this sense, the term "combustion instability" is less appropriate for this investigation, as it will use a stable model of sector rig and add driving broadband stochastic disturbance to account for the observed pressure oscillations. Of course, in a very lean condition, a self-excited model of pressure oscillations in industrial combustors will be more appropriate than a stable-driven model [1,7].

Experimentally determined frequency responses of the combustor pressure to the valve actuation voltage (Fig. 12) closely resembled linear systems with delay. A second-order model with delay was used to fit these dynamics with good agreement in the frequency range of 150–400 Hz. In principle, these empirical fits are necessary but not sufficient to conclude that the combustor dynamics were, in fact, linearly stable (as opposed to perhaps limit-cycling behavior), as a limit-cycling system may produce a frequency response resembling that of a stable-driven system. However, there are several additional arguments that a stable-driven system is indeed a good model of the observed behavior. First, the uncontrolled pressure PSD can be closely matched using a noise-driven stable model. Second, Fig. 13 shows that the probability distribution of pressure from experiments is very well approximated by Gaussian distribution, which is a typical distribu-
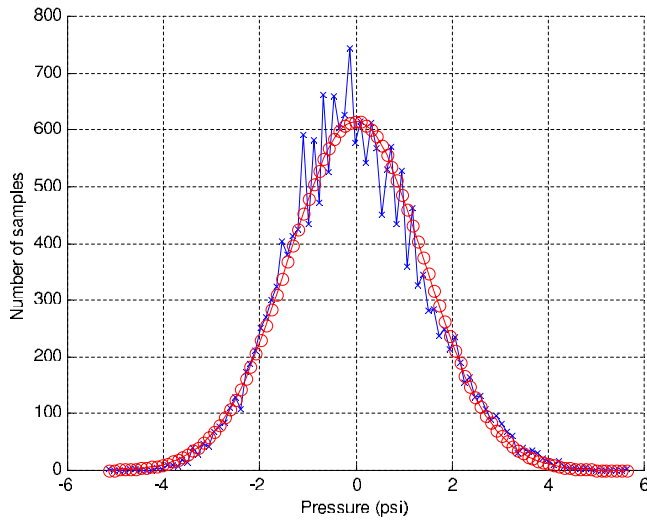
Fig. 13 Distribution of 20,000 samples of uncontrolled un-steady combustor pressure (x) and a fit with a Gaussian distribution (○)

Fig. 15 Second-order model of combustor with delay reproduces peak-splitting phenomenon (Fig. 11) in closed-loop simulation

tion of an output of a linear system driven by Gaussian input. A noise-driven limit-cycling system would show a double-hump distribution [8,9] of pressure. Last, it will be shown that the stable-driven model reproduces the peak-splitting effect of the controller in simulations with encouraging fidelity to data.

The transfer function of combustor pressure to valve command voltage was measured via open-loop swept-sine tests actuating one of the three nozzles. The first step in fitting a measured transfer function was to identify the time delay from the slope of the phase in the frequency range of 220–260 Hz. Next, the phase lag due to delay was subtracted from the experimental phase lag yielding a nearly classical second-order response with the phase dropping 180 deg through the magnitude response peak. A stable second-order transfer function with 2 poles and 1 zero was fitted numerically.

A schematic of the closed-loop simulation block diagram is shown in Fig. 14. The plant $G_0(j\omega)$ is the empirical second order system with delay representing the combustor dynamics. With the controller off, the standard deviation of the white Gaussian noise was adjusted in the simulation to match the PSD of the pressure data from experiment. A likely physical source of the driving disturbance is the turbulent flow fluctuations driving the acoustic mode directly or through the heat release process.

The effect of multiple nozzles was simulated by linearly scaling the controller output by the number of nozzles, which was consistent with experimental open-loop forcing results.

Figure 15 shows that the simulation exhibited a peak-splitting phenomenon similar to those observed in the experiments. The amplitude at the dominant oscillation frequency was attenuated while the secondary peaks were amplified by adding more nozzles and therefore more authority. The simulation showed symmetric splitting because the three on-off valves were modeled as one on-off valve with variable "on" level, denoted by b on Fig. 14. The slight asymmetry of peaks after the third valve was turned on in experiment can be attributed to a different phase lag of the third valve relative to the first two.

Even though a linear, stable system driven by white Gaussian disturbance was a good model of the sector combustor during the experiments, using on-off valves for control made the closed-loop system strongly nonlinear. Thus, an analysis of peak splitting using linear control theory tools [6] may not seem immediately relevant. However, it has been argued by Banaszuk et al. [10] that a quasilinear analysis using random-input describing functions is appropriate to study the nonlinear dynamics of the combustion model with on/off valves in the presence of large-amplitude noise (Fig. 16), as is the case with this closed-loop model. In this technique, the signals in the model were approximated as sums of constant, sinusoidal, and random components with Gaussian distribution. The static nonlinear elements were replaced with equivalent gains called random-input describing functions. The values of constant components, amplitudes and frequencies of sinusoidal components, and standard deviations of Gaussian components in the system can be found by solving system of nonlinear equations.

Fig. 14 Schematic of closed-loop combustor simulation block diagram
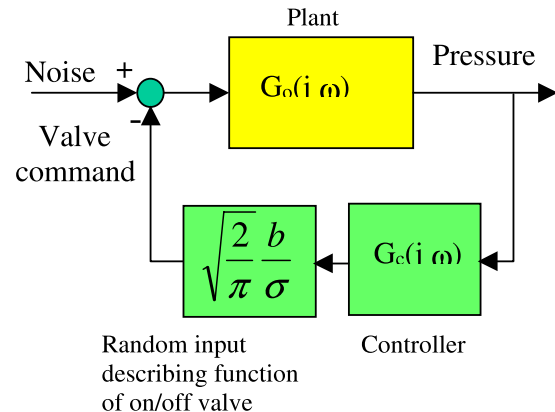
Fig. 16 Model of the closed-loop combustor with the on-off valve characteristic simulated with its random-input describing function
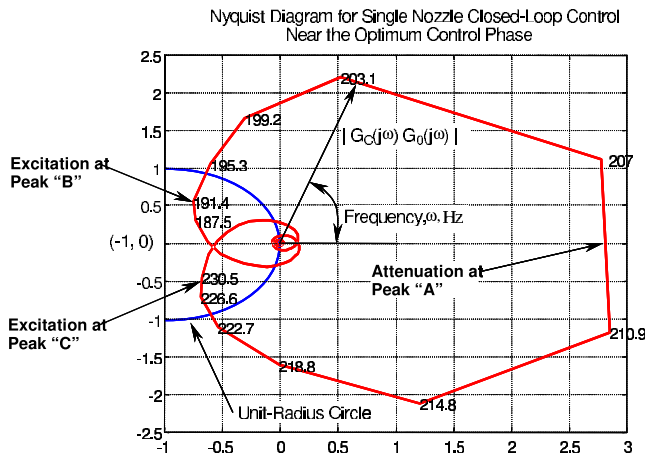
Fig. 17 Nyquist diagram for single-nozzle closed-loop control near the optimum control phase, showing that the controller excited secondary peaks ("B" and "C") and attenuated the primary peak ("A")

It can be shown that the system of Fig. 14 with the identified standard deviation of Gaussian input has low effective gain of the on-off valve for the sinusoidal signal so that a limit cycle oscillation cannot be sustained. Therefore, only the balance of Gaussian processes in the loop has to be carried out to approximately "predict" the PSD of the combustor pressure under closed-loop control. The random-input describing function for the on-off valve with "on" level denoted by b is

$$N(\sigma) = \sqrt{\frac{2}{\pi}} \frac{b}{\sigma}$$

where σ is the standard deviation of the Gaussian process at the input of the valve. One can show that, given the noise input PSD $\Phi_{ii}(j\omega)$, σ can be found from the Gaussian process balance equation

$$\sigma = \sqrt{\frac{1}{2\pi} \int_{-\infty}^{\infty} \left| \frac{G_0(j\omega)G_c(j\omega)}{1 + \sqrt{\frac{2}{\pi}} \frac{b}{\sigma} G_0(j\omega)G_c(j\omega)} \right|^2 \Phi_{ii}(j\omega) d\omega}$$

which can be solved numerically. Once the value of σ is known, the pressure PSD $\Phi_{pp}(j\omega)$ can be obtained from the formula

$$\Phi_{pp}(j\omega) = |G_0(j\omega)/(1 + G_0(j\omega)G_C(j\omega)N(\sigma))|^2 \Phi_{ii}(j\omega)$$

The closed-loop transfer from noise to pressure is $G_0(j\omega)/(1 + G_0(j\omega)G_C(j\omega)N(\sigma))$, indicating the following:

- For $|1 + G_0(j\omega)G_C(j\omega)N(\sigma)| < 1$, the pressure oscillations are amplified by the controller.
- For $|1 + G_0(j\omega)G_C(j\omega)N(\sigma)| > 1$, the pressure oscillations are attenuated by the controller.

Figure 17 shows the Nyquist plot of $|G_0(j\omega)G_C(j\omega)N(\sigma)|$ in the complex plane for the value of b corresponding to three valves. (For this plot $G_0(j\omega)G_C(j\omega)$ and σ were obtained from model simulation rather than calculation, the main reason being that the controller $G_C(j\omega)$ used in the experiments and in the simulation was a nonlinear phase-shifting controller based on a frequency-tracking extended Kalman filter, which does not have a simple linear transfer function, even though for a fixed central frequency of oscillations, it can be closely approximated by a linear transfer function.)

We see that the controller can either amplify or attenuate pressure oscillations at certain frequency bands. The two nearly symmetric branches of the Nyquist plot that cross into the unit-radius

circle, centered at $(-1, 0)$, for frequencies greater than 225 Hz and less than 195 Hz were the root causes of the secondary peaks. While adding more nozzles and therefore more actuator authority increased the control gain in the attenuation band, it also increased the control gain in the excitation band as well, imposing a limit on the phase-shifting controller's effectiveness. Note, however, that increasing the number of actuated nozzles does not correspond to proportional gain increase, as the standard deviation σ of the Gaussian process at the input of the valve is a function of b.

The large delay in the sector combustor made broadband attenuation of pressure oscillations difficult. Because of the large delay between the valve command signal and pressure pulsations, the plant phase changed rapidly over a relatively wide range of frequencies near the resonant frequency where the plant had considerable gain and where the phase and gain of the controller were approximately flat. Therefore, the Nyquist plot of $|G_0(j\omega)G_C(j\omega)N(\sigma)|$ entered the unit circle centered at $(-1, 0)$ for the frequencies on both sides of the attenuation band. The quickly rolling plant phase due to the large plant delay resulted in positive feedback control on both sides of an attenuation band centered at the resonant frequency, yielding an apparent splitting of the dominant oscillation mode.

Similar peak-splitting phenomena were observed in combustion experiments by Langhorne et al. [11] Fleifil et al. [12] Saunders et al. [6], and others. Langhorne et al. [11] used on-off valves in the reported experiments. They noticed a large delay in the plant. They used sinusoidal input describing functions to replace the on-off valves and interpreted the effect of control as reduction of a magnitude of a limit cycle. However, the analysis always predicted a system in a limit cycle and did not allow for an explanation of peak splitting. The missing element in the analysis was the effect of driving noise essentially linearizing the valves and stabilizing the limit cycles. Fleifil et al. [12] attributed secondary peaks to destabilization of the flame dynamics. Saunders et al. [6] dealt with limit-cycling model of combustion instability in an academic rig controlled with acoustic drivers. After the limit cycle was stabilized, the secondary peaks were observed. As in the present paper, the secondary peaks were attributed by Saunders et al. [6] to the controller destabilizing the sidebands. However, no model matching results of experiment was presented.

Experiments of Seume et al. [7] and Cohen et al. [1] with active control of combustion instability did not show peak-splitting phenomenon. This could be attributed to the fact that in the above mentioned experiments either the delay was lower (pilot fuel modulation rather than the main fuel modulation in experiments of Seume et al. [7], shorter fuel lines in experiments of Cohen et al. [1] or damping of the plant was low (lean conditions in experiments of Seume et al. [7], no acoustic liner in experiments of Cohen et al. [1], so that the plant gain was low in the sidebands where feedback was positive. We believe that in both cases, a self-excited mechanism was dominant and a stable, noise-driven model would not be appropriate. Banaszuk et al. [10] provide some analysis on the effect of delay and plant damping on peak splitting.

The contribution of the present paper to explanation of peak splitting is as follows. The role of combustion delay associated with using the main fuel system for control of lean premix combustion was explained. The importance of taking into account the turbulence-induced noise has been indicated. For the first time, a simple model closely reproducing the peak splitting observed in experiment has been provided. Lastly, it was shown why quasilinear approaches like random-input describing function methods are valid approximate analysis tools for nonlinear combustion models including Gaussian disturbance.

Summary

Active control of pressure oscillations was demonstrated on a three-nozzle sector combustor, using engine hardware. The control system was scaled up from a previous system designed for use

in a single-nozzle combustor. This system used solenoid valve actuators to modulate a portion of the fuel delivered to each of the premixing fuel nozzles. A phase-shifting control algorithm, using a frequency-tracking observer to identify and track the pressure oscillations, acted on the sensed combustor pressure fluctuations.

Testing of the uncontrolled combustor demonstrated that the dominant oscillations occurred at a frequency of approximately 200 Hz, dependent on the operating conditions.

Open-loop forcing tests illustrated that coordination of the three different actuation systems was insensitive to the relative phasing between the systems over a broad range of phase differences. Overall actuation authority increased linearly with the number of fuel nozzles actuated.

Demonstration of the closed-loop control system showed that reductions of 6.5 dB were possible using dual-nozzle actuation. The combustor emissions did not change relative to uncontrolled operation. Although the open-loop forcing tests demonstrated that overall actuator authority increased linearly with the number of fuel nozzles actuated, closed-loop control tests showed that the *incremental* reductions in combustor pressure oscillations diminished with the number of fuel nozzles actuated. This was a direct result of the controller "splitting" the dominant spectral peak, a fundamental limitation of phase shifting controllers in systems with large delays. The peak-splitting phenomenon could be reproduced in simulation using an empirical second-order system with delay representing combustor dynamics driven by noise.

Acknowledgment

References

[1] Cohen, J. M., Rey, N. M., Jacobson, C. A., and Anderson, T. J., 1998, "Active Control of Combustion Instability in a Liquid-Fueled Low-NO_x Combustor," ASME Paper No. 98-GT-267.

[2] Snyder, T. S., Rosfjord, T. J., McVey, J. B., and Chiappetta, L. M., 1994, "Comparison of Liquid Fuel/Air Mixing and NO_x Emissions for a Tangential Entry Nozzle," ASME Paper No. 94-GT-283.

[3] John, R. R., and Summerfield, M., 1957, "Effect of Turbulence on Radiation Intensity from Propane Air Flames," Jet Propul., **27**, pp. 169–179.

[4] Samaniego, J.-M., Egolfopoulos, F. N., and Bowman, C. T., 1995, "CO2* Chemiluminescence in Premixed Flames," Combust. Sci. Technol., **109**, pp. 183–203.

[5] Gysling, D. L., Copeland, G. S., McCormick, D. C., and Proscia, W. M., 1998, "Combustion System Damping Augmentation With Helmholtz Resonators," ASME Paper No. 98-GT-268.

[6] Saunders, W. R., Vaudrey, M. A., Eisenhauer, B. A., Vandsburger, U., and Fannin, C. A., 1999, *37th AIAA Aerospace Sciences Meeting*, Reno, Jan., AIAA Paper No. 99-0717.

[7] Seume, J. R., Vortmeyer, N., Krause, W., Hermann, J., Hantschk, C.-C., Zangl, P., Gleis, S., Vortmeyer, D., and Orthmann, A., 1997, "Application of Active Combustion Instability Control to a Heavy Duty Gas Turbine," presented at the *ASME Asia '97 Congress and Exhibition*, Singapore, Oct., ASME Paper No. 97-AA-119.

[8] Banaszuk, A., Jacobson, C. A., Khibnik, A. I., and Mehta, P. G., 1999, "Linear and Nonlinear Analysis of Controlled Combustion Processes. Part II: Nonlinear Analysis," *Proceedings of Conference on Control Applications*, Hawaii, Aug.

[9] Lieuwen, T. C., and Zinn, B. T., 2000, "Investigation of Limit Cycle Oscillations in an Unstable Gas Turbine Combustor," *38th AIAA Aerospace Sciences Meeting*, Reno, Jan., AIAA Paper No. 2000-0707.

[10] Banaszuk, A., Jacobson, C. A., Khibnik, A. I., and Mehta, P. G., 1999, "Linear and Nonlinear Analysis of Controlled Combustion Processes. Part I: Linear Analysis," *Proceedings of Conference on Control Applications*, Hawaii, Aug.

[11] Langhorne, P. J., Dowling, A. P., and Hooper, N., 1988, "Practical Active Control System of Combustion Oscillations," J. Propul. Power, **6**, pp. 324–333.

[12] Fleifil, M., Annaswamy, A. M., Hathout, J. P., and Ghoniem, A. F., 1997, "The Origin of Secondary Peaks With Active Control of Thermoacoustic Instability," *Proceedings of the AIAA Joint Propulsion Conference*, Seattle.

Effects of Temperature and Particle Size on Deposition in Land Based Turbines

Jared M. Crosby

Scott Lewis

Jeffrey P. Bons

Department of Mechanical Engineering,
Brigham Young University,
Provo, UT 84602

Weiguo Ai

Thomas H. Fletcher

Department of Chemical Engineering,
Brigham Young University,
Provo, UT 84602

Four series of tests were performed in an accelerated deposition test facility to study the independent effects of particle size, gas temperature, and metal temperature on ash deposits from two candidate power turbine synfuels (coal and petcoke). The facility matches the gas temperature and velocity of modern first stage high pressure turbine vanes while accelerating the deposition process. Particle size was found to have a significant effect on capture efficiency with larger particles causing significant thermal barrier coating (TBC) spallation during a 4 h accelerated test. In the second series of tests, particle deposition rate was found to decrease with decreasing gas temperature. The threshold gas temperature for deposition was approximately 960°C. In the third and fourth test series, impingement cooling was applied to the back side of the target coupon to simulate internal vane cooling. Capture efficiency was reduced with increasing mass flow of coolant air; however, at low levels of cooling, the deposits attached more tenaciously to the TBC layer. Postexposure analyses of the third test series (scanning electron microscopy and X-ray spectroscopy) show decreasing TBC damage with increased cooling levels. [DOI: 10.1115/1.2903901]

Keywords: deposition, syngas, turbines

Introduction

The effects of solid particles ingested into gas turbines are a universal problem shared by both land based and aircraft turbines. Due to the large air flow that gas turbines require, these particles cannot economically be entirely eliminated from the inlet air flow even with the best filtration and cleanup systems. Internal particulate sources include combustion products of fossil fuels, eroded turbomachinery components, and secondary chemical reactions. External particulate sources vary widely depending on operating environment (marine, desert, and industrial) and level of filtration (aeroengine, remote power microturbine, or large industrial power plant). These contaminants are heated in the combustor and either follow the flow out of the engine or impact against the turbine blades, which results in erosion, corrosion, and deposition. Erosion and deposition are competing phenomena and depend on the phase of the particulate impacting the blade surfaces. While there are numerous secondary parameters influencing these processes, generally the particulate erodes the blades when it is below the softening temperature and adheres to the blades when above the softening temperature. This threshold temperature depends on the particulate type, but has been shown to occur between 980°C and 1150°C [1–5].

The primary factors affecting the extent of deposition on turbine blades include gas temperature, turbine surface temperature, net particle loading, particulate chemical composition, turbine blade exposure time, and geometric boundaries imposed on the flow. Previous turbine tests with coal-derived fuels by Wenglarz and Fox [4] show a dramatic increase in deposition rate as the gas temperature is raised above the particulate melting point. In their study, coated turbine superalloy specimens were subjected to 2–5 h of deposition from three coal-water fuel (CWF) formulations. The coal had been cleaned to simulate ash levels (~1%) that would be considered acceptable for use in a gas turbine. The

fuel was burned in a low-emission subscale turbine combustor at realistic flow rates (e.g., impact velocities ~180 m/s) and gas temperatures (1100°C). With the turbine specimens located at two different streamwise locations downstream of the combustor exit, the influence of gas temperature on deposition rate could be studied. It was noted that the upstream specimens (operating at gas temperatures ~1100°C) experienced one to two orders of magnitude higher deposition rates compared to the downstream specimens (operating at gas temperatures ~980°C). Compared to a previous series of tests with lower ash content (0.025%) residual fuel oil, the deposit levels with CWFs were two to three orders of magnitude larger for the same operating temperature. An aeroengine deposition study performed by Kim et al. with volcanic ash showed that the rate, at which deposition occurs, increases with time for a given turbine inlet temperature (TIT) and dust concentration, i.e., the vanes become better captors of material as the deposits on the vanes increase [5]. It was also found that once deposition begins, the mass of material deposited is proportional to dust concentration for a given TIT and dust exposure time.

Wenglarz and Fox [4] also explored the possibility of subcooling the upstream turbine specimens and found a factor of 2.5 reduction in deposits for a 200°C drop in metal surface temperature. Lower deposit formation in areas of reduced surface temperature was also noted by Bons et al. [6] in their study of serviced turbine hardware. Cooled turbine vanes, which exhibited large (1–2 mm thick) marine deposits over their entire surface, were noticeably free of deposits in the film cooling flow path where surface temperatures are significantly lower. This effect created substantial troughs or "furrows," which extended for more than ten hole diameters downstream of the cooling hole exit. These results confirm the important role of gas and surface temperature in determining deposition rates from ash-bearing fuels.

Due to current economic and political pressures, alternate fuels such as coal, petcoke, and biomass are being considered to produce substitute syngas fuels to replace natural gas in power turbines. Given the present volatility in natural gas markets and the uncertainty regarding projected fuel availability over the 20–30 year design lifetime of newly commissioned power plants, coal and petroleum derivative fuels are already being used at a

Copyright © 2008 by ASME
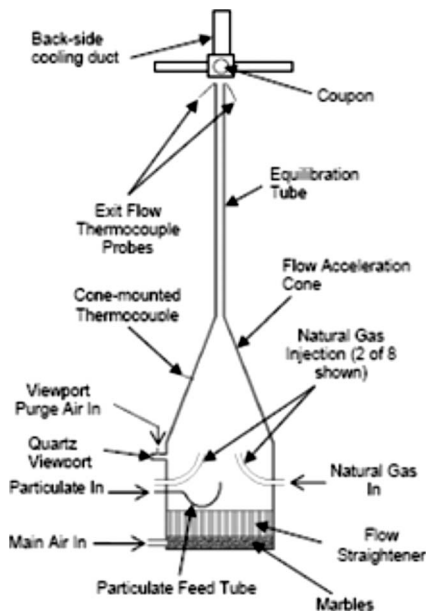
Fig. 1 BYU Turbine Accelerated Deposition Facility schematic

Fig. 2 Equilibration tube exit temperature profile for standard testing conditions ($M=0.25$ and $T=1183°C$)

handful of gas turbine power plants worldwide. In addition, intermediate goals of the DOE Future Gen and DOE Turbine Program focus on coal syngas as a turbine fuel in an effort to reduce dependency on foreign supplies of natural gas. Thus, the stage is set for broader integration of alternate fuels in gas turbine power plants. Studies of potential sources of deposition from these syngas fuels are necessary so that their adverse effects can be minimized. Deposition has numerous adverse results that can range from decreased engine performance to catastrophic failure of the blades. For monetary as well as safety reasons, it is highly desirable to reduce or eliminate these effects. In all but the most severe conditions, deposition is a relatively slow process and its study on an actual turbine is neither time nor cost efficient. To remedy this, an accelerated turbine facility has been developed, which simulates 8000 h of exposure time in a 4 h test. This is done by matching the net particle throughput mass at realistic combustor gas exit temperatures and velocities. The validation of this hypothesis was the subject of a previous paper by Jensen et al. [7]. Subsequently, this facility has been used to study alternate fuel deposition at constant operating conditions and the evolution of deposits with repeated exposure. The present study uses this facility to characterize the effects of deposition from coal- and petcoke-derived fuels on turbine blade materials as the particle size, gas temperature, and back side cooling level are varied independently.

Experimental Facility

Modifications. The Turbine Accelerated Deposition Facility (TADF) was originally built in 2004 (Fig. 1). Jensen et al. [7] described the facility in detail and provided validation of accelerated testing principles using airborne particulate. Its basic features include a partially premixed natural gas burning combustor capable of operating at an exit Mach number of 0.3 and an exit temperature of 1150°C, thus simulating the conditions at the entrance of a typical first stage nozzle guide vane for an F-class power generation turbine. One flow parameter that is not simulated is static pressure (deposition occurs at approximately atmospheric conditions). Jensen et al. cited a number of sources for facilities that also operate at lower pressures than an operating gas turbine engine and all concluded that particle temperature, concentration, and residence time are the critical parameters for proper simulation and not static pressure. A small fraction of the high pressure air is directed through a particle feed system, con-

sisting of a syringe driven by a frequency controlled motor, which can be adjusted to yield the desired feed rate. Particulate from the syringe is entrained into the flow and enters at the base of the combustor. The particulate is then heated in the combustor and brought to thermal and velocity equilibrium in the 1 m long equilibration tube before impacting on a circular turbine blade specimen held at a desired impingement angle within one jet diameter of the tube exit.
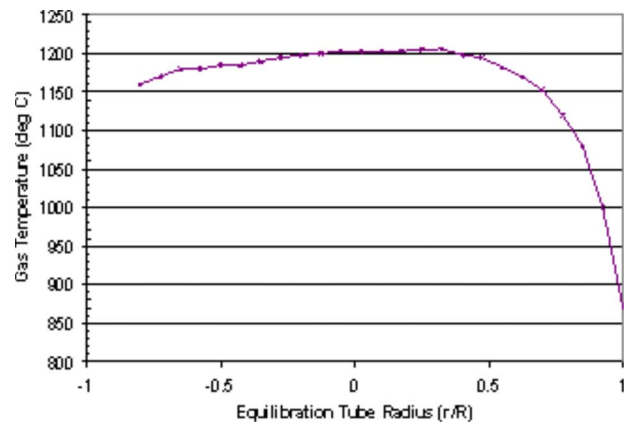
Since its design, the TADF has been used for numerous deposition studies involving airborne particulate, biomass, coal, and petcoke [7–10]. In all previous studies, the fixture used to hold the test sample produced a nearly isothermal profile through the target specimen thickness. Modern engines employ significant internal and film cooling schemes to help protect blade materials. In order to more closely model these conditions, modifications were made to the TADF. Minor modifications to the combustor included: increasing the equilibration tube diameter to 2.54 cm to allow for a more uniform temperature profile and increasing the number of flame holders from 4 to 8 to maintain flame stability. The increase in tube diameter resulted in a slight decrease in exit velocity with the Mach number reduced to 0.25 for the operating temperature of 1183°C. Primary air flow was measured with a choked flow orifice to an uncertainty of ±3%. Figure 2 shows the temperature profile at standard test operating conditions (gas exit temperature = 1183°C, Mach=0.25). The profile was measured by traversing a high temperature thermocouple probe across the lip of the tube exit. The thermocouple was not shielded and a radiation correction of 33°C at 1150°C was estimated using an emissivity of 0.5 for the oxidized Omegaclad™ probe surface. The thermocouple uncertainty was less than 15°C and the uncertainty in calculated Mach number was ±0.021.

The NASA Lewis chemical equilibrium code [11] was used to determine the composition of the combusted gas stream at 1183°C, based on the composition and flow rates of natural gas and air. For base condition in the TADF (1183°C, 0.0214 kg/s of inlet air, 0.000471 kg/s of inlet natural gas), the compositions of the combusted gas (in mol %) were 12.9% O_2, 3.8% CO_2, 7.2% steam, and the balance N_2.

A completely new specimen holder was designed to allow for impingement cooling (Fig. 3). Cool air is brought in through the center tube, impinges on the back side of the sample, and exits through the outer tube. The entire fixture is insulated with ceramic batting to minimize 3D heat transfer losses. When impingement cooling is used, the back side temperature of the sample is measured using two welded *K*-type thermocouples. Inlet and exit coolant temperatures are measured using *K*-type thermocouples as well. The sample's front side temperature is measured using a red-green-blue (RGB) camera through a technique described in the next section. A radiation shield helps vs minimize radiative
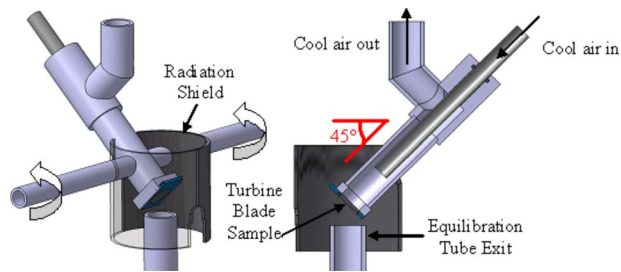
Fig. 3 Fixture designed to allow impingement cooling of turbine blade sample

Fig. 4 Measured front side and back side temperatures as a function of cooling

losses while also providing optical access through a cutout (Fig. 3) for the RGB camera as well as digital video recording. The specimen holder can be rotated to hold the turbine sample at any impingement angle. All the tests in this study were conducted at 45 deg, as shown in Fig. 3, since this is representative of the leading edge stagnation region of a first stage vane. This impingement angle was found to produce the maximum surface degradation in tests conducted by Jensen et al. over a range of angles from 30 deg to 90 deg [7].

Three sets of circular turbine blade samples, all approximately 2.54 cm in diameter, were obtained from multiple industry sources for this study. In order to respect proprietary concerns of the manufacturers, strict source anonymity has been maintained for all data presented in this publication. The samples are representative of a high performance turbine material system: A nickel based superalloy substrate approximately 0.3 cm thick was common to all three sets, an MCrAlY bond coating approximately 225 μm thick for the first set, 200 μm for the second, and 175 μm for the third, and an air plasma sprayed (APS) yttrium stabilized zirconium (YSZ) thermal barrier coating (TBC) layer approximately 0.45 mm thick for the first set, 0.40 mm for the second, and 0.17 mm for the third. The samples were polished to a centerline average roughness (Ra) value of $1–1.5$ μm.

Each of the three sets of coupons was used for a different test series, as will be explained in later sections; therefore, consistency for each test series was maintained. A small groove was machined around the circumference of each sample to allow it to be held in the cooling fixture with adequate sealing to contain the coolant. For all tests, pre- and post-test masses were measured as well as digital images taken. Uncertainty in the mass measurement is ± 5 mg. A Hommel T8000 profilometer was used for post-test measurements of the deposit surface roughness. Environmental scanning electron microscopy (ESEM) was employed as a post-test diagnostic to determine the extent of deposition and material system degradation. To prepare the samples for the ESEM, the samples were placed in epoxy, to preserve the deposit, cross sectioned, placed in Bakelite, and then polished.

During facility operation, the coupon front side surface temperature was measured with a Sony charge-coupled device (CCD) camera using a two-color technique based on previous work by Lu [12]. Figure 4 shows the variation in front side temperature as a function of coolant mass flow rate. The temperature uncertainty was estimated at $15.4\,^{\circ}$C. Back side temperatures from thermocouples welded to the back side of the coupon are also shown in the plot. The temperature difference between the front and back sides increases as the cooling flow rate increases, as expected, with temperature differences ranging from $200\,^{\circ}$C to $400\,^{\circ}$C. An additional front side temperature measurement was made with an IR thermometer. A surface emissivity of 0.2 was used to match the two-color temperature measurement for the lowest cooling rate. The IR temperature measurements seem to follow the average of the two-color measurements with this constant emissivity value. At the highest coolant flow rate indicated in the plot, the surface heat flux was estimated to be nearly 1000 kW/m^2 using a simple
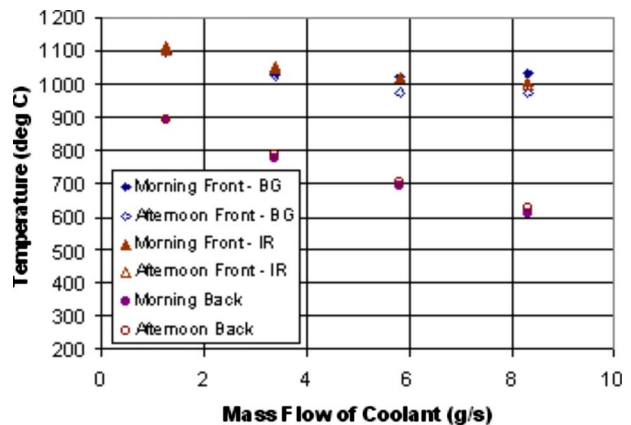
one-dimensional heat flow approximation—a value consistent with heat flux levels in modern first stage gas turbines.

Particulate Preparation. The coal and petcoke samples used in this study are the same as those described in Bons et al. [8], with the exception that the particle sizes have been substantially reduced. This was accomplished using a mechanical grinder with a collector to trap the particles exhausted out of the air filter. Subbituminous coal fly ash was obtained from an operating power plant, while the petcoke ash is boiler slag obtained from a combined cycle gas turbine power plant operating with a blend of 55% petcoke and 45% coal. The ash was characterized using an ESEM to perform X-ray spectroscopy, which can identify the elemental composition down to the atomic number of carbon. An independent elemental analysis was also conducted on the ash samples by ALS Chemex using inductively coupled plasma atomic emission spectroscopy (ICP-AES). The results were similar with only slight variation in the weight percentages of silicon, which were attributed to the ESEM measurements being spot measurements while the ICP-AES were bulk measurements.

To simulate ash that could be entrained by the flow leading to the turbine, the particles must be small enough to pass through the various gas cleanup systems. Filtration systems in modern gas turbine power plants are designed to remove all particles with diameters greater than 10 μm and a majority of particles larger than 1 μm. With inadequate or degraded filtration, these levels can be exceeded. This study focuses only on contamination from the fuel gas system. In addition to particles from the fuel stream, sand and dirt from the inlet air and rust from the gas turbine flow path can also form deposits resulting in spallation and TBC loss. This study is intended to supplement other studies performed by the authors, in which sand, biomass, and other synfuels have been used [7–10].

After grinding, the size of the ash samples was determined using the laser-based Coulter counter. The Coulter counter operates using a laser beam to illuminate the particles contained in a water slurry, which scatter light according to their size. Photodetectors convert the scattered light to particle size distributions. A more detailed explanation of the Coulter counter is given in Bons et al. [8]. Table 1 shows the particle size and elemental composition of the particulate used in the majority of the tests conducted in this study. The bulk density of each ash sample was measured in a graduated cylinder, and the apparent density (mass per particle exterior volume) was calculated using an estimated packing factor of 0.5.

Results and Discussion

Particle Size Series. Three series of tests were conducted to study the effects of particle size, gas exit temperature, and metal

Table 1   Ash particle summary statistics: size, density, and average elemental composition

	Coal	Petcoke
Mass mean diameter (μm)	3.1–16	6.3
Bulk density (g/cm^3)	0.99	1.45
Apparent density (g/cm^3)	1.98	2.90
Element	wt %	wt %
Na	6.9	4.3
Mg	3.6	2.2
Al	17.8	14.5
Si	47.4	38.3
P	1.6	0.0
S	1.8	1.0
K	2.6	2.5
Ca	8.7	7.5
Ti	1.6	0.8
V	0.0	3.4
Fe	6.4	22.9
Ni	0.0	0.9

Fig. 5   Coal particle size distribution for four sizes tested

temperature on deposition. The first test series looked at the effects of particle size on deposition. For the case of erosion, Hamed et al. [13] calculated the trajectories of various sizes of particles (10–50 μm) in a modern low pressure turbine (LPT) stage using a semiempirical particle rebound model. They found that larger particles actually have multiple rebounds between neighboring blades while smaller particles primarily impact the pressure surface only. To explore the effect of particle size on deposition, the present study used standard combustor operating conditions (gas exit temperature=1183°C, Mach=0.25) with the first set of 1 in. diameter turbine samples. The tests were run with no cooling air and the interior passage of the cooling fixture was insulated with blanket insulation material. The back side temperature was measured with two welded K-type thermocouples and found to be approximately 990°C, which is roughly 200°C below the combustor exit temperature.

Recently, Wammack et al. [9] conducted a deposition study using polished TBC turbine samples where the specimens were subjected to four consecutive testing cycles, returning the sample to room temperature between each test. They measured a significant increase in TBC surface roughness following the first thermal cycling. As a result, this roughened surface was much more susceptible to deposit accumulation compared to the highly polished surface prior to the first test cycle. To account for this effect in the current test series, an initial 1 h "burn-in" test was conducted with particulate injection, following which the combustor was shut down. The sample was allowed to cool without removing it from the fixture. Following this, the combustor was again brought to steady state and a standard 4 h test was conducted. Coal ash particulate was used in this test series, with four different sizes, each obtained from different locations in the mechanical grinder. The four particle size distributions (shown in Fig. 5) were obtained using the Coulter counter. The data shown in the figure are in wt %, so in all samples there are a majority of particles (by number) in the range below the mass mean diameter. ESEM images of the largest and smallest samples show a representative distribution of particle sizes (Fig. 6).

Using the pre-test and post-test mass measurements, the net specimen mass gain during exposure was assessed (Table 2). In some cases, the deposit was very fragile and much of it flaked off following the test as it cooled. The separated deposit percentage, defined as the amount of deposit that separated after the test ended divided by the net specimen mass gain, is also shown in the table. Percentages greater than 100% are indicative of significant spallation of the TBC layer where the mass of the separated deposit (plus TBC) weighed more than the net specimen mass gain. The
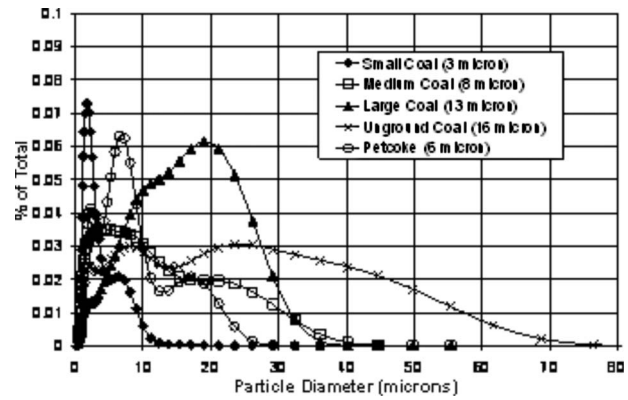
increasing percentage of separated deposit with increasing particle size indicates that TBC is more prone to spall with larger deposit formations.

Figure 7 shows two post-test images of the 13 μm particle test coupon. The first image was taken immediately after combustor shutdown while the second image was taken after the sample had cooled to room temperature. Streamwise aligned deposit structures are evident in the hot deposit image (Fig. 7(a)). These structures are similar to fuel deposit structures previously measured on a serviced turbine blade pressure surface by Bons et al. [6] (Fig.
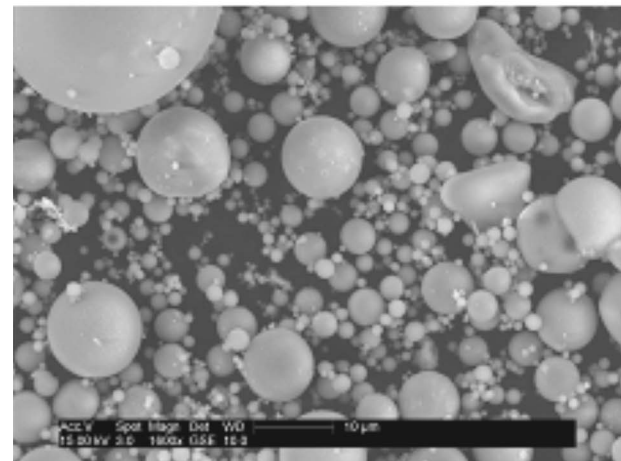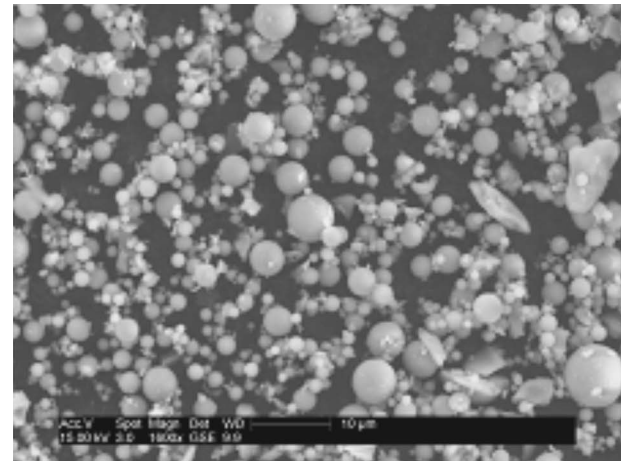
Fig. 6   ESEM images of smallest (top) and largest (bottom) size coal particles

Table 2   Deposition results from particle size test series

Particle size (μm)	Preburn button mass (g)	Button mass change (mg)	Separated deposit mass (mg)	Separated deposit (%)	Net deposit mass (mg)	Deposition rate (mg/cm²h)	Net particulate mass added to flow (mg)	Net capture efficiency (%)
3	14.73	70	300	81	370	14.6	10,050	3.68
8	14.88	60	450	88	510	20.13	10,350	4.93
13	14.12	−10	880	101	870	34.34	12,720	6.84
16	14.99	−140	1220	113	1080	42.63	13,390	8.07

8). The deposits in Fig. 8 were considerably more tenacious than the accelerated coal deposits in this case, since they were still intact on the blade surface after cooldown. With rapid cooling, the mismatch in thermal expansion coefficients between the metal, the TBC, and the deposit results in the removal of most of the deposit with some of the TBC as well. TBC spallation is evident primarily along the leading edge of the circular specimen (Fig. 7(*b*)), even though the deposit thickness is approximately uniform over the entire coupon (Fig. 7(*a*)). Wammack et al. observed similar behavior in their deposition tests and attributed this to the impingement of deposit-laden gas at the exposed metal/TBC interface [8]. Thus, material system degradation (e.g., TBC spallation) was always most significant at the leading edge of the turbine specimen. In a gas turbine, similarly exposed TBC/metal interfaces are evident at each of the film cooling holes in the stagnation region of the blade. This explains the common occurrence of TBC spallation adjacent to stagnation film holes as described by Bons et al. [6]. The extent of spallation and material system degradation will be discussed further using ESEM images.

Dividing the net deposit mass by the exposed coupon surface area and the test duration yielded deposition rate measurements from 14 mg/cm²h to 43 mg/cm²h for the smallest and largest size particles (Table 2). Figure 9 shows the effect of particle size on net capture efficiency (mg/h of deposit divided by mg/h of

particulate added to the flow). Capture efficiency increases asymptotically with particle size with a more than 50% increase from 3 μm to 16 μm. These results suggest that with filter degradation, deposition problems as well as turbine hardware damage are likely to increase considerably. Additionally, it is important to note that even the smallest size particles tested showed significant deposition. This would indicate that even with properly functioning filtration systems, the problems associated with deposition and spallation cannot be entirely eliminated. These deposition rates are lower than previous measurements in the same facility reported by Bons et al. (70–140 mg/cm²h) and those reported by Wenglarz and Fox (200–400 mg/cm²h) [7,4]. This may be due to the lower particulate loadings used in the present study compared to Bons et al. [8] (less than 100 ppmw h versus 150–600 ppmw h, respectively).

Despite the larger particle size and increased capture efficiency, roughness measurements of the deposit surface did not show a significant trend with particle size. Four 15 mm long profilometer traces were made on each coupon following the combustor shutdown. Loose deposits that flaked off during cooldown were not evaluated for this assessment. Roughness statistics taken from these four residual deposit measurements were averaged to yield typical values for each coupon. While the residual deposit surfaces were considerably more rough (Ra$\cong$7 μm and Rt $\cong$50 μm) than the pre-test coupon surface (Ra$\cong$1 μm), average roughness values for the 3 μm and 16 μm particles were approximately the same.

Gas Temperature Series. The second test series was performed using coal ash with a mass mean diameter (MMD) of 3 μm with no cooling air and the interior of the coolant passage still insulated. Six tests were performed at five different gas exit temperatures using the second set of samples. Two of the tests were performed at a gas exit temperature of 1183°C, which is typical in many modern first stage gas turbine engines while the other tests were at lower temperatures. All of the tests experienced a nominal particulate loading of 96 ± 12 ppmw h. This loading is intended to simulate an engine operating for one year (8000 h) at a low particulate concentration of 0.01 ppmw. This standardization of ppmw h has been used previously [7–9] to simulate long
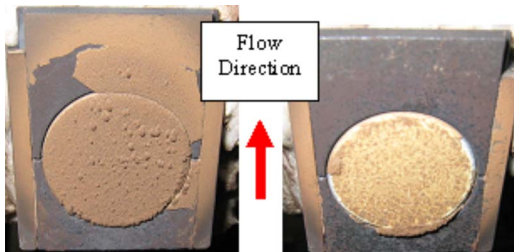
Fig. 7   Post-test images of coupon subjected to 13 μm particle size
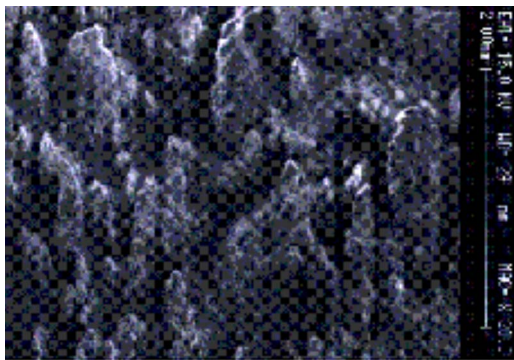
Fig. 8   Micrograph image taken of turbine blade pressure surface deposits (flow direction is bottom to top)
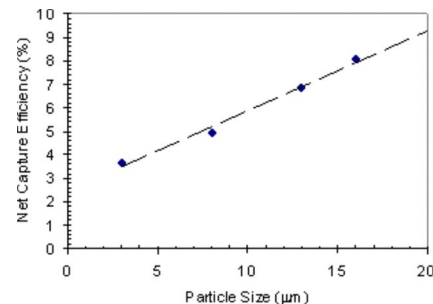
Fig. 9   Effect of particle size on net capture efficiency

Table 3 Deposition results from gas temperature test series

Gas temperature (°C)	Preburn button mass (g)	Button mass change (mg)	Separated deposit mass (mg)	Separated deposit (%)	Net deposit mass (mg)	Deposition rate (mg/cm² h)	Net particulate Mass (mg)	Net capture efficiency (%)
1183	13.66	40	100	71	140	6.91	7880	1.78
1183	13.66	40	110	73	150	7.4	8220	1.82
1074	13.64	60	0	0	60	2.96	7590	0.79
1020	13.64	30	0	0	30	1.48	7820	0.38
966	13.69	10	0	0	10	0.49	7360	0.14
860	13.62	0	0	0	0	0	7860	0

duration turbine operation. A similar metric was used by Caguiat [14], in which accelerated compressor fouling caused by salt water ingestion was studied. By using this metric, the results can be interpreted to a wide range of applications. Airflow was adjusted to maintain an exit velocity of 170 m/s for each test, which at the gas temperatures tested yielded Mach numbers ranging from 0.23 to 0.26. Since the mode of deposition for particles on the order of 3 μm is inertial impaction, this constant jet velocity condition maintains the same kinetic energy at particle impact. Accordingly, the only relevant variable in this test series is the particle temperature, which was calculated to be in thermal equilibrium with the gas at the exit of the 1 m long equilibration tube. Once the facility reached steady state, particle seeding commenced and lasted for 4 h, after which the facility was immediately shut down. The initial 1 h burn-in test was not performed for this test series.

Deposits were very similar to the 3 μm test from the particle size series. The same flaking was observed for the tests run at 1183°C, but very little flaking was noticed at lower temperatures. Deposition results are summarized in Table 3. Repeated tests were run at an exit temperature of 1183°C to show the repeatability of the facility. The deposition rate decreased by approximately 58% with the first 100°C drop in gas temperature. This was followed by another 50% decrease with an additional 50°C drop. An additional 50°C drop in gas temperature to 966°C resulted in a 67% decrease in deposition rate. At 860°C, no deposit formed indicating a gas temperature threshold for deposition around 960°C for this study. This compares well with studies performed previously by Wenglarz and Fox using coal-derived fuel, Kim et al. using volcanic ash, and Jensen et al. using airborne dust. Since these gas temperatures are all lower than the melting temperature of the ash compounds, the rising deposition rate with gas temperature is likely due to the increased tendency for deposit sintering at elevated temperatures. Sintering creates large deposit masses that are less susceptible to removal by erosion from subsequent particle impacts. Figure 10 shows the corresponding decrease in net capture efficiency with gas temperature. It is noted that the capture efficiency at 1183°C in Fig. 10 is approximately 50% of that shown in Fig. 9 for the same 3 μm particle size. This is due to the effect of the burn-in, which was not performed for this test series.
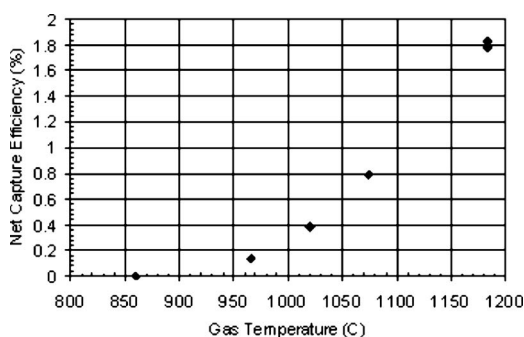
Figures 11(a)–11(c) show digital images of specimens at 1183°C, 1074°C, and 966°C. Note the large amount of separated deposit for the high temperature case and the lack of substantial deposits at low temperature (though the coupon is still discolored at the lower edge near jet impact). Based on the trend in Fig. 10, we would expect deposition rates to increase for G- and H-class engines, which operate above 1500°C. However, some of the constituents may be in a vapor phase at these temperatures so the degree to which deposition would increase might not be exponential, as indicated in Fig. 10. The authors are unaware of any deposition tests in the open literature that operate at higher temperatures than those in this study.

A similar trend with gas temperature is noted in the deposit roughness measurements shown in Fig. 12. All three statistical roughness metrics (centerline average [Ra], average peak height [Rz], and peak height [Rt]) increase as gas temperature is increased above the deposition threshold temperature of 960°C. It should be noted that due to extensive deposit flaking at 1183°C, the roughness measurement shown in Fig. 12 is actually taken from a separated flake of deposit rather than from the residual deposit on the coupon surface.

The strong dependency of deposition rate on gas (and particle) temperature has important implications for modern turbine blade rows where the gas temperature can drop by 150–250°C per stage. If the turbine inlet temperature is high enough so that particles are molten or sinter readily, they may collect primarily near the leading edge—since with falling temperatures through the
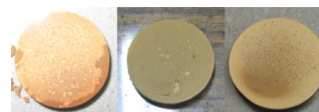
Fig. 11 Digital images of postburn coupons at (from left to right) 1183°C, 1074°C, and 966°C

Fig. 10 Effect of gas temperature on net capture efficiency
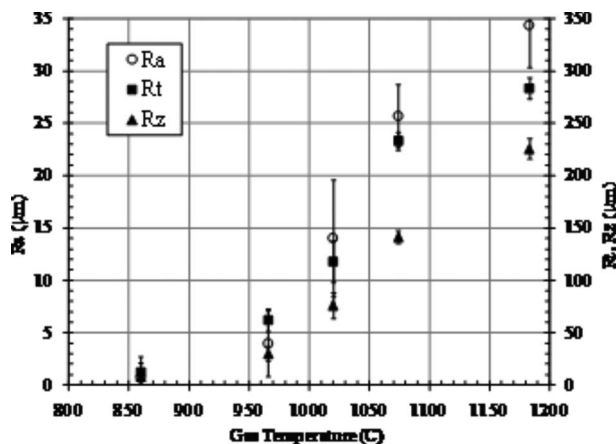
Fig. 12 Effect of gas temperature on deposit roughness

Table 4 Deposition results from impingement cooling test series using coal

Mass flow of coolant (g/s)	Heat flux (kW/m²)	Preburn button mass (g)	Button mass change (mg)	Separated deposit mass (mg)	Separated deposit (%)	Net deposit mass (mg)	Deposition rate (mg/cm² h)	Net particulate mass (mg)	Net capture efficiency (%)
0	0	14.73	70	300	81	370	14.6	10050	3.68
1.26	500.68	30.56	130	90	41	220	8.68	8480	2.59
3.38	1049.21	30.69	120	20	14	140	5.53	9270	1.51
5.81	1404.35	30.53	100	0	0	100	3.95	8120	1.23
8.33	1614.26	30.93	0	0	0	0	0	9540	0

vane passage, sintering may no longer be possible. If, however, the gas temperature at the vane inlet is so high that corrosive elements are in the vapor phase, then they may not deposit on the vane. Rather, they may wait until the temperature drops and then begin to condense on the surface—perhaps in the subsequent blade row. Another factor affecting deposit buildup is of course the flow angle relative to the local surface. The flow is directly impinging at the leading edge, whereas it is mostly parallel to the wall at midspan.

Impingement Cooling Series. The third test series was performed to study the effects of impingement cooling on deposition. The insulation was removed from the interior of the cooling fixture and two K-type thermocouples were welded to the back side of each sample to measure the back side temperature. This test series used the same set of samples as in the particle size series. The RGB camera was used to measure the sample front side temperature and two K-type thermocouples were used to measure the incoming and outgoing coolant temperatures. Four tests were run at varying mass flows of coolant. The same coal ash was used as in the gas temperature series (3 μm diameter) and the standard combustor operating conditions, as used in the particle size series, were used including the initial 1 h burn-in test. All of the tests experienced a nominal particulate loading of 110 ± 7 ppmw h, only slightly higher than the gas temperature series due to the additional 1 h burn-in test.

The deposits formed in this test series were much more tenacious than the previous ones. Appreciable deposit flaking was only observed for the 1.26 g/s cooling case and it was minimal. This result is consistent with the behavior of the gas temperature series, in which the lower gas temperatures showed a more tenacious deposit. The applied coolant lowers the temperature of the TBC surface producing a thinner deposit layer. Thin deposit layers are not as susceptible to flaking induced by thermal contraction during cooldown. Table 4 provides a summary of the deposition results. The deposition rate was reduced by approximately 40% with the initial level of cooling. This was followed by further reductions as the amount of cooling was increased. Corresponding
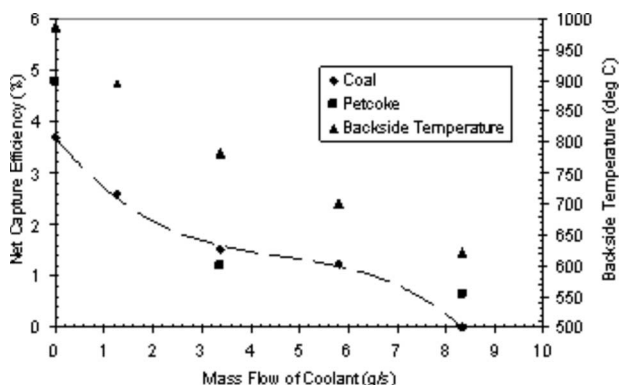
trends in net capture efficiency are shown in Fig. 13. For this series, spallation occurred, but was limited to very small portions of the edge at the base of the sample. The amount of visible spallation decreased slightly with increased coolant mass flow. The drop in capture efficiency noted in Fig. 13 is similar to the result of Wenglarz and Fox [4] who observed a factor of 2.5 reduction in deposits for a 200°C drop in metal surface temperature produced by subcooling. The present results show a factor of 4 reduction in deposits for a 360°C drop in back side temperature (100°C drop in front side temperature—see Fig. 4) with cooling. These results clearly show the benefits of cooling in reducing deposition. However, in G- and H-class engines, the amount of cooling needed to obtain the necessary drop in front side temperature could be prohibitive. These results also suggest that film cooling could provide an additional reduction in deposition and spallation. However, Bons et al. [6] noted that film cooling holes introduce exposed TBC/metal interfaces that are actually more prone to spallation.

To further assess the level of TBC degradation, the test articles from this test series were analyzed using the ESEM. The cross sectioned samples were first used to measure the thickness of deposit remaining on the surface (Fig. 14). Three images were taken of the cross sectioned sample: one at the bottom of the sample (closest to the combustor exit), one near the middle, and one at the top. Figure 15 shows a typical series of images taken from the 5.81 g/s cooling level sample.
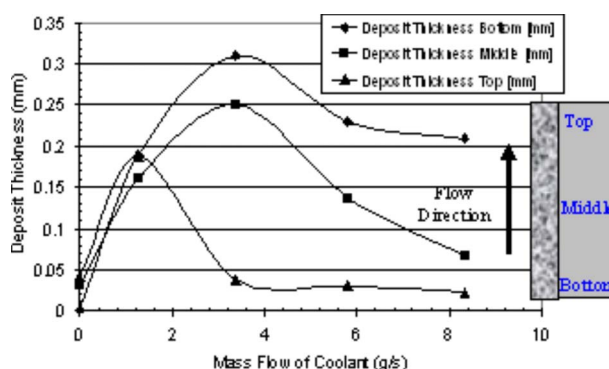
Fig. 14 Remaining deposit thickness versus cooling level
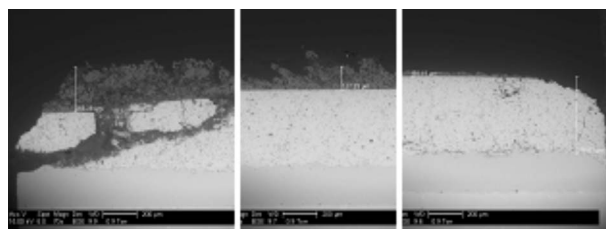
Fig. 15 Typical image series of bottom (left), middle, and top (right) portions of 5.81 g/s coolant test sample

Fig. 13 Effect of cooling on net capture efficiency
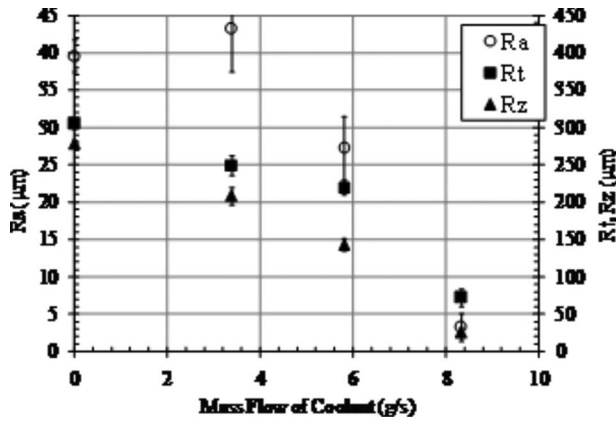
Fig. 16 Effect of cooling on deposit surface roughness

Fig. 17 Elemental comparison of ash, deposit, and penetration for coal impingement cooling series

As seen in Fig. 14, residual deposit thickness is fairly uniform for the no cooling and lowest level of cooling cases. This is indicative of the large percentage of separated deposit for these two cases as noted in Table 4. As the amount of cooling was increased to 3.3 g/s, the top deposit thickness dropped off considerably while the middle and bottom continued to increase because of the more tenacious deposit formation near the leading edge. Since the top of the coupon was furthest from the jet, it experienced the lower temperatures and thus less deposition. Further increases in the amount of coolant result in decreasing deposit thicknesses at all locations. This spatial variation in deposit thickness is similar to what occurs in an actual turbine with deposition buildup at the hottest spots near the leading edge [6]. Figure 15 shows the level of spallation, which occurred at the leading edge as a result of deposit penetration. Similar spallation was seen in the particle size test series. Wammack et al. [9] observed a similar deposit penetration effect although with a different TBC material system. With the exception of the highest cooling case, all other tests in this series had varying amounts of spallation damage caused by penetration of the deposit along the cross section.

Figure 16 contains the surface roughness data for the impingement cooling test series. As expected, the roughness falls off as the deposit is reduced due to increased back side cooling. The roughness measurement for the no cooling case was taken from a separated deposit flake to ensure consistency with the more tenacious deposits at the higher cooling levels.

X-ray spectroscopy was conducted to determine the elemental constituents in the surface deposit, as well as the penetrating deposits. Figure 17 shows the elemental composition in wt % compared with the ash. The surface deposits showed a similar makeup as the ash; however, there was a significant increase in Ca while Na and Si showed large decreases. The figure also clearly shows that the TBC studied is penetrated by Si, Ca, and Al from the ash. The spallation appears to be the result of the difference in coefficients of thermal expansion between the TBC and the penetrating ash elements. Upon shutdown of the facility, this mismatch in contraction rates causes significant thermal stresses in the TBC, resulting in separation of the TBC layer particularly near the edges of the coupon.
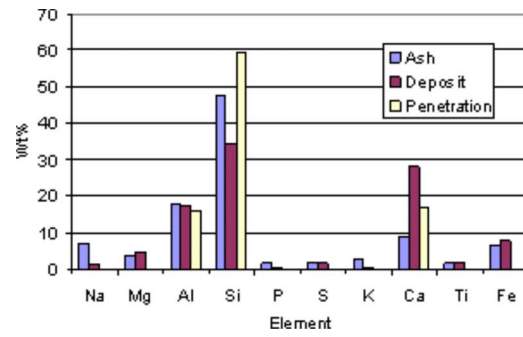
Petcoke Series. A final series of tests were performed using the petcoke/coal blend particulate. Three tests were conducted using particles with a MMD of 6 μm. The third set of samples described earlier was used in this test series. First, a no cooling test was performed with the interior of the coolant fixture insulated as in the gas temperature and particle size test series. Following this, two impingement cooling levels were tested in the same configuration as the coal series. The same standard operating conditions were used, namely, $T=1183°C$, Mach=0.25. The deposits looked similar to those of the coal impingement cooling series. The same large amount of flaking occurred on the no cooling case; however, there was more flaking on the cooling cases compared to the coal series perhaps due to the larger particle size. There was slightly more spallation of the TBC in the no cooling case compared to the coal; however, the different MMD makes a direct comparison difficult. A summary of the deposition results is shown in Table 5. Trends in net capture efficiency are included in Fig. 13 with the coal.

Conclusions

Four series of tests were performed in an accelerated deposition test facility to study the independent effects of particle size, gas temperature, and metal temperature on ash deposits from two candidate power turbine synfuels. Testing was conducted in the TADF by matching gas temperature, velocity, and net throughput of particulate out of the combustor with that experienced by a modern power turbine. Nominal combustor exit flow conditions are Mach number of 0.25 and gas temperature of 1183°C. Testing with four different sizes of coal ash particles showed greater than double the deposition rate as particle mass mean diameter was increased from 3 μm to 16 μm. In the second series of tests, different gas temperatures were studied while the facility maintained a constant exit velocity of 170 m/s (Mach=0.23–0.26). Particle deposition rate was found to decrease with decreasing gas temperature. The threshold gas temperature for deposition was approximately 960°C. Ground coal and petcoke ash particulates were used in the third and fourth test series with impingement cooling on the back side of the target coupon. Deposition rates decreased with increasing mass flow of coolant air, as expected. Deposit surface roughness levels decreased with decreasing gas

Table 5 Deposition results from impingement cooling test series using petcoke

Mass flow of coolant (g/s)	Heat flux (kW/m²)	Preburn button mass (g)	Button mass change (mg)	Separated deposit mass (mg)	Separated deposit (%)	Net deposit mass (mg)	Deposition rate (mg/cm² h)	Net particulate mass (mg)	Net capture efficiency (%)
0	0	13.8	10	360	97	370	14.60	7720	4.79
3.38	1049.20	29.4	40	60	60	100	3.95	7680	1.22
8.33	1614.26	29.42	20	30	60	50	1.97	8200	0.65

temperature and increasing coolant flow, consistent with the trend in particulate capture efficiencies for both cases. Postexposure analyses of the third test series (scanning electron microscopy and X-ray spectroscopy) show decreasing TBC damage with increased cooling levels. Work is currently under way to study the effects of different TBC application techniques on deposition.

Acknowledgment

Nomenclature

M = Mach number
Q = heat flux (W)
Ra = centerline average roughness
Rt = peak roughness
Rz = average peak roughness
T = temperature
c_p = specific heat at constant pressure (J/kg K)
m = mass flow rate (kg/s)

References

[1] Wenglarz, R. A., and Wright, I. G., 2002, "Alternate Fuels for Land-Based Turbines," *Proceedings of the Workshop on Materials and Practices to Improve Resistance to Fuel Derived Environmental Damage in Land-and Sea-Based Turbines*, Oct. 22–24, Colorado School of Mines, Golden, CO.
[2] Smialek, J. L., Archer, F. A., and Garlick, R. G., 1992, *The Chemistry of Saudi Arabian Sand: A Deposition Problem on Helicopter Turbine Airfoils* Advances in Synthesis and Processes, SAMPLE, 3, pp. M92–M101.
[3] Toriz, F. C., Thakker, A. B., and Gupta, S. K., 1988, "Thermal Barrier Coatings for Jet Engines," presented at the Gas Turbine and Aeroengine Congress Amsterdam, The Netherlands, June 6–9, Paper No. 88-GT-279.
[4] Wenglarz, R. A., and Fox, Jr., R. G., 1990, "Physical Aspects of Deposition From Coal-Water Fuels Under Gas Turbine Conditions," ASME J. Eng. Gas Turbines Power, **112**, pp. 9–14.
[5] Kim, J., Dunn, M. G., Baran, A. J., Wade, D. P., and Tremba, E. L., 1993, "Deposition of Volacanic Materials in the Hot Sections of Two Gas Turbine Engines," ASME J. Eng. Gas Turbines Power, **115**, pp. 641–651.
[6] Bons, J. P., Taylor, R., McClain, S., and Rivir, R. B., 2001, "The Many Faces of Turbine Surface Roughness," ASME J. Turbomach., **123**, pp. 739–748.
[7] Jensen, J. W., Squire, S. W., Bons, J. P., and Fletcher, T. H., 2005, "Simulated Land-Based Turbine Deposits Generated in an Accelerated Deposition Facility," ASME J. Turbomach., **127**, pp. 462–470.
[8] Bons, J. P., Crosby, J., Wammack, J. E., Bentley, B. I., and Fletcher, T. H., 2007, "High Pressure Turbine Deposition in Land-Based Gas Turbines With Various Synfuels," ASME J. Eng. Gas Turbines Power, **129**, pp. 135–143.
[9] Wammack, J. E., Crosby, J., Fletcher, D., Bons, J. P., and Fletcher, T. H., 2006, "Evolution of Surface Deposits on a High Pressure Turbine Blade—Part I: Physical Characteristics," ASME J. Turbomach., **130**, p. 021020.
[10] Bons, J. P., Wammack, J. E., Crosby, J., Fletcher, D., and Fletcher, T. H., 2006, "Evolution of Surface Deposits on a High Pressure Turbine Blade—Part II: Convective Heat Transfer," ASME J. Turbomach., **130**, p. 021021.
[11] McBride, B. J., and Gordon, S., 2006, "Computer Program for Calculation of Complex Chemical Equilibrium Compositions and Applications II. User's Manual and Program Description," http://www.grc.nasa.gov/WWW/CEAWeb/RP-1311P2.htm.
[12] Lu, H., 2006, "Experimental and Modeling Investigations of Biomass Particle Combustion," Ph.D. dissertation, Chemical Engineering Department, Brigham Young University, Provo, UT.
[13] Hamed, A., Tabakoff, W., Rivir, R. B., Das, K., and Arora, P., 2004, "Turbine Blade Surface Deterioration by Erosion," ASME Paper No. GT2004-54328.
[14] Caguiat, D., 2002, "Rolls Royce/Allison 501-K Gas Turbine Anti-Fouling Compressor Coatings Evaluation," ASME Paper No. GT2002-30261.

Investigation of the Effect of Incomplete Droplet Prevaporization on NO$_x$ Emissions in LDI Combustion Systems

Christian H. Beck

e-mail: christian.beck@its.uka.de

Rainer Koch

Hans-Jörg Bauer

Institut für Thermische Strömungsmaschinen,
Universität Karlsruhe (TH),
76128 Karlsruhe, Germany

The influence of incomplete liquid fuel prevaporization on the emissions of nitric oxides in a swirl stabilized model gas turbine combustor is investigated experimentally and numerically. The design of the model combustor enables the variation of the degree of prevaporization. This is achieved by using two liquid fuel injectors. One injector is located far upstream of the combustor and generates a fully prevaporized and premixed air fuel mixture. The second injector is located at the combustor inlet. Consequently, the liquid fuel mass flow split between the two injectors determines the fraction of nonprevaporized fuel present in the reaction zone. The NO/NO$_2$ measurements were performed with a chemoluminescence analyzer. In accordance to the findings of other researchers, the present experimental study revealed that the influence of prevaporization on nitric oxide emissions is of significance for practical applications. The experimental studies were accompanied by numerical studies of partially prevaporized lean combustion in an abstracted configuration. The purpose of this numerical study is to gain a detailed understanding of the influence of droplet slip on droplet flame position and peak temperature. The droplet slip velocity was found to have a significant impact on the peak temperature of the droplet flame and, therefore, NO formation rates within the droplet flame. The combustion system used for the experimental investigation was characterized regarding droplet slip velocities with an extended laser Doppler anemometry technique. The comparison between numerical and experimental results shows that the droplet slip velocities in the macroscopic reaction zone are within the transition range from an envelope to a wake flame. It is concluded that small-scale mixing effects play a significant role in the formation of nitric oxides in spray combustion systems with incomplete prevaporization. [DOI: 10.1115/1.2906185]

Introduction

As of today, the reduction of aero-gas-turbine emissions has become the main driving force for the development of new combustor concepts. The predominant idea is to achieve a reduction of NO$_x$ emissions by minimizing the temporal and spatial inhomogeneities of the temperature in the reaction zone. In lean flames, temperature fluctuations increase NO formation because of the nonlinear dependence of the NO formation on temperature.

Theoretically, a lean perfectly premixed and prevaporized combustion system does offer a significant NO$_x$ emission reduction potential [1]. However, the high combustor pressure levels of modern aeroengines make complete prevaporizing and premixing practically impossible due to the fast onset of autoignition at these conditions [2,3].

The lean direct injection (LDI) concept is characterized by a global lean equivalence ratio and incomplete prevaporization of the liquid fuel. While complete prevaporization is not achieved, large-scale mixture inhomogeneities are avoided. However, the presence of liquid fuel droplets in the macroscopic reaction zone can create mixture inhomogeneities on a microscopic length scale, if a near stoichiometric burning envelope flame is established around individual droplets.

The first question to be addressed in the present work is to what extent the NO$_x$ emissions are affected by the fraction of liquid fuel present in the macroscopic reaction zone. This question was previously investigated by other authors [4,5]. In the first study, a two-injector system was used where the degree of prevaporization is adjusted like in the rig used in the present study. The liquid fuel mass fraction α was varied between $0.3 \leqslant \alpha \leqslant 0$ at ϕ=0.6; 0.72. The operating pressure was 0.3 MPa and the preheat temperature was 600–700 K. The author reports a piecewise linear dependence of NO$_x$ emissions on α. At higher equivalence ratios, the influence of prevaporization on emissions was found to decrease.

The second study was performed at atmospheric pressure with air preheat temperatures of 323–376 K. The degree of prevaporization was varied by adjusting the premixing duct length and the preheat temperature. The degree of prevaporization was evaluated from phase Doppler (PDA) liquid phase flux measurements. For flame stabilization, an electrically heated wire ring was used. The generally very low preheat temperature causes low adiabatic flame temperatures at lean conditions. The authors report a piecewise linear dependence of emissions on α for $\alpha < 0.5$. For $0.5 < \alpha < 1$, emissions were found not to vary with the degree of prevaporization.

The main difference between the experimental setups of the previous studies and the present one is the type of flame stabilization. In the present study, a generic swirl-stabilized burner is used. The stabilization mechanism is expected to have a significant impact on the flame structure. In addition, the droplet slip is fundamentally different in a swirl-stabilized flame, where gas

Copyright © 2008 by ASME

phase velocities significantly change along the droplet trajectories compared to a pipe flow. Therefore, the setup used in the present study can be expected to represent the characteristics of a gas turbine combustor to a greater extent than previous studies.

In the second part of the paper, a detailed analysis of the NO formation in lean flames with partial droplet prevaporization is presented. The linear dependence of NO_x emissions on the degree of prevaporization suggests that the variation of the degree of prevaporization may be abstracted as the superposition of two flame types: droplet flame and premixed flame. The flame type causing high emissions is the individual burning droplet. In order to gain a better understanding of the prevailing NO formation mechanism, the emission formation of a single droplet flame will be numerically studied. It is known that significant droplet slip velocities can cause the stoichiometric envelope flame to extinguish and a wake flame to establish. The influence of this flame type transition on the NO formation of a single droplet flame will be discussed.

First experimental studies on droplet flame extinction were performed by Spalding [6]. Recently, Pope [7] presented a correlation based on these early experiments and new numerical results. The numerical results are based on a setup quite similar to the one used here. The authors report a nonlinear relation between droplet diameter and extinction velocity. Furthermore, the extinction velocity was found to exponentially vary with ambient gas temperature. In general, the study presented by Pope [7] focuses on the point at which extinction of the envelope flame at the forward stagnation point occurs. Investigations using similar numerical setups were performed by Raghavan et al. [8] and Jiang et al. [9]. Both studies focus on the flame type transition caused by the variation of droplet slip velocity. In all available numerical studies on droplet flame extinction, chemical reaction is modeled with a single step global reactions. In the present study, the detailed mechanism from Held et al. [10] is used for several reasons. First, the position of the droplet wake flame is mainly determined by the chemical time scales. Since the droplet flame position was found to have a significant effect on emissions, detailed modeling of the chemical processes is of importance. Second, the formation of nitric oxides is to be modeled. Again, a detailed mechanism from Hewson [11] is used since the accuracy of simplified NO formation rate expressions is limited.

The final experimental investigation presented in this paper will discuss the range of droplet slip velocities found in typical swirl-stabilized combustion systems. By using the results from the numerical investigation, the droplet flame type, which is present in the macroscopic reaction zone of typical swirl-stabilized flames, will be deduced.

Experimental Investigation

Concept and Design of the Experimental Setup. The combustion system used in this study is specifically designed to allow the variation of droplet prevaporization. The setup contains two liquid fuel injectors (see Fig. 1). One injector is positioned far upstream while the second injector is placed in the proximity of the reaction zone. The upstream injector is used to generate a prevaporized and perfectly premixed fuel air mixture, while the downstream injector is used to directly inject droplets into the flame. By varying the fuel mass flow split between the upstream and the downstream injector, the fraction of nonprevaporized fuel present in the reaction zone can be adjusted.

The fraction of liquid fuel present in the flame front is to be determined from fuel mass flow measurements. Therefore, it is necessary that the droplets injected by the downstream injector do not significantly vaporize before they reach the macroscopic reaction zone. This is ensured by injecting the liquid fuel at a temperature of only T_f=263 K. An accompanying numerical study confirmed that an injection temperature of 263 K is sufficient to minimize droplet mass loss due to vaporization for the droplet size
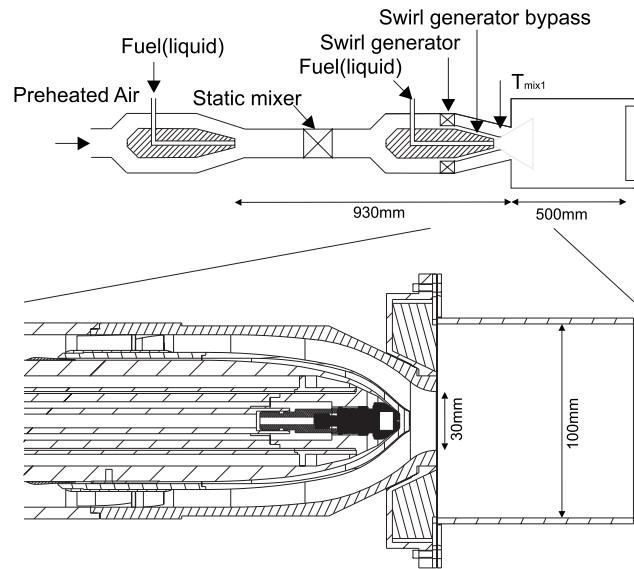
Fig. 1 Schematic of the rig; detail of the burner and combustion chamber

distribution, fuel, air temperature, and residence time of this combustor. Flame stabilization is achieved by generating a vortex breakdown.

Operating Conditions. In the experimental setup, all oxidizer and fuel mass flows are measured using calibrated sensors. The combustor inlet temperature T_{mix1} is controlled as well as the liquid fuel temperature inside the injector. The pressure level behind the combustor exit is atmospheric. An overview of the operating conditions relevant for this paper is given in Table 1.

The combustion system is fed with preheated air. A preheat temperature of T_{mix2}=473 K was chosen. This temperature is a compromise between minimizing liquid fuel prevaporization from the downstream injector and achieving realistic adiabatic flame temperatures (1650–1850 K) at lean conditions ($\phi \leq 0.6$). The preheat temperature is defined here as the temperature of the unburnt mixture under the premise that all fuel is vaporized and mixed (T_{mix2}). The combustor inlet temperature T_{mix1} is calculated from this virtual temperature by Eq. (1), in which the temperature change due to heating and vaporization of the nonprevaporized fuel mass flow is accounted for. If T_{mix2} remains constant, the adiabatic flame temperature is independent of the degree of prevaporization α and the liquid fuel temperature. For T_{mix2}=473 K and ϕ=0.5, T_{mix1} linearly varies between 473 K$\leq T_{mix1} \leq$497 K for $0 \leq \alpha \leq 1$. The enthalpy of fuel and oxidizer used in Eq. (1) is

Table 1 Operating conditions

Quantity	Value	Comment
ϕ	0.5, …, 0.6	
α	0, …, 0.8	Liquid fuel fraction
T_{mix2}	473 K	
T_f	263 K	Measured in atomizer
$\dot{m}_{Ox}$	14.9 g/s	Total oxidizer mass flow
$\dot{m}_{core}$	0.7 g/s	Swirl generator bypass mass flow
$\dot{m}_{atom}$	0.1, …, 0.25 g/s	Downstream atomizer air mass flow
Fuel	Heptane	
s	0.46	Swirl number at the combustor inlet
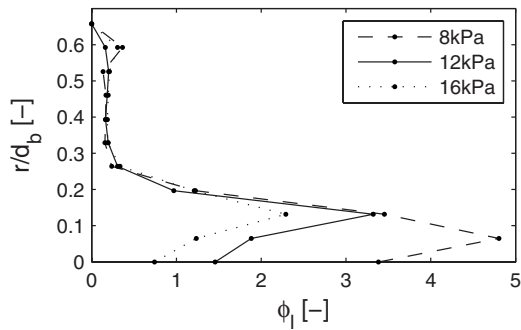
Fig. 2 Radial distribution of liquid fuel equivalence ratio for three atomizer air pressure levels, $\phi=0.55$, $\alpha=0.5$

Fig. 3 CDF of liquid fuel equivalence ratio for three atomizer air pressure levels, $\phi=0.55$, $\alpha=0.5$

calculated as a function of temperature. The thermodynamic data provided with the reaction mechanism [10] are used.

$$(h_{air} + Y_f h_f)|_{T_{mix\ 2}} = (1 - \alpha)Y_f(\Delta h_{lg} + h_f)|_{T_f} + (h_{air} + \alpha Y_f h_f)|_{T_{mix\ 1}}$$
(1)

Experimental Investigation of Mixture Characteristics. For the injection of liquid fuel, two air assist atomizers are used. The upstream injector was chosen based on the requirement to generate a fine spray suitable for fast prevaporization and premixing. The mixing length is approximately 1 m with a mean residence time of 200 ms. The performance of the premixing system was evaluated in a previous study [12] and was found to deliver a very homogeneous mixture ($\sigma_\phi=0.008$). A traverse mounted gas sampling system and a flame ionization detector were used for the characterization of mixture homogeneity. The measurements were performed 0.4 m downstream of the upstream injector, implying that the standard deviation at the combustor inlet is lower than the value reported above.

For the downstream injector, the key requirements are that the spray characteristics are independent of liquid mass flow, and that the liquid fuel equivalence ratio in the macroscopic reaction zone is as homogeneous as possible. Since these requirements cannot be ideally met, the impact of the deviation from ideal conditions regarding the effects investigated in this study is assessed.

The downstream injector was characterized at reacting conditions with a standard phase Doppler anemometry system setup for a scattering angle of 74 deg. The simultaneous characterization of liquid and gas phase flow was achieved by using the recorded particle diameter as phase discrimination criterion ($d_{disc}=3$ μm). Since the data rate of small fuel droplets is very low, spherical glass particles with $d<3$ μm and a refractive index of $n\approx1.5$ were added by a "Palas RGB 1000" particle dispenser. A seeding volume flow was chosen, which is $<0.5\%$ of the liquid fuel volume flow. At the chosen scattering angle, the PDA technique is relatively insensitive to particle refractive index [13]. The difference between the expected refractive index of the fuel droplets ($n=1.4$) and the gas tracer particles causes a sizing error $<3\%$. This sizing error for tracer particles is considered insignificant for the purpose of phase discrimination. The data were sampled at $x/d_b=0.33$ downstream of the combustor inlet. The radial range covered is $0<r/d_b<0.66$. This location is at the beginning of the macroscopic reaction zone (see Fig. 8).

The radial distribution of liquid fuel equivalence ratio $\phi_l=f_l\rho_l/(c_g\rho_g z)$ was obtained from the PDA measurements (see Fig. 2). The data are shown for an operating condition with 50% prevaporization and $\phi=0.55$ at three atomizer air pressure levels. For all atomizer pressure levels, the liquid fuel equivalence ratio is rich near the center axis. The high liquid fuel equivalence ratio in this region is due to the low gas phase velocity near the center axis (see Fig. 9).

In order to assess the importance of the rich region near the
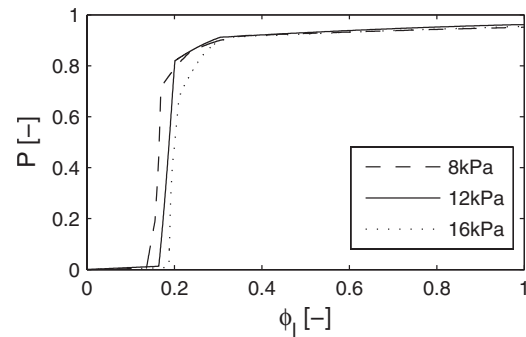
center axis, the mixture mass flow weighted cumulative distribution function for the mean liquid fuel equivalence ratio was derived. Mixture mass flow weighting is used since the local mixture mass flow represents the importance of a region for the overall characteristics of the combustion system. The cumulative distribution function (CDF) of the liquid fuel equivalence ratio is shown in Fig. 3. The distribution of the liquid fuel equivalence ratio is relatively narrow in all three cases. Approximately 10% of the mixture mass flow has a liquid fuel equivalence ratio higher than the mean value.

The inhomogeneity of liquid fuel placement could bias the dependence of NO_x emissions on the degree of prevaporization by formation of large-scale temperature inhomogeneities. Since it is not clear to what extent the inhomogeneity of liquid fuel placement affects the overall NO_x emissions of the combustor, a practical test regarding the sensitivity of NO formation on liquid fuel placement was performed. The variation of the atomizing air pressure has a significant effect on the liquid fuel equivalence ratio in the proximity of the burner axis (see Fig. 2). However, the overall NO emissions of the combustion system change by less than 2.5% when a variation of atomizer air pressure is performed (see Table 2). It is concluded that the effect of inhomogeneities in liquid fuel placement, as they are present in the experimental setup, is more than two orders of magnitudes smaller than the effect of the degree of prevaporization on emissions (see Fig. 4). For the emission measurements presented later, an atomizer air pressure level of $p_{atom}=12$ kPa was chosen. The low sensitivity of NO_x emissions regarding liquid fuel placement can be explained by multiple effects.

1. The mass flow in the region where the inhomogeneities of liquid fuel equivalence ratio are present (burner axis) is small.
2. The length of the droplet trajectories within the macroscopic reaction zone is of the order of the linear diameter. Furthermore, the droplets in the macroscopic reaction zone do not reach momentum equilibrium (see Fig. 9). Therefore, the heat release caused by nonprevaporized fuel is distributed over a large volume. Consequently, the inhomogeneous distribution of liquid fuel at the beginning of the reaction zone does not necessarily imply the existence of a macroscopic

Table 2 Effect of variation of fuel placement on emissions, $\phi=0.55$, $\alpha=0.5$

Case	p_{atom} (kPa)	EI_{NO} (g/kg)	$\bar{D}_{32}$ (μm)
1	8	0.53	52
2	12	0.52	45
3	16	0.52	37
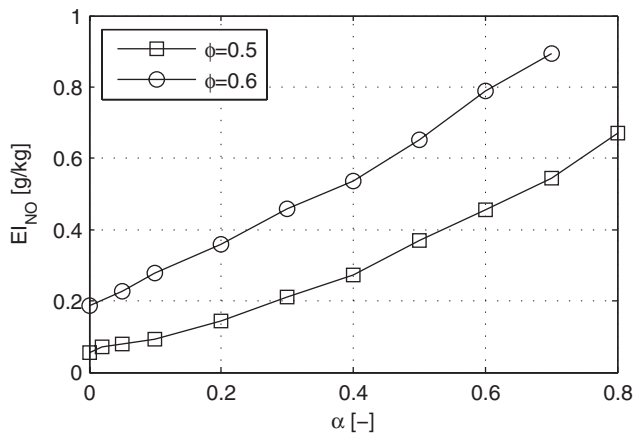
Fig. 4 Influence of liquid fuel mass fraction on overall NO emissions

Fig. 5 Abstracted flame structure of partially prevaporized combustion

temperature inhomogeneity and, thus, high NO formation rates.

3. In the present experimental configuration, the gaseous fuel equivalence ratio is not affected by inhomogeneities of the liquid fuel placement, since liquid fuel prevaporization from the downstream injector is minimized by cooling the liquid fuel. An inhomogeneity of the gaseous fuel distribution would cause a macroscopic hot spot and high NO formation rates. Therefore, the impact of liquid fuel placement in the experiment is fundamentally different from real combustors, where the liquid fuel placement has a major impact on gaseous fuel distribution.

An additional source of uncertainty is the dependence of spray properties on the injector liquid mass flow. PDA measurements demonstrated a sensitivity of the liquid mass flow weighted Sauter diameter on the atomizer fuel mass flow. For a variation of the liquid fuel mass fraction between $0.1 < \alpha < 0.8$, the mean Sauter diameter varied within $40~\mu m < \overline{D}_{32} < 49~\mu m$. Considering the low sensitivity of NO emissions regarding mean droplet diameter (see Table 2), the variation of the mean droplet diameter with the liquid fuel mass fraction is not of significance for the emission measurements to be presented later.

Experimental Investigation of the Influence of Prevaporization on NO$_x$ Emissions. The experimental setup previously described was used to investigate the influence of incomplete prevaporization on the NO$_x$ emissions. The variation of α was performed for two equivalence ratios $\phi = 0.5$ and 0.6. The adiabatic flame temperatures corresponding to these equivalence ratios are $T = 1650$ K and 1837 K. The NO/NO$_x$ measurements were performed with a chemoluminescence analyzer. Since the measured NO$_2$ concentrations were virtually zero for all operating conditions, only the NO concentration will be reported.

For both overall equivalence ratios, a significant influence of the liquid fuel fraction α on overall NO emissions is observed (Fig. 4). The relation between NO emissions and the liquid fuel mass fraction is almost linear for both equivalence ratios. This linear dependence of NO emissions on α can be explained by the superposition of two flame types: premixed combustion and droplet burning. Lean premixed flames cause very low emissions of nitric oxides (see Fig. 4, $\alpha = 0$) while droplet flames, which may burn at a near stoichiometric equivalence ratio, can cause significant formation of nitric oxides.

Numerical Investigation

Introduction. The experimental results presented in the previous section show that the presence of nonprevaporized droplets in the macroscopic reaction zone has a significant effect on overall combustor NO$_x$ emissions. While the experimental setup allows the variation of global parameters, detailed measurements are extremely difficult to perform and analyze since the quantities of interest show significant fluctuations in time and space due to turbulence. Therefore, spray combustion was also numerically studied. The primary objective of the numerical study is to identify and understand the effects governing the NO formation in partially prevaporized spray flames. An abstracted structure of such a flame is shown in Fig. 5.
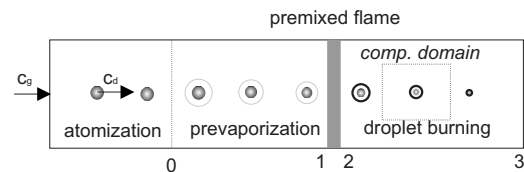
In the case of a high degree of prevaporization, there will be a stable premixed flame front, which is traversed by droplets. If the degree of prevaporization is reduced, the premixed flame front will extinguish. Then, an alternative flame structure will be formed. This flame structure will still be characterized by an equilibrium of upstream heat transport, which initiates chemical reaction that in turn will cause downstream heat release. A detailed discussion of plausible flame structures is given by Borghi [14].

For a perfectly prevaporized mixture, the temperature of the premixed flame front will be at its maximum value. In contrast, the global NO$_x$ emissions for this case are at a minimum (see Fig. 4). If the degree of prevaporization is reduced, the temperature of the premixed flame front will decrease and cause the region to become less important to overall NO formation. Therefore, the focus of the numerical investigation is on the processes in the proximity of the droplet during droplet burning, which is likely to predominantly contribute to overall emissions.

It is known that the droplet slip velocity influences the burning mode of an individual burning droplet [6]. Two characteristic flame types can be observed: An envelope flame, which encloses the droplet and burns as a diffusion flame at near stoichiometric conditions. At higher slip velocities, the envelope flame extinguishes at the forward stagnation point and a wake flame is established. Since this transition from one flame type to another is expected to be accompanied by changes of the peak flame temperature, NO formation will also be affected by the flame type transition.

For the reasons previously discussed, the effect of droplet slip velocity on flame type transition and NO formation was numerically investigated. The results of the numerical simulation will be discussed considering the droplet slip velocities measured in the presented burner.

Concept of the Numerical Simulation. For the numerical simulation, a configuration representing a partially prevaporized flame burning in a constant area duct with isotropic droplet spacing is considered (Fig. 5). For a given equivalence ratio, degree of prevaporization, oxidizer, and fuel temperature, the local temperature and mixture composition at Position 2, which is the beginning of the computational domain, are calculated. This is done under the assumption that all prevaporized fuel is burnt in the premixed flame and that the mixture has reached chemical equilibrium. From the ratio of the gas and droplet velocity, the local liquid and gas phase density, the overall equivalence ratio, and the degree of prevaporization, the dimensionless droplet spacing l/d can be determined from Eq. (2). The fuel mass fraction Y_f is calculated from the global equivalence ratio.

$$l/d = \left(\frac{(1 - Y_f\alpha)\pi\rho_f \dfrac{c_d}{c_g}}{6Y_f\alpha\rho_g} \right)^{1/3} \quad (2)$$

For conditions covered by the experimental investigation, the dimensionless spacing varies between $40 < l/d < 75$. According to Annamalai and Ryan [15], the interaction between burning droplets is small to negligible for this droplet spacing range. Interaction between burning droplets is referred to as group combustion. Various regimes exist, which are generally characterized by the presence of high gaseous fuel concentrations outside flammability limits surrounding a group of droplets in the reaction zone [15]. In lean spray flames with homogeneous fuel placement, such a condition is unlikely to exist since a homogeneous fuel placement implies that the local equivalence ratio is identical to the overall equivalence ratio. Therefore, nonprevaporized droplets will individually burn in LDI combustion systems. Consequently, the simulation does include just one individual droplet. The computational domain is a 2D rectangle, assuming rotational symmetry. The computational domain covers $-20 \le x/d \le 100$ in the streamwise direction and $0 \le r/d \le 37.5$ in the radial direction relative to the droplet center. The domain is initialized with the temperature and mixture composition present at the inlet. An initial droplet temperature of 300 K was chosen. The droplet flame establishes itself due to autoignition. This initial condition is more realistic than initializing an envelope flame [16].

Numerical Modeling. In the present setup, the liquid phase inside the droplet as well as the gas phase is fully discretized. Hence, the modeling of vaporization and interphase heat transfer requires an interface condition. For modeling of hydrocarbon oxidation, a detailed mechanism for n-heptane is used [10]. Additionally, a detailed chemical mechanism developed by Hewson [11] is used to model nitric oxide formation. In the gas phase region, transport equations for momentum, enthalpy, and species mass fractions are solved. The derivation of the transport equation is discussed in detail by Warnatz et al. [17]. In the liquid phase region, only the enthalpy equation is solved.

For the modeling of heat conduction and concentration driven species diffusion, mixture averaged coefficients are used. The thermal conductivity $\bar{\lambda}$ is calculated from the mixture averaged dynamic viscosity assuming a Prandtl number $\mathrm{Pr}=0.7$ with $\bar{\lambda}=\bar{\mu}\bar{c}_p/\mathrm{Pr}$. The diffusion coefficient $\bar{D}$ is calculated from $\bar{D}=\bar{\mu}/(\bar{\rho}\mathrm{Sc})$ with $\mathrm{Sc}=0.7$.

The interface condition is based on the assumption of phase equilibrium at the droplet surface. The vapor pressure required for the coupling of the species transport equation of the fuel was calculated from the Antoine equation (Eq. (3)). The resulting local evaporation flux is needed to set the interface condition for energy and mass conservation (Eq. (4)). The latent heat of vaporization required for the energy interface condition is calculated as a function of temperature (Eq. (5)). The conservation of mass at the interface is technically implemented by locally deforming the grid (Eq. (6)). For spatial discretization, the central differencing scheme was employed. For time stepping, the Crank–Nicolson scheme was used.

$$Y_{f,s} = \frac{M_f}{\bar{M}} \exp\left(A - \left(\frac{B}{T_{g,s} + C} \right) \right) \quad (3)$$

$$c_{f,s,g} = \frac{-\bar{D}\left(\dfrac{\partial(Y)_f}{\partial r} \right)_s}{1 - Y_{f,s}} \quad (4)$$

$$\lambda_{f,l} \frac{dT}{dr} = \rho_{f,g} c_{f,s} h_{l,g}(T_{s,l}) \quad (5)$$
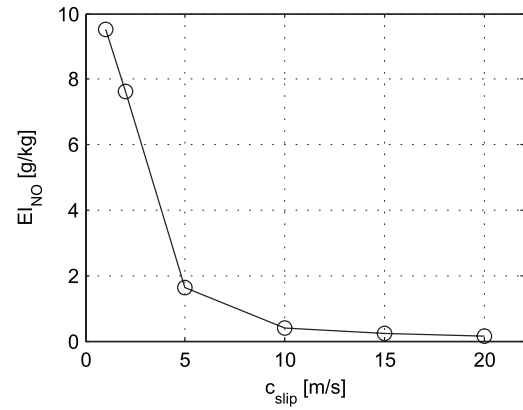
Fig. 6 Dimensionless NO formation rate of single droplet flames

$$c_{f,s,g}\rho_{s,g}Y_{s,f} = c_{f,s,l}\rho_{f,s,l} \quad (6)$$

Results. A variation of the droplet slip velocity was performed for one operating condition characterized by the preheat temperature $T_{mix2}=673$ K, liquid fuel fraction $\alpha=0.1$, global equivalence ratio $\phi=0.5$, and $p_{amb}=0.1$ MPa. For these boundary conditions, the temperature downstream of the premixed flame and at the beginning of the computational domain is 1805 K. The initial droplet diameter is $d=50$ μm. The droplet slip velocity was varied between 1 m/s $< c_{slip} <$ 20 m/s, which corresponds to a droplet Reynolds number of $0.18 < \mathrm{Re}_D < 3.6$.

Since the simulation is transient, a time for comparison of the nonintegral quantities needs to be chosen. For the operating conditions considered here, the droplet flames have reached a stable burning mode after $t=85,\dots,350$ μs, depending on the flame type. The comparison was performed at a simulation time $t=500$ μs.

For the investigation of the influence of the slip velocity on NO formation, the ratio of the NO formation rate integrated over the domain volume (Eq. (7)) and the vaporization fuel mass flow of the droplet is used to quantify NO formation. In a global context, this is referred to as the emission index EI_{NO}.

$$\dot{m}_{NO} = M_{NO} \int \sum_{i=1}^{m} z_i R_i dV \quad (7)$$

In Fig. 6, the simulated effect of droplet slip on NO formation in the droplet flame is shown. For the range of droplet slip velocities considered, a variation of NO formation of almost two orders of magnitude was found. The relation between emissions and slip velocity exhibits a nonlinear transition in the slip velocity range of 2 m/s $< c_{slip} <$ 5 m/s. An explanation of this behavior can be obtained from a comparison of the flame structure.

The predicted temperature field for three different droplet slip velocities is shown in Fig. 7. The temperature field around the droplet is significantly affected by droplet slip. Toward higher slip velocities, it is becoming more homogeneous, while a decrease in peak temperature is observed. Additionally, the region of the temperature peak moves further away from the droplet.

From detailed analysis of the temperature and CH radical mass fraction fields, it was concluded that the mass fraction peak of the CH radical correlates quite well with the location of the heat release (Fig. 7). For the smallest slip velocity of 2 m/s, an envelope flame is observed. However, the temperature and CH mass fraction at the forward stagnation point are lower than in the wake region. In the case of a slip velocity of 5 m/s, no significant heat release is observed in the upstream region of the droplet as the local temperature does not exceed the inlet temperature. Therefore, the extinction of the droplet flame at the forward stagnation

$c_s=2$ m/s $c_s=5$ m/s $c_s=10$ m/s
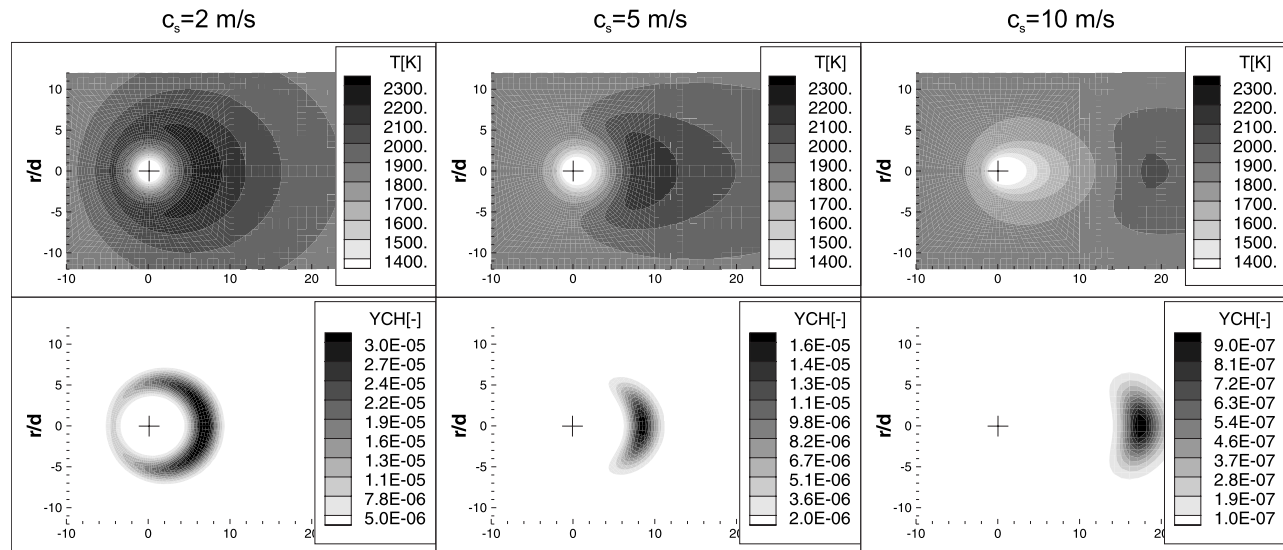
Fig. 7 Effect of slip velocity on temperature and CH mass fraction

point must occur for a slip velocity of $2,\ldots,5$ m/s. If the slip velocity is further increased, the flame position moves further downstream. The transition between the two droplet flame types explains the nonlinearity in the relation between droplet slip and NO formation, as shown in Fig. 6.

Considering the results of the numerical investigation, the effect of droplet slip on NO formation in a droplet flame can be explained by the following mechanism.

1. The flame position is determined by a chemical time scale and a convective time scale. An increase of the slip velocity results in a decrease of the convective time scale and, consequently, the distance between droplet and flame increases.
2. The distance between droplet and flame exerts a significant influence on the equivalence ratio of the droplet flame. In the case of a large distance, mixing is improved, resulting in a lower equivalence ratio of the droplet flame.
3. The equivalence ratio at the position of the droplet flame determines the flame temperature. Due to the nonlinear dependence of NO formation on temperature, the equivalence ratio has a significant impact on NO formation in the flame.

In the present analysis, radiative heat transfer was not considered. Radiative heat transfer can reduce the peak temperature of the droplet flame. Furthermore, the vaporization rate of the droplet can be increased if the droplet absorbs radiation. The effect of thermal radiation is, however, not expected to qualitatively alter the effect of slip velocity on NO formation in droplet flames.

Experimental Investigation of Droplet Slip Velocities

In the previous section, it was shown that the droplet slip velocity has a strong impact on the microscopic droplet flame shape as well as local peak temperature, which in turn significantly affects NO formation. In the experimental investigation, it was found that the presence of liquid fuel in the macroscopic reaction zone has a significant effect on overall emissions. In order to show which magnitude of droplet slip velocities and, consequently, droplet flame type can be expected in a swirl-stabilized burner, the droplet slip velocity was measured in the generic burner. As a prerequisite, the location of the macroscopic reaction zone had to be identified. Then, the mean gas phase and droplet velocities were acquired in this region.

Identification of the Macroscopic Reaction Zone. In order to determine the mean slip velocities of the burning droplets, first the region where there is a high probability of the presence of burning

droplets needs to be identified. The recording of time averaged chemiluminescence intensity and subsequent deconvolution is a technique well suited to obtain this information. For the deconvolution, the Abel transformation is used.

In the deconvoluted chemiluminescence recordings, two separate regions are visible where significant chemiluminescence intensities are observed (see Fig. 8). The main flame burns in the shear layer between fresh mixture and recirculated mixture. The second region is located near the center axis in the inner recirculation zone. The extent of the inner recirculation zone and the position of the shear layer is characterized by the contour plot of the axial gas phase velocity shown in Fig. 9.

Measurement of Droplet Slip in the Reaction Zone. For the determination of droplet slip velocities, the disperse phase as well as the gas phase velocities were simultaneously measured. An LDA setup in combination with a phase discrimination technique is used. Phase discrimination is performed by particle diameter. The particle diameter is obtained from the recorded scattering intensity. A discrimination diameter of $d=2$ μm was chosen. The effect of Gaussian laser intensity distribution in the measurement volume on the scattering intensity is reduced by rejecting particles, which do not traverse the near center region of the measurement volume. This is achieved by calculating the particle trajectory length within the measurement volume and defining a boundary value $l_{\text{bound}}=0.8d_{\text{probevol}}$. The results of the extended LDA technique are in good agreement with disperse phase veloc-
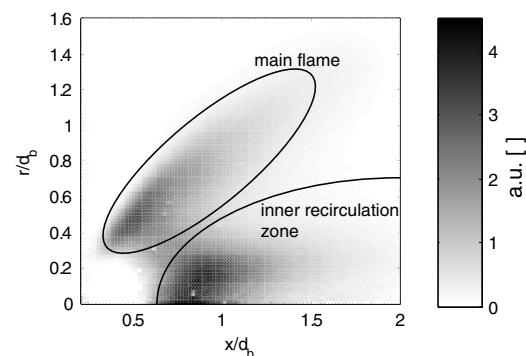
Fig. 8 Chemiluminescence intensity, time averaged and deconvoluted, band pass filtered for CH* emission around 431 nm; $\phi=0.5$, $\alpha=0.5$
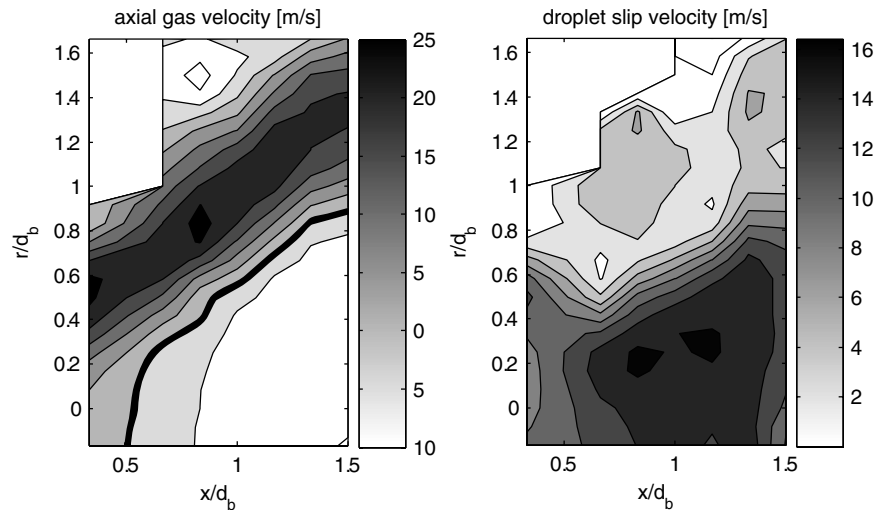
Fig. 9 Axial gas phase velocity and droplet slip velocity magnitude, ϕ=0.5, α =0.5, thick black line: c_{ax}=0 m/s

ity measurements obtained with the PDA technique. The extended LDA technique was preferred over the PDA technique for these measurements since the optical access window available for LDA was less susceptible to degradation by tracer particles.

The mean value of the axial and tangential velocity component was obtained for both phases. The resulting droplet slip velocity is shown in Fig. 9. The highest droplet slip velocities of 12 m/s $<c_{slip}<16$ m/s are observed near the center axis, where the inner recirculation zone is located. Further outside, there exists a region with lower slip velocities of 2 m/s $<c_{slip}<5$ m/s. This is the region of the main heat release. Thus, two regions characterized by different droplet combustion modes can be discriminated.

1. The inner recirculation zone, where high droplet slip velocities prevail. According to the numerical study previously presented (Fig. 7) at high slip velocities, a wake flame burning behind the droplet is expected to exist. The wake flame is characterized by low flame temperatures and, thus, a minor contribution to the overall NO_x emissions.
2. The main flame, where low droplet slip velocities are observed. In this region, the numerical simulation predicts the existence of both envelope and wake flames since the slip velocities are within the range of the flame type transition. As a consequence, the droplet flame temperature is higher, which results in higher NO formation rates.

Summary

The experimental study shows that the degree of prevaporization has a significant impact on the NO_x emissions of a swirl-stabilized model gas turbine combustor. Thus, the reduction of nonprevaporized fuel in the reaction zone does offer a significant NO_x emission reduction potential for LDI combustion systems. With increasing overall equivalence ratio, the emission reduction potential decreases. The effect of the degree of prevaporization on the NO_x emissions is a consequence of the presence of droplets in the macroscopic reaction zone. The droplet density in the reaction zone is in the range in which individual droplet burning is expected. The absence of group combustion phenomena is a general feature of LDI combustion systems with homogeneous fuel placement.

An almost linear relation between the degree of prevaporization and the overall nitric oxide emissions was found. The linearity suggests that a superposition of two NO formation mechanisms exists. While nitric oxide formation in lean premixed flames is minimal, a near stoichiometric droplet flame can be a significant source of nitric oxides. Therefore, the amount of nonprevaporized fuel which is burnt in droplet flames is directly proportional to the overall NO_x emissions.

As a major result of the present study, an alternative method for the NO_x emission reduction in LDI combustion systems was identified. NO formation can be minimized for a given degree of prevaporization by maximizing the droplet slip velocity in the macroscopic reaction zone. The effect of the droplet slip velocity on NO_x emissions is governed by the following mechanism: An increase in droplet slip velocity will increase the droplet/flame distance, and due to an increase of the mixing length, the mixture fraction at the flame position is reduced. Consequently, the peak temperature as well as the NO formation rates are lowered.

The mean droplet slip velocities in the swirl-stabilized model combustor investigated in the present study were measured. In the main reaction zone, relatively low droplet slip velocities were measured, which are within the transition range between envelope and wake flame. In the inner recirculation zone, relatively high slip velocities were measured, suggesting the presence of wake flames. Thus, it is concluded that major contributions to the NO_x emissions under nonprevaporized conditions stem from droplets burning in the main reaction zone.

The final conclusion of the present study is that a reliable prediction of the NO_x emissions of LDI combustors must include a submodel that accounts for single droplet burning and the nitric oxides formed within these droplet flames.

Acknowledgment

Nomenclature

Latin Letters

c = velocity magnitude (m/s)
D = diffusion coefficient (m²/s)
d = diameter (m)
D_{32} = Sauter mean diameter (SMD) (m)
f = flux (m³/(m² s))
h = total enthalpy (J/(kg K))
l = droplet spacing (m)
M = molar mass (kg/mol)

$\dot{m}$ = mass flow (kg/s)
R = species source term (kg/s)
s = swirl number
T = temperature (K)
u = velocity component (m/s)
X = molar fraction
Y = mass fraction
z = stoichiometric factor

Greek Letters

α = ratio of liquid to total fuel mass
ϕ = equivalence ratio
λ = thermal conductivity (W/(m K))
ρ = density (kg/m^3)

Subscripts

ax = axial
b = burner
f = fuel
g = gas phase
l = liquid phase
mix1 = condition after mixing of prevaporized fuel fraction
mix 2 = virtual condition after complete vaporization
ox = oxidizer
r = radial
s = droplet surface

References

[1] Bauer, H.-J., 2004, "New Low Emission Strategies and Combustor Designs for Civil Aeroengine Applications," Prog. Comput. Fluid Dyn., **4**, pp. 130–142.
[2] Aggarwal, S. K., 1998, "A Review of Spray Ignition Phenomena, Present Status and Future Research," Prog. Energy Combust. Sci., **24**, pp. 565–600.
[3] Cano-Wolff, M., Meisl, J., Koch, R., and Wittig, S., 1998, "The Influence of Evaporation on the Autoignition-Delay of n-Heptane Air Mixtures Under Gas Turbine Conditions," *27th International Symposium on Combustion*, pp. 2025–2031.
[4] Cooper, L. P., 1980, "Effect of the Degree of Prevaporization Upon Emissions for a Premixed Partially Vaporized Combustion System," NASA Technical Paper No. 1582.
[5] Baessler, S., Moesl, K. G., and Sattelmayer, T., 2006, "NO$_x$ Emissions of a Premixed Partially Vaporized Kerosene Spray Flame," ASME Paper No. GT2006-90248.
[6] Spalding, D. B., 1953, "The Combustion of Liquid Fuels," *Fourth International Symposium on Combustion*, pp. 847–864.
[7] Pope, D. N., and Gogos, G., 2005, "Numerical Simulation of Fuel Droplet Extinction Due to Forced Convection," Combust. Flame, **142**, pp. 89–106.
[8] Raghavan, V., Babu, V., Sundararajan, T., and Natarajan, R., 2005, "Flame Shapes and Burning Rates of Spherical Fuel Particles in a Mixed Convective Environment," Int. J. Heat Mass Transfer, **48**, pp. 5354–5370.
[9] Jiang, T. L., Chen, W. S., Tsai, M. J., and Chiu, H. H., 1995, "A Numerical Investigation of Multiple Flame Configurations in Convective Droplet Gasification," Combust. Flame, **103**, pp. 221–238.
[10] Held, T. J., Marchese, A. J., and Dryer, F. L., 1997, "A Semi-Empirical Reaction Mechanism for n-Heptane Oxidation and Pyrolysis," Combust. Flame, **123**, pp. 107–146.
[11] Hewson, J. C., 1997, "Pollutant Emissions From Nonpremixed Hydrocarbon Flames," University of California.
[12] Schaefer, O., 2005, "Experimentelle und Numerische Analyse des Flammenrueckschlags bei der Mageren Vormischverbrennung," ITS, University of Karlsruhe.
[13] Maier, G., and Wittig, S., 1999, "Fuel preparation and Emission Characteristics of a Pressure Loaded LPP Combustor," AIAA Paper No. 99-3774.
[14] Borghi, R., 1996, "Background on Droplets and Sprays," Lecture Series-von Karman Institute, Vol. 2, pp. 1–39.
[15] Annamalai, K., and Ryan, W., 1992, "Interactive Processes in Gasification and Combustion. Part 1: Liquid Drop Arrays and Clouds," Prog. Energy Combust. Sci., **18**, pp. 221–295.
[16] Chiu, H. H., 1996, "Multiple-State Phenomena and Hysteresis of a Combusting Isolated Droplet," Atomization Sprays, **6**, pp. 1–26.
[17] Warnatz, J., Maas, U., and Dibble, R. W., 2001, *Combustion*, Springer, New York.

R. A. Huls[1]

Faculty of Engineering Technology,
Section of Applied Mechanics,
University of Twente,
P.O. Box 217,
7500 AE Enschede, The Netherlands

J. F. van Kampen

Faculty of Engineering Technology,
Section of Thermal Engineering,
University of Twente,
P.O. Box 217,
7500 AE, Enschede, The Netherlands

P. J. M. van der Hoogt

Faculty of Engineering Technology,
Section of Applied Mechanics,
University of Twente,
P.O. Box 217,
7500 AE Enschede, The Netherlands

J. B. W. Kok

Faculty of Engineering Technology,
Section of Thermal Engineering,
University of Twente,
P.O. Box 217,
7500 AE Enschede, The Netherlands

A. de Boer

Faculty of Engineering Technology,
Section of Applied Mechanics,
University of Twente,
P.O. Box 217,
7500 AE Enschede, The Netherlands

Acoustoelastic Interaction in Combustion Chambers: Modeling and Experiments

To decrease NO_x emissions from combustion systems, lean premixed combustion is used. A disadvantage is the higher sensitivity to combustion instabilities, leading to increased sound pressure levels in the combustor and resulting in an increased excitation of the surrounding structure: the liner. This causes fatigue, which limits the lifetime of the combustor. This paper presents a joint experimental and numerical investigation of this acoustoelastic interaction problem for frequencies up to 1 kHz. To study this problem experimentally, a test setup has been built consisting of a single burner, 500 kW, 5 bar combustion system. The thin structure (liner) is contained in a thick pressure vessel with optical access for a traversing laser vibrometer system to measure the vibration levels of the liner. The acoustic excitation of the liner is measured using pressure sensors measuring the acoustic pressures inside the combustion chamber. For the numerical model, the finite element method with full coupling between structural vibration and acoustics is used. The flame is modeled as an acoustic volume source corresponding to a heat release rate that is frequency independent. The temperature distribution is taken from a Reynolds averaged Navier Stokes (RaNS) computational fluid dynamics (CFD) simulation. Results show very good agreement between predicted and measured acoustic pressure levels. The predicted and measured vibration levels also match fairly well.
[DOI: 10.1115/1.2938391]

1 Introduction

Air pollution has become an important issue in the past few decades. An important component of the pollution is nitrogen oxide or NO_x, which is, amongst others, formed during combustion of fossil fuels in gas turbines. To decrease this formation, lean combustion is applied, using an excess of air to combust the fuel. This leads to lower NO_x emissions, but also to increased acoustic pressure levels in the combustion chamber caused by a higher sensitivity to combustion instabilities [1]. Because of the high temperatures in the combustion chamber, the surrounding structure, the so-called liner, has to be thin and is therefore flexible. The acoustic pressure perturbations induce vibrations of the structure, leading to fatigue problems. This paper deals with the interaction between combustion, acoustics, and vibrations with emphasis on frequencies below 1 kHz. Extensive literature is available on the interaction between combustion and acoustics [2] and much work is also available on the interaction between acoustics and vibration [3,4]. The work presented in this paper attempts to combine these three fields in order to calculate the vibrations of the liner.

For the experiments, a test rig has been built. A cross section of the test rig is depicted in Fig. 1. The combustion chamber is a square tube of 150×150 mm^2 with a length of approximately 1.8 m. It consists of three main sections. The left part is the combustion section, consisting of the plenum (1, the last chamber upstream of the burner), a generic burner (2, in which the air gets a swirling motion and fuel, which is natural gas, is injected), and the first part of the combustion chamber (3, where the combustion takes place in a partially premixed flame). The middle section is the structural section, in which the vibration of the liner can be measured using laser vibrometry through windows (4) in the pressure vessel. In the combustion section and the structural section, a relatively thin structure, called the liner (5), is present within a much thicker pressure vessel (6). Cooling air flows between the liner and the pressure vessel. In the structural section, the liner consists of thicker end parts (4 mm) and a thinner part (7, 1.5 mm) in between. The structural vibration is measured on this thinner part. Acoustic pressure in the combustion chamber can be measured with pressure transducers p_2 and p_3 (there are more pressure transducers in the test rig, but they are not used in this paper). The most right part is the water cooler in which the cooling air is mixed with the combustion air and the hot gases are cooled down by water injection to temperatures that the throttle valve can withstand. The combustion channel in the structural section and the water cooler are separated by a tube to separate the acoustics of the water cooler and the rest of the system to a certain degree, because acoustic waves hardly travel from the structural section through the tube (8) to the water cooler and back.

First, the acoustoelastic coupling is explained. Subsequently, the flame model and its use in the acoustoelastic model, as used for calculating the acoustic and structural responses during combustion, is treated. The implementation of temperature effects is

---
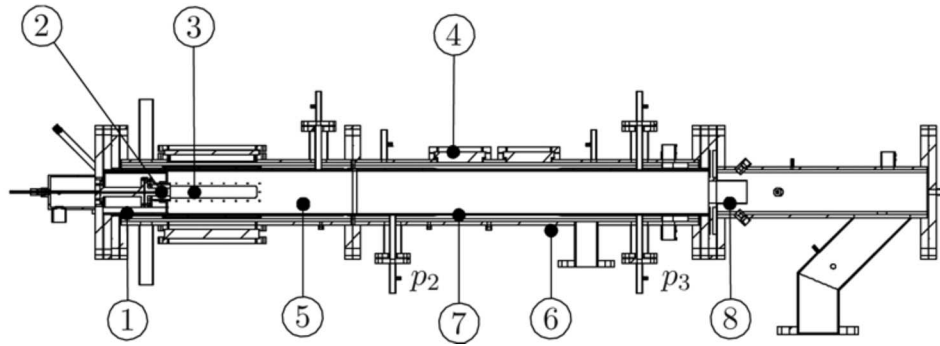
Fig. 1 Cross section of the test rig: 1=plenum, 2=burner, 3=combustion chamber, 4=windows, 5=liner, 6=pressure vessel, 7=thin liner part, and 8=exit tube

then described for the acoustic behavior and the structural behavior. Numerical and experimental results are then compared and conclusions are drawn.

2 Modeling

2.1 Acoustoelastic Model. Assuming that the effects of flow and viscosity are small, the governing equation for the acoustic domain is the wave equation as follows:

$$\frac{1}{c_0^2}\frac{\partial^2 p}{\partial t^2} - \rho_0 \frac{1}{\partial x_i}\left(\frac{1}{\rho_0}\frac{\partial p}{\partial x_i}\right) = 0 \qquad (1)$$

in which c_0 denotes the speed of sound, ρ_0 density, p is the fluctuating part of the pressure, x_i coordinate direction i $(i=1,2,3)$, and t time. The second term on the left-hand side can be rewritten as

$$\rho_0 \frac{1}{\partial x_i}\left(\frac{1}{\rho_0}\frac{\partial p}{\partial x_i}\right) = \rho_0\left(\frac{1}{\partial x_i}\left[\frac{1}{\rho_0}\right]\frac{\partial p}{\partial x_i} + \frac{\partial^2 p}{\partial x_i \partial x_i}\right) \qquad (2)$$

Density ρ_0 is of the order 1, pressure is of the order 10^5, and x is similar to the length of the combustion chamber and thus of the order 1. The first term on the right-hand side is therefore much smaller than the second and a simpler acoustic wave equation can be used as follows:

$$\frac{1}{c_0^2}\frac{\partial^2 p}{\partial t^2} - \frac{\partial^2 p}{\partial x_i \partial x_i} = 0 \qquad (3)$$

On the boundary, either pressure or velocity can be prescribed as follows:

$$p = 0 \qquad (4)$$

$$\frac{\partial p}{\partial n} = -\rho\frac{\partial^2 w}{\partial t^2} \qquad (5)$$

in which n is the unit normal on the boundary surface and w is the displacement in this direction. Discretization of the wave equation subject to these boundary conditions using the finite element method (FEM) leads to the following system of equations [5]:

$$\mathbf{M^p \ddot{p}} + \mathbf{K^p p} = -\mathbf{R^p} \qquad (6)$$

in which $\mathbf{M^p}$ is the acoustic mass matrix, $\mathbf{p}$ is the vector containing the nodal pressures, $\mathbf{K^p}$ is the acoustic stiffness matrix, a dot denotes differentiation with respect to time, and $\mathbf{R^p}$ contains the discretization of the prescribed boundary condition. The accelerations consist of prescribed accelerations contained in $\mathbf{R}$ (Eq. (10)) and, where the boundary is coupled to the structure, those of the structure $\mathbf{R^w}$. This generates a coupling mass matrix $\mathbf{M^{fs}}$ that depends on the accelerations from the structural problem and therefore the influence of the structure on the acoustic behavior is included.

Because the structure consists of thin flat plates, the plate bending equations (without membrane stresses) for a plate of uniform thickness and material properties are used to describe the dynamic structural behavior [6] as follows:

$$h\rho\frac{\partial^2 w}{\partial t^2} + D\left(\frac{\partial^4}{\partial x_1^4} + 2\frac{\partial^4}{\partial x_1^2 \partial x_2^2} + \frac{\partial^4}{\partial x_2^4}\right)w = -p \qquad (7)$$

in which ρ is the density and D is the bending stiffness given by

$$D = \frac{Eh^3}{12(1-\nu^2)} \qquad (8)$$

in which E is Young's modulus, h is the thickness of the plate, and ν is Poisson's ratio. The equations are discretized using shell elements [5], giving the following system of equations:

$$\mathbf{M^w \ddot{w}} + \mathbf{K^w w} = \mathbf{F^t} \qquad (9)$$

in which $\mathbf{M^w}$ is the structural mass matrix, $\mathbf{w}$ is the vector containing the nodal out-of-plane displacements and rotations, $\mathbf{K^w}$ is the structural stiffness matrix, and $\mathbf{F^t}$ is the vector containing the external loads (moments and forces). These external loads consist partially of the loads imposed by the acoustic pressure $\mathbf{F^p}$ and partially of structural external loads $\mathbf{F}$. Because the loads imposed by the acoustic domain on the structure are related to pressure times area, they generate a coupling stiffness matrix $\mathbf{K^{fs}}$ depending on the acoustic pressure. This means that the influence of the acoustics on the structural behavior is included. If the acoustic and structural meshes on the interface coincide, coupling the equations results in

$$\begin{bmatrix} \mathbf{M^w} & \mathbf{0} \\ \mathbf{M^{fs}} & \mathbf{M^p} \end{bmatrix}\begin{Bmatrix} \mathbf{\ddot{w}} \\ \mathbf{\ddot{p}} \end{Bmatrix} + \begin{bmatrix} \mathbf{K^w} & \mathbf{K^{fs}} \\ \mathbf{0} & \mathbf{K^p} \end{bmatrix}\begin{Bmatrix} \mathbf{w} \\ \mathbf{p} \end{Bmatrix} = \begin{Bmatrix} \mathbf{F} \\ \mathbf{R} \end{Bmatrix} \qquad (10)$$

These equations include two-way interaction between acoustic and structural behaviors. The asymmetric matrices are only created at interfaces that are marked as fluid-structure interfaces. For the determination of the matrices, reference is made to the ANSYS manual [7]. The total $\mathbf{M}$ and $\mathbf{K}$ matrices in this system of equations are asymmetric due to the off-axis $\mathbf{M^{fs}}$ and $\mathbf{K^{fs}}$ parts and therefore an asymmetric solver that is, in general, substantially slower than a symmetric solver is required. Furthermore, modal superposition cannot be applied for asymmetric matrices in the ANSYS software package used (which is version 8.1) and therefore a series of harmonic analysis is used to generate the frequency dependent responses. The coupling procedure was validated on a simple setup consisting of a stiff box covered with a flexible plate [8].

For the geometry considered in this paper, the acoustic field induces structural vibrations, but the vibrations only weakly influence the acoustic field. Thus, one-way coupling would probably
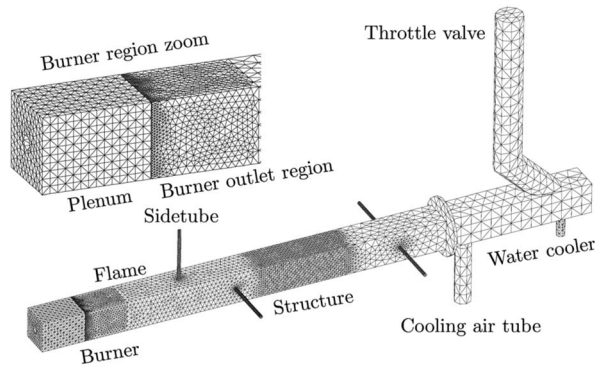
Fig. 2 Mesh of the acoustoelastic finite element model

be sufficient. However, this may not always be the case. When the vibration causes a net change in volume of the combustion chamber, the vibration can substantially influence the acoustics [9]. Furthermore, the cooling channel between the liner of the combustion chamber and the pressure vessel can also have a significant influence on the vibration of the wall, especially if there is substantial acoustic damping [10]. The method proposed allows for inclusion of such effects.

The finite element model used consists of the plenum, the combustion chamber, and the water cooler and is depicted in Fig. 2. It consists of linear acoustic elements. The inlet of the plenum consists of an acoustic decoupler plate and therefore a zero velocity boundary condition is imposed here for the acoustic domain. At the location of the throttle valve, also a zero velocity boundary is imposed. At the location of the burner, the flow path through the burner is meshed using linear acoustic elements, causing reflection due to the smaller cross-sectional area of the burner compared with the plenum and combustion chamber. No additional damping or reflection is specified in the burner flow path.

The sidetubes, in which the pressure sensors are located, have a specific acoustic absorption of 1 at the end, resulting in an anechoic end, simulating the acoustic absorber at the end of the tube. Details of the finite element implementation of this condition can be found in Ref. [7].

The structural model, consisting of linear shell elements, is present at the location of the thinnest part of the liner in the structural section of the test rig. The boundaries of this square tube section are taken as clamped, because the thicker liner parts should impose a clamped condition on the thinner part in between. The cooling passage between the liner and the pressure vessel as well as the pressure vessel itself are not included in the model, because their influence is mostly small [10].

2.2 Flame Model. The flame acts as an acoustic monopole source or a number of monopole sources. There are several methods to implement such a source in a finite element code, be it for flame noise calculations or with a thermoacoustic feedback mechanism. Nowak et al. [11] and Fannin [12] both used LMS SYSNOISE [13] and applied the same technique. They applied a velocity boundary condition on the acoustic domain at the location of the flame front, such that it generates a volume source that is equivalent to the unsteady heat release of the flame. Pankiewitz and Sattelmayer [14] employed COMSOL FEMLAB [15], which allows for more control on the way the finite element code works. They discretized the source term caused by unsteady heat release together with the wave equation, including the thermoacoustic feedback mechanism. The FEM package ANSYS does not allow for a direct implementation like Pankiewitz and Sattelmayer used. To model unsteady heat release, a volume source Q is used, which is defined as a nodal flow rate with dimensions (m^3/s^2) and which acts as a monopole source. This method is similar to that of Nowak et al. and Fannin, although the implementation is different.

The relation between this source and the unsteady heat release rate is first derived. The spectrum of the flame as autonomous source is subsequently discussed. Thermoacoustic feedback is not included, although it can have substantial influence on the acoustic response [16]. Methods to include this feedback mechanism include large eddy simulation using one-way coupling between acoustics and vibrations [17], transfer function formulations [10], and time domain simulations [14].

The inhomogeneous wave equation describing the relation between acoustics and specific heat release rate $\bar{q}$ is given by [18]

$$\frac{1}{c_0^2}\frac{\partial^2 p}{\partial t^2} - \frac{\partial^2 p}{\partial x_i \partial x_i} = \frac{\gamma-1}{c_0^2}\frac{\partial \bar{q}}{\partial t} \tag{11}$$

in which γ is the ratio of specific heats c_p/c_v, with c_p the specific heat at constant pressure and c_v the specific heat at constant volume. Only one monopole source is used as a representation of the flame and therefore the source is lumped to one node. Heat release is therefore expressed as the volume integrated heat release rate q with dimensions (J/s), integrated over the entire flame zone. The right-hand side of Eq. (11) thus becomes

$$\int_V \frac{\gamma-1}{c_0^2}\frac{\partial \bar{q}}{\partial t}dV = \frac{\gamma-1}{c_0^2}\frac{\partial q}{\partial t} \tag{12}$$

A relation between the nodal flow rate Q used in the finite element calculations and this volume integrated heat release rate q is needed. The dimensions of Eq. (12) are in kg/s^2. The nodal flow rate is expressed in m^3/s^2 and therefore a division by the mean density is still needed. The nodal flow rate can thus be expressed in terms of the volume integrated heat release rate as

$$Q = \frac{\gamma-1}{\rho_0 c_0^2}\frac{\partial q}{\partial t} \tag{13}$$

Assuming harmonic perturbations as $q = \hat{q}e^{i\omega t}$, this expression can be written as

$$\hat{Q} = \frac{i\omega(\gamma-1)}{\rho_0 c_0^2}\hat{q} \tag{14}$$

The calculations and measurements in this paper are all for steady combustion. An expression is therefore still needed for the frequency dependency of the heat release rate $\hat{q}$. This dependency can be described by

$$\hat{q} = Af^n \tag{15}$$

in which A is a constant, n is the exponent-that determines the shape of the spectrum, and f is frequency. By combining Eqs. (14) and (15), the acoustic volume source, representing the flame, can now be written as

$$\hat{Q} = \frac{i2\pi A(\gamma-1)f^{n+1}}{\rho_0 c_0^2} \tag{16}$$

Experiments to determine the heat release were performed on the test rig by measuring CH* radicals using chemiluminescence [19]. The presence of CH* is linearly related to heat release [20]. The spectrum created from these measurements is almost flat, suggesting that, for the frequency range measured (up to 400 Hz), the heat release rate spectrum is flat. The parameter n is therefore taken as 0.

In literature, free field acoustic pressure measurements are often made to characterize flame noise. It can be shown that for free-field radiation (outside a combustion chamber) from an acoustic volume source Q (which acts as a monopole source of sound), the pressures in the field are proportional to Q [21]. The pressure spectrum measured in the free field, as found in literature, can therefore be used to determine the exponent n. Below 1 kHz, the value of 0 is also found in literature [22,23]. For turbulent noise without combustion, a clear peak is normally found in the pres-
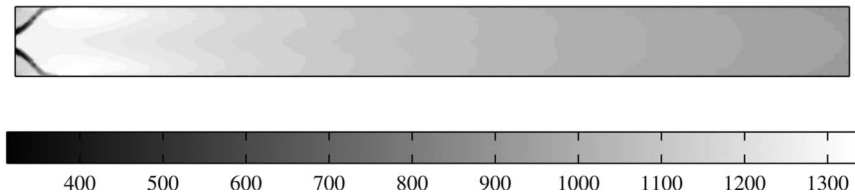
Fig. 3 Cross section of the temperature field in the combustion chamber from CFD used in the FEM model (°C)

sure spectrum, but this peak disappears for the reacting flow [24]. The volume source applied here is therefore given by

$$\hat{Q} = Bf \qquad (17)$$

Constant B has been obtained by comparing experimental and numerical results for pressure sensor p_2 and is 1×10^{-3} m^3 s^{-1}.

2.3 Temperature Dependent Acoustic Properties. For the acoustic behavior of the combustion chamber during combustion, the density and speed of sound are adjusted to the temperature field calculated with computational fluid dynamics (CFD), which is depicted in Fig. 3 for combustion at a pressure of 1.5 bars with an air factor of 1.8 and a thermal power of 125 kW. The mesh size of the CFD model should be at least as small as the smallest flow details to be resolved (for more details on the CFD model, see Ref. [19]), whereas the acoustic mesh size is prescribed by the geometry and the smallest acoustic wavelength to be solved. Because the mixing of fuel and air as well as the combustion process require high spatial detail, the acoustic mesh is much coarser than the CFD mesh. The temperature data of the CFD mesh are therefore interpolated on the acoustic mesh. A Delaunay triangulation is first made of the nodes from the CFD mesh. This makes a set of tetrahedral elements from the given nodes, in which no nodes are contained in each tetrahedral. For each node in the acoustic mesh, these tetrahedral elements for the CFD mesh are used to find the point in the CFD mesh nearest to the node in the FEM mesh. The temperature from this node in the CFD mesh is then used as nodal temperature for the FEM mesh. Because the CFD mesh is much finer than the FEM mesh, especially in regions of high thermal gradients, this interpolation is accurate enough. The temperature in the water cooler is taken the same as the outlet temperature of the combustion chamber, which is sufficient to provide a realistic acoustic boundary condition for the combustion chamber.

2.4 Temperature Dependent Structural Properties. The properties of the structure are a function of temperature (just as those of the fluid). Figure 4 shows the dependence of Young's modulus on temperature for Hastelloy X [25], which is a high
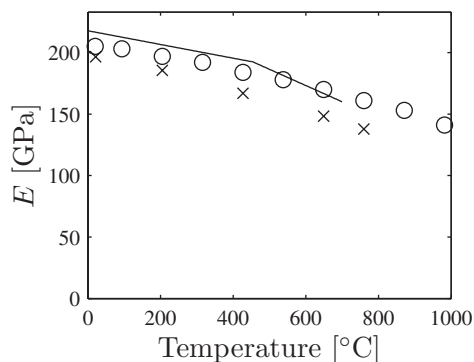
performance alloy used in gas turbines, for SS310 [26], which is used in the test rig and for an expression for a typical stainless steel [27]. All three materials show the same behavior with Young's modulus dropping slowly from just above 200 GPa at 20°C to 150 GPa at 800°C. The eigenfrequencies of a plate, as indication of the vibrational behavior of the liner, scale with the root of Young's modulus. Young's modulus decreases by approximately 25% for a temperature increase from 20°C to 800°C. This causes a change in eigenfrequency of 13%. A very accurate prediction (better than ±20°C) of the temperature of the structure is therefore not really important to determine the material properties. However, different temperatures over the structure may lead to thermal stresses [28], which can significantly influence eigenfrequencies and even result in buckling. This is not further examined in this paper. The temperature T_s of the structure is taken as the average of the temperature in the combustion chamber T_{comb} and in the cooling passage T_{cool}, so [29]

$$T_s = \frac{T_{\mathrm{comb}} + T_{\mathrm{cool}}}{2} \qquad (18)$$

The structural material behavior is governed by Young's modulus E and Poisson's ratio ν. Values for Poisson's ratio at high temperatures are rarely measured. Measurements at lower temperatures show little temperature dependence, with values ranging from 0.29 to 0.31. A constant Poisson's ratio of 0.3 is therefore used here. The density is also taken constant as 7800 kg/m^3.

In the test setup, the thin part of the structure is entirely downstream of the flame. CFD calculations show that the gases in the combustion chamber at the location of the thin section have a temperature of about 1380 K (1107°C). The cooling air enters the cooling passage at 20°C and leaves it at around 300°C. The cooling air temperature is therefore taken as 160°C, which gives a temperature for the structure of 633°C (906 K). At this temperature, Young's modulus is approximately 150 GPa and this value is used for the calculations.

Figure 5 shows the construction for liner temperature measurements schematically and the measured temperature of the liner during the measurement. Two thermocouples are mounted on the thick parts of the structural liner, just before and just after the flexible section. The thermocouples lie against the liner, but are not embedded in it, and are partially shielded from the cooling air by a protective shield. The measured temperature before the flexible section is 580°C and after the flexible section 530°C. Because the thermocouples are not embedded in the liner material and are only partially protected from the cooling air, these readings are indicative and are likely to be lower than the real values. The temperature was also measured through the laser vibrometer windows using a pyrometer, which resulted in a temperature of 720°C. Considering the weak dependence on temperature of the structural properties and the range of the measured temperatures, Young's modulus estimate of 150 GPa is good enough.

3 Experiments

A test rig with a thermal power of 500 kW at a maximum pressure of 5 bars has been built, in which measurements are carried out on the combustion process, the acoustic response in the

Fig. 4 Temperature dependence of Young's modulus E. (—) typical stainless steel, (×) stainless steel 310, and (○) Hastelloy X.
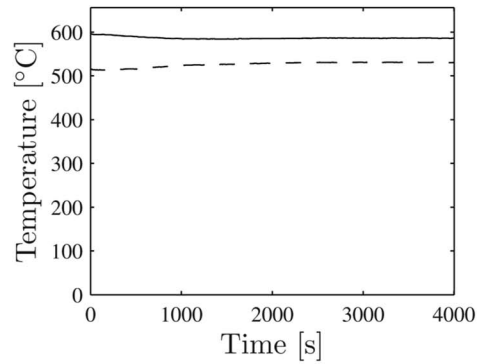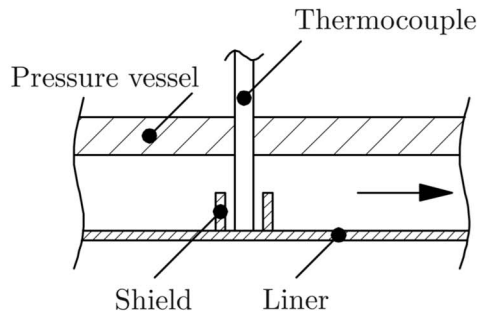
Fig. 5 Construction for liner temperature measurement (left) and the temperature measured (right). (—) before the flexible section and (– –) after the flexible section.

combustion chamber, and the resulting vibrations of the liner. In the combustion zone, windows are available in both pressure vessel and liner. The already mentioned CH* chemiluminescence measurements were made through these windows to measure the heat release by the flame.

To obtain the acoustic response of the system due to combustion, pressure measurements are made using relatively cheap Kulite pressure transducers. To allow measurements at high temperatures, they are placed in an anechoic sidetube. The high static pressure is compensated by connecting the back intake from the transducer by a long thin tube, a volume, and another thin tube to the test rig. The thin hoses and volume diminish dynamic pressures on the back side, providing a static back pressure. The sensor signal is amplified and subsequently acquired using a SIGLAB data acquisition system at a sample frequency of 2.56 kHz. In this paper, measurements made using pressure sensors p_2 and p_3 are used (see Fig. 1); other sensors yielded highly similar results.

Structural vibrations are measured using a Polytec laser vibrometer and a traverse system. Because the liner is surrounded by a pressure vessel, glass windows have been constructed in the pressure vessel to allow optical access to the liner. The measurements in this paper have all been performed through a slit window in the pressure vessel and therefore lie on one line. The slit window lies on the same location as the square windows visible in Fig. 1, although on a different side. The traverse system moves the laser vibrometer to a point. The SIGLAB system is then used to acquire the laser vibrometer signal during a specified period. Subsequently, the traverse system moves the laser vibrometer to the next point and the next measurement is made. For further information on the test rig, reference is made to Ref. [10].

4 Results

In this section, the measured and calculated acoustic responses are first treated. Subsequently, the structural response is discussed.

4.1 Acoustic Response. Table 1 lists the calculated and measured acoustic eigenfrequencies of the combustion chamber. The acoustic modes are denoted by a subscript a and numbered after the number of half waves in the three directions, so the $(100)_a$ has

Table 1 Calculated and measured acoustic eigenfrequencies (Hz) of the combustion system during combustion

Mode	$(100)_a$	$(200)_a$	$(300)_a$	$(400)_a$	$(500)_a$
Expt.	250	445	639	846	1050
FEM	259	432	622	812	1011
LES-Helmholtz [30]	250	433	642	844	1045
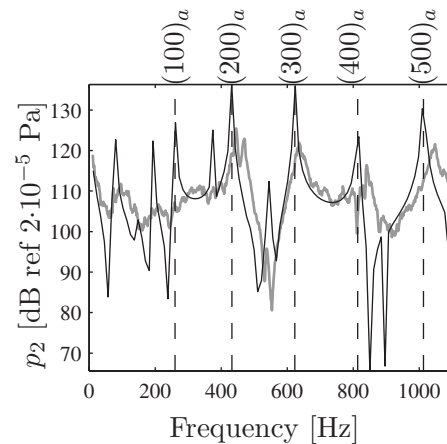
Fig. 6 Calculated (black) and measured (gray) autospectra for sensor p_2 (combustion chamber) with flame noise excitation. The dashed lines denote calculated acoustic eigenfrequencies.

Table 2 Calculated and measured structural eigenfrequencies during combustion (Hz)

Mode	$(11)_{ss}$	$(12)_{ss}$	$(11)_{h1}$	$(11)_{h2}$	$(12)_{h1}$	$(13)_{ss}$	$(11)_{cc}$	$(13)_{h1}$
Expt.	195	257	284	302	323	342	411	542
Model	166	242	237	237	300	361	329	406

approximately one half wave[2] in the length direction and none in the other directions (e.g., it is a one-dimensional mode). The acoustic eigenfrequencies that are predicted show an excellent match with the experimentally determined ones. Acoustic calculations using a temperature field from a large eddy simulation (LES) in a Helmholtz solver show highly similar acoustic eigenfrequencies (Ref. [30] and Table 1), which is a further indication that these results are correct.

Figure 6 shows the pressure measured by sensor p_2, which is located in the combustion chamber (see also Fig. 1), and the response to the volume source representing the flame calculated with the acoustic finite element model. The measured and calculated pressure amplitudes agree well. In both measurement and calculation, high acoustic response is found for the second and higher acoustic eigenmodes of the combustion chamber. The am-

---

[2]Because the boundary conditions of the combustion chamber are not zero velocity at the ends due to the plenum and the water cooler, not exactly one half wave fits in.

$(11)_{ss}$ $(11)_{h1}$ $(11)_{cc}$
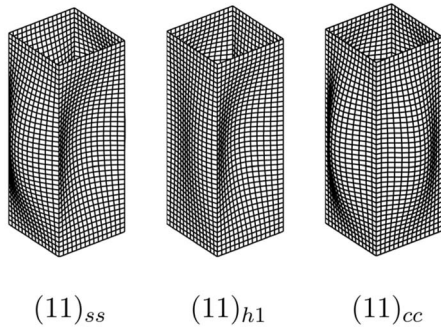
Fig. 7 Different structural mode shapes of the (11) mode

Fig. 8 Shape of the liner in the structural section; gases flow from left to right

$(11)_{ss}$ $(12)_{ss}$ $(11)_{h1}$ $(11)_{h2}$ $(12)_{h1}$ $(13)_{ss}$ $(11)_{cc}$ $(13)_{h1}$
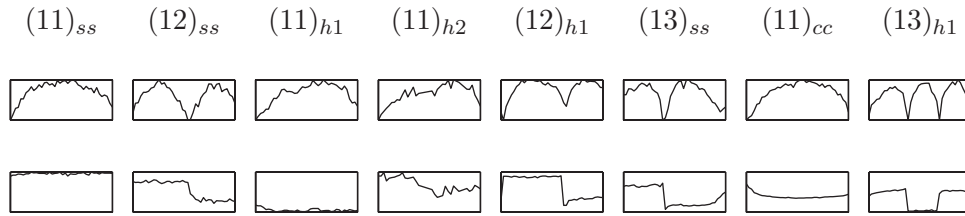
Fig. 9 Amplitude (top) and phase with respect to pressure sensor p_3 (bottom) of the mode shapes measured during combustion

plitude of the resonances is higher in the calculations, which is a clear indication that there is some acoustic damping present in the experimental setup. The first acoustic mode of the combustion chamber, which is the $(100)_a$ mode, is not present very strongly in the measurement, which is caused by a feedback mechanism that damps the acoustic oscillations [10]. Further damping mechanisms include damping in the burner, damping at the exit, damping caused by the turbulent flow field, and acoustic losses through liner vibrations.

4.2 Structural Response. The structural eigenfrequencies are obtained from the autospectrum of the laser vibrometer signal, which is averaged over all the measurement points. This assures that modes are not missed due to measurements on a nodal line. The spectrum is divided by the average pressure measured by the acoustic sensors to suppress acoustic modes. The resulting measured and calculated structural eigenfrequencies are listed in Table 2.

The structural eigenfrequencies are also numbered according to the number of half waves seen on a side of the square tube in a direction, so the (12) mode has two half waves in the length direction and one half wave in the width direction. The subscripts ss, $h1$, $h2$, and cc denote different combinations on the different sides of the square tube that can arise of such a pattern (Fig. 7). Subscript ss stands for simply supported and is used for modes in which the corners rotate to create a structural boundary condition for a side of the liner, which is similar to a simply supported plate. Sides that connect at a corner move in opposite directions for such modes. Subscript cc is used when the corners hardly rotate, giving a clamped boundary condition and sides that move in equal directions. Subscripts $h1$ and $h2$ are used for modes with different vibration patterns on different sides (modes that always come in pairs, one a 90 deg rotated version of the other).

Table 2 shows that the eigenfrequencies do not match well. This has several causes. First, the structural model only includes the thin part of the liner in the structural section (Fig. 8). The structural boundaries of this thin section are modeled as clamped, but the thick sections are only 4 mm thick and therefore this boundary is not entirely stiff. This is also observed in structural models that include the thick sections. A second cause for the differences are the welds made during the production of the liner (Fig. 8), which
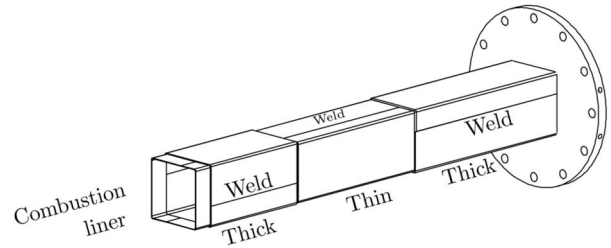
are not taken into account in the structural model. The eigenfrequencies can also change due to acoustoelastic coupling [31], prestress, and irregular heating, which are all not taken into account in the model.

The measured mode shapes behind the slit window are depicted in Fig. 9. By comparing Fig. 9 with Fig. 7, it can be seen that, although the match between calculated and measured eigenfrequencies is not very well, the mode shapes match well. The structural model used can therefore still give relevant results. The only exception is the $(13)_{ss}$ mode, for which its measured shape looks like a (12) type of mode. This mode shape propagates into the thicker parts of the structural liner, which are not visible behind the slit window. This could be an explanation for the fact that the shape behind the slit does not really look like the $(13)_{ss}$ shape. Another explanation could be that the mode shape has been changed due to, for instance, thermal prestress.

Figure 10 shows the average vibration level of the liner and the part correlated with p_3.[3] Above 200 Hz, the measured vibration is very coherent with the measured pressure, which shows that the structure responds to the acoustic field generated in the combustion chamber by the flame. The measured vibration level matches well with the calculation, starting near −120 dB (1 μm/s) for low frequencies and increasing to −60 dB (1 mm/s) around 500 Hz, after which it decreases again.

In Fig. 10, the structural eigenfrequencies are depicted by dotted lines, whereas the dashed lines denote acoustic eigenfrequencies. The first two structural eigenfrequencies, $(11)_{ss}$ and $(12)_{ss}$, show very distinct vibration peaks in the measurement (Fig. 10(a)). In the calculation (Fig. 10(b)), the peaks are not visible at all. This is caused by the lack of any welds or other asymmetry in the structural model. Because the acoustic field is almost one dimensional in the model, the symmetric acoustic pressure load on the liner does not couple with these asymmetric structural mode shapes and therefore these modes are not excited. In the experiment, the acoustic excitation is not entirely symmetric and the mode shapes are not symmetric either (because of the welding), so

---

[3]The correlated part is determined as $S_{11} = S_{12}S_{21}/S_{22}$, in which S_{22} denotes an autospectrum and S_{12} denotes a cross spectrum [32].
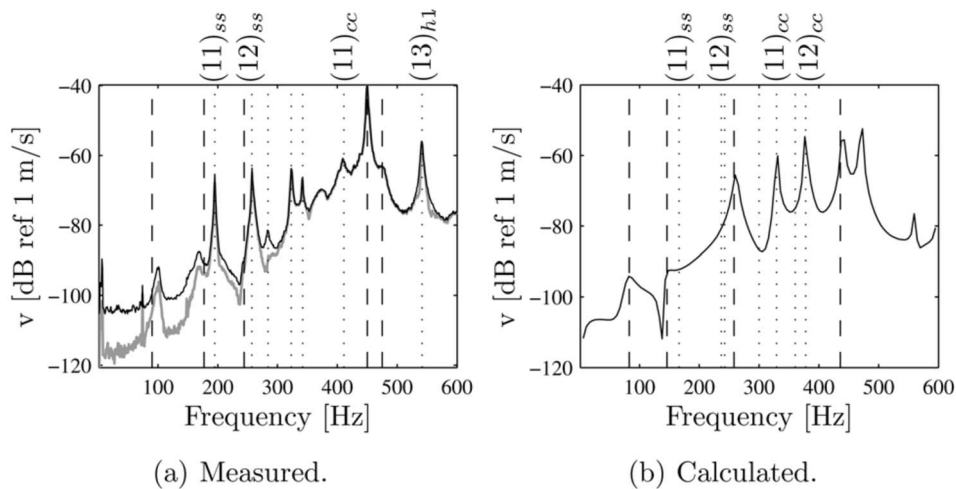
Fig. 10 Measured and calculated autospectra of the mean vibration of the liner; gray is the part correlated with p_3. The dashed lines denote acoustic eigenfrequencies and the dotted lines denote structural eigenfrequencies.

these modes are excited.

To get an indication of the influence of asymmetry, Fig. 11 shows the calculated response when an asymmetric structural model is made by giving the elements at the weld location Young's modulus of 2100 GPa. In this model, the $(11)_{ss}$ mode has an eigenfrequency of 183 Hz and the $(12)_{ss}$ has an eigenfrequency of 274 Hz. It is clear that this model does show the high vibration amplitudes for these modes seen in the measurement.

5 Conclusions

An acoustoelastic modeling procedure has been developed to predict structural vibrations in combustion chambers, including full interaction between acoustics and structural vibrations. Temperature fields for the fluid are extracted from a Reynolds averaged Navier Stokes (RaNS) CFD model including heat losses and structural temperatures are also calculated using the CFD results. These temperatures are used in a fully coupled acoustoelastic finite element model, in which the flame is represented by an acoustic volume source. The acoustic response of this model is successfully validated with measurements made in a custom built test rig that is representative for an industrial combustion system. The predicted structural vibration shapes also match with the experiment. Coupling of the structural and acoustic model in a fully
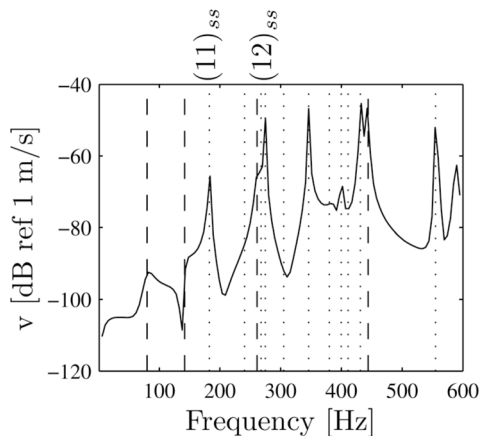
coupled fashion yields a predicted structural vibration spectrum that matched well with the vibration spectrum found in the experiment, indicating that the coupled model is sufficiently accurate.

References

[1] Lieuwen, T. C., and Yang, V., eds., 2005, *Combustion Instabilities in Gas Turbine Engines: Operational Experience, Fundamental Mechanisms, and Modeling*, American Institute of Aeronautics and Astronautics, Reston, VA.
[2] Lieuwen, T., 2003, "Modeling of Premixed Combustion-Acoustic Wave Interactions: A Review," J. Propul. Power, **19**(5), pp. 765–781.
[3] Fahy, F., 1985, *Sound and Structural Vibration: Radiation, Transmission, and Response*, Academic, London.
[4] Junger, M. C., and Feit, D., 1972, *Sound, Structures, and Their Interaction*, MIT, Cambridge, MA.
[5] Cook, R. D., Malkus, D. S., and Plesha, M. E., 2002, *Concepts and Applications of Finite Element Analysis*, Wiley, New York.
[6] Hansen, C. H., and Snyder, S. D., 1997, *Active Control of Noise and Vibration*, E&FN Spon, London.
[7] 2004, ANSYS HTML Online Documentation, ANSYS 8.1, Ansys Inc.
[8] Huls, R. A., van Kampen, J. F., Kok, J. B. W., and de Boer, A., 2003, "Fluid Structure Interaction to Predict Liner Vibrations in an Industrial Combustion System," *Proceedings of the Tenth International Congress on Sound and Vibration*, Stockholm, Sweden.
[9] Huls, R. A., Kok, J. B. W., and de Boer, A., 2003, "Vibration of the Liner in an Industrial Combustion System Due to an Acoustic Field," *Proceedings of the International Forum on Aeroelasticity and Structural Dynamics*, Amsterdam, The Netherlands.
[10] Huls, R. A., 2006, "Acousto-Elastic Interaction in Combustion Chambers," Ph.D. thesis, University of Twente, The Netherlands.
[11] Nowak, D., Bellucci, V., Cerny, J., and Toqan, M., 2004, "Numerical Modeling of Thermoacoustic Oscillations in a Gas Turbine Combustion Chamber," *Proceedings of the 11th International Congress on Sound and Vibration*, St. Petersburg, Russia.
[12] Fannin, C. A., 2000, "Linear Modeling and Analysis of Thermoacoustic Instabilities in a Gas Turbine Combustor," Ph.D. thesis, Virginia Polytechnic Institute and State University, Blacksburg, VA.
[13] LMS SYSNOISE, http://www.lmsintl.com/SYSNOISE, LMS International, Researchpark Z1, Interleuvenlaan 68, 3001 Leuven, Belgium.
[14] Pankiewitz, C., and Sattelmayer, T., 2003, "Time Domain Simulation of Combustion Instabilities in Annular Combustors," ASME J. Eng. Gas Turbines Power, **125**(3), pp. 677–685.
[15] COMSOL FEMLAB, http://www.comsol.com, COMSOL AB, Tegnérgatan, 23, SE-111 40, Stockholm, Sweden.
[16] Huls, R. A., de Boer, A., and Kok, J. B. W., 2004, "A Transfer Function Approach to Structural Vibrations Induced by Thermoacoustic Sources," Proceedings of the 11th International Congress on Sound and Vibration, St. Petersburg.
[17] Huls, R. A., Sengissen, A. X., van der Hoogt, P. J. M., Kok, J. B. W., Poinsot, T., and de Boer, A., 2007, "Vibration Prediction in Combustion Chambers by

Fig. 11 Calculated autospectrum of the mean vibration of the liner for an asymmetric structure

Coupling Finite Elements and Large Eddy Simulations," J. Sound Vib., **304**(1–2), pp. 224–229.

[18] Dowling, A. P., 2003, "Singing Flames—The Coupling of Acoustics and Combustion," *Proceedings of the Tenth International Congress on Sound and Vibration*, Stockholm, Sweden.

[19] van Kampen, J. F., 2006, "Acoustic Pressure Oscillations Induced by Confined Turbulent Premixed Natural Gas Flames," Ph.D. thesis, University of Twente, The Netherlands.

[20] Hardalupas, Y., and Orain, M., 2004, "Local Measurements of the Time-Dependent Heat Release Rate and Equivalence Ratio Using Chemiluminescent Emission From a Flame," Combust. Flame, **139**, pp. 188–207.

[21] Bies, D. A., and Hansen, C. H., 1996, *Engineering Noise Control, Theory and Practice*, 2nd ed., E&FN Spon, London.

[22] Flemming, F., Nauert, A., Sadiki, A., Janicka, J., Brick, H., Piscoya, R., Ochmann, M., and Koeltzsch, P., 2005, "A Hybrid Approach for the Evaluation of the Radiated Noise From a Turbulent Non-Premixed Jet Flame Based on Large Eddy Simulation and Equivalent Source & Boundary Element Methods," *Proceedings of the 12th International Congress on Sound and Vibration*, Lisbon, Portugal.

[23] Rajaram, R., and Lieuwen, T., 2002, "Parametric Studies of Acoustic Radiation From Turbulent Flames," Paper No. AIAA-2002-3864.

[24] Rajaram, R., and Lieuwen, T., 2004, "Effect of Approach Flow Turbulence

[25] Characteristics on Sound Generation from Premixed Flames," Paper No. AIAA-2004-0461.

[25] Haynes International, 2005, Hastelloy X®, Haynes International.

[26] Haynes International, 2005, Haynes® HR-120™, Haynes International.

[27] Zinkle, S. J., Robertson, J. P., and Klueh, R. L., 1998, "Thermophysical and Mechanical Properties of Fe-(8-9)%Cr Reduced Activation Steels (4/25/98 Draft)," Technical Report, Oak Ridge National Laboratory.

[28] Tinga, T., van Kampen, J. F., de Jager, B., and Kok, J. B. W., 2007, "Gas Turbine Combustor Liner Life Assessment Using a Combined Fluid/Structural Approach," ASME J. Eng. Gas Turbines Power, **129**, pp. 69–79.

[29] Lefebvre, A. H., 1999, *Gas Turbine Combustion*, 2nd ed., Taylor & Francis, London.

[30] Sengissen, A. X., van Kampen, J. F., Huls, R. A., Stoffels, G. G. M., Kok, J. B. W., and Poinsot, T., 2007, "LES and Experimental Studies of Cold and Reacting Flow in a Swirled Partially Premixed Burner With and Without Fuel Modulation," Combust. Flame, **150**(1–2), pp. 40–53.

[31] Huls, R. A., Kok, J. B. W., and de Boer, A., 2003, "Vibration of the Liner in an Industrial Combustion System Due to an Acoustic Field," *Proceedings of the International Forum on Aeroelasticity and Structural Dynamics*, Amsterdam, The Netherlands.

[32] Lavrentjev, J., Abom, M., and Bodén, H., 1995, "A Measurement Method for Determining the Source Data of Acoustic Two-Port Sources," J. Sound Vib., **183**(3), pp. 517–531.

An Acoustic-Energy Method for Estimating the Onset of Acoustic Instabilities in Premixed Gas-Turbine Combustors

Z. M. Ibrahim

F. A. Williams

S. G. Buckley

Center for Energy Research,
Department of Mechanical and Aerospace
Engineering,
University of California, San Diego,
La Jolla, CA 92093

C. Z. Twardochleb
Combustion Technology,
Solar Turbines Incorporated,
San Diego, CA 92108

For given acoustic frequencies of premixed gas-turbine combustors, a classical method not currently in use is explored for assessing whether acoustically driven oscillatory combustion will occur. The method involves cataloging linear amplification and attenuation mechanisms and estimating magnitudes of their rates. Linear approximations to nonlinear mechanisms are included in an effort to obtain a reasonably complete description. A stability index is defined such that oscillation is predicted to occur when the value of the index exceeds unity. The method is tested on the basis of new experiments and experimental data available in literature. Moderate success is achieved in rationalizing these experimental results. The objective of the method is to enable quick and inexpensive decisions to be made for a wide variety of potential design configurations and operating conditions, without the complexity of computational fluid dynamics. The approach therefore may complement other approaches already in use. [DOI: 10.1115/1.2938393]

Introduction

Many current combustor designs in the gas-turbine industry employ lean premixed combustion for the purpose of mitigating pollutant emissions. Such combustors, however, have been prone to combustion oscillations that detract from performance, reduce combustor lifetimes, and increase operating expenses. Economical tools to help minimize the chances of encountering oscillatory combustion in new and existing combustor designs for low-emission gas turbines are worthy of investigation.

Significant advances in computational approaches for predicting oscillatory combustion have been achieved in recent years [1]. Although fully resolved direct-numerical simulation of turbulent combustion in practical-scale combustors remains beyond current capabilities, there are a variety of well-developed modeling approaches employing different types of computational fluid dynamics (CFD), e.g., large eddy simulation approaches [2], that now can be brought to bear on the problem. Another class of modeling approaches works with a flame transfer function which, based on a flame model, ultimately provides both the oscillation frequency and the amplification rate of an acoustic disturbance [3–5]. Nonlinear CFD methods, including approaches employing Galerkin or finite-difference techniques [1,6,7], yield predictions of both frequencies and limiting oscillation amplitudes, dependent, of course, on the turbulence and combustion models employed. Since all such approaches are computationally intensive, there is motivation for investigating less expensive approaches that are capable of addressing a wide variety of combustor configurations and operating conditions in a reasonable amount of time.

Advantage may be taken of the fact that observed oscillation frequencies often do not differ greatly from natural acoustic frequencies of the combustion chamber. Determination of the frequency may then be treated separately from determination of whether amplification occurs. In the present work, it is assumed that potential oscillation frequencies will be identified indepen-

dently, from acoustic analysis, parallel CFD investigations, experiments or estimates based on experience, and the likelihood of oscillation occurring is therefore assessed as a function of frequency. The likelihood is estimated from analysis of amplification and attenuation rates by different physical and chemical mechanisms presumed to occur within the combustion system. Since acoustic amplification and attenuation are fundamentally linear concepts, linear approximations to nonlinear processes are employed in this approach.

We introduce simplified models of potentially relevant processes including, for example, different flame configurations ranging from distributed reactions to localized heat release, and different interaction mechanisms, such as pressure-sensitive combustion and mixture-ratio variations. Time lags play a central, crucial role in these models, which make use of simplified descriptions for approximating mode shapes of acoustic fields. The user must estimate the combustor and operational parameters as inputs to the model to obtain the amplification coefficients and time lags. The output is the stability index, which determines whether amplification or damping is likely to occur as a function of frequency. The approach is shown to be capable of explaining a number of experimental observations, thereby providing some confidence in the utility of the method in future applications.

Summary of the Basic Formulation

Elements of the problem formulation have been presented previously [8]. Beginning with a formal definition of the acoustic energy [9,10], an amplification term, such that the energy increases with time t in proportion to $e^{2\alpha t}$, can be identified as

$$\alpha = \left[\frac{-\int_A \langle p' u'_i \rangle dA_i - \int_A \langle e \overline{u_i} \rangle dA_i + \int_V \langle \Phi \rangle dV}{2\langle \hat{e} \rangle V} \right] \quad (1)$$

where p and u_i denote pressure and velocity, Cartesian tensor notation with the summation convention being adopted, dA_i is the outward-pointing surface area element of the chamber (which has a total surface area A), V is its volume, e represents the local instantaneous acoustic energy density, and Φ is the difference between the local instantaneous acoustic amplification and attenuation rate per unit volume. Notation adopted throughout will be that primes denote acoustic perturbations, overbars denote local

average values, angular brackets denote a time average over an acoustic oscillation cycle, a caret denotes a volume average over the entire chamber, and a tilde denotes an acoustic oscillation's amplitude. Turbulent fluctuations are not identified explicitly in this formulation, it is convenient to include them implicitly as part of the unperturbed mean flow.

In Eq. (1),

$$e = \frac{p'^2}{2\gamma\overline{p}} + \overline{\rho}\frac{u'_i u'_i}{2} \tag{2}$$

where ρ denotes density and γ is the ratio of specific heats, and

$$\Phi = \frac{\gamma-1}{\overline{\rho c^2}}p'q' - \frac{\partial u'_i}{\partial x_j}\boldsymbol{\tau}'_{ij} \tag{3}$$

c representing the speed of sound, $\boldsymbol{\tau}_{ij}$ the viscous stress tensor, and q the rate of heat release per unit volume. The three terms in the numerator of Eq. (1) describe, respectively, the boundary work, the acoustic energy advected across the control surface by the mean flow, and the net internal acoustic amplification rate, while the denominator is twice the acoustic energy in the chamber, the average acoustic energy per unit volume given by

$$\langle \hat{e} \rangle = \frac{1}{T}\int_0^T \frac{1}{V}\int_V e\,dV\,dt \tag{4}$$

in which T denote the oscillation period.

A simple, generic way of expressing acoustic pressure and velocity fluctuations in cylindrical coordinates in the absence of a radial dependence is

$$p'(x,\theta,t) = \widetilde{p}\cos(\omega t)\cos(kx)\cos(m\theta)$$

$$u'(x,\theta,t) = \left(\frac{\widetilde{p}}{\rho c}\right)\cos(\omega t + \varphi)\cos(kx + \ell)\cos(m\theta + \psi) \tag{5}$$

where t is the time, x is the axial coordinate, u denotes the component of velocity in the direction of wave propagation, typically the x direction, θ is the azimuthal angle, ω denotes frequency, and k and m are the wave numbers in the axial and circumferential directions, respectively, while φ, ℓ, and ψ denote phase differences between the velocity and pressure perturbations. Although radially dependent acoustic perturbations generally involve Bessel functions [10], they typically are of higher frequency and of lesser importance, and therefore when they are included, they will be approximated by additional sinusoidal factors in Eq. (5) dependent on the radius. The phase angles appearing in Eq. (5) depend on the boundary conditions.

Several mechanisms make contributions to α in Eq. (1). Some contributions are positive and are denoted by α_{amp}, while others are negative, and their magnitudes are denoted by α_{damp}. A stability index may then be defined as the ratio of the sum of amplification rates to the sum of attenuation rates,

$$S(\omega) = \frac{\Sigma\,\alpha_{amp}}{\Sigma\,\alpha_{damp}} \tag{6}$$

This index may be used to examine all frequencies in the region of interest (typically around the acoustic natural modes of the geometry being studied). With this definition, $S(\omega) > 1$ indicates the possibility of oscillations while $S \leq 1$ indicates a neutral or damped system.

Models for Perturbations of the Rate of Heat Release

All terms in the numerator of Eq. (1) contribute to α and thereby to $S(\omega)$ of Eq. (6). The last term, however, is of major importance to gas-turbine oscillatory combustion. The first term, the boundary work, is of dominant importance for acoustic instabilities in solid-propellant rockets, but in gas turbines, it is at most an attenuation term at the walls, if the walls are lined with Helm-

holtz resonators, for example. The second term, the difference between the advection of acoustic energy into the chamber at the inlet and the advection out at the exit, typically is not negligible locally, but the inward and the outward advection tend to cancel, including turbulent contributions thereto, so that often the net contribution is not dominant. The third term, the difference between the net Rayleigh-criterion amplification and the homogenous acoustic damping according to Eq. (3), generally has components in each of these categories that cannot be neglected. Wall damping, for example, often is not negligible and has an influence described by a boundary-layer treatment of the last term in Eq. (3) [10], and damping by liners, which could be viewed as coming from either the first term in Eq. (1) or the last term in Eq. (3), generally always needs to be taken into account in practical combustors. The main amplification comes from the first term in Eq. (3), and therefore ultimately it requires relating the perturbations in the rate of heat release to the pressure perturbations. If only this term is retained, then Eq. (1) becomes

$$\alpha = \frac{(\gamma-1)}{2\overline{\rho c^2}\langle\hat{e}\rangle V}\int_V \langle p'q'\rangle dV \tag{7}$$

Different mechanisms for producing this kind of coupling are addressed here.

Pressure-Sensitive Reactors With Spatially Distributed Reactions Having Fixed Time Lags. One of the earliest models considered was the $n-\tau$ model, first introduced by Crocco and Cheng [11] in the 1950s during a period of research aimed at understanding oscillations in liquid-propellant rocket engines. The model starts from the observation that the rate of heat release q depends on local pressure, concentrations, and temperatures of reactants. Acoustic pressure fluctuations give rise to fluctuations in the rate of heat release, but it takes some time τ for the heat-release rate to respond to pressure because of finite-rate chemistry or transport. To describe this, the heat-release rate can then be taken as proportional to the pressure raised to a power (i.e., $q \propto p^n$), with the pressure evaluated at a time τ earlier, the value of which is locally fixed by the processes occurring at the point in question. Perturbing the resulting expression and linearizing the outcome gives what has been referred to as the $n-\tau$ model,

$$q' = n\overline{q}\frac{p'(t-\tau)}{\overline{p}} \tag{8}$$

With this model, the heat-release-rate perturbation at any particular position in the chamber may be considered to be proportional to pressure perturbations at the same point at an earlier time.

Pressure variations in acoustic fields are uniquely related to variations of the other state variables, temperature and density, but velocity variations have different phase relationships to pressure variations at any given position, depending on the acoustic mode and the boundary conditions. Therefore, in general, if pressures were replaced by velocities in Eq. (8), the outcome for q' would be different, and the value of α calculated from Eq. (7) would be changed. Models can be constructed in which q' responds to velocity fluctuations u' with a locally determined time lag τ, as will be illustrated later, but (with one important exception) such models tend to be unrealistic for homogenous reactors and are not addressed presently. To define the simplest model for a homogenous reactor, τ is taken to be constant throughout the reactor illustrated in Fig. 1, and Eq. (8) may then be used in Eq. (7) to show that the corresponding contribution to α is

$$\alpha = \frac{\left[n(\gamma-1)\dfrac{\overline{q}}{\overline{p}}\right]\dfrac{1}{T}\int_0^T\int_V \dfrac{p'(t)p'(t-\tau)}{\overline{\rho c^2}}dV\,dt}{2\langle\hat{e}\rangle V} \tag{9}$$
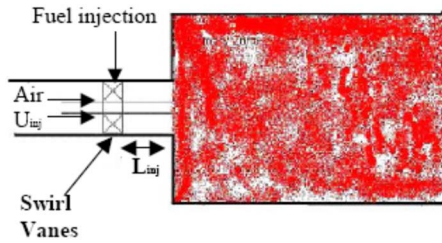
Fig. 1 Schematic of a homogenous reactor

In applying this result, values are needed for both n and τ. The simplest approach is to select constant values for each [8], such as $n = 0.05$ and

$$\tau = \frac{L_{\text{inj}}}{U_{\text{inj}}} \qquad (10)$$

where L_{inj} is the distance from the fuel nozzle to the combustor entrance, and U_{inj} is the average flow velocity in the injector stream, illustrated schematically in Fig. 1. Depending on the combustor configuration, instead of employing a design-dependent τ, it may be better to select a design-independent value based on expected heat-release time lags for the local combustion process.

Irrespective of how τ is determined, as long as it is a known constant, Eq. (9) can be used to calculate this contribution to α once the acoustic field is specified. With the description given in Eq. (5), use may be made of Eqs. (2) and (4) in Eq. (9) to show that

$$\alpha = \left[n(\gamma - 1) \frac{\bar{q}}{\bar{p}} \right] \frac{\cos(\omega\tau)}{2} \qquad (11)$$

This is a simple but general result for this constant-τ limiting case of the homogenous model, which, in turn, represents a limiting case in which the combustion fills the entire chamber. When the values of the five parameters n, γ, τ, $\bar{q}$, and $\bar{p}$ are known, Eq. (11) may be employed to calculate the associated contribution to α as a function of ω. This contribution may then be positive or negative, depending on the frequency as determined by the sign of $\cos(\omega\tau)$.

There may be interest in applying this model to a reactor in which combustion does not fill the entire chamber. For this extension, a factor $f < 1$ must be placed in Eq. (11), where f denotes the ratio of pressure contribution to the acoustic energy over the portion of the chamber in which combustion occurs to the total pressure contribution to the acoustic energy in the chamber. The value of f may be calculated from an acoustic-mode analysis of the chamber, once the portion of the chamber in which combustion occurs is specified. As an especially simple example, for a chamber of length L in which the pressure oscillation is proportional to $\cos(\pi x/2L)$ and combustion occurs only in the region between $x = 0$ and $x = x_f$, it is found that $f = 2/\pi[(x_f/L)\sqrt{1-(x_f/L)^2} + \sin^{-1}(x_f/L)]$. In most configurations, a simple formula like this cannot be obtained for f, and instead a numerical calculation of f is required.

Pressure-Sensitive Reactors With Spatially Distributed Reactions Having Space-Dependent Time Lags. If τ is not constant but instead varies in space, then the value of α obtained from Eq. (9) differs from the simple result in Eq. (11) and depends on both the shape of the acoustic mode and the spatial dependence of τ. In one model of this kind, τ may be assumed to vary linearly with the axial coordinate x through the chamber, the coefficient of variation being $1/u_\tau = d\tau/dx$, which may be positive or negative. By setting

$$\tau = \tau_0 + u_\tau^{-1} x \qquad (12)$$

in Eq. (8), with τ_0 and u_τ both constant, it is found from Eqs. (4) and (5) with $m = 0$, and (9) that if

$$k = \frac{\pi}{2L} \qquad (13)$$

then

$$\alpha = \frac{n(\gamma - 1)}{2(\omega L/u_\tau)} \frac{\bar{q}}{\bar{p}} \frac{1}{\left[1 - \left(\frac{\omega L}{\pi u_\tau} \right)^2 \right]}$$
$$\times \left\{ \left[1 - \left(\frac{\omega L}{\pi u_\tau} \right) - \left(\frac{\omega L}{\pi u_\tau} \right)^2 \right] [\cos(\omega\tau_0)] \left[\sin\left(\frac{\omega L}{u_\tau} \right) \right] \right.$$
$$\left. + [\sin(\omega\tau_0)] \left[2 \left(\frac{\omega L}{\pi u_\tau} \right)^2 - 1 + \cos\left(\frac{\omega L}{u_\tau} \right) \right] \right\} \qquad (14)$$

Equation (13) corresponds to a chamber with an acoustically closed injector end at $x = 0$ and an acoustically open end at $x = L$, for which Eq. (5) reduces to

$$p'(x,t) = \tilde{p} \cos(\omega t)\cos\left(\frac{\pi x}{2L} \right)$$
$$u'(x,t) = \frac{\tilde{p}}{\bar{\rho} c} \sin(\omega t)\sin\left(\frac{\pi x}{2L} \right) \qquad (15)$$

the values $m = 0$, $\psi = 0$, $\varphi = -\pi/2$, and $\ell = -\pi/2$, for example, in Eq. (5) producing this result. The formulas are different with different boundary conditions.

The six parameters whose values must be given to use Eq. (14) for finding α as a function of ω are n, γ, τ_0, $\bar{q}$, $\bar{p}$, and u_τ/L. Although more complicated than Eq. (11), Eq. (14) yields a result which approaches that of Eq. (11) as $u_\tau/\omega L$ approaches infinity. For small values of $u_\tau/\omega L$, however (high frequencies), the magnitude of the result in Eq. (14) becomes smaller by the factor $u_\tau/\omega L$ as a result of cancellation of contribution from different parts of the chamber. If combustion were to occur only in part of the chamber, then the integration in Eq. (9) would extend only over that part, but a formula as simple as Eq. (14) would not be obtained; in this case, depending on which part of the chamber experiences combustion, the resulting value of α may be decreased or increased.

Mode-dependent results also occur for models that introduce Lagrangian time lags, which follow fluid elements. If the fluid is convected downstream, in the x direction, with the constant mean velocity U_c, and if the perturbations to the heat release at position x at time t result only from the pressure perturbation at position $x - U_c\tau_L$, at time $t - \tau_L$, then a space lag must be taken into account in addition to the Lagrangian time lag τ_L (unless U_c is sufficiently small), causing p' in Eq. (8) to be evaluated at a different spatial position than q'. This result arises from the fact that, in this model, each fluid element moves a distance $U_c\tau_L$ before releasing heat. These complications in general would require the integrals in Eq. (9) to be evaluated numerically, with $p'(t - \tau)$ evaluated at a spatial position different than that of $p'(t)$. This would preclude the derivation of simple analytic formulas such as those given in Eqs. (11) and (14). A wide variety of possible models for reactors with distributed reactions thus exist, the results in Eqs. (11) and (14) representing two special simple limiting cases.

Pressure-Sensitive Reactors With Spatially Localized Reactions. The opposite limit from that of spatially distributed reactions is the limit of spatially localized reactions. It is worthwhile to consider this opposite limiting case, which is simpler to analyze than the general case. In applications, then, judgments can be made as to whether the combustion is approximated better by the distributed-reaction or localized-reaction model, and the result
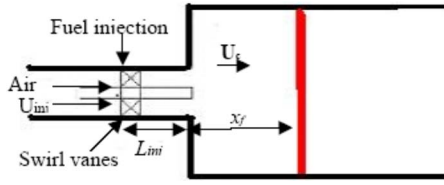
Fig. 2 Schematic of an anchored flame at a fixed location

for the model judged to be closest to reality can be used. Alternatively, some components of both limits may be judged to be present, and the combustion may then be partitioned between the two.

The $n - \tau$ description underlying Eq. (8) may still be considered for the localized limit. Results for α in this limit, however, have a greater dependence on the chamber configuration and on the acoustic mode than does the result in Eq. (11). It is simplest to consider a one-dimensional configuration in which the chamber, of length L, extends from $x = 0$ to $x = L$, and a planar flame is anchored at the position $x = x_f$, as shown in Fig. 2. In this case, Eq. (8) is modified to

$$q' = n\bar{q}\frac{p'(t - \tau)}{\bar{p}}\delta(x - x_f)L \quad (16)$$

For the acoustic field of Eq. (15), use of Eqs. (4), (5), and (16) in Eq. (7) results in

$$\alpha = n(\gamma - 1)\frac{\bar{q}}{\bar{p}}\left[\cos\left(\frac{\pi x_f}{2L}\right)\right]^2 \cos(\omega\tau) \quad (17)$$

Application of Eq. (17) requires knowledge not only of the values of the five parameters n, γ, τ, $\bar{q}$, and $\bar{p}$, which were needed in Eq. (11), but also the value of x_f/L. The sign of α, however, again depends only on the value of $\omega\tau$.

The possible choices for τ in this formula parallel those in Eq. (11), although if the design-dependent τ is selected, then Eq. (10) would better be replaced by

$$\tau = \frac{L_{\text{inj}}}{U_{\text{inj}}} + \frac{x_f}{U_c} \quad (18)$$

where U_c is the average flow velocity in the chamber. The method of determining the value of n depends on the model selected for the localized heat release. If, for the configuration corresponding to Eq. (15), a model of premixed turbulent-flame propagation is selected, with the planar flame stabilized at $x = x_f$, then the average total rate of heat release in the chamber of volume V, with cross-sectional area A, is

$$\bar{q}V = (\overline{Q_r \rho S_T})A \quad (19)$$

in which Q_r denotes the heat released per unit mass of mixture consumed and S_T is the turbulent burning velocity. With $q \propto \delta(x - x_f)L$, the corresponding perturbation is [12]

$$\frac{q'}{\bar{q}} = \frac{Q_r'}{Q_r} + \frac{\rho'}{\bar{\rho}} + \frac{S_T'}{S_T} \quad (20)$$

indicating that perturbations in Q_r, ρ, and S_T all contribute to n in Eq. (16). The pressure dependences of these three parameters therefore affect n in this model. Expressions for n would be different in other models, and the simplest approach would be to merely select a value, as indicated above (Eq. (10)).

Velocity-Sensitive Reactors With Spatially Localized Reactions. For localized reactions, there are more physically reasonable models with velocity-sensitive responses than there are for distributed reactors. Results necessarily will be configuration dependent and mode dependent, and for the configuration that led to Eq. (16), that equation becomes

$$q' = n\bar{q}\frac{\gamma u'(t - \tau)}{\bar{c}}\delta(x - x_f)L \quad (21)$$

where in Eq. (8) $p'/\bar{p}$ is replaced by $\gamma u'/\bar{c}$, u being the velocity in the x direction. This selection is better than $u'/\bar{u}$ because in acoustics, it is $\gamma u'/\bar{c}$ rather than $u'/\bar{u}$ that is of the same order of magnitude as $p'/\bar{p}$.

Equation (7) still applies for this contribution, and for the mode considered, which has $\langle\hat{e}\rangle = |\tilde{p}^2|/(2\gamma\bar{p})$, Eqs. (5) and (21) result in

$$\alpha = \frac{n(\gamma - 1)}{4}\frac{\bar{q}}{\bar{p}}\sin\left(\frac{\pi x_f}{L}\right)\sin(\omega\tau) \quad (22)$$

which differs from Eq. (17) in that $\left\{\left[\cos\left(\frac{\pi x_f}{2L}\right)\right]^2 \cos(\omega\tau)\right\}$ is replaced by $\left\{\frac{1}{4}\sin(\pi x_f/L)\sin(\omega\tau)\right\}$ as a consequence of the pressure sensitivity being replaced by the velocity sensitivity. Although the results are generally similar, the amplitudes are somewhat less for the same value of n (the maximum possible value being $1/4$ of the previous maximum), and the phase difference is altered, amplification now peaking at $\omega\tau = \pi/2$ instead of at $\omega\tau = 0$.

Flamelet-Area Fluctuations. In the turbulent-flame model of Eqs. (19) and (20), explicit velocity sensitivity can arise for the flamelet regime. In this regime, as is well known [10],

$$S_T A = S_L A_f \quad (23)$$

where S_L is the laminar burning velocity and A_f is the wrinkled flame area, and the wrinkled flame area may be considered to be proportional to the velocity fluctuations, whence

$$\frac{S_T'}{S_T} = \frac{S_L'}{S_L} + \frac{A_f'}{A_f} = \frac{S_L'}{S_L} + \frac{u'}{\bar{u}} \quad (24)$$

The only velocity-dependent term that arises when Eq. (24) is substituted into Eq. (20) is

$$\frac{q'}{\bar{q}} = \frac{u'}{\bar{u}} \quad (25)$$

which, in Eq. (21), corresponds to

$$n = \bar{c}/\gamma\bar{u} \quad (26)$$

which is a large number even if $\bar{u}$ is taken to be the mean convection velocity. In many models, the $\bar{u}$ in Eq. (25) should instead be the root-mean-square turbulent fluctuation velocity, which causes n in Eq. (26) to be even larger. Equation (25), however, assumes that the acoustic velocity fluctuations are fully effective in increasing the wrinkled flamelet area. In many models, only the turbulent velocity fluctuations increase the flamelet area, and the acoustic fluctuations may have a small or negligible effect on the turbulent fluctuations. A correction factor that is generally small therefore belongs to the right-hand side of Eq. (25), resulting in a correspondingly small factor in Eq. (26). This model nevertheless can lead to responses having magnitudes larger than those associated with pressure-sensitive responses. Clearly, there are many uncertainties concerning the magnitude of n for this model.

The appropriate time lag τ for this model can be of the order of a large-eddy turnover time,

$$\tau = d/\bar{u} \quad (27)$$

where d is a large-eddy diameter and $\bar{u}$ a representative turbulent fluctuation velocity, resulting in a numerical value that may often be comparable with values obtained from Eq. (10). As with n, however, there are significant uncertainties in expressions and values for τ.

Since most gas-turbine conditions tend to lie in the thin-reaction-zone regime rather than in the flamelet regime, this potentially large effect may not be representative for most applications. In the thin-reaction-zone regime, Eq. (23) does not apply, but instead, the turbulent burning velocity is proportional to the

square root of a turbulent diffusivity, which if proportional to u' would produce a factor of $\frac{1}{2}$ in Eq. (26) and would again require a small multiplicative factor if the acoustics are ineffective in generating turbulent diffusivity fluctuations.

Equivalence-Ratio Fluctuations. Equivalence-ratio fluctuations are another mechanism that is often identified as being an important candidate for a velocity-sensitive response. When the fuel and air flow rates within the injector respond differently to acoustic oscillations, the instability generates local fluctuations of the equivalence ratio, which are convected downstream to the turbulent flame, where they produce fluctuations in the heat-release rate. Under the proper circumstances, these fluctuations can couple with the pressure closing the instability loop.

Specifics depend on details of the injection process, but in many cases, the fuel feed pressure is high enough that the injector can be considered to be choked, giving a constant flow rate, while the air flow rate past the injector responds to the acoustic oscillations. If the air flows in the x direction at velocity u at the injector, then the fluctuations in the equivalence ratio ϕ are given by [1]

$$\frac{\phi'}{\bar{\phi}} = -\left(\frac{u'}{\bar{u}} + \frac{\rho'}{\bar{\rho}} \right) \qquad (28)$$

in which the local density fluctuations at the injector are usually of a lesser importance and can be neglected, giving a velocity-sensitive response with the time lag of Eq. (18). Since

$$\frac{q'}{\bar{q}} = \left(\frac{dq}{d\phi} \frac{\bar{\phi}}{\bar{q}} \right) \frac{\phi'}{\bar{\phi}} \qquad (29)$$

with this mechanism, in Eq. (21),

$$n = \left(\frac{dq}{d\phi} \right) \left(\frac{\bar{\phi}}{\bar{q}} \right) \frac{1}{\gamma M_{\text{inj}}} \qquad (30)$$

where the air Mach number at the injector is

$$M_{\text{inj}} = \frac{U_{\text{inj}}}{\bar{c}_{\text{inj}}} \qquad (31)$$

and $u'(t-\tau)$ is to be evaluated at the injector, leading to p' and q' being evaluated at different spatial locations in Eq. (7).

The potential for this to be a large effect is evident from the presence of the Mach number in the denominator in Eq. (30). It does, however, become necessary to address the acoustic velocity fluctuation u' in the injection region, and this can be small, offsetting the influence of the Mach number. For example, for the simple configuration considered in deriving Eq. (14), if the injection is at $x=0$, then $u'=0$ there, and equivalence-ratio fluctuations (which also can be called mixture-ratio or mixture-fraction fluctuations) occur only through the density fluctuations (related to the pressure fluctuations), which have been neglected as being small. If the acoustic field is given by Eq. (15) and the injection of fuel is at $x=x_{\text{inj}}$, then use of Eqs. (21) and (30) in Eq. (7) gives

$$\alpha = -\left[\frac{(\gamma-1)}{2\gamma M_{\text{inj}}} \left(\frac{dq}{d\phi} \frac{\bar{\phi}}{\bar{q}} \right) \frac{\bar{q}}{\bar{p}} \right] \left[\cos\left(\frac{\pi x_f}{2L} \right) \sin\left(\frac{\pi x_{\text{inj}}}{2L} \right) \right] \sin(\omega\tau) \qquad (32)$$

Comparison of Eq. (32) with Eqs. (17) and (22) shows that if the fractional change in the rate of heat release with the fractional change in the equivalence ratio is of order unity, then this effect can be relatively large. It produces amplification for $0 < \omega\tau < \pi$ (attenuation for $\pi < \omega\tau < 2\pi$) when $\pi x_{\text{inj}}/2L$ is small and negative and attenuation for $0 < \omega\tau < \pi$ when it is small and positive. Expressions will be different for other modes or other configurations.

To use this result numerically, it is necessary to evaluate $dq/d\phi$. For the flamelet regime, from Eqs. (19), (20), and (24) it may be seen that

$$\frac{dq}{d\phi} \frac{\bar{\phi}}{\bar{q}} = \frac{dQ_r}{d\phi} \frac{\bar{\phi}}{\bar{Q}_r} + \frac{dS_L}{d\phi} \frac{\bar{\phi}}{\bar{S}_L} + \frac{d\rho}{d\phi} \frac{\bar{\phi}}{\bar{\rho}} + \frac{dA_f}{d\phi} \frac{\bar{\phi}}{\bar{A}_f} \qquad (33)$$

while for the thin-reaction-zone regime, the last term in this approximation is replaced by a corresponding fractional change in diffusion coefficient. In both regimes, the first two terms are dominant and may be evaluated from thermodynamic data and from data on laminar burning velocities.

Turbulent diffusion can be an important phenomenon in modifying the influence of equivalence-ratio fluctuations. The mixture nonuniformities introduced at the injector tend to be washed out by diffusion processes as a fluid element flows downstream. This phenomenon has been addressed previously [13,14] by models more complex than the simple estimate to be adopted here. If Eq. (27) is employed as an estimate of a decay time τ_d for equivalence-ratio fluctuations, then a result such as Eq. (32) requires an additional factor of e^{-t_L/τ_d}, taken here as a reasonable approximation accounting for this effect, where t_L is the space-dependent Lagrangian transit time for the fluid element, given, for example, by Eq. (18). This factor accounts for the reduction in amplitude of the equivalence-ratio fluctuations by diffusion and causes the effect to diminish as the distance downstream increases.

Velocity-Sensitive Reactors With Spatially Distributed Reactions. The equivalence-ratio fluctuations just described can also be important when there are distributed reactions. This would involve a spatially dependent time lag, as in Eq. (12), and it would give, for the configuration to which Eq. (32) applies, the formula

$$\alpha = -\frac{(\gamma-1)}{\pi \gamma M_{\text{inj}}} \left(\frac{dq}{d\phi} \frac{\bar{\phi}}{\bar{q}} \right) \frac{\bar{q}}{\bar{p}} \frac{\sin\left(\dfrac{\pi x_{\text{inj}}}{2L} \right)}{\left[1 - \left(\dfrac{2\omega L}{\pi u_t} \right)^2 \right]}$$
$$\times \left\{ \cos\left(\frac{\omega L}{u_\tau} \right) \sin(\omega\tau_0) - \left(\frac{2\omega L}{\pi u_\tau} \right) \left[1 - \sin\left(\frac{\omega L}{u_\tau} \right) \right] \cos(\omega\tau_0) \right\} \qquad (34)$$

in which τ_0 and u_τ may best be obtained from Eq. (18). For small values of $\omega L/u_\tau$, this result is quite similar to that of Eq. (32), the difference being that $\cos(\pi x_f/2L)$ is now replaced by $2/\pi$, but for large values of this parameter, the magnitude becomes smaller by a factor $u_\tau/\omega L$, as in Eq. (14). If combustion were to occur only in part of the chamber, then again the integral in Eq. (7) would extend only over that part, precluding a result as simple as that in Eq. (34) from being derived and, in general, requiring numerical integration for evaluating α. The limiting case in which the distributed combustion is mainly localized toward the upstream end of the chamber would correspond to Eq. (32) with $(\pi x_f/2L)=1$.

Equation (34) does not take into account the reduction in amplitude of equivalence-ratio fluctuations by diffusion. When this effect is included, the formula becomes more complicated than Eq. (34), and α is best calculated by numerical integration. The effect can be very substantial, lessening the influence of the downstream portion of the chamber greatly and thereby removing most of the destructive interference effects that lead to rapid variations of α with ω.

Vortex Shedding. Vortex shedding is basically a nonlinear phenomenon, and a linear approximation is needed to apply the present approach. The viewpoint to be adopted is that vortices are shed from an object with a characteristic dimension d, a rod diameter (as in the case of fuel spokes in an injector) or a boundary-layer thickness at an edge, and with a characteristic length L_V, the length of the rod or of the edge. The gas entrained in the vortex burns at a time τ after the vortex is shed, where τ may, for example, be considered to be an induction time for ignition, and the heat is released over a period of time comparable with the vortex

turnover time. The shedding frequency ω in the absence of the acoustic field is determined by the Strouhal number

$$\text{St} = \frac{\omega d}{U_c} \tag{35}$$

a representative value of which is about 0.2 [15].

If this were all that were involved, then there would be no contribution to acoustic amplification because there would be no coupling between the phase of the shedding and of the acoustics. Coupling is provided by the fact that the shedding frequency increases with the velocity, as implied by Eq. (35). The velocity increase associated with the acoustics promotes shedding, so that shedding can be triggered in the high-velocity portion of the acoustic oscillations, thereby synchronizing the shedding with the acoustic field. This coupling clearly is nonlinear, since it depends on the magnitude of the acoustic velocity, and the shedding phase is thus a function of the acoustic amplitude. Moreover, by modifying the shedding frequency through Eq. (35), the nonlinearity can lead to synchronization of shedding over a range of frequencies.

However, since the acoustics, under combustor operating conditions of greatest practical interest, may be expected not to make a large change in the shedding as an approximation, it may be assumed that interaction will occur only over frequencies differing by a small factor r, perhaps about 10%, from the natural shedding frequency of Eq. (35) for the mean velocity U_c. The frequency dependence of the magnitude of the fluctuation in the heat-release rate per unit volume is therefore taken to be

$$|q'| = |q'|_{\max}\left[1 - \left(\frac{\omega - \omega_0}{r\omega_0}\right)^2\right] \tag{36}$$

for $(1-r)\omega_0 < \omega < (1+r)\omega_0$ and 0 otherwise, where ω_0 is the value obtained from Eq. (35) with U_c being the average velocity at the shedding point. Equation (36) is preferred over a Gaussian, for example, because there is no interaction if the frequencies are too different.

To use Eq. (36), it is necessary to evaluate $q'_{\max}$, the value that occurs when the acoustic and shedding frequencies coincide. The value of q' may be approximated as being zero outside the vortex and constant inside. If the vortex is approximated as having diameter d and length L_V, and if the circulation is estimated as $U_c(U_c/\omega) = U_c^2 d/\text{St}$, then its turnover time, d^2 divided by its circulation, is $d\text{St}/U_c$, so that

$$|q'|_{\max} = \frac{Q_r\rho U_c}{d\text{St}} \tag{37}$$

If x_v denotes the value of x at which the vortex is shed, then Eqs. (36) and (37) give

$$q'(x_v + U_c\tau, t) = \frac{Q_r\rho U_c}{d\text{St}}\left[1 - \left(\frac{\omega - \omega_0}{r\omega_0}\right)^2\right]\frac{u'(x_v, t - \tau)}{0.1 U_c} \tag{38}$$

where the magnitude of the velocity fluctuations has been approximated as 10% of the mean velocity. The final factor in Eq. (38) couples the heat-release fluctuations with the acoustic-triggered shedding. Equation (38) applies over a volume of diameter d and length L_V centered at position $x_v + U_c\tau$, and q' is zero outside this volume, in this approximation.

For the configuration and acoustic conditions of Eq. (15), with the rod or edge normal to the flow direction, use of Eq. (38) in Eq. (7) results in
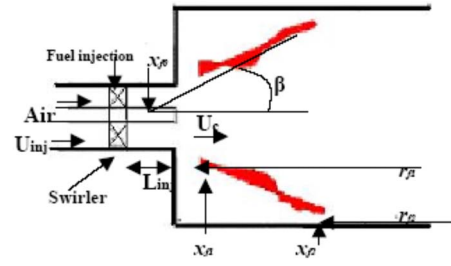
Fig. 3 Schematic of an anchored conical flame

$$\alpha = \frac{\pi(\gamma - 1)dL_V Q_r}{0.8\text{St}Vc}\left[1 - \left(\frac{\omega - \omega_0}{r\omega_0}\right)^2\right]$$
$$\times \sin(\omega\tau)\sin\left(\frac{\pi x_v}{2L}\right)\cos\left(\frac{\pi(x_v + U_c\tau)}{2L}\right) \tag{39}$$

provided that the vortex diameter is small compared with the wavelength of the acoustic field. If there is more than one rod or edge in the system, then Eq. (39) is to be applied separately for each, the sum contributing to α. Since the derivation neglects vortex growth through entrainment during its transit, if $U_c\tau$ is large enough, then an entrainment factor, perhaps $1 + 0.1 U_c\tau/d$, may appropriately be included in Eq. (39). The result predicts amplification if $x_v > 0$ for $0 < \omega\tau < \pi$ when ω is close enough to ω_0 (α is zero for $|\omega - \omega_0| > r\omega_0$), and the amplification increases with increasing ratio of vortex volume to chamber volume.

Pressure-Sensitive Cylindrical Reactors With Conical Anchored Flames. This case is between two limiting cases discussed earlier (the distributed-reaction limit and the spatially-localized-reaction limit) and is more appropriate for some applications. The flame in this example is anchored between two axial and radial locations, (x_{f1}, r_{f1}) and (x_{f2}, r_{f2}), as shown in Fig. 3.

The modeling challenges for this case are similar to those of the spatially localized flame in that it may be difficult to determine the exact location of the reaction zone. The heat release is assumed to occur only at the flame sheet, and the heat-release rate is written as

$$q' = n\bar{q}\left[\frac{p'(t - \tau)}{\bar{p}}\right]\delta(\eta)\frac{R^2 L \sin\beta}{(r_{f_2}^2 - r_{f_1}^2)} \tag{40}$$

where η is a coordinate perpendicular to the flame sheet defined by

$$\eta = (r - r_f)\cos\beta - (x - x_f)\sin\beta \tag{41}$$

obtained by transforming the axial (x) and radial (r) coordinates into a system perpendicular to and parallel to the flame sheet. The heat-release perturbation is taken here to be proportional to the pressure perturbations occurring at the flame location, evaluated at a time τ earlier, as in Eq. (16). It clearly would also be possible to address, in this geometry, velocity-sensitive heat release, as in Eq. (21), and the result from equivalence-ratio fluctuations is to be discussed below.

The use of Eqs. (40) and (41) in Eq. (7) gives

$$\alpha = n(\gamma - 1)\frac{\bar{q}}{\bar{p}}\left(1 + \frac{[\cos^2(\xi_2) - \cos^2(\xi_1)] + [(\xi_2 - \xi_0)\sin(2\xi_2) - (\xi_1 - \xi_0)\sin(2\xi_1)]}{[(\xi_2 - \xi_0)^2 - (\xi_1 - \xi_0)^2]}\right)\cos(\omega\tau) \tag{42}$$

where $\xi = \pi x_f / 2L$, and x_{f0} is the point where the extrapolated flame meets the x axis (forming an angle β). Following Putnam [16] in Eq. (42), one may consider setting

$$\tau = \frac{L_{\text{inj}}}{U_{\text{inj}}} + \frac{x_{f1}}{U_c} + \frac{x_{f2} - x_{f1}}{3U_c} \tag{43}$$

as an approximation in the spirit of Eq. (18), although the resulting value for τ often is too large to produce reasonable results, so that a smaller, design-independent value is preferred. The growth-rate results obtained by this model tend to fall between the two limits discussed before and can be positive or negative depending on the frequency.

Velocity-Sensitive Cylindrical Reactors With Conical Anchored Flames. If the heat-release perturbations in the above example are assumed to be sensitive to velocity perturbations only, then in the spirit of Eq. (21), these perturbations can be approximated by

$$q' = n\bar{q}\left[\frac{\gamma u'(t-\tau)}{\bar{c}}\right]\delta(\eta)\frac{R^2 L \sin\beta}{(r_{f_2}^2 - r_{f_1}^2)} \tag{44}$$

For equivalence-ratio fluctuations, the u' in Eq. (44) is evaluated at the injector location, and the growth rate for a variable time lag, which is more physically plausible because combustion occurs along the flame sheet, can be expressed analytically if turbulent diffusion is neglected; however, the formula is complicated, even more so than Eq. (42), so that it is simpler to calculate α numerically from the formula

$$\alpha = \left[\frac{(\gamma-1)}{2\gamma M_{\text{inj}}}\left(\frac{dq}{d\phi}\frac{\bar{\phi}}{\bar{q}}\right)\frac{\bar{q}}{\bar{p}}e^{-\tau_0/\tau_d}\sin(\beta)\sin(\xi_{\text{inj}})\right]$$
$$\times \left(\frac{2L}{\pi R}\tan(\beta)\right)^2 \left\{\sin(\omega\tau_0)\int_{\xi_1}^{\xi_2}(\xi - \xi_0)e^{-c\xi}\cos(\xi)\cos(b\xi)d\xi\right.$$
$$\left. + \cos(\omega\tau_0)\int_{\xi_1}^{\xi_2}(\xi - \xi_0)e^{-c\xi}\cos(\xi)\sin(b\xi)d\xi\right\} \tag{45}$$

in which $b = 2\omega L/\pi u_\tau$, $c = 2L/\pi u_\tau \tau_d$, $\tau_0 = L_{\text{inj}}/U_{\text{inj}}$, $u_\tau = U_c$, and $\tau_d = d/\bar{u}$. In this expression, the reduction in amplification through turbulent diffusion has been included, d being the size of the large eddies and $\bar{u}$ the turbulent fluctuation velocity.

More Complex Configurations. Equation (45) involved performing a numerical integration along the length of the flame. The amplification rate α in general can be evaluated by numerical integration when the necessary information is available, and in most complex configurations, numerical integration is required. In flame-sheet approximations, the integration is carried over the area of the sheet, and in distributed-reaction approximations, the integration is carried over the volume of the chamber. The latter situation is the most general in that a flame sheet can always be approximated as a flame of nonzero thickness, and q' can be taken to be large inside this thickness and zero outside. The information that is required for determination of α should be clear from Eq. (7).

First of all, it is necessary to know the average acoustic energy per unit volume defined in Eq. (4). Since $\langle\hat{e}\rangle$ is proportional to the square of the pressure amplitude $\bar{p}^2$, this formally involves knowing the amplitude of the acoustic fluctuations, but, in fact, that is irrelevant since $\bar{p}^2$ also occurs in the numerator of Eq. (7) and so cancels out in the expression for α. In other words, the amplitude can be assigned an arbitrary value at a selected position. What is needed for calculation of $\langle\hat{e}\rangle$ by numerical integration is only therefore the shape of the acoustic mode under consideration. This should be available from chamber-acoustic programs, so that $\langle\hat{e}\rangle$ can be calculated for the given amplitude.

The only other factor in α in Eq. (7) is the ratio of the volume integral (over the entire chamber) of the amplification rate per unit volume to the chamber volume. This ratio can also be evaluated by numerical integration (for the selected amplitude), given the acoustic mode and the information concerning the amplification mechanism that determines q'. This information is, of course, quite different for different mechanisms. Equation (8) provides the simplest example. Time lags often are involved, and Eq. (12) often will be a reasonable approximation, in which x becomes the distance along a particle path and u_τ the particle velocity along the path. If this velocity varies appreciably in the model, then $u_\tau^{-1}x$ is better replaced by $\int u_\tau^{-1}dx$. To complete the specification of q', either the amplitude factor n is simply given or a formula such as Eq. (20), (29), or (38) is used, with quantities appearing there given, for example, by Eq. (24) or Eqs. (28) and (33).

Depending on the mechanism, the shape of the acoustic mode will appear in different ways in the evaluation of q'. The integration over the volume is, however, straightforward once the acoustic mode, the mechanism, and the values of the associated parameters are known. The computational times will vary depending on the geometry and mechanisms of choice, but are much shorter than the times required for approaches implementing CFD, although the latter, of course, give nonlinear behaviors, which the present approach is incapable of doing.

Because the present approach is only an approximate one, it is consistent with the spirit of the method to address various additional simplified approximations of the acoustic field, the chamber and the flame configurations, the physical mechanisms of the heat-release perturbations, and the time lags. One prevalent design configuration is an annular chamber with a number N of axially directed injectors distributed uniformly around the annulus. Acoustic modes observed in such units often are circumferential, so that Eq. (5) can be applied with $k = \ell = 0$. If interactions of flames from different injectors, tendencies of flames to spread conically, and distributed-reaction effects are neglected, then the flame from each injector can be approximated by a circular cylindrical sheet of radius r_f, centered on the injector axis. Moreover, r_f may be considered small enough that the phase of the acoustic field for the entire flame of injector k may be approximated as the phase of the azimuthal angle θ_k of the center of that injector. With these simplifications, the analog of Eq. (16) for pressure-sensitive reactors becomes

$$q' = n\frac{\bar{q}}{\bar{p}}\sum_{k=1}^{N}p'(\theta_k,t-\tau)\delta(r_k - r_f)\frac{L(R_o - R_i)}{Nr_f} \tag{46}$$

where L is the length of the annular combustor, R_o and R_i are its outer and inner radii, respectively, and r_k is a radial coordinate from the axis of the injector k, appearing in the argument of the delta function.

If Eq. (12) is employed for τ, then use of Eq. (46) in Eq. (7) gives, for the tangential mode considered,

$$\alpha = \frac{(\gamma-1)n\bar{q}u_\tau}{\omega N\bar{p}(R_o + R_i)}\left[\sum_{k=1}^{N}\cos^2(m\theta_k)\right]\times\left\{\cos(\omega\tau_0)\sin\left(\frac{\omega L}{u_\tau}\right)\right.$$
$$\left. - \sin(\omega\tau_0)\left[1 - \cos\left(\frac{\omega L}{u_\tau}\right)\right]\right\} \tag{47}$$

where m is an integer ($m = 1$ for the fundamental mode). In the limit of $u_\tau = 0$, so that τ is constant, the braces in Eq. (47) approach $(\omega L/u_\tau)\cos(\omega\tau_0)$. With these same geometrical approximations applied to equivalence-ratio fluctuations, Eqs. (29) and (33) continue to hold, and

$$\alpha = \frac{B(\gamma - 1)n\bar{q}u_\tau}{\omega N \bar{p}(R_o + R_i)}$$

$$\times \left\{ \sum_{k=1}^{N} \cos(\psi)\cos^2(m\theta_k) - \sin(\psi)\cos(m\theta_k)\sin(m\theta_k) \right\}$$

$$\times \left\{ \cos(\varphi)\left[\cos(\omega\tau_0)\sin\left(\frac{\omega L}{u_\tau}\right) - \sin(\omega\tau_0)\left\{1 - \cos\left(\frac{\omega L}{u_\tau}\right)\right\}\right] \right.$$

$$\left. + \sin(\varphi)\left[\sin(\omega\tau_0)\sin\left(\frac{\omega L}{u_\tau}\right) + \cos(\omega\tau_0)\left\{1 - \cos\left(\frac{\omega L}{u_\tau}\right)\right\}\right]\right\}$$

(48)

in which the phase angles ψ and φ are those that appear in Eq. (5), and B, less than unity but often of order unity, denotes the ratio of the axial velocity fluctuations in the injector to the tangential velocity fluctuations in the chamber. For a traveling wave, $\psi = \varphi = 0$, while a standing wave can be described by setting $\varphi = 0$ and $\psi = -\pi/2$, for example, in both cases eliminating the $\sin(\varphi)$ term in Eq. (48), and essentially reverting to Eq. (47) in the first case, and replacing $\cos^2(m\theta_k)$ in Eq. (47) by $\cos(m\theta_k)\sin(m\theta_k)$ in the second case. These results neglect turbulent dissipation, and although analytic results could be obtained including that effect, numerical evaluation of the integral over x is just as easy.

Models for Attenuation of Acoustic Energy

Acoustic-energy dissipation occurs through a variety of mechanisms in practical combustion systems, the most common of which are wall damping and damping by perforated liners that target certain acoustic modes. Other mechanisms of acoustic attenuation are generally less significant and have been addressed reasonably thoroughly in literature [1,10]. These other mechanisms therefore are not addressed here.

Wall Damping. This damping is due to the oscillatory boundary layer near the wall, and it depends on the frequency, the surface area, and the flow properties near the wall. Detailed analysis of wall damping mechanisms is given in several references [9,10,17]. An expression is derived by Williams [10] starting from a simplified time-dependent momentum equation (with t time and y distance normal to the wall), namely,

$$\rho_w \frac{\partial v}{\partial t} = \frac{\partial\left(\mu_w \frac{\partial v}{\partial y}\right)}{\partial y}$$

(49)

where ρ_w, μ_w, and ν are the density, viscosity, and velocity near the wall. This equation has a solution

$$v = \left(\frac{\theta_w}{\theta_c}\right)\text{Re}\{Ve^{-(1+i)\sqrt{\omega\rho_w/2\mu_w}\,y}\}$$

(50)

where θ_w, θ_c, V, and ω are the temperature at the wall, the temperature in the core, the complex oscillatory velocity amplitude outside the oscillating boundary layer, and the frequency of the oscillation, respectively.

From this velocity solution, an energy-dissipation expression (per unit area of combustor wall) can be derived as

$$e_{\text{wd}} = \int_0^\infty \frac{1}{2}\rho_w \omega \left[\frac{\theta_w}{\theta_c}Ve^{-(1+i)\sqrt{\omega\rho_w/2\mu_w}\,y}\right]^2 dy = \frac{1}{2}\left(\frac{\theta_w}{\theta_c}\right)^2|V|^2\sqrt{\frac{\omega\rho_w\mu_w}{2}}$$

(51)

This solution then needs to be integrated over the wall boundary surfaces to obtain the total rate of dissipation by wall damping

$$\alpha_{\text{wd}} = \frac{\int_A e_{\text{wd}}\,dA}{2\langle\hat{e}\rangle V}$$

(52)

Damping by Perforated Liners. Perforated liners are common in gas-turbine applications; their primary use is the provision of cooling to prevent severe temperatures from damaging the hardware. This cooling is provided by air impinging on the liner external walls and/or by film cooling to the interior walls. The latter can contribute significantly to acoustic-energy attenuation, as has been explained by Howe [17,18], Hughes and Dowling [19], and Eldredge and Dowling [20]. The physical mechanism for the removal of acoustic energy is vortex shedding at the edge of the cooling apertures through which there is a mean flow rate. The vortices are moved away from the liner by the mean flow and eventually decay to turbulence.

If the cavity depth (distance from the perforated liner to the wall that backs it) is larger than the aperture diameter, and if both of these dimensions are much smaller than the acoustic wavelength, then the acoustic properties of an aperture can be expressed as [19]

$$\frac{\partial p'}{\partial y} = \eta[p']_{y=-0}^{y=+0} \quad \text{at } y = 0$$

(53)

where y denotes distance normal to the aperture pointing into the chamber, and η is an effective compliance found from an expression developed by Howe [18] based on the Rayleigh conductivity for an aperture and can be expressed as

$$\eta = \frac{2a\chi}{d^2}$$

(54)

in which a is the aperture radius and d the distance between the centers of the apertures. Here,

$$\chi = \lambda - i\delta$$

(55)

where

$$\lambda = \frac{I_1^2(\text{St})\left[1 + \frac{1}{\text{St}}\right] + \frac{4}{\pi^2}e^{2\text{St}}\cosh(\text{St})K_1^2(\text{St})\left[\cosh(\text{St}) - \frac{\sinh(\text{St})}{\text{St}}\right]}{I_1^2(\text{St}) + \frac{4}{\pi^2}e^{2\text{St}}\cosh^2(\text{St})K_1^2(\text{St})}$$

(56)

and

$$\delta = \frac{\left[\frac{2}{\pi\text{St}}\right]I_1(\text{St})e^{2\text{St}}K_1(\text{St})}{I_1^2(\text{St}) + \frac{4}{\pi^2}e^{2\text{St}}\cosh^2(\text{St})K_1^2(\text{St})}$$

(57)

in which $I_1(\text{St})$ and $K_1(\text{St})$ denote modified Bessel functions of the first and second kinds [21]. The Strouhal number is defined here as

$$\text{St} = \frac{\omega a}{U}$$

(58)

with U being the mean gas velocity through the aperture.

An expression for the attenuation rate can be developed by looking at the acoustic admittance (the inverse of the acoustic impedance) defined as $Y = \tilde{u}/\tilde{p}$, in which $\tilde{u}$ refers to the complex amplitude of the average outward normal velocity. The average rate of acoustic energy extraction per unit area can be expressed as [10] $\langle p'u'\rangle = [p'^2/2]\text{Re}\{Y\}$. Upon employing this result in Eq. (1), it follows that the contribution of the perforated liner to the damping is
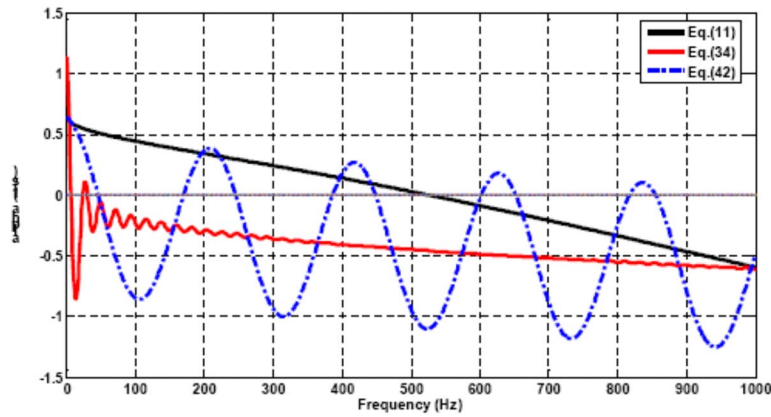
Fig. 4   Growth-rate results obtained from Eqs. (11), (34), and (42) with a fixed $n = 0.05$

$$\alpha_{p\ell} = \frac{\gamma \bar{p}}{2} \frac{\int_A p'^2 \text{Re}\{Y\} dA}{\int_V p'^2 dV} \tag{59}$$

Furthermore, if we define a Helmholtz number as

$$\hbar = \frac{\omega l}{c} \tag{60}$$

where l is the distance from the aperture to the backing wall, and introduce

$$\beta = \frac{\omega d^2}{2ac} \tan(\hbar) \tag{61}$$

then use of the results of Hughes and Dowling [19], given in the first part of their paper, this results finally in

$$\alpha_{pl} = \frac{\int_A p'^2 \left[\dfrac{\beta \delta \tan(\hbar)}{\beta^2 + \lambda^2 + \delta^2 - 2\beta\lambda} \right] dA}{\int_V p'^2 dV} \tag{62}$$

Comparison With Experimental Results

Experiments in four different, increasingly more complex types of combustor configurations are addressed here as means for testing the usefulness of the method that has been proposed. While most of the experiments were performed as part of the present work, some results are taken from the existing literature. The experiments include both atmospheric-pressure and high-pressure rigs and address both single-injector chambers and chambers with full annular sets of injectors. Wide ranges of conditions are thus represented. The approach will be to investigate how well the experimental results can be interpreted on the basis of the preceding models.

Single-Injector, Atmospheric-Pressure, Quartz Combustor. Experiments were performed with a transparent combustor for the purpose of testing the utility of the method being developed here. The intent was to observe under what conditions oscillatory combustion occurred and to attempt to determine which of the preceding models, if any, could lead to rational interpretations of the experimental results. The experimental design and operation have been described more fully previously [8]. The vertically oriented combustion chamber, 8 in. in inside diameter and 20 in. in length, was open to the exhaust system at the top and fed from the bottom by a lean mixture of air and natural gas, injected through a model single-element swirl premixer about 2 in. in diameter, having eight fuel spokes. The air, preheated to 283°F, entered the premixer at 0.12–0.17 lb/s from a cylindrical plenum, coaxial with the combustor and acoustically isolated from it by annular plates, so that the acoustic field in the combustor could reasonably be

approximated by Eq. (15). The fuel-flow rate was between 0.005 lb/s and 0.007 lb/s, and the pressure in the combustor was maintained at atmospheric pressure. Oscillations were detected by measuring pressure variations, monitored through piezoelectric transducers and microphones, and by visual, high-speed-camera and charge coupled device (CCD)-camera observations.

The fundamental acoustic frequency in the chamber during combustion was 250 Hz. At the lower fuel-flow rates, oscillatory combustion did not occur, and the flame appeared to be approximately conical, as illustrated in Fig. 3. Oscillations at 250 Hz were recorded at the higher fuel-flow rates, and under oscillatory conditions on the average, the flame appeared to fill approximately the entire lower portion of the combustor.

Results for α based on different models which can be used to interpret these observations appear in Eqs. (11), (14), (17), (22), (32), (34), (39), (42), and (45), and possible variations of these results have been discussed previously in connection with the equations. One of the first questions is to ask whether a model can predict amplification at the 250 Hz frequency. Some indeed can, as may be seen from results for Eqs. (11), (34), and (42) plotted in Fig. 4. The results for Eqs. (11) and (42) include modifications for the effect of wall damping from Eq. (52), as described previously [8]. Even without turbulent dispersion taken into account to diminish effects of equivalence-ratio fluctuations, the destructive interference from the variable time lag of Eq. (18) eliminates amplification from Eq. (34) for this distributed-reaction model. The pressure-sensitive result for the simple distributed-reaction model of Eq. (11) is seen to produce amplification. It is more appropriate, however, from the flame-shape observations to employ the conical-flame model of Eq. (42), and while the second amplification region for this curve does not exactly coincide with the observed frequency, the inaccuracies are such that the model could well predict amplification where observed. It seems better to base this linear stability analysis on the conical flame rather than the distributed reaction because that is the configuration which is observed prior to the onset of oscillations, so that is the configuration which would have to be linearly unstable.

It is widely believed that equivalence-ratio fluctuations tend to be the primary cause of oscillations. For the conical flame, this effect is described most accurately by Eq. (45), the prediction of which is plotted in Figs. 5 and 6, in combination with the vortex-shedding prediction of Eq. (39). The values of parameters employed for these calculations were 0.5 cm for d, 0.95 cm for L_V, 5 cm for $L_{inj} = -x_v$, 0.63 for ϕ, 14.5 m/s for U_{inj}, 1.8 m/s for U_c, 10% of U_c for $\bar{u}$, and 1.4×10^7 J/kg for Q_r in Eq. (39), and 2.54 cm for x_{f1}, 17.8 cm for x_{f2}, 4.78 cm for r_{f1}, 10.16 cm for r_{f2}, and 3.4 cm for d, along with other parameters having the same values as above, in Eq. (45). In evaluating ξ_{inj}, the positive value $x_{inj} = L_{inj}$ was employed, it being clear that the phase of the oscil-
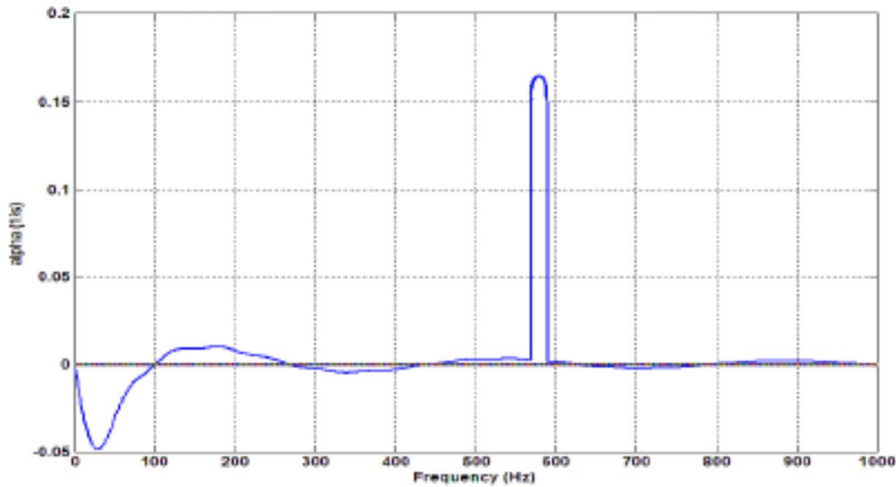
Fig. 5 Growth-rate results obtained from Eqs. (39) and (45)

lations at the injector is the same as that near the upstream end of the chamber and L_{inj} representing the order of magnitude of the displacement away from the velocity node. It is seen from the figures that the equivalence-ratio fluctuations for the conical fame do indeed provide a small amplification effect at the observed frequency, and although the vortex-shedding effect is larger, its potential frequency range is too high, unless U_c is taken to be unreasonably small or d unreasonably large. The small wiggles of the curve in Fig. 6 arise from interference of the amplification effects of different parts of the conical flame.

Testing the predictions of different mechanisms against the present experimental results serves to provide experience in ascertaining how useful the various models may be. Predictions of the vortex-shedding model depend strongly on the shedding frequency, which is seen from Eq. (35) to increase with increasing velocity and with decreasing size of the elements from which the shedding occurs. The shedding frequencies estimated here (as well as for the experiments discussed later) are too high for this phenomenon to be significant; they would correspond to a higher mode of oscillations, for which damping effects would be stronger, or they would operate only over a frequency range too narrow

to correspond to an acoustic mode. Even though there are uncertainties in estimating sizes, very large elements would be needed to reduce the frequencies into the range observed; yet, after oscillation develops, vortex shedding may be involved in the limit cycle. A general aspect of the predictions of all of the other mechanisms is that the magnitude of the effect tends to increase with increasing fuel-flow rate. This occurs because over the range of equivalence ratios tested, the only parameter that varied significantly with increasing fuel-flow rate was the heat release, expressed per unit mass of mixture through Q_r in Eq. (39) and per unit volume of mixture through $\bar{q}$ in the other equations. The other mechanisms are thus all consistent with the experimental observation that combustion oscillations occurred only at the higher fuel-flow rates, provided that the mechanism does predict amplification rather than attenuation at the frequency of interest.

The tentative explanation of the experimental results is that fluctuations of the equivalence ratio induced the oscillations through the amplification seen in Fig. 6. In this same experimental apparatus, tunable diode lasers were employed to detect oscillations in methane concentration at the injector outlet, and
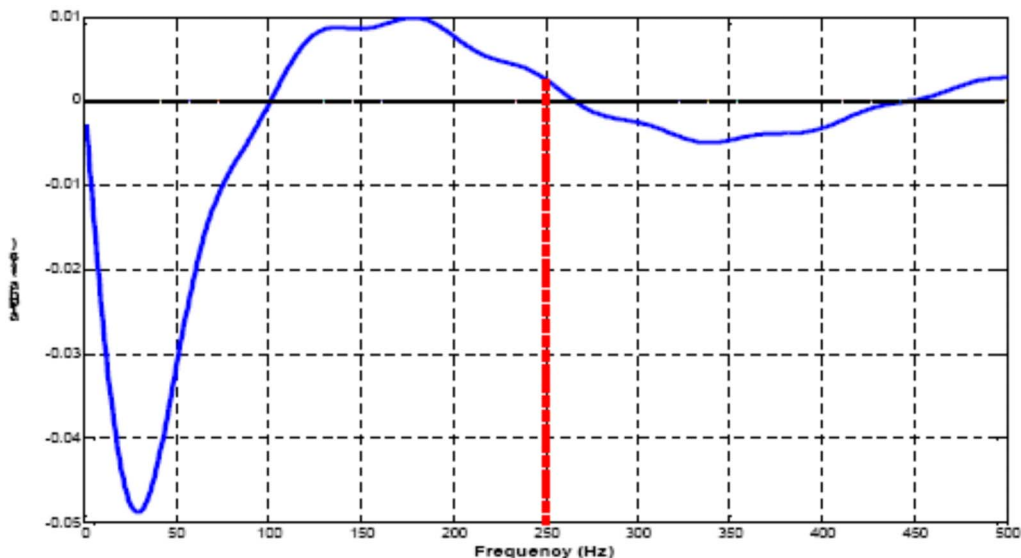
Fig. 6 Growth-rate results (zoomed in near 250 Hz) from effects of equivalence-ratio fluctuations, as obtained from Eq. (45)
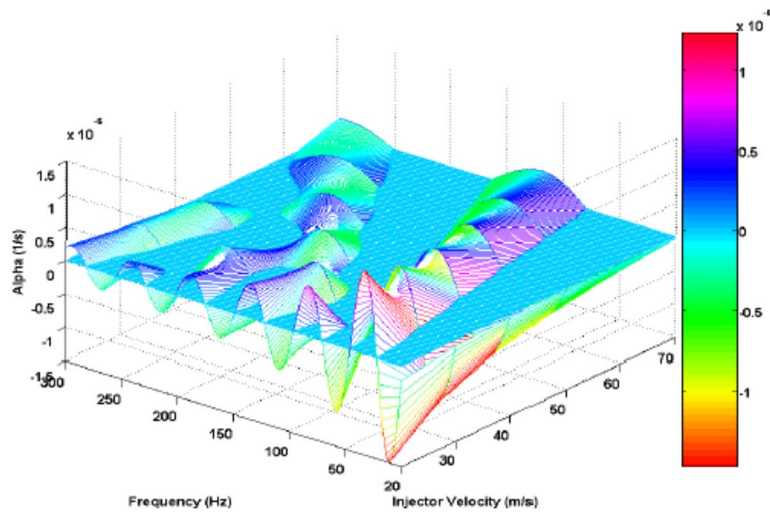
Fig. 7 Growth-rate results obtained from Eq. (45) (at a fixed pressure of 7.5 atm and equivalence ratio of 0.65) for the high-pressure experiments as a function of injection velocity and frequency

equivalence-ratio fluctuations were established to exist [22]. There is, however, some uncertainty as to whether they were sufficiently large to drive the instability. The values of the parameters employed in using Eq. (45), which correspond to $n = 2.94$ in Eq. (44), are seen from Fig. 6 to provide growth times as long as a few minutes, even though damping phenomena other than turbulent dispersion were not taken into account. The experiences during the experiment do not rule out growth times that long, and moreover, uncertainties in values of parameters are large enough that predicted growth times could be appreciably shorter.

This underscores the rough nature of the general approach proposed here and the possibility that a priori predictions by this method will be inconclusive, especially in marginal cases, which therefore might best be avoided in design selections. An observation that can be made on the basis of the present theoretical work is that in the present tests, if the experimental conditions had been closer to lean blowout, then other parameters, such as the burning-velocity variation in Eq. (33), could have been larger, leading to oscillations being associated with decreasing (rather than increasing) fuel-flow rate, if complete blowout could be avoided.

Single-Injector High-Pressure Combustors. Since practical gas turbines operate at elevated pressures, efforts were made to study measurements made in experiments like those of the quartz combustor but instead run at high pressures. An extensive program of such measurements has been completed [23–25]. The inside diameter of the cylindrical combustor, 7.8 in., was quite close to that of the quartz combustor, and the preheated air was supplied at 600°F. Chamber pressures in the tests ranged from 5 atm to 10 atm and equivalence ratios of the natural gas from 0.59 to 0.77. An adjustable exhaust plug allowed the fundamental longitudinal frequency to be changed, but most results were obtained with this frequency between about 200 Hz and 250 Hz, comparable to that of the quartz combustor. The fuel and air entered the combustor coaxially through an annular premixer with swirl vanes and fuel spokes, having inner and outer diameters of 1.5 in. and 2.5 in., respectively. Because of the exhaust plug and the characteristics of the premixer, a better approximation than Eq. (15) to the fundamental acoustic field is

$$p'(x,t) = \tilde{p}\cos(\omega t)\sin\left(\frac{\pi x}{2L}\right)$$

$$u'(x,t) = \left(-\frac{\tilde{p}}{\rho c}\right)\sin(\omega t)\cos\left(\frac{\pi x}{2L}\right) \tag{63}$$

corresponding to a pressure node at the chamber entrance and a velocity node at the chamber exit. This leads to modifications in the formulas for α, for example, replacing $\cos(\omega\tau)$ by $\sin(\omega\tau)$ in Eq. (11).

The primary results of measurements that were reported in the references were amplitudes and frequencies of pressure oscillations as functions of operating conditions. Extensive variations of parameters were made, especially in the premixer configuration and fuel-injection pattern. There are, however, a number of irregularities in the results, such as the observation of different amplitudes on different days, oscillations at apparently subacoustic frequencies under certain conditions, and differences in effects of equivalence ratios under different conditions, over the range of equivalence ratios tested. Many of these irregularities are likely attributable to nonlinearities that are not addressed in the present analysis. Since no systematic effect of equivalence ratio or pressure could be extracted from the results over the range tested, it is assumed here that the results are representative of an average condition, 7.5 atm, and an equivalence ratio of 0.65. The main variable that clearly did affect the oscillation amplitude was the mean velocity in the premixer. In general, amplitudes were large at injection velocities of 40 m/s and below and (except at subacoustic frequencies) small at injection velocities of 50 m/s and above. The task of the present analysis therefore is to develop an interpretation for this effect of injection velocity.

Just as for the quartz combustor, it is assumed that high-amplitude oscillations will develop only if the combustor with the flame under nonoscillating conditions is linearly unstable. In this experiment, however, independent information on the shape of this flame is not available. It nevertheless seems reasonable to assume a conical-flame shape, since swirl-stabilized flames often are conical. This focuses attention on Eqs. (42) and (45), although it was also of interest to investigate predictions for distributed reactions, such as Eq. (34). The results for constant time lags, as in Eq. (11), etc., seem likely to be less relevant for this experiment. The predictions from Eqs. (34) and (42) did not provide a very good correspondence to the experimental results. The results for Eq. (45), however, are much more promising, as may be inferred from Fig. 7 to be explained below. This figure was obtained

employing the values 4.8 cm for $L_{inj}=-x_v$, 0.65 for ϕ, 20–70 m/s for U_{inj}, 0.22–0.77 m/s for U_c, 10% of U_c for $\bar{u}$, 1.4×10^7 J/kg for Q_r, 2.5 cm for x_{f1}, 17.0 cm for x_{f2}, 4.5 cm for r_{f1}, 10.3 cm for r_{f2}, and 3.5 cm for d, again with ξ_{inj} positive and $x_{inj}=L_{inj}$. The interaction index n was obtained from Eq. (30) by use of Eq. (33), in which the contribution to n from the laminar burning velocity was 3.0, that from the heat release was 0.9, and that from the other terms was negligible. The agreement to be now described is consistent with the prevailing viewpoint that equivalence-ratio fluctuations were responsible for the oscillatory combustion observed in these experiments.

Figure 7 shows the amplification rate evaluated from Eq. (45) in a plane of frequency and injection velocity. To aid in visualizing regions where amplification may occur, a plane is passed through the three-dimensional figure at zero amplification rate, and only regions above that plane are highlighted. In general, there are mountain chains of amplification that peak at frequencies, which increase with increasing injection velocities. This is due to the decrease in the time lag τ_0 with increasing injection velocity. At low injector velocities, the fundamental longitudinal frequencies of the combustor fall within the second mountain chain. This mountain chain passes to higher frequencies at an injection velocity of about 50 m/s, which is where the large pressure amplitudes are observed experimentally to disappear. This calculation therefore provides a potential interpretation of the experimental observation. Explanations based on other previous equations do not work as well. For example, the vortex-shedding result of Eq. (39) gives amplification only for frequencies that range from about 400 Hz at an injection velocity of 20 m/s to about 1400 Hz at an injection velocity of 70 m/s, all much higher than the observed frequencies. Stronger damping mechanisms at these higher frequencies are likely to prevent oscillations from occurring there. Of all of the present results, therefore, Eq. (45) is most attractive for these experiments, as well as for the experiments with the quartz combustor.

A Twelve-Injector, Atmospheric-Pressure, Annular Combustor. To investigate more complex configurations, measurements were made on an annular combustor having 12 development premixed injectors, equally spaced around the annulus and directed axially downstream. The combustor, which had an effusion-cooled liner, operated at normal atmospheric pressure in a test rig that had a 1 ft space, open to the laboratory, between the combustor exit and the exhaust system that deflected the exhaust gases upward. Although the setup, which has been used to test various injector designs, was equipped with four rakes to collect temperature profiles at four different angles across the open area and a video camera facing forward to view the flame, the primary data were obtained from 12 pressure transducers, one mounted on each injector, and from visual observation of the flame, which could be seen by peering upstream at an angle through the open area. The piezoelectric transducers, dynamic data from which were acquired by an Alta-Solutions Spectra-Shield box, were mounted in tees off the spuds of the pilot fuel line, seen schematically in Fig. 8. The transducers were connected to 50 ft copper coils in efforts to minimize acoustic interference.

The annular combustor was 0.38 m in length, 0.26 m in inner radius, and 0.34 m in outer radius. Each injector, of outer diameter 0.1 m and shown schematically in Fig. 8, had ten swirl vanes equipped with six fuel-injection holes each, an inner radius of 0.40 m, and an axial distance of 0.05 m between the fuel-injection point and the injector's interface with the combustion chamber.

The flow rates were selected to keep the equivalence ratio close to 0.63, where oscillations could be observed. The airflow rate, through a preheater providing air at 283°F, was fixed at 3.07 lb/s. The fuel flow was varied between 140 lb/h and 199 lb/h, with oscillations observed to occur near 194 lb/h, the values for which data are addressed here. Pilot flow rates from about 2% to 10% were explored, and oscillations were observed at the lower pilot

Fig. 8 A schematic of the development injector used in the experiments

flow rates, 2%–4%, as expected. Measurements were made at 4% pilot flow rates, for which representative pressure amplitudes are shown in Fig. 9. The dominant frequency observed, 250 Hz, is consistent with a first fundamental circumferential mode, calculated from $\bar{c}/(2\pi R)$ (where R is the arithmetic mean of the radius of the annulus and $\bar{c}=826$ m/s) to be 247 Hz.

Relative amplitudes and phases of the 12 different pressure signals were obtained from SPECTRA SHIELD software in typically ten snapshots recorded at 3 Hz. The phase results, within the accuracy of the measurements, were consistent with an assumption that the combustor experienced a standing circumferential wave; there were very few variations of relative phases between different snapshots for most transducers, and indicated that phase differences were small, most within 20 deg and all within 70 deg; these differences corresponding to time differences on the order of 1 ms and likely attributable to small differences in acoustic path lengths and time synchronization for different transducers. The relative amplitude data, shown in Fig. 10, are also consistent with the standing fundamental circumferential wave (shown by a curve in the figure), within the accuracy of the data. In this figure, the angle $\theta=0$ has been adjusted to coincide with the location of the torch employed for ignition, the presence of which may anchor the velocity node.

For the assumed mode, from Eq. (5), the acoustic field is given by

$$p'(\theta,t) = \tilde{p}\cos(\omega t)\cos(\theta)$$

$$u'(\theta,t) = \frac{\tilde{p}}{\rho\bar{c}}\sin(\omega t)\sin(\theta)$$

(64)

where u' is now the component of velocity in the θ direction. To estimate amplification, the flame-shape approximations that led to Eq. (46) are adopted. Visual observation suggested that the flame shape may best be approximated by solid cones, but within the
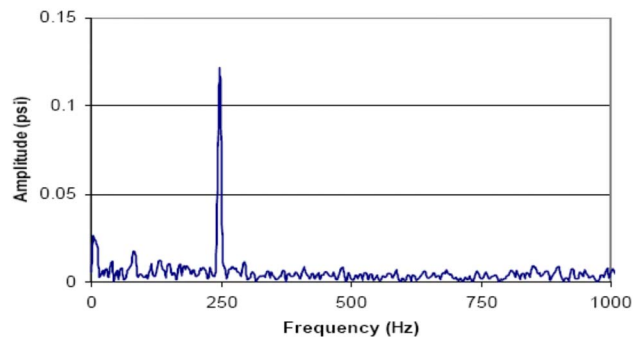
Fig. 9 Dynamic pressure measurements during oscillation for an annular combustor at atmospheric-pressure conditions
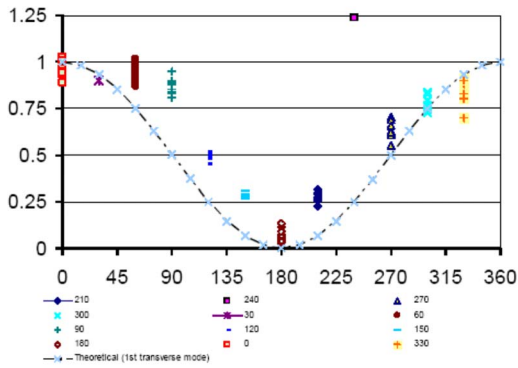
Fig. 10 Measured relative pressure amplitudes as functions of circumferential angle

accuracy of the present crude approach, differences from the assumed hollow cylindrical shape are not likely to affect predictions substantially. Consideration of possible amplification mechanisms led to the belief that, just as in the previous two types of experiments, mixture-ratio variations seemed likely to contribute the main source. With this in mind, a velocity-sensitive model was addressed for which

$$q' = n \frac{\gamma \bar{q}}{\bar{c}} \sum_{\kappa=1}^{N} u'(\theta_\kappa, t - \tau) \delta(r_\kappa - r_f) \frac{L(R_o - R_i)}{N r_f} \qquad (65)$$

Although u' here is the acoustic velocity in the circumferential direction, it is assumed that this same velocity is transmitted locally to the axial flow in the injector, thereby generating the equivalence-ratio oscillations. Axial velocity fluctuations at twice this frequency may also be expected, but for the standing wave, there should also be a contribution at this fundamental frequency. An efficiency of transmission at the fundamental, can however, be introduced, for example, by including an additional factor less than unity in n.

Rather than working with an explicit formula such as Eq. (48), a numerical integration of Eq. (7) was performed utilizing the expressions obtained in Eqs. (64) and (65) with the time-lag expression in Eq. (10), and employing the values 5 cm for L_{inj}= $-x_v$, 0.63 for ϕ, 22.8 m/s for U_{inj}, 8.5 m/s for U_c, 10% of U_c for $\bar{u}$, 2.407×10^7 J/kg for Q_r, 1.8 cm for x_{f1}, 13.2 cm for x_{f2}, 3.8 cm

for r_{f1}, and 33.5 cm for r_{f2}. The interaction index n was obtained from Eq. (30) by use of Eq. (33), in which the contribution to n from the laminar burning velocity was 2.9, that from the heat release was 0.95, and that from the other terms was negligible. In the numerical integration, besides these equivalence-ratio fluctuations, effects of vortex shedding, wall damping, and damping due to the perforated-wall lining were taken into account, using data given in the Appendix. The results for the growth rate, shown in Fig. 11, indicate a possible instability peaking around the combustion chamber's fundamental frequency of 250 Hz. The vortex-shedding frequency was found to be around 915 Hz and had only a small impact on the overall growth rate, while the liner and wall damping had a larger effect and were mainly responsible for the negative slope shown in the figure at the higher frequencies. Figure 11 therefore is consistent with most of the amplification at the fundamental frequency being due to the equivalence-ratio fluctuations.

Other modes in this combustor are at higher frequencies and generally would be predicted to be stable according to Fig. 11. For example, the frequency of the first standing axial-mode frequency is estimated from $\bar{c}/(2L)$ to be 1094 Hz, which is beyond the range of positive amplification. Since the liner was designed only for cooling, not for acoustic attenuation, a modified liner design may have eliminated the oscillation at the fundamental azimuthal frequency.

A Twelve-Injector, High-Pressure, Annular-Combustor Engine. To investigate the effect of high pressure in a multiple-injector, annular configuration, an actual engine with development injectors was tested. The platform chosen was the Solar Turbines Taurus-70 (a 7.5 MW package). The engine test is an extension of the previous atmospheric annular test in that it uses the same set of injectors and a similar liner, but it operates at a higher pressure. The engine has a 14-stage axial compressor (instead of preheated air) and a few components downstream (turbine and exhaust), all of which might have had a contribution to the overall recorded oscillation and thereby introduce added uncertainty in estimates. The experiment, however, does serve to illustrate application of the approach in a practical engine environment.

The instrumentation, similar to that adopted for the annular atmospheric rig, used dynamic pressure sensors mounted as before on the pilot fuel line to monitor oscillations. In this test, there were 13 dynamic pressure sensors, an extra one having been
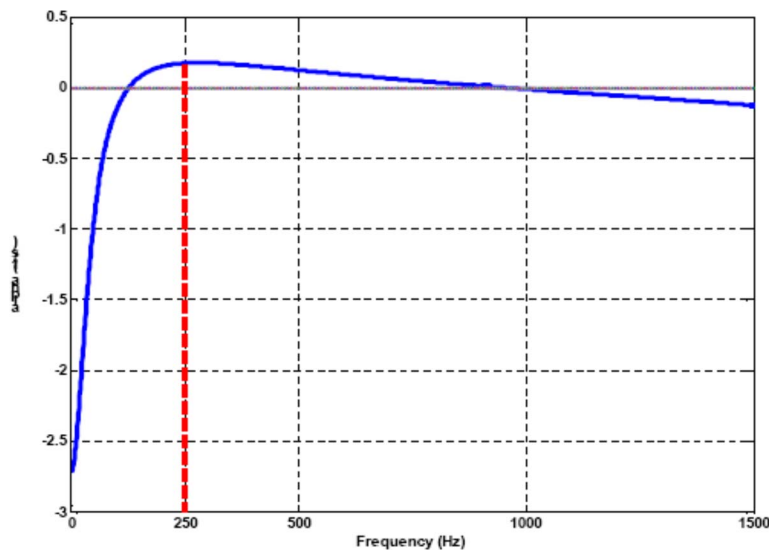
Fig. 11 Growth-rate predictions for the atmospheric-pressure, annular combustor
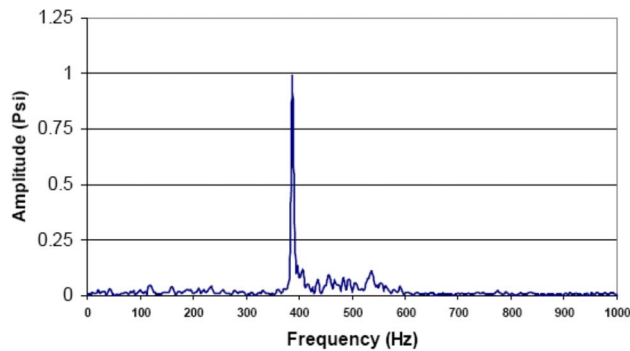
Fig. 12 Dynamic pressure spectrum obtained during oscillation on a Taurus-70 engine test (full load, 4% pilot flow, and primary zone at 2853°F)

mounted on the torch to give phase information with respect to the torch. Dynamic pressure data were collected using the same instrumentation described previously.

The flow rates tested were adjusted to keep the equivalence ratio between 0.60 and 0.72, where oscillations could be observed. The air flow rate was fixed at 54 lb/s, with a compressor outlet pressure between 160 psi and 240 psi, and the fuel flow was varied between 1800 lb/h and 3500 lb/h, with the dominant oscillations observed to arise near 3400 lb/h. This is consistent with the predictions, indicated earlier, that amplification rates are largest at the highest heat-release rates. Pilot flow rates from about 2% to 10% were explored, and oscillations were observed at the lower pilot flow rates, 2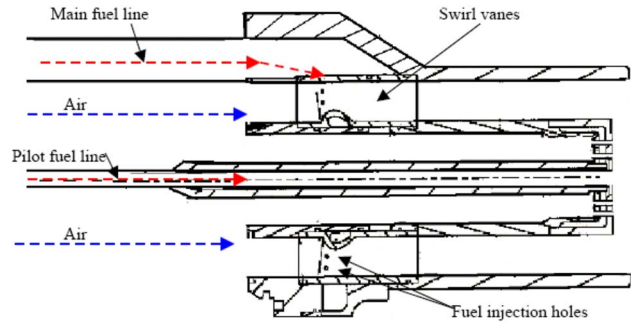%–4%, just as with the atmospheric rig. Measurements were made at 4% pilot flow rates, for which representative pressure amplitudes are shown in Fig. 12, where the dominant frequency, seen to be about 387 Hz, is consistent with a first mixed (axial/circumferential) mode.

This oscillation, at a frequency on the order of 400 Hz, occurring at full load and low pilot percentage, was the highest-intensity oscillation observed under any conditions. To map out the instability characteristics further, measurements were also made at idle, 50% load and 75% load, with variable pilot percentages, and under different conditions, there were indications of low-frequency oscillations (rumble at ~37 Hz), of oscillations at a midrange frequency (200 Hz), and of a low-amplitude high-frequency instability (screech at ~1050 Hz), but all of these were much less intense than the 400 Hz oscillation, which occurred at both 75% and full load. Unlike in the atmospheric rig, there was

no indication of a purely circumferential mode, at a frequency on the order of 250 Hz, possibly because of damping influence of the guide vanes at the entrance to the turbine in the engine, which would tend to impede circumferential motion. In the present work, therefore, attention was focused on the first mixed mode, the presence of which was consistent with observed irregular and variable phase relations between signals from the different pressure sensors and with corresponding relative amplitude results. With so many rotating parts, namely, compressor, turbine, generator (fixed at 60 Hz), etc., it is difficult to isolate the combustion-related oscillations. A mixed mode, standing axially but rotating circumferentially, therefore finally was assumed for purposes of comparison with predictions.

In modeling the engine, the boundary conditions for the combustor-premixer assembly were assumed to provide a pressure node at the injector and a velocity node at the combustor exit (taken at the inlet guide vane to the turbine), where the flow is assumed to approach choked conditions. Equation (5) for the first mixed mode then simplifies to

$$p'(x,\theta,t) = \tilde{p}\cos(\omega t)\sin\left(\frac{\pi x}{2L}\right)\cos(\theta)$$

$$u'(x,\theta,t) = \left(-\frac{\tilde{p}}{\bar{\rho}c}\right)\sin(\omega t)\cos\left(\frac{\pi x}{2L}\right)\cos(\theta)$$

(66)

with u' again representing the circumferential component, which is proportional to the axial component. Numerical integration of Eq. (7), utilizing expressions obtained in Eqs. (65) and (66) with the time-lag expression in Eq. (10), and employing 0.63 for ϕ, 89 m/s for U_{inj}, 2.1 m/s for U_c, 10% of U_c for $\bar{u}$, 2.407 $\times 10^7$ J/kg for Q_r, and the same dimensions as those used for the annular atmospheric rig, gives the results shown in Fig. 13. The interaction index n was obtained from Eq. (30) by use of Eq. (33), in which the contribution to n from the laminar burning velocity was 2.9, that from the heat release was 0.95, and other terms were negligible, just as for the atmospheric rig. In the numerical integration, besides these equivalence-ratio fluctuations, effects of vortex shedding, wall damping, and damping due to the perforated-wall lining were taken into account, using the data given in the Appendix. The results for the growth rate, shown in Fig. 13, indicate a possible instability around the frequency of the first mixed mode of the combustion chamber, about 400 Hz. The vortex-shedding frequency was found to be much higher (over 1500 Hz) and had a small impact on the overall growth rate. Figure 13 therefore is consistent with most of the amplification being due to the equivalence-ratio fluctuations, just as in the other
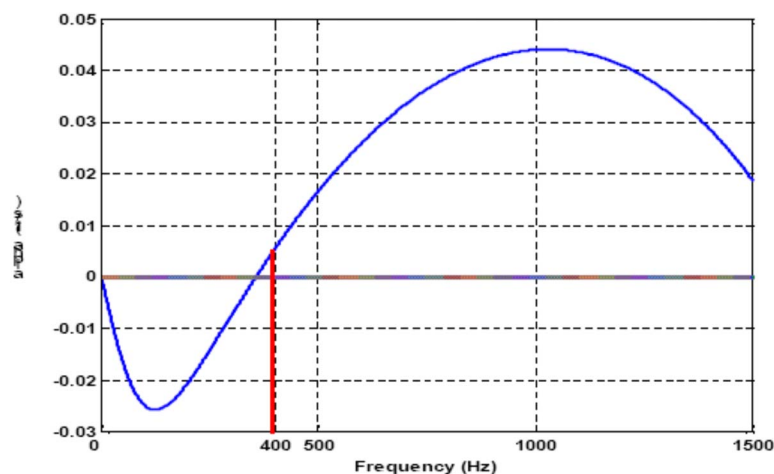
Fig. 13 Predicted growth-rate results for the annular high-pressure engine test
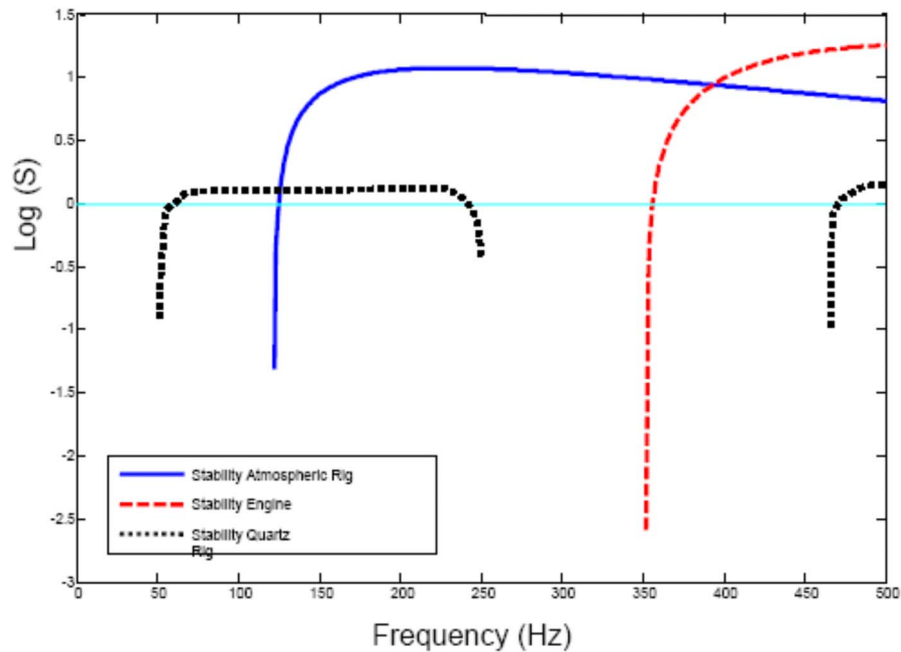
Fig. 14 Predicted stability results for the three performed experiments (1–500 Hz)

experiments.

Except for the difference in the acoustic mode, the preceding model for the engine is quite similar to that for the atmospheric rig. There are, however, significantly greater uncertainties in the modeling results for the engine. The amplification rate at 400 Hz, seen in Fig. 13, is small, comparable with that found in the atmospheric rig. Moreover, much higher amplification rates are seen to be predicted at higher frequencies, and it is unlikely that the increased damping for these higher acoustic modes can be large enough to offset the large predicted increase in amplification. Even the vortex-shedding mechanism, with a frequency above 1500 Hz, might be thought to result in screech amplitude in excess of the observed oscillation at 387 Hz. One aspect of Fig. 13 that may be considered favorable is the predicted attenuation at 250 Hz, which makes it unnecessary to appeal to extraneous factors such as guide vanes for eliminating the fundamental circumferential mode. This difference from results shown in Fig. 11 for the atmospheric rig is a consequence of the different mode, including now an axial component and also a traveling rather than standing circumferential component. Another criticism of these predictions is that, with a traveling circumferential component (perhaps in the direction of rotor rotation), it is less likely that velocity fluctuations at this frequency can be transferred efficiently to the axial-component fluctuations in the injectors, needed to generate equivalence-ratio fluctuations; double-frequency oscillations in the axial velocities in the injectors may be expected to be more pronounced, calling into question Eq. (65). Equivalence-ratio fluctuations may well be the driver of the instability, but the mode shape assumed in Eq. (66) may be incorrect, the phase information from the pressure transducers being inconclusive. There may, for example, be a standing circumferential component that helps drive the equivalence-ratio oscillations. Even without this, however, the axial component can generate axial velocity fluctuations in the injectors, leading again to Eq. (65), given the same types of assumptions that were employed in its derivation. The main advantage of Eq. (66) is that its associated natural oscillation frequency is close to the observed frequency, but there are other possible mode shapes with this frequency that would modify Fig. 13. These observations underscore the importance of investigating all possible mode shapes, in general, in applying the approach developed here during design investigations.

Conclusions

The paper presents a simplified approach in analyzing combustion-driven acoustic oscillations in premixed gas-turbine combustors. The method works by examining the acoustic energy content in a control volume of interest (usually an injector/combustor assembly). It identifies some of the physical mechanisms that contribute to the growth and decay of acoustic energy within the combustion volume, calculates growth/attenuation rates for the described mechanisms, and thus predicts whether the combustion system will experience oscillations. The approach, as described, is linear and utilizes linear approximations when nonlinear events are encountered.

Simplified models for equivalence-ratio fluctuations (including turbulent dissipation) and vortex shedding were developed, along with other models. Results from the first of these models (namely, that for equivalence-ratio fluctuations) were shown to compare reasonably well with experimental results obtained from a single-injector quartz combustor operating at atmospheric conditions as well as from a single-injector high-pressure combustors. It was found to be possible to use this same mechanism to rationalize results obtained from experiments on a 12-injector, annular, atmospheric-pressure rig. Measurements made on an engine with this same combustor configuration were, however, less conclusive, although they could be consistent with the same mechanism. A stability-index chart, based on Eq. (6), for all three experiments performed in connection with the present work is shown in Fig. 14. The figure illustrates the strong tendency for oscillations to occur in the 12-injector, atmospheric rig at frequencies between 120 Hz and 500 Hz and indicates a comparatively marginal instability range for the quartz combustor under the experimental conditions. Higher fuel-flow rates would have increased the strength of and range of predicted instability for the quartz combustor, while modified liner designs may have reduced the potential instability for the atmospheric rig (as well as for the engine).

All of the tests of the approach that were reported here involved efforts to explain, after the fact, what was observed experimentally. This would not be possible in using the approach as a design tool. In design, it would be necessary to identify all of the possible acoustic frequencies and acoustic-mode shapes in the combustion chamber, and for each of these to address each of the amplification

and damping mechanisms, to determine from Eq. (6) whether oscillation is predicted to occur. This entails appreciable effort and also involves significant uncertainties. The nature of the uncertainties has been illustrated in the four different applications to experiments reported here. Not only do dimensions and operating conditions need to be estimated but also expected flame shapes need to be hypothesized. As a result, there are likely to be significant ranges of uncertainties in the predictions, and value judgments will need to be made. Similar kinds of uncertainties arise in early applications [6,7] of the Galerkin approach, where the accuracy of the mode description as well as the chosen model for the heat-release perturbations affect the predictions to a great extent. While the Galerkin method works by identifying a set of acoustic modes then following their growth or decay by marching in time, the current approach is simpler, in that the mode shapes are approximated in a less complicated fashion, and predictions are made only for a growth rate, which does not involve integrating numerically in time. This makes the calculations simpler and less expensive.

The main advantage of the approach is that, beyond helping to increase the understanding of specific aspects of the types of oscillations that may occur, each individual calculation can be performed much more quickly and less expensively than calculations requiring CFD or other numerically demanding approaches. Since there are also uncertainties in other methods of prediction, the method proposed could find a useful place alongside other tools used in premixed gas-turbine combustor design.

Acknowledgment

Appendix

The values used to calculate the damping rate by the perforated-wall liner are as follows: Chamber properties and liner dimensions:

- the annular combustor was 0.38 m long
- inner radius of the combustor was 0.26 m
- outer radius of the combustor was 0.34 m
- Mean temperature of $1273\,°K$ calculated from the temperature of the fresh reactants and the adiabatic flame temperature

Perforated-wall holes were of two types:

(1) radius 0.0013 m spaced at 0.0219 m apart
(2) radius 0.0020 m spaced at 0.0585 m apart

Both sets of holes were 0.01 m from the backing wall.

References

[1] Lieuwen, T., and Yang, V., 2006, *Combustion Instabilities in Gas Turbine Engines: Operational Experience, Fundamental Mechanisms, and Modeling*, AIAA, Reston, VA.
[2] Martin, C., Benoit, L., Sommerer, Y., Nicoud, F., and Poinsot, T. J., 2006, "Large Eddy Simulation and Acoustic Analysis of a Swirled Staged Turbulent Combustor," AIAA J., **44**(4), pp. 741–750.
[3] Keller, J. J., 1995, "Thermoacoustic Oscillations in Combustion Chamber of Gas Turbines," AIAA J., **33**(12), pp. 2280–2287.
[4] Polifke, W., Paschereit, C. O., and Dobbeling, K., 2001, "Constructive and Destructive Interference of Acoustic and Entropy Waves in Premixed Combustor With A Choked Exit," Int. J. Acoust. Vib., **6**(3), pp. 135–146.
[5] Dowling, A. P., and Stow, S. R., 2003, "Acoustic Analysis of Gas Turbine Combustors," J. Propul. Power, **19**(5), pp. 751–764.
[6] Culick, F. E. C., 1970, "Stability of Longitudinal Oscillations With Pressure and Velocity Coupling in a Solid Propellant Rocket," Combust. Sci. Technol., **2**, pp. 179–201.
[7] Zinn, B. T., and Lores, M., 1972, "Application of the Galerkin Method in the Solution of Non-Linear Axial Combustion Instability Problems in Liquid Rockets," Combust. Sci. Technol., **4**, pp. 269–278.
[8] Ibrahim, Z. M., Williams, F. A., Buckley, S. G., and Lee, J. C. Y., 2006, "An Acoustic Energy Approach to Modeling Combustion Oscillations," ASME Paper No. GT-2006-90096.
[9] Landau, L. D., and Lifshitz, E. M., 1987, *Fluid Mechanics*, Pergamon, Oxford, UK.
[10] Williams, F. A., 1985, *Combustion Theory*, Addison-Wesley, Redwood City, CA.
[11] Crocco, L., and Cheng, S. I., 1956, *Theory of Combustion Driven Instabilities in Liquid Rocket Motors*, Butterworths Scientific, London, UK.
[12] You, D., Huang, Y., and Yang, V., 2005, "A Generalized Model of Acoustic Response of Turbulent Premixed Flame and Its Application to Gas-Turbine Combustion Instability Analysis," Combust. Sci. Technol., **177**, pp. 1109–1150.
[13] Scarinci, T., and Freeman, C., 2000, "The Propagation of a Fuel-Air Ratio Disturbance in a Simple Premixer and Its Influence on Pressure Wave Amplification," ASME Paper No. GT-2000-0106.
[14] Sattelmayer, T., 2000, "Influence of The Combustion Aerodynamics on Combustion Instabilities From Equivalence Ratio Fluctuations," ASME Paper No. GT-2000-0082.
[15] Wang, A. B., Travnicek, Z., and Chia, K. C., 2000, "On the Relationship of Effective Reynolds Number for the Laminar Vortex Shedding of a Heated Circular Cylinder," Phys. Fluids, **12**(6), pp. 1401–1416.
[16] Putnam, A. A., 1971, *Combustion-Driven Oscillations in Industry*, American Elsevier, New York.
[17] Howe, M. S., 1998, *Acoustics of Fluid-Structure Interactions*, Cambridge University Press, Cambridge, UK.
[18] Howe, M. S., 1979, "On the Theory of Unsteady High Reynolds Number Flow Through a Circular Aperture," Proc. R. Soc. London, Ser. A, **366**(1725), pp. 205–223.
[19] Hughes, I. J., and Dowling, A. P., 1990, "The Absorption of Sound by Perforated Linings," J. Fluid Mech., **218**, pp. 299–335.
[20] Eldredge, J. D., and Dowling, A. P., 2003, "The Absorption of Axial Acoustic Waves by a Perforated Liner With Bias Flow," J. Fluid Mech., **485**, pp. 307–335.
[21] Abramowitz, M., and Stegun, I., 1964, *Handbook of Mathematical Functions with Formulas, Graphs, and Mathematical Tables*, Dover, New York.
[22] Gharavi, M., Ibrahim, Z. M., Borchers, M., Williams, F. A., Buckley, S. G., and Arellano, L., 2007, "Tunable Diode Laser Measurements of Equivalence-Ratio Fluctuations for Premixed Gas-Turbine Applications," Fifth US Combustion Meeting, San Diego, CA.
[23] Richards, G. A., and Janus, M. C., 1998, "Characterization of Oscillations During Premix Gas Turbine Combustion," ASME J. Eng. Gas Turbines Power, **120**, pp. 294–302.
[24] Straub, D. L., and Richards, G. A., 1998, "Effect of Fuel Nozzle Configuration on Premix Combustion Dynamics," ASME Paper No. GT-1998-492.
[25] Straub, D. L., and Richards, G. A., 1999, "Effect of Axial Swirl Vane Location on Combustion Dynamics," ASME Paper No. GT-1999-109.

Autoignition of Hydrogen and Air Inside a Continuous Flow Reactor With Application to Lean Premixed Combustion

D. J. Beerer

V. G. McDonell
e-mail: mcdonell@ucicl.uci.edu

UCI Combustion Laboratory,
University of California,
Irvine, CA 92697-3550

With the need to reduce carbon emissions such as CO_2, hydrogen is being examined as potential "clean" fuel for the future. One potential strategy is lean premixed combustion, where the fuel and air are allowed to mix upstream before entering the combustor, which has been proven to curb NO_x formation in natural gas fired engines. However, premixing hydrogen and air may increase the risk of autoignition before the combustor, resulting in serious engine damage. A flow reactor was set up to test the ignition delay time of hydrogen and air at temperatures relevant to gas turbine engine operations to determine maximum possible mixing times. The results were then compared to past experimental work and current computer simulations. The current study observed that ignition is very sensitive to the initial conditions. The ignition delay times follow the same general trend as seen in previous flow reactor studies: ignition within hundreds of milliseconds and relatively low activation energy. An experimentally derived correlation by Peschke and Spadaccini (1985, "Determination of Autoignition and Flame Speed Characteristics of Coal Gases Having Medium Heating Values," Research Project No. 2357-1, Report No. AP-4291) appears to best predict the observed ignition delay times. Homogenous gas phase kinetics simulations do not appear to describe ignition well in these intermediate temperatures. Therefore, at the moment, only the current empirical correlations should be used in predicting ignition delay at engine conditions for use in the design of gas turbine premixers. Additionally, fairly large safety factors should still be considered for any design to reduce any chance of autoignition within the premixer.
[DOI: 10.1115/1.2939007]

Introduction

With the need to reduce carbon emissions such as CO_2, hydrogen is being examined as potential "clean" fuel for the future. Hydrogen has been employed in the past as a rocket fuel, yet relatively little work has been done to determine the suitability of the fuel for gas turbine applications. However, the potential use of hydrogen produced from gasification for gas turbines in an "integrated gasification combined cycle (IGCC)" has led to an increase in interest. Although examples of gas turbines operating on hydrogen (or high hydrogen content fuels such as syngas) are found in the literature [1,2], current IGCC developments require extremely low NO_x emission levels. As a result, for hydrogen fired gas turbine applications in the future [3], low emission strategies must be considered. However, hydrogen poses a greater challenge than hydrocarbon fuels for a number of reasons [4–7]. Natural gas fired gas turbines have successfully adopted lean premixed combustion as a key enabler for ultralow emission levels, which leads one to ask if such engines could be converted for hydrogen use. In a lean premixed combustor, fuel and air are allowed to mix upstream before entering the combustor. This is desirable, as an overall lean mixture will have a lower flame temperature, which inhibits NO_x formation, and by premixing the fuel and air, this eliminates any "pockets" of high fuel concentration, which could burn at higher temperatures. It is essential to know the maximum allowable mixing time (which will be less than the ignition delay time) for the fuel and air at the pressures and temperatures typically observed inside premixers in order to avoid autoignition and engine damage.

Typical inlet temperatures lie in an intermediate temperature range (600–950 K) and pressures from 4 atm to 30 atm. Recently, a number of papers have reported ignition delay times for both syngas/air and hydrogen/air at these elevated temperatures and pressures, along with explanations for the observed ignition delay times [8–10]. There is a considerable difference between observed results using various experimental techniques and models using simple homogenous reactor systems and current chemical mechanisms. This discrepancy poses a challenge to engineers designing premixers because a reliable way of predicting the ignition delay time for hydrogen fueled systems under realistic engine conditions is not yet available and is the subject of this study.

In this paper, results and observations from the experiments performed in a high pressure continuous flow reactor, which try to simulate the conditions inside gas turbine premixers, are presented and compared with other autoignition experiments using different test apparatuses. It is hoped that these results will shed further light on this issue of autoignition along with insight and suggestions on engine premixer design.

Background

The gas phase oxidation of hydrogen with either oxygen or air is probably the most intensely studied and well-understood reactant systems. A number of investigators have measured ignition delay times of hydrogen/oxygen or air systems at intermediate temperatures in shock tube devices [11–18], while others have used flow reactors that better simulate the conditions seen inside a gas turbine premixer. For instance, Peschke and Spadaccini [19] used a continuous flow reactor with undiluted syngas fuel ($H_2/CO/CO_2$) with varying mole fractions of H_2 and H_2O to determine ignition delay times at temperatures between 630 K and 780 K and pressures from 12 atm to 23 atm. This work concluded

Table 1 Experimentally derived correlation of ignition delay for undiluted hydrogen/air, syngas/air, and hydrogen/oxygen at intermediate temperatures. Concentrations are in terms of mol/cc for Peschke's correlation and mol/l for Walker's corrrelations, and temperature is in kelvin for all four.

Author	Mixture	Method	Correlation	T (K)	P (atm)	Φ
Peschke and Spadaccini	Syngas/air	Continuous flow reactor	$\tau\,(\mathrm{s})\cdot[O_2]^{0.5}[F]^{0.25}=1.29\times10^{-7}\exp(3985/T)$	630–780	12.5–23	0.3–0.6
Walker	Hydrogen/air	Shock heated flow	$\log_{10}[O_2]\cdot\tau\,(\mathrm{s})=-6.016+\dfrac{1604}{4.58T}$	550–850	6.5–20	1
Walker	Hydrogen/air	Shock tube reflected shock	$\log_{10}[O_2]\cdot\tau\,(\mathrm{s})=-12.683+\dfrac{30{,}419}{4.58T}$	765–1160	1.15–19	1
Steinberg and Kaskan	Hydrogen/oxygen	Shock tube reflected shock	$\tau\,(\mu\mathrm{s})=3.4\times10^{-4}\exp(11{,}000/T)$	775–930	7.5–25	1

that the ignition delay time is nearly independent of the CO or CO_2 concentration, indicating that the ignition properties of syngas are dominated by hydrogen kinetics. As a result, the measured syngas ignition delay results are comparable with hydrogen/air results.

Table 1 lists a number of experimentally derived correlations for ignition delay from a number of investigators in the temperature range between 630 K and 1000 K [17,19,20]. These correlations are for hydrogen/air, syngas/air, or hydrogen/oxygen systems autoigniting in various devices: shock tube, continuous flow reactor, and shock-heated flow apparatus. A comparison of these correlations along with experimental results is presented in Fig. 1. The points represent experimental data, while the lines represent empirically derived correlations from past investigators. The lines are plotted in the temperature range under which they are valid. Peschke and Spadaccini's correlation was for a mixture at 15 atm, Walker's was for a mixture at 5 atm, and Steinberg and Kaskan's was for 10 atm. It is interesting how each device and temperature range can give such drastically different results both in magnitude of ignition delay time and in activation energy (slope). For an engineer to know which correlation to use and its accuracy for predicting autoignition in a specific premixer may not be a straightforward task.

In addition to autoignition tests of hydrogen/air mixtures, species and temperature profiles of the "post-induction" region (after the initial mixing and induction period) in homogenous gas phase reactions were studied in flow reactors as far back as Glassman and Sawyer [21]. Experiments were performed in plug flow reactors under highly diluted conditions with special wall materials (quartz or silica) along with large diameters to reduce wall effects and spatial gradients. Dryer and co-workers continued these plug flow reactor experiments over the past few decades, which re-

sulted in a number of popular mechanisms for the oxidation of hydrogen, with their more recent revision being published in 2007 [22]. None of these studies tried to quantify the induction time (or ignition delay time) because results obtained from flow reactors are very sensitive to mixing and other perturbations [23].

Of all the existing data on ignition and kinetics of hydrogen/air systems, the autoignition study by Peschke and Spadaccini performed in a turbulent flow reactor best represents the conditions inside gas turbine premixers and is hence likely to simulate ignition in a premixer most accurately. Because their results do not match closely with other autoignition studies (perhaps due to experimental techniques), it is desirable to reproduce their results with a similar device. Additionally, experiments conducted outside the validation range will allow one to estimate the accuracies of the correlations when extrapolated out to new temperatures, pressures, and equivalence ratios.

As a result, the two objectives of this paper are (1) to present recent experimental work on autoignition in a similar device to that used previously and (2) to compare these results to an extensive literature review for autoignition of hydrogen/air mixtures in order to advise on the suitability of hydrogen as a fuel in a premixed engine configuration.

Approach

Because different techniques appear to give varying results, it is desirable to use an apparatus that would closely simulate the condition inside a premixer, so that the results obtained could be confidently applied to a premixer. Therefore, a continuous flow reactor is used in the current study. This type of a device has the following features: isobaric, turbulent, and subsonic, with wall or boundary layer effects possible. The current flow reactor used can experimentally determine ignition delay times for flowing hydrogen air mixtures at intermediate temperatures (600–900 K) and elevated pressures (4–7 atm). Unfortunately, facility limitations prevented testing at pressures above 7 atm where many gas turbine premixers operate.

Experiment

The test procedure and vessel in the current study have been described in detail in past reports [24,25]. However, a brief summary is presented here as well. The device used in the current study is a stainless steel flow reactor like the one used by Peschke and Spadaccini [19] during their syngas/air ignition experiments. Lefebvre et al. [26] also used a similar flow reactor in the past to measure the ignition delay times of hydrocarbon fuels. A schematic is shown in Fig. 2. The flow reactor produces a fully developed turbulent flow of preheated air (Re~30,000–150,000) in which the fuel is injected. A 72 kW electric heater is used to raise air temperatures between 700 K and 950 K. Similarly, fuel is preheated to any temperature from room temperature to 600 K using a smaller inline heater.
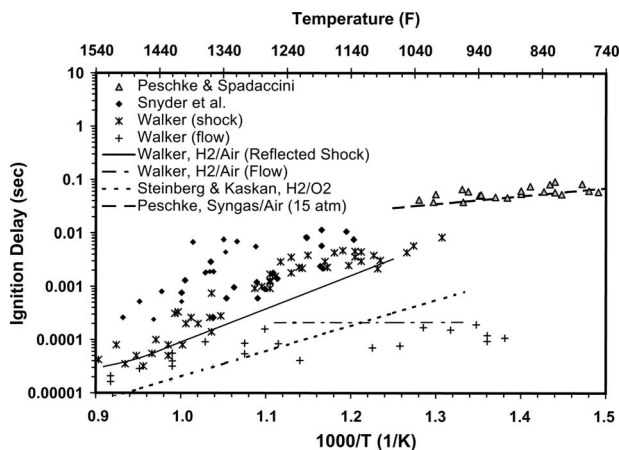
Fig. 1 Comparison of current data with past ignition delay studies
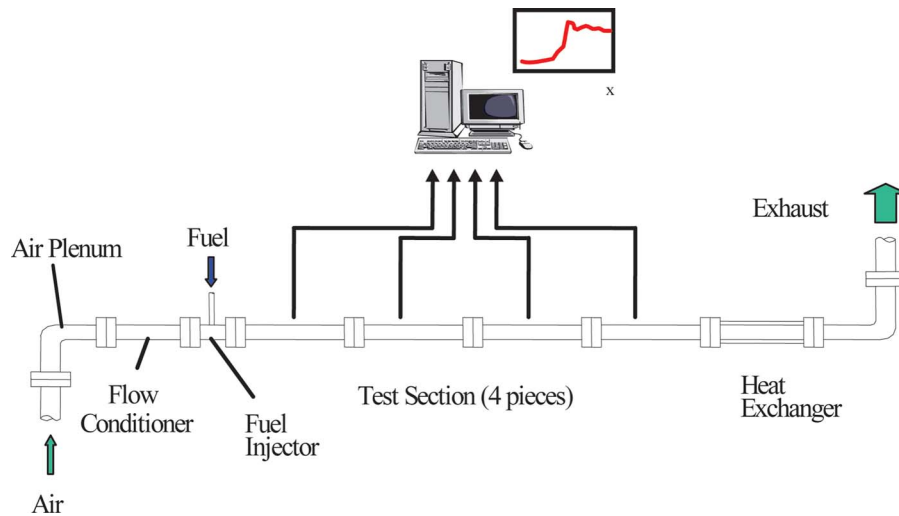
Fig. 2 Schematic of the continuous flow reactor

The air enters a venturi nozzle after a flow conditioner. At the throat, the fuel is injected perpendicular to the flow from a series of small orifices aiming radially inward. The injector was designed to produce rapid mixing (within 140 mm downstream of injection). The mixture then proceeds down a 38.1 mm inner diameter smooth steel pipe. The test section length is 3.8 m. Clamshell heaters and aluminum silica insulation blankets surround the first 3.1 m of the test section in order to approximate a near adiabatic condition. The latter part (where optical and temperature equipment is located) is surrounded by only insulation blankets, resulting in a small loss of heat (temperature drop over this section is normally ~15 K). However, the measurement error of the ignition delay due to this drop should be fairly small.

One key difference between the current flow reactor and those used previously is that in the current reactor the walls are maintained at the same temperature as the flowing air, while in the flow reactor of Peschke and Spadaccini the reactor walls were cooled with water to quench any ignition originating in the boundary layer. As real premixers will not have cooled walls, the current device was designed without water cooled walls.

Monitoring the reaction within the vessel is a Hamamatsu R106UH photomultiplier tube (PMT) mounted at the end of the test section looking axially down the vessel and monitors all light in the visible spectrum. If any reaction occurs, resulting in chemiluminescence, the PMT will detect this and send a signal to a computer. In addition to the PMT, a number of Omega® type-K thermocouples are mounted near the end of the test section to confirm ignition from a rise in temperature.

An analysis of the flow field within the test section was conducted in previous studies. Computational fluid dynamics (CFD) modeling of the fuel injector and mixing was performed by Chen et al. [24] and was confirmed through measurements using a flame ionization detector (FID) device and other diagnostic procedures. The velocity profile (Fig. 3) and FID tests (Fig. 4) were repeated under cold flow conditions prior to these tests to confirm the previous measurements. FID measurements were performed by injecting a dilute propane/nitrogen mixture through the venturi and measuring the concentration downstream. Results showed only a 2% variation in concentration along the profile of the pipe; however, fuel concentration was slightly higher near the walls.

The traditional procedure for determining ignition delay times in the studies of Peschke and Spadaccini [19] and also Lefebvre et al. [26] was as follows: The residence time of the fuel and air would be adjusted within the test section (based on flow rates) to a desired value. This was followed by incrementally raising the temperature of the mixture until ignition occurred within the test

section. The ignition delay time for the temperature at which the mixture autoignited was then estimated to be that of the bulk residence time of the flow within the test section

As mentioned previously, the works of both Sawyer and Dryer have caution against trying to find precise induction or ignition delay times based solely on the bulk residence time because of the sensitivity of the flow to small perturbations. With this in mind,
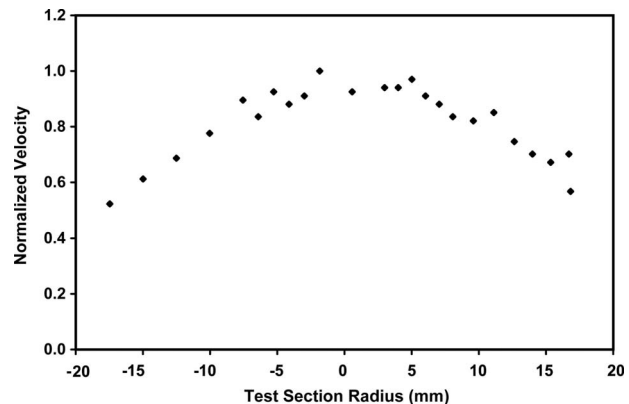
Fig. 3 Velocity profile in the test section during cold flow test. Reynolds number=125,000.
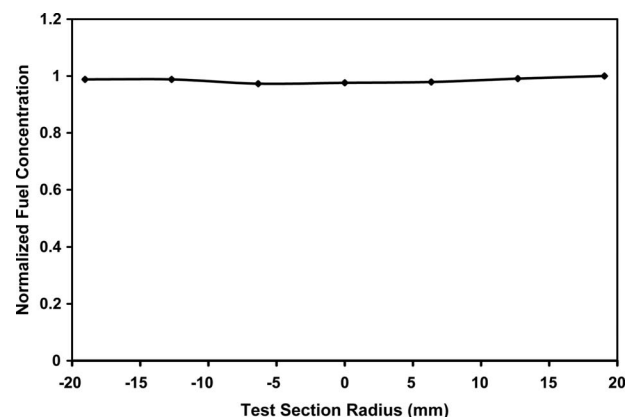
Fig. 4 Fuel concentration profile in the test section during the FID test

Table 2 Results of the current study for hydrogen/air ignition

Test	Pressure (atm)	Air (K)	Fuel (K)	Φ	T mix (K)	1000/T (1/K)	Residence time (ms)	Ignition
1	5.8	801	301	0.28	753	1.33	192	Yes
2	5.8	804	301	0.28	7563	1.32	190	Yes
3	5.8	807	301	0.28	747	1.34	189	No
4	5.8	808	301	0.28	748	1.34	189	No
5	5.8	798	341	0.28	745	1.34	190	No
6	5.8	800	452	0.28	755	1.32	187	No
7	5.8	803	451	0.37	745	1.34	183	No
8	5.8	825	478	0.37	780	1.28	178	Yes
9	6.0	830	477	0.32	771	1.30	183	No
10	5.6	832	477	0.28	784	1.28	174	No
11	5.7	833	477	0.29	786	1.27	180	No
12	5.7	834	477	0.45	781	1.28	168	Yes
13	5.7	835	477	0.45	764	1.31	172	No
14	5.7	837	505	0.45	769	1.30	171	No
15	5.7	836	505	0.45	769	1.30	171	No
16	5.8	837	505	0.28	805	1.24	179	Yes
17	5.8	838	505	0.28	807	1.24	178	Yes
18	5.8	837	505	0.28	795	1.26	178	No
19	5.8	838	505	0.14	810	1.23	184	No
20	5.8	838	509	0.45	786	1.27	168	Yes
21	5.8	845	508	0.45	792	1.26	167	Yes
22	5.1	809	300	0.33	744	1.34	155	No
23	5.1	808	300	0.33	755	1.32	155	No
24	5.1	812	300	0.33	762	1.31	153	No
25	5.3	802	300	0.33	768	1.30	161	No
26	5.3	807	300	0.33	772	1.30	161	No
27	5.3	809	300	0.40	783	1.28	132	No
28	5.3	811	300	0.40	783	1.28	132	No
29	5.1	781	300	0.33	777	1.29	111	No
30	5.1	779	300	0.33	777	1.29	111	No
31	5.1	721	300	0.27	747	1.34	92	No
32	5.1	672	300	0.24	714	1.40	92	No
33	5.1	668	300	0.24	711	1.41	92	No
34	5.1	669	300	0.27	710	1.41	90	No
35	5.3	699	300	0.28	730	1.37	413	No
36	5.4	699	300	0.28	730	1.37	413	No
37	5.5	699	300	0.28	730	1.37	413	No
38	5.5	699	300	0.28	730	1.37	413	No
39	5.1	755	300	0.46	779	1.28	383	No
40	5.2	794	300	0.46	721	1.39	364	No
41	5.4	811	300	0.46	735	1.36	356	No
42	5.1	819	300	0.28	769	1.30	353	No
43	5.1	824	300	0.28	773	1.29	390	No
44	5.2	824	300	0.46	738	1.36	390	No
45	5.1	826	300	0.52	771	1.30	389	No
46	6.1	827	300	0.31	772	1.30	454	No
47	6.4	832	300	0.31	778	1.29	451	Yes
48	6.4	832	300	0.31	796	1.26	450	No
49	6.4	834	300	0.20	748	1.34	451	No
50	6.4	834	300	0.52	777	1.29	452	No

the current study has adopted two independent methods for determining delay time to study this potential problem.

First, the traditional approach used in the previous flow reactor studies was implemented. Here, the residence time pressure and temperature were set to a desired value, and fuel was injected until a steady state condition was achieved. If ignition occurred, the ignition delay was estimated to be roughly equal to the residence time. By performing multiple tests over a range of conditions, the ignition delay time for this pressure/temperature region could be mapped.

In the second method, the difference in time between when fuel enters the vessel and when ignition occurs as detected by the PMT was measured and estimated to be the ignition delay. This method has been used successfully for measuring ignition delay times for aviation fuels and ethylene with air [27,28]. The benefits of this method include the fact that it eliminates the need to know the conditions of the flow inside the vessel to calculate the delay time.

However, it suffers from some ambiguity associated with finding the exact instance fuel enters the vessel because of the small time it takes the fuel to travel from the fuel valve to the injector ports. Nonetheless, comparing these two independent techniques can provide some insight relative to the concerns raised in the past about the residence time method.

Results

Tests were conducted over a series of several weeks. The results of each test are shown in Table 2. The points where ignition occurred are plotted against previous studies and their derived correlations in Table 1. The fuel used in this study was hydrogen, which was undiluted and mixed with air at an equivalence ratio between 0.2 and 0.6. The range of mixture temperatures is 700–800 K with pressures of 5–7 atm.
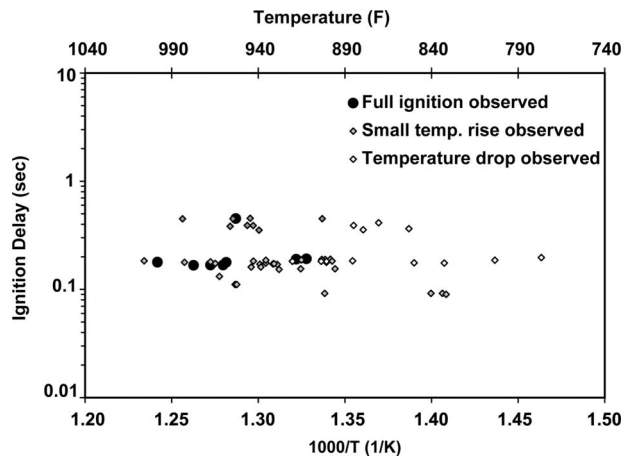
Fig. 5 Classification of ignition events

Fig. 6 Comparison of current results with previous measurements and correlations

One observation made during the testing was that the ignition tendency of the mixture was highly sensitive to the testing conditions. To illustrate this sensitivity, Fig. 5 plots all the points where tests were conducted and classifies the nature of the ignition event. In these tests, the air flow was set to a specified residence time, pressure, and temperature, and fuel was injected and the system was left to obtain a steady state. In some cases, a full ignition was observed while others only showed a small temperature rise or no rise at all. Full ignition (temperature rise of several hundred degrees) only occurred at higher temperatures but was rather sporadic, occurring only roughly one-half of the time within the time scale of the measurement. Details of the tests are provided in Table 2. To give an example of the sporadic ignition behavior, at residence time of 180 ms, ignition was seen as low as 750 K. However, for another run at 795 K with the same residence time, ignition did not occur. Further, when the flow rate was reduced to allow a residence time of nearly 400 ms, it would be expected to see ignition at a lower temperature compared to previous tests. However, ignition was not observed until 780 K. This observation suggests that perhaps the aerodynamics of the flow affects the delay time, either through mixing, turbulence levels, or effects in the boundary layer. Such effects have not been quantified yet in this or any previous study, which leads to interest in further investigations.

Uncertainties in estimating the residence times based of the bulk flow rate is in the range of 15% based on comparison from pitot tube measurements performed under cold flow conditions. Further investigation is being conducted at this time on the diffusion of fuel with respect to convective flow rates. Additionally, any uncertainties in timing the ignition delay from the PMT primarily lie in measuring the time at which fuel injection takes place. The estimated uncertainty in this has been studied and estimated to be around ±20 ms. The tests to compare the two methods were done at fairly low temperatures and slow flow rates (longer ignition delay times) to minimize the effects of these uncertainties on the results. During one test, for example, the residence time method estimated an ignition delay of 400 ms, while the PMT estimated a delay of 600 ms. A possible explanation for this significant difference would be that the mixture may be igniting in a region where local flow has a longer residence time than the bulk flow (in an eddy or boundary layer perhaps). Overall, this suggests that measuring ignition based only on the residence time may only have limited precision. However, because of the log scale presentation of the results, both methods give comparable results when given the variation found in the literature, as shown in Table 1 and Fig. 2.

Finally, the uncertainty of the temperature in the test section is estimated to be ±20 K based on the variation (both axially and radially) in the test section due to heat loss to the walls during normal operating conditions.
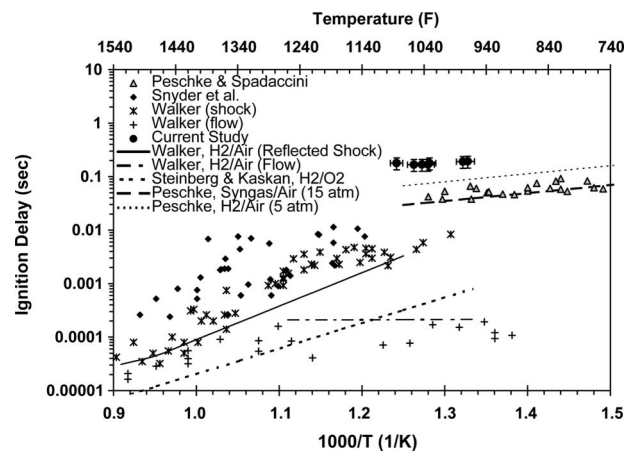
Despite the inconsistencies observed in the nature of the ignition events at lower temperatures, the current results appear to follow the same general trend observed by Peschke and Spadaccini [19]. Generally, higher pressures and higher temperatures both result in shorter ignition delay times. Additionally, the overall activating energy (given by the slope) is rather small. When Peschke and Spadaccini's correlation is applied to the lower pressure (but similar temperatures range) in the current study, as seen in Fig. 6, it appears that the correlation predicts a shorter delay time by roughly a factor of 2. Additionally, in the current study, ignition was never seen below 750 K, while Peschke and Spadaccini observed ignition down to 660 K under similar time scales. The differences in the results might be attributed to the slightly different designs of the two flow reactors. However, further investigation is still warranted.

One interesting observation made in this study was that at temperatures just shy of a full ignition event, the temperature increase at the walls, based on thermocouple readings, was much higher than at the axis of the flow reactor (for the same axial length downstream). In some cases, the difference in temperature rise between wall and axis was as much as 20 K. This means that either the local residence time at the walls is longer (slower flow), allowing more time to react, which results in an increase in temperature, or possibly some sort of catalytic reaction occurs at the wall. Further investigation is needed to determine the cause of this and its affect on the results.

As has been performed in previous papers [8–10], experimental results are compared with a simple kinetics model simulated in CHEMKIN 4.0 [29]. The reactor model was implemented in the AURORA® (PSR) module with the following assumptions: homogenous, zero dimensional, isobaric, and adiabatic. This simple reactor model has accurately determined ignition delay times of hydrogen/oxygen mixtures (compared with high temperature shock tube results) at temperatures above 1000 K in the past [30], so it would be desirable that such simulations could be accurate as well in the intermediate temperature regime below 1000 K where gas turbine engines run. The results of the simulations with respect to experimental values are presented in Fig. 7. The simulations for the present work utilized the reaction mechanism of O'Conaire et al. [30]. However, other mechanisms do exist and perform in a similar manner [25,31], especially in the context of the comparison shown in Fig. 7. Unfortunately, the observed and simulated results do not agree at all; the flow reactor measurements are orders of magnitude shorter than the simulations. As shown in Fig. 7, at higher temperatures (above 1000 K), the
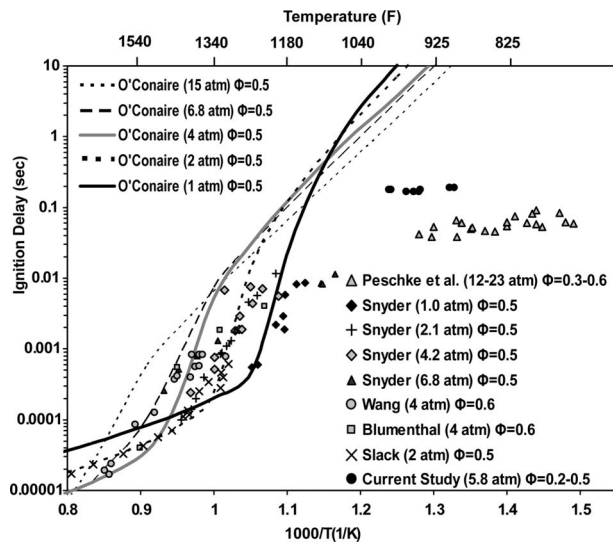
Fig. 7 Comparison of experimental work to homogenous simulations (mechanism by O'Conaire et al. [30])

Fig. 8 Hydrogen-oxygen explosion limit chart with experimental test conditions identified. The shaded region represents typical gas turbine combustor inlet temperatures and pressures.

model and experiment do agree fairly well. However, at lower temperatures, the measured ignition delays are far shorter than the model. In the context of the gas turbine premixer, this is disturbing since these lower temperatures are precisely where these devices operate. A possible reason for the discrepancy has been discussed recently in a number of papers and is summarized partly in the following section, with its implications for utilizing hydrogen or syngas in premixed combustors.

Discussion

The ignition delay time for hydrogen is linked to the hydrogen-oxygen explosion limits [32,33]. In the strong ignition region, which occurs at temperatures to the right of the second explosion limit, the elementary reactions involve a number of chain branching reactions involving H, O, and OH radicals. In the mild ignition region at intermediate temperatures and pressures above the third and "extended" second explosion region, the reactions occur through reactions involving the less reactive HO_2 and H_2O_2 radicals. The pressures and temperatures that will be seen in a gas turbine premixer typically lie within the shaded region seen in Fig. 8 based on the pressure and temperature values obtained from Table 3. It is seen that this area lies within the mild ignition and

the steady reaction regions. It is interesting that data from Peschke and Spadaccini [19] show comparable ignition delay times within both the mild ignition and steady action regions.

Additionally, test conditions for previous experimental work by Snyder et al. [13], Blumenthal et al. [15], and Wang et al. [16] are presented in Fig. 8 as well. If one examines these points carefully in the context of the explosive limit plot along with the resulting delay times, as shown in Fig. 7, it can be seen that the disagreement with the model occurs with experimental data points in the "mild" ignition region upon crossing over the extended second limit. This may give a clue regarding where to begin searching for a solution to the observed discrepancy between simulations and measurements.

Because the homogenous model and the experimental values show disagreement in only the mild ignition region, this may at first suggest a problem with the rates of the elementary reactions involving H_2O_2 and HO_2 since these species control the regime boundaries. However, Sabia et al. [34] analyzed these reactions using sensitivity analysis to explore the extent to which they would need to be modified in order to better match the experimental work of Snyder et al. [13]. Their conclusion was that the modi-

Table 3 List of current commercial engines with their approximate combustor inlet pressure and temperature, along with estimations of ignition delay times given by correlations from Peschke and Spadaccini, a CHEMKIN homogeneous model, and a methane correlation by Li and Williams

Engine	Pressure (atm)	Air temperature (K)	Estimated ignition delay time (ms)		
			H_2 correlation (Ref. [19])	H_2 CHEMKIN (Model)	CH_4 (Ref. [37])
GE 9H[a]	23	705	85	11,805	2336
Solar Taurus 65	15	670	153	[b]	8713
Solar Taurus 60	12.3	644	221	[b]	21,985
Solar Mercury 50[c]	9.9	880	59	4941	189
GE LM6000[a]	35	798	35	34,850	214
Siemens V-94.3A[a]	17.7	665	141	[b]	8448
Siemens V-94.2[a]	12	600	336	[b]	88,406
Capstaone C60[c]	4.2	833	140	1869	917

[a]Inlet temperature estimated from ideal gas isentropic compression.
[b]Represents no ignition within 1 min.
[c]Recuperated engine.

fications to the mechanism needed to gain agreement are well outside the established uncertainty factor attributed to these reactions. Hence, other factors are likely the culprit for the observed discrepancies.

Ströhle and Myhvold [31] postulated that the experimental conditions in the mild ignition tests deviate so far from the assumed ideal homogenous and zero dimension behavior that a simple homogenous reactor alone is no longer sufficient to predict accurately the delay time. This conclusion can be reinforced by examining the observations of previous low temperature shock tube ignition studies. Through rapid imaging of the ignition processes inside a shock tube, a number of investigators [15,35,36] have all observed two distinct ignition phenomena depending on whether the mixture is in the mild or in the strong ignition region. In the strong ignition region (at high temperatures where chain branching occurs), the mixture heated by the shock results in a uniform ignition through the cross section of the vessel that proceeds to a detonation wave. In the mild ignition, on the other hand, small flame kernels sporadically appear within the shock-heated mixture that eventually united to form the detonation wave. In short, the strong ignition case shows a uniform ignition and explosion, while the mild ignition shows a very nonhomogenous ignition.

In normal gas turbine operation, shocks and detonations will not be present inside the premixer; however, it is possible that nonhomogenous ignition could still be present and therefore dominate the behavior in practical systems. This nonhomogenous ignition could also be responsible for the short ignition seen inside the flow reactors as well. Thus far, little progress has been made to quantitatively model the nonhomogenous ignition in the mild ignition region, making the present time experimental results and their empirically derived correlations the only reliable way of predicting the ignition delay for conditions seen inside a gas turbine premixer with a fair amount of accuracy.

To put the issue in the context of how long ignition delay times for hydrogen/air premixers will likely be, Table 3 presents the estimated ignition delay times for some current engines if they were hypothetically converted to use hydrogen utilizing their current pressure and estimated inlet combustor temperature and using the correlation of Peschke and Spadaccini and the simple CHEMKIN simulation. Additionally, a correlation by Li and Williams for methane is given as well to show the differences between hydrogen and methane at these temperatures and pressures [37].

Ignition delay times are considerably shorter than any model. However, they are still at least an order of magnitude greater than most premixer times. However, due to the variability of delay times between different test apparatuses and to the sporadic nature of delay in the same apparatus under slightly different conditions, it would be recommended that very large safety factors should be utilized in order to avoid autoignition under all conditions. Hence, while autoignition should remain a concern, it will not be an immediate problem for most engines unless considerable premixing times are required or until even higher combustor inlet pressures and temperatures are used for greater efficiency.

Conclusions

A flow reactor was set up to test the ignition delay time of hydrogen and air at temperatures relevant to gas turbine engine operations. The results were then compared to past experimental work and current computer simulations.

The current study revealed that ignition would not always occur on a consistent basis. The delay times follow the same general trend as seen in previous flow reactor studies, where ignition is within a fraction of a second and at relatively low activation energy. The current results are best described by a correlation by Peschke and Spadaccini; however, a more sophisticated correlation may be needed in the future to account for effects caused by the flow field. For now, use of the current correlation gives good approximations. However, a fairly large safety factor (between 5

and 10) is recommended to ensure that ignition delay will never be shorter than the mixing time within the premixer.

Due to the inability to properly model the ignition delay time in the mild ignition region using simple computer models, the only way of confidently predicting ignition delay times at present are from the experimentally derived correlations.

Finally, while autoignition should remain a concern, it will not be a significant problem for most engines, only those with considerably long premixing times or ones with high inlet combustor temperatures or pressures.

References

[1] Conrad, W. E., and Corrington, L. C., 1957, "NACA Research Memorandum: Hydrogen for Turbojet and Ramjet Powered Flight," Report No. NACA RM E57D23.

[2] Sampath, P., and Shum, F., 1985, "Combustion Performance of Hydrogen in a Small Gas Turbine Combustor," Int. J. Hydrogen Energy, **10**(2), pp. 829–837.

[3] Dennis, R. A., and Harp, R., 2007, "Overview of the U.S. Department of Energy's Office of Fossil Energy Advanced Turbine Program for Coal Based Power Systems With Carbon Capture," ASME Paper No. GT2007-28338.

[4] Chiesa, P., Lozza, G., and Mazzocchi, L., 2005, "Using Hydrogen as Gas Turbine Fuel," ASME J. Eng. Gas Turbines Power, **127**, pp. 73–80.

[5] Therkelsen, P. L., Mauzey, J. L., McDonell, V. G., and Samuelsen, S., 2006, "Evaluation of a Low Emission Gas Turbine Operated on Hydrogen," *ASME Turbo Expo*, Barcelona, Spain, May, Paper No. GT2006-90725.

[6] Lieuwen, T., McDonell, V., Petersen, E., and Santavicca, D., 2008, "Fuel Flexibility Influences on Premixed Combustor Blowout, Flashback, Autoignition, and Stability," ASME J. Eng. Gas Turbines Power, **130**, p. 011506.

[7] Dryer, F. L., Chaos, M., Zhao, Z., Stein, J., Alpert, J., and Homer, C., 2007, "Spontaneous Ignition of Pressurized Releases of Hydrogen and Natural Gas Into Air," Combust. Sci. Technol., **179**, pp. 663–694.

[8] Petersen, E. L., Kalitan, D. M., Barrett, A. B., Reehal, S. C., Mertens, J. D., Beerer, D. J., Hack, R. L., and McDonell, V. G., 2007, "New Syngas/Air Ignition Data at Lower Temperature and Elevated Pressure and Comparison to Current Kinetics Models," Combust. Flame, **149**(1–2), pp. 244–247.

[9] Dryer, F. L., and Chaos, M., 2008, "Ignition of Syngas/Air and Hydrogen/Air Mixtures at Low Temperatures and High Pressures: Experimental Data Interpretation and Kinetic Modeling Implications," Combust. Flame, **152**(1–2), pp. 293–299.

[10] Kalitan, D. M., Mertens, J. D., Crofton, M. W., and Petersen, E. L., 2007, "Ignition and Oxidation of Lean Syngas CO/H2 Fuel Blends in Air," J. Propul. Power, **23**(6), pp. 1291–1304.

[11] Slack, M. W., 1977, "Rate Coefficient for H+O₂+M=HO₂+M Evaluated From Shock Tube Measurements of Induction Times," Combust. Flame, **28**, pp. 241–249.

[12] Bhaskaran, K. A., Gupta, M. C., and Just, Th., 1973, "Shock Tube Study of the Effect of Unsymmetrical Dimethyl Hydrazine on the Ignition Characteristics of Hydrogen-Air Mixtures," Combust. Flame, **21**, pp. 45–48.

[13] Snyder, A. D., Robertson, J., Zanders, D. L., and Skinner, G. B., 1965, "Shock Tube Studies of Fuel/Air Ignition Characteristics," Report No. AFAPL-TR-65-93-1965.

[14] Craig, R. R., 1966, "A Shock Tube Study of the Ignition Delay of Hydrogen-Air Mixtures Near the Second Explosion Limit," Report No. AFAPL-TR-66-74.

[15] Blumenthal, R., Fieweger, K., Komp, K. H., and Adomeit, G., 1996, "Gas Dynamic Features of Self Ignition of Non-Diluted Fuel/Air Mixtures at High Pressure," Combust. Sci. Technol., **113–114**, pp. 137–166.

[16] Wang, B. L., Olivier, H., and Groenig, H., 2003, "Ignition of Shock-Heated H₂-Air-Stream Mixtures," Combust. Flame, **133**, pp. 93–106.

[17] Walker, D. W., 1969, "An Investigation of the Shock Ignition Characteristics of Static and Flowing Combustible Mixtures," Ph.D. thesis, Ohio State University.

[18] Neer, M. E., 1972, "An Investigation of Spontaneous Ignition of Flowing Hydrogen Air Mixtures," Ph.D. thesis, Ohio State University; Neer, M. E., 1975, "Autoignition of Flowing Hydrogen-Air Mixtures," AIAA J., **13**(7), pp. 924–928.

[19] Peschke, W. T., and Spadaccini, L. J., 1985, "Determination of Autoignition and Flame Speed Characteristics of Coal Gases Having Medium Heating Values," Research Project No. 2357-1, Report No. AP-4291.

[20] Steinberg, M., and Kaskan, W., 1955, "Ignition of Combustible Mixtures by Shock Waves," *Fifth Symposium (International) on Combustion*, pp. 664–672.

[21] Glassman, I., and Sawyer, R., 1969, "The Reaction of Hydrogen With Nitro-

gen Dioxide, Oxygen, and Mixtures of Nitric Oxide," *12th Symposium (International) on Combustion*, pp. 469–479.

[22] Li, J., Zhao, Z., Kazakov, A., Chaos, M., Dryer, F. L., James, J., and Scire, S., 2007, "A Comprehensive Kinetic Mechanism for CO, CH2O, and CH3OH Combustion," Int. J. Chem. Kinet., **39**(3), pp. 109–136.

[23] Gokulakrishnan, P., Kazakov, A., and Dryer, F., 2003, "Comparison of Numerical and Experimental Kinetic Data for Flow Reactor Systems: Mixing Effects," Third U.S. Joint Meeting of the Combustion Institute.

[24] Chen, J., Jermakian, V., McDonell, V., and Samuelsen, S., 2003, "Correlation of Ignition Delay With Fuel Composition and State for Application to Gas Turbine Combustion," AGTSR Subcontract 00-01-SR084CS under DOE NETL Contract No. DE-FC21-92MC29061, University of California, Irvine Combustion Laboratory, Final Report (http://www.clemson.edu/scies/utsr/SR084.htm).

[25] Beerer, D. J., Greene, M. U., McDonell, V. G., and Samuelsen, G. S., 2006, "Correlation of Ignition Delay With IGCC and Natural Gas Fuels," South Carolina Institute for Energy Studies, Contract No. 03-01-SR112, Final Report. (http://www.clemson.edu/scies/utsr/SR112.htm).

[26] Lefebvre, A. H., Freeman, W., and Cowell, L., 1986, "Spontaneous Ignition Delay Characteristics of Hydrocarbon Fuel/Air Mixtures," NASA Contractor Report No. 175064.

[27] Gokulakrishnan, P., Gaines, G., Currano, J., Klassen, M. S., and Roby, R. J., 2007, "Experimental and Kinetic Modeling of Kerosene-Type Fuels at Gas Turbine Operating Conditions," ASME J. Eng. Gas Turbines Power, **129**, pp. 655–663.

[28] Sims, G.-J., Clague, A. R., Copplestone, R. W., Menzies, K. R., and MacQuisten, M. A., 2005, "The Measurement and Prediction of Gaseous Hydrocarbon Fuel Auto-Ignition Delay Time at Realistic Gas Turbine Operating Conditions," ASME Paper No. GT-2005-68736.

[29] Kee, R. J., Rupley, F. M., Miller, J. A., Coltrin, M. E., Grcar, J. F., Meeks, E., Moffat, H. K., Lutz, A. E., Dixon-Lewis, G., Smooke, M. D., Warnatz, J., Evans, G. H., Larson, R. S., Mitchell, R. E., Petzold, L. R., Reynolds, W. C., Caracotsios, M., Stewart, W. E., Glarborg, P., Wang, C., and Adigun, O., 2007, CHEMKIN Collection, Release 4.0, Reaction Design, Inc., San Diego, CA.

[30] O'Conaire, M., Curran, H., Simmie, J., Pitz, W., and Westbrook, C., 2004, "A Comprehensive Modeling Study of Hydrogen Oxidation," Int. J. Chem. Kinet., **36**(11), pp. 603–622.

[31] Ströhle, J., and Myhvold, T., 2007, "An Evaluation of Detailed Reaction Mechanisms for Hydrogen Combustion Under Gas Turbine Conditions," Int. J. Hydrogen Energy, **32**, pp. 125–135.

[32] Yetter, R. A., Dryer, F. L., and Golden, D. M., 1992, *Major Research Topics in Combustion*, M. Y. Yussaini, A. Kumar, and R. G. Voigt, eds., Springer, New York, p. 309.

[33] Yetter, R. A., Rabitz, H., and Hedges, R. M., 1991, "A Combined Stability-Sensitivity Analysis of Weak and Strong Reactions of Hydrogen/Oxygen Mixtures," Int. J. Chem. Kinet., **23**, pp. 251–278.

[34] Sabia, P., Schiesswohl, E., de Joannon, M. R., and Cavaliere, A., 2006, "Numerical Analysis of Hydrogen Mild Combustion," Turk. J. Eng. Environ. Sci., **30**, pp. 127–134.

[35] Voevodski, V. V., and Soloukhin, R. I., 1965, *Tenth Symposium (International) on Combustion*, The Combustion Institute, Pittsburgh, pp. 279–283.

[36] Meyer, J., and Oppeneheim, A. K., 1971, "On the Shock-Induced Ignition of Explosive Gases," *13th Symposium (International) on Combustion*, The Combustion Institute, Pittsburgh, p. 1153.

[37] Li, S. C., and Williams, F. A., 2002, "Reaction Mechanism for Methane Ignition," ASME J. Eng. Gas Turbines Power, **124**, pp. 471–480.

Sonny Martin
Control and Instrumentation Research Group,
Department of Engineering,
University of Leicester,
LE1 7RH Leicester, UK
e-mail: sm342@le.ac.uk

Iain Wallace
Alstom Aerospace,
Cambridge Road,
LE8 6LH Whetstone, UK

Declan G. Bates
Control and Instrumentation Research Group,
Department of Engineering,
University of Leicester,
LE1 7RH Leicester, UK
e-mail: dgb3@le.ac.uk

Development and Validation of a Civil Aircraft Engine Simulation Model for Advanced Controller Design

1 Introduction

Computer simulation is a powerful tool for the mechanical and control system design of gas turbines. A high fidelity computer simulation can be used as a substitute for a real engine in many applications. For example, it is possible to simulate critical transients that must be avoided on the actual plant due to the risk of damage. Turbine engines can be modeled at various levels of detail, from full 3D descriptions of the gas path (e.g., NASA's numerical propulsion system simulation (NPSS) [1]) that can require distributed computers or supercomputers to simplified algebraic equations [2] and even simple overall transfer functions. It is generally accepted that a 1D simulation is sufficient for accurate dynamic performance modeling and, therefore, controller design. The simulation method used in this study is known as an aerothermal transient performance model [3]. This method avoids iterative calculations by arranging the component equations to follow the direction of the gas path and by introducing storage volumes between components to account for the unsteady balance of mass at the compressor discharge, at the combustion chamber, and between the turbines [4]. Relative to an iterative model, there is some loss of accuracy, but this is negligible from the point of view of engine control system development and is offset by a superior execution time, particularly if a small time step is used. If a constant time step is chosen for numerical integration, then this method can provide a model with a predictable run time. If the simulation is designed to run in real time, then it can also be used with real hardware, although, clearly, the computer program outputs have to be generated at least as fast as the predicted physical phenomena for the model to run side by side with an engine [5]. In this paper, we present a full aerothermodynamic model of a two-spool, high-bypass turbofan engine with an unmixed exhaust together with a switched, gain-scheduled aeroengine controller with bumpless transfer and antiwindup. The engine simulation in conjunction with this controller achieves dynamic performance representative of that of a real aeroengine. Model implementation is in the MATLAB-SIMULINK® environment. Full flight-envelope validation of both the model and the controller has been performed with the assistance of Alstom Aerospace, with the exception of engine startup as this is not within the scope of the model.

The features of the presented model are its modularity, ease of implementation, and adherence to the underlying physics. Empirical approximations have been avoided wherever possible, with the aim of improving the model's flexibility and providing physical justification for the approximations used (as opposed to empirical approximations whose boundary of validity is often unknown). Most of the model's current implementation details are provided by initialization scripts. Therefore, tuning the model is a simple matter of changing script details without the need to extensively modify SIMULINK modules; i.e., most variables are dynamically intialized from the MATLAB workspace. For example, the gain schedule is provided by variables in the workspace, and the parameters of the scaling of the compressor maps (this is performed online while the simulation runs) are also provided by external scripts. The model is also compatible with the Real-Time-Workshop, a toolbox available in the MATLAB-SIMULINK environment that is able to automatically generate a source code in C language from the SIMULINK scheme. This feature can be useful in developing a code for hardware-in-the-loop applications. The purpose of the model is the development of advanced control strategies. Therefore, a base line controller that closely mirrors industrial practice has been designed to validate the closed-loop performance properties of the model. The controller has itself a modular approach, allowing easy extension of the number of parameters regulated by the controller. The model is also provided with a "dashboard" that permits inspection during the simulation's progress of significant parameters, such as mass flow, temperature, and pressure at each engine station.

There are relatively few papers in the literature that deal specifically with civil aircraft engines. Several papers provide an architecture for simulating gas turbines [4,6–12], but most are applied to industrial turbines and few provide details of implementations suitable for civil aircraft aeroengines [2]. This paper includes additional details specific to civil aircraft engines: The fan of the engine (this absorbs a significant proportion of the power output by the engine, and an accurate model is highly desirable) is modeled as two separate sections, a core section and a duct section, with different pressure ratios and efficiencies as would be the case for a real engine. A nozzle module suitable for an aerothermal model (i.e., that does not require iterative procedures) and a model of the duct (as a nozzle) are also provided, so that fan power consumption may be accurately calculated. Transfer of heat to and from the engine components is also taken into consideration by providing heat storage modules for each major component. Heat soak can have a significant effect on the dynam-
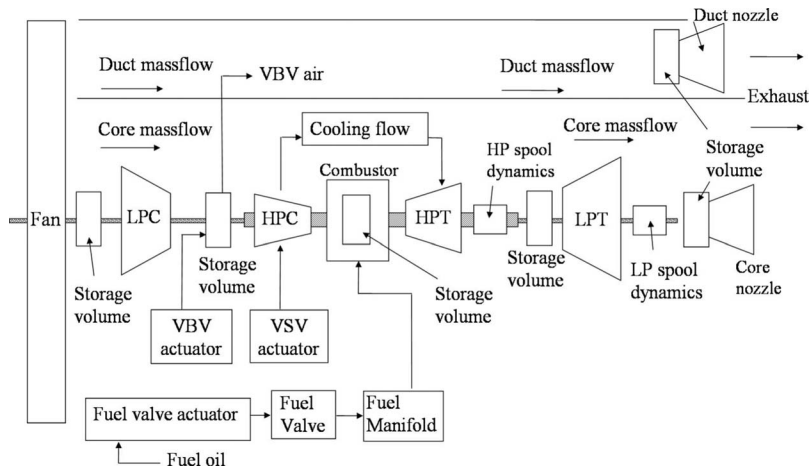
Fig. 1 The main components of a turbofan engine

ics of the engine, particularly at high altitude where the mass flow through the engine is greatly reduced. Indeed, the range of environmental and operating conditions that an aeroengine can be expected to undergo is much greater than those of industrial engines. An aeroengine must be able to perform and satisfy stringent requirements under dramatically varying environmental conditions and very different regimes, e.g., rapid acceleration/deceleration, takeoff, and idle. For a validation of the model under these varying conditions, a gain-scheduled controller is provided.

There are also relatively few papers that discuss in detail the architecture and design of industrially applicable control schemes for civil aircraft engines. Several papers discussing advanced control of military aircraft engines may be found in the literature since these engines have more controller inputs and thus require multivariable controllers; some examples are: Refs. [13–17]. A high-level general introduction to aircraft engine feedback control is contained in Ref. [18]. Another useful source is Ref. [11]. The latter has many useful details regarding engine and actuator dynamics, and provides detailed performance figures that are backed up directly by industry, but, like Ref. [18], it falls short of providing a comprehensive overview of the controller architecture and practical methods of implementation that would allow replication of the design.

The paper is structured as follows. Section 2 provides a description of the main engine components that are included in the model. An introduction to civil aircraft engine controllers can be found in Sec. 3, with the details of the model's controller following in Sec. 4. A review of simulation issues can be found in Sec. 5. The validation and performance results of the simulation are discussed in Sec. 6.

2 Modular Construction of the Mathematical Model

A gas turbine engine is a highly complex nonlinear system requiring an accurate dynamic model for controller design and evaluation. For the purpose of development and testing of advanced aeroengine controllers, a full aerothermodynamic simulation of a jet engine has been developed and implemented in the MATLAB-SIMULINK® environment. The plant controlled is a generic high-bypass separated flow turbofan. This has been found to be the optimum configuration for a high subsonic commercial aircraft [19]. The model is therefore representative of the jet engine of a midrange aircraft, such as the highly successful Airbus A320 family. The model has two shafts, variable bleeds and stator vanes, actuator dynamics, heat soak dynamics, cooled turbines, a model of the duct, and a fixed convergent exhaust nozzle. It has been developed in a modular fashion to permit the easy implementation of failure scenarios and adaptation to multiple engine configurations. The model, in its current implementation, develops a maxi-

mum thrust of above 30,000 lbf (133 kN) and has been validated, in collaboration with an industrial partner, via comparison with steady state and dynamic data for a comparable engine. Although the model as developed is nonproprietary, some specific performance figures of this configuration have on this occasion been omitted for reasons of commercial sensitivity.

A turbofan's airflow is split into two main sections (as shown in Fig. 1). The outer, "duct" or "bypass," airflow is accelerated by a fan situated at the front of the engine. This section provides most of the engine's thrust by moving a large mass of air at a relatively low speed. The inner or "core" section provides the power to drive the fan. Airflow through this section is compressed via two sequential compressors: a low pressure compressor (LPC) and a high pressure compressor (HPC). The HP flow at the exit of the HPC is in part combusted, expands through the HP turbine (this powers the HPC), and then flows into the LP turbine (this powers the LPC and the fan). A further expansion to atmospheric pressure is via a fixed convergent nozzle placed at the rear of the LP turbine. The shaft connecting the fan, the LP compressor, and the LP turbine is called the "LP shaft." Similarly, the shaft connecting the HP compressor and the HP turbine is known as the "HP shaft." These two shafts are concentric—the LP shaft extends beyond and rotates within the HP shaft. Figure 1 outlines how these turbofan components are interconnected. The variable bleed valve (VBV) placed between the LPC and the HPC improves the surge characteristics [10,11] by purging air directly into the duct (surge is a violent oscillatory reversal of the gas stream's flow). For the same reason, the HPC module is provided with a model of variable stator vanes (VSVs). The operation of both these components is open loop scheduled with corrected shaft speed. The simulation uses "lumped" elements: The engine components are simplified to volumeless elements, thereby reducing the partial differential equations that describe their distributed properties to ordinary differential equations that describe the evolution of key properties over time. The aim is to derive a set of explicit first order differential equations that can be solved using an integration algorithm to accurately describe the dynamic characteristics of the modeled components. The unsteady mass balance between components is modeled via storage volumes (plena).

The simulation of a gas turbine's components requires the application of the following thermodynamic conservation laws or continuity equations:

- conservation of mass (basic physical principle)
- conservation of energy (first law of thermodynamics)
- conservation of momentum (Newton's second law)

Additionally, relationships describing heat transfer processes and

fluid mechanics must also be applied. Finally, shaft dynamics are added by making mechanical connections between the component models. Engine acceleration is provided by integrating the shafts' power imbalance over time.

There currently exist several approaches to modeling gas turbines: The most accurate are iterative models based on thermodynamic conservation laws and continuity equations. An engine equilibrium point is calculated (this is the component matching phase), and from this all engine parameters are derived via an iterative solution of the system of equations (initial guesses are usually provided). These models assume as constant the mass flow for the required matching of the compressors and turbines. The type of model presented here, called an "aerothermal transient performance model" [3] or "aerothermodynamic model," [4] avoids iteration by arranging the equations to follow the direction of the gas path and by introducing storage volumes between components to account for the unsteady balance of mass at fan and compressor discharge, combustion chamber, between the turbines, and between the turbines and the nozzle [4]. This is the most accurate of the many noniterative models used for modeling engine performance transient parameters [3]. Other models are more suitable for flight simulators where lower accuracy is permissible and generally use transfer functions relating fuel flow and parameter outputs [3]. Relative to iterative models, all other approaches suffer from some loss of accuracy, but in the case of the aerothermal model considered here, this is negligible for the purpose of engine control system development, particularly if a small time step is used. This loss is also offset by a superior execution time. The size of the volumes (plena) included between the turbomachinery is important [3], as they have their own time constant [4], and this will affect the maximum permissible time step. Clearly, the update time step should stay below the plena time constant. For small plenum volumes, there is a very steep rate of variation in pressure for any variation in mass influx or efflux. Should the time step of the system be large, this would lead to situations whereby the system would respond to large changes in pressure rather than to the gradual change that would occur for a smaller sample time. An unphysical situation would arise when these changes in pressure would result in exceeding the pressure ratio boundaries of the compressor or turbine maps either downstream or upstream of the plenum. From this perspective, the smallest possible time step is desirable. However, one should also consider that the turbomachinery characteristic maps are in themselves approximations, and an extremely small time step will thus not necessarily improve the simulation accuracy in practice, although it will indeed improve the solution accuracy. Because the model incorporates numerous component maps, the tradeoff between solution accuracy and time step is not readily quantifiable analytically, and the determination of an overall limiting time step is not easy. Plenum size is therefore a limiting factor to the permissible time step, and solution accuracy needs to be carefully tested should very small volumes be used. This is, however, likely to become an issue only when simulating multistage turbomachinery in a stage-by-stage fashion (this is not the case for the present simulation as the model uses lumped components). A practical way of testing for this is to repeatedly halve the time step until no difference in solution accuracy is noticed for an engine rapid transient such as what would occur during a pilot slam request. A good, conservative, constant time step for the current simulation is 10^{-4} s. This works comfortably even with basic Euler numerical integration (MATLAB ODEL).

Other simulation methods, such as the iterative "thermodynamic matching model" presented in Ref. [10] and also discussed in Ref. [3], are much slower and usually do not have a predictable run time as the solution time to convergence may vary. Furthermore, the iterative method produces noise on the output parameters due to solutions at each time step falling at random places within the permitted tolerance band. This noise may prevent assessment of system stability due to the perturbations produced [3].

For real-time applications, in order to reduce the computational time, techniques based on the linearization of the model have often been adopted [4,5,19]. However, simulations based on linearized models should be used only in the neighborhood of the working point about which the linearization has been carried out and are therefore particularly unsuitable for aeroengine simulation.

In summary, calculations in the current model are performed in a feed-forward manner, thus allowing for a direct noniterative calculation of the engine cycle and performance. Once atmospheric conditions, namely, altitude, Mach number, temperature deviation from the International Standard Atmosphere (ISA), and the value of the control variables, e.g., fuel flow, and other control parameters that are open loop scheduled (e.g., bleed valve position) have been specified, the operating point follows via a feed-forward calculation that propagates along the engine's direction of flow. A few notable exceptions are addressed via the use of SIMULINK "memory blocks" (please refer to Sec. 5) so that thermodynamic properties can be based on a component's mean temperature and the compressors can be provided with pressure data from downstream components.

2.1 Component Models. Each modular component can be viewed as an operator the purpose of which is to compute the thermodynamic state of the fluid (typically mass flow $\dot{w}$ (kg s^{-1}), total temperature, and pressure) at the outlet of the module based on the inlet conditions and some additional parameters. Each component model relies on the equations for mass, momentum, and energy balances and on empirical information derived from rig tests or advanced computational fluid dynamics calculations, e.g., compressor and turbine characteristic maps. The stagnation conditions at the engine inlet are computed with Saint-Venant–Wantzel relations [19] as a function of altitude, variation from ISA day temperature, and Mach number. This accounts for ram recovery at the engine's inlet.

The thermodynamic properties of the air stream and combustion gases will vary due to the range of environmental and operating conditions at which the engine must operate. This makes an accurate evaluation of the gas stream's thermodynamic properties highly desirable for an aeroengine. Lookup tables may be used (tables containing the values of the specific heats have been published in many works [6,20]), or, as in the present case, algebraic curve-fitting expressions [3] may be used. Therefore, in the present work, the working fluids are not considered as perfect gases of constant specific heats, as this is mainly appropriate for preliminary design calculations [19]. This has the advantage of both improved accuracy and preserves a computational architecture that allows for complex scenarios to be simulated, e.g., ingestion of water vapor and dramatic changes in inlet temperature. The specific heat at constant pressure, c_p, was provided by the polynomial fits provided in Ref. [3] and is temperature and fuel air ratio (FAR) dependent. The gas constant R is temperature independent and FAR dependent. The ratio of specific heats, γ, is temperature and FAR dependent and can be expressed as a function of the specific heat capacity c_p and the gas constant R. It should be noted that for formulas using c_p and γ, it is most accurate to base these values on the mean temperature for each component, i.e., the arithmetic mean of the inlet and outlet values. It is less accurate to evaluate c_p and γ at inlet and outlet, and then take a mean value for each [3].

2.2 Plena. Because turbomachinery, compressor, and turbine units are considered as volumeless elements, a plenum is placed at the compressor outlet in order to take into account the unsteady mass balance at compressor discharge within the combustion chamber and between the turbines and the LP turbine and the nozzle. Mass conservation implies

$$w = \int (\dot{w}_{\text{in}} - \dot{w}_{\text{out}}) \cdot dt + w_0 \tag{1}$$

where w is the mass present in the casing, $\dot{w}$ represents gas stream mass flow (kg s^{-1}), and w_0 is the initial value of the mass present in the plenum. Pressure inside the plenum is then calculated via the ideal gas law,

$$p_{\text{out}} = w \cdot \frac{T \cdot \bar{R}}{V} \tag{2}$$

where $\bar{R}$ is the specific gas constant of the gas stream (J kg^{-1} K^{-1}). Each plenum also includes a module to calculate the heat soak of the component upstream. If this was not included, the plenum's outlet temperature would be equal to the inlet temperature. Energy accumulation due to transient effects, such as volume packing [3], is neglected. Pressure losses are also not considered although these are easily implemented if desired [19,21].

2.3 Heat Soakage. Each turbomachinery component includes heat transfer effects, such as the heat transfer to turbine blades and casings. Only convective heat transfer is considered based on simplified equations for turbulent flow over a flat plate and assuming a constant Prandtl number [22]. By considering a lump of metal (e.g., a blade) in a hot gas flow, a simple first order heat soak equation can be developed. The time constant τ can be calculated from the heat transfer coefficient and the mass and specific heat capacity of the metal. The heat transfer coefficient is calculated for the design point conditions and modified at off-design conditions depending on mass flow and temperature as both alter the flow's Reynolds number. It has been demonstrated that heat soak effects play an important role in determining a gas turbine's dynamic performance [5], yet they are extremely difficult to predict in the absence of good test data. In the absence of such data, the heat soak released upon an abrupt deceleration of an industrial engine [23] was scaled down for the current model. The time constant was similarly reduced. The overall heat soak quantity was then distributed amongst the components according to their mass and temperatures. Key equations for the implementation of a heat soak module follow. The most fundamental equation is Newton's law of cooling,

$$q = \bar{h}A \cdot \Delta T = \bar{h}A(T_m - \bar{T}) \tag{3}$$

where q is the heat flow [W], $\bar{h}$ is the average heat transfer coefficient over the surface (W m^{-2} K^{-1}), T_m is the component average temperature, $\bar{T}$ is the gas stream's mean temperature, and A is the heat transfer area (m^2). The heat transfer coefficient is temperature and flow dependent, and this dependency can be approximated with the following relationship [24]:

$$Y \propto T^{0.23} \dot{w}^{0.8} \tag{4}$$

where $\dot{w}$ is mass flow rate and

$$Y = \bar{h}A \tag{5}$$

In experimental conditions, the easiest parameter to measure will be the time constant τ. This can be obtained by rapidly increasing or decreasing the gas stream temperature from a starting condition, with the gas and metal mass in thermodynamic equilibrium at a known temperature,

$$\frac{dT_m}{dt} = -\frac{q}{Mc_{pm}} \tag{6}$$

where T_m is the metal temperature, M is the metal mass, and c_{pm} is the metal specific heat capacity. Equations (6) and (3) above can be combined to give

$$\frac{dT_m}{dt} = -\frac{\bar{h}A(T_m - \bar{T})}{Mc_{pm}} \tag{7}$$

Since the time constant is

$$\tau = \frac{Mc_{pm}}{\bar{h}A} \tag{8}$$

it then follows that

$$\frac{dT_m}{dt} = -\frac{1}{\tau}\Delta T \tag{9}$$

Therefore, the time constant of the system can be experimentally determined. Once this is known, for a system of similar mass and area, the following equations can be applied:

$$Y_d = \bar{h}A = \frac{1}{\tau_d}Mc_{pm} \tag{10}$$

where Y_d is the value of Y established under the experimental conditions T_d, $\dot{w}_d$, and τ_d. From this, it follows that

$$q = Y \cdot \Delta T = \Delta T \cdot Y_d \cdot \frac{\tau_d}{\tau} = \Delta T \cdot Y_d \cdot \left(\frac{\tau}{\tau_d}\right)^{-1}$$
$$= \Delta T \cdot Y_d \cdot \left[\left(\frac{\bar{T}}{T_d}\right)^{-0.23} \left(\frac{\dot{w}}{\dot{w}_d}\right)^{-0.8} \right]^{-1} \tag{11}$$

This is because

$$\tau = \tau_d \left[\left(\frac{\bar{T}}{T_d}\right)^{-0.23} \left(\frac{\dot{w}}{\dot{w}_d}\right)^{-0.8} \right] \tag{12}$$

This last relationship follows from the following considerations. Since

$$\tau = \frac{Mc_{pm}}{\bar{h}A} \approx \frac{k}{\bar{h}} \tag{13}$$

where k is a constant and from Eq. (4),

$$\bar{h} \approx k_1 \cdot T_d^A \cdot \dot{w}_d^B \tag{14}$$

it then follows that

$$\tau_d = \left(\frac{k}{k_1}\right) \cdot T_d^{-A} \cdot \dot{w}_d^{-B} = k_d^* \cdot T_d^{-A} \cdot \dot{w}_d^{-B} \tag{15}$$

Considering a new time constant τ at different temperature and mass flow conditions,

$$\tau = k^* \cdot T^{-A} \cdot \dot{w}^{-B} \tag{16}$$

and, therefore,

$$\frac{\tau}{\tau_d} = \frac{k^* \cdot T^{-A} \cdot \dot{w}^{-B}}{k_d^* \cdot T_d^{-A} \cdot \dot{w}_d^{-B}} \tag{17}$$

and if

$$k_d^* = k^* \tag{18}$$

which holds for components of similar geometries [22], then,

$$\frac{\tau}{\tau_d} = \frac{T^{-A} \cdot \dot{w}^{-B}}{T_d^{-A} \cdot \dot{w}_d^{-B}} = \left(\frac{T}{T_d}\right)^{-A} \left(\frac{\dot{w}}{\dot{w}_d}\right)^{-B} \tag{19}$$

Therefore, if Y_d and τ_d have been established experimentally, then formula (11) can be applied to get the heat transferred q (W) over a range of temperatures and mass flows. This heat can then be added or subtracted to the enthalpy of the gas stream.

2.4 Fan and Compressors. The fan placed at the front of the turbofan provides the majority of the engine's thrust. The fan

simulation module is divided into two sections: a core and a duct section. The ratio between the duct and core mass flows is known as the bypass ratio (BPR),

$$BPR = \frac{\dot{w}_{duct}}{\dot{w}_{core}} \quad (20)$$

Each section is modeled via a characteristic map, describing the steady state performance of the component. The performance can be specified by curves of delivery pressure and temperature plotted against mass flow for various fixed values of rotational speed. These characteristic curves are, however, dependent on other variables such as the conditions of pressure and temperature at entry and the physical properties of the working fluid. By using dimensional analysis, the variables involved may be combined to form a smaller and more manageable number of dimensionless groups, and these characteristic curves can then be plotted on a nondimensional basis, i.e., stagnation pressure ratio and isentropic efficiency η_i against the nondimensional mass flow rate $\dot{w}_c$ for fixed values of the nondimensional speed $(n/\sqrt{\theta})^3$. The fan's corrected mass flow is provided by the characteristic map once the fan's pressure ratio and corrected shaft speed have been provided. Applying the conservation equations, the temperature increase over the fan is described by

$$T_{out} = T_{in} \cdot \left[1 + \frac{1}{\eta_i}(\pi^{(\gamma-1)/\gamma} - 1) \right] \quad (21)$$

where π is the pressure ratio over the core or duct section of the fan, γ is the ratio of specific heats, and η_i is the isentropic efficiency. The power required to drive the fan is then

$$P_{fan} = c_p \cdot \dot{w} \cdot (T_{out} - T_{in}) \quad (22)$$

and is positive since it is supplied to the air.

The air that flows through the core section of the engine is compressed via two compressors in series. These are modeled in a similar fashion to the fan, except that there is no splitting of the mass flow. Characteristic maps are again at the core of the compressor models, and the constitutive equations are the same. More complex models would split the compressor into stages separated by small plena and solve gas flow equations based on a knowledge of blade angle and stage performance, but the approach adopted here is more practical, particularly for a generic turbofan model where data requirements are not too onerous [25].

Between the two compressors, there is an open-loop-scheduled VBV. This extracts air from the core flow and exhausts directly into the duct. The percentage of mass flow extracted is scheduled with the corrected LP shaft speed. For more information on the predicted effect of VBVs, the reader is referred to Ref. [10].

The second of the compressors in series, the HPC also includes customer bleeds (these power aircraft accessories) and VSVs. The latter are to improve the surge margin of the HPC and are modeled by a percentage reduction in corrected mass flow. This reduction is open loop scheduled against corrected HP shaft speed. The reader is referred to Ref. [10] for plots of the effects of VSVs on compressor maps. The customer bleeds are modeled by extracting a percentage of the inlet airflow. This air will not be available for work in the compressor, and this is reflected in the formula for HPC power,

$$HPC_{power} = c_p \cdot \dot{w} \cdot (T_{out} - T_{in}) \cdot [k_1 x_1 + k_2 x_2 + (1 - k_1 - k_2)] \quad (23)$$

where k_1 and k_2 are the proportion of air removed via bleeds 1 and 2, respectively, and x_1 and x_2 are scalars from 0 to 1, which represent the proportion of the total temperature rise to be expected at that stage.

Cooling air is also extracted prior to the combustor, at the outlet of the HPC. Cooling flow is an important element of the model because the total percentage of engine inlet mass flow extracted before the combustor may be up to 25% for a high technology

aero or industrial engine [3], and cooling flow will represent a significant proportion of this. Cooling flow is often modeled simply as a percentage of the engine's mass flow [19], but in this case it was preferred to use a relation that, although empirical, is based on the ratio of the pressure of the air source (the HPC) and that of the sink (the high pressure turbine (HPT)) [4,26],

$$\dot{w}_{cool} = K \sqrt{1 - \frac{p'_{out}}{p_{in}}} \frac{p_{in}}{\sqrt{T_{in}}} \quad (24)$$

where K is the discharge coefficient, p_{in} and T_{in} are, respectively, the pressure and temperature at the bleed point, and p'_{out} is the static pressure at the exit of the cooling circuit. In this work, this is approximated by the pressure value at the cooling flow exit. This is reasonable since the velocity of the gas stream is relatively low at this stage and the dynamic pressure remains a low proportion of the total up to approximately a Mach number of 0.4 [3].

2.5 Combustor. The air at the outlet of the HPC is passed into a combustion chamber. This increases the enthalpy of the working fluid via the combustion of fuel. The flame temperatures in the model are obtained from 2D lookup tables that were calculated using the NASA program SP273. These data were extracted from Ref. [27]. Therefore, the exit temperature of the combustor is provided as a function of excess air factor λ and inlet temperature. To account for the unsteady mass balance between the HPC, combustor, and HPT, a storage volume is included in the combustor.

2.6 Turbines. The hot gas stream exits the combustor and is expanded via two turbines in series. A characteristic map is used to represent each turbine. The constitutive equation for the temperature drop across the turbine is

$$T_{inlet} - T_{outlet} = \eta_t T_{in} \left[1 - \left(\frac{1}{p_{in}/p_{out}} \right)^{\gamma-1/\gamma} \right] \quad (25)$$

where η_t is the turbine isentropic efficiency. The HPT, although not modeled as a multistage cooled turbine, does include injection of cooling air from the HPC. Cooling air is injected into the main stream at the turbine inlet. Therefore, a mixing procedure has to be included in the module. For calculations of work, the whole flow is used; i.e., both the hot gases and the cooling air do work in the turbine. The mixing block takes the mass fraction of cooling air and calculates the temperature of the mixed flow,

$$T_{mix} = \frac{x T_{cool} c_{p,cool} + (1 - x) T_{inlet} c_{p,hot}}{x c_{p,cool} + (1 - x) c_{p,hot}} \quad (26)$$

where x is the mass fraction of cooling air. The temperature of the mixture of hot and cold gas, T_{mix}, is then substituted for T_{inlet} in Eq. (25).

2.7 Exhaust System. Exhaust air exits the turbofan engine in two separate unmixed streams: duct air and core section air. Both the duct and core exhaust are modeled as convergent nozzles, each of a fixed area. At current levels of cycle pressure ratio, virtually all turbojets (note that these engines do not have a duct section) operate with the nozzle choked during takeoff, climb, and cruise, and the nozzle only becomes unchoked when thrust is significantly reduced. Thus, the nozzle is liable to be unchoked only when preparing to land or when taxiing [19]. The situation is rather different for a turbofan, and the core nozzle can be assumed to be unchoked over the operating range of the engine. The duct nozzle, due to the inherently low speed of the duct gas stream, is also unchoked. The core and bypass flows are therefore expanded through the core and bypass nozzles to the pressure of ambient air. A converging nozzle is used because the exhaust flow is subsonic, and for subsonic flow, a convergent nozzle accelerates the gas. The "throat" or minimum area of the nozzle will regulate the amount of flow that can be exhausted through the nozzle. The object of a turbine nozzle is to produce as much kinetic energy as possible from given inlet conditions and pressure drop. There will

inevitably be some frictional losses—maximum efficiency is reached when there is no friction and the process is perfectly isentropic. The efficiency of the nozzle is the ratio of the actual kinetic energy produced to this theoretical maximum. As the nozzle efficiency falls below unity, the expansion will be a mixture of isentropic and isothermal [28]. Conditions at the inlet of the nozzle shall be denoted with subscript 0, e.g., p_0, v_0, and T_0 for the pressure, specific volume, and temperature, respectively. Similarly, conditions at the exit of the nozzle are denoted with subscript 1. Conditions at the nozzle throat are denoted with subscript t.

The nozzles of a gas turbine receive a gas that already possesses an appreciable velocity. Therefore, the equations used to model the nozzle must incorporate factors to account for these significant inlet velocities. The non-negligible gas velocity may be accounted for by using the concepts of stagnation pressure, p_{0T}, and stagnation temperature, T_{0T}. For a gas undergoing an isentropic expansion,

$$p v^\gamma = \text{const} \tag{27}$$

where γ, the ratio of specific heats, is known as the adiabatic index because this is an isentropic (i.e., adiabatic and reversible) process. For a frictionally resisted adiabatic expansion, this becomes

$$p v^m = \text{const} \tag{28}$$

where the polytropic exponent m is a function of the adiabatic index γ and nozzle efficiency η_N,

$$m = \frac{\gamma}{\gamma - \eta_N(\gamma - 1)} \tag{29}$$

The nozzle throat will pass flow at speeds up to and including sonic but cannot support supersonic flow (a convergent nozzle slows down supersonic fluids). Sonic flow will be reached when the ratio of throat pressure p_t to inlet stagnation pressure p_{0T} has reached a critical value (the nozzle is "choked"),

$$\frac{p_{tc}}{p_{0T}} = \left(\frac{2}{\gamma + 1}\right)^{m_c/(m_c - 1)} \tag{30}$$

where p_{tc} and m_c are, respectively, the throat pressure and polytropic exponent at these critical conditions.

Furthermore, assuming that nozzle efficiency is constant over the length of the nozzle (the variation for a convergent-only nozzle has been found in practice to be small up to and including sonic velocity [28]) and assuming that pressure and specific volume in the stagnation state are related to temperature by

$$p_{0T} v_{0T} = \bar{R} T_{0T} \tag{31}$$

where $\bar{R}$ is the specific gas constant, the nozzle's mass flow is then

$$\dot{w} = A \sqrt{2 \frac{\gamma}{\gamma - 1} \frac{p_{0T}}{v_{0T}} \left(\left(\frac{p_1}{p_{0T}}\right)^{2/m_0} - \left(\frac{p_1}{p_{0T}}\right)^{(m_0+1)/m_0}\right)} \tag{32}$$

for

$$\frac{p_1}{p_{0T}} \geq \left(\frac{2}{\gamma + 1}\right)^{m_c/(m_c - 1)} \tag{33}$$

i.e., for subsonic flow. A is the throat area and is the same as the exit area for a convergent-only nozzle.

An important issue is that there is no value for the specific volume at stagnation conditions, v_{0T}, in the model at this stage, but this can easily be calculated from the relationship in Eq. (31). Under the assumption that $m_c = m$, i.e., the polytropic index is not greatly varied at critical conditions [28], the model can be provided with an architecture that can also cope with sonic flow if the following equation is also included in the nozzle module:

$$\dot{w} = A \sqrt{\left(\frac{2}{\gamma + 1}\right)^{(m_c+1)/(m_c-1)} \gamma \frac{p_{0T}}{v_{0T}}} \tag{34}$$

for

$$\frac{p_1}{p_{0T}} < \left(\frac{2}{\gamma + 1}\right)^{m_c/(m_c - 1)} \tag{35}$$

This raises the question of how to determine the throat pressure given only the inlet and outlet pressures for the nozzle, which will be the usual case. Because for a convergent-only nozzle the nozzle throat and outlet are adjacent, the throat pressure will be the same as the outlet pressure until the ratio of the outlet to inlet pressure falls below the critical value (i.e., the nozzle becomes choked), and thereafter the throat pressure will remain at the critical value.

2.8 Shafts. Speeds at time t are calculated using unbalanced powers, speeds from the previous point, and spool inertias. The rotational acceleration of the shaft can be found from the shaft dynamic balance. For example, for the LP shaft,

$$\frac{d\omega}{dt} = \frac{1}{I\omega}(P_{\text{LPT}} - P_{\text{LPC}} - P_{\text{fan}} - P_{\text{losses}}) \tag{36}$$

where P is the power, I is the shaft moment of inertia, and ω is the shaft angular speed. Power losses are caused by friction and engine accessories and can be modeled as a simple percentage of the total power provided to the shaft or as a loss that is proportional to shaft speed.

2.9 Actuators. Models for mechanical actuators, such as those of the fuel system valve, the VBVs, and the VSVs, are also included. These are modeled in terms of first and second order Laplace transforms (transfer functions) [11]. The temperature sensor (transducer) also has its own dynamics, and these too are represented in the model via transfer functions according to the representation in Ref. [29]

3 Specifications and Constraints for Civil Aircraft Engine Controllers

One of the key objectives of an aircraft engine is to achieve maximum thrust with minimum engine weight. Therefore, although a gas turbine is inherently in itself a stable system [5], feedback control is an essential part of jet engines because of the requirement to run close to the engine's operating limits. Transient conditions do exist for which operation is unstable, but because these are conditions that may seriously damage the engine (an example of this is surge, a violent oscillatory reversal of the gas stream's flow), they are considered as areas of the operating envelope that are to be avoided. This is achieved via open-loop-scheduled controls on some of the engine components (e.g., bleed valves and stator vanes) and by closed-loop limiting of both shaft acceleration and the rate of change of fuel flow. Therefore, these unstable conditions are not part of the feedback control problem for civil aircraft engines. The main aim of the engine controller is therefore to guarantee that the engine will be maintained within its operating limits at all times, regardless of how the operator may move the throttle lever or of inlet conditions (e.g., altitude and Mach number). The engine's operating limits may be of a mechanical, thermal, or aerodynamic nature (e.g., surge). In addition to these constraints, the overall engine performance is also subject to both regulatory standards and the requirements of the airframe manufacturer.

What a pilot wants to achieve when moving the thrust lever is a certain percentage of the maximum thrust available at the current flight conditions, not a specific net thrust from the engine. Since thrust itself is not measurable in flight, the relative thrust command given by the power lever angle (PLA) setting must be translated into a command change of a measured variable. Thrust corresponds well with the LP shaft speed (after taking into account aircraft speed and environmental conditions such as pressure and
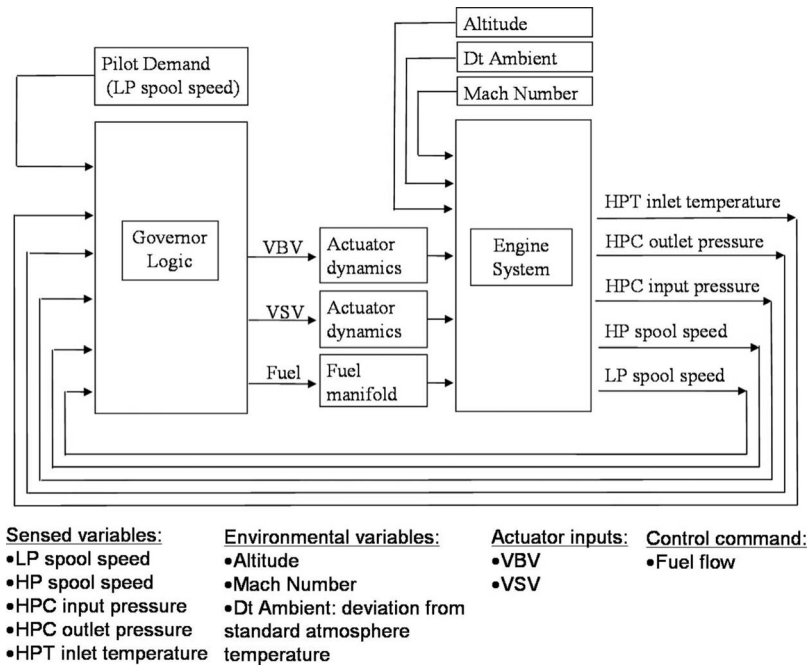
Sensed variables:
- LP spool speed
- HP spool speed
- HPC input pressure
- HPC outlet pressure
- HPT inlet temperature

Environmental variables:
- Altitude
- Mach Number
- Dt Ambient: deviation from standard atmosphere temperature

Actuator inputs:
- VBV
- VSV

Control command:
- Fuel flow

Fig. 2 Diagram of the current model's closed-loop system

temperature), particularly in the case of a high-bypass turbofan, where the majority of the thrust is provided by the fan. Therefore, it is common practice to choose fan speed as the controlled parameter (this, for example, is the choice adopted by General Electric [5], although other vendors may and do choose other indirect measurements of thrust). Fuel flow is the sole control input available as other engine components that may modify the engine's operating point, such as bleed valves or VSVs, are, in this instance, open loop scheduled. On an advanced civil aircraft, these may be "tweaked" according to the operating condition and past history of the engine, but they are not, in any case, truly feedback controlled as would occur in multivariable military jet engine control schemes. Furthermore, the exhaust nozzle on a civil aircraft is fixed and as such cannot be used to modify the engine's operating point as occurs on military engines. A diagram of the current model's closed-loop system is provided in Fig. 2.

The engine's operating limits may be divided into two groups: maximum limits are those that must not be exceeded from below, and minimum limits are those that must not be exceeded from above. Maximum limits are as follows: fan speed (i.e., LP spool speed), fuel flow increase rate, HP spool speed (the shaft that joins the HP turbine and the HP compressor), HP spool acceleration, HP turbine inlet temperature, HP compressor discharge pressure, and fuel flow. Minimum limits are as follows: LP spool speed, fuel flow decrease rate, HP spool speed, HP spool deceleration, and fuel flow. With the exception of fan speed demand, minimum LP spool speed, and maximum fuel and fuel flow rate (the latter is scheduled against HP compressor pressure ratio), all of the above are currently set to fixed values. However, the architecture would be able to cope with these variations according to operating conditions or different engine requirements following, say, a failure. The engine's idle condition may be any of the minimum limits on LP spool speed, HP compressor delivery pressure, or fuel, according to the engine's operating condition and environmental factors.

The engine is maintained within its operating limits by fuel regulators, and these can also be split into two categories: steady state control regulators and transient control regulators. The steady state regulators consist of fixed limits that prevent the engine operating outside fixed bounds, for example, to limit against overtemperature, overspeed, fuel metering valve high and low limits, minimum idle limits, and flameout limits. These are maxi-

mum and minimum HP shaft speed, fan speed control, maximum turbine inlet temperature, maximum and minimum fuel flow, maximum and minimum fuel flow rate, and compressor delivery pressure ratio. For the transient control regulators, the aim is to control the HP shaft rate of acceleration and fuel rate during sharp acceleration demands and for sharp deceleration conditions, minimum core speed and fuel rate decelerations are also controlled. There are several regulators within the designed controller, and some are there as a backup to the others, for example, the duplication of acceleration and deceleration regulators (thereby allowing control of the acceleration rate of both shafts). An important motivation for the development of the model is to allow investigation of robust and adaptive control solutions to specific failure modes. Should a failure mode affect the fuel system, then the acceleration profiles would need to be controlled via the speed rate regulators. Should a failure mode affect the variable geometry or bleed systems, the compressor delivery pressure and the consequent pressure regulators could be significantly affected. The performance of the engine under these failure modes needs to be assessed, and so several regulators have been implemented.

Indeed, the engine's operational limits also need to be considered in the context of engine degradation or failure. As an example, the acceleration of a healthy engine is usually limited by the maximum permissible rate of acceleration of any of the engine's shafts (note: this is not a mechanical limit but is meant to avoid surge; therefore, the maximum rate of acceleration of the HP shaft tends to dominate the acceleration profile), the allowed fuel flow rate of increase, and possibly the maximum permitted fuel flow (for an aggressive acceleration profile). A healthy engine can therefore successfully reach its maximum rated power without encountering any further limits. However, for a condition of low ambient pressure with extreme bleed and high ambient temperature, the maximum turbine inlet temperature may instead become the operating envelope's limiting factor, and the engine may not reach maximum power but will instead settle at the maximum turbine inlet temperature. Furthermore, transient turbine inlet temperature is higher than that permitted during a steady state operation. Therefore, the maximum power achievable would be further reduced after a short period of time. Another consideration is that these operating limits may not always be set at a fixed value. For example, the engine's minimum LP spool speed is increased at
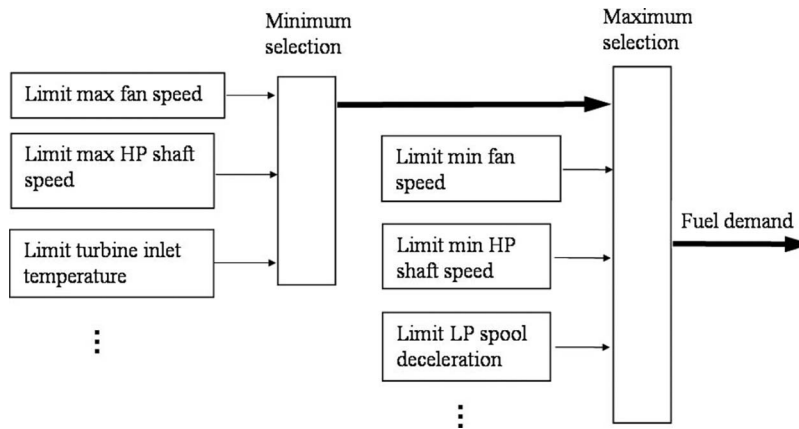
Fig. 3 Selection logic architecture

high altitude or during landing (to allow for a rapid increase in thrust in case of an aborted landing), and the fuel flow rate of change is scheduled according to the engine's operating point. A further example of this is a software upgrade by the engine manufacturer: It is current practice that an engine's performance may be capped to increase life span and fuel economy. However, should the aircraft owner have a requirement for improved performance, he may pay for a software upgrade to remove some of these limitations.

In addition to the engine operating limits, there are also the regulatory requirements on the overall behavior of the engine. These standards are issued by an international or national authority, for example, the U.S. Federal Aviation Authority (FAA). Typical requirements for a civil aircraft [5] are that upon receiving a demand for an increase in thrust, the engine must not overshoot its target by more than 2%, with a maximum steady state deviation of 1%. The engine's time to accelerate to maximum thrust is also regulated; this is a specification of the airframe manufacturer and often takes the form of a requirement that the engine must be able to accelerate at sea level static (SLS) from within 15% of idle to full throttle within a specified time frame, e.g., 10 s, and to preserve this acceleration profile over a given altitude range.

4 Controller Architecture and Design

The controller's input is relative thrust demand (a percentage of the maximum thrust available at the engine's operating point, here considered proportional to fan speed), and the output is fuel flow demand. Performance requirements are satisfied while maintaining the engine within its operating limits by assigning a gain-scheduled proportional-integral (PI) controller to each of the individual constraints. A selection logic then chooses amongst these so that at any point of its operating envelope the engine is governed by an appropriate controller. The gains of each PI controller are scheduled as a function of engine rpm and altitude using lookup tables that are dynamically initialized from the workspace over a flight envelope from sea level to 35,000 ft and over values of engine rpm from idle to maximum thrust. Bumpless transfer and antiwindup are also provided by the controller architecture. For the purpose of clarity, in the rest of this paper, each individual PI loop will be referred to as a "regulator," with only the overall architecture and resultant control system referred to as "the controller."

4.1 Regulator Selection Logic. All of the regulators that control a "maximum" limit (e.g., fan speed and HP turbine inlet temperature) are routed into a "minimum" selection block that selects the smallest output of these regulators. The resultant signal is then passed into a maximum selection block along with the output of

all the regulators assigned to minimum limits. This maximum selection block then chooses the greatest of these signals. A diagram of this architecture is shown in Fig. 3. A useful feature of this minimum/maximum selection architecture is that it inherently provides bumpless transfer since a switchover between regulators may only occur at a crossover point: when one of the inactive regulators' outputs intersects that of the active regulator. What this means in practice is best illustrated by a diagram: Fig. 4 shows the individual fuel demands of the active regulators during a pilot request—in this case an abrupt increase in thrust demand at SLS to 98% of the maximum thrust in a time span of half a second. It is immediately apparent that it is the maximum regulators (i.e., limits not to be exceeded from below) that intervene on the engine's behavior during an acceleration. Conversely, it is the minimum regulators that intervene during a deceleration, as shown in Fig. 5. Figure 6 shows the final controller demand after the selection logic has been applied to the output of all regulators. By comparing this with Fig. 4, it is apparent that the controller has selected the smallest of the regulators' demands during acceleration and that the transfer between these is smooth. Conversely, it has selected the largest of the regulators' demands during deceleration. Note that the controller's output is converted to fuel flow units ($kg\ s^{-1}$) in a module external to the controller to allow for an easy implementation of different fuels should the model be adapted in the future to a different configuration, e.g., an industrial aeroderivative engine. The switchover between regulators is evident in the next plot: Fig. 7 shows which regulator is controlling the engine at any moment of time. The numbers along the ordinate of the plot indicate the active regulator: 1 is the fan speed (LP shaft) regulator, 8 is the fuel flow increase rate regulator, 4 is the HP shaft rate of the acceleration regulator, 7 is the maximum fuel regulator, 15 is the fuel flow decrease rate regulator, 12 is the HP shaft rate of the deceleration regulator, and 13 is the minimum fuel regulator. At steady state, until time $t=50$, the engine is controlled by the fan speed demand regulator, then upon the pilot's request at $t=50$ for an abrupt acceleration, the fuel demand of the fan speed regulator rapidly ramps up. At approximately $t=50.01$, the active regulator is switched over to regulator 8, the fuel flow increase rate. During the remainder of the acceleration, the engine is controlled by the HP shaft maximum acceleration rate regulator, the fuel flow increase rate regulator, and the maximum fuel regulator. Finally, toward the end of the acceleration, control is again switched over to the fan speed regulator. The inverse process occurs after $t=105.5$, upon engine deceleration: The fuel flow decrease rate regulator is the first regulator to take over from fan speed but is subsequently replaced by the HP shaft deceleration regulator and the minimum fuel regulator. The overall controller
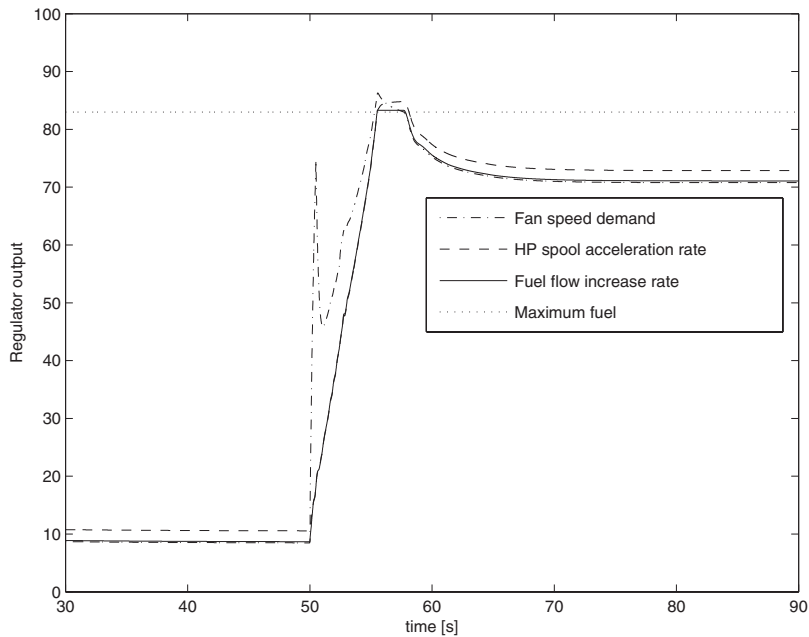
Fig. 4 Active regulators' output during acceleration

output is a smooth ramp, and engine acceleration proceeds accordingly until maximum thrust has been achieved. This can be seen clearly in Fig. 8.

4.2 Preventing Integrator Windup. The bumpless transfer logic in the controller works well, as indeed it must because it is an inherent property of the architecture of the controller: a minimum and maximum selection logic applied successively to groups of individual regulators. However, although this bumpless transfer is inherent to the minimum/maximum selection logic, this switching between controllers could not in practice occur with just a PI control for each regulator—each PI regulator must have a procedure in place to prevent the integrator's output from growing indefinitely when that particular regulator is not active. This would otherwise break the logic of the architecture. Consider if the maxi-

mum LP shaft acceleration regulator did not have an integrator reset in place. Then, while the engine is at steady state, its integrator's output would grow without bounds and switchover to the acceleration limit (upon a demand for increased thrust) would only occur after the maximum acceleration limit had already been greatly exceeded or not at all if the engine had been running at steady state for a long enough period of time. A highly effective antiwindup architecture that ensures that the integrator's output does not grow without bounds is shown in Fig. 9. When a regulator is active (it is notified of this by a module that tracks which is the active regulator), the switch selector (as seen in Fig. 9) will pass the regulator's own signal around the feedback loop, and at point B the output will be zero and the regulator will see an unmodified error signal. When the controller is inactive, the
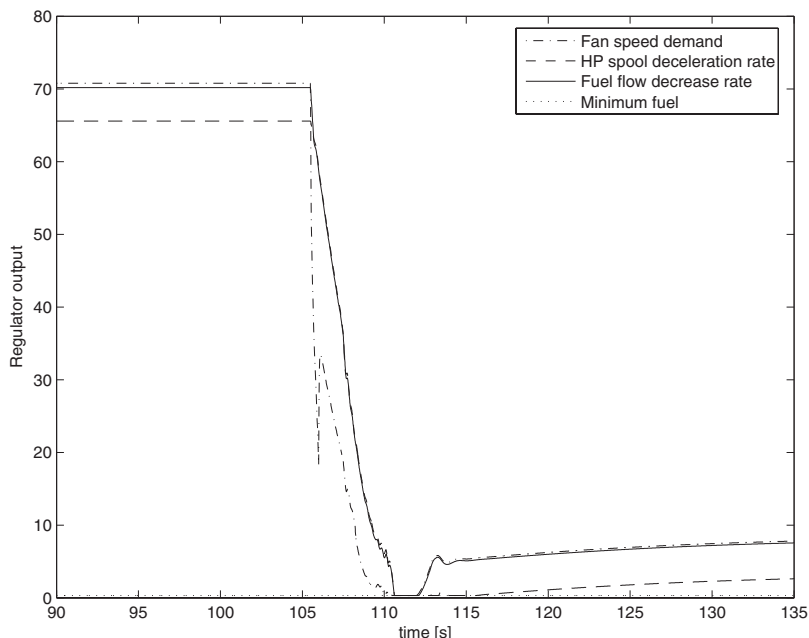
Fig. 5 Active regulators' output during deceleration
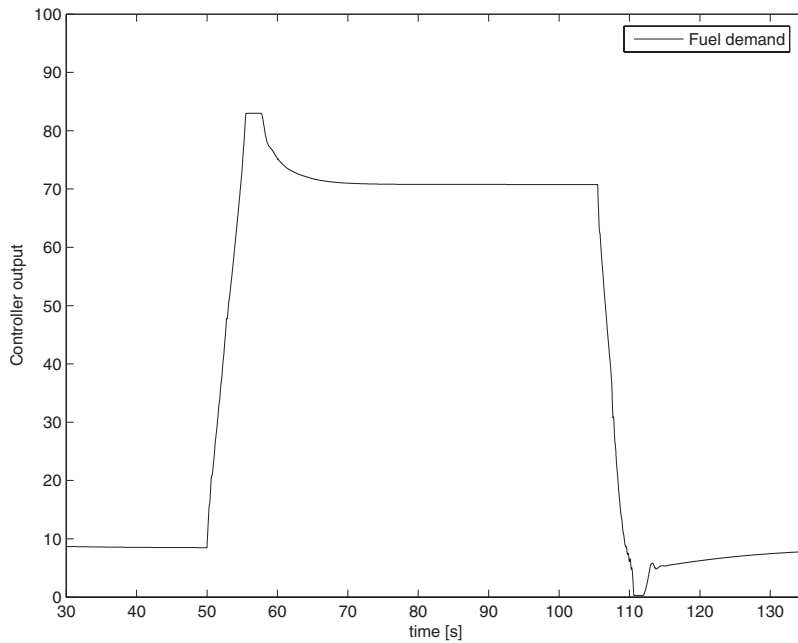
Fig. 6   Controller fuel demand

switch will pass the value of the current active regulator. This is then fed back via point B, after being subtracted from the signal at point A and then multiplied by the gain W_G—the result is then subtracted from the error, thereby effectively reducing the error seen by the inactive regulator and thus reducing its value. When the output of the active controller is below the regulator's target, the tracking will reach a value slightly above that of the active regulator, and vice versa—when the output of the active controller is above the regulator's target, it will rest at slightly below the active signal (i.e., the regulator's output will track the active sig-

nal from above and below). This property, in conjunction with a maximum and minimum selection logic, is what allows the overall architecture to function.

The value of the gain W_G underpins the operation of the anti-windup loop. For example, one may wish to know the value of a regulator when it is inactive and the engine has reached a steady state—e.g., the condition before an abrupt acceleration. Simple inspection leads to the following conclusion: the output of an inactive controller will reach a fixed value when
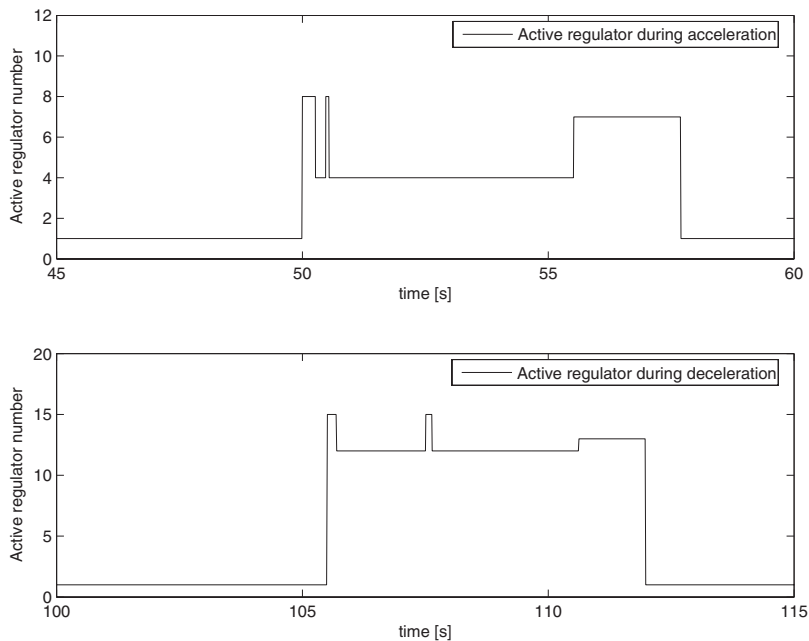
Fig. 7   The ordinate gives the number of the active regulator: 1 is the fan speed (LP shaft) regulator, 4 is the HP shaft rate of the acceleration regulator, 8 is the fuel flow increase rate regulator, 7 is the maximum fuel flow regulator, 15 is the fuel flow decrease rate regulator, 12 is the HP shaft rate of deceleration regulator, and 13 is the minimum fuel regulator
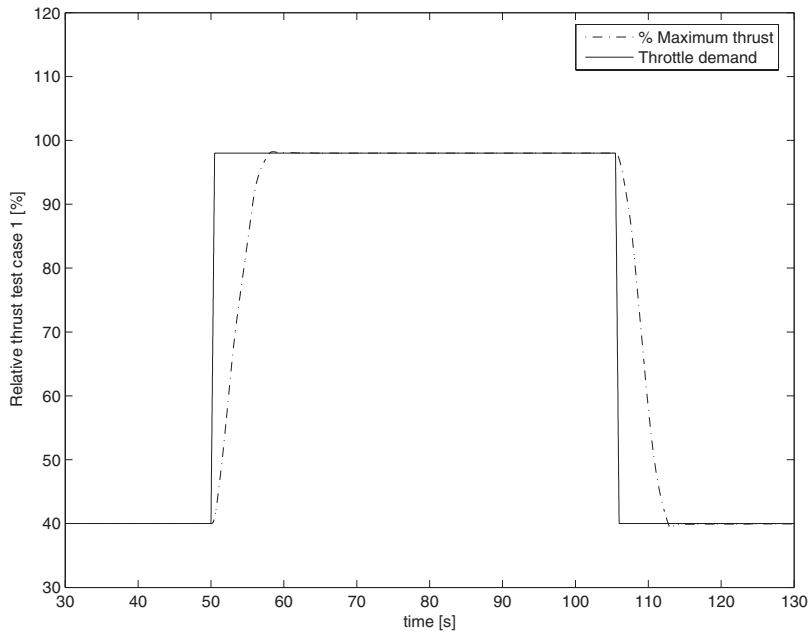
Fig. 8 Thrust response to large throttle demand

$$(A - C)W_G = E$$

which if rearranged gives the steady state value of A as

$$A = E/W_G + C \qquad (37)$$

It would seem from this that during a steady state operation it is desirable to have a large W_G, so that E/W_G tends to zero and $A \approx C$, where C is the value to be tracked. Under these conditions, a maximum limit regulator would track the active regulator's output asymptotically from above, while a minimum limit regulator would track the active regulator's output asymptotically from below. The requirements for this to occur are readily highlighted under the assumption of a discrete model (as all simulated models are, in practice, due to numerical integration) and a single, small, time step update Δt. For a maximum limit, assuming constants E and C, the change in the value of A over one time step is approximately

$$I_G(E - (A - C)W_G)\Delta t \qquad (38)$$

Since $A > C$ for a maximum limit, the major requirement is that the value subtracted from A during one time step must be less than

$A - C$. Consider the worst case scenario of a negligible error value (since a large error value helps in satisfying the above condition),

$$(A - C)W_G I_G \Delta t < (A - C) \qquad (39)$$

simplified to

$$\Delta t W_G I_G < 1 \qquad (40)$$

Similarly, for a minimum limit, since now $C > A$, the requirement is that the value added to A during one time step must be less than $C - A$, i.e.,

$$-(A - C)W_G I_G \Delta t < (C - A) \qquad (41)$$

which again reduces to the expression in Eq. (40),

$$\Delta t W_G I_G < 1 \qquad (42)$$

These considerations may tempt one to arrive at the conclusion that W_G should be as large as possible subject to the above constraint—but first we need to consider what happens during a single time step update for a time-varying controller output C, assuming a constant error E. Under such circumstance,
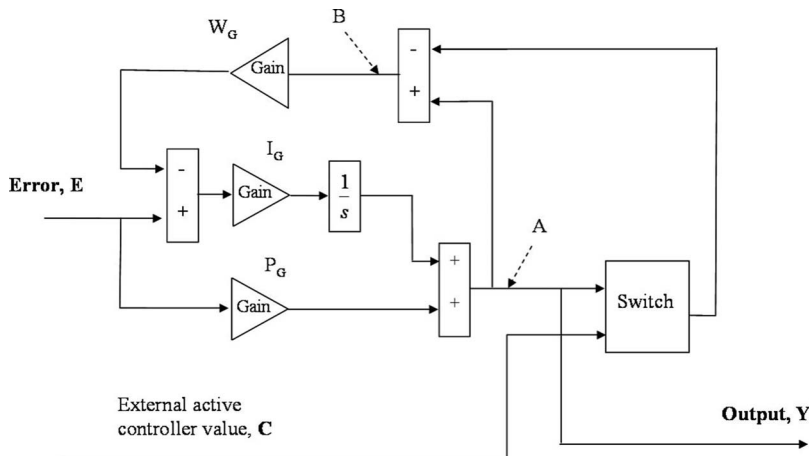
Fig. 9 PI controller structure with integrator antiwindup

Journal of Engineering for Gas Turbines and Power   SEPTEMBER 2008, Vol. 130 / **051601-11**
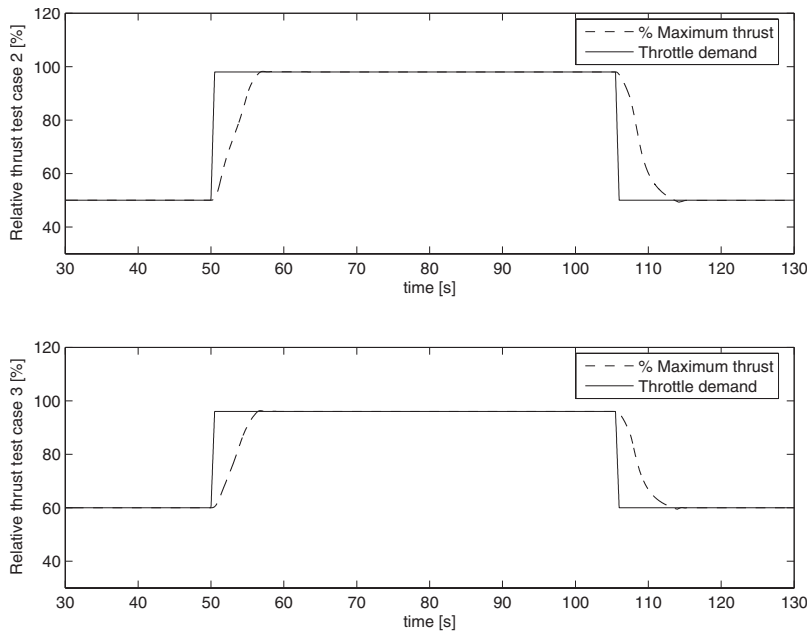
Fig. 10 Thrust response to large throttle demand. Case 2 (top): from 50% to 98% of the maximum thrust, 15,000 ft (≈4500 m), and Mach number of 0.45. Case 3 (bottom): from 60% to 96% of the maximum thrust, 35,000 ft (≈10,000 m), and Mach number of 0.8.

$$A(t + \Delta t) = P_G E + I(t) + I_G\{E - [A(t) - C(t + \Delta t)]W_G\}\Delta t \tag{43}$$

where

$$I(t) = I_G\{E - [A(t - \Delta t) - C(t)]W_G\} \tag{44}$$

The requirement for a maximum limit to retain a margin of safety, i.e., how much its signal rides above the signal to be tracked, is then

$$I_G\{E(t) - [A(t) - C(t + \Delta t)]W_G\}\Delta t \geqslant \Delta C \tag{45}$$

Similarly, for a minimum limit,

$$I_G\{E(t) - [A(t) - C(t + \Delta t)]W_G\}\Delta t \leqslant \Delta C \tag{46}$$

under all conditions. This is aided by a small Δt, but too large a value of W_G can indeed lead to the value of A dipping below that of C when C should rise very rapidly. For the system under consideration, it has been found that this would require very large values of W_G—of the order of 10^3 or more—and that excellent tracking of C is achievable with values in the order of 10^2, without fear of the tracking regulator's output crossing over C. However, in general, one must be aware that a safe value of W_G depends on the system considered—and, in particular, on the maximum rate of increase of C and E—and that possible variations in the time step Δt are also of consequence. The implications of a time-varying error during transients are a logical extension of the above. In summary, it is not possible to provide an absolute guarantee that a certain value of W_G will be appropriate for all conditions unless clear boundaries on E, C, and their rate of increase are established. Therefore, the value of W_G must, in general, be verified for the range of conditions expected.

4.3 Reference Tracking: Requirements and Consequences. How closely an inactive regulator must track the active regulator depends on how rapidly switchover must occur. It must not, however, track the active regulator too closely, thereby providing a "safety margin" in case of a rapid change in the value of C. Time for switchover also depends on the size of the gains P_G and I_G—with sufficiently large gains it has been found that the time

for switchover is negligible and a good safety tracking margin can be achieved with no fear of switchover being delayed enough for any of the regulator limits to be exceeded by more than 1%. It is clear then that this controller architecture requires extensive validation and tuning to the dynamics of the controlled plant: The architecture does not guarantee that no limits will be exceeded should the plant's dynamics be significantly faster than those predicted during testing, although this does not pose a serious problem for gas turbines, whose dynamics are well known and predictable. Furthermore, the presence of multiple regulators also provides a degree of redundancy.

5 Simulation Issues

5.1 Model Initialization. The model described in this paper has been developed for the purpose of investigating advanced strategies for robust fault tolerant aeroengine control. Clearly, it is of great benefit to provide an implementation architecture that allows for rapid alteration of the model to simulate faults and adaptation to different engine configurations if so wished. One way of doing this is to initialize as much of the model as possible from scripts. For example, all SIMULINK tables where possible are initialized using workspace vectors. Scripts can assign initialization values to all lookup tables, enabling the model to be rapidly changed if required. In the same way, major parameters can be made time dependent if their values are provided via "from workspace" blocks. For the same reason, the scaling of each characteristic map is performed online as the model runs, with each of the scaling parameters provided by a workspace variable. The number of states included in the model is 41.

5.2 Algebraic Loops. Algebraic loops occur if a module requires data from elements downstream. This is a major issue for the compressors and turbines because outlet pressure data are required to calculate the pressure ratio across the component and, thus, via the characteristic map, the component's mass flow. It is also good practice to calculate thermodynamic parameters based on a component's average temperature (see Sec. 2), but this re-
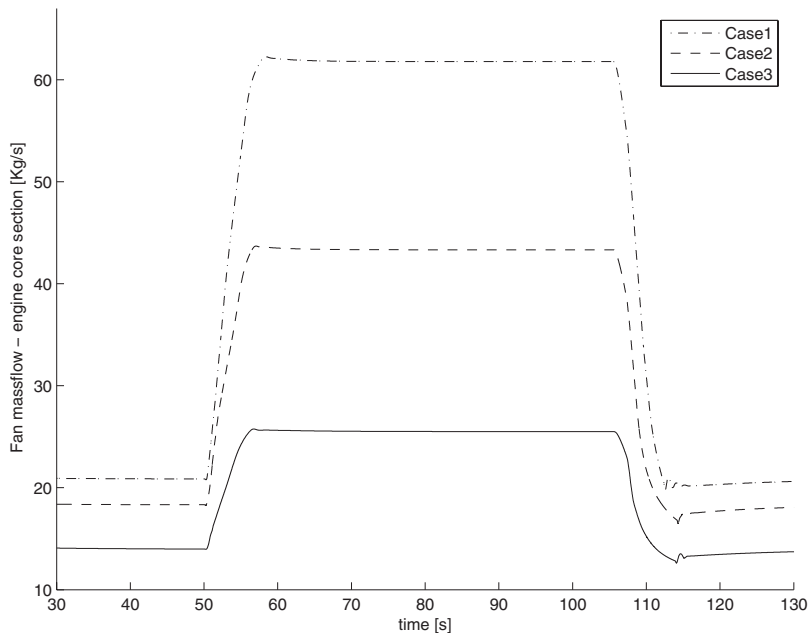
Fig. 11 Mass flow through the engine core

quires knowledge of the component's outlet temperature prior to its calculation by the simulation module. If these algebraic loops are not specifically eliminated, the SIMULINK loop solver uses Newton's method to iteratively find a solution [30]. Although the method is robust, it is possible to create loops for which the loop solver will not converge without a good initial guess for the algebraic states. An initial guess for a line in an algebraic loop can be specified by placing an initial condition (IC) block which is normally used to specify an initial condition for a signal on that line. Another way to specify an initial guess is to use an algebaic constraint block. An alternative method that is particularly advantageous for the current model is to specify a one-time-step delay by using a memory block, thereby avoiding the need for iterative calculations that would slow down the simulation considerably.

Thanks to the use of these delays, the solution can be reached without the iterative procedure that is generally required for the solution of the nonlinear equation system. This is made possible by means of the approximations that are applicable to real-time gas turbine dynamic models in consideration of the very short time step used in the simulation.

6 Closed-Loop Performance Validation

Several methods of gas turbine simulation dynamic performance validation have been used in the past, e.g., Ref. [2] used GASTURB [21], a commercial software dedicated to gas turbine modeling, and Ref. [7] matches calculated performance to previously published results [11].
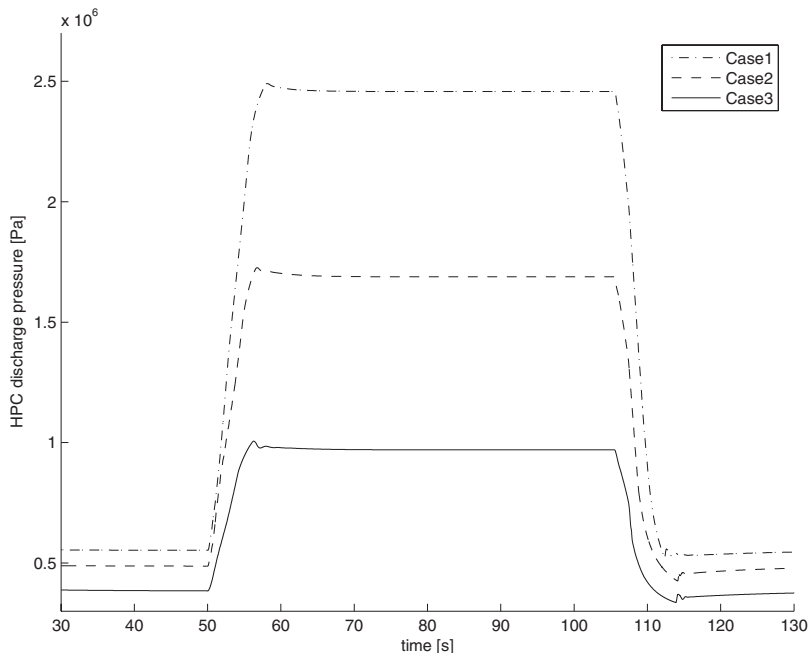
Fig. 12 HP compressor discharge pressure
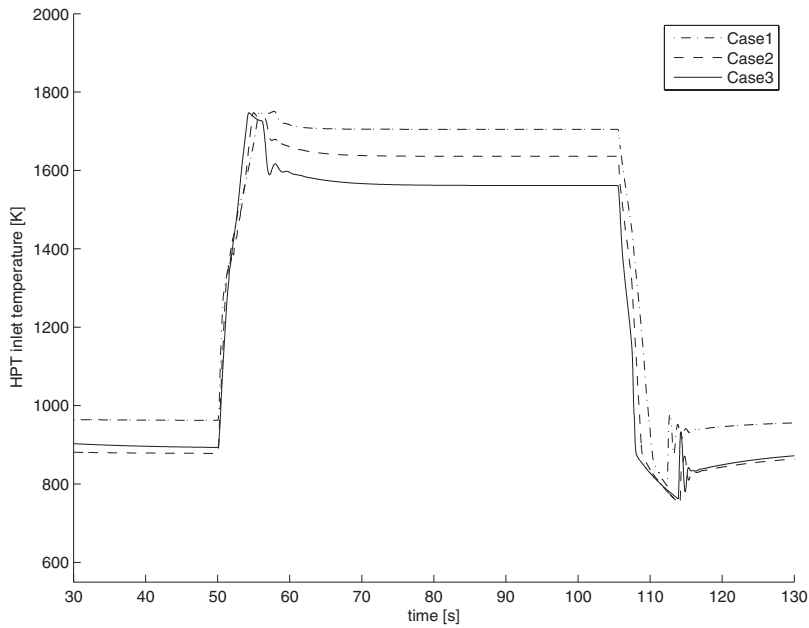
Fig. 13 HPT inlet temperature

The current model and controller have been validated against dynamic performance data for a comparable engine by analyzing the resulting closed-loop performance properties for a range of different pilot thrust demands against the type of responses required from a real turbofan engine. Some snapshots of the overall performance of the model and controller can be seen in Figs. 4–8 and 10–14. Figure 4 shows the individual fuel demands of the active regulators during a pilot request—in this case, an abrupt increase in thrust demand at SLS to 98% of maximum thrust in the time span of half a second. Figure 5 shows the active regulators' demands during a deceleration. Figure 6 shows the final controller demand after the controller's selection logic has been applied to the output of all regulators. By comparing this with Figs. 4 and 5, it is apparent that the controller has selected the smallest

of the regulators' demands during acceleration and that the transfer between these is smooth. Conversely, it has selected the largest of the regulators' demands during deceleration. The overall controller output is a smooth ramp, and engine acceleration proceeds accordingly until the maximum thrust has been achieved. This is apparent in Fig. 8, which shows the engine's response to the pilot's demand: Although the request is abrupt, the engine acceleration is smooth. Although this is not evident in the plot, there is a slight overshoot and undershoot of about 0.4%, but this is well within the FAA requirement of a deviation in thrust of not more than 2% [5] and can be reduced further, although at the cost of an increase in acceleration time. Plots of characteristic performance during three test cases are provided (see Figs. 4–8 and 10–14),
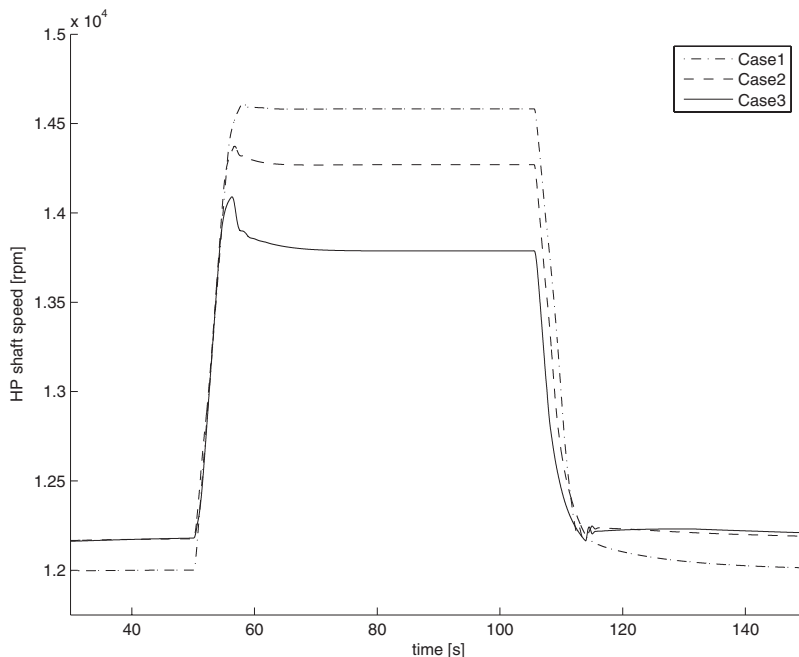
Fig. 14 HP shaft speed

and these show engine characteristic response at different points in the operating envelope. The test cases are as follows:

(1) Case 1. SLS: from 40% to 98% of the maximum thrust.
(2) Case 2. Environment conditions: 15,000 ft (4572 m); Mach number 0.45. From 50% to 98% of maximum thrust.
(3) Case 3. Environment conditions: 35,000 ft (10,067 m); Mach number 0.8. From 60% to 96% of maximum thrust.

Figure 8 shows the response to an abrupt pilot demand at SLS, and Fig. 10 plots the response to test cases 2 and 3 for a similar pilot demand, i.e., a request for an abrupt acceleration over a short time of 0.5 s. Additional plots show some fundamental engine characteristics during the three test cases: Fig. 11 shows the core mass flow (exit of fan), Fig. 12 the HPC discharge pressure, Fig. 13 the HPT inlet temperature, and Fig. 14 the HP shaft speed.

7 Conclusions

This paper has presented details of the design and validation of a complex nonlinear real-time simulation model for a civil turbofan aircraft engine. The model was developed in a modular fashion using wherever possible the underlying physics and avoiding empirical approximations. A switched gain-scheduled feedback controller incorporating bumpless transfer and antiwindup functionality was designed and implemented on the engine model in accordance with current industrial practice. Together, the engine and controller cover the full flight envelope and achieve dynamic performance that closely matches that of a real engine. The control scheme corresponds closely to current industrial practice and delivers high-performance tracking of pilot demands while ensuring that the operating constraints of the engine are met at all times. Future work on this project will focus on extending the model to include various sources of uncertainty, fault, and failure scenarios and on extending the control scheme to deliver robust fault tolerant performance.

Acknowledgment

Nomenclature

T = temperature (K)
V = volume (m^3)
w = mass of gas stream (kg)
w_0 = initial value of mass present in plenum (kg)
$\dot{w}$ = gas stream mass flow (kg s^{-1})
R = gas constant (J K^{-1} mol^{-1})
$\bar{R}$ = specific gas constant of the gas stream (J kg^{-1} K^{-1})
c_p = specific heat at constant pressure (J kg^{-1} K^{-1})
γ = ratio of specific heats
τ = heat soak time constant (s)
M = metal mass (kg)
q = heat flow (W)
$\bar{h}$ = average heat transfer coefficient over a surface (W m^{-2} K^{-1})
T_m = metal component average temperature (K)
$\bar{T}$ = gas stream mean temperature (K)
A = heat transfer area (m^2)
c_{pm} = metal specific heat capacity (J kg^{-1} K^{-1})
Y_d = value of Y established under experimental conditions
τ_d = heat soak time constant established under experimental conditions (s)

η_i = isentropic efficiency
η_t = turbine isentropic efficiency
π = pressure ratio
P_x = power consumption of component x (W)
p = total pressure (all pressures are total pressure unless otherwise stated) (Pa)
p' = static pressure (Pa)
I = moment of inertia (kg m^2)
ω = angular velocity (rad s^{-1})

References

[1] Litt, J. S., Parker, K. I., and Chatterjee, S., 2003, "Adaptive Gas Turbine Engine Control for Deterioration Compensation due to Aging," 16th International Symposium on Airbreathing Engines, Cleveland, OH.
[2] Borguet, S., Kelner, V., and Leonard, O., "Cycle Optimisation of a Turbine Engine: An Approach Based on Genetic Algorithms," Aerospace and Mechanical Engineering Department, University of Liege, Technical Report.
[3] Walsh, P., and Fletcher, P., 1998, *Gas Turbine Performance*, 1st ed., Blackwell Science, Oxford.
[4] Camporeale, S. M., Fortunato, B., and Mastrovito, M., 2006, "A Modular Code for Real Time Dynamic Simulation of Gas Turbines in Simulink," ASME J. Eng. Gas Turbines Power, **128**, pp. 506–514.
[5] Kreiner, A., and Lietzau, K., "The Use of Onboard Real-Time Models for Jet Engine Control," 2001, MTU Aero Engines, Technical Report.
[6] Al-Hamdan, Q. Z., and Ebaid, M. S. Y., 2006, "Modeling and Simulation of a Gas Turbine Engine for Power Generation," ASME J. Eng. Gas Turbines Power, **128**, pp. 302–311.
[7] Camporeale, S. M., Fortunato, B., and Dumas, A., 1998, "Dynamic Modeling and Control of Regnerative Gas Turbines," ASME Paper No. 98-GT-172.
[8] Camporeale, S. M., Agresti, M., and Fortunato, B., 2000, "An Object-Oriented Program for the Dynamic Simulation of Gas Turbines," ASME Paper No. 2000-GT-42.
[9] Camporeale, S. M., Dambrosio, L., and Fortunato, B., 2002, "One-Step Ahead Adaptive Control for Gas Turbine Power Plants," ASME J. Dyn. Syst., Meas., Control, **124**, pp. 341–348.
[10] Kim, J. H., Song, T., Kim, T., and Ro, S., 2001, "Model Development and Simulation of Transient Behavior of Heavy Duty Gas Turbines," ASME J. Eng. Gas Turbines Power, **123**, pp. 589–594.
[11] Rowen, W. I., 1983, "Simplified Mathematical Representations of Heavy-Duty Gas Turbines," ASME J. Eng. Power, **105**, pp. 865–869.
[12] Visser, W. P. J., Kogenhop, O., and Oostveen, M., 2006, "A Generic Approach for Gas Turbine Adaptive Modeling," ASME J. Eng. Gas Turbines Power, **128**, pp. 13–19.
[13] Garg, S., 1996, "A Simplified Scheme for Scheduling Multivariable Controllers and Its Application to a Turbofan Engine," Presented at the ASME International Gas Turbine and Aeroengine Congress and Exhibition, Birmingham, UK, June, Paper No. 96-GT-104.
[14] Larkin, L. J., and Philpott, J., 2004, "Implementation of a Multivariable Control," ASME J. Eng. Gas Turbines Power, **126**, pp. 472–474.
[15] Postlethwaite, I., Samar, R., Choi, B.-W., and Gu, D.-W., 1995, "A Digital Multi-Mode h-Infinity Controller for the Spey Turbofan Engine," European Control Conference.
[16] Samar, R., Murad, G., Postlethwaite, I., and Gu, D.-W., 1995, "A Discrete Time h-Infinity Observer-Based Controller and Its Application to an Aero-Engine," American Control Conference.
[17] Watts, S., and Garg, S., 1995, "A Comparison of Multivariable Control Design Techniques for a Turbofan Engine Control," ASME 40th Gas Turbine and Aeroengine Congress and Exposition, Houston, TX, June.
[18] Spang, A. H., and Brown, H., 1999, "Control of Jet Engines," Control Eng. Pract., **7**, pp. 1043–1059.
[19] Saravanamuttoo, H., Cohen, H., and Rogers, G., 1996, 4th ed., *Gas Turbine Theory*, Longman, New York.
[20] Archer, R. D., and Saarlas, M., 1996, *An Introduction to Aerospace Propulsion*, Prentice-Hall, Englewood Cliffs, NJ.
[21] Kurzke, J., GASTURB software.
[22] Welty, J., Wicks, E., Wilson, R., and Rorrer, G., 2001, *Fundamentals of Momentum, Heat, and Mass Transfer*, Wiley, New York.
[23] Pike, A. W., 2000, "Development of the gtx100 Gas Turbine Simulink Dynamic Model," Alstom, Technical Report.
[24] Incropera, F., and Dewitt, D., 1990, *Fundamentals of Heat and Mass Transfer*, Wiley, New York.
[25] Ricketts, B. E., 1997, "Modelling of a Gas Turbine: A Precursor to Adaptive Control," *IEEE Colloquium: Adaptive Controllers in Practice*, pp. 7/1–7/5.
[26] McGreehan, W. F., and Schotsch, M. J., 1998, "Flow Characteristics of Long Orifices With Rotation and Corner Radiusing," ASME J. Turbomach., **110**, pp. 213–217.
[27] Alstom GTX100 dynamic simulation program.
[28] Thomas, P., 1999, *Simulation of Industrial Processes for Control Engineers*, Butter-Heinemann, Oxford.
[29] Hannett, L. N., and Khan, A., 1993, "Combustion Turbine Dynamic Model Validation From Tests," IEEE Trans. Power Syst., **8**, pp. 152–158.
[30] Mathworks 2005, Simulink Manual.

Comparative Study of Two Low CO₂ Emission Power Generation System Options With Natural Gas Reforming

Na Zhang[1]

Institute of Engineering Thermophysics,
Chinese Academy of Sciences,
Beijing 100080, P.R.C.
e-mail: zhangna@mail.etp.ac.cn

Noam Lior

Department of Mechanical Engineering and
Applied Mechanics,
University of Pennsylvania,
Philadelphia, PA 19104-6315

Two power plant schemes that reduce CO_2 emission and employ natural gas reforming were analyzed and discussed. The first one integrates natural gas reforming technology for efficiency improvement with an oxy-fuel combined power system (OXYF-REF), with water as the main work fluid. The reforming heat is obtained from the available turbine exhaust heat, and the produced syngas is used as fuel with oxygen as the oxidizer. The turbine working fluid can expand down to a vacuum, producing a high-pressure ratio and thus more net work. The second system integrates natural gas reforming in a precombustion decarbonization scheme using chemical absorption technology for the CO_2 removal (PCD-REF). The gas turbine is the conventional air-based one with compressor intercooling. Supplementary combustion is employed to elevate the turbine exhaust temperature and thus achieve a much higher methane conversion rate (96.9%). Both systems involve internal heat recuperation from gas turbine exhausts, and particular attention has been paid to the integration of the heat recovery chain to reduce the related exergy destruction. The systems are simulated and their thermal efficiency, overall and component exergy losses, and CO_2 removal capacity are compared. The OXYF-REF system has a higher energy efficiency, of 51.4%, and higher CO_2 removal, but the product CO_2 has lower purity, of 84%. The PCD-REF system has a thermal efficiency of 46%, the captured CO_2 is 99% pure, and the CO_2 specific emission is 58.5 g/kW h.
[DOI: 10.1115/1.2904895]

1 Introduction

CO₂ separation and sequestration is increasingly regarded as an effective strategy to limit greenhouse gas emissions in fossil-fuel-based power plants. The main three removal strategies are [1–3] (1) postcombustion decarbonization, (2) oxy-fuel power systems, and (3) precombustion decarbonization. Each of these strategies has some relative advantages and disadvantages, and they all decrease power generation efficiency and increase its cost. In this paper, we propose, analyze, and compare two power systems with low CO₂ emissions, employing natural gas reforming technology for fuel conditioning, where one of the systems employs the concepts of an oxyfuel system and the other of precombustion decarbonization, and compare the thermal performance of these two different strategies. To place these systems in the context of CO₂ removal strategies, a brief overview follows.

Postcombustion decarbonization separates CO₂ from the flue gas; it requires minimal modifications to the power system, but large gas quantities must be treated because CO₂ is diluted by the large amounts of nitrogen that are introduced with the combustion air. Chemical absorption of CO₂ is considered to be the most suitable method for this case because of the low CO₂ partial pressure [4].

Oxy-fuel systems are based on close-to-stoichiometric combustion with enriched oxygen and recycled flue gas. The combustion is thus accomplished in the absence of the large amounts of nitrogen, and produces only CO₂ and H₂O. CO₂ separation is accomplished by condensing out the water, typically at ambient tempera-

tures, from the flue gas and therefore requires only a small amount of energy. At the same time, however, a relatively large amount of energy, 7—9% of the total system input, is needed for the oxygen production. The main (and the recycled) working fluid commonly used in the referenced studies is either CO₂ [5–10] or H₂O [11–14]. Also, using CO₂ as the working fluid, we proposed and analyzed semiclosed oxyfuel systems with integration of the LNG (liquefied natural gas) cold exergy utilization [15,16].

To reduce the oxygen production energy efficiency penalty, new technologies have been developed, such as chemical looping combustion (CLC) [17–19] and the advanced zero emissions power plant (AZEP) concept [20,21]. The adoption of these new technologies shows promising performance because no additional energy is then necessary for oxygen separation, but they are still under development [22].

Precombustion decarbonization is accomplished by conversion of the fuel to CO- and H₂-enriched syngas by partial oxidation [1,23] or steam reforming [24,25], followed by a shift process in which CO is converted to CO₂ that is then separated out. Compared to the postcombustion decarbonization from the exhaust, it allows reduced equipment size and lower energy requirements because of much lower quantities of the conditioned gas. Depending on the operational conditions (mainly the pressure and CO₂ concentration), the CO₂ removal can be accomplished by either physical or chemical absorption.

The two low-CO₂ emission power generation systems we propose and analyze in this paper employ natural gas reforming technology for fuel conditioning but with different fuel conversion rates, each having a different improvement objective. In the oxy-fuel semiclosed power system, the steam reforming process is mainly used for the efficiency improvement by turbine exhaust heat recuperation. Similar to that in the chemically recuperated gas turbine (CRGT) cycle [26–28], it utilizes the turbine discharge heat to improve the fuel heating value by producing H₂. Only a

---
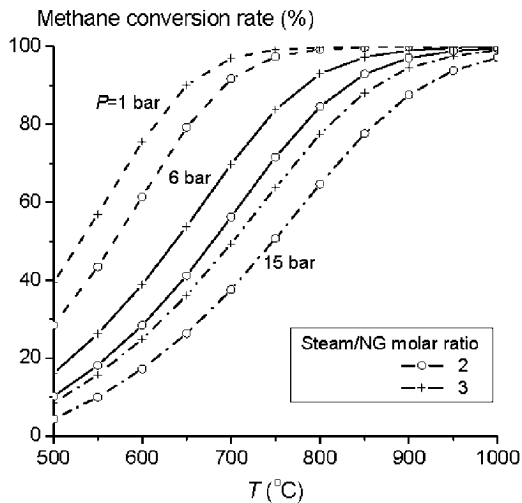
Fig. 1 Methane conversion rate predicted by chemical equilibrium

Table 1 Molar composition and some properties for feed streams

	Natural gas	Oxygen	Air
CH_4 (mol %)	91.18		
C_2H_6 (mol %)	4.41		
C_3H_8 (mol %)	0.1		
N_2 (mol %)	4.31	2	77.3
O_2 (mol %)		95	20.74
CO_2 (mol %)			0.03
H_2O (mol %)			1.01
Ar (mol %)		3	0.92
Temperature (°C)	25	25	25
Pressure (bar)	40	2.38	1.013
Lower heating value (kJ/kg)	46,300	—	
Power consumption for O_2 production (kJ/kg)		812	

medium conversion rate of methane is obtained with the available turbine discharge temperature, and the fact that the CO_2 capture is accomplished by the oxyfuel combustion method is, as explained above, an important advantage. Water vapor is employed as the main working fluid.

In the system with precombustion decarbonization, we employ the steam reforming (together with shift) process for the CO_2 removal. For this reason, supplementary combustion is used to elevate the turbine exhaust temperature and thus allow a much higher precombustion methane conversion rate ($>95\%$) to CO_2. This is intended to minimize the amount of CH_4 that enters the combustor and produces CO_2 emissions from the plant.

In both system configurations, steam is produced by heat recuperation inside the system, both for the reforming process and for combustion injection. The latter increases the working fluid mass flow rate for power generation while demanding very little pumping work for the injected (and then vaporized) water pressure elevation. Particular attention has been paid to the integration of the turbine exhaust heat recovery with both the reforming and the recuperation process.

2 Natural Gas Reforming Process

Chemical recuperation is one of the innovative concepts for improving the performance of natural gas fired gas turbine cycles [26–28]. The natural gas reforming process absorbs heat from the turbine exhaust to produce hydrogen, thus converting some of the turbine exhaust heat into the reforming product heating value.

The reforming process involves the following main reactions [2]:

$$CH_4 + H_2O \leftrightarrow CO + 3H_2 \quad \Delta H = 206.11 \text{ kJ/(mol } CH_4)$$

$$CO + H_2O \leftrightarrow CO_2 + H_2 \quad \Delta H = -41.17 \text{ kJ/(mol CO)}$$

$$C_nH_m + nH_2O \rightarrow nCO + (m/2 + n)H_2$$
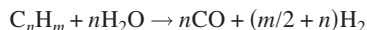
The first reaction is the methane reforming. It is highly endothermic and the methane conversion rate is a function of temperature, pressure, and steam/methane ratio, as shown in Fig. 1, which is obtained with ASPEN PLUS software and RK-Soave property method [29], assuming chemical equilibrium, for the natural gas composition given in Table 1.

Low-pressure, high temperature, and high steam consumption increase the reforming conversion. As pointed out by Lozza and Chiesa [25], for power cycles adopting precombustion decarbonization, a methane conversion rate higher than 95% is needed for over 90% CO_2 removal, necessitating large steam consumption

and high temperature operation. The typical gas turbine exhaust temperature, 550–600°C, is not sufficiently high for elevated conversion even under low pressure. Therefore, autothermal reforming [23] or supplementary firing [24], in which a fraction of the natural gas is used as fuel, are necessary to increase the turbine exhaust temperature.

The second reaction is known as the shift reaction. In the precombustion decarbonization scheme, the syngas must be shifted as it enriches the CO_2 concentration for CO_2 removal. The third reaction is the reforming of the heavier hydrocarbons contained in the natural gas, which is usually considered irreversible.

The situation is quite different from that in the CRGT cycles, in which turbine exhaust heat is recovered for improving the fuel heating value by methane conversion to H_2 and CO. High conversion of methane is, however, not essential in CRGT because the unconverted reactants are utilized as fuel. In addition, the methane conversion rate is very sensitive to the temperature in the mid-level temperature region (Fig. 1). Supplementary combustion is therefore not essential for the CRGT cycles, in which the fuel conversion is thus based on the available gas turbine exhaust heat and reaches only a moderate level. High methane conversion rate is, as explained above, necessary in the system with precombustion decarbonization we propose because the unconverted CH_4 would otherwise generate CO_2 in the subsequent combustion process.

3 Configuration I: The Oxyfuel System Integrated With Steam Reforming (OXYF-REF)

The conceptual plant configuration analyzed in this section integrates the CRGT concept with oxyfuel combustion [30]. Heat is extracted from the turbine exhaust for reforming with a medium methane conversion rate. An air separation unit is needed to produce oxygen as the combustion oxidizer. CO_2 is removed by water condensation and is subsequently compressed for liquefaction and storage.

The system configuration is shown in Fig. 2. It can be roughly divided into four sections: reforming process (2-3-4-5-6-7-8), power generation, exhaust heat recovery for steam generation (22-23-24-25), and CO_2 compression and liquefaction (28-30).

In the *reforming process section*, the steam and natural gas mixture (State Point 2) (of 2:1 molar ratio) is preheated to (3) by syngas heat recovery and enters the adiabatic reactor PRE-REF, where the heavier hydrocarbons are reformed. The reforming gas temperature drops due to the endothermality of the process (3-4), and it is preheated again before feeding to the reformer REF. The reformer operates at approximately the combustion pressure ($\sim$15 bar). It may adopt the conventional counterflow design with the reformer tubes filled with suitable catalyst (such as nickel catalyst pellets) [26]. The cold-side fuel gases flow through this
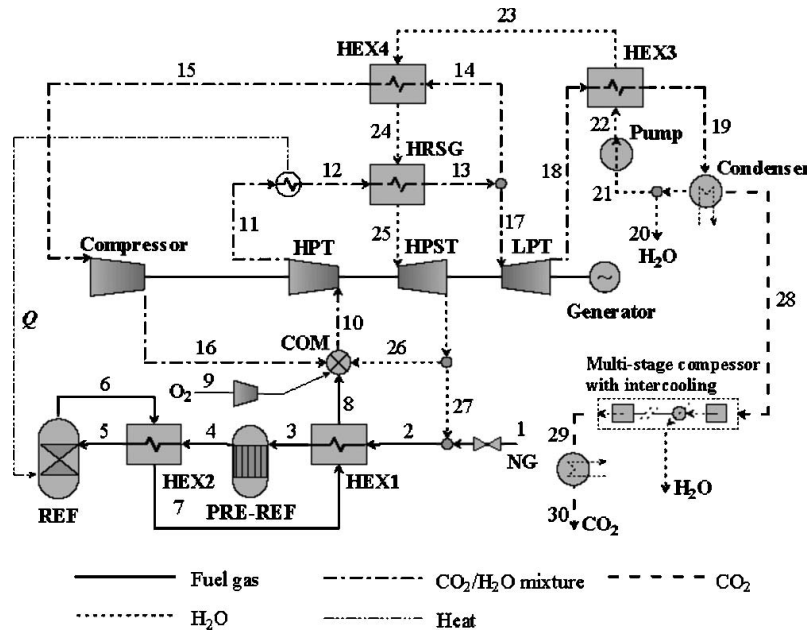
Fig. 2   Process flowsheet of Configuration I: OXYF-REF

packed bed. The heat necessary for reforming is provided by the high-pressure turbine (HPT) exhaust (11-12) flowing on the shell side. Before feeding to the combustor, the syngas (6) is cooled in HEX1 and HEX2 to an assumed maximum temperature of 250°C for preheating the reactants.

The combustion is near stoichiometric with oxygen as the oxidizer. A 2% excess oxygen is assumed. The oxygen is assumed to be produced in a conventional cryogenic vapor compression air separation plant with the specific energy consumption of 812 kJ/kg O_2 [22]. The combustion product is a mixture of mainly CO_2 and H_2O.

The *power generation section* consists of two gas turbines (HPT and LPT), one compressor and one steam turbine (HPST). It can be regarded as a combination of a recuperated oxy-fuel gas turbine cycle with steam injection and a steam Rankine-type cycle. The recuperated gas turbine cycle provides heat (in 11-12 and 12-13) for the reforming process and for steam generation in the HRSG. The steam Rankine cycle recovers the exhaust heat from the gas turbine (GT) cycle and provides steam for both combustion injection (26) and steam reforming (27). The heat recovery section, including HEX3, HEX4, and HRSG, serves as the boiler for the Rankine-like cycle.

The HPT flue gas is divided into two streams (Streams 14 and 17). Stream 14 preheats the Rankine cycle working fluid in HEX4 and then flows to the compressor and combustor of the GT cycle. Stream 17 further expands in LPT to a fairly low-pressure level (0.08 bar in this study), and the water contained is condensed and partly recycled as the Rankine cycle working fluid (21). The configuration of the power generation section is basically similar to the Graz cycle [15]. The arrangement of the higher-pressure (higher heat capacity) but lower mass flow rate fluid on the Rankine cycle side of the heat recovery section, with the lower-pressure (lower heat capacity) but higher mass flow rate fluid on the Brayton cycle side, is for reduction in heat transfer irreversibilities in the heat exchangers.

The combustion-generated CO_2 is separated and compressed to 110 bar (29) in a separate seven-stage compressor with intercooling.

4   Configuration II: The Precombustion Decarbonization Gas Turbine System (PCD-REF)

The GT system with integrated upstream fuel decarbonization and CO_2 removal is shown in Fig. 3. These processes are intended to reduce the amount of carbon entering the combustor and thus of the amount of CO_2 produced in it. Since the CO_2 separation is performed before addition of the oxidant, air can be used without the nitrogen-related energy penalties of postcombustion decarbonization. Basically, it has four main sections too: power generation section, fuel conditioning (reforming and shifting process), CO_2 removal (chemical absorption), and CO_2 compression and liquefaction.

The *power generation section* consisted of two-stage compressors (LPC and HPC) with intercooling and one GT. Similar in principle to the system proposed by Fiaschi et al. in Ref. [24], it is based on a recuperative GT power cycle with steam injection (8) to the combustor, fueled by the CO_2-free, H_2 enriched, syngas (32). The injected steam is produced by heat recuperation from the compressor intercooling and turbine exhaust. Different from Configuration I in the previous section, the GT uses air (1) as the basic working fluid.

The *fuel conditioning chain* consists of one reformer (REF) and two-stage shift reactors HTS (high temperature shift reactor) and LTS (low temperature shift reactor). The reformer works at a relatively lower-pressure level (~6 bar) to avoid the need for large steam addition. The GT exhaust temperature is not high enough to obtain a high methane conversion rate. Supplementary combustion (in SC) is thus adopted, which is sustained by excess oxygen in the turbine exhaust (10) and a fraction of the treated syngas (31), to avoid producing CO_2. The turbine exhaust (11-12) with elevated temperature provides heat for the endothermic reaction in REF. The necessary steam is produced by heat recovery inside the fuel conditioning section at the natural gas feed pressure (40 bar). Before feeding to the reformer, the mixture (22) of the produced steam and preheated natural gas (in molar ratio of 2:1) is expanded in the expander to the reformer operation pressure and a temperature of 411°C (23). The produced syngas composition is obtained assuming chemical equilibrium at the REF exit at the

Fig. 3 Process flowsheet of Configuration II: PCD-REF

temperature set at 900°C. Higher steam/natural gas ratios are not considered because more heat would have been needed to be extracted from the turbine exhaust that would have led to lower combustion inlet temperature (Streams 5 and 8) and to less available heat for the amine regeneration. The conversion of CO to CO_2 is advanced in two-stage shift reactions (HTS and LTS). The shift reactions are exothermic and the heat is recuperated for steam generation and natural gas preheating (in HEX3, HEX4, and HEX5). Before being sent to the CO_2 removal section, the syngas (29) is cooled down to near-ambient temperature, and part of the water content is removed by condensation.

The CO_2 removal section follows the conventional chemical absorption concept. It consists substantially of an absorber and stripper (regenerator). The solution for CO_2 absorption is a mixture of water and methyl diethanolamine (MDEA) (40% by mass), selected to reduce the reboiler heat duty, as MDEA requires less heat for regeneration than other amines, monoethanolamine (MEA) and diethanolamine (DEA), for example [2]. The rich solution from the absorber is preheated in HEX6 by the lean solution and regenerated in the stripper by extracting heat from the turbine exhaust (13-14) downstream of the recuperator HEX2. The minimal temperature difference in the HEX6 and the reboiler was chosen to be about 10°C. The largely CO_2-free fuel gas from the top of the absorber feeds the combustor and the supplementary combustor (SC). A fuel compressor is necessary to overcome the pressure loss.

The CO_2 compression and liquefaction section is the same as that in the OXYF-REF system configuration. The CO_2 enriched gas (34) from the top of the stripper is compressed to 84 bar and liquefied, making liquid CO_2 (35) available for storage.

5 Calculation Assumptions and Method

The proposed systems have all been simulated with the ASPEN PLUS software [29], in which the component models are based on the energy balance and mass balance, with the default relative convergence error (the relative difference between the iteration used and the one before) tolerance of 0.01%. For example, Tables 4 and 5 are the proof of mass balance satisfaction, and Table 6 is the exergy balance. The ELECNRTL and the RK-Soave thermo-

dynamic models were selected for the thermal property calculations for the chemical absorption section and other parts of the systems, respectively. The ELECNRTL property method is the most versatile electrolyte property method. It can handle very low and very high concentrations. It can handle aqueous and mixed solvent systems. It can deal with any liquid electrolyte solution unless there is association in the vapor phase.

The RK-SOAVE property method uses the Redlich–Kwong–Soave (RKS) cubic equation of state for all thermodynamic properties except liquid molar volume. It is recommended for gas-processing, refinery, and petrochemical applications. Example applications include gas plants, crude towers, and ethylene plants. The RK-SOAVE property method can be used for nonpolar or mildly polar mixtures. Examples are hydrocarbons and light gases, such as carbon dioxide, hydrogen sulfide, and hydrogen. This property method is particularly suitable in the high temperature and high-pressure regions, such as in hydrocarbon processing application or supercritical extractions. Reasonable results can be expected at all temperatures and pressures. It is consistent in the critical region, although results are least accurate in the region near the mixture critical point.

The principal reactors (PRE-REF, REF) have been simulated by the Gibbs reactor [2] available in the ASPEN PLUS model library, which determines the equilibrium conditions by minimizing Gibbs free energy. For the chemical absorption section, both absorber and stripper have been simulated using the RadFrac model in the ASPEN PLUS library. Some properties of feed streams are reported in Table 1, and the main assumptions for simulations are summarized in Table 2, and the performance results are reported in Table 3. The calculations use the same natural gas input to provide a common comparison basis.

Some stream state parameters for both system configurations, including temperature, pressure, and composition, are presented in Tables 4 and 5, respectively.

The net system efficiency is defined as

$$\eta = \left[\left(\sum W_T - \sum W_C - \sum W_P - W_{ASU} \right) \eta_{mec} \eta_{gen} \right] / m_f LHV$$

(1)

Table 2 Main assumptions for the calculation

Reformer REF	Pressure loss (% of inlet pressure)	5
	Minimum heat transfer temperature difference gas/gas (°C)	23
Preformer	Pressure loss (% of inlet pressure)	3
Shift reactors	Pressure loss (% of inlet pressure)	2
Compressors	Isentropic efficiency (%)	88
	Fuel and O_2 compressor efficiency (%)	85
Gas turbines	HPT inlet temperature (°C)	1300
	HPT isentropic efficiency (%) (including blade cooling effects)	89
	LPT inlet temperature (°C)	400
	LPT isentropic efficiency (%)	90
	Expander efficiency (%)	85
Steam turbine	HPST inlet pressure (bar)	150
	HPST isentropic efficiency (%)	90
Combustor	Excess O_2 (%) (in the oxyfuel system)	2
	Pressure loss (% of inlet pressure)	3
	Maximum fuel temperature (°C)	250
Heat exchangers	Pressure loss (% of inlet pressure)	1
	Minimum heat transfer temperature difference gas/gas (°C)	20
	Minimum heat transfer temperature difference gas/liquid (°C)	15
Chemical absorption system	Absorber pressure (bar)	5.5
	Stripper pressure (bar)	1.8
	Minimum heat transfer temperature difference (°C)	10
Multistage compressor for CO_2 compression	Number of stages	7
	Stage isentropic efficiency (%)	80
	Intercooler temperature (°C)	35
Pump	Efficiency	85
Ambient state	Temperature (°C)	25
	Pressure (bar)	1.013

$$\varepsilon = \left[\left(\sum W_T - \sum W_C - \sum W_P - W_{ASU} \right) \eta_{mec} \eta_{gen} \right] / A_f \quad (2)$$

$$A_{loss} = \sum A_{in} - \sum A_{out} \quad (3)$$

The exergy dead state is 25°C/1.013 bar.

The system boundary is defined to include all units that contribute to the net system efficiency. In the OXYF-REF system, the process material streams are inflows of fuel (natural gas), and O_2,

Table 3 Performance summary and comparison

Configuration	OXYF-REF	PCD-REF
Natural gas molar flow rate (kmol/h)	3600	3600
Air mass flow rate (kg/s)	—	610
O_2 mass flow rate (kg/s)	68.47	—
Combustor steam injection rate (kg/s)	71.6	59.3
Methane conversion rate (%)	47.12	96.88
Supplementary fuel fraction (%)	—	29.1
HPT power (MW)	548.13	600.36
LPT power (MW)	88.59	—
HPST power (MW)	64.16	—
Expander power (MW)	—	29.98
HPC power (MW)	173.48	135.05
LPC power (MW)	—	99.97
Fuel compressor power (MW)	—	10.93
Water pump power (MW)	1.987	0.166
MDEA pump power (MW)	—	0.244
CO_2 compression power (MW)	36.68	10.64
O_2 production work (MW)	55.59	—
O_2 compression work (MW)	15.31	—
Generator and mech. loss (MW)	8.36	7.47
Net power output (MW)	409.47	365.87
Natural gas LHV input (MW)	796.61	796.61
Energy efficiency (%)	51.40	45.93
CO_2 specific emission (g/kW h)	0.0	58.5

outflows of pressurized CO_2 and condensed H_2O, and cooling water (in and outflow). In the PCD-REF system, the inflows and outflows across the system boundary include all those mentioned above except the O_2 stream; in addition, the process material streams also include air, the injected water streams for both combustion and reforming, and the flue gas. The energy streams include electricity output and the power consumed for O_2 production (only in the OXYF-REF system). Other energy loss contributors (include mechanical loss and generator loss) are taken into account by assuming a 2% reduction in the gross power output.

6 Exergy Analysis

Using Eqs. (2) and (3), an exergy analysis was performed to examine the exergy losses in all system components, and in the entire system, for obtaining guidance for component and system improvements. The results for the components are shown in Table 6.

Additional information indicating the exergy effectiveness of interactions between heat-exchanging components is obtained by using graphical exergy analysis via the exergy utilization diagram (EUD) method [31]. In this method, an energy donor and an energy acceptor are defined in each energy-transformation/exchange system. For the energy donor and the acceptor, energy change, expressed as the process enthalpy change ΔH, is released by the former and is accepted by the latter, and the corresponding exergy exchange is expressed as

$$\Delta A = \Delta H - T_0 \Delta S \quad (4)$$

They defined the "availability factor" or the "energy level" E as the ratio of the exergy change to the enthalpy (energy) change.

$$E = \Delta A / \Delta H = 1 - T_0 (\Delta S / \Delta H) = 1 - \frac{T_0}{T} \quad (5)$$

It is an intensive value and represents the energy quality. We can calculate E for the acceptor and the donor, expressed as E_{ed} and E_{ea}, respectively. By plotting E_{ed} and E_{ea} against the transformed energy ΔH (or Q in a heat exchange process), we obtain the donor-to-acceptor process exergy destruction represented as the area between these curves.

This method has the following advantages: (i) the area between the energy donor and energy acceptor curves, E_{ed} and E_{ea}, represents a characteristic feature of each process equal to the exergy destruction of the corresponding section of the system, and (ii) the energy-level difference ($E_{ed} - E_{ea}$) represents the driving force to make the process proceed. When its value becomes the smallest, a pinch point is found at that location.

The E-Q (ΔH) diagrams of some key processes are shown in Figs. 4 and 5. It should be pointed out that the system configurations and operating parameters are not necessarily optimal for each system. A few comments that are valid for the chosen configurations and parameters can be made on the exergy analysis results.

- While the natural gas input exergy A_f was chosen to be the same for both systems (taken as 100%), the OXYF-REF system contains an additional 1.33% amount of exergy input contained in the O_2 stream from the *ASU*.
- On the output side, it is also noteworthy that the pressurized CO_2 streams separated from each system possess exergy (corresponding to the reversible work that could have been produced by isothermal expansion of the pressurized CO_2 to its partial pressure in the environment) amounting to 4.9% and 4.4% of A_f for Systems I and II, respectively. If we consider the captured high-pressure CO_2 stream also as an exergy-valuable product of the system, the total exergy efficiencies would be 53.5% and 47.8% for these two systems.
- The combustion-associated exergy loss is, as usual, the highest loss, amounting to 26.6% in the OXYF-REF system

Table 4 Main stream states of the OXYF-REF system (the state point numbers refer to Fig. 2)

No.	T (°C)	P (bar)	m (kg/s)	Molar composition (%)								
				CH₄	C₂H₆	H₂	CO	CO₂	H₂O	O₂	N₂	Ar
	Reforming section											
2	192.3	16.95	53.24	30.4	1.5				66.7		1.4	
3	550	16.8	53.24	30.4	1.5				66.7		1.4	
4	453.8	16.35	53.24	28.7		9.9	0.1	2.8	57.2		1.4	
5	639.7	16.2	53.24	28.7		9.9	0.1	2.8	57.2		1.4	
6	740	15.6	53.24	11.9		43.8	6.6	6.3	30.3		1.1	
8	250.3	15.45	53.24	11.9		43.8	6.6	6.3	30.3		1.1	
	Power generation section											
10	1300	15	471.06					11	86.9	0.4	0.9	0.7
11	763.4	1.05	471.06					11	86.9	0.4	0.9	0.7
12	649.3	1.04	471.06					11	86.9	0.4	0.9	0.7
17	400	1.03	193.32					11	86.9	0.4	0.9	0.7
18	134.3	0.082	193.32					11	86.9	0.4	0.9	0.7
25	620.8	150	107.62						100			
26	292	16.95	71.59						100			
	CO₂ compression											
28	35	0.08	74.29					39.8	52.7	1.6	3.4	2.5
29	35	110	50.40					84	0.2	3.3	7.2	5.3

and to 29.2% of A_f in the PCD-REF system. The higher latter loss is because (cf. Ref. [32]) one of the two combustors, SC, operates at a lower temperature than the combustor in the former system and because the mass flow rate through the combustors in the latter system is higher.

- The reforming section includes the reactors and the heat exchangers. The syngas heat is largely recuperated internally by preheating the reactants. The EUDs in the reforming section are shown in Figs. 4(a) and 4(b), and the exergy loss represented by the shaded area is obviously larger in the PCD-REF system. In the OXYF-REF system, the reformer has two sections: the adiabatic section 5-5′ and endothermic section 5′-6. The reaction in PRE-REF is also adiabatic, with limited conversion rate. The adiabatic reactions in both

PRE-REF (3-4) and REF (5-5′) each are designed to undergo a temperature drop of nearly 100 °C to allow the turbine exhaust to be cooled to a low value, so that to increase both the exhaust heat recovery for reforming and the final reforming temperature. The exergy loss is found to be 16.8 MW, which is about 2% of the natural gas input exergy A_f. In the PCD-REF system, the reforming process requires a higher heat input because of the high reforming temperature of 900 °C. Compared to 107 MW in the OXYF-REF configuration, the heat duty of REF is 286 MW here, leading to larger exergy loss in REF. The syngas heat is recuperated by feedwater and natural gas preheating in HEX3, HEX4, and HEX5 that are included in the reforming section

Table 5 Main stream states of the PCD-REF system (the state point numbers refer to Fig. 3)

No.	T (°C)	P (bar)	m (kg/s)	Molar composition (%)								
				CH₄	C₂H₆	H₂	CO	CO₂	H₂O	O₂	N₂	Ar
	Power generation section											
1	25	1.013	610					0.03	1.0	20.7	77.3	0.9
5	600	15.45	610					0.03	1.0	20.7	77.3	0.9
8	600	15.45	59.3						100			
9	1300	15	679.03					0.3	24.3	11.5	63.1	0.7
10	658.8	1.06	679.03					0.3	24.3	11.5	63.1	0.7
11	935.2	1.04	683.03					0.4	28.1	9.1	61.7	0.7
12	633	1.03	683.03					0.4	28.1	9.1	61.7	0.7
13	233.2	1.02	683.03					0.4	28.1	9.1	61.7	0.7
14	124	1.013	683.03					0.4	28.1	9.1	61.7	0.7
	Fuel conditioning section											
22	629.4	40	53.24	30.4	1.5				66.7		1.4	
23	410.9	6.3	53.24	30.4	1.5				66.7		1.4	
24	900	6.1	53.24	0.6		61.5	16.3	3.4	17.3		0.9	
26	493.9	5.95	53.24	0.6		69.7	8.1	11.5	9.2		0.9	
28	256.9	5.8	53.24	0.6		77.4	0.4	19.3	1.4		0.9	
	CO₂ removal section											
30	35	5.7	52.63	0.6		78	0.4	19.4	0.8		0.9	
31	48.8	5.5	4.0	0.6		94.5	0.5	1.4	2		1.1	
32	178.7	15.45	9.73	0.6		94.5	0.5	1.4	2		1.1	
34	35	1.8	38.79	0.4				96.3	3.2		0.1	
35	35	83.69	38.35	0.4				99	0.5		0.1	

Table 6 Exergy analysis results and comparison

Configuration	OXYF-REF		PCD-REF	
	MW	%	MW	%
Exergy input				
Natural gas	843.41	100	843.41	100
O_2 feed stream	11.25	1.33		
Exergy output				
Net power output	409.5	48.55	365.87	43.38
Energy for O_2 production	55.59	6.59		
CO_2 stream	41.48	4.92	37.42	4.44
Exergy loss				
Combustor	224.01	26.56	245.88	29.15
Reforming process	16.83	2.0	41.93	4.97
Turbine HPT/LPT/ST/expander	31.62	3.75	27.23	3.23
Compressors (including O_2 compressor)	9.99	1.18	17.08	2.03
Heat exchangers[a]	43.11	5.11	27.64	3.28
Chemical absorption	—	—	33.57	3.98
CO_2 compression	15.49	1.84	3.52	0.42
Flue gas	—	—	35.05	4.16
Mechanical and generator losses	8.36	0.99	7.47	0.89

[a]HEX1, HEX2 and HRSG in OXYF-REF; HEX1 and HEX2 in PCD-REF

too, to reduce the HTS and LTS inlet temperatures to 400 °C and 160 °C. As shown in Fig. 4(*b*), the exergy loss in HEX5 is relatively large because of the poor thermal
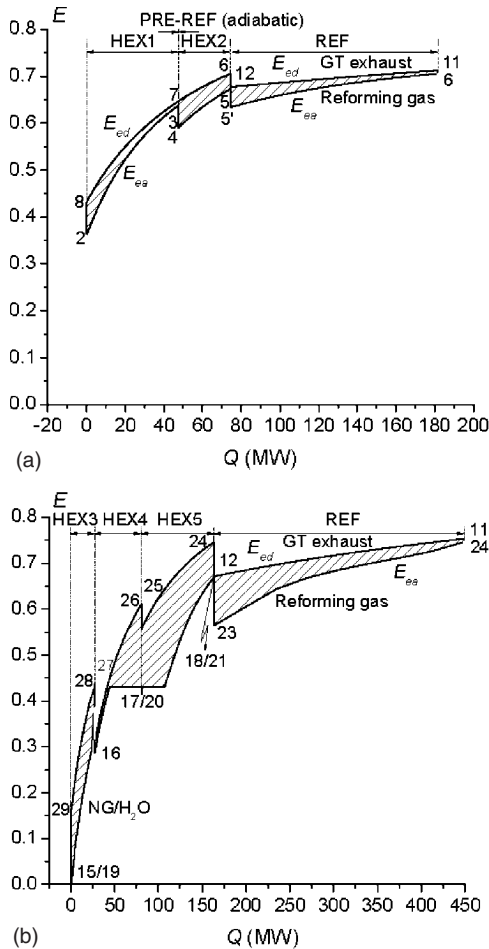
Fig. 4 (*a*) EUD in the reforming section of the OXYF-REF cycle and (*b*) EUD in the reforming section of the PCD-REF cycle
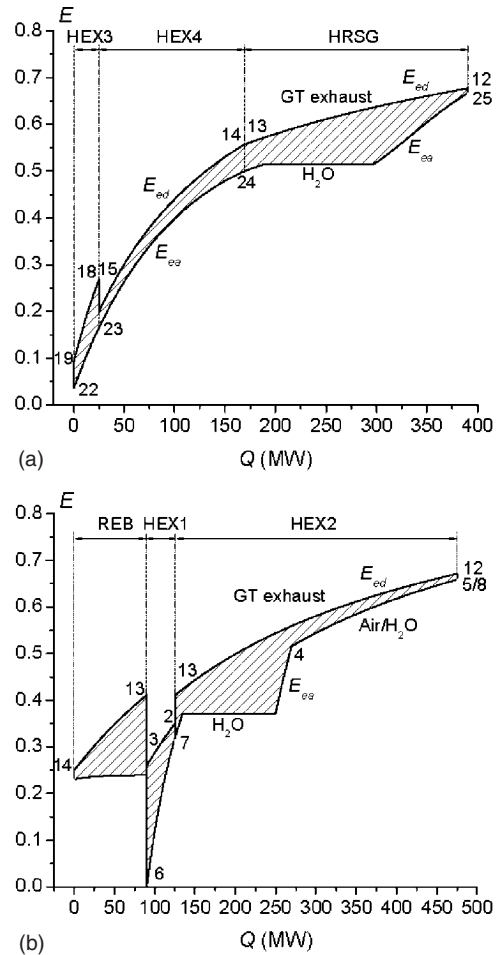
Fig. 5 (*a*) EUD in the turbine exhaust heat recovery process of the OXYF-REF cycle and (*b*) EUD in the heat recovery process of the PCD-REF cycle

match with the isothermal steam evaporation process. The total exergy loss in the reforming process is 41.9 MW, accounting for 5% of the natural gas input exergy A_f. As indicated by the EUD, a way to reduce the exergy losses is to reduce the difference between E_{ed} and E_{ea}. Smaller ($E_{ed} - E_{ea}$) means a closer match between the energy donor and acceptor. In a heat exchange process, this would be accomplished by choosing a smaller average heat transfer temperature difference, which also leads to the need for larger heat transfer area or/and higher heat transfer coefficients and thus higher cost.

- We now examine the exergy losses in the heat recovery sections, composed of several heat exchangers, of both systems. In the OXYF-REF system, Fig. 5(*a*) is the EUD of the water preheating and steam generation process in HEX3, HEX4, and HRSG, and the related exergy loss was computed to be about 43 MW, 5.1% of the total natural gas exergy input. Part of the HPT flue gas is directly recycled (at Point 14 in Fig. 2) to the compressor and then to the combustor, its sensible heat is mainly utilized to preheat water (in HEX4), and this also helps to reduce the compressor power consumption; therefore, the recycle fraction (m_{14}/m_{13}) is determined by the heat demand of the water side considering the minimal heat transfer temperature difference, and it also has influence on the compressor power consumption and the turbine power output. The recycled fraction is found to be 59% in this calculation, which means

Table 7 The CO₂ enriched mixture composition after the multistage compression

Configuration	State point	T (°C)	P (bar)	Vapor fraction	Mass flow rate (kg/s)/molar composition (%)					
					CH_4	CO_2	H_2O	O_2	N_2	Ar
OXYF-REF	29	35	110	1		44.14/84	0.037/0.2	1.27/3.3	2.4/7.2	2.55/5.3
PCD-REF	35	35	83.7	0	0.062/0.4	38.19/99	0.079/0.5		0.013/0.1	

that the working fluid mass flow rate of LPT is 41% of that of HPT.

In the PCD-REF system, besides providing heat for the reforming and recuperation (in HEX2), the turbine exhaust also sustains the reboiler heat duty. The reformer REF, the recuperator HEX2, and the reboiler are configured in a cascade according to the temperature levels, intending also to reduce the heat transfer related exergy destruction. The reformer is upstream of the SC exhaust, taking advantage of the possibly highest temperature available (11-12). The recuperator HEX2 produces steam for combustion injection and also preheats the combustion air (and steam) to 600 °C. The steam injection rate (the mass flow rate ratio between the injected steam and the compressor inlet air) is 9.7% in this calculation. Larger steam injection is favorable to the global energy efficiency, but would lead to less heat available to the reboiler.

Downstream the cascade, the exhaust heat (13-14) is used for regeneration of amine in the CO₂ removal section. The exhaust gas enters the reboiler at 233 °C and leaves at 124 °C, providing 90.2 MW heat for the amine regeneration. The exhaust heat recovered percentages in REF, HEX2 and the reboiler are 39.4%, 48.2%, and 12.4%, respectively.

Figure 5(b) is the EUD for the reboiler REB, HEX1, and HEX2 in system PCD-REF. The match between the isothermal heat sink of steam evaporation and the sensible heat resource of GT exhaust gas leads to relatively large exergy loss (23.2 MW) in HEX2. The total exergy losses in HEX1 and HEX2 are found to be 27.6 MW, accounting for 3.3% points of the fuel exergy input A_f. As mentioned before, the exergy loss in the heat exchangers can be reduced with smaller ($E_{ed}-E_{ea}$). This can be accomplished by parameter optimization or rearrangement of the match between the energy donor and acceptor (configuration optimization).

- In the power generation section, the turbine related exergy loss is 31.6 MW in the OXYF-REF system, slightly larger than that in the PCD-REF system, because of the higher power output. However, the compressor-related exergy loss in the PCD-REF system is 7 MW larger than that in the OXYF-REF system because more working fluid is treated, resulting in higher compression work demand. The turbine and compressor exergy loss can be reduced if more efficient components are employed.
- In the OXYF-REF system, about 55.6 MW power (6.6% of the natural gas exergy input) is used for O₂ production, and this is treated as an exergy outflow from the system.
- The PCD-REF system employs a chemical absorption section for CO₂ removal. The related exergy loss includes the absorption, amine regeneration (in REB), heat exchange, and the remaining processes, and is found to be 33.6 MW, accounting for 4% of the total exergy input. The turbine flue gas exhausts (State 14) at a temperature of 124 °C, after providing heat to the reboiler, lead to a 35 MW (4.2% of A_f) loss to the environment. The relatively high exhaust temperature is mandated by the heat transfer temperature difference in REB. The flue gas exergy loss can be reduced by further utilization of the exhaust heat for heat production.

7 Overall Performance Comparison and Discussion

We recall now that the two system configurations differ in several ways, basically based on the different CO₂ removal strategies (Table 7). OXYF-REF and PCD-REF have, respectively,

- different working fluids: the mixture of H₂O/CO₂ and air
- different system configurations in the power generation section: a combined gas/steam cycle and a recuperated GT cycle
- different operation parameters: most notably different REF operation conditions and different turbine exhaust conditions, where in the OXYF-REF system, the turbine working fluid can expand down to a vacuum, significantly enlarging the overall working pressure region

7.1 Power Generation Section. The OXYF-REF system has a net power output of 409.5 MW, with an energy efficiency of 51.4%. Most of the power (78.2%) is generated by the HPT GT. The compressor consumes more power than that produced by the LPT and HPST turbines.

The CO₂ multistage compressor power demand is 36.7 MW, which is much higher than that for the PCD-REF system, because of the larger amount of the gases compressed and the presence of a large quantity of noncondensable gases.

The energy consumption for O₂ production and compression is 70.9 MW, which accounts for 8.9% of the total system energy input.

The PCD-REF system has a net power output of 365.9 MW, lower by about 10.6% than that of the OXYF-REF system, largely because only 71% of the fuel gas feeds the combustor, with the remaining 29% used for the SC needed to support the reforming, resulting in an overall energy efficiency of 45.9%. This efficiency is higher by ~3% points than the efficiency reported in Ref. [24] for a similar recuperative GT cycle but with atmospheric pressure reforming, and approaches the 46%–48% efficiencies reported for the gas/steam combined cycle configurations proposed in other studies [1,2,25]. As to the PCD-REF system, it is noteworthy that it can be regarded as a combined gas/steam turbine cycle (since steam is injected into the combustor) with some of its advantages but having a much simpler configuration.

7.2 Fuel Conditioning Section. The methane conversion rate depends on the reforming conditions. The reformers work at different pressures and temperatures in each of the two systems, but with the same steam/natural gas molar ratio. In the OXYF-REF system, the reformer products exit at a temperature of 740 °C, restricted by the turbine exhaust temperature (which is higher than that of the conventional air-based GT exhaust because of the different working fluids). It achieves a medium methane conversion rate of 47.1%. The syngas molar compositions are 43.8% H₂, 6.3% CO₂, 6.6% CO, 11.9% CH₄, and 30.3% H₂O. The CO₂ and H₂O compositions were then elevated to 11% and 87% by combustion in COM.

In the PCD-REF system configuration, a methane conversion rate of 96.9% is achieved, the high value attributed to lower reforming pressure and the supplementary combustion in SC. Such supplementary combustion typically has a negative effect on the

Table 8 Main results for the CO_2 removal section in the PCD-REF system

Solvent mass flow rate (kg/s)	500
Reboiler heat duty (MW)	90.2
Absorber feed CO_2 (kg/s)/(mol %)	42/19.4
CO_2 in the fuel gas (kg/s)/(mol %)	2.43/1.4
CO_2 in distillate (kg/s)	38.19
Removal efficiency (%)	90.9

overall efficiency because the associated supplementary fuel energy is not fully exploited for power production and is used only at a lower temperature level. In this analysis, this supplementary fuel fraction is 29%. 97.5% of CO in the syngas was converted to CO_2 after the two-stage shift process. Compared to the first configuration, the syngas after CO_2 removal is much more enriched in H_2 (with a molar fraction of 94.5%), leading to a very high heating value of this clean fuel.

7.3 CO_2 Removal/Compression Section. In the multistage CO_2 compressor, water is removed after each stage of intercooling. In the OXYF-REF system, the captured CO_2 stream is a gaseous mixture at 110 bar/35 °C. In the PCD-REF system, the captured CO_2 stream is in the liquid state already at 84 bar/35 °C.

As shown in Table 7, the CO_2 volume content in the OXYF-REF system configuration is 84%; the O_2, N_2, and Ar amount to 15.8%, mainly depending on the oxygen purity, natural gas composition, and the excess oxygen rate beyond the stoichiometric combustion. Further purification might be required to remove some of the gas components prior to transportation and storage. According to Ref. [22], purifying CO_2 would incur a power cycle efficiency reduction up to 0.4% points and would add to the overall cost. Davison [33] mentioned an oxy-fuel natural gas fired combined cycle plant in which the flue gas with a CO_2 concentration of 88 mol % dry basis is compressed and the CO_2 concentration is increased to 96 mol % by a cryogenic unit for removal of inert gases that is integrated with the compression unit. In this paper, the mixture is compressed to 110 bar, and the presence of the noncondensable species increases the compression power requirement. Further purification and its effect were not taken into consideration, and the calculation indicates that the pressurized stream can be liquefied at a near-ambient temperature of 16.5 °C. Assuming 100% capture, the final liquid pure CO_2 mass flow rate is 44.1 kg/s. However, a trace amount of CO_2 will in any case be dissolved in the water.

In the PCD-REF system configuration, the CO_2 molar composition of the absorber feed stream is 19.4% and reduced to 1.4% in the fuel gas after CO_2 removal. The removal efficiency of the chemical absorption is 90.9% (Table 8), and it increases by increasing the heat input to the reboiler. The actual captured CO_2 of 38.2 kg/s is 86.5% of that in the OXYF-REF system. The total CO_2 emission (does not include those introduced with air) in the flue gas plus those escaped from the chemical absorption is 5.95 kg/s, making the specific emission of 58.5 g/kW h, compared, e.g., to 41–43 g/kW h reported in Refs. [1,2,25] with combined cycle configurations and 155 g/kW h in Ref. [24] adopting a recuperative GT cycle. It is noticed that 13.6% of the unconverted CH_4 (mass flow rate of 0.062 kg/s) was removed together with CO_2 in the chemical absorption plant, which takes account of ~0.4% of the total CH_4 input to the system. This fraction of CH_4 will be released during the CO_2 liquefaction process and is lost for both power generation and CO_2 capture. Since methane has a greenhouse effect that is 20–30 times higher than that of CO_2 for the same concentration, it is important to minimize its release to the atmosphere. Methane emissions in the proposed systems are,

however, not higher than methane emissions from any other power generation system that uses methane as fuel and chemical absorption for CO_2 capture.

7.4 Technology Considerations. The hardware challenge associated with the oxyfuel system is mainly the CO_2/H_2O turbine. The mixture of CO_2/H_2O has different expansion characteristics than the combustion gas in conventional GTs, resulting in higher exhaust temperatures for the same pressure ratio and turbine inlet temperature. The optimal pressure ratio is also higher than that for the air-based turbines. The CO_2/H_2O turbine calls for a new design since the existing turbines cannot be easily adapted to the new working fluid.

The combustor is another technological challenge for both the oxyfuel system and the one with precombustion decarbonization. For the oxyfuel system, it involves the combustion in a pure oxygen environment. A review about the oxyfuel combustion technology was given in Ref. [34] but focused on coal based systems. Another one by Pronske et al. [35] summarized the development of oxyfuel turbine and combustor technology by the Clean Energy Systems (CES) company and Siemens Power Generation for the 300–600 MW coal syngas plant with zero emissions.

For the precombustion capture plant with reforming, the major problem of the combustor is NO_x emission control when burning hydrogen-enriched fuel, which has very high heating value and flame temperature. Premixed combustion is difficult to apply for hydrogen combustion due to its high reactivity. Some studies suggested that fuel dilution with steam or nitrogen, accompanied with certain efficiency loss, might be a feasible solution [36].

The technological difficulties are different for the reformers in the two configurations. In the environments containing carbon and hydrogen compounds in the critical temperature range of about 400–800°C, metal dusting can potentially be a severe corrosion problem [37]. Some known techniques to minimize the effects of metal dusting include additional steam injection and preoxidation to build and maintain a stable, adherent, healable oxide surface layer on the exposed metal surfaces. In the OXYF-REF system, the reformer is susceptible to metal dusting because it produces syngas at the temperature of 740°C, which may necessitate the use of materials that exhibit good resistance to metal dusting attack. The metal dusting is avoided in the PCD-REF configuration by designing the operation to take place above the critical temperature range. However, the high temperature reformer in the PCD-REF configuration may cause some technological difficulties too, mainly the material stress, operation lifetime and cost, etc. In this study, the temperature above 900°C is used to obtain a desired conversion rate with limited steam addition. The pressurized reforming process is used, and it allows reduced equipment size. Considering the great influence of the pressure on performance and hardware, a thermoeconomic comparison with an atmospheric reforming process would be useful.

Another technological issue in the PCD-REF system is associated with the entrainment of amine traces (MDEA) by the clean synfuel, which may be corrosive to the turbine blades and combustor. The calculation results from ASPEN PLUS indicate that the residual MDEA mass fraction in the clean fuel is 2 ppm. The negative effect of such a small amount is assumed in this study to be negligible; so, further processes/equipment for removing these trace amounts were not considered. Prevention of the amine contamination requires an adequate design of the amine droplet separation system, as addressed in Refs. [23,24].

8 Concluding Remarks

Steam reforming is an effective strategy for CO_2 capture from natural gas fuel power plants. Chemical recuperation for fuel conversion is also considered to result in higher plant efficiency than the conventional physical recuperation with heat transfer.

The paper presented two novel systems that integrate steam reforming, one with oxyfuel cycle technology that eliminates

air-N_2 input to the GT working fluid and thus allows simple separation of the CO_2 from its exhaust, and the other with precombustion decarbonization technology employing chemical absorption, for CO_2 removal in natural gas fired power plants. The two systems were then thermodynamically simulated and compared. To increase efficiency, they both employ high temperature internal combustion, with steam injection into the combustor.

Considering that 100% of the CO_2 was captured, the OXYF-REF system is better in that respect than the PCD-REF one, but the captured CO_2 is mixed with other gases, and emerges in gaseous state at a concentration of 84%. Additional energy would hence be necessary for its further purification and liquefaction, and the penalty to the overall efficiency is estimated to be 0.4% points in Ref. [22]; this effect is not considered in this analysis. The PCD-REF has a 58.5 g/kW h specific CO_2 emission, achieving 86.5% CO_2 removal that is thus lower than the 100% removal for the oxyfuel system. The captured CO_2 is, however, at high purity of 99% and in liquid state. In PCD-REF, 10% of the uncaptured CO_2 escapes with the flue gas and 3% remains unseparated from the amine during the stripping process using the reboiler. In this calculation, the reboiler heat demand is fully sustained by the turbine exhaust heat recovery and is restricted by the minimal temperature difference in the reboiler.

The PCD-REF system, which employs a recuperated GT cycle, has a global energy efficiency lower by 5.4% points than that found for the OXYF-REF combined system, mainly due to additional fuel demand for the supplementary firing. Its efficiency of 46% is, however, comparable to some other systems employing a combined gas/steam cycle configuration.

As to the hardware requirement, the OXYF-REF system includes an air separation unit, consuming about 7% of the total system energy input. It also employs an additional turbine, a HP steam turbine for additional power generation. The PCD-REF system employs a more complicated fuel conditioning section with two-stage shift reactors and a chemical absorption unit for CO_2 removal. It achieves the energy efficiency of around 46% without inclusion of a closed steam cycle (thus eliminating steam turbine, condenser, and associated hardware). An economic analysis was not performed but is obviously necessary for a more comprehensive comparison.

The turbine exhaust heat is largely recuperated internally in both configurations. The heat recovery chains were carefully arranged to reduce the heat transfer related exergy destruction. An exergy analysis was performed to examine the exergy losses in all system components and in the entire system, also with the aid of the EUD method, for obtaining guidance for component and system improvements. It is found that the system exergy efficiencies (based on the electricity generated) are 48.6% for OXYF-REF and 43.4% for PCD-REF. The OXYF-REF system has lower exergy losses in both the combustion and reforming processes, but the O_2 production energy consumption is 6.6% of the fuel exergy input. Comparatively, the PCD-REF system has an additional exergy loss of 4% of A_f in the chemical absorption process and also has a flue gas related exergy loss of 4.2% of A_f.

Acknowledgment

Nomenclature

A = exergy (kW)
E = $\Delta A / \Delta H$, Eq. (5)
H = enthalpy (kW)
LHV = lower heating value (kJ/kg)
m = mass flow rate (kg/s)
P = pressure (bar)
T = temperature (°C)
Q = heat duty (MW)
W = power (MW)
ε = exergy efficiency (%)
η = energy efficiency (%)

Subscripts

0 = ambient state
$1,2,\ldots,35$ = states on the cycle flow sheet
ASU = air separation unit
C = compressor
ea = energy acceptor
ed = energy donor
f = fuel
gen = generator
in = inlet
mec = mechanical
out = outlet
P = pump
T = turbine

Component

COM = combustor
HEX = heat exchanger
HPC = high-pressure compressor
$HPST$ = high-pressure steam turbine
HPT = high-pressure gas turbine
$HRSG$ = heat recovery steam generator
HTS = high temperature shift reactor
LPC = low-pressure compressor
LPT = low-pressure gas turbine
LTS = low temperature shift reactor
$PRE\text{-}REF$ = prereformer
REF = reformer

References

[1] Lozza, G., and Chiesa, P., 2002, "Natural Gas Decarbonization to Reduce CO_2 Emission From Combined Cycles—Part I: Partial Oxidation," ASME J. Eng. Gas Turbines Power, **124**, pp. 82–88.
[2] Corradetti, A., and Desideri, U., 2005, "Analysis of Gas-Steam Combined Cycles With Natural Gas Reforming and CO_2 Capture," ASME J. Eng. Gas Turbines Power, **127**, pp. 545–552.
[3] Chiesa, P., and Consonni, S., 2000, "Natural Gas Fired Combined Cycles With Low CO_2 Emissions," ASME J. Eng. Gas Turbines Power, **122**, pp. 429–436.
[4] Desideri, U., and Paolucci, A., 1999, "Performance Modeling of a Carbon Dioxide Removal System for Power Plants," Energy Convers. Manage., **40**, pp. 1899–1915.
[5] Mathieu, P. and Nihart, R., 1999, "Zero-Emission MATIANT Cycle," ASME J. Eng. Gas Turbines Power, **121**, pp. 116–120.
[6] Mathieu, P. and Nihart, R., 1999, "Sensitivity Analysis of the MATIANT Cycle," Energy Convers. Manage., **40**, pp. 1687–1700.
[7] Yantovski, E. I., Zvagolsky, K. N., and Gavrilenko, V. A., 1996, "The COOPERATE—Demo Power Cycle," Energy Convers. Manage., **37**(6–8), 861–864.
[8] Yantovski, E. I., 1996, "Stack Downward Zero Emission Fuel-Fired Power Plants Concept," Energy Convers. Manage., **37**, pp. 867–877.
[9] Staicovici, M. D., 2002, "Further Research Zero CO_2 Emission Power Production: The "COOLENERG" Process," Energy, **27**, pp. 831–844.
[10] Bolland, O., and Mathieu, P., 1998, "Comparison of Two CO_2 Removal Options in Combined Cycle Power Plants," Energy Convers. Manage., **39**, pp. 1653–1663.
[11] Anderson, R., Brandt, H., Doyle, S., Pronske, K., and Viteri, F., 2003, "Power Generation With 100% Carbon Capture and Sequestration," Second Annual Conference on Carbon Sequestration, Alexandria, VA.
[12] Marin, O., Bourhis, Y., Perrin, N., Zanno, P. D., Viteri, F., and Anderson, R., 2003, "High Efficiency, Zero Emission Power Generation Based on a High-Temperature Steam Cycle," 28th International Technical Conference on Coal Utilization and Fuel Systems, Clearwater, FL.
[13] Jericha, H., Gottlich, E., Sanz, W., and Heitmeir, F., 2004, "Design Optimization of the Graz Cycle Prototype Plant," ASME J. Eng. Gas Turbines Power, **126**, pp. 733–740.
[14] Martinez-Frias, J., Aceves, S. M., Smith, J. R., and Brandt, H., 2004, "Thermodynamic Analysis of Zero-Atmospheric Emissions Power Plant," ASME J. Eng. Gas Turbines Power, **126**, pp. pp.2–8.
[15] Zhang, N. and Lior, N., 2006, "A Novel Near-Zero CO_2 Emission Thermal Cycle With LNG Cryogenic Exergy Utilization," Energy, **31**, pp. 1666–1679.
[16] Zhang, N. and Lior, N., 2006, "Proposal and Analysis of a Novel Zero CO_2 Emission Cycle With Liquid Natural Gas Cryogenic Exergy Utilization," ASME J. Eng. Gas Turbines Power, **128**, pp. 81–91.

[17] Ishida, M., and Jin, H., 1997, "CO_2 Recovery in a Novel Power Plant System With Chemical-Looping Combustion," Energy Convers. Manage., **38**(19), pp. 187–192.

[18] Ishida, M., and Jin, H., 1994, "A New Advanced Power-Generation System Using Chemical-Looping Combustion," Energy, **19**, pp. 415–422.

[19] Naqvi, R., and Bolland, O., 2005, "Off-Design Evaluation of a Natural Gas Fired Chemical Looping Combustion Combined Cycle With CO_2 Capture," *Proceedings of ECOS2005*, Trondheim, Norway, pp. 827–834.

[20] Griffin, T., Sundkvist, S. G., Asen, K., and Bruun, T., 2005, "Advanced Zero Emissions Gas Turbine Power Plant," ASME J. Eng. Gas Turbines Power, **127**, pp. 81–85.

[21] Moller, B. F., Torisson, T., Assadi, M., Sundkvist, S. G., Sjodin, M., Klang, A., Asen, K. I., and Wilhelmsen, K., 2005, "AZEP Gas Turbine Combined Cycle Power Plants—Thermo-Economic Analysis," *Proceedings of ECOS2005*, Trondheim, Norway, pp. 819–826.

[22] Kvamsdal, H. M., Jordal, K., and Bolland, O., 2007, "A Quantitative Comparison of Gas Turbine Cycles With CO_2 Capture," Energy, **32**, pp. 10–24.

[23] Fiaschi, D., Lombardi, L., and Tapinassi, L., 2003, "The Recuperative Auto Thermal Reforming and Recuperative Reforming Gas Turbine Power Cycles With CO_2 Removal—Part I: The Recuperative-Auto Thermal Reforming Cycle," ASME J. Eng. Gas Turbines Power, **125**, pp. 933–939.

[24] Fiaschi, D., Lombardi, L., and Tapinassi, L., 2004, "The Recuperative Auto Thermal Reforming and Recuperative Reforming Gas Turbine Power Cycles With CO_2 Removal—Part II: The Recuperative Reforming Cycle," ASME J. Eng. Gas Turbines Power, **126**, pp. 62–68.

[25] Lozza, G., and Chiesa, P., 2002, "Natural Gas Decarbonization to Reduce CO_2 Emission From Combined Cycles—Part II: Steam-Methane Reforming," ASME J. Eng. Gas Turbines Power, **124**, pp. 89–95.

[26] Adelman, S. T., Hoffman, M. A., and Baughn, J. W., 1995, "A Methane-Steam Reformer for a Basic Chemically Recuperated Gas Turbine," ASME J. Eng. Gas Turbines Power, **117**, pp. 16–23.

[27] Abdallah, H., Facchini, B., Danes, F., and De Ruyck, J., 1999, "Exergetic Optimization of Intercooled Reheat Chemically Recuperated Gas Turbine," Energy Convers. Manage., **40**, pp. 1679–1686.

[28] Kesser, K. F., Hoffman, M. A., and Baughn, J. W., 1994, "Analysis of a Basic Chemically Recuperated Gas Turbine Power Plant," ASME J. Eng. Gas Turbines Power, **116**, pp. 277–284.

[29] ASPEN PLUS®, Aspen Technology, Inc., Version 11.1, http://www.aspentech.com/, Aspen Physical Property System, Physical Property Methods and Models 11.1, Sept. 2001, Aspen Technology, Inc., Cambridge, MA.

[30] Zhang, N., and Lior, N., 2006, "Configuration Analysis of Oxy-Fuel Cycles With Natural Gas Reforming and CO_2 Capture," *Proceedings of ECOS2006*, Crete, Greece, pp. 1619–1628.

[31] Ishida, M., and Kawamura, K., 1982, "Energy and Exergy Analysis of a Chemical Process System With Distributed Parameters Based on the Energy-Direction Factor Diagram," Ind. Eng. Chem. Process Des. Dev., **21**, pp. 690–695.

[32] Dunbar, W. R., and Lior, N., 1994, "Sources of Combustion Irreversibility," Combust. Sci. Technol., **103**, pp. 41–61.

[33] Davison, J., 2007, "Performance and Cost of Power Plants With Capture and Storage of CO_2," Energy, **32**, pp. 1163–1176.

[34] Buhre, B. J. P., Elliott, L. K., Sheng, C. D., Gupta, R. P., and Wall, T. F., 2005, "Oxy-Fuel Combustion Technology for Coal-Fired Power Generation," Prog. Energy Combust. Sci., **31**, pp. 283–307.

[35] Pronske, K., Trowsdale, L., Macadam, S., Viteri, F., Bevc, F., and Horazak, D., 2006, "An Overview of Turbine and Combustor Development for Coal-Based Oxy-Syngas System," ASME Paper No. GT2006-90816.

[36] Damen, K., Troost, M., Faaij, A., and Turkenburg, W., 2006, "A Comparison of Electricity and Hydrogen Production Systems With CO_2 Capture and Storage. Part A: Review and Selection of Promising Conversion and Capture Technologies," Prog. Energy Combust. Sci., **31**, pp. 215–246.

[37] Hazeldine, P., and Baker, B. A., 2007, "Utilization of Alloy 693 in Metal Dusting Environments," *NACE International Corrosion 2007 Conference and Expo*, Nashville, TN, Mar. 11–15, Paper No. 07430.

System Study on Partial Gasification Combined Cycle With CO$_2$ Recovery

Yujie Xu

Institute of Engineering Thermophysics,
Chinese Academy of Sciences,
Beijing 100190, P.R.C.;
Graduate University,
Chinese Academy of Sciences,
Beijing 100190, P.R.C.

Hongguang Jin

e-mail: hgjin@mail.etp.ac.cn

Rumou Lin

Wei Han

Institute of Engineering Thermophysics,
Chinese Academy of Sciences,
Beijing 100190, P.R.C.

A partial gasification combined cycle with CO$_2$ recovery is proposed in this paper. Partial gasification adopts cascade conversion of the composition of coal. Active composition of coal is simply gasified, while inactive composition, that is char, is burnt in a boiler. Oxy-fuel combustion of syngas produces only CO$_2$ and H$_2$O, so the CO$_2$ can be separated through cooling the working fluid. This decreases the amount of energy consumption to separate CO$_2$ compared with conventional methods. The novel system integrates the above two key technologies by injecting steam from a steam turbine into the combustion chamber of a gas turbine to combine the Rankine cycle with the Brayton cycle. The thermal efficiency of this system will be higher based on the cascade utilization of energy level. Compared with the conventional integrated gasification combined cycle (IGCC), the compressor of the gas turbine, heat recovery steam generator (HRSG) and gasifier are substituted for a pump, reheater, and partial gasifier, so the system is simplified obviously. Furthermore, the novel system is investigated by means of energy-utilization diagram methodology and provides a simple analysis of their economic and environmental performance. As a result, the thermal efficiency of this system may be expected to be 45%, with CO$_2$ recovery of 41.2%, which is 1.5–3.5% higher than that of an IGCC system. At the same time, the total investment cost of the new system is about 16% lower than that of an IGCC. The comparison between the partial gasification technology and the IGCC technology is based on the two representative cases to identify the specific feature of the proposed system. The promising results obtained here with higher thermal efficiency, lower cost, and less environmental impact provide an attractive option for clean-coal utilization technology.
[DOI: 10.1115/1.2938273]

1 Introduction

Clean-coal technologies have been the general orientation of coal-fired power plants, and the coal-fired combined cycle is a potential technology for clean conversion of coal, which has made it a subject of interest to researchers worldwide [1–6]. The integrated gasification combined cycle (IGCC) and pressurized fluidized bed combined cycle (PFBCC) have shown outstanding advantages and potential advancements, but they also have severe flaws [3]. The IGCC system provides higher efficiency, better environmental protection, and easy integration with other technologies to form multifunctional energy systems. However, the IGCC system is complex and involves the addition of large pieces of hardware to power plants, which results in higher investment costs. In contrast, the PFBCC system is relatively simple in terms of plant configuration and emission control, resulting in lower investment costs. The first-generation PFBCC system does not allow the use of high-temperature high-efficiency gas turbine due to a limitation on the highest cycle temperature of the combustion bed, and though the initial temperature of second-generation PFBCC system has been improved by adding a topping combustion chamber, the difficult problem of solid particles and alkali metals of fuel gas harming the gas turbine has still not been overcome. Furthermore, IGCC and PFBCC systems cannot effectively separate and sequester CO$_2$. Therefore, research on a novel coal-fired combined cycle system, synthesizing the advantages of IGCC and PFBCC and eliminating their disadvantages, will be

extremely important in the future. The partial gasification combined cycle is an advisable choice, and in recent years, it has been widely studied by researchers in many countries [4–7]. However, a related study is still in the stage of conceptual design, and a system with excellent synthetical performance has not been found.

The present paper is devoted to integrating a new system of partial gasification combined cycle with CO$_2$ recovery on the basis of analysis of related technologies, such as the IGCC, PFBCC, and GRAZ cycle [8,9], and to fully analyzing the new system's thermodynamic performance.

2 Description of the System

Figure 1 shows the plant scheme of the partial gasification combined cycle with CO$_2$ recovery. This system mainly includes several subsystems, which are partial gasification subsystem, gas turbine subsystem, boiler subsystem, and CO$_2$ treatment subsystem. Coal is partially gasified and produces syngas and char. The char is burnt in a boiler to produce superheated steam. The syngas is burnt with pure oxygen in the combustor to produce high-temperature work fluid. The rankine and Brayton cycles are integrated by injecting steam from Rankine cycle to Brayton cycle. CO$_2$ produced by syngas can be separated by cooling. The detailed description of the system is as follows.

A partial gasifier—a fluidized bed gasifier (A)—is fed by coal (1), steam (2) extracted from a high-pressure steam turbine (HPT) (V), sorbent, (3) and oxygen (4). The oxygen comes from a low-pressure air separate unit (ASU) (T) outlet and is further compressed by a compressor (U). It should be noted that air (43) piped to the ASU produces not only oxygen (44) but also a nitrogen (45) by-product. In the fluidized bed gasifier, coal is converted into two products—syngas (5) and char (6). The depressurized char and particulate (11) from a cyclone (C) are burnt with air (39) as
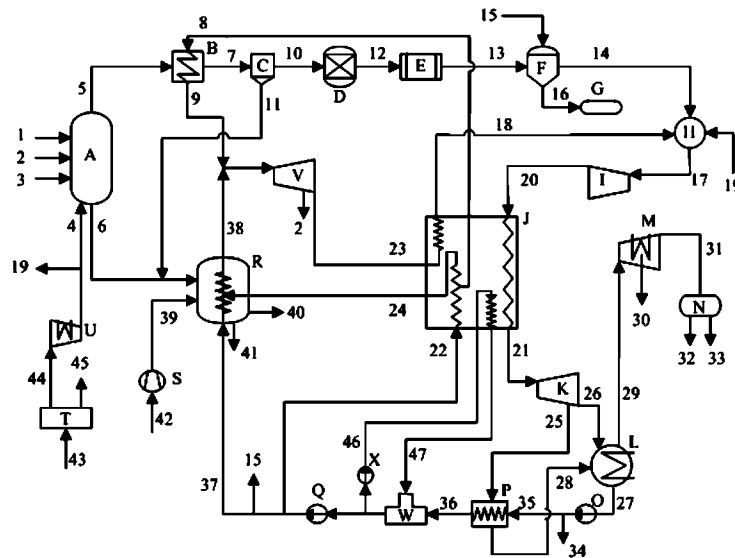
Fig. 1 Plant scheme of the partial gasification combined cycle with CO_2 recovery; A-gasifier; B-syngas cooler; C-cyclone; D-hydrolyzer, E-dry desulfurizer; F-scrubber; G-waste-disposal unit; H-combustion chamber; I-HTT; J-reheater; K-LTT; L-condenser; M-compressor; N-refrigeration machine; O-pump; P-reheater; Q-pump; R-boiler; S-compressor; T-ASU; U-compressor; V-HPT; W-deaerator; X-pump

oxidant in a boiler (R), and the air is compressed in a compressor (S) fed by air (42). In the boiler, the superheated steam (38) is produced, and slag (41) and exhaust gas (40) are discharged. Steam (38) along with steam (9) from a syngas cooler (B) is expanded in the HPT (V), and then the expanded steam (23) is heated in a reheater (J) and injected into a combustion chamber (H). Raw syngas (7) exiting the syngas cooler is processed through the cyclone, a hydrolyzer (D), a dry desulfurizer (E), and a scrubber (F) in order to obtain clean syngas (14). Oxy-fuel combustion of the clean syngas, together with the stoichiometric mass flow of oxygen (19), occurs in the combustion chamber with the injection of steam (18), and the products (17) are CO_2 and H_2O. The high-temperature working fluid (17) is expanded primarily to a pressure of 1.055 bar in a high-temperature gas turbine (HTT) (I). Due to the addition of the steam in the combustion chamber, the steam content in the working fluid increases to about 92.3%. It is evident that a further expansion down to condenser pressure would not end at a reasonable condensation point for the water component, so the hot exhaust gas is cooled in the following reheater to heat feed water (22) and the steam of the HPT outlet (23). After this, it is further expanded in a low-temperature gas turbine (LTT) (K) to a condenser pressure of 0.08 bar. In the condenser (L), CO_2 is separated automatically by water condensation. The unwanted water (34) of the cycle is discharged after a pump (O), while the rest (35) is preheated in a reheater (P). In order to remove dissolved gases (N_2, O_2, and CO_2) in the feed water, the deaerator (W) is arranged in front of the feed pump. The feed water (36) is heated close to saturation temperature in the deaerator using the steam (47) from the reheater (J). The deaerated water is piped to the boiler, the reheater (J), and the scrubber, respectively. In the reheater (J), a part of the water (8) is piped to the syngas cooler, while the other (24) is piped to an appropriate position of the boiler and converges with the heated feed water (37). Because water and other impurities are present in CO_2 (29) in the condenser, it is compressed to 70 bars by an intercooled compressor (M) and the water (30) is separated, and then CO_2 (31) is further cooled by a refrigeration machine (N) to obtain liquid CO_2 (32) and the other mixed gas (33).

3 Thermodynamic Performance

From the above description shown in Fig. 1, the idea of cascade conversion of coal was used to construct a new system. The system combined combustion of char in the boiler with combustion of syngas in the combustion chamber of a gas turbine to connect in series with different temperature ranges—a HPT cycle, HTT cycle, and LTT cycle. This increased the working temperature range from 25°C to 1400°C, making the cascade utilization of energy levels possible.

This paper presents an evaluation of the system with the ASPEN PLUS software. The coal composition is shown in Table 1. The pressure in the gasifier was 45 bars, and the mole ratio of the oxygen rich, 96% content O_2, to steam is 16.9/3 in the oxidant. The excess air ratio was 1.2 in the boiler. The exhaust gas temperature was 130°C. The excess oxygen-rich ratio was 1.03 in the combustion chamber. Isentropic efficiencies of the HTT, the HPT, and the LTT were 0.9, 0.88, and 0.86, respectively. The isentropic

Table 1 Coal composition

Industrial analysis (by wt %)	
Moisture	5.000
Fixed carbon	34.087
Volatile	49.043
Ash	16.870
Ultimate analysis (by wt %)	
Ash	16.870
Carbon	67.274
Hydrogen	4.478
Oxygen	5.924
Nitrogen	1.239
Sulfur	4.185
Chlorine	0.030
Coal LHV (kJ/kg)	25,898

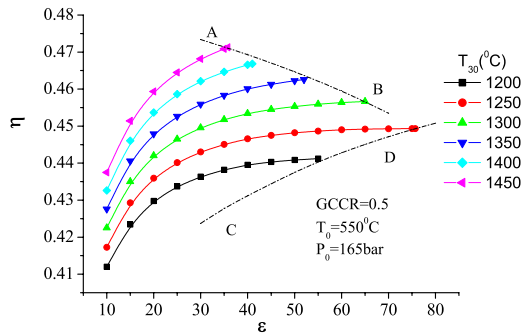Fig. 2   Variation of thermal efficiency with T_{30} and ε of the HTT

Fig. 3   Variation of thermal efficiency with GCCR and ε

efficiency of the pump was 0.78. The approach temperature difference and minimum temperature difference between hot input and cool output in the reheater were, respectively, 11°C and 30°C. The temperature of water existing in the condenser was 25°C.

In the new system, tars and oil vapors are not considered in the syngas exiting the gasifier with around 900°C of temperature. This is because some researches show that lime-based sorbents may be injected into the gasifier not only to capture sulfur but also to catalytically enhance tar cracking. The test results of the second-generation PFBC of Foster Wheeler Development Corporation show that no tars and oil vapors the present in the syngas exiting a circulating PFB with 871°C of temperature [10].

On the basis of analysis of the degree of freedom of the system model, this system has five independent variables: (i) gasifier carbon conversion ratio (GCCR). This is a ratio, by weight, of the carbon converted into syngas to the total carbon input. When pressure and the oxidant parameters are fixed in the gasifier, the GCCR is the key parameter to determine the components of syngas: (ii) the initial temperature T_0 of the HPT, (iii) the initial pressure P_0 of the HPT, (iv) the initial temperature T_{30} of the HTT, and (v) the pressure ratio ε of the HTT.

Figure 2 illustrates the variation of the overall thermal efficiency η of the system with varying initial temperature T_{30} and pressure ratio ε of the HTT. When GCCR, T_0, and P_0 are fixed, T_{30} and ε can only vary in the area enveloped between curve AB and curve CD. Curve AB represents the maximal value of T_{30} at different ε when the steam of the HPT outlet is heated in the reheater and the temperature difference between the hot input and cool output in the reheater is equal to 30°C. Curve CD represents the minimum value of T_{30} at the different ε when the steam of the HPT outlet directly pipes into the combustion chamber and is not heated in the reheater. On the envelope curve AB, max T_{30} and η decrease with the increase of ε. The reason is mainly that when the quantity of heat of syngas combustion is fixed and the temperature difference between hot input and cool output in the reheater is minimum, the exhaust gas temperature of the HTT decreases with the increase of ε, resulting in the decrease of the temperature of the steam injected into the combustion chamber. On the envelope curve CD, min T_{30} and η increase with the increase of ε. The reason is mainly that under the no-reheating condition and increase of ε, the expansion ratio of the HPT decreases, resulting in the increase of the temperature of exhaust steam that piped into the combustion chamber of the HPT. In addition, for a given ε, η will increase with the increase of T_{30}, and for a given T_{30}, η will increase with the increase of ε. When ε has a lower value, the increment of η is greater than that when ε has a higher value. Theoretically, for each T_{30}, there is a ε_{opt} to get a maximum of η, but few ε_{opt} can be reached due to the limitation of the envelope of the curves.

Figure 3 illustrates the overall thermal efficiency η of the system as it varies with the GCCR and pressure ratio $\varepsilo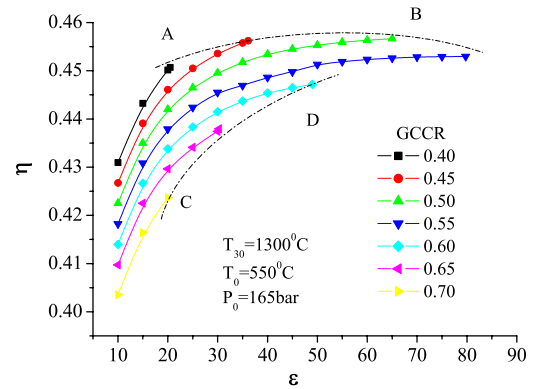n$. It is similar to Fig. 2 in that the family of curves shown in Fig. 3 is enveloped by curves AB and CD when T_{30}, T_0, and P_0 are fixed. Curves AB and CD represent, respectively, the minimum GCCR and the maximum GCCR at different ε. The reasons are also similar to those given in Fig. 2. On the envelope curve AB, the minimum GCCR increases and η varies slowly with ε increase. The reason is that under the reheating condition and minimum temperature difference between hot input and cool output of 30°C in the reheater, with the increase of ε, the HTT exhaust temperature decreases and the steam temperature injected into the combustion chamber also decreases. This will make the fuel demand increase to reach the same T_{30}. On the envelope curve CD, the maximum GCCR decreases with the increase of ε. The reason is that under the no-reheating condition, with the increase of ε, the temperature of the steam injected into the combustion chamber increases, so that it will make the fuel demand decrease. Moreover, for the given ε, η will be decreased with the increase of GCCR. The reason is that, with the same ε, the increase of GCCR will make the temperature difference between hot input and cool output in the reheater increase and more middle-level thermal energy will be lost; additionally, the energy to separate CO_2 will be increased. According to curve AB, when other variables are given, there is a special set of GCCR and ε to get an optimal η.

If the leak of steam of the HPT is not considered, η will always increase with the increase of P_0, but this is in conflict with what is actually happening. In fact, the value of η increases firstly and then decreases because the leak of steam increases with the increase of P_0 and becomes more and more rapid. Here, the leak of steam is considered in the HPT. Figure 4 illustrates that the overall thermal efficiency η of the system varies with T_0 and P_0 when GCCR, T_{30}, and ε are fixed. For a given P_0, η will increase with the increase of T_0 because energy destruction decreases in the
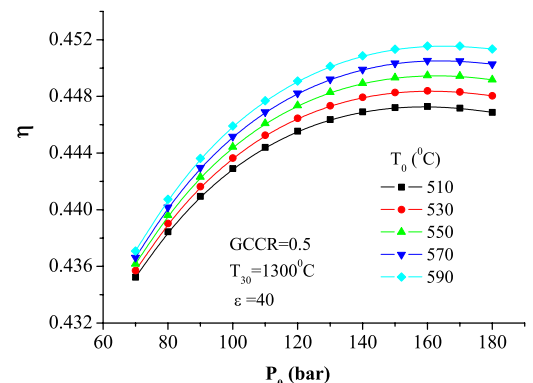

Fig. 4   Variation of thermal efficiency with T_0 and P_0 of the HPT

Table 2 Main parameters of the system

Point in Fig. 1	Pressure (MPa)	Temperature (°C)	Mass flow (kg/s)	Point in Fig. 1	Pressure (MPa)	Temperature (°C)	Mass flow (kg/s)
1 coal	4.500	15.0	18.24	24 steam*	17.000	303.6	64.00
2 steam	4.500	354.6	0.60	25 steam*	0.080	97.9	13.99
4 oxygen	4.500	281.5	3.38	26 steam*	0.008	44.7	111.98
5 syngas	4.500	900.0	14.03	27 water	0.008	25.0	102.00
7 syngas	4.400	200.0	14.03	28 water	0.080	42.1	13.99
8 steam	17.000	190.0	7.23	29 CO$_2$*	0.008	25.0	23.97
9 steam	16.500	550.0	7.23	30 water	0.101	25.0	3.45
10 syngas	4.400	200.0	12.86	31 CO$_2$*	7.000	25.0	20.52
11 particle	4.400	200.0	1.17	32 liquid CO$_2$	7.000	5.0	18.12
12 syngas	4.400	202.3	12.86	33 gas	7.000	5.0	2.40
13 syngas	4.350	202.3	12.09	34 water	0.120	25.0	2.74
14 syngas	4.300	134.2	12.65	35 water	0.120	25.0	99.26
15 water	5.000	108.5	1.80	36 water	0.120	90.0	99.26
16 waste water	4.300	136.4	1.24	37 water	17.000	106.4	26.22
17 steam*	3.800	1250	125.97	38 steam	16.500	550.0	90.22
18 steam	3.920	538.2	96.86	39 air	0.104	17.9	88.27
19 oxygen	4.500	281.5	16.46	40 exhaust	0.101	130.0	94.70
20 steam*	0.106	573.9	125.97	42 air	0.101	15.0	88.27
21 steam*	0.101	117.0	125.97	44 oxygen	0.101	15.0	19.84
22 water	17.000	106.4	71.23	46 water	0.130	104	2.75
23 steam	4.000	339.3	96.86	47 steam	0.130	150	2.33

* Note: "steam*" is the mixture of steam and other gas but is mainly steam and CO_2. "CO_2*" is the mixture of CO_2 and other gas but is mainly CO_2

boiler. For a given T_0, the increment of η at a lower value of P_0 is more than that at a higher value of P_0, and there is a P_0 that can make the combined cycle reach the highest η.

4 Exergy Analysis of the System

To understand clearly the characteristics of the new system, this paper analyzes a case in detail. The five variables, GCCR, T_{30}, ε, P_0, and T_0, were chosen as 0.4482, 1250°C, 38, 165 bars, and 550°C, respectively. The other assumptions are the same as those given in Sec. 3. The parameters of the main points of the system are listed in Table 2. In this case, the thermal efficiency of the system is 44.95% (lower heating value (LHV) base), with a CO_2 recovery of 41.21%.

The results show that the new system provides similar high efficiency as in the IGCC system. At the same time, it separates a part of the CO_2. Therefore, its efficiency is higher than that of an IGCC with CO_2 recovery. In order to identify the internal phenomena, this paper makes use of exergy analysis and compares the new system with an IGCC system.

Figure 5 is the simplified flow chart of the IGCC system. This system contains four subsystems, which are the gasification and cleanup subsystem, the high-pressure cryogenic ASU, the gas turbine subsystem, and the HRSG and steam turbine subsystem. A
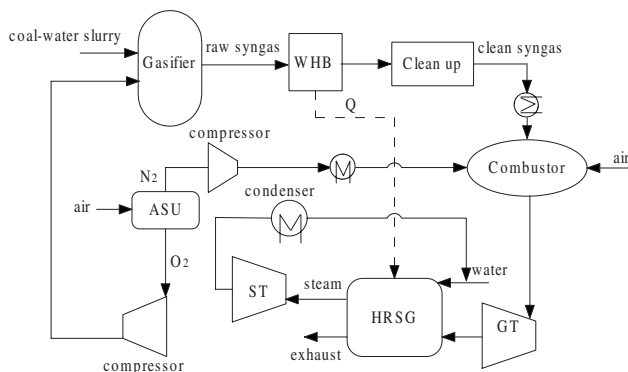
Fig. 5 The simplified flow chart of the IGCC system

Texaco gasifier is used in this system. Coal-water slurry and 98% oxygen rich from the ASU enter the gasifier to produce raw syngas. The operating pressure of the gasifier is equal to 28.6 bars, and the conversion rate of carbon is 98% in the gasifier. The temperature of the raw syngas exiting the gasifier is 1346°C. The raw syngas is cooled to about 200°C in a cooling unit, and high-temperature steam is produced. The cooled syngas is inducted into a cleanup subsystem. In this subsystem, a solid particulate of the syngas is removed in a cyclone and a venturi scrubber, and then sulfur of the syngas is removed by the use of the Selexol method. The separated H_2S will be inducted into the Claus/SCOT unit to recover sulfur. The temperature of the syngas exiting to the cleanup subsystem is equal to 40°C. The clean syngas and the N_2 from the ASU are heated to 300°C and then inducted into the combustion chamber of the gas turbine. The temperature of the turbine inlet is 1250°C, and the pressure ratio is 16.1. The HRSG and steam turbine subsystem adopts a triple pressure reheat cycle. The efficiencies of high-pressure, middle-pressure, and low-pressure steam turbine are 81%, 90%, and 81%, respectively.

In the new system, a dry desulfurizer is used to clean syngas. In order to make the comparison consistent between the new system and the IGCC, the same wet desulfurization technology as the IGCC substitutes for the dry desulfurization in the new system. The thermal efficiency of the new system will be decreased by 0.48%, from 44.95% to 44.47%. Table 3 shows a comparison of distribution of exergy destruction of the new system and the IGCC system with/without CO_2 recovery [11]. Here, the highest initial temperature of the IGCC is 1250°C, and the approach temperature difference of the heat exchanger and the efficiency of the corresponding assembly are the same as in the new system. Correspondingly, the exergy efficiency of the new system is about 43.49%, while that of the IGCC without CO_2 recovery is 44.91%. Based on related literature [12,13], when an IGCC system separates CO_2 by conventional physical and chemical absorption, its thermal efficiency will be decreased by 8–12% on a relative basis. Thus, its efficiency will be decreased by 3–5%, which is 39.91%–41.91%, when the IGCC separates the same ratio (41.21%) of CO_2 as the new system.

In order to analyze more clearly the internal phenomena of integration of the systems, this paper adopts the energy-utilization diagram (EUD) methodology developed by Ishida and Kawamura

Table 3 Exergy destruction comparison between the new system and IGCC system

Items	The new system (%)		IGCC (%)	
	Exergy (kJ)	Ratio of exergy to total exergy (%)	Exergy (kJ)	Ratio of exergy to total exergy (%)
Total exergy input				
Fuel exergy	26,486	100	26,486	100
Exergy destruction				
Gasifier	1221.0	4.61	3776.9	14.26
Cleanup unit	384.0	1.45	386.7	1.46
Cool unit	79.5	0.3	778.7	2.94
Boiler	5387.3	20.34	0.0	
Combustion chamber	3302.8	12.47	5522.3	21.16
Turbine	847.6	3.20	1030.3	3.88
Compressor	161.6	0.61	688.6	2.6
HSRG (or reheater)	987.9	3.73	733.7	2.87
ASU	1022.3	3.86	1054.1	4.01
Condenser	656.9	2.48	357.6	1.36
Auxiliary	259.6	0.98	259.6	0.98
CO_2 recovery	654.2	2.47	0	0 (without CO_2 recovery)
			794.6–1324.3	3–5 (with CO_2 recovery)
Exergy output				
Work output	11,518.8	43.49	11,894.9	44.91 (without CO_2 recovery)
			10,570.6–11100.3	39.91–41.91 (with CO_2 recovery)
Sum total				
	26,483.4	99.99	26,483.4	99.99

[14] and Ishida [15]. The EUD is determined by the energy level (A) versus the energy-transformation quantity (ΔH). The energy level (A) is equal to the exergy change ($\Delta \varepsilon$) divided by the energy change (ΔH), that is, $A = \Delta \varepsilon / \Delta H$. For an energy-transformation system, the energy is released by the energy donor and is accepted by the energy acceptor. In the EUD, the exergy destruction can be obtained easily from the area between the curves for the energy donor (A_{ed}) and energy acceptor (A_{ea}).

4.1 Gasification Subsystem. Figures 6(a) and 6(b) show, respectively, the EUDs for the gasification subsystem of the IGCC and the new system [16]. For the gasifier in the IGCC, the partial combustion acts as an energy donating reaction, represented by the curve of A_{ed}, the gasification reaction as an energy accepting reaction (A_{ea4}), and the three feed streams, the water (A_{ea1}), the oxygen (A_{ea2}), and the coal (A_{ea3}), energy acceptors which are heated to the temperature of gasification. As a result, the exergy destruction of gasification in the IGCC is equivalent to the shaded area between the curves of the energy donor (A_{ed}) and the energy acceptors (A_{ea1} through A_{ea4}), 3776.9 kJ/kg coal. For the gasifier in the new system, the partial combustion acts as an energy donating reaction, represented by the curve of A_{ed}. The gasification reaction (A_{ea5}) and pyrogenation reaction (A_{ea3}) act as energy accepting reactions, and the water and the oxygen (A_{ea1}), the coal (A_{ea2}), and the char and coal (A_{ea4}) are energy acceptors, which are heated to gasification temperature. This exergy destruction, the shaded area shown in Fig. 6(b), is equal to 1221 kJ/kg coal.

It is clear that exergy destruction in the gasification subsystem of the new system is less than one-third of the exergy destruction of the IGCC system. This is mainly a benefit from the cascade conversion of coal. In the partial gasifier, the only active composition of coal is gasified, the heat demand is less, and the temperature required is lower, so less material takes part in the reaction, resulting in less exergy destruction of reaction. However, in the IGCC, coal is gasified completely, and in contrast to partial gasification, its exergy destruction is greater.

4.2 Combustion Subsystem. Figures 7(a) and 7(b) show, respectively, the EUDs for the combustion subsystems of the IGCC
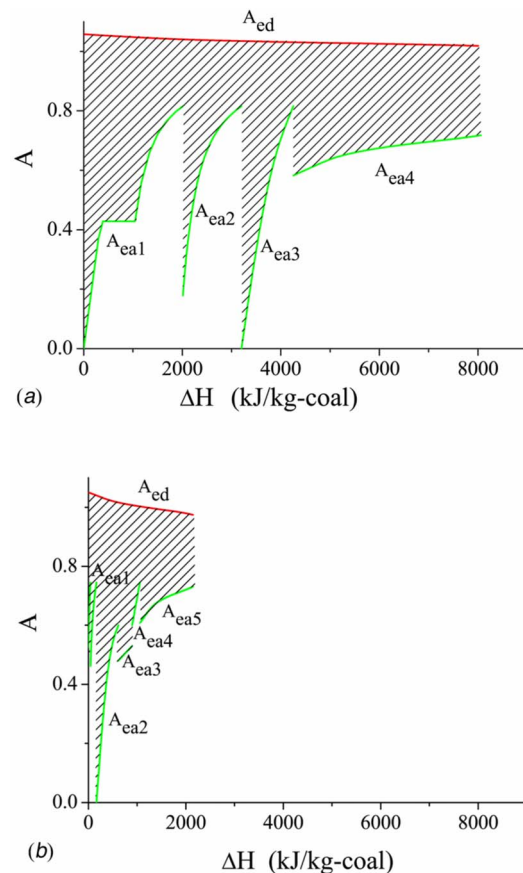
Fig. 6 (a) EUDs for the gasification subsystem of IGCC. (b) EUDs for the gasification subsystem of the new system.
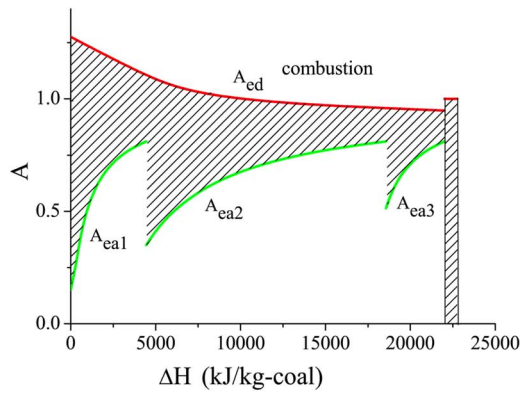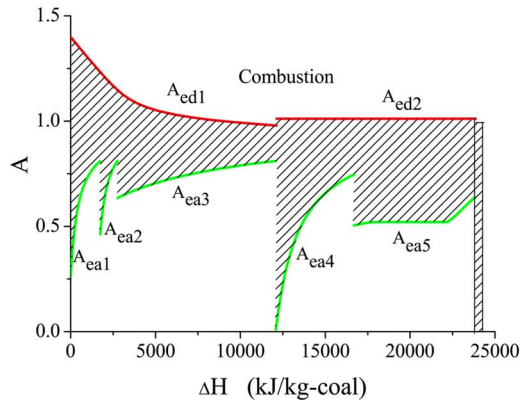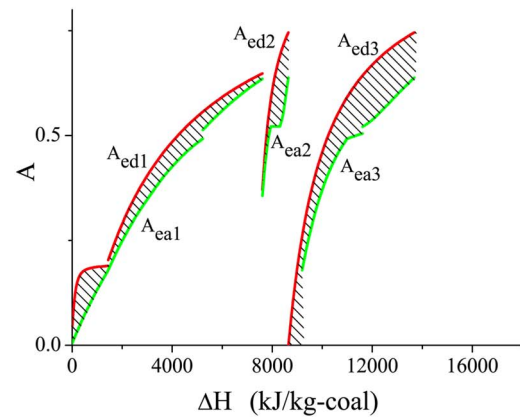
Fig. 7 (*a*) **EUDs for the combustion subsystem of IGCC.** (*b*) **EUDs for the combustion subsystem of the new system.**


Fig. 8 (*a*) **EUDs for the heat-exchange subsystem of IGCC.** (*b*) **EUDs for the heat-exchange subsystem of the new system.**

and the new system. The combustion acts as an energy donating reaction (curve A_{ed} in Fig. 7(*a*) and curves A_{ed1} and A_{ed2} in Fig. 7(*b*)). The three feed streams in Fig. 7(*a*)—the nitrogen (A_{ea1}), the air (A_{ea2}), and the syngas (A_{ea3})—act as energy acceptors that are preheated to the specified combustion temperature. However, in Fig. 7(*b*), there are two combustions: in the combustion chamber and in the boiler. The former combustion is similar to Fig. 7(*a*), and its energy acceptors are the syngas (A_{ea1}), the oxygen (A_{ea2}), and the steam (A_{ea3}), while in the latter combustion reaction, air (A_{ea4}) preheated to the specified combustion temperature and the superheated steam (A_{ea5}) act as energy acceptors. The total shaded areas between the curves of A_{ed} and A_{ea} represent exergy destruction. Due to greater irreversibility of the burning process as well as the irreversibility during the mixing of the input streams, the exergy destructions of the two systems are greater. Especially for the combustion process in the boiler, there is an evaporating heating process, so that exergy destruction in the boiler is much higher than in the combustion chamber. As a result, total exergy destruction of combustion is 8690.1 kJ/kg coal in the new system and 5522.3 kJ/kg coal in the IGCC.

4.3 Heat-Exchange Subsystem. Figures 8(*a*) and 8(*b*) show, respectively, the EUDs for the heat-exchange subsystem of the IGCC and the new system. The new system contains three heat-exchange processes shown in Fig. 8(*b*). The exhaust gas (A_{ed1}) of the HTT acts as an energy donator, and the feed water of the boiler and the steam of the HPT outlet (A_{ea1}) act as energy acceptors in the reheater following the HTT. In the syngas cooler, the raw syngas (A_{ed2}) and the water (A_{ea2}) are a pair of energy donator and energy acceptor, and in the boiler, fuel gas (A_{ed3}) and water (A_{ea3}) are energy donator and energy acceptor. Two heat-exchange
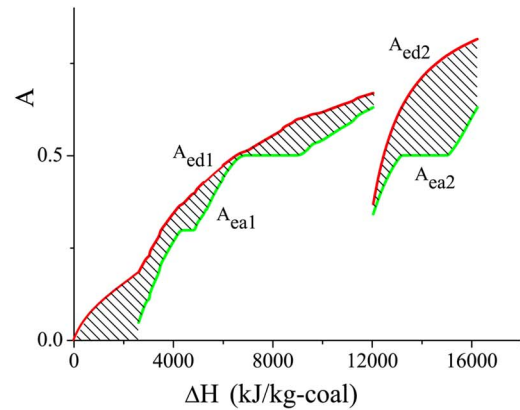
processes in the IGCC system, from left to right in Fig. 8(*a*), are, respectively, in the HRSG and in the syngas cooler, which are similar to the relevant process of the new system. Comparing the two figures, temperature matching of the new system is more likely to result in smaller exergy destruction. The main reason is that the product of syngas combustion, as a working fluid, is not discharged to air in the new system, while in the IGCC, it is discharged to air with temperatures above 90 °C existing in the HRSG. The other main reason is that the temperature of raw syngas existing in the gasifier is much lower in the new system than that in the IGCC, so that it decreases the temperature difference of heat exchange. As a result, the total exergy destruction is 1869.9 kJ/kg coal in the IGCC and 1724.2 kJ/kg coal in the new system.

4.4 Power Subsystem. Figures 9(*a*) and 9(*b*) show the EUDs for the power subsystem of the IGCC and the new system, respectively. The abscissa of these diagrams indicates the work. For turbines, gas expansion is the energy donor, and the energy level becomes greater than unity. The work generated is equal to width of curve A_{ed}, and the energy level is unity. The shaded area between curve A_{ed} and the horizontal line with $A_{ea}=1$ represents the exergy destruction in the turbine because the generated work is accepted by a work sink with the energy level $A_{ea}=1$. For the compressor, gas compression is the energy acceptor, and the energy level becomes less than unity. The work required is equal to the width of curve A_{ea}, and the energy level is unity. Since the required work is donated by a work source with the energy level $A_{ed}=1$, the shaded area between the horizontal line with $A_{ed}=1$ and the curve represents the exergy destruction in the compressor.
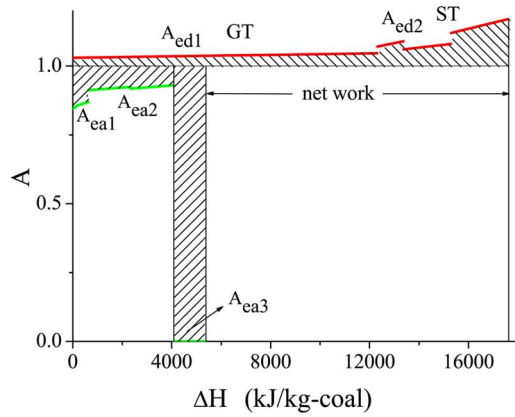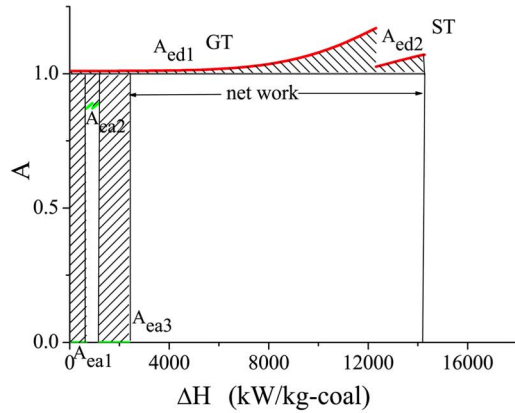
Fig. 9   (*a*) EUDs for the power subsystem of IGCC. (*b*) EUDs for the power subsystem of the new system.

The work generated by the new system includes gas turbine (HTT and LTT) expansion (A_{ed1}) and steam turbine (high pressure) expansion (A_{ed2}), and the work required includes the CO_2 compressor (A_{ea1}), the O_2 compressor (A_{ea2}), and the ASU (A_{ea3}). The work generated by the IGCC includes gas turbine expansion (A_{ed1}) and steam turbine (high pressure, middle pressure, and low pressure) expansion (A_{ed2}), and the work required includes O_2 and N_2 compressors (A_{ea1}), the compressor (A_{ea2}) of the gas turbine, and the ASU (A_{ea3}). From the figures, on the one hand, the gross work generated by the new system is less than that of the IGCC. In the new system, coal is partially gasified, so that the only energy of syngas is used in high-temperature and high-performance gas turbine and the energy of char is used by the lower temperature steam turbine. However, in the IGCC, coal is fully gasified so that the total energy of coal is used by the high-temperature and high-performance gas turbine. On the other hand, the work required by the new system is also less than that of the IGCC. The main reason is that the compressor of the gas turbine in the IGCC consumes a great deal of work, while in the new system, the compressor of the gas turbine is replaced by a pump. The exergy destruction of the power subsystem was found to be 2524.1 kJ/kg coal in the new system and 2773.1 kJ/kg coal in the IGCC. As a result, the net work is 11,518.8 kJ/kg coal in the new system and 11,894.9 kJ/kg coal in the IGCC; hence, the efficiencies of the two systems are similar. On the basis of the above comparison, the positive and negative aspects allow the new system to get the similarly high efficiency as the IGCC without CO_2 recovery.
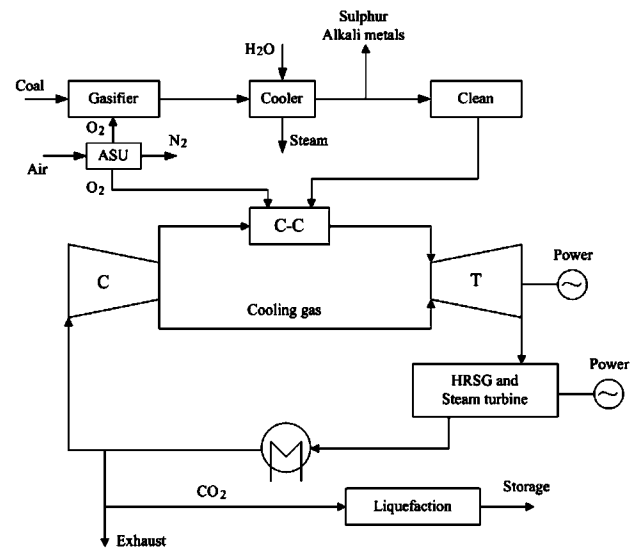
Fig. 10   The flow chart of the IGCC with a semiclosed O_2/CO_2 cycle

5   Economic and Environmental Performance

5.1   Analysis of Environmental Performance. Figure 10 shows the flow chart of the IGCC with a semiclosed O_2/CO_2 cycle [17]. In this system, clean syngas is burnt in a combustion chamber with pure oxygen. The gas existing HRSG is partly re-injected to the combustion chamber, and the other is treated and CO_2 is separated and liquefied.

The partial gasification combined cycle with CO_2 recovery provides a friendly environment. Not only are emissions of SO_x, NO_x, and solid particles lower, but CO_2 produced by syngas is also separated with low energy consumption. Figure 11 shows that thermal efficiencies of the new system and the IGCC with semiclosed O_2/CO_2 cycle [17] vary with the ratio of separated CO_2 X_{CO_2} and the initial temperature T_{30} of the gas turbine. In the new system, the ratio of CO_2 separated X_{CO_2} is approximately equal to the GCCR. When X_{CO_2} and T_{30} are given, the values of the three variables are equal to the optimal value for the maximum efficiency of the system. In the IGCC, when X_{CO_2} and T_{30} are given, the other variable, pressure ratio of the gas turbine, is equal to the optimal value for the maximum efficiency of the IGCC. From the figure, it is obvious that when T_{30} is fixed, the efficiency of the IGCC decreases as CO_2 increases since the larger X_{CO_2} results in more work consumption for compressing CO_2. At the same time, when T_{30} is fixed, the efficiency of the new system varies from an
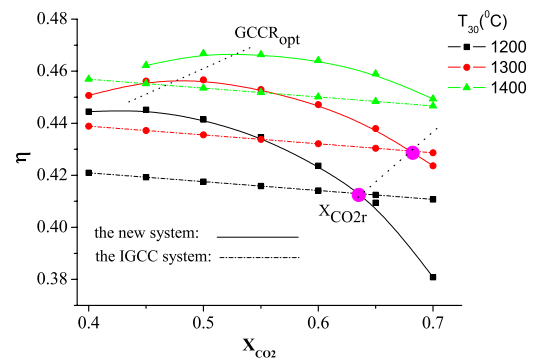
Fig. 11   Variation of the thermal efficiency of the new system and semiclosed IGCC with CO_2 recovery with X_{CO_2} and T_{30}

Table 4 Specific investment cost estimation of the new system and the IGCC system. Note: The O_2 consumption is 1.033×10^{-4} kg/kW s in the new system and 1.86×10^{-4} kg/kW s in the IGCC.

Items	Specific investment cost	
	New system ($/kW)	IGCC with semiclosed O_2/CO_2 cycle ($/kW)
Gasification subsystem	311$/kW (including boiler)	455
ASU subsystem	192	264
Power subsystem	435	402
CO_2 recovery subsystem	55	55
Cost of utilities	70	82
Total specific investment cost	1063	1258

increase to a decrease with X_{CO_2} increase, and there exists an optimal X_{CO_2}. The optimal X_{CO_2} is also the optimal GCCR $GCCR_{opt}$ when the efficiency is at the optimal value. In addition, a critical value of CO_2 recovery $X_{CO_{2_r}}$ is present, shown in the figure. On the left of the value $X_{CO_{2_r}}$, the efficiency of the new system is higher than that of the IGCC. On the right of the value $X_{CO_{2_r}}$, the efficiency of the IGCC is higher. It should be noted that the value of $X_{CO_{2_r}}$ increases with increasing T_{30}.

5.2 Economic Evaluation. The future application of a technology and the selection of a power plant mainly depend on the economical benefit. Therefore, an economic comparison of the proposed system and an IGCC power plant was performed. The new combined cycle power plant demonstrated better economical performance according to the technical analysis as follows: (i) Compared with the conventional gasifier in the IGCC, the partial gasifier decreases technical requirements, and its gasification temperature is about $800-1000\,°C$, which is much lower than that of the IGCC. Hence, the size of the partial gasifier will be smaller than that of the conventional gasifier, and simultaneously, its cost is much lower. (ii) The temperature of raw syngas existing in the gasifier is much lower, and there is less slag of syngas in the new system than that in the IGCC, so that the material requirement of the syngas cooler along with its cost is lower. (iii) The new system combines spray calcium desulfuration in the gasifier and dry desulfuration of syngas. Because 90% sulfur in coal is removed in the gasifier, the conventional wet desulfuration, which is complex and expensive, is not required. (iv) The new system does not have a gas turbine compressor, which is replaced by the pump. It also omits the HRSG, which is replaced by the reheater. Accordingly, the related equipment is simplified, and the cost is also lower.

Since the oxygen requirement and CO_2 removal vary with the GCCR, the cost of related equipment is also changed. Table 4 [9,17] shows comparisons of the approximate estimation of investment costs between the new combined cycle and the IGCC with a semiclosed O_2/CO_2 cycle when the GCCR of the new system is equal to 0.5, and the initial temperatures of HTT in the new system and gas turbine in the IGCC are equal to $1300\,°C$. The thermal efficiencies of the new system and the IGCC are 45.32% and 43.25%, respectively. The costs indicate engineer-purchase-construct (EPC) costs but exclude interest during construction and startup costs.

For the IGCC with a semiclosed O_2/CO_2 cycle, the cost of the gasification subsystem (455$/kW), quotes from literature [18], and that of the power subsystem (402$/kW) is the cost of a turn-key contract from literature [19]. While for the new system, the gasification subsystem is composed of the partial gasifier and the boiler of a circulating fluidized bed (CFB) that is chosen. The capacity of the partial gasifier is almost half of the gasifier of IGCC, hence, on the basis of the approximate cost-estimate coefficient 0.8 of a gasifier, the cost of the partial gasifier is equal to 261$/kW, which derives from 455$/kW divided by $2^{0.8}$. The cost

of the CFB based in China is supplied by the China Huadian Engineering Corporation, Ltd., and due to the international cost of the CFB is about 1.5–2.0 times more than Chinese one, the international cost can be deduced. The cost of the CFB based on international in this paper is equal to 38–50$/kW, and the maximum 50$/kW is used in this paper. So, the cost of the gasification subsystem of the new system is 311$/kW. From the literature [9], the investment costs per kW of power subsystem of new system is similar as that of S-GRAZ cycle, that is 435$/kW. From the literature [20], the cost of ASU is 40,400k$ when the capacity of pure O_2 production is 1839 tons/day, and the scale factor of ASU is 0.5. The O_2 consumptions of the new system and the IGCC are 22.12 kg/s (1.033×10^{-4} kg/kW s) and 38.01 kg/kg s (1.86×10^{-4} kg/kW s), respectively. Based on these data, the costs of the ASUs of the new system and the IGCC are obtained, which are 192$/kW and 264$/kW, respectively. Furthermore, from the literature [9], the cost of CO_2 recovery unit is 550,000$/(kg CO_2/s). The cost of utilities is equal to 7% of the EPC cost. As a result, through simple estimation, compared with the IGCC with semiclosed O_2/CO_2 cycle, the total investment of the new system will be reduced by about 16%.

6 Conclusions

This paper proposes a novel coal-fired combined cycle system on the basis of three main key technologies, including partial gasification of coal, oxy-fuel combustion of syngas, and injecting steam. The system contains five independent variables. Among them, the initial temperature T_{30} and pressure ratio ε of the HTT and GCCR are key variables. Due to the adoption of partial gasification and integration of the Brayton and Rankine cycles, an envelope of a family of curves is presented. At the envelope curve, when T_{30} is fixed and GCCR varies from 0.4 to 0.7, the optimal efficiency of the system becomes around 0.46 (LHV base). The efficiency is nearly the same as that of an IGCC without CO_2 recovery.

By use of exergy analysis, the internal phenomenon of the system inefficiency was revealed and compared with an IGCC. Due to the partial gasification of coal, exergy destruction of gasification is 9.65% lower in the new system than in the IGCC. However, the new system contains a boiler, so the exergy destruction of combustion is 11.65% higher in the new system than in the IGCC. In addition, oxy-combustion makes the separation of CO_2 consume less energy, so the exergy destruction of the new system is about 2% lower in the new system than in IGCC.

This paper provides a simple analysis of the economic and environmental performance and compares the new system with a semiclosed IGCC with CO_2 recovery. Since the new system adopts the more simple partial gasification, much of the equipment is simplified, and the total investment cost is about 16% lower than a semiclosed IGCC with CO_2 recovery. Simultaneously, when the ratio of CO_2 recovery X_{CO_2} is equal to 0.4482, the exergy efficiency of the new system is 1.5–3.5% higher than

that of an IGCC with CO_2 recovery. The comparison between the partial gasification technology and the IGCC technology is based on the two representative cases to identify the specific feature of the proposed system. The new system realizes effective utilization of energy based on cascade utilization of energy level and integration of thermodynamic cycle and CO_2 recovery.

Acknowledgment

Nomenclature

$$T_0 = \text{initial temperature of HPT (°C)}$$
$$P_0 = \text{initial pressure of HPT (bar)}$$
$$T_{30} = \text{initial temperature of HTT (°C)}$$
$$\varepsilon = \text{pressure ratio of HTT}$$
$$\eta = \text{thermal efficiency (LHV)}$$
$$\Delta\varepsilon = \text{exergy change (kJ/kmol)}$$
$$\Delta H = \text{enthalpy change (kJ/kmol)}$$
$$A = \text{energy level}$$
$$X_{CO_2} = \text{the ratio of } CO_2 \text{ separated}$$
$$X_{CO_2} = \text{critical value of } X_{CO_2}$$

Subscripts

$$\text{opt} = \text{optimal value}$$
$$\text{ed} = \text{energy donor}$$
$$\text{ea} = \text{energy acceptor}$$

References

[1] U.S. DOE Assistant Secretary for Fossil Energy, 1993, "Clean Coal Technology Demonstration Program," DOE/ASME Report No. 9309152.

[2] Cai, R., Lin, R., Xiao, Y., and Xu, D., 1993, "Coal-Fired Combined Cycle Power Generation Technology With High Efficiency, Low Pollution, and Low Water Consumption," UNESCO, Senior Conference of Cleaning Coal-Fired Technology, Beijing, China.

[3] Lin, R., Cai, R., and Jiang, L., 1999, "Performance Analysis and Comparison of Three Coal-Fired Combined Cycle Systems," Gas Turbine Technology in China, **12**(3), pp. 22–28.

[4] Lozza, G., Chiesa, P., and DeVita, L., 1996, "Combined-Cycle Power Stations Using "Clean-Coal Technologies:" Thermodynamic Analysis of Full Gasification Versus Fluidised Bed Combustion With Partial Gasification," ASME J.

[5] Foster Wheeler Development Corporation, 2003, "Development of Pressurized Circulating Fluidized Bed Partial Gasification Module (PGM)," Department of Energy, Contract No. DE-FC26-00NT40972.

[6] Makoto, T., Noriyuki, I., Keiji, U., 2002, "Development of Advanced PFBC Technology," *Proceedings of the Eighth SCEJ Symposium on Fluidization*, Kitakyusyu, Japan, pp. 38–45.

[7] Rao, A., Verma, A., and Samuelsen, G., 2005, "Engineering and Economic Analyses of a Coal-Fueled Solid Oxide Fuel Cell Hybrid Power Plant," ASME Paper No. GT2005-68762.

[8] Jericha, H., Gottlich, E., Sanz, W., and Heitmeir, F., 2004, "Design Optimization of the Graz Cycle Prototype Plant," ASME J. Eng. Gas Turbines Power, **127**(4), pp. 765–772.

[9] Sanz, W., Jericha, H., Moser, M., and Heitmeir, F., 2005, "Thermodynamic and Economic Investigation of an Improved GRAZ Cycle Power Plant for CO_2 Capture," ASME J. Eng. Gas Turbines Power, **127**(4), pp. 765–772.

[10] Robertson, A., Van Hook, F., Burkhard, O., Carli, O., 1996, "Second-Generation PFBC Systems Research and Development—Phase 2, Circulating PFBC Test Results," Report No. DOE/MC/21023-94/C0352.

[11] Liu, Z., Jin, H., and Lin, R., 2000, "Exergy Analysis of Integration Between Air Separation Process and IGCC," *Proceedings of ASME Turbo Expo 2000*, Munich.

[12] Chiesa, P., and Lozza, G., 1999, "CO_2 Emission Abatement in IGCC Power Plants by Semiclosed Cycles—Part A: With Oxygen-Blown Combustion," ASME J. Eng. Gas Turbines Power, **121**, pp. 635–641.

[13] Audus, H., 2000, "Leading Options for the Capture of CO_2 at Power Stations: IEA Greenhouse Gas R&D Programme," *Proceedings of the Fifth International Conference on Greenhouse Gas Control Technologies*, Australia.

[14] Ishida, M., and Kawamura, K., 1982, "Energy and Exergy Analysis of a Chemical Process System With Distributed Parameters Based on the Energy-Direction Factor Diagram," Ind. Eng. Chem. Process Des. Dev., **21**, pp. 690–702.

[15] Ishida, M., 2001, *Thermodynamics Made Comprehensible*, Nova Science, New York.

[16] Zheng, D., Moritsuka, H., and Ishida, M., 1986, "Graphic Energy Analysis for Coal Gasification—Combined Power Cycle Based on Energy Utilization Diagram," Fuel Process. Technol., **13**, pp. 125–138.

[17] Xu, G., Lin, R., and Jin, H., 2005, "The Multi-Objective and Unified Scale Evaluation Criterion for IGCC System," Journal of Engineering Thermophysics in China, **26**(4), pp. 545–548.

[18] Davison, J., Bressan, L., and Domenichini, R., 2004, "CO_2 Capture in Coal-Based IGCC Power Plants," *Proceedings of the Seventh International Conference on Greenhouse Gas Control Technologies*, Canada, Sep. 5–9.

[19] Farmer, F., 2002, *Gas Turbine World 2001-02 GTW Handbook for Project Planning, Design and Construction*, Pequot Publishing, Inc., Fairfield, CT.

[20] Kreutz, R., Williams, S., Consonni, P., and Chiesa, P., 2005, "Co-Production of Hydrogen, Electricity and CO2 From Coal With Commercially Ready Technology. Part B: Economic Analysis," Int. J. Hydrogen Energy, **30**, pp. 769–784.

R. T. Deam
e-mail: rdeam@groupwise.swin.edu.au

E. Lemma
e-mail: elemma@swin.edu.au

Faculty of Engineering and Industrial Sciences,
Industrial Research Institute Swinburne,
P.O. Box 218,
Hawthorn, Victoria 3122, Australia

B. Mace
e-mail: bm@alphalink.com.au

R. Collins
e-mail: racoll@ozemail.com.au

Micromachines Ltd.,
20 Queen Street,
Melbourne, Victoria 3000, Australia

On Scaling Down Turbines to Millimeter Size

The purpose of this work is to establish the maximum theoretical efficiency that a viscous flow turbine (such as a Tesla turbine) can achieve. This is very much in the spirit of the Betz limit for wind turbines. The scaling down of viscous flow turbines is thought not to alter this result, whereas the scaling down of conventional turbines, whether axial or radial flow, results in an ever lowering of their efficiencies. A semiempirical scaling law is developed for conventional gas turbines using published machine performance data, which is fitted to a simple boundary layer model of turbine efficiency. An analytical model is developed for a viscous flow turbine. This is compared to experimental measurements of the efficiency of a Tesla turbine using compressed air. The semiempirical scaling law predicts that below a rotor diameter of between about 11 mm and 4 mm, a practical Brayton cycle is not possible. Despite that, however, and for rotor diameters less than between about 7 mm and 2 mm, a viscous flow turbine, compressor, or pump will be more efficient than a conventional design. This may have a significant impact on the design of microelectromechanical system devices. [DOI: 10.1115/1.2938516]

Keywords: Brayton cycle, scaling law, expansion efficiency, viscous flow turbine, power MEMS

1 Introduction

It is well known that the principles used to design a Jumbo Jet are not appropriate for the design of a flying device the size of an insect. There have been many studies of the scaling laws comparing the performance of molecular machinery, animals, and man-made machines, for example, Marden and Allen [1]. This work examines the problem of designing a microelectromechanical system (MEMS) turbine, that is, a device with a power output of less than a few hundred watts. Although an insect and a Jumbo Jet in flight obey the same laws of physics (the Navier–Stokes equations), one of the main differences between them is the value of the Reynolds number of the flow in which they operate. A Jumbo Jet works in a highly turbulent world, whereas an insect swims in a much more viscous dominated world, for example, see Wang [2].

This work examines the design principles that might be used to design a MEMS turbine. The scaling laws for modern turbines tend to favor larger sizes due to their increased efficiencies. However, turbines are complex machines and therefore their scaling laws are not well understood. This is probably because the loss mechanisms in turbines are still the subject of research and development as described by Denton [3], who listed the main loss mechanisms as being categorized historically under the headings of the following:

- profile loss (loss generated in the boundary layers away from the end walls)
- endwall loss (sometimes called secondary loss)
- tip leakage loss (which is reduced by the effect of clearance seals)

It is not our objective here to treat these important loss mechanisms individually. We will assume that for a particular size of working gas turbine, the parameters associated with these loss mechanisms have been optimized to arrive at the best performance that can be achieved for the size designed. It is how these optimized machines scale down that is studied here.

When studying turbine efficiencies, it is important to distin-

guish between the overall (or thermal) efficiency, from now on referred to as Brayton cycle thermal efficiency, and the expansion (or isentropic) efficiency of a turbine, from now on referred to as the turbine component efficiency. The Brayton cycle thermal efficiency is usually defined as the net mechanical power output of the turbine divided by the rate of heat generation from burning the fuel. The inverse of the Brayton cycle thermal efficiency is often quoted by the manufacturers as the heat rate. The heat rate is usually quoted in units of BTU/kW h or kJ/kW h (for example, a 30% overall efficiency corresponds to a heat rate of 12,000 kJ/kW h). In contrast to the Brayton cycle thermal efficiency, the turbine component efficiency is a measure of the fluid dynamic effectiveness of the turbine. It is the ratio of the network output per unit mass flowing through the machine divided by the theoretical amount of work that could have been extracted per unit mass, if the gas flowing through the machine had been adiabatically (reversible and isentropic) expanded between the turbine's inlet and outlet pressures.

Working turbines in service range from 750 MW (with the largest rotor diameter of about 4 m) to 3 kW (with a rotor diameter of about 100 mm). The former are steam turbines used in power stations while the latter are miniature gas turbines used for model airplanes. When designing very small turbines (less than 100 mm rotor), it is important to know what Brayton cycle thermal efficiencies can be achieved in practice. To this end, a survey of what can be achieved at present has been undertaken.

2 Fluid Dynamic Scaling Laws for Gas Turbines

2.1 Experimental Efficiency Data. Data were collected for a range of production gas turbines. The data for the heat rates of commercial turbines (from about 200 kW to 200 MW output) from Refs. [4,5] were converted to Brayton cycle thermal efficiencies. In addition, the data from Ref. [5] were also used to determine the efficiencies of Capstone microturbines while data for miniature gas turbines (primarily for model jet airplane applications) were used from Ref. [6]. The model turbine data range in output from just under 3 kW to just under 40 kW (Table 1). The Brayton cycle thermal efficiency is calculated using the published power output and fuel consumption figures assuming that the heat of combustion of the fuel is 37 MJ/l.

These data are plotted in Fig. 1. Note that the Brayton cycle

Table 1 Model turbine Brayton cycle efficiency data

Name of engine	Fuel consumption (ml/min)	Output (MW)	Brayton cycle thermal efficiency
PHT4	230	0.005	3.53%
PJ-W-R 1)	150	0.0035	3.78%
PJ-W	150	0.0027	2.92%
PHT3 helicopter	195	0.0035	2.91%
Phoenix HF 65 turboprop	750	0.0371	8.02%

thermal efficiency is plotted against the power output, where the power output is on a logarithmic scale. All the gas turbines operate on an air breathing Brayton cycle; therefore have a compressor and combustion chamber to drive the turbine. Data from Rankine cycle turbines (usually steam turbines) are not plotted.

There is an obvious trend of decreasing efficiency with decreasing maximum output. However, there is a fair amount of scatter and one of the reasons for this is because there has been no effort made to distinguish stationary engines from aeroengines. Moreover, unlike the data for the other turbines, the data for Capstone microturbines that are used for power generation stand out because they employ a regenerator. In addition, the scatter in Fig. 1 also reflects the range of maximum gas temperatures entering the turbine (after the compressor and combustion chamber).

From this limited survey of data, an engineer might conclude that gas turbines with a maximum power output below about 1 kW are not going to be a practical proposition. Model jet airplane enthusiasts certainly appreciate this point. The flying time of a model jet aircraft is severely limited by the poor fuel consumption of their model gas turbines or, in other words, the very low Brayton cycle thermal efficiency of their engines. The lower Brayton cycle thermal efficiency at smaller sizes is due to the individual turbine component efficiencies decreasing with size, since all these engines use similar kerosene fuels.

2.2 Simple Model for Turbine Efficiencies. As Denton [3] has shown, modeling the losses in practical turbines and compressors that are used in Brayton cycle engines is complex and still the subject of research. What is needed here is a semiempirical guide that elucidates the trends, rather than accurately predicting losses and therefore efficiencies.

The overall efficiency at maximum power output from a Brayton cycle (Brayton cycle thermal efficiency) is given by

$$\eta = \frac{\eta_{exp}\tau + \frac{1}{\eta_{exp}} - 2\sqrt{\tau}}{\tau + \frac{1}{\eta_{exp}} - 1 - \sqrt{\tau}} \qquad (1)$$

See Dixon [7], where τ is the ratio of the absolute inlet gas temperatures to the turbine and compressor, respectively, and η_{exp} is the turbine component efficiency. It is assumed that the compressor and turbine component efficiencies are the same, although in practice compressor losses tend to be greater than turbine losses. A Brayton cycle with regenerator can utilize some of the heat generated by the compressor and turbine inefficiencies. In this case, the overall cycle thermal efficiency at maximum power output from a Brayton cycle with a perfect regenerator is given by Decher [8]

$$\eta = 1 - \frac{1}{\eta_{exp}\sqrt{\tau}} \qquad (2)$$

Equations (1) and (2) are plotted in Fig. 2, for a selection of turbine inlet temperatures assuming a 20°C compressor inlet temperature.

The plot demonstrates that turbine component efficiencies (turbine and compressor) have to be above about 50% to get power from a practical Brayton cycle. Both equations (1) and (2) show that for any net power output to be possible:

$$\eta_{exp} \geq \frac{1}{\sqrt{\tau}} \qquad (3)$$

Thus, the lowest possible turbine component efficiency is limited by the maximum operating temperatures of the material that the turbine is built from. A regenerator will not compensate for efficiency losses, if the turbine and compressor performance are too poor. It is important to note that in this simple analysis the losses from friction (e.g., bearing losses), incomplete combustion, and heat losses (from the engine casing or by conduction through engine components) have not been considered. These additional losses would require higher turbine component efficiencies to get power from a practical Brayton cycle. In any case, Eq. (3) represents one important constraint; a Brayton cycle will have to overcome as it is scaled down.

Heat Losses From the Casing. We will now estimate how the heat losses from the casing scale with engine size. Engineers expect the usual 2/3rds power law, which is simply due to the ratio of surface area to volume of the machine. Approximate equations
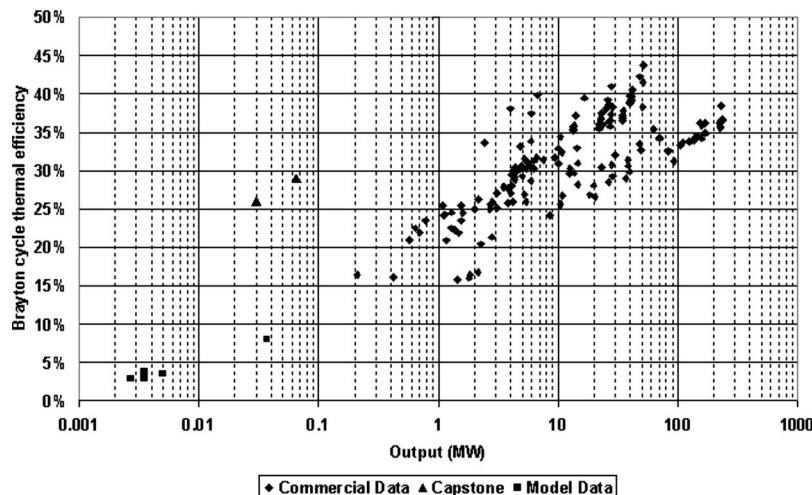
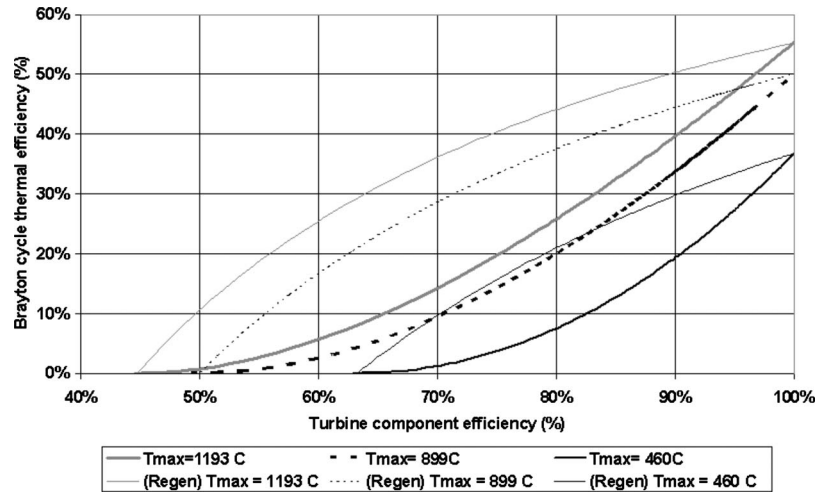**Fig. 1 Practical air breathing Brayton cycle machine efficiencies**

Fig. 2 Brayton cycle thermal efficiency versus turbine component efficiency, assuming 20°C inlet temperature to the compressor (**thick lines simple cycle; thin lines with regenerator**)

for the flow of heat from the casing to the environment and the flow of heat convected through the machine can be written as

$$Q_L \approx \text{Nu } kD\Delta T \tag{4}$$

where the length of the machine is of the same order of magnitude as the diameter.

$$Q_C \approx Mc\rho C_p D^2 \Delta T \tag{5}$$

See Fig. 3 for a schematic of the heat flows.

The worst case is assumed; heat conduction through the gas in the machine to the casing dominates the process of heat flow to the environment. That is, the Biot number very much less than 1, thus the conductivity of the material from which the turbine is made is so large that it can be ignored and thus the driving temperature differences are on the gas side.

In Eq. (4), Q_L is the rate of heat loss from the casing, where Nu is the Nusselt number, k the thermal conductivity of the gas flowing through the machine, D the typical length scale for the machine (the rotor diameter), and ΔT the maximum temperature difference. While in Eq. (5), Q_C is the rate of heat flow through the machine that is convected by the gas; M is the Mach number, c the velocity of sound, and ρC_p the specific heat per unit volume of the gas.

This leads to an estimation of the ratio of heat losses to convective heat flow as

$$\frac{Q_L}{Q_C} = \frac{\text{Nu}}{M} \frac{\nu_{\text{th}}}{c} \frac{1}{D} \tag{6}$$

The thermal diffusivity ($\nu_{\text{th}} = k/\rho C_p$) divided by the speed of sound for air at 800°C is about 5.5×10^{-7} m. For laminar flow, the Nusselt number is about 2, so the worst case is for turbulent flow where the Nusselt number would behave similarly to the correlation developed by Partridge (see McAdams [9]):
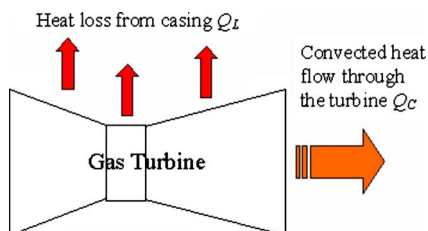
Fig. 3 Schematic of heat losses from turbine casing

$$\text{Nu} = 0.023 \, \text{Re}^{0.8} \, \text{Pr}^{0.4} \tag{7}$$

which would yield Nusselt numbers of about 100 for rotor diameters of 1 mm. Using a value of 100 for the ratio of the Nusselt number to Mach number, Eq. (6) estimates the heat loss for a 1 mm diameter turbine at 6%. Thus, for rotor sizes of 1 mm and above, heat losses from the turbine are small, relative to the heat flowing through the turbine. The heat losses in a small combustion chamber require the modeling of the chemical kinetics of the combustion process. In contrast to that, with a small diameter turbine, the losses may become significant for a small (1 mm or less combustion chamber), see Shan et al. [10]. For the simple model being developed here, heat losses will not be directly included. However, it will be assumed that all loss mechanisms are in some way related to the Reynolds number.

2.3 Model Assumptions. The model assumptions will be kept as simple as possible, in the spirit of developing a semiempirical model. The turbine component efficiencies of a conventional gas turbine will be assumed to depend only on the Reynolds number, so that all losses will be attributed in some way to the boundary layer. This is not unreasonable; since both the profile loss, which is generated in the boundary layers away from the end walls and the endwall loss (or secondary loss), will depend strongly on the Reynolds number. The tip leakage loss, which depends on the tolerance of clearance seals, will depend on the manufacturing method used and so will be optimized by the designer. The performance optimization at a particular machine size means that the ratios of the seal clearances and blade span to machine diameter will scale with machine size in some way, and so will be related to the Reynolds number.

The assumptions are as follows:

1. Both the turbine and compressor efficiencies are equal at any size (in practice compressor efficiencies are somewhat less than turbine efficiencies).
2. There is negligible heat loss.
3. 100% turbine component efficiencies outside the boundary layer.
4. The boundary layer does not contribute to the turbine component efficiencies.
5. The boundary layer grows like the flow over a flat plate at zero incidence angle.

A mathematical model using these assumptions will be used to obtain a *semiempirical fit* with the commercially available Brayton cycle data displayed in Fig. 1. This model, being a semiempir-

Journal of Engineering for Gas Turbines and Power

SEPTEMBER 2008, Vol. 130 / **052301-3**

ical model, should be primarily judged by how well the results fit the data. Obviously, there will be other parameters that will affect the scaling laws for a Brayton cycle, but hopefully they will be small enough for the model to give reasonable predictions for engineers to use as a guide as to the expected performance for a particular size of machine.

2.4 Scaling Equations. The purpose of building this simple mathematical model is to try and predict the scaling laws for Brayton cycle turbines (gas turbines). First of all, a simple expression for the turbine component efficiencies will be derived; this expression will then be related to the power output of a machine and its Brayton cycle thermal efficiency. The Brayton cycle thermal efficiency depends on whether or not the machine has a regenerator and the parameter τ, which is the ratio of the absolute temperature of inlet gas to the turbine to that of the compressor. Thus, there are two families of resultant curves to fit against practical data. The final expression has one free parameter $\dot{W}_0$, which is used to fit the practical Brayton cycle efficiency data shown in Fig. 1.

The turbine component efficiencies will be modeled by estimating the fraction of a turbine's flow cross sectional area that is filled by the boundary layer. The starting point of the model is the thickness of the boundary layer δ for turbulent flow over a flat plate at zero angle of incidence. From Schlichting [11], this is given by

$$\delta = 0.036 L \left(\frac{\nu}{UL} \right)^{1/5} \tag{8}$$

where ν is the kinematic viscosity of the fluid, L the length downstream from the start of the plate, and U the fluid's bulk velocity. Applying this to a turbine, L becomes the downstream distance from the entrance to the turbine, thus

$$\delta \propto L \left(\frac{\nu}{UL} \right)^{1/5} \tag{9}$$

Suppose that the turbine component efficiency η_{exp} is proportional to the fraction of the flow area that is not in the boundary layer. Thus,

$$\eta_{\mathrm{exp}} = \frac{D^2 - \phi \delta D}{D^2} = 1 - \phi \frac{\delta}{D} \tag{10}$$

where $\phi \approx 4 N_{\mathrm{blades}}/\pi$, N_{blades} is the number of blades and D is the effective flow diameter, such that $\pi D^2 = \pi (D_{\mathrm{tip}}^2 - D_{\mathrm{hub}}^2)$, D_{tip} is the diameter at the tip of the rotor and D_{hub} is the diameter of the hub.

The dimensionless geometric shape factor ϕ would have a value of about 40 for a turbine with 30 blades. Substituting δ from Eq. (9) into Eq. (10):

$$\eta_{\mathrm{exp}} = 1 - \phi_1 \frac{L}{D} \left(\frac{\nu}{UL} \right)^{1/5} \tag{11}$$

The dimensionless constant $\phi_1 = 0.036\phi$ is about unity. Equation (11) will now be used to predict the turbine component efficiencies as a function of machine power output and Brayton cycle thermal efficiency.

The power output from the turbine $\dot{W}$ depends on the flow through the turbine and its Brayton cycle thermal efficiency η:

$$\dot{W} = \eta \rho U D^2 C_p \Delta T \tag{12}$$

Thus,

$$\eta_{\mathrm{exp}} = 1 - \left(\frac{\eta \dot{W}_0}{\dot{W}} \right)^{1/5} \tag{13}$$

where

$$\dot{W}_0 = \nu \left(\frac{L^4}{D^3} \right) \rho C_p \Delta T \phi_1^5 \tag{14}$$

This result depends on the power output, Brayton cycle thermal efficiency (and therefore the maximum operating temperature of the cycle), as well as the diameter and length of the machine. The parameter $\dot{W}_0$ has the units of power and depends on the length

$$\left(\frac{L^4}{D^3} \right) = \lambda \tag{15}$$

The optimum performance of the machine will depend on choosing an optimum aspect ratio (D/L) for any particular size of machine. Thus, the length λ may scale with the power of the machine. Suppose that λ scales as the machine power output to some power α.

$$\lambda \propto \dot{W}^\alpha = \lambda_0 \left(\frac{\dot{W}}{\dot{W}_0} \right)^\alpha \tag{16}$$

Then Eq. (13) simplifies to

$$\eta_{\mathrm{exp}} = 1 - \eta^{1/5} \left(\frac{\dot{W}_1}{\dot{W}} \right)^\beta \tag{17}$$

where

$$\dot{W}_1 = \left(\frac{\nu \lambda_0 \rho C_p \Delta T \phi_1^5}{\dot{W}_0^\alpha} \right)^{(1+\alpha)} $$

where $\beta = 1 - \alpha/5$, and $\dot{W}_0$ is a constant to be determined that has the dimension of power and will depend on the kinematic viscosity of the working fluid. From Eq. (15) and (16), the aspect ratio of a machine scales as

$$\left(\frac{D}{L} \right) = \left(\frac{L}{\lambda_0} \right)^{1/3} \left(\frac{\dot{W}}{\dot{W}_1} \right)^{-\alpha/3} \tag{18}$$

If $\alpha = 0$, then $\beta = \frac{1}{5}$ and $\dot{W}_1 = \dot{W}_0$, so that

$$\dot{W}_0 = \nu \rho C_p \Delta T \lambda_0 \phi_1^5 \tag{19}$$

For this scaling law to be true, the aspect ratio of the turbines must scale only with the cube root of the machine length, $(D/L) = (L/\lambda_0)^{1/3}$. If this were true, it would mean that very large axial machines would become slightly "fatter" in proportion to their smaller cousins. However, this would happen only as the cube root of the machine length. The result would be different for radial machines since L was defined as the downstream distance from the entrance to the turbine inlet, which for a radial turbine would be D, and thus would lead to a scaling law for radial machines, $(D/L) = (\lambda_0/D)^{1/4}$. Further work would be necessary to find the correct value of α, but α is expected to be close to zero. The only effect of a nonzero value of α would be to change the value of β slightly in the scaling law (Eq. (17)).

A value of $\beta = \frac{1}{5}$ will be used for the purpose of analyzing the collected data shown in Fig. 1.

For a Brayton cycle machine with an air inlet pressure of 1 atm and with a temperature rise of $700\,°\mathrm{C}$ in the combustor ($\Delta T = 700$), Eq. (19) reduces to $\dot{W}_0 \approx 13 \lambda_0 \phi_1^5$ W. The value of $\lambda_0 \phi_1^5$ would have to be determined by a more rigorous fluid dynamic analysis. However, empirically the constant $\dot{W}_0$ can be determined from the data displayed in Fig. 1 (all the machines surveyed burn hydrocarbons in air). Different working fluids will have different values for the parameter $\dot{W}_0$.

2.5 Machine Minimum Diameter Estimation for a Brayton Cycle. If Eq. (17) with $\beta = \frac{1}{5}$ is taken as a reasonable estimate of the scaling law for practical Brayton cycle machines, then by
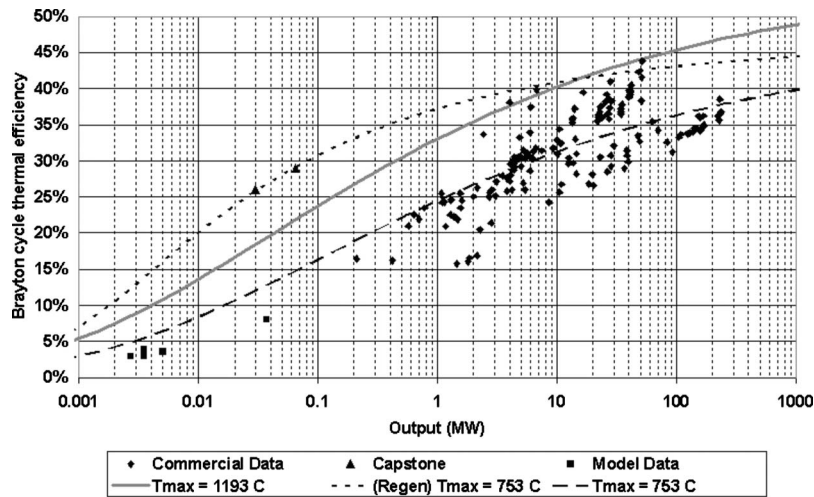
Fig. 4 Comparison of practical Brayton cycle machine efficiencies with the semiempirical scaling law for different turbine inlet temperatures with $\dot{W}_0$ = 200 W

combining Eq. (12) and (17), and assuming that the quantity $(\nu\lambda_0\phi_1^2/U)^{1/2}$ does not vary significantly with the size of machine, an estimate of the minimum practical diameter of a machine may be made from the following expression:

$$D_{min} = D_{set}\left[\frac{1 - \eta_{exp\ set}}{1 - \eta_{exp\ min}}\right]^{5/2} \qquad (20)$$

The minimum size may be estimated by taking the minimum turbine component efficiency, $\eta_{exp\ min}$, to be 50% (from Fig. 2) and data from Gerendás and Pfister [12] who have built a working turbine with a 74 mm diam rotor attaining a turbine efficiency of 85% and a compressor efficiency of 77%. Using these two figures for the turbine component efficiencies yields a minimum diameter of between about 11 mm and 4 mm. It means that a Brayton cycle turbine would just have enough power to turn over and smaller machines would not work at all. This estimate is uncomfortably close to the MEMS size range.

3 Comparison of the Scaling Law With Engineering Data

3.1 Data From Air Breathing Machines. The data displayed in Fig. 1 can now be fitted to Eq. (17) with $\beta = \frac{1}{5}$, and using Eqs. (1) and (2) for the Brayton cycle thermal efficiency for a given temperature ratio τ. These equations form the basis of a semiempirical scaling law for Brayton cycle machines and are compared to the practical data already shown in Fig. 1. The compressor inlet temperature is taken as 20°C, and the curves are fitted for values of τ of 5 and 3.5 for a simple cycle and 3.5 for a cycle with a regenerator. The same value of the free parameter $\dot{W}_0$ (200 W) is used for all three curves that are shown in Fig. 4, this value gives a good fit to the data. The value of 200 W for $\dot{W}_0$ corresponds to a scaling length λ_0 of about 2.5 m, for a shape factor ϕ of 40.

The semiempirical scaling law seems to exhibit the correct behavior compared to the collected data. The conclusion from these data and the semiempirical scaling law is that there is a minimum physical size that a practical working Brayton cycle machine can attain. This size is estimated to be between about 4 mm and 11 mm according to Eq. (20). Attempts have been made to build MEMS scale conventional Brayton cycle machines; in particular, Epstein [13] has been a pioneer in this field and has built a radial machine with 8 mm compressor and 6 mm turbine rotor diam-

eters. It should be noted that all the foregoing analysis applies to conventional axial turbomachines, and the conclusion is the smaller they are; the worse their expansion efficiency.

3.2 Brayton Cycle Machines With Atypical Working Fluids. Air is the working fluid normally used by Brayton cycle machines. However, NASA has carried out an extensive development program for closed cycle Brayton engines suitable for power generation in space applications using other working fluids. To extend the foregoing analysis for these working fluids, data have been taken from Mason et al. [14], Shaltens and Mason [15], Shaltens and Boyle [16], and Shaltens [17]. The Brayton cycle machines in these studies use a mixture of helium and xenon (with a mean molecular weight of either 40 g/mol or 84 g/mol) pressurized to operate at a compressor inlet pressure of 0.5 MPa as the working fluid [18].

These data for the Brayton cycle engines with a regenerator and a working fluid, which is a mixture of helium and xenon, are plotted in Fig. 5. It should be noted that the efficiency data point at 2 kW was the result of an extensive experimental test program. The empirical value of $\dot{W}_0$ (200 W) that was found for machines that use air as the working fluid now has to be scaled using Eq. (19). The viscosity of the He/Xe mixture is taken from Johnson [19] and the values of the specific heat were calculated assuming a perfect gas law, and a temperature rise ΔT of 700°C. The semiempirical scaling law is plotted on the same figure for temperature ratios 5, 4, and $\dot{W}_0$ = 66 W, to be compared to the data using a He/Xe with a mean molecular weight of 84. Also plotted is the semiempirical scaling law for a temperature ratio of 3 and $\dot{W}_0$ = 140 W for comparison to the data using a mean molecular weight of 40.

The turbines produce a remarkable performance for their size, in part, because the working fluid has lower specific heat than air, although the dynamic viscosity is slightly higher. This scales the value of $\dot{W}_0$ down compared to air, from Eq. (19), and therefore leads to higher expansion efficiencies at lower powers compared to air.

The next section will look at the expansion efficiency of viscous transfer turbines of which the Tesla turbine is a good example. Unfortunately, efforts to develop Tesla turbines have concentrated on competition with conventional turbines at the scales were they do best (multi kilowatt and above). Rice [20] is prob-
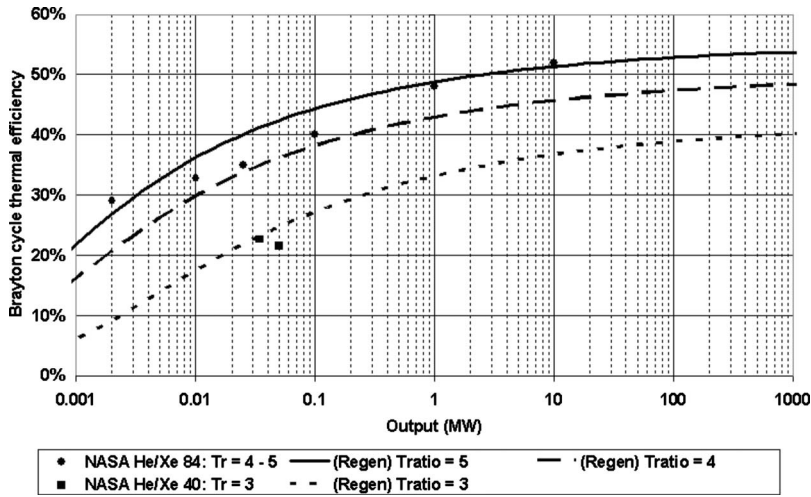
Fig. 5 Comparison of NASA closed Brayton cycle machine efficiencies with the semiempirical scaling law

4 One Dimensional Viscous Flow Turbines

4.1 Incompressible Flow. In order to understand the limits of a practical viscous flow turbine, an analysis of a one dimensional viscous flow turbine will be carried out. The analysis will assume incompressible flow. The one dimensional viscous flow turbine is not a practical engineering proposition, but merely a way to help understand what limits the performance of a viscous flow turbine. Figure 6 below shows an implementation of a one dimensional viscous flow turbine. There are of course no blades, in common with a practical viscous flow turbine, such as a Tesla turbine. The sides of the belts are not considered, and both belts are geared to run at the same speed.

The pressure at the outlet has a numerical value of zero, that is, P_{res} is the pressure difference between the reservoir and the atmosphere. The continuity equation in the turbine is very simple, since there is incompressible flow and no area change:

$$\frac{\partial V}{\partial x} = 0 \qquad (21)$$

Therefore, V is a constant and equal to the outlet velocity of the fluid from the turbine. The energy equation is integrated to give

$$P + \frac{1}{2}\rho V^2 + C_p T = h = P_{res} \qquad (22)$$

There is no enthalpy added so the inlet pressure to the turbine P_{in} is given by
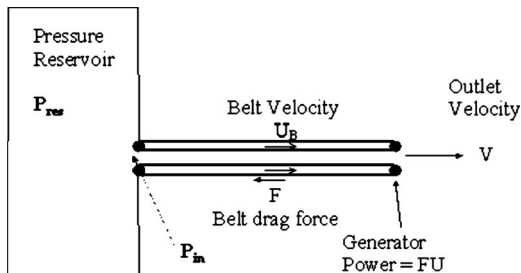
Fig. 6 1D viscous flow turbine

$$P_{in} = P_{res} - \frac{1}{2}\rho V^2 \qquad (23)$$

The momentum equation in the turbine predicts the pressure drop

$$\Delta P_{turbine} = \chi P_{res} f(\theta) \qquad (24)$$

$$F = A\chi P_{res} f(\theta) \qquad (25)$$

The pressure drop has been expressed, as a fraction χ of P_{res}. Note that no assumption has been made as to what type of flow there is in the turbine (laminar or turbulent).

This is expressed as a function $f(\theta)$, where $\theta = U_B/V$. F is the total drag force on both the belts that make up the turbine. A is the cross-sectional area of the flow channel (the height of the channel between the belts times their width). Also, the energy equation enables the pressure drop to be expressed in terms of P_{res} and the kinetic energy of the exiting fluid:

$$\Delta P_{turbine} = P_{in} = P_{res} - \frac{1}{2}\rho V^2 \qquad (26)$$

Thus,

$$V = \sqrt{\frac{2P_{res}(1 - \chi f(\theta))}{\rho}} \qquad (27)$$

Power extracted from the turbine is then calculated by

$$\dot{W}_{1D} = FU = AP_{res}\chi f(\theta) U_B \qquad (28)$$

$$\dot{W}_{1D} = AP_{res} V\chi f(\theta)\theta \qquad (29)$$

The maximum power that could possibly be collected from any machine working between the pressure reservoir and atmosphere is given by

$$\dot{W}_{max} = AP_{res} V_1 = A\frac{1}{2}\rho V_1^3$$

$$V_1 \text{ velocity at } \theta = 1 \qquad (30)$$

Therefore,

$$\dot{W}_{max} = A\frac{1}{2}\rho \left(\frac{2P_{res}}{\rho}\right)^{3/2} \qquad (31)$$

The turbine component efficiency of the turbine is defined in terms of the power extracted divided by the maximum power that is available:

$$\eta_{1D} = \frac{\dot{W}_{1D}}{\dot{W}_{max}} = \frac{VP_{res}\chi f(\theta)\theta}{\frac{1}{2}\rho\left(\frac{2P_{res}}{\rho}\right)^{3/2}} \tag{32}$$

Thus,

$$\eta_{1D} = \frac{\sqrt{\frac{2P_{res}(1-\chi f(\theta))}{\rho}}P_{res}\chi f(\theta)\theta}{\frac{1}{2}\rho\left(\frac{2P_{res}}{\rho}\right)^{3/2}} \tag{33}$$

Therefore,

$$\eta_{1D} = \sqrt{(1-\chi f(\theta))}\chi f(\theta)\theta \tag{34}$$

The maximum turbine component efficiency for a given velocity ratio θ is found by finding the optimum geometry through the parameter χ.

$$\frac{\partial \eta_{1D}}{\partial \chi} = f(1-\chi f)^{1/2}\theta - \frac{1}{2}f^2\chi(1-\chi f)^{-1/2}\theta \tag{35}$$

If $\chi f \neq 1$ and $f\theta \neq 0$

$$0 = (1-\chi f) - \frac{1}{2}\chi f \tag{36}$$

Therefore,

$$\chi f = \frac{2}{3} \tag{37}$$

Thus,

$$\eta_{\chi opt} = \frac{2}{3}\left(\frac{1}{3}\right)^{1/2}\theta \tag{38}$$

The maximum turbine component efficiency is obtained as $\theta \rightarrow 1$,

$$\eta_{max} = \frac{2}{3\sqrt{3}} = 38.49\% \tag{39}$$

This is the maximum turbine component efficiency of a one dimensional viscous flow turbine using incompressible flow. The flow of power through the system is summarized below.

In available power,

$$AP_{res}V_1 \quad 100\%$$

In maximum power collected by belt,

$$AP_{res}V_1\frac{2}{3}\frac{1}{\sqrt{3}} \quad 38.49\%$$

In maximum power not collected by belt,

$$AP_{res}V_1\left(1-\frac{2}{3\sqrt{3}}\right) \quad 61.51\%$$

The uncollected power can be attributed to the following:

(a)   exit losses,

$$(1-\chi f)AP_{res}V_1 = \frac{1}{3}AP_{res}V_1 \quad 33.33\%$$

(b)   heat dissipated to fluid,

$$AP_{res}V_1\frac{2}{3}\left(1-\frac{1}{\sqrt{3}}\right) \quad 28.18\%$$

4.2 Compressible Flow. An analysis of a compressible flow viscous turbine is more difficult and will not be covered here. However, the work reported in this paper was motivated by an extensive experimental test program carried out on a 50 mm diam

Table 2 Experimental maximum turbine component efficiencies: measured and inferred allowing for bearing losses

P inlet (kPa)	Maximum efficiency (dynamometer)	Maximum efficiency (no losses)	Fraction of incompressible limit
111	18.0%	37.3%	0.97
121	22.0%	42.0%	1.09
131	23.5%	44.2%	1.15
142	23.0%	43.8%	1.14
151	22.5%	41.1%	1.07
170	21.0%	41.5%	1.08

rotor Tesla type turbine, which will be reported separately in Experimental Thermal and Fluid Science. The tests were carried out using compressed air, the turbine exit venting to atmosphere with turbine inlet pressures from 110 kPa to 170 kPa (170 kPa is about the stagnation pressure of sonic flow at 100 kPa).

A summary of the test results is reported below in Table 2. This shows the maximum efficiency (as measured at the dynamometer) for each inlet pressure, together with the maximum efficiency that would be expected when the parasitic losses from the bearings are included. The rotation speed at maximum efficiency was between 25,000 rpm and 70,000 rpm. A viscous turbine under incompressible flow would be expected to have a maximum efficiency of 38.5%, so the inferred no loss efficiency is also shown as a fraction of the incompressible limit. These measurements show that the maximum expansion efficiency of a viscous flow turbine with compressible flow is very close to the incompressible flow value.

5 Discussion

In the foregoing analysis, we have explored the effect of scaling down on the performance of Brayton cycle turbomachineries. Traditionally, turbomachines scale up well, i.e., the bigger the machines, the more efficient they are. Scaling down is a problem, however, with viscous losses making miniature turbines less efficient at smaller sizes. Despite that, highly compact microturbomachineries directed toward satisfying the demonstrated need for generating power at device size and output levels suitable for use in portable electronic appliances and other devices have been proposed [13,21]. In addition, and at somewhat larger sizes, such compact microturbomachineries have also been proposed for use as a combined heat and power source for residential buildings [22,23].

The preliminary work here has shown that a Brayton cycle might not be the appropriate cycle to use with these highly compact turbines as has been attempted by some of the reported research work [24–26]. It is interesting that the possibility of a Rankine cycle has been explored for MEMS sized turbines by Fréchette et al. [27], to avoid this problem.

Peirs et al. [24] have measured the turbine component efficiency of a Brayton cycle microturbine with a 10 mm rotor, generating up to 28 W mechanical power output. They report a turbine component efficiency of 18.4% at 160,000 rpm. Although later testing by the same authors [25] raises this value to between 20% to 24%. According to the semiempirical scaling laws proposed in Sec. 2.4 (Eq. (20)) and the estimate of the minimum rotor size that could sustain a Brayton cycle (between about 4 mm and 11 mm, at 50% turbine component efficiency), the expected maximum turbine component efficiency of their turbine would be between about 48% and 59%. Since their turbine rotation speed was limited by the maximum speed of their bearings, they would have expected higher turbine component efficiency, if they had been able to run at their design rotation speed of 210,000 rpm. These data are not a definitive test of the semiempirical scaling, but are consistent with it. It should be remembered that to make predic-
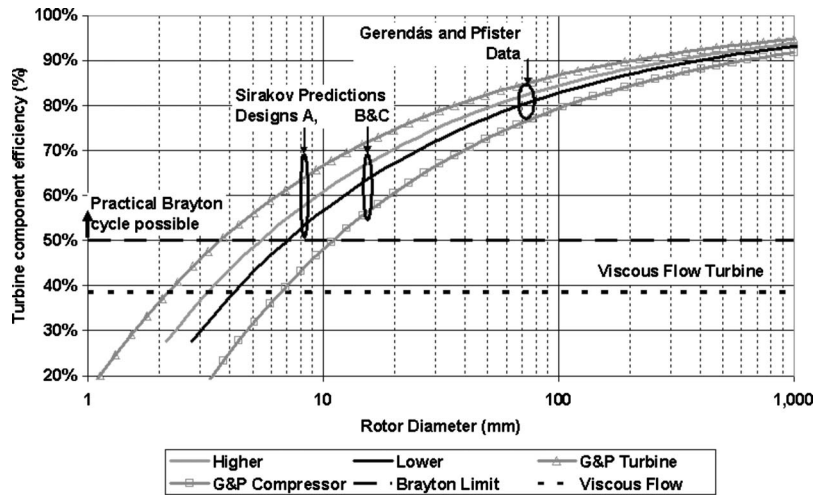
Fig. 7 Possible scaling laws for viscous and conventional turbines at MEMS scale

tions at MEMS sizes (below about 20 mm) the semiempirical scaling law has been extended beyond the range of collected data that it has been fitted to.

This was also the case with the 38.49% maximum turbine component efficiency of a viscous flow turbine that restricts the type of cycle that can be used for power generation. However, viscous flow turbines, although starting from a low base, have the advantage that they hold the promise to scale down well as was indicated by the preliminary analysis of a one dimensional turbine and the performance measurements of the 50 mm diam rotor Tesla type turbine. In other words, these preliminary results indicate that the expansion efficiency is not likely to change much as the turbine is scaled down. Further work is being undertaken to show experimentally that viscous flow machines have a maximum turbine component efficiency of 38.49% and that this figure does not change as the turbine is scaled down to MEMS sizes. A conventional bladed turbine may also behave as a viscous flow turbine as the design is scaled down; if when the viscous forces dominate, there is a net torque to turn the rotor. However, since bladeless, viscous flow turbines are easier to construct; any application (such as a micropump) would take advantage of the simplicity of the design offered by a viscous flow turbine.

These ideas are summarized in Fig. 7, which shows that for rotor diameters smaller than between about 11 mm and 4 mm, a practical Brayton cycle is no longer possible and for rotor diameters smaller than between about 7 mm and 2 mm a viscous flow turbine will be more efficient than a conventional turbine. Also plotted are the experimental data of Gerendás and Pfister [12] and the model predictions of Sirakov [28], see Table 3. These data are plotted as ovals covering the turbine efficiency (top of the oval) and the compressor efficiency (bottom of the oval), since the scaling law assumes that the turbine and compressor efficiencies are the same. The curves labeled higher and lower are the scaling law fits from Fig. 3 for values of τ of 4 and 3. The curves labeled G&P Turbine and G&P Compressor use the turbine and compressor

Table 3 Data from microturbines

	Rotor diameter (mm)	Turbine efficiency	Compressor efficiency
Gerendás and Pfister (measured)	74	85%	77%
Sirakov Prediction Design A	8.8	69%	50%
Sirakov Prediction Design B	16	69%	59%
Sirakov Prediction Design C	16	65%	54%

efficiencies from Gerendás and Pfister [12] in Eq. (20). The curves give an indication of the minimum practical size for a working Brayton cycle.

A great deal of experimental work will have to be done to check the ideas presented here. However, a better understanding of the scaling laws for MEMS machines is a major part of the research effort that is being undertaken worldwide. Modern commercial turbines have been developed over the last 50 years; perhaps in the next 50 years commercial MEMS machines may carry the same importance as is presently enjoyed by the large turbines of today.

6 Conclusions

The case has been made that MEMS sized turbomachinery should be based on viscous transfer design principles because conventional bladed designs are likely to have much poorer turbine component efficiencies for rotor diameters less than 7–2 mm. Practical MEMS sized machines are most likely to be used with a Rankine cycle, a Brayton cycle being impractical for rotor diameters less than 11–4 mm.

Acknowledgment

Nomenclature

c = velocity of sound
C_p = specific heat per unit mass of the gas
D = rotor diameter (the typical length scale for the machine)
D_{min} = minimum practical diameter for a working machine
D_{set} = rotor diameter of a working machine with a measured turbine component efficiency $\eta_{exp\,set}$
A = cross-sectional area of the flow channel in the belt turbine
F = drag force on both the belts that make up the belt turbine
h = enthalpy of the fluid
k = thermal conductivity of the gas flowing through the machine
L = length of the machine
M = Mach number
N_{blades} = number of blades in a stage

Nu = Nusselt number

P = pressure

P_{in} = inlet pressure to belt turbine

P_{res} = reservoir pressure for the belt turbine

Pr = Prandtl number=$\mu C_p / k$

$\Delta P_{\mathrm{turbine}}$ = pressure drop across belt turbine

Q_C = rate of heat flow through the machine convected by the gas

Q_L = rate of heat loss from the casing

Re = Reynolds number=UL/ν

T = absolute temperature

ΔT = maximum temperature difference between the gas in the machine and ambient

U = bulk velocity of gas in the machine

U_B = velocity of belt in belt turbine

V = fluid outlet velocity from the belt turbine

$\dot{W}$ = power output (as work rate) from the machine

$\dot{W}_0$ = empirical constant used in model scaling equation (units Watts)

$\dot{W}_1$ = parameter used in model scaling equation (units Watts)

$\dot{W}_{1\mathrm{D}}$ = power extracted from belt turbine

$\dot{W}_{\mathrm{Max}}$ = maximum power extracted from belt turbine

x = Cartesian distance along belt turbine

α = exponent in power law for aspect ratio scaling (Eq. (16))

β = exponent in turbine scaling law (Eq. (17))

δ = boundary layer thickness

η = Brayton cycle thermal efficiency

η_{exp} = turbine component efficiency (turbine expansion efficiency or compressor efficiency)

$\eta_{\mathrm{exp\,set}}$ = measured turbine component efficiency for a rotor diameter D_{set}

$\eta_{\mathrm{exp\,min}}$ = minimum turbine component efficiency for a working machine ($\sim 50\%$)

$\eta_{1\mathrm{D}}$ = turbine component efficiency of belt turbine

$\eta_{\chi\mathrm{opt}}$ = optimum turbine component efficiency of belt turbine as a function of θ

η_{max} = maximum turbine component efficiency of belt turbine

τ = ratio of the absolute inlet gas temperatures to the turbine and compressor respectively

ρ = gas density

μ = dynamic viscosity of the gas

ν = kinematic viscosity

ν_{th} = thermal diffusivity of the gas

θ = ratio of belt velocity to outlet fluid velocity

ϕ = dimensionless geometric shape factor

ϕ_l = dimensionless geometric shape factor =0.036ϕ

λ = length associated with machine aspect ratio (Eq. (15))

χ = pressure drop in the belt turbine expressed as a fraction of P_{res}

References

[1] Marden, J. H., and Allen, L. R., 2002, "Molecules, Muscles, and Machines: Universal Performance Characteristics of Motors," Proc. Natl. Acad. Sci. U.S.A., **99**(7), pp. 4161–4166.

[2] Wang, Z. J., 2005, "Dissecting Insect Flight," Annu. Rev. Fluid Mech., **37**, pp. 183–210.

[3] Denton, J. D., 1993, "Loss Mechanisms In Turbomachines," ASME J. Turbomach., **115**(4), pp. 621–656.

[4] Nye, M., 1996, "Gas-Turbines By Heat Rate," http://www.gas-turbines.com/specs/heatrt.htm

[5] Capstone, 2006, "Capstone Turbine Corporation—Technology Tour—Data Sheets," http://microturbine.com/prodsol/techtour/downloads/datasheets.asp

[6] Martens, T., 2004, "Model Turbine Specification List," http://www.airtoi.nl/turbines.php3

[7] Dixon, S. L., 1998, *Fluid Mechanics and Thermodynamics of Turbomachinery*, Butterworth-Heinemann.

[8] Decher, R., 1994, *Energy Conversion: Systems, Flow Physics and Engineering*, Oxford University Press, New York.

[9] McAdams, W. H., and 1954, *Heat Transmission*, McGraw-Hill, New York.

[10] Shan, X. C., Wang, Z. F., Jin, Y. F., Wu, M., Hua, J., Wong, C. K., and Maeda, R., 2005, "Studies on a Micro Combustor for Gas Turbine Engines," J. Micromech. Microeng., **15**(9), pp. 215–221.

[11] Schlichting, H., 1979, *Boundary-Layer Theory*, McGraw-Hill, New York.

[12] Gerendás, M. P. R., 2000, "Development of a Very Small Aero-Engine," 45th ASME International Gas Turbine and Aeroengine Technical Congress and Exposition, Munich, Germany.

[13] Epstein, A. H., 2004, "Millimeter-Scale, Micro-Electro-Mechanical Systems Gas Turbine Engines," ASME J. Eng. Gas Turbines Power, **126**(2), pp. 205–226.

[14] Mason, L. S., Shaltens, R. K., Dolce, J. L., and Cataldo, R. L., 2002, "Status of Brayton Cycle Power Conversion Development at NASA GRC," Space Technology and Applications International Forum (STAIF-2002) sponsored by the American Institute of Aeronautics and Astronautics Albuquerque, NM.

[15] Shaltens, R. K., and Mason, L. S., 1999, "800 Hours of Operational Experience From a 2 kWe Solar Dynamic System," Space Technology and Applications International Forum Albuquerque, NM.

[16] Shaltens, R. K., Boyle, R. V., 1995, "Initial Results From the Solar Dynamic (SD) Ground Test Demonstration (GTD) Project at NASA Lewis," 30th Intersociety Energy Conversion Engineering Conference, Orlando, FL.

[17] Shaltens, R. K., 2002, "Advanced Solar Dynamic," http://www.grc.nasa.gov/WWW/tmsb/dynamicpower/doc/adv_sd_tech.html

[18] Johnson, P. K., and Mason, L. S., 2006, "Performance and Operational Characteristics for a Dual Brayton Space Power System With Common Gas Inventory," The Fourth International Energy Conversion Engineering Conference and Exhibit (IECEC), San Diego, CA.

[19] Johnson, P. K., 2006, "A Method for Calculating Viscosity and Thermal Conductivity of a Helium-Xenon Gas Mixture," Paper No. NASA CR-2006–214394.

[20] Rice, W., 1965, "An Analytical and Experimental Investigation of Multiple-Disk Turbines," ASME J. Eng. Power, **87**, pp. 29–36.

[21] Muller, N., and Frechette, L. G., 2002, "Performance Analysis of Brayton and Rankine Cycle Microsystems for Portable Power Generation," American Society of Mechanical Engineers, New Orleans, LO, pp. 513–522.

[22] Jacobson, S. A., Epstein, A. H., 2003, "An Informal Survey of Power MEMS," The International Symposium on Micro-Mechanical Engineering, Tsuchiura, Japan.

[23] Yagoub, W., Doherty, P., and Riffat, S. B., 2006, "Solar Energy-Gas Driven Micro-CHP System for an Office Building," Appl. Therm. Eng., **26**(14–15), pp. 1604–1610.

[24] Peirs, J., Reynaerts, D., and Verplaetsen, F., 2003, "Development of an Axial Microturbine for a Portable Gas Turbine Generator," J. Micromech. Microeng., **13**(4), pp. 190–195.

[25] Peirs, J., Reynaerts, D., and Verplaetsen, F., 2004, "A Microturbine for Electric Power Generation," Sens. Actuators, A, **113**(1), pp. 86–93.

[26] Isomura, K., Murayama, M., Yamaguchi, H., Ijichi, N., and Kawakubo, T., 2002, "Feasibility Study of a Micromachine Gas Turbine," Ishikawajima-Harima Eng. Rev., **42**(3), pp. 177–183.

[27] Fréchette, L. G., Lee, C., Arslan, S., Liu, Y. C., 2003, "Preliminary Design of a MEMS Steam Turbine Power Plant on-a-Chip," Third International Workshop on Micro & Nano Tech. for Power Generation & Energy Conv. (PowerMEMS'03), Makuhari, Japan.

[28] Sirakov, B. T., 2005, "Characterization and Design of Non-Adiabatic Micro-Compressor Impeller and Preliminary Design of Self-Sustained Micro Engine System," Massachusetts Institute of Technology.

Static and Dynamic Characteristics for a Pressure-Dam Bearing

Bader Al-Jughaiman

Rotating Equipment Engineer
Saudi Aramco,
Dhahran 31311, Saudi Arabia
e-mail: bader.jughaiman@aramco.com

Dara Childs

The Leland T. Jordan Professor of Engineering
Texas A&M University,
College Station, TX 77843-3123
e-mail: dchilds@tamu.edu

*Measured rotordynamic force coefficients (stiffness, damping, and added mass) and static characteristics (eccentricity and attitude angle) of a pressure-dam bearing are presented and compared to predictions from a Reynolds-equation model, using an isothermal and isoviscous laminar analysis. The bearing's groove dimensions are close to the optimum predictions of Nicholas and Allaire (1980, "Analysis of Step Journal Bearings-Infinite Length and Stability," ASLE Trans., **22**, pp. 197–207) and are consistent with current field applications. Test conditions include four shaft speeds (4000 rpm, 6000 rpm, 8000 rpm, and 10000 rpm) and bearing unit loads from 0 kPa to 1034 kPa (150 psi). Laminar flow was produced for all test conditions. A finite-element algorithm was used to generate solutions to the Reynolds-equation model. Excellent agreement was found between predictions and measurements for the eccentricity ratio and attitude angles. Predictions of stiffness and damping coefficients are in reasonable agreement with measurements. However, experimental results show that the bearing has significant added mass of about 60 kg at no-load conditions, versus zero mass for predictions from the Reynolds-equation model and 40 kg using Reinhardt and Lund's (1975, "The Influence of Fluid Inertia on the Dynamic Properties of Journal Bearings," ASME J. Lubr. Technol., **97**, pp. 159–167) extended Reynolds-equation model for a plain journal bearing. The added mass quickly drops to zero as the load increases. Measured results also show a whirl frequency ratio near 0.36 at no-load conditions; however, a zero whirl frequency ratio was obtained at all loaded conditions, indicating an inherently stable bearing from a rotordynamics viewpoint.* [DOI: 10.1115/1.2906173]

Introduction

As illustrated in Fig. 1, pressure-dam bearings are used in many types of rotating machinery because of their higher threshold speed of instability compared to plain journal bearings. They are also easier to manufacture and have better manufacturing tolerances than multilobe bearings [1]. The improvement in stability comes from the step or dam cut in the upper surface of the bearing that produces a pressure rise near the step and a downward force on the journal. Because of this induced load, the rotor operates at a higher eccentricity ratio. The bottom pad is normally deeply grooved to create a circumferential relief track. This track reduces the effective bearing length, reducing load capacity and increasing the nominal journal eccentricity. The bearing in Fig. 1 has a step at the top (unloaded pad) and a relief track at the bottom pad. The figure shows the most important design parameters for pressure-dam bearing, namely, step film thickness ratio $k' = h_1/h_2$, dam axial length ratio $\bar{L}_d = L_d/L$, and relief track axial length ratio $\bar{L}_t = L_t/L$.

Allaire et al. [1] compared the theoretical pressure profile for an infinite-length pressure-dam bearing calculated by finite element method to experimental results. They found that the inertia theory that includes both flow turbulence and pressure drop at the step agrees well with the experimental results. However, they also found that the pressure drop at the step can be neglected for bearings with Reynolds number smaller than 1500. Laminar flow theory fails for Reynolds number greater than 50.

Nicholas and Allaire [2] analyzed the stability of finite length pressure-dam bearings and found, that for maximum stability, that the bearing should be designed for $k' = 3 - 6$ and θ_s

$= 125 - 160$ deg. They predicted the whirl-frequency ratio (WFR) for an optimum bearing to be between 0.33 and zero depending on the bearing design and operating conditions.

Nicholas et al. [3], Leader et al. [4], and Lanes et al. [5] reported experimental WFR results for near-optimum pressure-dam bearings supporting flexible rotors to be 0.35, 0.36, and 0.34, respectively. These measured WFRs were determined by comparing the rotor maximum speed just before high subsynchronous vibration is produced to the rotor critical speed. This approach does not provide a full stability map, i.e., WFR versus bearing load, and provides no information about the bearing stiffness, damping, and inertia coefficients.

The effect of fluid-film inertia is ignored in developing the Reynolds-equation because the C_r/R ratio is on the order of 0.001 and produces small Reynolds number (order of 1). The bearing force coefficients based on Reynolds model can be written as

$$-\begin{bmatrix} f_{bx} \\ f_{by} \end{bmatrix} = \begin{bmatrix} K_{xx} & K_{xy} \\ K_{yx} & K_{yy} \end{bmatrix} \begin{bmatrix} \Delta x \\ \Delta y \end{bmatrix} + \begin{bmatrix} C_{xx} & C_{xy} \\ C_{yx} & C_{yy} \end{bmatrix} \begin{bmatrix} \Delta \dot{x} \\ \Delta \dot{y} \end{bmatrix} \qquad (1)$$

Reinhardt and Lund [6] showed that fluid inertia effects could be significant for Reynolds number on the order of 100 without affecting the assumption of laminar flow. Reinhardt and Lund's model is

$$-\begin{bmatrix} f_{bx} \\ f_{by} \end{bmatrix} = \begin{bmatrix} K_{xx} & K_{xy} \\ K_{yx} & K_{yy} \end{bmatrix} \begin{bmatrix} \Delta x \\ \Delta y \end{bmatrix} + \begin{bmatrix} C_{xx} & C_{xy} \\ C_{yx} & C_{yy} \end{bmatrix} \begin{bmatrix} \Delta \dot{x} \\ \Delta \dot{y} \end{bmatrix} + \begin{bmatrix} M_{xx} & M_{xy} \\ M_{yx} & M_{yy} \end{bmatrix}$$
$$\times \begin{bmatrix} \Delta \ddot{x} \\ \Delta \ddot{y} \end{bmatrix} \qquad (2)$$

This paper presents measured results for both static and dynamic performance of a near-optimum pressure-dam bearing and compares them to predictions from a laminar, isothermal, and inertialess flow model.

Fig. 1 Schematic view of pressure-dam bearing after Ref. [3]

Test Rig Description

Figure 2 shows the bearing test rig. Rodrigeuz and Childs [7] and Al-Ghasem and Childs [8] previously used it in measurements of a flexure pivot-pad bearing. The shaft is connected to a 65 kW air turbine with a high-speed flexible disk coupling and can run up to 16,000 rpm. The test shaft is made from stainless steel and

machined to a precise diameter of 116.8 mm (4.600 in.) at the bearing location. It is supported on the pedestals through angular-contact ball bearings, spaced approximately 457 mm (18 in.) apart. An oil-mist system lubricates the ball bearings.

The stator section holds the test bearing and all the associated instrumentation, namely, noncontacting eddy-current proximity sensors, accelerometers, pressure transducers, and thermocouples. A pneumatic loader and two hydraulic shakers apply static and dynamic loads to the bearing stator. Six pitch stabilizers control the angular alignment between the bearing and the shaft. ISO VG32 turbine oil is delivered to the test section from an oil-supply system that can deliver oil up to a maximum pressure of 82.7 bars and a volumetric flow rate of 75 l/min. A heat exchanger and a set of pneumatically driven valves allow for control of the oil-supply temperature. Temperature probes are located in the oil-inlet chamber as well as the downstream end caps. A static pressure probe measures the oil pressure at the inlet and outlet locations.

Four proximity probes, located in the stator end caps, measure the relative motion of the rotor with respect to the stator for each direction of excitation. Two proximity probes are placed in a plane at the nondrive end and two at a parallel plane at the drive end. The measurement of the stator position in two parallel planes allows monitoring and control of the stator's pitch and yaw. Piezoelectric accelerometers measure the stator absolute acceleration in both the x and y directions.

Experimental Procedures

Static Test Procedure. During a typical test, the bearing stator is centered on the shaft from results of a contact test using the shakers to proceed from one bearing surface to the other. Once the bearing is centered ($e_x = e_y = 0$), the rotor is run at a low speed, usually 4000 rpm. Then, the bearing is loaded using the static loader to the required load. Once the rotor reaches the required steady state, the following data are taken:

Fig. 2 Test rig cross section

(1) stator x and y positions in both drive end and nondrive end planes (e_x, e_y)
(2) rotor speed, ω
(3) oil volumetric flow rate, Q
(4) static load applied by the static loader, W
(5) oil-inlet temperature, T_i
(6) oil exit temperature, T_e
(7) bearing pad temperatures

This procedure is repeated with increasing bearing load, keeping the rotor speed constant, until the bearing eccentricity ratio $\varepsilon_0 = 0.85$ is reached. Then, the test is repeated again at a higher speed. Testing stops once the specified maximum test speed is reached (10,000 rpm), or excessive vibration or excessive temperature (ball bearing) is encountered. At each test condition, the bearing static characteristics, including eccentricity ratio ε_0 and attitude angle ψ, are calculated.

$$\varepsilon_0 = \frac{e}{C_r} = \frac{\sqrt{(e_x^2 + e_y^2)}}{C_r} \tag{3}$$

$$\psi = \tan^{-1}\left(\frac{e_x}{e_y}\right) \tag{4}$$

Dynamic Test Procedure. For a given static load, the rotor is brought up to the steady state conditions of speed and oil-inlet temperature. Then, the bearing stator is alternately excited using the hydraulic shakers with a prespecified pseudorandom dynamic excitation wave form with frequencies from 20 Hz to 300 Hz in 10 Hz increment in two orthogonal directions, i.e., x direction and the y direction (static load direction). The following data are collected for each test condition:

(1) transient excitation-force components in the x and y directions (f_x, f_y)
(2) transient stator acceleration in both the x and y directions (x, y)
(3) transient, relative rotor-stator displacement in both the x and y directions $(\Delta x(t), \Delta y(t))$

Each individual test result consists of 32 separate shakes that are averaged in the frequency domain.

Tests are repeated at different load conditions keeping the rotor speed constant until reaching the bearing eccentricity ratio $\varepsilon_0 = 0.80$. Dynamic tests are operated at lower maximum eccentricities than static tests to avoid rubbing while shaking. The same procedure is repeated for each test speed. Testing stops when either the top test speed is reached or either excessive vibrations or excessive ball-bearing temperatures are encountered.

The bearing force coefficients are calculated for each test condition using the parameter-identification procedure described by Childs and Hale [9]. The equations of motion for the stator mass M_s can be written as

$$M_s \begin{bmatrix} \ddot{x}_s \\ \ddot{y}_s \end{bmatrix} = \begin{bmatrix} f_x \\ f_y \end{bmatrix} - \begin{bmatrix} f_{bx} \\ f_{by} \end{bmatrix} \tag{5}$$

Substituting Eq. (2) into Eq. (5) and rearranging net

$$\begin{bmatrix} f_x - M_s \ddot{x}_s \\ f_y - M_s \ddot{y}_s \end{bmatrix} = -\begin{bmatrix} K_{xx} & K_{xy} \\ K_{yx} & K_{yy} \end{bmatrix}\begin{bmatrix} \Delta x \\ \Delta y \end{bmatrix} - \begin{bmatrix} C_{xx} & C_{xy} \\ C_{yx} & C_{yy} \end{bmatrix}\begin{bmatrix} \Delta \dot{x} \\ \Delta \dot{y} \end{bmatrix}$$
$$- \begin{bmatrix} M_{xx} & M_{xy} \\ M_{yx} & M_{yy} \end{bmatrix}\begin{bmatrix} \Delta \ddot{x} \\ \Delta \ddot{y} \end{bmatrix} \tag{6}$$

The left-hand vector of Eq. (6) is defined in terms of known measured applied force and stator acceleration vectors. On the right-hand side, $\Delta x(t)$ and $\Delta y(t)$ are also measured functions of time. Restating Eq. (6) in the frequency domain gives

Table 1 Test matrix

P (kPa) rpm	0	172	345	517	690	862	1034
4000	s,d	s	s,d	s	s,d	s	
6000	s,d	s	s,d	s	s,d	s	
8000	s,d	s	s,d	s	s,d	s	s,d
10,000	s,d	s	s,d	s	s,d	s	s,d

$$\begin{bmatrix} \mathbf{F_x} - M_s \mathbf{A_x} \\ \mathbf{F_y} - M_s \mathbf{A_y} \end{bmatrix} = -\begin{bmatrix} \mathbf{H_{xx}} & \mathbf{H_{xy}} \\ \mathbf{H_{yx}} & \mathbf{H_{yy}} \end{bmatrix}\begin{bmatrix} \mathbf{D_x} \\ \mathbf{D_y} \end{bmatrix} \tag{7}$$

The elements of the bearing dynamic stiffness function $\mathbf{H_{ij}}$ are related to the coefficients defined in Eq. (2) by

$$\mathbf{H_{ij}} = K_{ij} - \Omega^2 M_{ij} + \mathbf{j}(\Omega C_{ij}) \tag{8}$$

Equation (7) provides only two equations for four unknowns $\mathbf{H_{xx}}$, $\mathbf{H_{xy}}$, $\mathbf{H_{yx}}$, and $\mathbf{H_{yy}}$. To provide four independent equations, alternate shakes about a given steady-state rotor position are conducted on the stator in orthogonal directions (x and y) yielding the following four equations in four unknowns:

$$\begin{bmatrix} \mathbf{F_{xx}} - M_s \mathbf{A_{xx}} & \mathbf{F_{xy}} - M_s \mathbf{A_{xy}} \\ \mathbf{F_{yx}} - M_s \mathbf{A_{yx}} & \mathbf{F_{yy}} - M_s \mathbf{A_{yy}} \end{bmatrix} = -\begin{bmatrix} \mathbf{H_{xx}} & \mathbf{H_{xy}} \\ \mathbf{H_{yx}} & \mathbf{H_{yy}} \end{bmatrix}\begin{bmatrix} \mathbf{D_{xx}} & \mathbf{D_{xy}} \\ \mathbf{D_{yx}} & \mathbf{D_{yy}} \end{bmatrix} \tag{9}$$

For each experimental condition, ten consecutive tests are conducted to estimate the variability of the dynamic stiffness in the frequency range of 20–300 Hz.

From Eq. (8), the intercept and the curvature of the regression line of the real part provide estimates for the bearing stiffness K_{ij} and the added-mass M_{ij} coefficients, respectively. Similarly, the estimates for the damping coefficients C_{ij} are obtained from the slope of the linear regression of the imaginary part of the dynamic stiffness. Uncertainty values of the bearing force coefficients are also calculated from statistical analysis of the resulting curve fits.

Test Matrix

Table 1 summarizes the test conditions in terms of rotor speed and static load. The letter "s" refers to static test while the letter "d" refers to dynamic test. The bearing unit load is determined using the following equation:

$$p = \frac{W}{LD} \tag{10}$$

Table 2 gives the film-thickness Reynolds number at the test speeds and zero eccentricity ratios, showing the laminar flow. However, turbulent flow may arise in the recesses.

Test Bearing

The geometric parameters of the test bearing are given in Table 3. Note that the dam is formed by a fillet with a radius of 0.4 mm that blends into the recess, rather than the sharp step illustrated in Fig. 1. Most pressure-dam bearings are provided with a filleted step to cut manufacturing costs.

The measured results are compared to prediction from a finite-element based code. The code is based on a Reynolds-equation model with laminar, isothermal, isoviscous, and inertialess flow. The input temperature of the code is the average of inlet and exit

Table 2 Reynolds number at test speeds and centered bearing

Speed (rpm)	4000	6000	8000	10,000
Re	135	213	302	399

Table 3 Bearing Design Parameters

	Pressure-dam bearing
L	76.2 mm
C_r	0.133 ± 0.0063 mm
θ_s	130 deg
k'	3.4–4.2
D	117.1 ± 12.70 mm
$\bar{L}_d$	0.75
$\bar{L}_t$	0.25

oil temperatures. The oil-inlet temperature during the test varied between 39.7°C and 48.9°C, while the oil-outlet temperature varied between 44.0°C and 57.5°C. Table 4 lists the oil-inlet and oil-outlet temperatures for all test conditions in °C.

Static Results

Figure 3 compares the measured and predicted eccentricity ratios at 8000 rpm and 10,000 rpm. The code does not converge at the no-load condition, so the solid lines in the figures start from 200 kPa. The measured and predicted eccentricity ratios increase as the load increases, but the bearing eccentricity ratio slightly decreases as speed increases at the same load. Because of the dam, the bearing operates at high eccentricity even at light loads. Generally good agreement is shown between the measurement and prediction. The maximum difference is 15%. The same basic results occurred for the eccentricity ratio at 4000 rpm and 6000 rpm.

Figure 4 compares the measured and predicted attitude angles at 8000 rpm and 10,000 rpm. The measured and predicted attitude

Table 4 Lube oil-inlet and oil-outlet temperature centigrade

Bearing unit load (kPa)

rpm		0	345	690	1034
4000	T_{In}	42.2	40.2	39.9	
	T_{out}	44.8	44.0	44.0	
6000	T_{In}	43.3	44.4	44.4	
	T_{out}	47.2	47.6	49.4	
8000	T_{In}	46.1	46.6	45.5	46.67
	T_{out}	49.6	51.6	51.7	52.53
10,000	T_{In}	48.8	44.4	45.3	45.75
	T_{out}	56.3	55.2	56.3	57.05
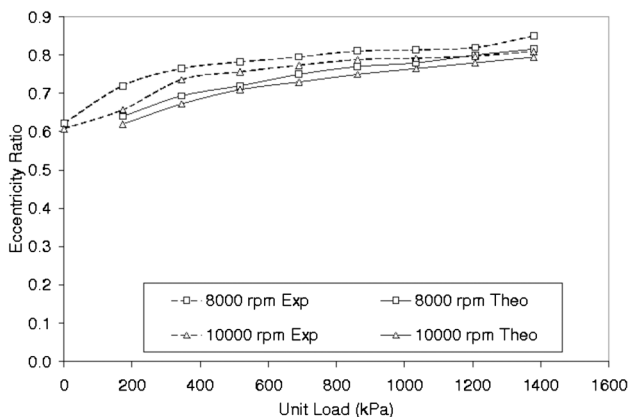
Fig. 3 Eccentricity ratio versus load
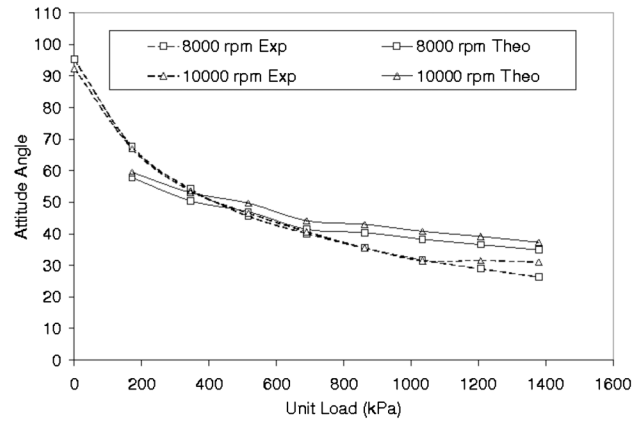
Fig. 4 Attitude angle versus load

angles decrease as the load increases, and the attitude angles slightly increase as speed increases at the same load. Generally good agreement between the measurements and predictions is obtained, with the maximum difference between the measured and predicted values at 25%. Similar results occurred for the attitude angles at 4000 rpm and 6000 rpm.

Dynamic Results

Stiffness Coefficients. Figures 5(a) and 5(b) compare the measured and predicted direct bearing stiffness coefficients at different rotor speeds and loads. K_{yy}, the direct stiffness in the load direction, agrees reasonably well with predictions except at the 690 kPa at 4000 rpm. K_{xx}, the direct stiffness in the nonload direction, agrees reasonably well with predictions for all conditions. The maximum uncertainty is $\pm 25\%$ at the 345 kPa load condition.

Figures 5(c) and 5(d) compare the measured and predicted cross-coupled stiffness coefficients at different rotor speeds and loads. In contrast to a plain journal bearing, for which $K_{yx} = -K_{xy}$ at zero eccentricity, and the two coefficients have opposite signs out to eccentricity ratios on the order of 0.7; for a pressure-dam bearing, the cross-coupled stiffness coefficients have the same signs for comparatively low loads. They are also quite different in magnitudes at no-load conditions. Measured values for K_{xy} in Fig. 5(c) are significantly higher than predicted, particularly for the 4000 rpm and 690 bar unit load condition. Measured values for K_{yx} in Fig. 5(d) are generally in good agreement with predictions for all load and speed conditions.

Damping Coefficients. Figure 6(a) shows the measured and predicted results for C_{yy} the direct damping coefficient in the load direction. Generally, predictions agree well with measurements. Figure 6(b) shows C_{xx} the direct damping coefficients in the no-load direction. Agreement is reasonable between measurements and predictions, except at the 390 bar load condition at 4000 rpm and 6000 rpm. Measured direct damping values are lower than predicted at the highest load condition.

Figures 6(c) and 6(d) show the cross-coupled damping coefficients. The 4000 rpm and 390 bar load case for C_{yx} is notably different from predictions. Otherwise, the predictions are in qualitative agreement with measurements, but measured cross-coupled damping values are lower than predicted.

Added-Mass Coefficients. Figure 7 illustrates M_{yy} at different rotor speeds and unit loads. Very large values occur at the no-load condition, steadily decreasing as running speed increases. The measured value of 60 kg compares to approximately 40 kg using Reinhardt and Lund's result for a plain journal bearing. As the load increases, the added mass term vanishes. Similar results oc-
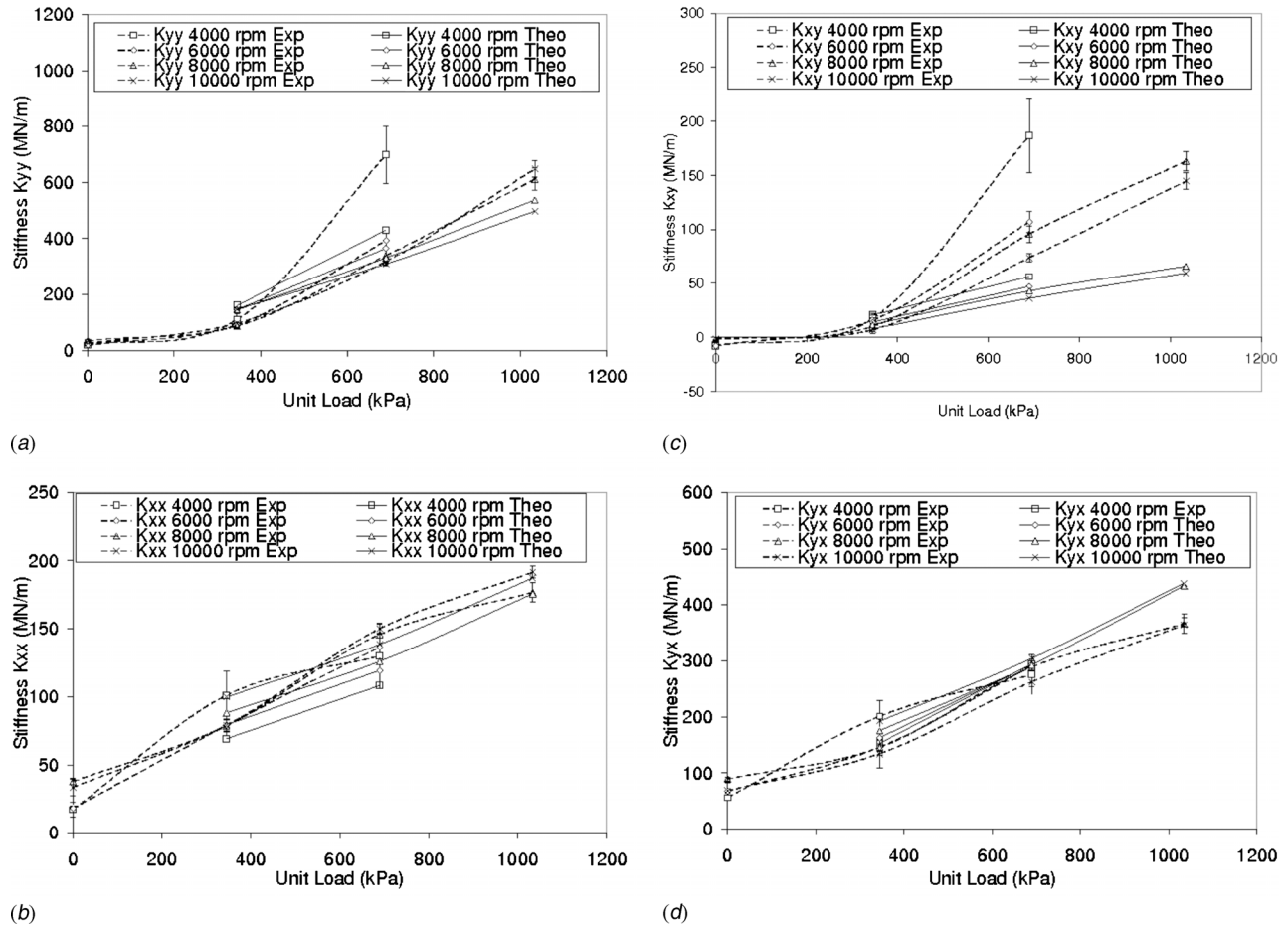
Fig. 5 (*a*) **Stiffness coefficients versus load;** (*b*) **stiffness coefficients versus load**

curred for M_{xx}. Cross-coupled added-mass terms estimated from the real parts of $\mathbf{H_{xy}}$ and $\mathbf{H_{xx}}$ are negligible, being of the same order of magnitude as their uncertainties.

Whirl Frequency Ratio (WFR). WFR is calculated from measured dynamic coefficients using

$$k_{eq} = \frac{k_{xx}c_{yy} + k_{yy}c_{xx} - c_{yx}k_{xy} - c_{xy}k_{yx}}{c_{xx} + c_{yy}} \qquad (11)$$

$$\text{WFR}^2 = \frac{(k_{eq} - k_{xx})(k_{eq} - k_{yy}) - k_{xy}k_{yx}}{c_{xx}c_{yy} - c_{xy}c_{yx}} = \left(\frac{\omega_f}{\omega}\right)^2 \qquad (12)$$

An analysis from San Andrés [10] accounts for the effects of fluid inertia on the WFR. However, in the absence of cross-coupled mass coefficients, the calculations show very small effect of the inertia terms on the WFR, and these coefficients are neglected in the results shown in Fig. 8. Those results show that the bearing is unconditionally stable at other than the no-load condition. The bearing is also more stable than predicted.

Summary and Conclusions

Results from a test program to determine the static and dynamic characteristics of a near-optimum pressure-dam bearing are reported. The results show that the bearing largely works as designed and predicted. It operates at a high eccentricity ratio even at light-load conditions. This intentional increase in eccentricity ratio dramatically improves the bearing's rotordynamic stability characteristics. The WFR results show that the test bearing is inherently stable for any loads greater than 345 kPa—significantly

more stable than predicted. Added-mass coefficients at the no-load condition are quite large, but quickly disappear as the load is increased.

In selecting bearings for turbomachinery applications, there is a general preference for tilting-pad bearings over other designs, particularly for high-speed applications. There may well be good reasons for this choice; however, superior stability behavior as measured by the WFR is not necessarily one of them.

Nomenclature

A_x, A_y = Fourier transformation of stator acceleration
C_{ij} = bearing damping coefficient (N s/m)
c_{ij} = dimensionless damping coefficient
C_r = bearing radial clearance (m)
D = bearing inner diameter (m)
D_x, D_y = Fourier transformation of Δx and Δy
e_x, e_y = average bearing displacement in the x and y directions, respectively (m)
f_{bx}, f_{by} = bearing reaction forces in the x and y directions, respectively (N)
f_x, f_y = measured excitation forces in the x and y directions, respectively (N)
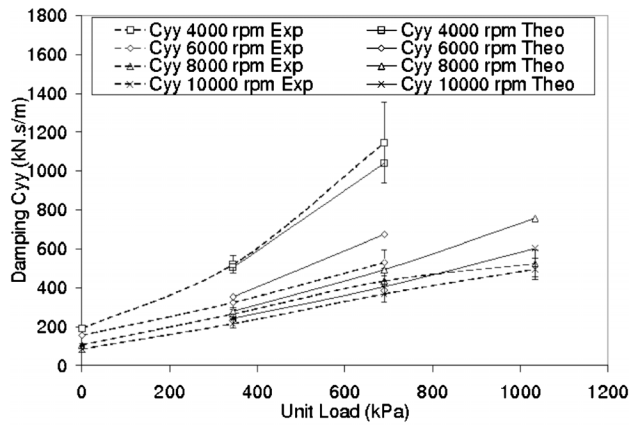
(a)
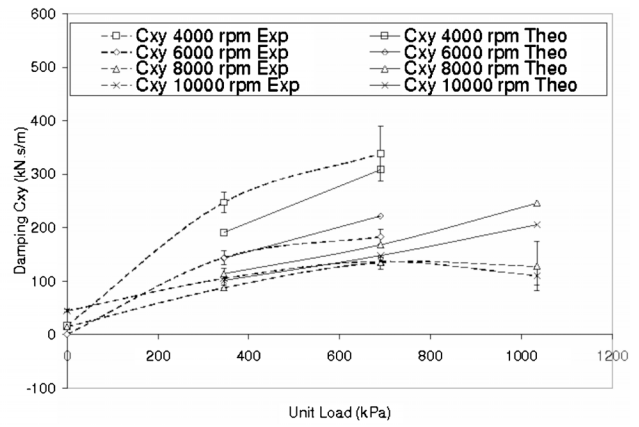
(c)
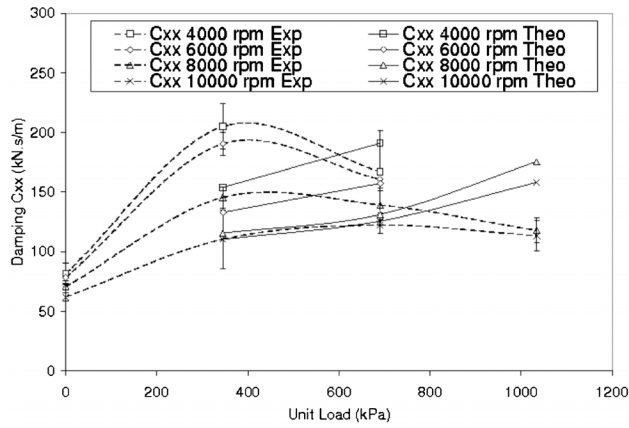
(b)
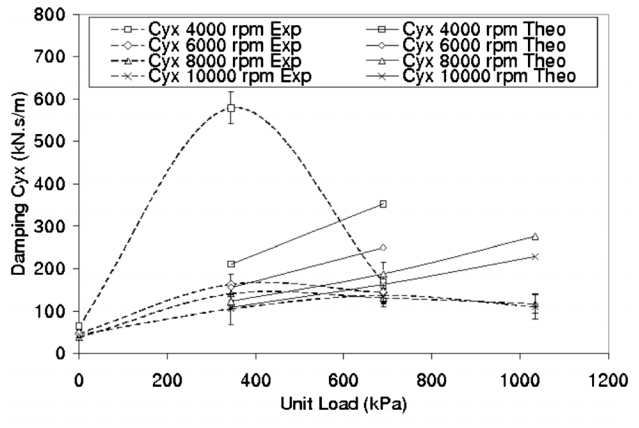
(d)

Fig. 6 (*a*) **Damping coefficients versus load;** (*b*) **damping coefficients versus load;** (*c*) **damping coefficients versus load;** (*d*) **damping coefficients versus load**
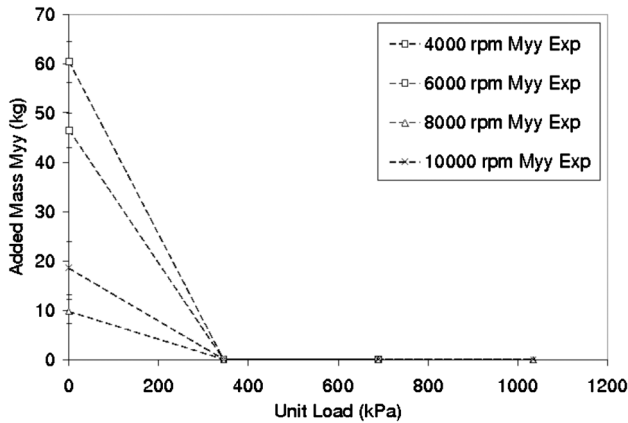
Fig. 7   Added-mass coefficients versus load
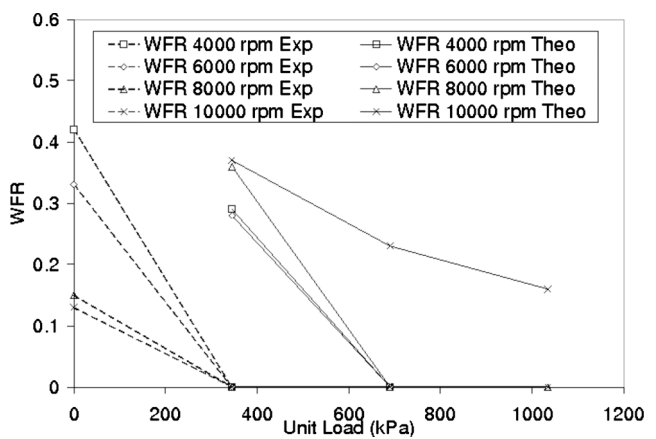
Fig. 8   WFR Versus load

$$F_x, F_y = \text{Fourier transformation of } f_x \text{ and } f_y, \text{ respectively}$$

H_{ij} = average dynamic stiffness (N/m)

i, j = subscript representing x and y

K_{ij} = bearing stiffness coefficient (N/m)

k_{ij} = dimensionless stiffness coefficient

k' = step film thickness ratio

L = bearing axial length (m)

L_d = dam axial length (m)

$\bar{L}_d$ = dam axial length ratio

L_t = relief track axial length (m)

$\bar{L}_t$ = relief track axial length ratio

M_{ij} = fluid inertia coefficient (kg)

M_s = stator mass (kg)

N = rotor speed (Hz)

R = bearing inner radius (m)

Re = Reynolds number $\text{Re} = \rho \omega R C_r / \mu$

W = bearing load (N)

x, y = displacement directions

z = bearing axial length

ε_0 = eccentricity ratio

ψ = attitude angle

θ_s = step angle

ω = rotor speed (rad/s)

Ω = excitation frequency (rad/s)

References

[1] Allaire, P., Nicholas, J., and Barrett, L., 1979, "Analysis of Step Journal Bearings-Infinite Length, Inertia Effects," ASLE Trans., **22**, pp. 333–341.

[2] Nicholas, J., and Allaire, P., 1980, "Analysis of Step Journal Bearings-Finite Length and Stability," ASLE Trans., **22**, pp. 197–207.

[3] Nicholas, J., Allaire, P., and Lewis, D., 1980, "Stiffness and Damping Coefficients for Finite Length Step Journal Bearings," ASLE Trans., **23**, pp. 353–362.

[4] Leader, M., Flack, R., and Allaire, P., 1980, "Experimental Study of Three Journal Bearings with a Flexible Rotor," ASLE Trans., **23**, pp. 363–369.

[5] Lanes, R., Flack, R., and Lewis, D., 1982, "Experiments on the Stability and Response of a Flexible Rotor in Three Types of Journal Bearings," ASLE Trans., **25**, pp. 289–298.

[6] Reinhardt, E., and Lund, J., 1975, "The Influence of Fluid Inertia on the Dynamic Properties of Journal Bearings," ASME J. Lubr. Technol., **97**, pp. 159–167.

[7] Rodriguez, L., and Childs, D., 2004, "Experimental Rotor dynamic Coefficient Results for a Load-on-Pad Flexible-Pivot Tilting-Pad Bearing With Comparison to Prediction From Bulk-Flow and Reynolds Equation Models," ASME J. Tribol., **128**, pp. 388–395.

[8] Al-Ghasem, A., and Childs, D., 2006, "Rotordynamic Coefficients; Measurements versus predictions for a High Speed Flexure-Pivot Tilting-Pad Bearing (Load-Between-Pad Configuration)," ASME J. Eng. Gas Turbines Power, **128**(4), pp. 896–906.

[9] Childs, D., and Hale, K., 1994, "A Test Apparatus and Facility to Identify the Rotor Dynamic Coefficients of High-Speed Hydrostatic Bearings," ASME J. Tribol., **116**, pp. 337–343.

[10] San Andrés, L., 1991, "Effect of Eccentricity on the Forced Response of a Hybrid Bearing," STLE Tribol. Trans., **34**(4), pp. 537—544.

Asynchronous Dynamic Coefficients of a Three-Lobe Air Bearing

Rafael O. Ruiz

Marcelo H. Di Liscia

Luis U. Medina

Sergio E. Díaz

Laboratorio Dinámica de Máquinas,
Universidad Simón Bolívar,
Caracas 1080-A, Venezuela

The study of dynamic whirl behavior of air bearings is fundamental for an adequate rotordynamic analysis and future validation of numerical predictions. This work shows the dynamic response of the air film on a three-lobe bearing under asynchronous whirl motion. One-dimensional multifrequency orbits are used to characterize the bearing rotordynamic coefficients. The test rig uses two magnetic bearing actuators to impose any given orbits to the journal. The dynamic forces are measured on the test bearing housing by three load cells. Journal whirling excitation is independent of the rotating speed, thus allowing asynchronous excitations. The multifrequency excitation is applied at each rotating speed up to 11,000 rpm, allowing the asynchronous characterization of the air film. The experimental procedure requires two linearly independent excitation sets. Thus, vertical and horizontal one-dimensional multifrequency orbits are applied as perturbations. Results show the synchronous and asynchronous dynamic coefficients of the air bearing. Asynchronous experimental results are compared to numerical estimation of the bearing force coefficients through solution of the isotropic ideal gas journal bearing Reynolds equation. Numerical dynamic coefficients are obtained as the effective coefficient values of the bearing when subject to a given orbit. A full characterization of the asynchronous rotordynamics coefficients of the bearing is presented in three-dimensional maps. [DOI: 10.1115/1.2772635]

Keywords: gas bearings, asynchronous response, dynamic coefficients

Introduction

The study of rotordynamic performance of rotor systems supported on gas bearings has gained noteworthy attention. Gas bearings have shown to be a successful alternative to support high-performance turbomachinery by solving some issues inherent to traditional fluid film journal bearings such as sealing and lubricant or working fluid contamination, the need of lubricant and cooling systems, and energy losses at high speeds. Industrial applications using gas bearings comprise turbo-compressor units, auxiliary power systems, microturbines, high-precision rotating machines, and those which demand oil-free environment [1–8].

The rotordynamic study of rotor-bearing systems requires understanding of the dynamic interactions between bearings and rotor. To take into account the dynamic contribution of bearings, it is compulsory to estimate dynamic bearing parameters. Identification of bearing rotordynamic characteristics represents a fundamental issue for dynamic behavior prediction, vibration control, and diagnosis or rotordynamic analysis in turbomachinery. Experimental and theoretical bearing identification have been conducted by several researchers, but there is still a need for standardization of the results presented in publications related to bearing identification [9].

Gas bearing modeling and identification are currently being developed. Viktorov et al. [10] propose a mathematical model for describing static and dynamic characteristics of externally pressurized gas journal bearings. Faria and San Andrés [11] developed a shape function especially suited for finite element modeling. Particularly in this work, one-dimensional Reynolds equation is solved for simple gas bearing geometries. A similar mathematical

procedure is considered by Heshmat et al. [12] to analyze the performance of gas lubricated foil thrust bearings. Thrust load is estimated numerically and compared with experimental data.

Experimental procedures have also been developed for dynamic characterization of air bearings. Wilde and San Andrés identified damping ratio, threshold speed of instability, and whirl frequency ratio for different pressure ratios of a simple gas hybrid bearing [13]. Zhu and San Andrés reported results from identification and modeling of a rotor supported on Rayleigh step gas bearings [14]. Similarly, structural stiffness of bump-type foil bearings is experimentally and theoretically examined by Rubio and San Andrés [15,16].

Swanson et al. [17] characterized a medium size gas turbine engine supported by magnetic, foil, and hybrid (magnetic and foil) bearings under different real conditions. Additional work is presented by the same authors, studying the ability of the foil bearing to function as a backup in case of magnetic bearing failure [18]. A different configuration for dynamic characterization of gas bearings, but based on a similar technology for applying excitation to a rotating shaft, is suggested by Bellabarba et al. [19]. This test rig uses two radial magnetic bearings as dynamic actuators to apply synchronous or asynchronous excitation to a rotating shaft. The test bearing is accommodated in an instrumented housing located at the shaft center section. Rotordynamic coefficients are estimated for a rigid three-lobe gas hydrostatic bearing with a non-spinning shaft.

The present article deals with the experimental identification of a three-lobe air bearing. It focuses on the experimental estimation of stiffness and damping coefficients for the air film bearing, obtained from the dynamic response of a rotor-bearing test rig subjected to multiharmonic one-dimensional orbit excitations. A brief overview of the test rig configuration and experimental procedure are presented. In addition, dynamic bearing parameters are reported graphically.

The goal of the precent work is the complete measurement of the rotordynamic coefficients in foil bearings; for this purpose,

step by step testing is absolutely necessary. First, the characterization of a three-lobe air bearing is the simplest initial test that could be conducted, allowing the test rig tuning and the validation of a simple numerical model for air film forces. Second, gradually increasing the complexity of the tests allows a numerical model improvement. Bellabarba et al. [19] reported measurements of rotordynamic coefficients for a nonrotating journal. Ruiz et al. [20] reported synchronous coefficients for a rotating journal under one-dimensional excitations. Ruiz et al. [21] studied the effect of two different excitation orbit shapes on the identified synchronous bearing coefficients. These works prove the capability of the rig test to identify the synchronous dynamic coefficients under different orbit shapes. The present work addresses the asynchronous behavior of the bearing, providing full speed-frequency coefficient maps.

Fig. 1   Test bearing section schematic

Experimental Setup

The test bearing is attached to the main chassis by three swiveling tip bolts that allow alignment. The shaft, with a built-in journal, is supported by one radial magnetic bearing on each end. The test rig uses these magnetic bearings to support and impose any given orbit to the journal. Each magnetic bearing has a load capacity of 76 N up to 550 Hz and can be controlled independently. This configuration permits common orbit shapes, white noise, multiharmonic motion, one-dimensional trajectories, cylindrical or conical modes, and others. Whirling of the rotor is independent of the shaft rotating speed, allowing asynchronous excitations. The journal can be located at any position within the air bearing clearance by the magnetic bearings [19]. All orbits for current tests are centered within the bearing. The magnetic levitation controller and the amplifier are able to reproduce the fed signals up to 1000 Hz. The rotor is driven by a dc motor, with maximum speed of 15,000 rpm.

Four variable reluctance sensors measure the shaft motion at each magnetic bearing; the precision in the measurement of the position of each magnetic journal is ± 0.1 μm. The motion of the journal is obtained as an interpolation of the motions at the magnetic journals by assuming a rigid rotor (experimental measurements and simulations confirm that the error due to this assumption is less than 3% in the worst case). Three piezoelectric load cells measure bearing loads (± 0.25 N) at the test bearing housing. A Hall effect sensor records the shaft speed. A data acquisition board (12 bits, 16 channels, 200 kHz) and proper ad hoc software are used to process and acquire the measurements. The air supply is controlled by a service unit with a pressure regulator, manometer, solid particles filter, and liquids trap.

A rigid three-lobe air lubricated bearing is tested. The test bearing has 30 mm length, 28.526 mm nominal diameter, 0.035 mm radial clearance, 0.02 mm preload, and three pairs of 1 mm feeding holes between pads. Each feeding hole is 3 mm from the midplane. Uncertainties on physical dimensions are within 2 μm. A groove on the bearing housing supplies air to the feeding holes at a constant pressure. A dial gauge measures the supply pressure at the feeding groove. The bearing is opened to the atmosphere at both ends, thus providing a symmetric pressure field about the bearing midplane. Figure 1 shows the orientation of the bearing lobes. Figure 2 shows the schematic of the test rig. Bellabarba et al. [19] described the test rig design considerations and features in further detail.

Experimental Procedure

The configuration of the magnetic bearing controller permits the centering of the journal into the air bearing. Synchronous and asynchronous orbits and/or perturbations are used as whirl excitations. The procedure identifies directly the dynamic coefficients of the air film, since the forces recorded correspond to the forces generated by the equivalent stiffness and damping of the air film.
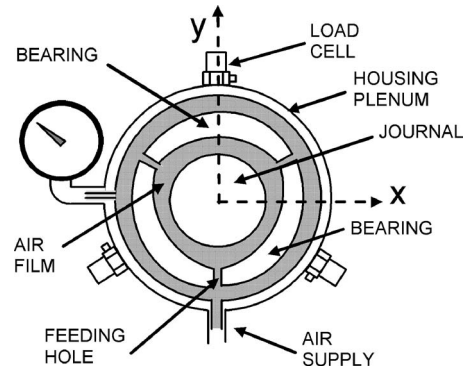
Equation (1) describes the linearized dynamic forced response in frequency domain, where H is the transfer function, and $C_{i,j}$ and $K_{i,j}$ represent the damping and stiffness:

$$(i\omega C_{i,j} + K_{i,j})u(\omega) = H(\omega)u(\omega) = F(\omega) \qquad (1)$$

The transfer function may be written as a function of the excitation and the response in matrix form, as given by Eq. (2) [20]. Note that this equation is valid only for each frequency.

$$H(\omega) = \begin{bmatrix} F_{x1} & F_{x2} \\ F_{y1} & F_{y2} \end{bmatrix}_{(\omega)} \begin{bmatrix} X_1 & X_2 \\ Y_1 & Y_2 \end{bmatrix}_{(\omega)}^{-1} \qquad (2)$$

To compute all terms on the right hand side of Eq. (2), two linearly independent excitations, denoted by subindices 1 and 2, must be performed at each rotating speed. It is important to note that the magnetic bearings are able to control the imbalance response, thus allowing cancellation of the unbalanced orbit if desired. Therefore, since the interest is to identify both synchronous and asynchronous coefficients, the imbalance response is cancelled for all tests performed.

Numerical Model

The modified isothermal Reynolds equation for gas lubricant, including feed flow from the orifices, is given in dimensionless form as

$$\frac{\partial}{\partial \theta}\left(\bar{h}^3 \bar{P} \frac{\partial \bar{P}}{\partial \theta}\right) + \left(\frac{D}{L}\right)^2 \frac{\partial}{\partial \bar{z}}\left(\bar{h}^3 \bar{P} \frac{\partial \bar{P}}{\partial \bar{z}}\right)$$

$$= \Lambda \frac{\partial(\bar{h}\bar{P})}{\partial \theta} - \frac{2\Lambda}{\Omega}\frac{\partial(\bar{h}\bar{P})}{\partial t} - \frac{2\Lambda}{\Omega}\frac{(\Re T)\dot{m}_{or}}{P_a C A} \qquad (3)$$

where
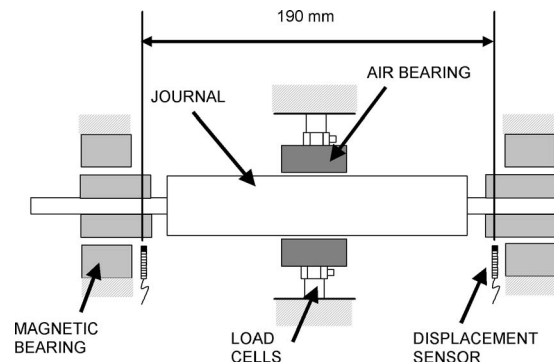
Fig. 2   Test rig schematic

$$\bar{z} = \frac{z}{L/2} \quad \bar{P} = \frac{P}{P_a} \quad \bar{h} = \frac{h}{C} \quad \Lambda = \frac{6\Omega\mu}{P_a}\left(\frac{R}{C}\right)^2$$

With the corresponding boundary conditions, $\bar{P}=1$ at $\bar{z}=\pm 1$, $\partial\bar{P}/\partial\bar{z}=0$ at $\bar{z}=0$ and $\bar{P}(\theta=0)=\bar{P}(\theta=2\pi)$. The last term on the right hand side of the Reynolds equation (3) is only considered for the inflow at the feeding holes. Away from the holes, where there is no external flow fed into the system, the last term is set to zero. Laminar flow is assumed in the film (modified flow Reynolds number from 13.7 to 37.6). The dynamic viscosity is assumed constant due to no significant variation of temperature during the experiment. The gas specific heat ratio is 1.4 for all calculations. The model takes account of the pressure loss through the feeding holes. Thus, the feed source mass flow rate is given by [22]

$$\dot{m}_{or} = \Phi m(P^*) g(\bar{h}) \quad \text{with } \Phi = \frac{\pi a^2}{\sqrt{\Re T}} P_S \tag{4}$$

$$m(P^*) = \begin{cases} \left(2\frac{k}{k+1}\right)^{1/2}\left(\frac{2}{k+1}\right)^{1/k-1} & \text{for } P^* < \bar{P}_{\text{choke}} \\ \alpha\left(2\frac{k}{k+1}\right)^{1/2} P^{*1/2}(1-P^{*k-(1/k)})^{1/2} & \text{for } P^* > \bar{P}_{\text{choke}} \end{cases} \tag{5}$$

$$\bar{P}_{\text{choke}} = \left(\frac{2}{k+1}\right)^{k/k-1} \quad g(\bar{h}) = \frac{\bar{h}}{(\bar{h}^2+\Delta^2)^{1/2}} \quad \Delta = \frac{a^2}{dC} \quad P^* = \frac{P}{P_s} \tag{6}$$

To solve the compressible Reynolds equation, an iterative numerical procedure is required. Thus, after some algebraic manipulation to Eq. (3), a finite difference scheme is implemented. For numerical purposes, the mass flow through each feeding hole is concentrated into a single node.

Due to the nonlinearity of the equation, an iterative procedure is used. The equation is separated into two terms, one containing the nonlinear contributions and the other the second order derivatives. The first pressure distribution (or seed for iteration) is set equal to ambient pressure. Next, the pressure solution is updated, always evaluating the nonlinear terms with the pressure profile of the previous iterations. Convergence of pressure is assumed when the largest difference between pressures of two successive iterations falls below 1%. Peng and Khonsari [23] used a similar iteration procedure to obtain the pressure distribution in foil bearings. Ruiz et al. [20,21], in previous works, showed this procedure in detail.

In previous works, Ruiz et al. [20] applied a zero-frequency finite perturbation to numerically estimate dynamic forces. The predicted stiffness coefficients follow the behavior of the experimental results for synchronous coefficients versus speed. However, the predicted damping has the same order of magnitude as the experimental values, but the numerical model predicts an almost constant value for direct and cross-coupled damping coefficients, which does not agree with the experimental behavior. This difference results from the simplification introduced by the use of zero-frequency perturbations.

A time domain least squares technique is hereby applied to obtain the dynamic forces. As the journal is forced to whirl at a known frequency (Ω) and orbit, the numerical model does not require calculation of the equilibrium position, which is irrelevant to the experiments.

The x and y coordinates and the x and y velocities of the center of the journal are expressed as follows:

$$x = r_x \sin(\Omega t) \quad y = r_y \cos(\Omega t) \tag{7}$$

$$\dot{x} = r_x\Omega \cos(\Omega t) \quad \dot{y} = -r_y\Omega \sin(\Omega t) \tag{8}$$

The forces F_x and F_y at any point i of the orbit can be written as
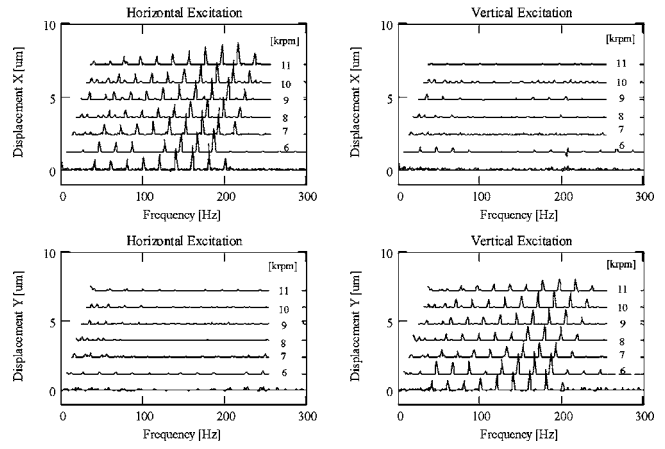
Fig. 3 Asynchronous excitations (P_s=5.2 bars, T_s=23°C)

$$fx_i = K_{xx}x_i + K_{xy}y_i + C_{xx}\dot{x}_i + C_{xy}\dot{y}_i \tag{9}$$

$$fy_i = K_{yx}x_i + K_{yy}y_i + C_{yx}\dot{x}_i + C_{yy}\dot{y}_i \tag{10}$$

For an amount of n time points that describe an entire orbit, Eqs. (9) and (10) can be expressed as follows:

$$\begin{bmatrix} f_{x1} & f_{y1} \\ f_{x2} & f_{y2} \\ \vdots & \vdots \\ f_{xn} & f_{yn} \end{bmatrix} = \begin{bmatrix} x_1 & y_1 & \dot{x}_1 & \dot{y}_1 \\ x_2 & y_2 & \dot{x}_2 & \dot{y}_2 \\ \vdots & \vdots & \vdots & \vdots \\ x_n & y_n & \dot{x}_n & \dot{y}_n \end{bmatrix} \begin{bmatrix} K_{xx} & K_{yx} \\ K_{xy} & K_{yy} \\ C_{xx} & C_{yx} \\ C_{xy} & C_{yy} \end{bmatrix} \tag{11}$$

or, in a simpler form,

$$[\mathbf{FXY}] = [\mathbf{XY}][\mathbf{KC}] \tag{12}$$

Since the positions and velocities matrix **XY** is not generally square, the values of coefficients in matrix **KC** can be estimated through the pseudoinverse:

$$[\mathbf{KC}] = \{[\mathbf{XY}]^T[\mathbf{XY}]\}^{-1}[\mathbf{XY}]^T[\mathbf{FXY}] \tag{13}$$

This equation gives the effective coefficient values of the bearing when subject to any given orbit. Ruiz et al. [21] used this expression to obtain the dynamic coefficients of a three-lobe air bearing under circular orbit excitations, obtaining good agreement with the experimental results and a nonconstant behavior of the synchronous damping coefficients.
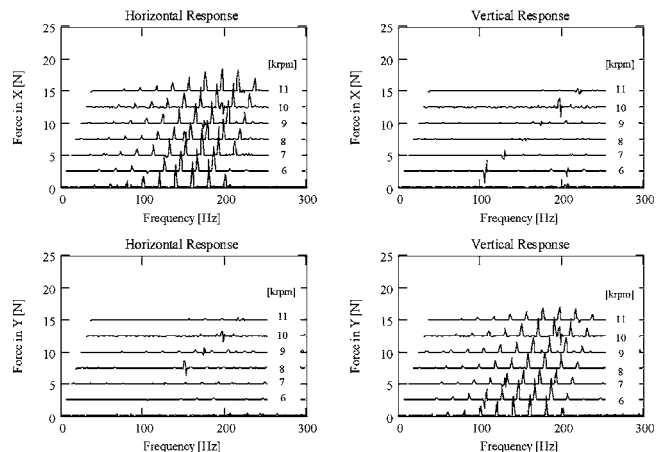
Fig. 4 Asynchronous fluid film response (P_s=5.2 bars, T_s=23°C)
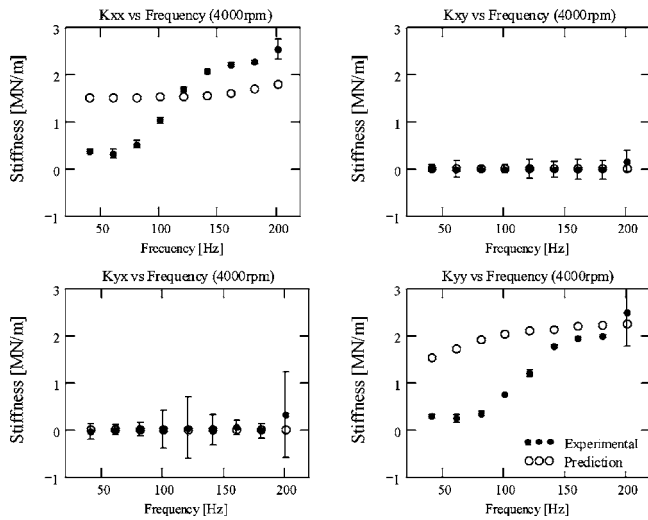
Fig. 5 Asynchronous stiffness at 4000 rpm (P_s=5.2 bars, T_s =23°C)
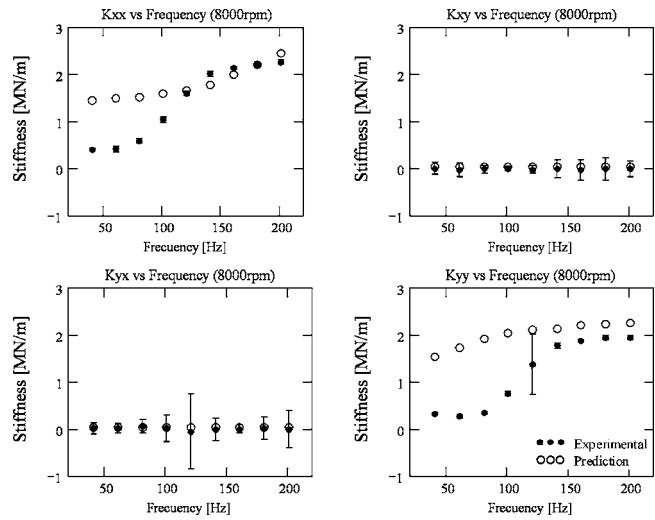
Fig. 7 Asynchronous stiffness at 8000 rpm (P_s=5.2 bars, T_s =23°C)

Results

A multifrequency excitation strategy is devised to calculate dynamic coefficients as a function of frequency. One-dimensional nine component harmonic excitation orbits in the horizontal and vertical axes are applied as perturbations over the position of the journal, generating two independent sets of data. The effect of unbalance is not present due to the capability of the magnetic bearing to control it. The phases of multifrequency excitation components were tuned to minimize the peak value of the orbit size, which results in orbit radii of approximately 5.6 μm.

Multifrequency perturbations in the *x* and *y* directions and their corresponding responses are presented in Figs. 3 and 4. These tests, performed from 4000 rpm to 11,000 rpm, allow the computation of stiffness and damping coefficients for each excitation frequency in the spectrum. The pure harmonic nature of the vertical and horizontal motions and responses are evident in Figs. 3 and 4, where cross-coupled effects are practically nil. All tests were conducted at 5.2 bars of air supply, as measured at the plenum ring before the feeding holes of the bearing.

Figures 5–10 correspond to effective asynchronous rotordynamic coefficients of the bearing under one-dimensional orbit ex-

citations for three different rotating speeds (4000 rpm, 8000 rpm, and 11,000 rpm). Using the same procedure used by Ruiz et al. [21] to obtain the transfer matrix for the two degrees of freedom model of the bearing, stiffness and damping coefficients (direct and cross-coupled) are estimated. Solid dots show the experimental measurements of the synchronous stiffness and damping coefficients as a function of the excitation frequency. Circles represent the predicted values for the same coefficients. Predictions correspond to one-dimensional perturbations at each excitation frequency. Experimental values of the dynamic coefficients were obtained as a media of six different measurements at each rotating speed. The error bars represent three times the standard deviation of the measurements, which is at least one order of magnitude larger than the uncertainty estimated through standard error propagation of the instrumentation uncertainties. In general, the measurements show high repeatability and coherence.

Direct stiffness is at least one order of magnitude higher than the cross-coupled one. The direct stiffness shows a growing trend with the excitation frequency both for the experiments and predictions. However, the growing trend is steeper for the experiments. Cross-coupled coefficients are practically null for the whole fre-
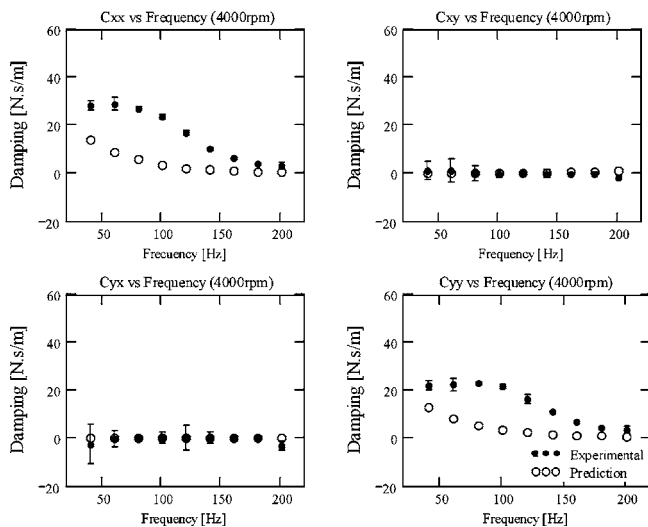
Fig. 6 Asynchronous damping at 4000 rpm (P_s=5.2 bars, T_s =23°C)
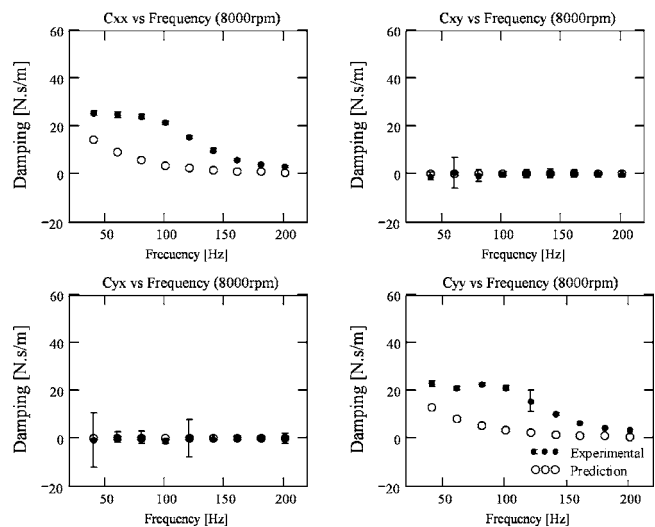
Fig. 8 Asynchronous damping at 8000 rpm (P_s=5.2 bars, T_s =23°C)
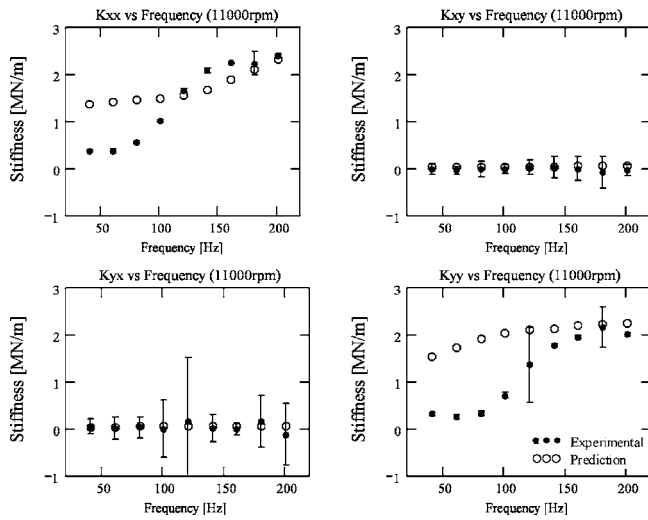
Fig. 9 Asynchronous stiffness at 11,000 rpm (P_s=5.2 bars, T_s=23°C)

quency range. Stiffness coefficients are nearly independent of rotor speed with the exception of K_{xx}, which decreases for decreasing speeds at the higher tested excitation frequencies. Also, in general, the stiffness and damping coefficients show orders of magnitude consistent with the asynchronous coefficients reported by Wilde and San Andrés [7].

The measured asynchronous direct damping coefficients are considerably larger than cross-coupled ones. In general, direct damping coefficients present a trend to decrease with frequency and are practically independent of rotor speed. However, measured coefficients remain nearly constant up to about 100 Hz, which is not predicted by the model. The predictions have a monotonous descending trend with the excitation frequency.

Experimental and numerical asynchronous rotordynamic coefficients show no significant speed dependency within the tested speed range (4–11 krpm), as Figs. 11 and 12 show. Thus, the excitation frequency dictates the coefficients' behavior in the test range independent of journal speed. Synchronous coefficients are indicated by solid lines in Figs. 11 and 12. Synchronous direct stiffness coefficients show a growing trend and the synchronous direct damping coefficients show a decreasing trend with rotating

Fig. 11 Asynchronous stiffness (P_s=5.2 bars, T_s=23°C)

speed, according to the hydrodynamic nature of the bearing. Early results from Ruiz et al. showed similar behavior [20,21].

Conclusions

Experimental measurements of the synchronous and asynchronous rotordynamic coefficients of a fixed geometry, gas lubricated bearing are presented. The speed-frequency maps presented show the following:

(1) Asynchronous coefficients show significant dependency on excitation frequency while being relatively independent of journal speed.
(2) Direct stiffness coefficients grow while direct damping coefficients decrease with excitation frequency.
(3) Both cross-coupled stiffness and damping coefficients are practically null regardless of the excitation frequency.

Fig. 10 Asynchronous damping at 11,000 rpm (P_s=5.2 bars, T_s=23°C)
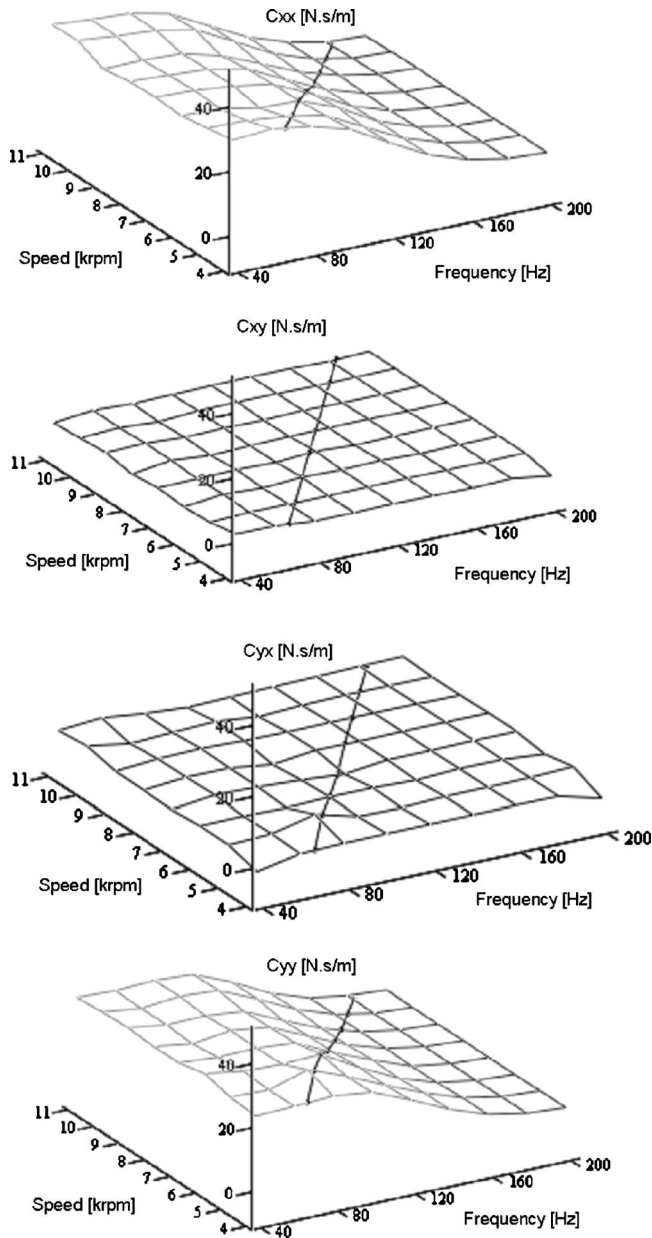
Fig. 12 Asynchronous damping (P_s=5.2 bars, T_s=23°C)

The least squares method used for the numerical identification of the dynamic coefficients significantly improves the results obtained by the zero-frequency perturbations used previously.

In spite of the simplicity of the finite difference method, the numerical model provides relatively good results. Further improvements could be obtained by inclusion of the energy equation together with an up-winding scheme and/or the use of finite volumes or finite element methods.

Acknowledgment

Nomenclature

a = orifice restrictor diameter (1×10^{-3} m)
A = effective orifice area (m^2)
C = nominal pad clearance (m)
$\mathbf{C}_{i,j}$ = damping matrix (N/m s)
D = journal diameter (m)
d = orifice discharge diameter (1×10^{-3} m)
F = Fourier transform of the hydrodynamic forces (N)
F_x = Fourier transform of the horizontal forces (N)
F_y = Fourier transform of the vertical forces (N)
g = orifice geometry function, Eq. (4)
h = film thickness (m)
$\bar{h}$ = dimensionless film thickness
$\mathbf{H}$ = transfer function matrix (N/m)
i = imaginary unit
k = gas specific heat ratio (1.4 for air)
$\mathbf{K}_{i,j}$ = stiffness matrix (N/m)
L = bearing axial length (m)
m = flow dimensionless factor
$\dot{m}_{or}$ = mass flow rate (kg/s)
P = hydrodynamic pressure (gage pressure) (N/m^2)
$\bar{P}$ = dimensionless hydrodynamic pressure
P_a = ambient pressure (gage pressure) (N/m^2)
P_s = supply pressure (gage pressure) (N/m^2)
P^* = orifice pressure ratio
$\bar{P}_{\text{choke}}$ = dimensionless hydrodynamic pressure
r_x = orbit x-axis projection
r_y = orbit y-axis projection
R = journal radius (m)
T = absolute temperature of air (K)
T_s = temperature of air supply (°C)
t = time (s)
u = Fourier transform of the displacement (m)
x = coordinate position of the journal center (m)
X = Fourier transform of the horizontal excitation (m)
y = coordinate position of the journal center (m)
Y = Fourier transform of the vertical excitation (m)
z = coordinate in axial direction
$\bar{z}$ = dimensionless coordinate in axial direction
α = empirical orifice lost coefficient (0.86)
Φ = orifice factor (kg/s)
Λ = bearing number (or compressibility number)
Δ = feed orifice geometric ratio
μ = fluid viscosity (1.882×10^{-5} N s/m^2)
Ω = journal angular speed (rad/s)
ω = asynchronous excitations (rad/s)
θ = circumferential coordinate (rad)
$\Re$ = gas constant (0.287 kJ/kg K)

References

[1] Heshmat, H., Walton, J. F., and Tomaszewski, M. J., 2005, "Demonstration of a Turbojet Engine Using an Air Foil Bearing," ASME Paper No. GT-2005-68404.

[2] Walton, J., Heshmat, H., and Tomaszewski, M., 2004, "Testing of a Small Turbocharger/Turbojet Sized Simulator Rotor," ASME Paper No. GT2004-53647.

[3] Heshmat, H., Heshmat, C., Valco, M. J., Radil, K. C., and Della Corte, C., 2005, "Foil Bearings Make Oil-Free Turbocharger Possible," ASME Paper No. WTC2005-63724.

[4] Swanson, E., and Heshmat, H., 2002, "Oil-Free Foil Bearing as a Reliable, High Performance Backup Bearing for Active Magnetic Bearing," ASME Paper No. GT-2002-30291.

[5] Swanson, E., Heshmat, H., and Shin, J., 2002, "The Role of High Performance Foil Bearing in an Advanced, Oil-Free, Integral Permanent Magnet Motor Driven, High-Speed Turbo Compressor Operating Above the First Bending Critical Speed," ASME Paper No. GT-2002-30579.

[6] Salehi, M., Heshmat, H., Walton, J., and Tomaszewski, M., 2004, "Operation of a Mesoscopic Gas Turbine Simulator at Speeds in Excess of 700.000 rpm on Foil Bearing," ASME Paper No. GT2004-53870.

[7] Wilde, D. A., and San Andrés, L., 2006, "Comparison of Rotordynamic Analysis Predictions With the Test Response of Simple Gas Hybrid Bearings for Oil

Free Turbomachinery," ASME J. Eng. Gas Turbines Power, **128**, pp. 634–643.

[8] Agrawal, G. L., 1997, "Foil Air/Gas Bearing Technology An Overview," ASME Paper No. 97-GT-347.

[9] Tiwari, R., Lees, A., and Friswell, M. I., 2004, "Identification of Dynamic Bearing Parameters: A Review," Shock Vib. Dig., **36**(2), pp. 99–124.

[10] Viktorov, V., Belforte, G., and Raparelli, T., 2005, "Modelling and Identification of Gas Journal Bearings: Externally Pressurized Gas Bearing Results," ASME J. Tribol., **127**, pp. 548–556.

[11] Faria, M. T., and San Andrés, L., 2000, "On the Numerical Modelling of High-Speed Hydrodynamic Gas Bearings," Trans. ASME, J. Tribol., **122**, pp. 124–130.

[12] Heshmat, C., Xu, D. S., and Heshmat, H., 2000, "Analysis of Gas Lubricated Foil Thrust Bearings Using Coupled Finite Element and Finite Difference Methods," Trans. ASME, J. Tribol., **122**, pp. 199–204.

[13] Wilde, D. A., and San Andrés, L., 2006, "Experimental Response of Simple Gas Hybrid Bearings for Oil-Free Turbomachinery," ASME J. Eng. Gas Turbines Power, **128**, pp. 626–633.

[14] Zhu, X., and San Andrés, L., 2005, "Experimental Response of a Rotor Supported on Rayleigh Step Gas Bearings," ASME Paper No. GT-2005-68296.

[15] Rubio, D., and San Andrés, L., 2005, "Structural Stiffness, Dry-Friction Coefficient and Equivalent Viscous Damping in a Bump-Type Foil Gas Bearing," ASME Paper No. GT-2005-68384.

[16] Rubio, D., and San Andrés, L., 2006, "Bump-Type Foil Bearing Structural

Stiffness: Experimental and Predictions," ASME J. Eng. Gas Turbines Power, **128**, pp. 653–660.

[17] Swanson, E., Walton, J., and Heshmat, H., 2002, "A Test Stand for Dynamic Characterization of Oil-Free Bearings for Modern Gas Turbine Engines," ASME Paper No. GT-2002-30005.

[18] Swanson, E., Heshmat, H., and Walton, J., 2002, "Performance of a Foil-Magnetic Hybrid Bearing," Trans. ASME: J. Eng. Gas Turbines Power, **124**, pp. 375–382.

[19] Bellabarba, E., Diaz, S., and Rastelli, V., 2005, "A Test Rig for Air Bearings Rotordynamic Coefficients Measurement," ASME Paper No. GT-2005–30005.

[20] Ruiz, R., Di Liscia, M., Medina, L., and Diaz, S., 2006, "Experimental Measurement of a Three Lobe Air Bearing Rotordynamic Coefficients," ASME Paper No. GT-2006-91068.

[21] Ruiz, R., Di Liscia, M., and Diaz, S., 2006, "Effect of the Orbit Shape on the Experimental Measurement of a Three Lobe Air Bearing," *Proceedings of the Seventh IFToMM Conference on Rotor Dynamics*, Vienna, Austria, Paper No. 284.

[22] San Andrés, L., and Wilde, D. A., 2001, "Finite Element Analysis of Gas Bearing for Oil-Free Turbomachinery," European Journal of Computational Mechanics, **10**(6–7), pp. 769–790.

[23] Peng, Z. C., and Khonsari, M. M., 2004, "Hydrodynamic Analysis of Compliant Foil Bearings With Compressible Air Flow," Trans. ASME, J. Tribol., **126**, pp. 542–546.

Modeling Cyclic Variability in Spark-Assisted HCCI

C. Stuart Daw

K. Dean Edwards
e-mail: edwardskd@ornl.gov

Robert M. Wagner

Johney B. Green, Jr.

Fuels, Engines, and Emissions Research Center,
Oak Ridge National Laboratory,
2360 Cherahala Boulevard,
Knoxville, TN 37932-6472

Spark assist appears to offer considerable potential for increasing the speed and load range over which homogeneous charge compression ignition (HCCI) is possible in gasoline engines. Numerous experimental studies of the transition between conventional spark-ignited (SI) propagating-flame combustion and HCCI combustion in gasoline engines with spark assist have demonstrated a high degree of deterministic coupling between successive combustion events. Analysis of this coupling suggests that the transition between SI and HCCI can be described as a sequence of bifurcations in a low-dimensional dynamic map. In this paper, we describe methods for utilizing the deterministic relationship between cycles to extract global kinetic rate parameters that can be used to discriminate multiple distinct combustion states and develop a more quantitative understanding of the SI-HCCI transition. We demonstrate the application of these methods for indolene-containing fuels and point out an apparent HCCI mode switching not previously reported. Our results have specific implications for developing dynamic combustion models and feedback control strategies that utilize spark assist to expand the operating range of HCCI combustion. [DOI: 10.1115/1.2906176]

Introduction

Homogeneous charge compression ignition (HCCI) is of considerable interest because it can significantly reduce peak in-cylinder temperatures and nitrogen oxide (NO_x) formation in internal combustion engines. In pure HCCI (that is, the ideal limit), ignition occurs as the result of compression heating of a premixed fuel-air charge, and the combustion reactions uniformly occur throughout the combustion chamber with little or no flame. This is very different from conventional diesel combustion, in which fuel is injected into air that has previously been compressed and heated prior to mixing. In the latter case, combustion occurs more slowly in the form of a well-defined diffusion flame. In between pure HCCI and conventional diesel, there are intermediate forms of combustion where a portion of the fuel and air are mixed prior to combustion. These HCCI-like combustion modes are generally referred to as low-temperature combustion modes, which are also of current interest to advanced engine researchers [1].

HCCI is also very different from conventional spark-ignited (SI) combustion in which a propagating flame is initiated by an electric spark in a premixed fuel-air charge [2]. Under some circumstances, it is possible for both HCCI and SI combustion to occur in the same cycle. One example of this dual-mode situation is illustrated in Fig. 1, where an initial SI propagating flame compresses and preheats unburned end gases in the cylinder to the point at which HCCI is initiated in the fuel-air portion that remains unburned. Our focus in this paper is on experimental studies of a gasoline-fueled engine where scenarios such as that illustrated in Fig. 1 can occur.

In order to achieve HCCI, it is typically necessary to preheat the fuel-air mixture to within a relatively narrow temperature window prior to compression. With too low an initial temperature, HCCI will not occur. With too high an initial temperature, the HCCI burning rate can be so rapid that mechanical damage results. Preheating is often achieved through exhaust gas recirculation (EGR), and some studies have shown that the presence of certain residual gas species can also affect ignition [3,4]. In practice, it is very difficult to achieve pure HCCI at all speeds and loads on most engines, so there is much ongoing research into

how to maximize the operating envelope for HCCI [1,5–7]. One promising approach being considered is to switch between HCCI and SI combustion as speed and load change. Several recent publications and presentations [8–11] have addressed SI-HCCI switching, but with few exceptions (e.g., Ref. [12]), there has been limited exploration of the fundamental processes involved in transitioning between a propagating flame and HCCI.

In this paper, we describe an analysis of experimental observations of unstable combustion in the SI-HCCI transition that occurs when SI is used to promote HCCI. Our goal is to understand the transition process in terms of global reaction kinetics. We are motivated to find ways of empirically observing these global kinetics directly with an engine because the results will account for in-cylinder details that would be present when trying to implement realistic on-board diagnostics and controls. We also want to correlate our phenomenological kinetics with the kinetics measured under more ideal laboratory conditions (e.g., rapid compression machines) or predicted from detailed computational models. By bridging these different perspectives, we hope to improve the overall understanding and utilization of HCCI.

We base the present discussion on experimental data from a single-cylinder gasoline engine, which has been specially modified to permit internal EGR. The level of internal EGR can be precisely controlled by adjusting the timing and lift of the intake and exhaust valves, so that it is possible to incrementally vary the combustion from pure SI to pure HCCI. We find that measurements of the unstable combustion occurring at intermediate EGR levels are rich in information about the kinetics that moderate the SI-HCCI transition.

Experimental Method

Our experimental observations were made using a 0.5-l single-cylinder AVL research engine with 11.34:1 compression ratio. This engine has two intake valves and one exhaust valve and is equipped with a full-authority hydraulic variable valve actuation (VVA) system. Internal EGR is achieved using negative valve overlap. Only a single intake valve was used in this study to promote swirl and mixing. The fuel (indolene and indolene-ethanol mixtures) was delivered by an intake mounted port fuel injector. Engine speed was maintained constant using an absorbing/motoring dynamometer. Nominal operating conditions corresponded to 1600 rpm and 3.4 bar indicated mean effective pressure (IMEP). Throughout the EGR range, spark timing was

Spark before TDC creates expanding flame front

Near TDC, HCCI begins as the unburned gas becomes sufficiently heated

HCCI completes after TDC as gas expands and cools and work is extracted
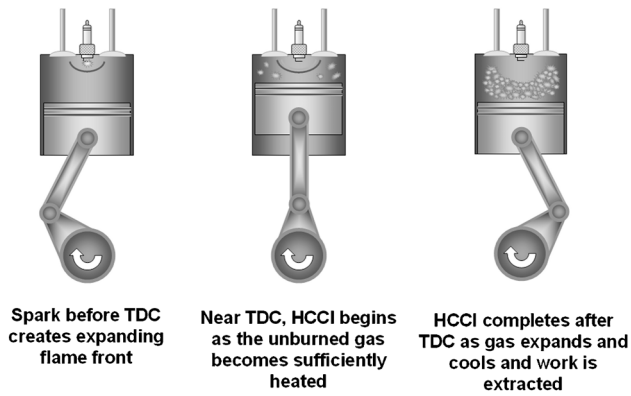
Fig. 1 Illustration of the possible role of the initial SI flame in spark-assisted HCCI. The SI flame stimulates subsequent HCCI by compressing and preheating the remaining unburned gases.

Fig. 3 HR profiles for the limiting cases of (*a*) no EGR (SI) and (*b*) maximum EGR (HCCI)

held fixed at 25°BTDC and coolant temperature maintained at 90°C. At EGR levels typically in excess of 55%, full HCCI operation was achieved, and the spark could be turned off with no impact on combustion. Fueling rate was maintained constant, and intake throttling used to maintain a stoichiometric air-fuel ratio. Typically, the throttle was wide open for pure HCCI operation.

In-cylinder pressure measurements were recorded at a resolution of 0.5 crank-angle degrees for each internal EGR level. To minimize noncombustion artifacts, all engine feedback controllers were shut off, and the engine was operated in open-loop mode except for the dynamometer speed controller and coolant temperature controller. Measurements at each specific EGR level typically included 2800 consecutive engine cycles. Standard exhaust gas instrumentation was used to provide a basic knowledge of the exhaust chemistry including steady-state measurements of CO, CO_2, HC, NO_x, and O_2 concentrations in the raw engine-out exhaust. The normal procedure following each incremental EGR adjustment was to allow the engine to run several minutes to reach "steady-state" (for oscillatory combustion states, this meant that the behavior became statistically stationary or consistent over time). Following this runout period, in-cylinder pressure and stan-

dard engine temperature and exhaust gas analyses were recorded for the required time. Cycle resolved heat release rate, integrated heat release (HR), and IMEP were calculated from the measured in-cylinder pressure measurements following standard procedures in the literature [2].

We note here that explicit measurements of the intake air-fuel ratio or in-cylinder charge stratification were not made in these experiments. As described in the next section, however, the steady-state cycle-to-cycle combustion consistency for pure SI (very low EGR) and HCCI (maximum EGR) implies that the intake charge was relatively well mixed.

Results and Discussion

The global trends observed for our SI-HCCI experiments are depicted in Fig. 2. These specific results are for indolene fueling, but similar trends were seen for indolene-ethanol fueling. As internal EGR increased (moving from left to right), combustion shifted from pure SI combustion (with a very low coefficient of variation (COV) in IMEP) to a complex mixture of SI and HCCI and finally to pure HCCI (again with a low COV) when the EGR level approached 60%. As seen in Fig. 3, average HR rate profiles at 0 and maximum EGR reflect the expected burn trajectories for pure SI and HCCI combustions, respectively. SI HR typically begins very soon after spark and is almost complete by TDC, while HCCI HR rises very rapidly near TDC and occurs over a much shorter interval.
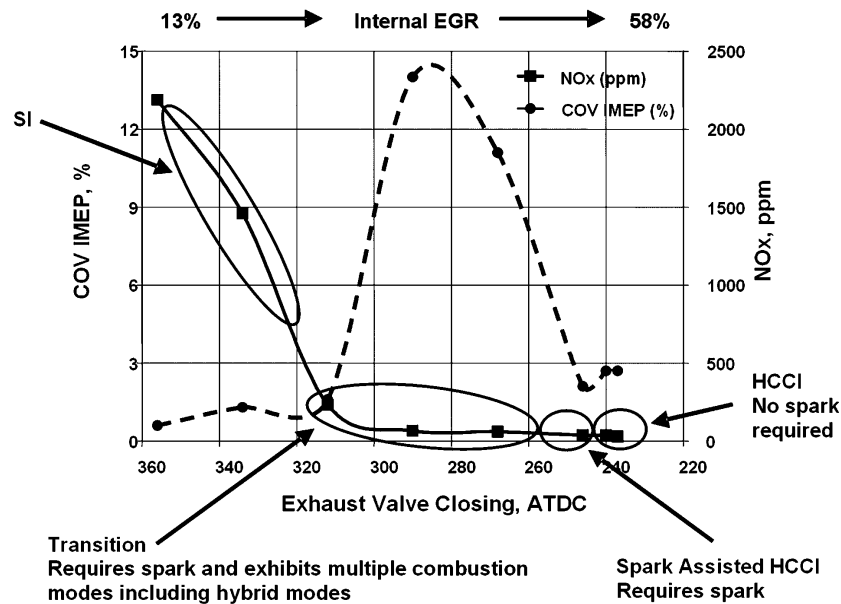
Fig. 2 General combustion trends observed in the SI-HCCI transition experiments

Relatively early in the transition with EGR, average NO_x emissions dropped rapidly, but there was also a concomitant rise in cyclic combustion variability (indicated by the large COV). High COV is highly undesirable because of the erratic power delivery and unacceptable vibration that would be experienced by the driver. In addition, the occasional misfires and excessively strong combustion events that create high COV result in momentary spikes in hydrocarbon and NO_x emissions, respectively (even though overall average emissions may be relatively low). Thus, there is a strong incentive to introduce some type of control to smooth the transition in a way that avoids such high COV.

Our subsequent discussion focuses on the analysis of sequential cyclic combustion measurements from an intermediate EGR condition (approximately 46%). The combustion state of the engine at this EGR roughly corresponds to the point of maximum COV in IMEP (approaching 15%) in Fig. 2. We now consider a cycle-resolved sequence of measured integrated HR values for the target engine condition determined using the usual procedures for interpreting cylinder pressure measurements [2]. We correct the computed HR values to account for cylinder-wall heat losses estimated using WAVE® engine simulation software [13]. For successive cycles (designated by indices $i-1$ and i), plots such as Fig. 4(a) and 4(b) (also referred to as first return maps) reveal the strong correlation between successive HR values [14–16]. Note that the large-scale cycle-to-cycle correlation features appear similar for both pure indolene fueling (Fig. 4(a)) and fueling with an 85/15 ethanol-indolene blend (Fig. 4(b)).

To better understand the reasons for the observed cycle-to-cycle HR correlations, it is helpful to consider the overall mass balance. For the fuel-air charge (assuming a stoichiometric inlet mixture), such a balance requires that

$$mr(i) = \frac{f}{1+f}\left(1 + mr(i-1) - \frac{HR(i-1)}{Q}\right) \quad (1)$$

where $f/(1+f)=r$, which is the specified EGR level. Equation (1) simply states that the amount of residual stoichiometric fuel-air mixture recycled from the current to the next cycle, $mr(i)$, is determined by the total initial air-fuel charge in the previous cycle (made up of fresh and previous residual charges), the amount of burning in the previous cycle, and the level of EGR (assuming uniform mixing of the cylinder contents). Thus, if we know $mr(i-1)$ and $HR(i-1)$, it is possible to calculate the residual fuel-air charge $mr(i)$. This process can be repeated ad infinitum as long as additional sequential HR measurements are available.

A practical problem in using Eq. (1) to compute residual charges from HR measurements is that the starting residual fraction, $mr(i-1)$, is not known a priori. This turns out not to be an insurmountable obstacle, however, because all subsequent iterates beyond the first are solely based on measured HR values. No matter what initial mr value is assumed, the resulting estimated series converges after a few cycles to the same values, as shown in Fig. 5. By discarding a few of the initial cycle estimates, the remaining estimated residual charge series is unique.

Figure 6 illustrates the resulting cyclic patterns in the estimated residual charge values estimated as described above for the nominal EGR condition. Here, we observe three distinct correlation trends between successive residual charges, implying three characteristically different types of combustion. For initial residual charges below 0.1, combustion throughout the cycle appears to be dominated by flame propagation from the spark (i.e., HCCI does not appear to happen). For initial residual charges >0.1, the data are clustered into two distinct families, which are traced with lines in the plot. As discussed below, these patterns appear to indicate that there are two distinct ways in which HCCI can occur after the initial pre-TDC SI burn.

A cycle-by-cycle heat balance similar to Eq. (1) above can also be used to estimate variations in residual gas temperature. Our
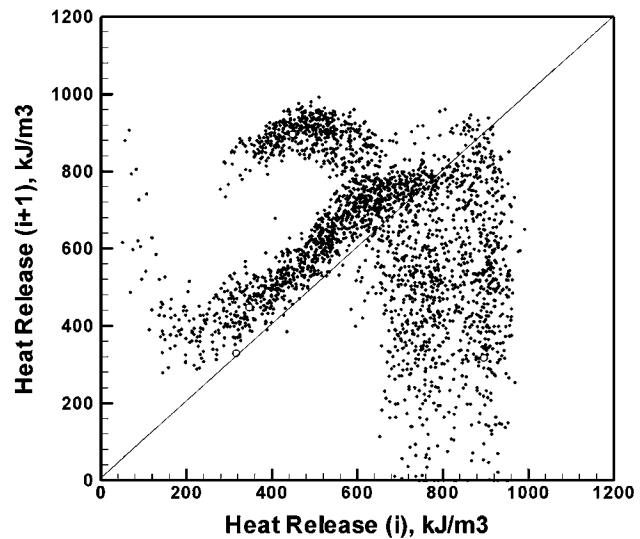
(a)
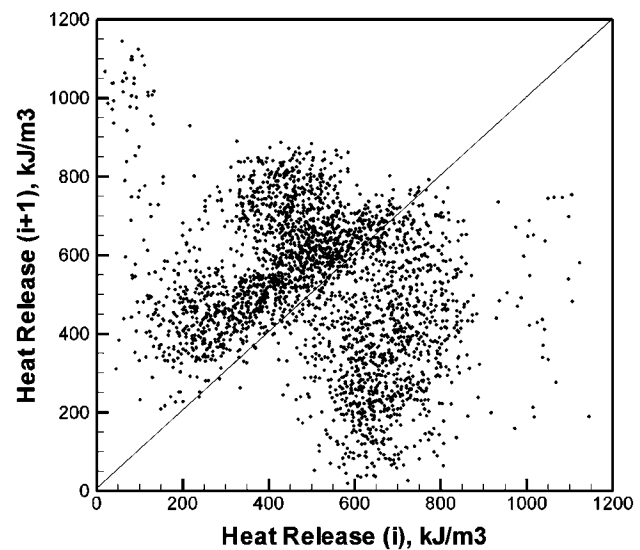
(b)

Fig. 4 First return maps of cyclic HR for (a) pure indolene and (b) E85 (85% ethanol, 15% indolene) at conditions near the maximum COV in HR

detailed analysis of residual gas temperatures using appropriate heat loss estimates during both the exhaust and intake strokes (obtained from a WAVE engine model of our engine) convinces us that variations in exhaust temperature tend to be slower and have less immediate impact (on a cycle-to-cycle basis) compared to the variations in residual fuel-air charge. Instead, exhaust temperature variations appear to be "filtered" by the thermal inertia of the combustion chamber and require multiple cycles over which to make substantial changes (e.g., when the nominal EGR level is changed).

The relatively large cyclic impact of residual charge on subsequent combustion becomes clearer when we consider how unburned charge preheating is affected by postspark combustion. As illustrated in Fig. 1, postspark propagating-flame combustion is critical to the onset of HCCI when EGR is insufficient to sustain HCCI-only combustion. In effect, the expanding flame front acts as an additional source of compression, which further boosts the preheating of the unburned gases to the point that they can ignite in the HCCI mode. Thus, the effective amount of compressive
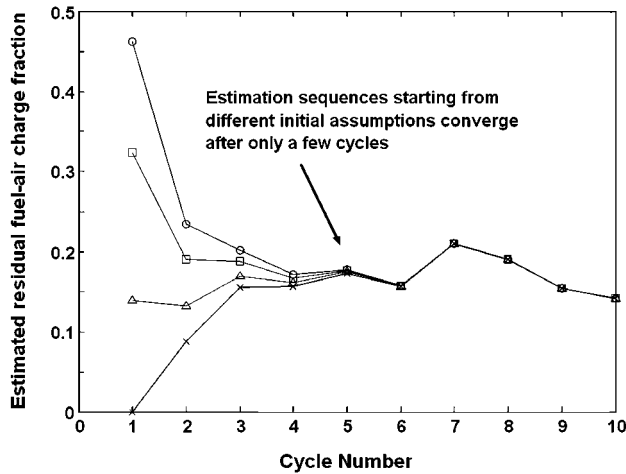
Fig. 5 Convergence of iterated residual fuel-air balances for a wide range of assumed initial residual charges. Convergence is driven by repeated input from observed values of HR(i).
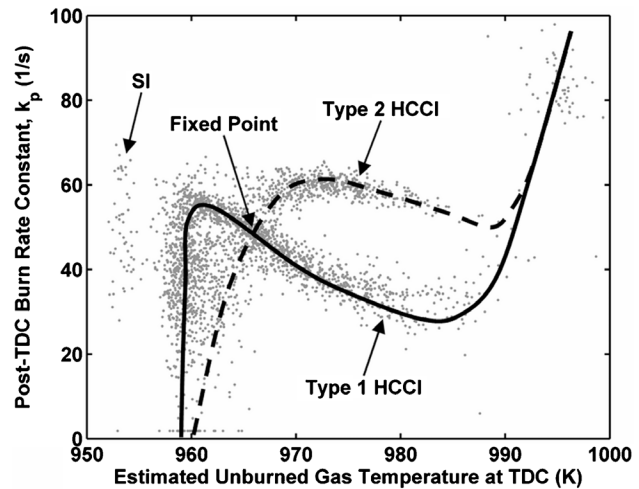

Fig. 7 Relationship between the estimated global post-TDC burn rate constant and unburned gas temperature at TDC

boost produced depends very much on the postspark flame speed, which is known to be highly dependent on charge dilution.

To develop quantitative estimates of the flame speed for our experiments, we estimated the nominal combustion rate for our engine under pure SI operation (no EGR) and then adjusted that rate for charge dilution with a standard flame speed correlation [2]:

$$\frac{S_L}{S_{L0}} = 1 - 2.06 x_b^{0.77} \qquad (2)$$

where

$$x_b = 1 - \frac{1 + \text{mr}}{1 + f} \qquad (3)$$

We then used a simple two-zone combustion model to estimate the unburned gas temperature at TDC in our engine at the reference nominal condition as a function of residual charge. For the subject engine condition, these estimates indicated that the unburned gas temperature at TDC can be as much as 140 K higher as the result of residual fuel-air charge coming from previous cycles.

Fig. 6 Characteristic patterns seen in the residual charge based on cycle-by-cycle mass balances

To quantify combustion rate in each cycle, we employed the concept of a global combustion efficiency, CE(i). The idea behind CE(i) is to quantify the fraction of the fuel-air charge consumed in each cycle, analogous to the idea of fractional conversion widely used for chemical reactors. Values of CE(i) for our experiments were determined from the estimated HR values and the relationship between HR and charge depletion:

$$\text{CE}(i) = \frac{\text{HR}(i)}{(1 + \text{mr}(i))Q} \qquad (4)$$

From the flame speed estimate and two-zone model described earlier, we estimated the fraction of combustion occurring as the result of spark ignition before TDC. The post-TDC contribution to combustion is then related to overall and pre-TDC combustion by

$$\text{CE}_p(i) = \frac{(\text{CE}(i) - \text{CE}_s(i))}{(1 - \text{CE}_s(i))} \qquad (5)$$

where $\text{CE}_s(i)$ and $\text{CE}_p(i)$ are the pre- and post-TDC combustion efficiencies for cycle i.

To relate the post-TDC fractional conversion to a global kinetic rate, we use a simplified global Wiebe-type relationship:

$$\text{CE}_p(i) = 1 - e^{(-k_p t_b)^n} \qquad (6)$$

where k_p is a global reaction rate constant, t_b is a burn time, and n is an empirical exponent. Note that taking the derivative of Eq. (6) with respect to time yields an expression that is proportional to in-cylinder HR rate. Comparisons with our experimental HR rate measurements indicate that this type of function does indeed provide a good fit using appropriate values for the three parameters.

Focusing on post-TDC combustion seems reasonable if we assume that the onset of HCCI tends to disrupt continuing flame propagation and that HCCI, when it occurs in the transition region, probably tends to initiate at or near TDC when the compression heating of the unburned gas is near maximum. Assuming that the post-TDC burn time is constant and the same for all cycles and fixed by the valve timings and engine speed, we can estimate a global post-TDC burn rate constant (k_p), which applies specifically to only that part of the combustion. We also assume that the empirical exponent is constant from cycle to cycle as well (as is typically the case for the analogous Wiebe parameter). Combining our estimates of k_p and temperature at TDC, we obtain plots such as Fig. 7.

We expect that the global post-TDC burn rate constant should be a strong function of temperature, but obviously the trend in Fig. 7 is more complex than a simple Arrhenius relationship. Ac-
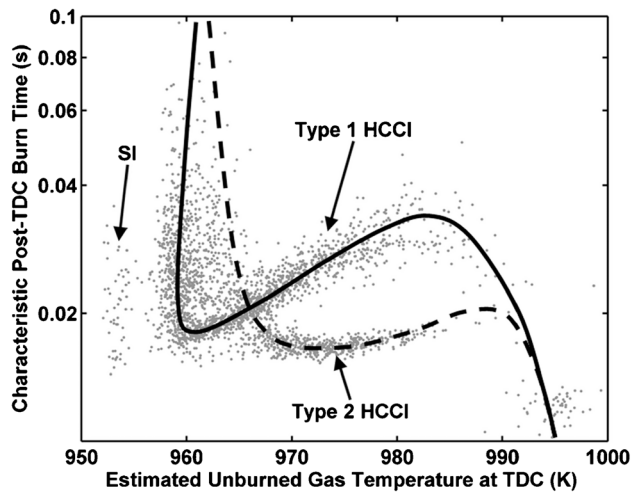
(a)
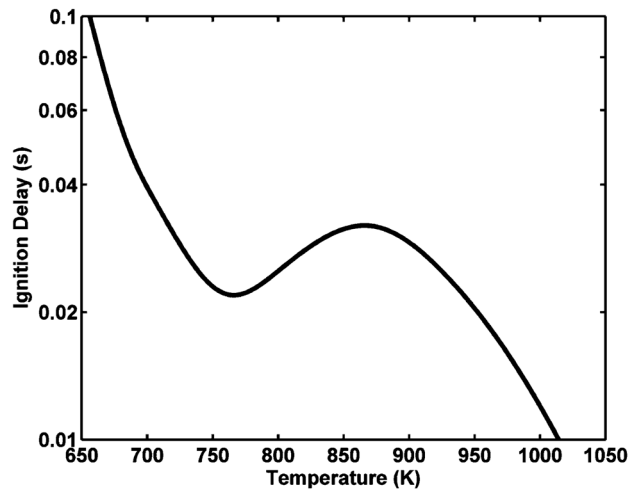
(b)

Fig. 8 Comparison of (a) observed post-TDC burn time ($1/k_p$) with (b) computed ignition delay for n-heptane

tually, there again appear to be three distinct trends (labeled in the figure) associated with the three different residual patterns noted earlier. In analyzing the post-TDC HR profiles for combustion events in these different regions, we see what appears to be an almost purely propagating-flame (SI) combustion occurring at low temperatures and two types of HCCI (or HCCI-like) combustion occurring at higher temperatures. Both types of HCCI combustion exhibit regions of negative temperature coefficient (NTC) behavior (i.e., the burn rate constant decreases with increasing temperature), but NTC is much more pronounced in one case than the other.

At one TDC temperature, the global kinetic rates of the two types of HCCI appear to cross (i.e., have the same value). We know from other analyses not presented here [14–16] that this particular point represents an unstable fixed point of the engine dynamical system. It represents the condition when the engine is most likely to shift from one type of HCCI to the other. This is an important point to recognize because it would be a natural point at which to target controls.

For comparison with detailed kinetics models and other laboratory measurements of NTC behavior (e.g., using rapid compression machines), it is useful to consider the reciprocal of k_p, which represents a global time scale for post-TDC combustion. Figure 8(a) illustrates the result for the same data plotted in Fig. 7. Here,

curves have been added to help distinguish the trends for the two different HCCI-like patterns. Note the similarity between the Type 1 HCCI trend in Figs. 8(a) and 8(b), which is a plot of ignition delay for n-heptane undergoing HCCI predicted by the Pitsch mechanism [17,18].

The strong similarity between the Type 1 HCCI and Fig. 8(b) suggests that at least part of the cycle-to-cycle combustion variations for our engine in the SI-HCCI transition involved n-heptane-like kinetics. Interestingly, the level of NTC behavior observed in these experiments has not been reported for indolene in other studies (as far as we have been able to determine). Although indolene is actually a complex mixture of alkanes and aromatics, it has been suggested that its behavior can be approximated by a mixture of surrogate fuels, n-heptane, iso-octane, and toluene [19–21]. This suggests to us that at least on some occasions, the appearance of n-heptane-like kinetics that characteristically have a strong NTC behavior should not be surprising for indolene.

What is perhaps more intriguing is the fact that in our engine there was a second type of HCCI for which the NTC behavior was much less pronounced but still present to a degree. This probably represents the effect of alternative kinetic pathways associated with the non-heptane-like components in indolene. The fact that the transitions between these different HCCI modes appears to occur predictably [14–16] indicates that there is probably a deterministic shifting of the residual composition between high and low heptane-like fractions.

To clarify, we conjecture that the heptanelike components are consumed in disproportionate amounts in some cycles, leading to one or more subsequent cycles where the non-heptane-like components dominate the chemistry and the HCCI reactions are exceptionally strong. Once the strong reactions consume the non-heptane residuals, the in-cylinder mixture returns to the higher n-heptane-like fraction present in the raw fuel. If such a residual composition shift is responsible for the kind of mode switching seen here, it might be exploited for purposes of control. For example, selected components might be deliberately added to the fresh fuel to steer the combustion away from or toward one or the other of the alternative HCCI combustion modes.

Finally, the strong similarity between the dynamical trends seen for both indolene and indolene-ethanol fuel mixtures suggests that the basic kinetic pathways for HCCI are not appreciably changed by the presence of up to 85% ethanol. This observation and those above should provide useful benchmarks for evaluating and improving the predictions of detailed in-cylinder HCCI kinetics models. Ultimately, the most useful kinetic models for HCCI will need to produce the kind of cycle-to-cycle trends reported here. In addition, the robustness of these trends in our experiments suggests that development of simplified in-cylinder combustion models based on global kinetic parameters should be possible and may be useful for correlating measurements and developing real-time diagnostics and controls.

Conclusions

Our results indicate that global kinetic parameters can be extracted from sequential unstable cycle-resolved combustion measurements in the SI-HCCI transition. For our experiments, enhancement of the pre-TDC compression heating by spark-initiated burning of the residual fuel-air charge had major impact on post-TDC combustion. When pre-TDC heating was less than a critical level, post-TDC combustion was dominated by a continuation of the initial SI burning. Above a critical level of preheating, two distinct types of HCCI combustion occurred after TDC, one exhibiting strong NTC and one weak NTC. Switching between the two HCCI modes occurred based on recent combustion history in previous cycles. The level of NTC behavior observed for indolene in these experiments does not appear to have been reported for

indolene in other studies. This same general type of behavior appears to occur even when indolene is diluted with up to 85% ethanol.

Acknowledgment

Nomenclature

$CE(i)$ = fraction of the total fuel-air charge in the cylinder in cycle i consumed by combustion

$CE_p(i)$ = fraction of the fuel-air charge left at TDC that is consumed by combustion after TDC

$CE_s(i)$ = fraction of the initial fuel-air charge consumed by combustion between the spark and TDC

f = mass of exhaust recirculated between cycles per unit mass fresh charge

$HR(i)$ = integrated heat release in cycle i (kJ/unit mass of fresh charge)

i = cycle index

$IMEP$ = indicated mean effective pressure (bar)

k_p = a global post-TDC reaction rate constant (1/s)

$mr(i)$ = mass of residual fuel-air charge input to cycle i per unit mass of fresh charge

n = empirical parameter used in Wiebe-like combustion expression

Q = heat released/unit mass of fuel-air charge burned (kJ/mass)

r = EGR fraction, that is, the fraction of the cylinder contents which is recycled into each new cycle

S_L/S_{L0} = ratio of laminar flame speed with dilution to undiluted flame speed

t_b = post-TDC burn time (s)

TDC = top-dead-center point of engine cycle

x_b = charge dilution fraction at spark

References

[1] Zhao, F., Assanis, D. N., Najt, P. M., Dec, J. E., Eng, J. A., and Asmus, T. N., 2003, *Homogeneous Charge Compression Ignition (HCCI) Engines: Key Research and Development Issues*, SAE International, Warrendale, PA.

[2] Heywood, J. B., 1988, *Internal Combustion Engine Fundamentals*, McGraw-Hill, New York.

[3] Shaver, G. M., Gerdes, J. C., Jain, P., Caton, P. A., and Edwards, C. F., 2003, "Modeling for Control of HCCI Engines," *Proceedings of the American Control Conference*, Vol. 1, pp. 749–754.

[4] Caton, P. A., Simon, A. J., Gerdes, J. C., and Edwards, C. F., 2003, "Residual-Effected Homogeneous Charge Compression Ignition at Low Compression Ratio Using Exhaust Reinduction," Int. J. Engine Res., **4**(3), pp. 163–177.

[5] Urushihara, T., Hiraya, K., Kakuhou, A., and Itoh, T., 2003, "Expansion of HCCI Operating Region by the Combination of Direct Fuel Injection, Negative Valve Overlap and Internal Fuel Reformation," SAE Paper No. 2003-01-0749.

[6] Olsson, J., Tunestal, P., and Johansson, B., 2004, "Boosting for High Load HCCI," SAE Paper No. 2004-01-0940.

[7] Duffy, K., Kieser, A., Fluga, E., and Milam, D., 2004, "Heavy-Duty HCCI Development Activities," 2004 Diesel Engine Emissions Reduction (DEER) Conference, www1.eere.energy.gov/vehiclesandfuels/pdfs/deer_2004/session7/2004_deer_duffy.pdf

[8] Weinrotter, M., Wintner, E., Iskra, K., Neger, T., Olofsson, J., Seyfried, H., Aldén, M., Lackner, M., Winter, F., Vressner, A., Hultqvist, A., and Johansson, B., 2005, "Optical Diagnostics of Laser-Induced and Spark Plug-Assisted HCCI Combustion," SAE Paper No. 2005-01-0129.

[9] Urushihara, T., Yamaguchi, K., Yoshizawa, K., and Itoh, T., 2005, "A Study of a Gasoline-Fueled Compression Ignition Engine—Expansion of HCCI Operation Range Using SI Combustion as a Trigger of Compression Ignition," SAE Paper No. 2005-01-0180.

[10] Santoso, H., Matthews, J., and Cheng, W. K., 2005, "Managing SI/HCCI Dual-Mode Engine Operation," SAE Paper No. 2005-01-0162.

[11] Hyvonen, J., and Johansson, B., 2005, "Operating Conditions Using Spark Assisted HCCI Combustion During Combustion Mode Transfer to SI in a Multi-Cylinder VCR-HCCI Engine," SAE Paper No. 2005-01-0109.

[12] Koopmans, L., Denbratt, I., and Backlund, O., 2002, "Cycle-to-cycle Variations: Their Influence on Cycle Resolved Gas Temperature and Unburned Hydrocarbons From a Camless Gasoline Compression Ignition Engine," SAE Paper No. 2002-01-0110.

[13] WAVE®, Version 7.2 Build 16, www.ricardo.com/software

[14] Wagner, R. M., Edwards, K. D., Daw, C. S., Green, J. B., Jr., and Bunting, B. G., 2006, "On the Nature of Cycle Dispersion in Spark-Assisted HCCI Combustion," SAE Paper No. 2006-01-0418.

[15] Edwards, K. D., Daw, C. S., Wagner, R. M., and Green, J. B., Jr., 2006, "Cyclic Variability During the Transition Between Spark-Ignited Combustion and HCCI," *Proceedings of the 2006 Technical Meeting of the Central States Section of The Combustion Institute*, Cleveland, OH, May 21–23.

[16] Daw, C. S., Wagner, R. M., Edwards, K. D., and Green, J. B., Jr., 2007, "Understanding the Transition Between Conventional Spark-Ignited Combustion and HCCI in a Gasoline Engine," Proc. Combust. Inst., **31**, pp. 2887–2894.

[17] Wooldridge, M. S., Walton, S. M., He, X., and Zigler, B. T., 2006, "Chemical Kinetics of Homogeneous Charge Compression Ignition and Other Low-Temperature Combustion Strategies," *Proceedings of the 2006 Technical Meeting of the Central States Section of the Combustion Institute*, Cleveland, OH, May 21–23.

[18] Liu, S., Hewson, J., Chen, J. H., and Pitsch, H., 2004, "Effects of Strain Rate on High-Pressure Nonpremixed *n*-heptane Autoignition in Counterflow," Combust. Flame, **137**(3), pp. 320–339.

[19] Andrae, J., Johansson, D., Björnbom, P., Risberg, P., and Kalghatgi, G., 2005, "Co-Oxidation in the Auto-Ignition of Primary Reference Fuels and *n*-Heptane/Toluene Blends," Combust. Flame, **140**, pp. 267–286.

[20] Ogink, R., and Golovitchev, V. I., 2003, "Reaction Mechanisms for Natural Gas and Gasoline in Homogeneous Charge Compression Ignition (HCCI) Engine Modeling," SAE Sixth International Conference on Engines for Automobiles, ICE2003, Naples, Italy, Sept.

[21] Fieweger, K., Blumenthal, R., and Adomeit, G., 1997, "Self-Ignition of S.I. Engine Model Fuels: A Shock Tube Investigation at High Pressure," Combust. Flame, **109**, pp. 599–619.

Experimental Examination of Prechamber Heat Release in a Large Bore Natural Gas Engine

Daniel B. Olsen

Allan T. Kirkpatrick

Engines and Energy Conversion Laboratory,
Mechanical Engineering Department,
Colorado State University,
Fort Collins, CO 80525

A common solution in reducing NO_x emissions to meet new emission regulations has been lean burn combustion. However, with very lean air/fuel (A/F) ratios, both carbon monoxide and hydrocarbon emissions become unacceptably high due to the spark misfiring and combustion instabilities. In order to mitigate this, a prechamber ignition system is often used to stabilize combustion at very lean A/F ratios. In this paper, the heat release in a retrofit prechamber system installed on a large bore natural gas engine is examined. The heat release analysis is based on dynamic pressure measurements both in the main chamber and prechamber. The Woschni correlation is utilized to model heat transfer. Based on heat release modeling and test data analysis, the following observations are made. Main chamber heat release rates are much more rapid for prechamber ignition compared to spark ignition. During combustion in the prechamber, much of the fuel flows into the main chamber unreacted. About 52% of the mass in the prechamber, at ignition, flows into the main chamber during prechamber combustion. Prechamber total heat release, pressure rise, and maximum jet velocity all increase with increasing prechamber equivalence ratio. Prechamber combustion duration and coefficient of variation of peak pressure are minimized at a prechamber equivalence ratio of about 1.09. [DOI: 10.1115/1.2906182]

Introduction

The topic of this paper is heat release modeling and characterization of a precombustion chamber (prechamber) for use on a large bore natural gas engine. A prechamber ignition system is a small chamber, usually 1–2% of the clearance volume, in which a near-stoichiometric mixture of fuel and air is ignited by a standard spark plug. The igniting mixture is propelled into the main chamber by the increasing pressure in the prechamber. This burning jet can have an ignition energy much greater than that from a normal spark plug, and ignition in the main chamber is initiated through multiple ignition sources or an elongated ignition source. One of the objectives of the paper is to better characterize the prechamber jet, such as the temperature and pressure profile, mass fraction burned as the jet propagates into the main chamber, and the overall combustion duration.

There are several advantages to this type of ignition system. A common solution in reducing NO_x emissions to meet new emission regulations has been lean burn combustion. However, with very lean air/fuel (A/F) ratios, both carbon monoxide and hydrocarbon emissions become unacceptably high due to the spark misfiring and combustion instabilities. Because the ignition energy is much higher and spatially distributed, prechambers can ignite a leaner overall mixture. Since the ignition volume in the main chamber is larger, ignition is less affected by mixture heterogeneity, thus resulting in more consistent combustion and reduced cycle-to-cycle combustion variations. This effectively extends the lean limit of combustion, allowing for cooler in-cylinder temperatures without significant cycle-to-cycle variations [1]. Consequently, NO_x emissions from the main combustion chamber can be reduced to much lower levels than for open chamber spark ignition. Also, due to the size of the fuel jet, the combustion flame front generally has a shorter distance to travel to complete the combustion process and thus reduces the combustion duration.

Prechambers are typically operated at near stoichiometric or rich equivalence ratios. It has been shown that the emissions from the prechamber can be a significant component of the exhaust emissions [2,3]. In particular a rich prechamber mixture, in comparison to a stoichiometric mixture, produces more CO, overall total hydrocarbons (THCs), higher THC percentages of VOCs, and possibly higher NO_x. Higher overall levels of THC may increase CH_2O [4,5] as well. In the experimental measurements by Gingrich et al. [3], it was shown that the prechamber significantly contributed to engine out NO_x emissions in a Waukesha 3521 four-stroke lean burn engine. Gas samples were obtained from the prechamber via a high temperature check valve. The composition of the prechamber sampled gas was compared to the gas composition in the exhaust. For nominal operating conditions, the NO_x originating from the prechamber was only about 10% of engine out NO_x emissions. At the lean limit of operation, however, the engine out NO_x consisted of approximately 85% prechamber NO_x. Thus, at engine operating conditions that minimize NO_x production, the primary source of the NO_x is the prechamber.

Heat Release Analysis

Heat release analysis is an important internal combustion engine analysis technique for determining combustion energy characteristics based on in-cylinder pressure profile data. There are generally two different techniques employed. One is the Rassweiler and Withrow [6] technique, in which the pressure change in the cylinder is assumed to be composed of the pressure change due to the volume change and the pressure rise due to the combustion. The pressure change related to the volume change is accounted for with a polytropic ideal gas relationship and the pressure rise due to the combustion is assumed to be proportional to the mass of fuel burned. Although this technique is widely used, it contains a number of approximations. For example, the wall heat transfer is accounted for by an empirical selection of the polytropic coefficient. However, the polytropic coefficient will not only vary from engine to engine but will also vary throughout the combustion process.

A more rigorous approach that incorporates heat transfer explicitly is a heat release approach using the energy equation. An example of this second approach is presented by Gatowski et al. [7]. By explicitly modeling heat transfer, both the total heat release and the net heat release can be determined. The fuel mass fraction burned can be computed by expressing the instantaneous total heat release as a fraction of the total heat release integrated over the combustion duration.

Heat Release Modeling. The heat release analyses in this paper are based on pressure measurements in the main chamber and the prechamber. Two heat release models were developed in order to compare the heat release from an engine with a prechamber to that from a conventional open (spark) ignition system. The first model is an overall heat release model combining both the main chamber and the prechamber, and the second is a heat release model of the prechamber. The heat release modeling includes wall heat transfer, and excludes fuel and crevice volume flow. For the overall heat release model where the combined chambers form the control volume system of interest, the energy balance equation in differential form is

$$\frac{dQ}{d\theta} = \left(\frac{C_p P}{R}\right)\frac{dV}{d\theta} + \left(\frac{C_v V}{R}\right)\frac{dP}{d\theta} - \frac{dQ}{d\theta}$$

In the overall model, the temperatures of the main and prechamber are assumed to be the same. Since the prechamber is only about 1% by volume of the main chamber volume when the piston is at top dead center, the impact of this assumption is small.

For the prechamber, the energy balance equation in differential form is

$$\frac{dQ_{pc}}{d\theta} = \left(\frac{C_v V}{R}\right)\frac{dP}{d\theta} - \frac{h\,dm}{d\theta} - \frac{dQ_{w\text{-}pc}}{d\theta}$$

The energy balance on the prechamber includes the fuel/air mass flow through the nozzle between the prechamber and the main chamber. The prechamber volume is fixed, so there are no terms that involve volume change. The ideal gas parameters C_p, C_v, R, and h are evaluated assuming air properties. These parameters, with the exception of R, vary with temperature. The temperature used to evaluate the enthalpy of the mass flowing into or out of the prechamber nozzle depends on the flow origin. If the mass is flowing out of the prechamber into the main chamber, then the average temperature of the gas in the prechamber is used. If the mass is flowing into the prechamber, then the average temperature in the main chamber is used. In both models, the mass flow of fuel into the prechamber is neglected.

For the calculations presented here, the prechamber analysis is only performed from prechamber spark ignition up until the time when significant combustion occurs in the main chamber. Combustion is assumed to begin in the main chamber when the pressure in the main chamber is greater than the pressure in the prechamber. During this period, the mass flow is from the prechamber into the main chamber.

Wall Heat Transfer. To carry out the energy balance analyses described above, it is necessary to know the instantaneous convective heat transfer coefficient of the main chamber and prechamber walls. A common heat transfer correlation used for instantaneous heat transfer in internal combustion engines is the Woschni correlation [8]. Although this correlation was developed for diesel engines, it has been frequently applied to spark ignition engines. In this paper, we first apply the correlation in its original form, then assess whether or not the model needs to be modified.

The convective heat transfer from the combustion gas to the cylinder wall is

$$\frac{dQ_w}{dt} = h_c A(T_w - T)$$

The Woschni correlation is as follows:

Fig. 1 The Cooper Bessemer GMV-4TF large bore natural gas engine

$$\text{Nu} = \frac{h_c B}{k} = 0.035\text{Re}^{0.8} = 0.035\left(\frac{\rho w B}{\mu}\right)^{0.8}$$

where

$$w = 2.28U_p + 0.00324CT_o\left(\frac{V_d}{V_o}\right)\left[\frac{(P_f - P_m)}{P_o}\right]$$

The original correlation, because it was developed for four-stroke cycle engines, references intake valve closing to indicate the end of the "breathing" process. Here, we reference exhaust port closure rather than intake valve closure to adapt to the two-stroke cycle application, since the exhaust ports typically close after the intake ports. Inclusion of an empirical constant C follows the work of Gatowski et al. [7]. A constant of $C=2.3$ was used. This adjusted both the total heat release and the slope of the total heat release versus the crank angle curve. The slope of the total heat release versus the crank angle curve should approach zero near the end of the expansion stroke.

Description of Experiment

Test Engine. The experimental data were obtained from a four-cylinder Cooper GMV-4TF large bore natural gas two-stroke cycle engine. A photograph of the engine is shown in Fig. 1. The engine is a slow speed (300 rpm) two-stroke cycle engine with a 14 in. (36 cm) bore, 14 in. (36 cm) stroke. It is loaded with a computer-controlled, water brake dynamometer to provide precise load control. The GMV-4TF is outfitted with an Altronic CPU2000 ignition and an Altronic-Hoerbiger Hyperfuel™ 500 psi (gauge) (3.5 MPa) high pressure fuel injection. The engine is instrumented with over 100 different engine parameters automatically recorded at each test point. The test conditions were typically at a 13.5 in. Hg intake pressure, 300 rpm, 440 bhp, and overall trapped equivalence ratio of 0.77. In operating the engine, the ignition timing was retarded by about 6 deg when changing from open to prechamber operation to maintain the same location of peak pressure at 16 deg after top dead center (atdc).

The dynamic pressure for each cylinder is measured with Kistler 6125A piezoelectric combustion pressure sensors. A Rosemount NGA 2000 five-gas bench is used for measurement of criteria pollutants, O_2, and CO_2. A Nicolet Magna Fourier transform infrared (FTIR) spectrometer is used to measure the emissions of criteria pollutants, CO_2, and hazardous air pollutants.

Prechamber. Figure 2 shows a cutaway profile of the prechamber. The locations of the inlet fuel, the spark plug, and the exit nozzle are indicated on the figure. The prechambers were designed to screw into the primary spark plug port in each cylinder. A schematic for the prechamber is provided in Fig. 3. Kistler 6052A piezoelectric pressure transducers were utilized to measure the pressure in the prechamber in each cylinder. A fast actuating
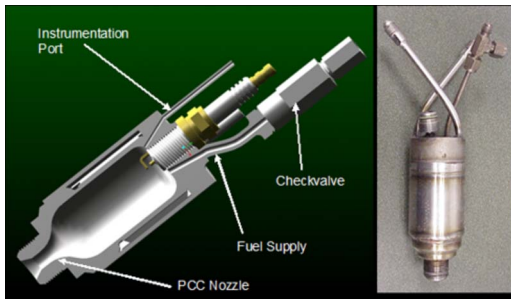
Fig. 2   Prechamber cutaway profile

sample valve was utilized to extract a gas sample from the prechamber on Cylinder 4. More details on the fast actuating sample valve can be found in Olsen et al. [9]. The gas samples were analyzed with the emission analyzers by way of a heated sample line.

As shown in Fig. 2, the fuel supply to the prechamber was controlled by using a pressure regulator and a check valve. Fuel was supplied to the prechamber while the prechamber pressure was less than the set point of the pressure regulator. The prechamber equivalence ratio was varied about a stoichiometric condition from 0.88 to 1.28, and was measured using a zirconia sensor with an AFRecorder 4800.

Results

Computation of Heat Release. Cylinder pressure profiles of the main and prechamber program were obtained from the Cooper test engine at nominal conditions of 300 rpm and a lean overall trapped equivalence ratio of 0.77 [10]. Using the program Engineering Equation Solver (EES) [11], the differential energy balance equations given above were integrated to determine the heat release rates in the prechamber and the main chamber. The mass flow through the prechamber nozzle to the main chamber was computed from the continuity equation, with the flow coefficient across the nozzle assumed to be 0.7. Based on the main chamber and prechamber pressure ratio data, the mass flow was computed to be subsonic throughout the prechamber combustion period.

Cylinder pressure profile data with an open cylinder with a spark ignition from the same test engine were used for comparison with the prechamber results. The pressure data were the average of 200 cycles, and were "smoothed" by averaging nine values, four on either side of a particular crank angle location. The main and cylinder temperatures were computed using the ideal gas equation.
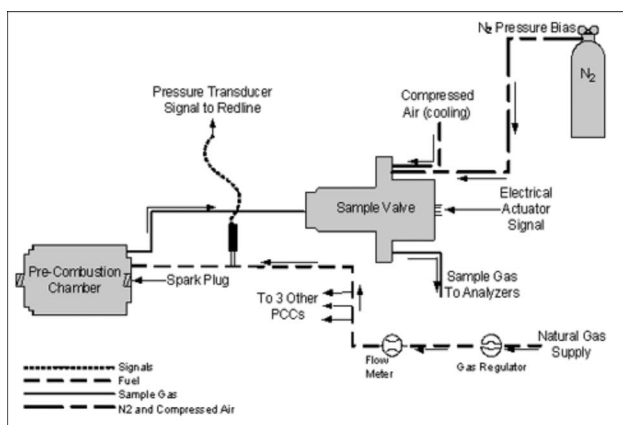
Fig. 3   Prechamber instrumentation schematic
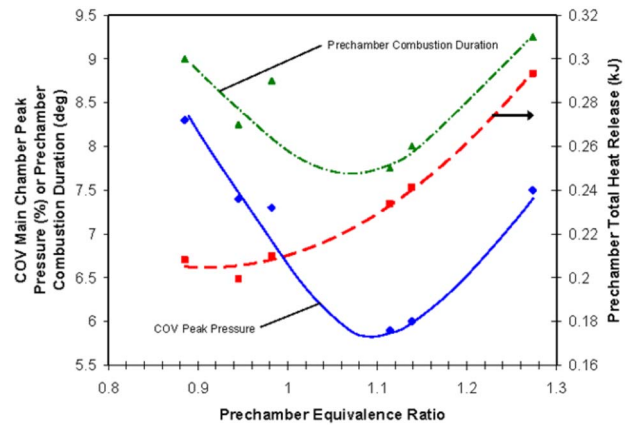
Fig. 4   Dependence of prechamber combustion on equivalence ratio

Prechamber Equivalence Ratio. With the use of a prechamber ignition system, the prechamber equivalence ratio must be chosen to minimize combustion instability. The COV of the main chamber peak pressure is typically used as a metric of combustion instability. Figure 4 shows the peak pressure COV as the equivalence ratio of the prechamber is varied from 0.88 to 1.28. The data indicate a minimum at an equivalence ratio of about 1.09, slightly rich. This is also the location of a minimum for the prechamber combustion duration.

The minima in the prechamber combustion duration at an equivalence ratio of about 1.09 can be associated with ignition phenomena. The flame kernel in a spark-ignited mixture begins as a laminar flame [12]. The laminar flame velocity is strongly related to the equivalence ratio and is maximized at a slightly rich equivalence ratio, between 1.05 and 1.10 for pure methane [13]. Laminar flame behavior is used here to provide insight; however, the overall combustion process in the prechamber is expected to be turbulent.

Combustion instability is a complex process and is associated with local variations in equivalence ratio and turbulence near the spark electrode [12,14]. Operation at an overall equivalence ratio that maximizes laminar flame speed will tend to minimize combustion instability.

The prechamber heat release model was utilized to gain more insight into prechamber combustion with increasing equivalence ratio. The prechamber total heat release is plotted in Fig. 4. Note that it does not follow the same trend as prechamber combustion duration and peak pressure. Rather, prechamber total heat release generally increases monotonically with prechamber equivalence ratio. Normally one would not anticipate an increase in total heat release as the equivalence ratio increases beyond 1.0. However, chemical analysis of prechamber gas samples shows a general trend of increasing combustion efficiency with increasing equivalence ratio.

Similarly, as shown in Fig. 5, the prechamber pressure rise and the maximum prechamber jet velocity increase with equivalence ratio for all data taken. The parameters in Fig. 5 show a general increasing trend with prechamber equivalence ratio. These parameters can be associated with total heat release in the prechamber. If the prechamber total heat release is larger, then one can expect a larger pressure rise and prechamber jet velocity.

Prechamber Mass Flow and Heat Release. The prechamber heat release analysis is performed on the data taken at a prechamber equivalence ratio of about 1.11, where the lowest COV of peak pressure occurs (see Fig. 4). The computed prechamber heat release is shown in Fig. 6. Also shown in Fig. 6 are the measured pressure profile, the computed mass flow from the prechamber into the main chamber, and the bulk temperature profile. This
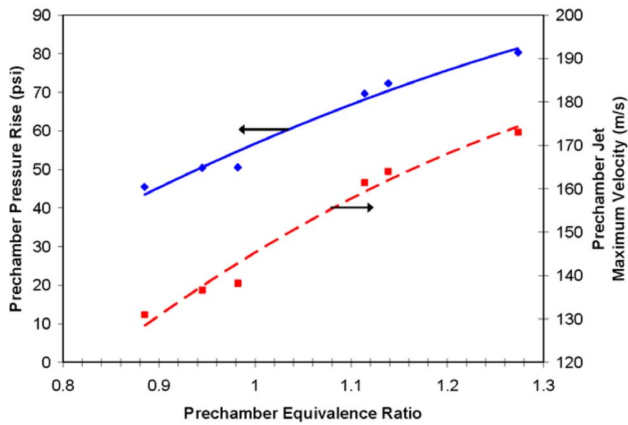
Fig. 5 Prechamber pressure rise and jet velocity

computation is performed during the interval between the prechamber ignition and start of combustion in the main chamber. It is interesting to note that the mass flow rate out of the prechamber peaks at about 0.1 kg/s about when the total heat release rate (slope of prechamber heat release curve) is a maximum. The mass flow analysis shows that about 52% of fuel/air mass present in the prechamber at the start of prechamber ignition flows into the main chamber during the prechamber combustion process.

The prechamber total heat release curve shown in Fig. 6 indi-
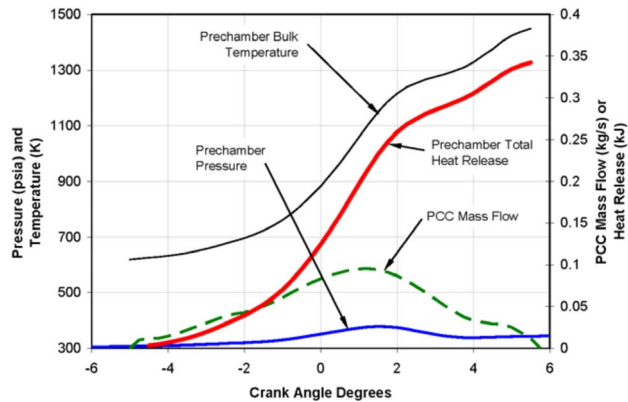
Fig. 6 Prechamber heat release characteristics versus crank angle
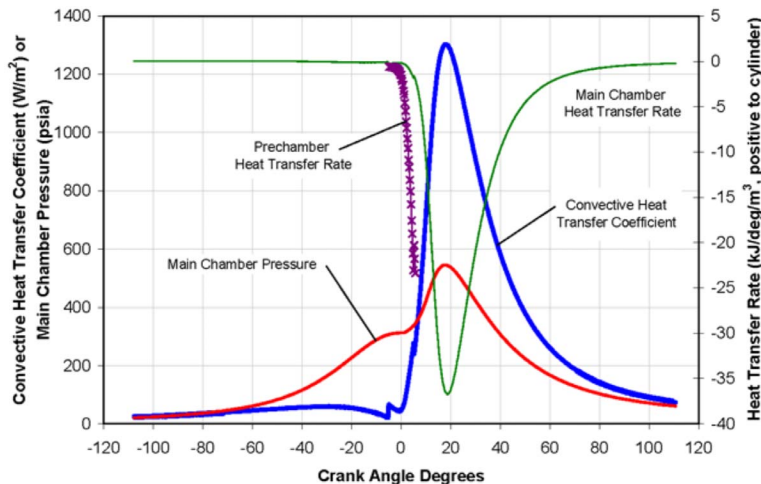
cates that 0.34 kJ is released during the prechamber combustion. Note that this value is higher than all the prechamber total heat release values in Fig. 4. The data in Fig. 6, however, were taken on a different, unrelated test run from the data in Fig. 4. There is about 1.1 kJ of chemical energy in the fuel-air mixture in the prechamber at ignition. The relative fraction of the chemical energy released in the prechamber is therefore less (31%) than that released in the main chamber (79%). Thus, as combustion occurs in the prechamber, one possibility is that much of the prechamber fuel is propelled into the main chamber unburned. It is also possible that much of the fuel is partially reacted and intermediate combustion products are injected into the main chamber.

The prechamber peak temperature (about 1450 K) is less than the main chamber peak temperature (about 1510 K). This is unexpected based on the difference in equivalence ratio. Combustion in the prechamber occurs at an equivalence ratio near stoichiometric, whereas combustion in the main chamber is very lean. Thus, the theoretical (i.e., adiabatic, constant volume) flame temperature in the prechamber is much higher. However, during combustion in the prechamber energy leaves via mass flow out the nozzle and the heat transfer surface to volume ratio is larger for the prechamber. These two effects combine to reduce the prechamber bulk temperature.

The temperature calculations provide an indication of NO_x production in the prechamber. It is generally accepted that the NO_x formation rate becomes significant at 2200 K. Thus, the temperature computation indicates that NO_x formation in the prechamber, for this design, is not large. This is consistent with in-cylinder sampling results from earlier work [11], where moderate levels ($\sim$600 ppm) of NO_x were measured in the prechamber near prechamber peak pressure. For future prechamber designs, it may be possible to more completely burn the fuel in the prechamber and inject a higher percentage of prechamber mass into the main chamber, while maintaining a peak prechamber temperature below the critical NO_x formation temperature.

Prechamber and Main Chamber Heat Transfer. The prechamber and main chamber wall heat transfer loss (kJ/deg m^3) profiles are plotted in Fig. 7. The heat transfer rates are normalized relative to the respective chamber volume. The convection heat transfer coefficient and the prechamber and main chamber wall heat transfer rates are also plotted. The prechamber wall heat transfer is shown in the plot during prechamber combustion only. The measured main chamber cylinder pressure is included for reference. The wall heat transfer losses are negative since the energy transfer is out of the cylinders. Note that during prechamber combustion the prechamber wall heat transfer loss is signifi-

Fig. 7 Prechamber and main chamber heat transfer versus crank angle
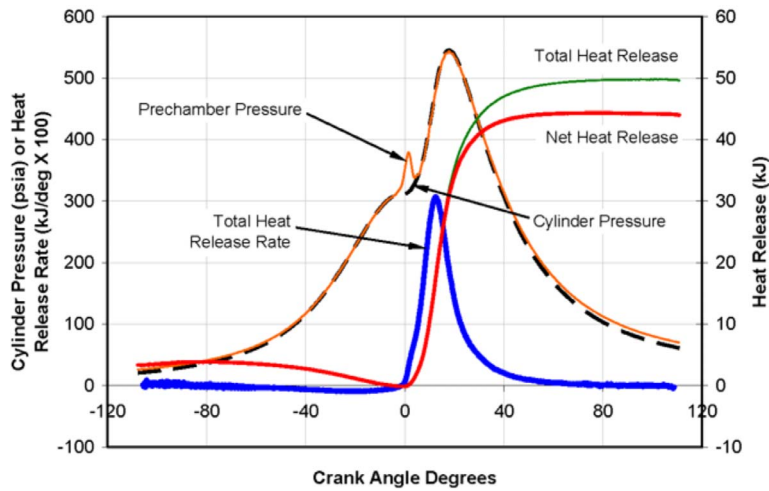
Fig. 8 Heat release versus crank angle for prechamber ignition

cantly greater than the main chamber heat transfer loss. The convection heat transfer coefficient is dependent on, among other parameters, instantaneous piston speed and pressure rise ($P_f - P_m$). During main chamber combustion, the piston is accelerating and the pressure rise is increasing. Consequently, a large increase in convection heat transfer coefficient is seen.

Comparison of Overall Heat Release. Figure 8 shows the heat release results with prechamber ignition. The open chamber (spark) ignition results are presented in Fig. 9. The main chamber pressure and prechamber pressure are plotted in the figures. Also plotted are the total heat release rate, and the total and net heat release. The difference between the total and net heat release is due to the wall heat transfer loss. The prechamber pressure profile follows the main chamber pressure profile except during the combustion process in the prechamber. Note that the magnitude of the pressure rise of the prechamber during combustion is about 25% of the pressure rise in the main chamber.

The heat release rates quickly rise during combustion, reach a maximum just before peak pressure, and then transition to zero at the end of the combustion process. Comparison of the heat release rate profiles in Figs. 8 and 9 indicates that combustion takes place in a shorter period of time with prechamber ignition. The increase in the heat release rate for prechamber ignition occurs over a smaller crank angle duration and reaches a peak value approxi-

mately 50% larger.

The net and total heat release curves in Figs. 8 and 9 are very similar. The net heat release peaks 58 deg after peak pressure then gradually decreases. This decrease occurs because late in the combustion process the rate of heat transfer from the cylinder is greater than the instantaneous rate of heat release due to the combustion.

The difference in magnitude between the total heat release and net heat release is due to the heat transfer. The net heat release curve was found to be independent of the heat transfer correlation. The total heat release curve should increase during combustion, then gradually transition to a slope of zero. The total heat release curve generally adheres to this behavior.

The total heat released can be compared to the chemical energy in the cylinder to ensure that the magnitude of the total heat release is appropriate. The chemical energy was computed from the lower heating value (47.7 MJ/kg) using the measured fuel gas composition, the trapped AF ratio (21.86) evaluated from the exhaust composition measurements [15], the scavenging efficiency (73%) determined from earlier scavenging measurements, and the trapped mass (41.1 g) computed from the air manifold temperature and the exhaust manifold pressure. The resulting chemical energy was calculated to be 62.7 kJ compared to a total heat re-
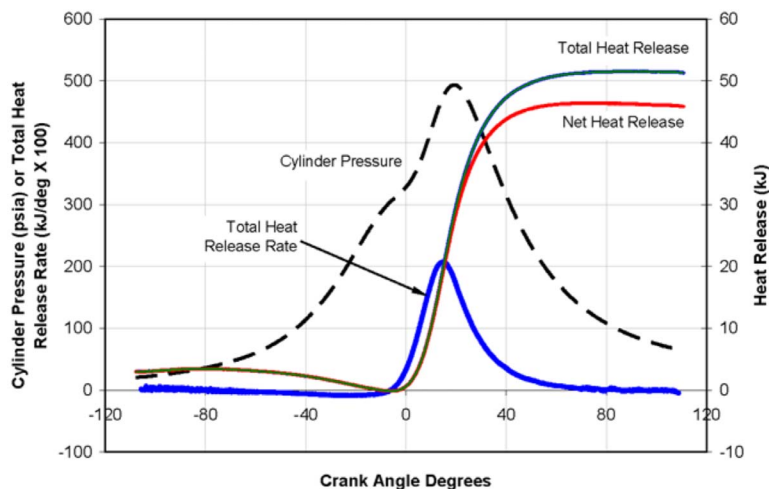
Fig. 9 Heat release versus crank angle for open chamber ignition
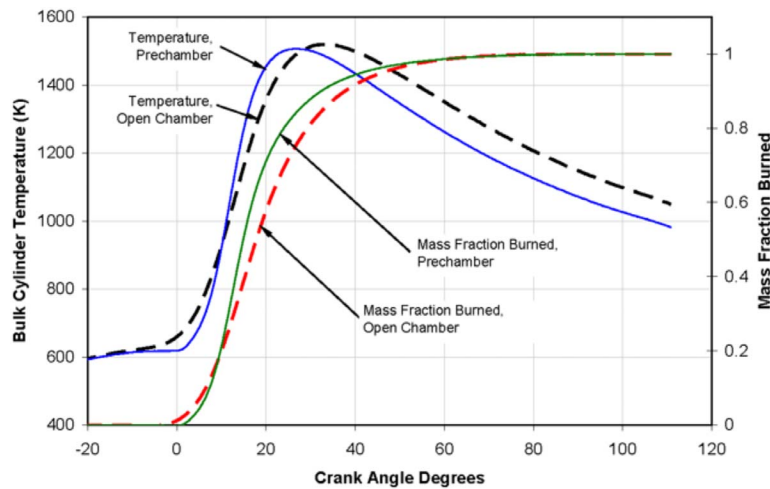
Fig. 10 Comparison of open chamber and prechamber ignition temperature and burn fraction

lease of 51.6 kJ. The total heat release is expected to be less than the chemical energy, since the chemical energy calculation is based on an ideal combustion process.

A direct comparison between open chamber and prechamber ignition of two parameters is made in Fig. 10. The two parameters are bulk, or average, main chamber temperature, and mass fraction burned. The mass fraction burned is the instantaneous heat release divided by the maximum heat release, which occurs at the end of the combustion process. The data show that the bulk cylinder temperature significantly peaks after peak pressure. Additionally, the peak bulk cylinder temperature is significantly below the adiabatic flame temperature, which is above 2000 K. Clearly, the rate of combustion is larger in the prechamber case, as illustrated earlier with total heat release rate. The mass fraction burned for prechamber ignition increases much more rapidly than for open chamber ignition. Consequently, the bulk temperature peaks earlier in the prechamber ignition case.

Summary and Conclusions

Heat release analysis based on cylinder pressure data and the first law of thermodynamics for the precombustion chamber has been developed. It was applied to a large bore natural gas two-stroke cycle engine. The Woschni correlation was utilized to model heat transfer. Heat release analysis was performed on test data from the large bore engine.

Based on heat release modeling and test data analysis, the following conclusions and observations are made.

- Main chamber heat release rates are much more rapid for prechamber ignition compared to spark ignition.
- Heat release analysis in the prechamber indicates that either the fuel is partially reacted or a significant fraction of the fuel flows into the main chamber unreacted.
- About 52% of the mass in the prechamber, at ignition, flows into the main chamber during prechamber combustion.
- Prechamber total heat release, pressure rise, and maximum jet velocity all increase with increasing equivalence ratio.
- Prechamber combustion duration and COV of peak pressure are minimized at a prechamber equivalence ratio of about 1.09.
- The above performance optimum does not correspond to the equivalence ratio where the most prechamber energy is released, which occurs at a larger equivalence ratio.

Nomenclature

A = cylinder wall area
B = cylinder bore
C = empirical constant
C_p = gas specific heat at constant pressure
C_v = gas specific heat at constant volume
h_c = convective heat transfer coefficient for combustion chamber walls
h = enthalpy of the mass flowing in/out of the prechamber
k = gas thermal conductivity
m = mass flowing through the prechamber nozzle, positive into prechamber
Nu = Nusselt number
P = instantaneous cylinder pressure
P_f = instantaneous firing cylinder pressure
P_m = instantaneous motored cylinder pressure
P_o = gas pressure at exhaust port closure
Q = combustion energy released in combined main chamber and prechamber
Q_w = heat transfer through cylinder walls
Q_{pc} = combustion energy released in the prechamber
$Q_{w\text{-}pc}$ = prechamber wall heat transfer, positive into prechamber
R = ideal gas constant
Re = Reynolds number
T = instantaneous cylinder temperature
T_o = temperature at exhaust port closure
T_w = cylinder wall temperature
t = time
U_p = mean piston speed
V = instantaneous cylinder volume
V_d = displacement volume
V_o = volume at exhaust port closure
V_{pc} = prechamber volume

θ = crank angle
ρ = gas density
μ = gas viscosity

References

[1] Iocco, D. E., 1995, "Retrofit Precombustion Chamber Helps Cut Engine NOx Emissions," Pipe Line and Gas Industry, **78**, pp. 41–46.

[2] Callahan, T. J., and Kubesh, J. T., 1997, "Contribution of Prechamber Combustion to Engine CO and HC Emissions," Gas Machinery Conference, 1997.

[3] Gingrich, J. W., Olsen, D. B., Puzinauskas, P., and Willson, B. D., 2006, "Precombustion Chamber NOx Emission Contribution to an Industrial High-Speed, Natural Gas Engine," Int. J. Engine Res., **7**(1), pp. 41–49.

[4] Mitchell, C. E., and Olsen, D. B., 2000, "Formaldehyde Formation in Large Bore Natural Gas Engines Part 1: Formation Mechanisms," ASME J. Eng. Gas Turbines Power, **122**(4), pp. 603–610.

[5] Olsen, D. B., and Mitchell, C. E., 2000, "Formaldehyde Formation in Large Bore Engines Part 2: Factors Affecting Measured CH2O," ASME J. Eng. Gas Turbines Power, **122**(4), pp. 611–616.

[6] Rassweiler, G. M., Withrow, L., and Cornelius, W., 1940, "Engine Combustion and Pressure Development," SAE J., **46**(1), pp. 25–48.

[7] Gatowski, J. A., Balles, E. N., Chun, K. M., Nelson, F. E., Ekchian, J. A., and Heywood, J. B., 1984, "Heat Release Analysis of Engine Pressure Data," Fuels and Lubricants Meeting & Exposition, Oct. 8–11, SAE Paper No. 841359.

[8] Woschni, G., 1967, "A Universally Applicable Equation for the Instantaneous Heat Transfer Coefficient in the Internal Combustion Engine," SAE Trans., **77**, pp. 3065–3083.

[9] Olsen, D. B., Holden, J. C., Hutcherson, G. C., and Willson, B. B., 2001, "Formaldehyde Characterization Utilizing In-Cylinder Sampling in a Large Bore Natural Gas Engine," ASME J. Eng. Gas Turbines Power, **123**(3), pp. 669–676.

[10] Olsen, D. B., Adair, J. L., and Willson, B. D., 2005, "Precombustion Chamber Design and Performance Studies for a Large Bore Natural Gas Engine," ASME Paper No. ICES2005-1057.

[11] Engineering Equation Solver, Version 7.721, ©1992-2006, S. A. Klein, F-Chart Software.

[12] Hiltner, J. D., 1997, "The Impact of Fuel Distribution on Cyclic Combustion Variations in a Natural Gas Fueled Spark Ignition Engine," Ph.D. thesis, Ohio State University.

[13] Andrews, G. E., and Bradley, D., 1972, "The Burning Velocity of Methane-Air Mixtures," Combust. Flame, **19**, pp. 275–288.

[14] Hamai, K., Kawajiri, H., Ishizuka, T., and Nakai, M., 1986, "Combustion Fluctuation Mechanism Involving Cycle-To-Cycle Spark Ignition Variation Due to Gas Flow Motion in S.I. Engines," *21st Symposium (International) on Combustion/The Combustion Institute*, pp. 505–512.

[15] Olsen, D. B., Hutcherson, G. C., Willson, B. D., and Mitchell, C. E., 2002, "Development of the Tracer Gas Method for Large Bore Natural Gas Engines: Part 2—Measurement of Scavenging Parameters," ASME J. Eng. Gas Turbines Power, **124**(3), pp. 686–694.

An Imaging Study of Compression Ignition Phenomena of Iso-Octane, Indolene, and Gasoline Fuels in a Single-Cylinder Research Engine

Bradley T. Zigler[1]
e-mail: bzigler@umich.edu

Stephen M. Walton

Dimitris Assanis

Elizabeth Perez

Margaret S. Wooldridge

Department of Mechanical Engineering,
University of Michigan,
Ann Arbor, MI 48109-2125

Steven T. Wooldridge
Ford Research and Advanced Engineering,
Ford Motor Company,
Dearborn, MI 48121-2053

High-speed imaging combined with the optical access provided by a research engine offer the ability to directly image and compare ignition and combustion phenomena of various fuels. Such data provide valuable insight into the physical and chemical mechanisms important in each system. In this study, crank-angle resolved imaging data were used to investigate homogeneous charge compression ignition (HCCI) operation of a single-cylinder four-valve optical engine fueled using gasoline, indolene, and iso-octane. Lean operating limits were the focus of the study with the primary objective of identifying different modes of reaction front initiation and propagation for each fuel. HCCI combustion was initiated and maintained over a range of lean conditions for various fuels, from $\phi = 0.69$ to 0.27. The time-resolved imaging and pressure data show that high rates of heat release in HCCI combustion correlate temporally to simultaneous, intense volumetric blue emission. Lower rates of heat release are characteristic of spatially resolved blue emission. Gasoline supported leaner HCCI operation than indolene. Iso-octane showed a dramatic transition into misfire. Similar regions of preferential ignition were identified for each of the fuels considered using the imaging data. [DOI: 10.1115/1.2898720]

Keywords: homogeneous charge compression ignition, imaging, optical engine

Introduction

Ignition and combustion are the most important processes in homogeneous charge compression ignition (HCCI) engines, and these phenomena are considered limited by chemical kinetics. HCCI engines have several potential advantages over traditional spark ignition (SI) and diesel engines [1,2]. HCCI offers greater fuel economy than SI engines, because they are capable of higher compression ratios and reduced throttling losses. HCCI engines also offer lower NO_x and particulate emissions than diesel engines, as a result of reduced local high-temperature zones and the homogeneous nature of the reaction. HCCI engines, however, present unique challenges, as chemical kinetics supplant traditional control strategies (i.e., SI and diesel injection timing).

Recent rapid compression facility (RCF) studies of iso-octane/air mixtures by He et al. [3] and Walton et al. [4–6] have demonstrated the presence of distinct ignition regimes. Under low fuel mole fraction conditions, only volumetric ignition was observed [3,4]. At higher fuel mole fractions, reaction fronts appeared to propagate throughout the test chamber of the RCF prior to volumetric ignition [4]. The presence of the reaction fronts served to accelerate ignition. The presence of similar phenomena during HCCI operation of a reciprocating piston engine could complicate ignition timing and the development of robust timing strategies. Additionally, Kaiser et al. [7,8] observed a dramatic change in the engine-out emissions at equivalence ratios of approximately 0.2 in their study of a single-cylinder engine operating in HCCI mode using gasoline fuel. Kaiser et al. proposed that the shift in emissions could be explained by flame "propagation over relatively short distances" for equivalence ratios less than 0.2. The debate over the presence of reaction fronts motivates in part the current work.

The primary objective of the new optical research engine facility at the University of Michigan (UM) is to provide improved understanding of the chemical and physical mechanisms that are important in advanced engine systems, including expanded HCCI and other low-temperature combustion strategies. Research conducted with the optical engine research facility complements that conducted using the UM RCF, expanding to experiments with multiple cycles in a flexible, production-based engine configuration. Specifically, the objective of the current work is to characterize the ignition phenomena observed during HCCI lean operating conditions for three classes of fuels: a reference fuel (indolene), a pump fuel (pump gasoline), and a chemical surrogate fuel (iso-octane). Iso-octane is often used as a chemical surrogate for gasoline, and indolene is used as a reference grade fuel for gasoline; thus, differences in the fuel performance and relationships to ignition phenomena provide insight into translating trends in prototype engine studies to production engines.

Exeperimental Approach

All experiments were conducted using the new UM single-cylinder optical research engine facility. This facility is based on an optical research engine donated to the UM by the Ford Motor Company. The optical research engine design is conceptually based on the optical research engine developed by Sandia National Laboratories [9]. The facility features a hydraulically supported, drop-down cylinder liner assembly with interchangeable fused silica and steel cylinder liners supporting a Bowditch-style piston extension with a quick-release top piston. The piston features a removable crown insert window, made of either fused

---
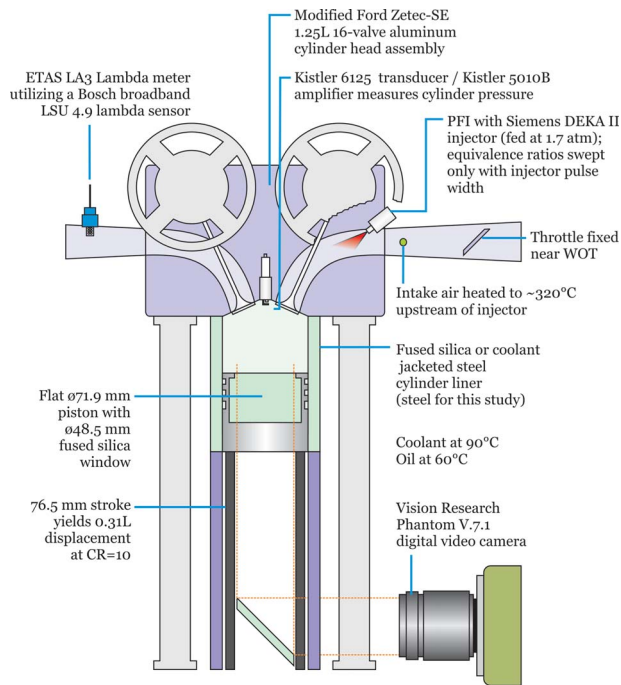
Copyright © 2008 by ASME

Fig. 1 Schematic of the single-cylinder optical research engine

silica or aluminum. An elliptical mirror is fixed in the piston extension for optical access through the $\phi 48.5$ mm piston window. The resulting facility offers excellent axial and orthogonal optical access through the piston window/mirror and the cylinder liner.

The optical research engine, depicted in Fig. 1, is built around a Ford Zetec-SE 1.25 L engine configuration. A modified production cylinder head is used, employing one of the four cylinders available. The aluminum cylinder head features fixed double-overhead cams timing four valves (twin $\phi 26.1$ mm intake, twin $\phi 22.1$ mm exhaust) around a centrally mounted spark plug. A flat-top $\phi 71.9$ mm piston with Torlon® rings strokes 76.5 mm for 0.31 L displacement at 10:1 compression ratio. Fuel is port injected slightly upstream of the intake ports.

The engine is driven by a Micro-Dyn 35 hydraulic dynamometer, which held the engine speed constant at 700 rpm for these experiments. Engine coolant and oil are auxiliary heated; coolant was maintained at 90°C and oil was maintained at 60°C.

Table 1 Experimental engine operating conditions considered in the current work

Fuel	ϕ	Intake air temperature (°C)
Indolene	0.69	317
Indolene	0.55	317
Indolene	0.44	317
Indolene	0.34	318
Iso-octane	0.68	319
Iso-octane	0.61	319
Iso-octane	0.45	319
Iso-octane	0.29	318
Gasoline	0.65	316
Gasoline	0.52	318
Gasoline	0.45	316
Gasoline	0.37	317
Gasoline	0.27	316

Fuel was fed to the Siemens DEKA II dual conical jet injector at 1.7 atm. An ECM spark and fuel injection controller is integrated with the dynamometer. All experiments in this study were run with the same near-WOT throttle plate setting, with the fuel injection pulse width varied to control the overall equivalence ratio of the fuel/air mixture. While this caused various equivalence ratios to have different engine loadings, the fixed throttle plate setting allowed fewer changes to the engine operating conditions to achieve HCCI for various equivalence ratios.

Fuel was injected very early onto a closed intake valve, at 50 deg BTDC during the compression stroke of the preceding cycle, to assist vaporization. Ambient air was preheated with a 1.4 kW heater and the intake manifold was heated using an auxiliary resistive heater to deliver intake air temperatures of approximately 320°C just upstream of the fuel injector. Cylinder pressure is measured by a piezoelectric transducer (Kistler 6125A) and charge amplifier (Kistler 5010B). Intake pressure is measured with an absolute pressure sensor in a water cooled fitting (Kistler 4045A2 with Kistler 4618 amplifier). Crank angle is encoded with a BEI encoder at 360 signal cycles per revolution. Equivalence

Fig. 2 Orientation of the imaged frames with respect to the cylinder geometry. Intake valves are on the bottom, and exhaust valves are on the top. The spark plug is shown at the center. The piston window is $\phi 48.5$ mm, which partially occludes the valves.
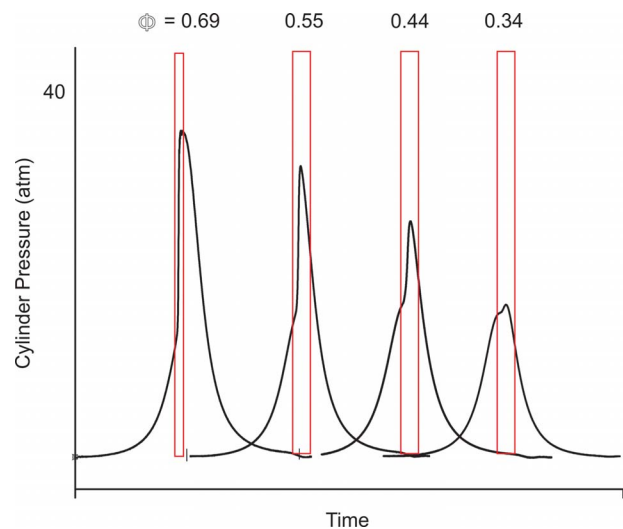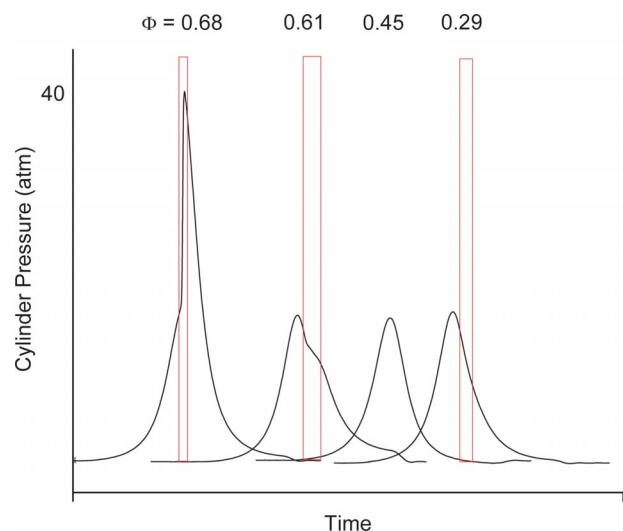

Fig. 3 Typical pressure traces versus time for engine conditions with indolene fuel. The data are superimposed for clarity. The boxed areas coincide with imaging sequences presented in Figs. 4–7.
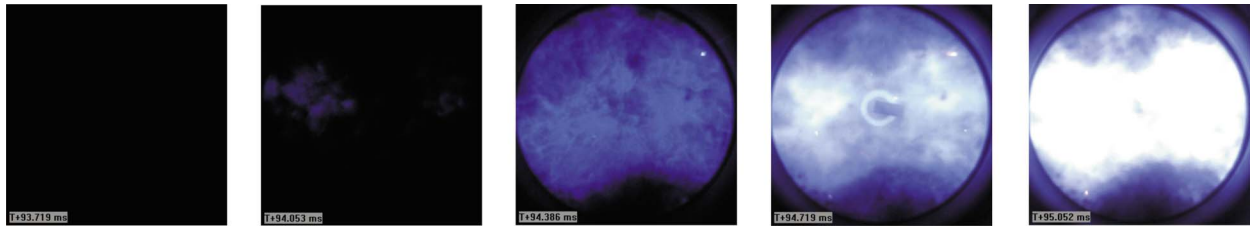
Fig. 4   Image sequence for indolene at $\phi = 0.69$

ratio is measured by an ETAS LA3 lambda meter utilizing a Bosch broadband LSU 4.9 lambda sensor. For the current work, the engine was run with a coolant-jacketed steel cylinder liner.

The fuels used in this work included iso-octane (2,2,4 trimethyl pentane; Sigma-Aldrich, anhydrous 99.8%), indolene (analyzed at 87.12% by weight carbon, <0.05% oxygen, 12.88% hydrogen; H/C=1.762 97.4 RON, 88.3 MON, 92.9 AKI), and commercial gasoline (Shell V-Power 93 octane (AKI) summer blend, assumed H/C=1.85 for lambda meter programming). The combustion chamber was imaged through the piston window using a high-speed color digital video camera (Vision Research

Phantom v7.1, color). The camera is capable of 800×600 pixel spatial resolution, and reduced resolution frame rates up to 160 kHz. A fast 50 mm lens (f/0.95 Nikor TV lens) and C-mount extension tubes are used with the camera to adjust the focal length and to reduce the focal depth along the cylinder axis. In this study, the camera was focused at a plane coinciding with the spark plug ground electrode and the camera settings were fixed at 320 $\times$ 320 pixels at 3000 fps (frames per second) with 309 μs exposure time. The camera sensor array was calibrated according to the
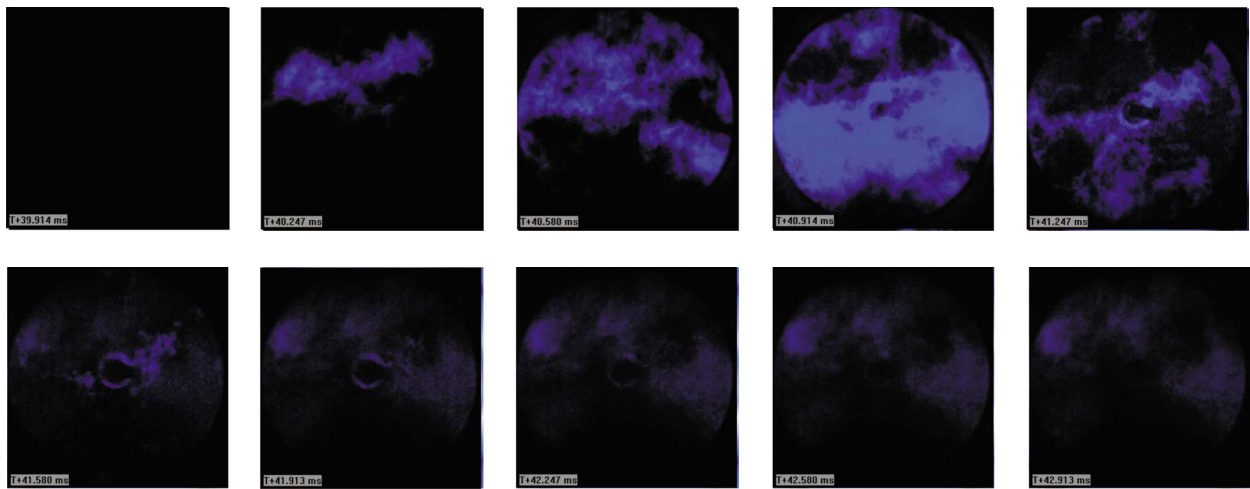
Fig. 5   Image sequence for indolene at $\phi = 0.55$

Fig. 6   Image sequence for indolene at $\phi = 0.44$

Journal of Engineering for Gas Turbines and Power   SEPTEMBER 2008, Vol. 130 **/** **052803-3**
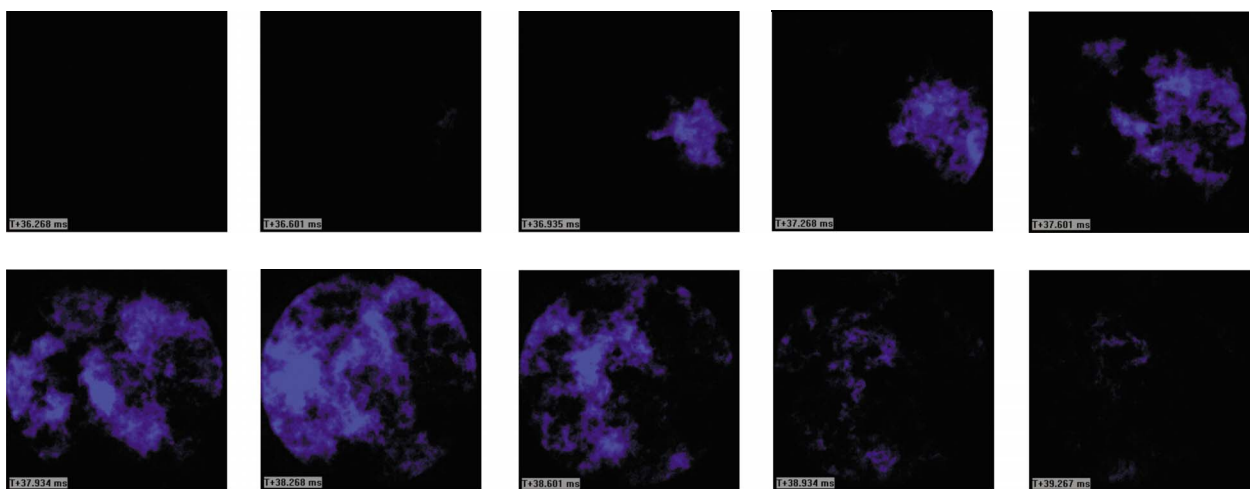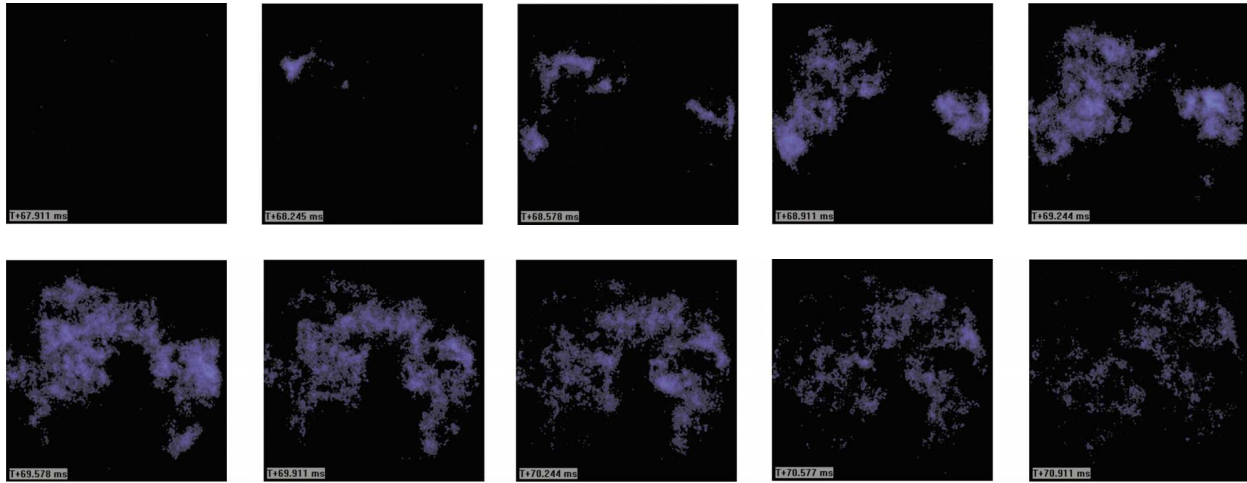
Fig. 7 Image sequence for indolene at $\phi = 0.34$

procedure outlined in Walton et al. [6]. Figure 2 depicts the orientation of the imaged frames and the engine valve geometry.

Results

Intake air preheating was required to achieve HCCI combustion. Once the engine speed was stabilized by the dynamometer and preheated air was introduced to the cylinder, HCCI combustion was initiated with fuel delivery only; no ignition spark was used to initiate firing and then transition to HCCI. The engine was operated through a range of lean conditions, as listed in Table 1. Initial studies were conducted with indolene; then the fuel was changed to iso-octane and later gasoline.

Indolene. Examples of typical pressure traces for each indolene equivalence ratio condition are shown in Fig. 3. The image sequences shown in Figs. 4–7 correlate to each of the pressure traces, as indicated in Fig. 3. The pressure traces for $\phi = 0.69$ and $\phi = 0.55$ showed little cycle-to-cycle variation; however, leaner conditions exhibited considerable irregularity. Pressure traces at conditions of $\phi = 0.69$ and 0.55 show ignition during compression and high heat release rates. Pressure traces at $\phi = 0.44$ showed ignition closer to TDC, with lower rates of heat release. For $\phi = 0.34$, the pressure traces show that HCCI combustion began during the expansion stroke, occurring later with leaner conditions.

Figures 4–7 show image sequences for HCCI combustion of indolene at various equivalence ratios. Each imaging frame represents a time interval of 333 μs, which at 700 rpm translates to 1.4 CAD. The time markers shown in the imaging frames are with respect to an arbitrary camera synchronization trigger signal for each run. All images have been saturation and gain adjusted for clarity.

All of the series show blue emission originating in a localized area in the combustion chamber. The time observed for the blue emission to expand from the point of origin to the remainder of the combustion chamber increased with leaner conditions. At $\phi = 0.69$, relatively uniform blue emission consistently developed across the combustion chamber within one image sequence (1.4 CAD) of the first indication of ignition. The data at $\phi = 0.55$ showed similar but slightly longer time to observe emission throughout the cylinder. At leaner conditions, the propagation required significantly longer times and emission never appeared simultaneously throughout the volume of the combustion chamber.

The images obtained at $\phi = 0.69$ (Fig. 4) showed bright white emission, which may be attributed to saturation of the camera array or thermal emission from soot particles. Further experiments, discussed below, indicate that the white emission is due to the camera pixel saturation. Leaner conditions did not produce white emission.

The rapid heat release rates characterized as rapid increases in the pressure trace data for $\phi = 0.69$ and 0.55 in Fig. 3 correspond temporally to the visualization of intense blue emission throughout the volume of the combustion chamber as seen in the imaging sequences of Figs. 4 and 5. The less pronounced heat release rate seen in Fig. 3 for $\phi = 0.44$ corresponds to the slightly less than complete volume, less intense blue emission data presented in Fig. 6. The spatially resolved, weaker blue emission seen in Fig. 7 for $\phi = 0.34$ corresponds to the small pressure rise on the expansion stroke seen in Fig. 3.

Iso-Octane. Examples of typical pressure traces for each iso-octane run are shown in Fig. 8. The image sequences shown in Figs. 9–12 correlate to the pressure traces where indicated in Fig. 8, with the exception of the image sequence for $\phi = 0.45$. The imaging sequence for that experiment was not synchronized with pressure data. Consequently, a typical but not matching sequence of images is presented for that condition.

The cylinder pressure traces for $\phi = 0.68$ showed ignition during compression, high heat release rates, and little cycle-to-cycle variation. Sequential pressure traces for $\phi = 0.61$ showed consid-
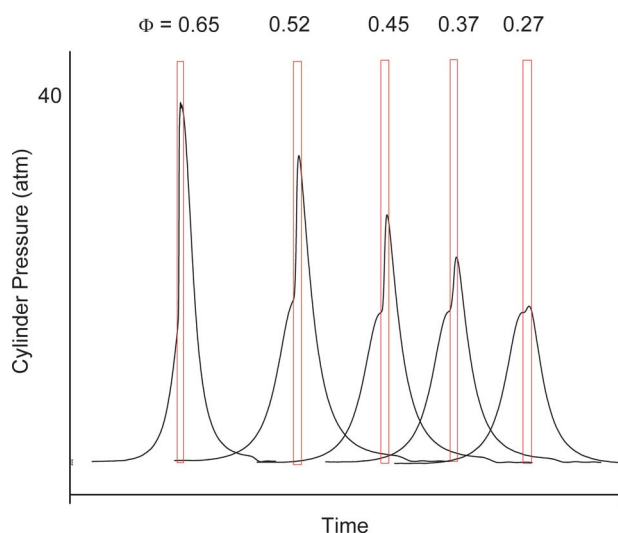

Fig. 8 Typical pressure traces versus time for engine conditions with iso-octane fuel. The data are superimposed for clarity. The boxed areas coincide with imaging sequences presented in Figs. 9, 10, and 12.
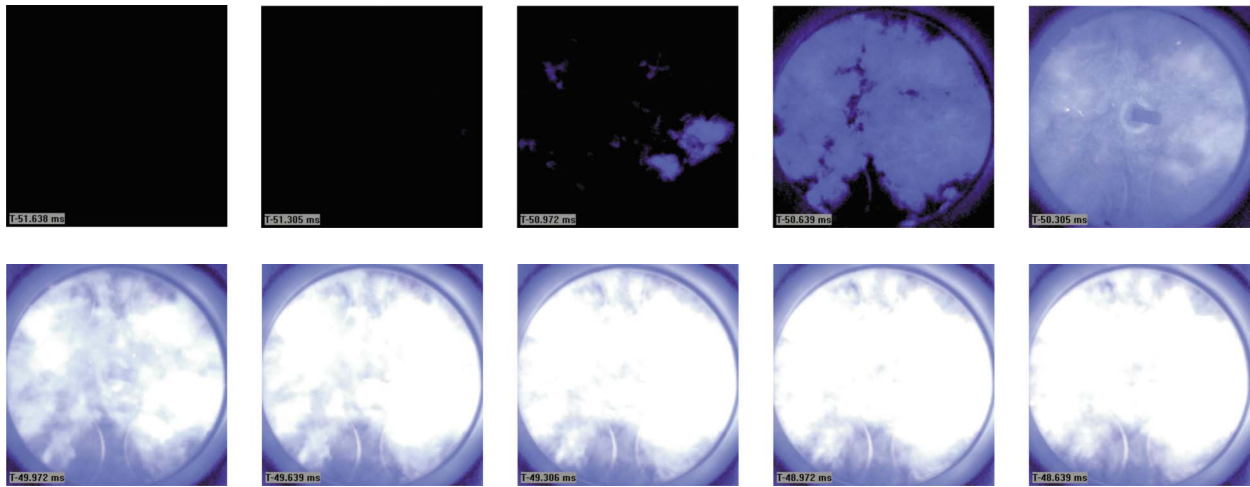
Fig. 9 Image sequence for iso-octane at $\phi=0.68$

erable variation, indicating misfire instability. The misfire conditions showed variation including ignition during compression, ignition during the expansion stroke, and pressure data resembling motoring conditions. Figure 8 contains an example of one of the most prevalent firing cycle behavior modes. The leaner $\phi=0.45$ and 0.29 conditions showed much less cycle-to-cycle variation in

the pressure profiles; however, the peak pressures were very low, resembling motoring pressure data. There was little obvious ignition-induced effect on pressure.

Figures 9–12 show image sequences for HCCI combustion of iso-octane at various equivalence ratios. All images have been saturation and gain adjusted for clarity. All of the iso-octane im-
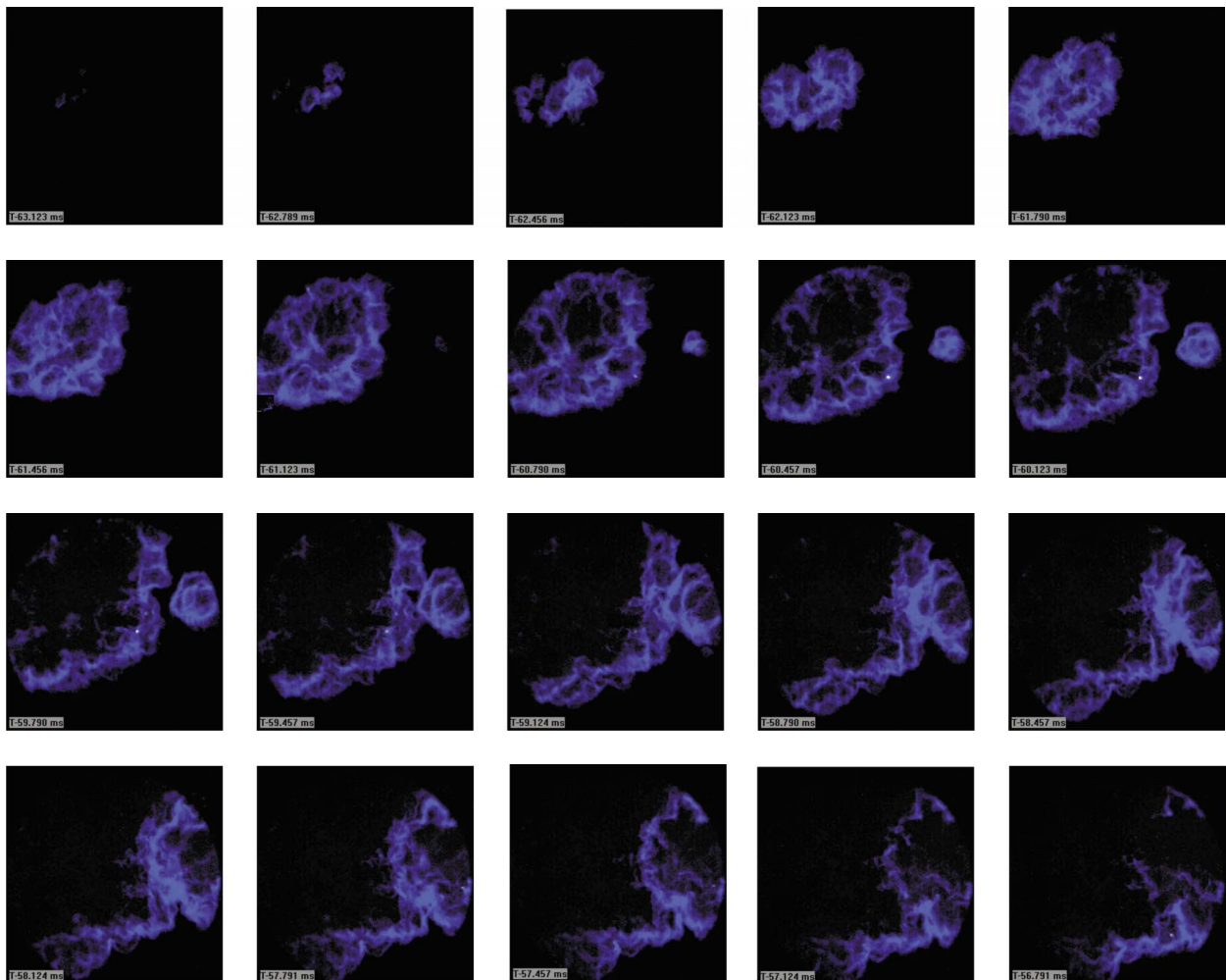
Fig. 10 Image sequence for iso-octane at $\phi=0.61$

Journal of Engineering for Gas Turbines and Power

SEPTEMBER 2008, Vol. 130 / **052803-5**
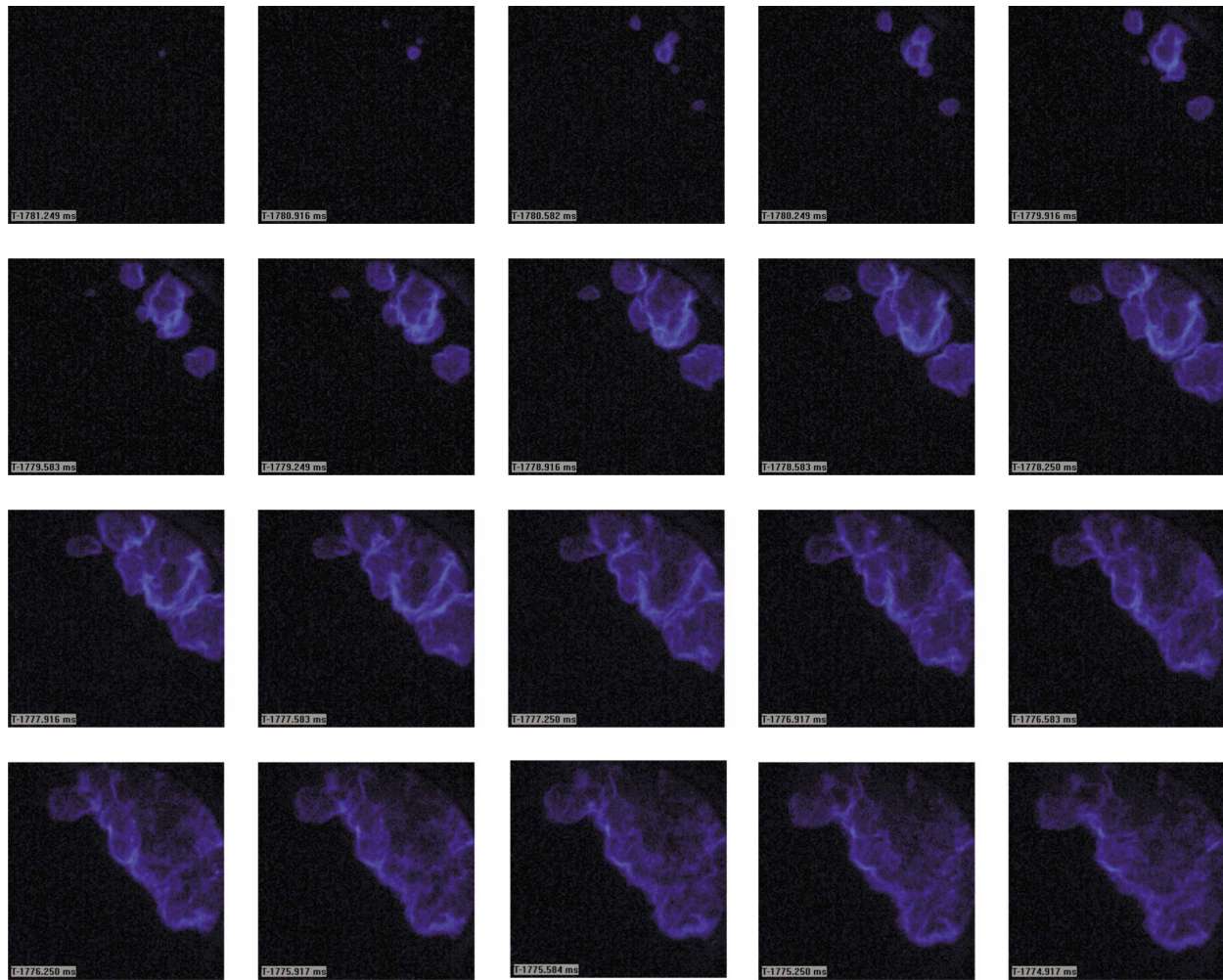
Fig. 11   Image sequence for iso-octane at $\phi = 0.45$

ages show blue emission originating in a localized area in the combustion chamber. The time required for the blue emission to expand from the point of origin to the remainder of the combustion chamber increased with leaner conditions. At $\phi = 0.68$, relatively uniform blue emission consistently developed across the combustion chamber within four images (5.6 CAD) of the first indication of ignition, as shown in Fig. 9. The next leaner condition, $\phi = 0.61$, showed extreme signs of misfire through variation in cylinder pressure and in ignition imaging. Figure 10 shows the image sequence associated with one of the more frequently observed phenomena, with blue emission extending for 45 image frames (63 CAD). Other image sequences for $\phi = 0.61$, not shown, contained emission spanning between 32 frames ($\sim$45 CAD) and 260 frames ($\sim$364 CAD). Blue emission never appeared simultaneously throughout the volume of the combustion chamber for conditions leaner than $\phi = 0.68$.

As observed with some indolene conditions, the images obtained for iso-octane at $\phi = 0.68$ showed bright white emission (see Fig. 9), and again leaner conditions did not produce white emission. At the leanest conditions studied for iso-octane, $\phi = 0.29$, blue emission was only occasionally observed during a cycle. Those cycles, which did exhibit emission, indicated very weak intensities that appeared to travel throughout the cylinder for long times (see Fig. 12), around 20–40 frames ($\sim$30–55 CAD).

The rapid heat release rate for $\phi = 0.68$ noted in Fig. 8 corresponds temporally to the fully volumetric, intense blue emission seen in Fig. 9. Leaner conditions exhibited neither simultaneous volumetric blue emission nor high rates of heat release on the pressure traces.

Gasoline. Examples of typical pressure traces for each gasoline run are shown in Fig. 13. The image sequences shown in Figs. 14–18 correlate to the pressure data, as indicated in Fig. 13. All images have been saturation and gain adjusted for clarity. The pressure data showed that ignition occurs during compression with high heat release rates for $\phi = 0.65$. Leaner conditions at $\phi = 0.52, 0.45, 0.37$, and 0.29 showed ignition near TDC with decreasing heat release rates. The pressure data also showed increasing cycle-to-cycle variation in cylinder peak pressure with leaner fuel mixtures. Unlike the leanest iso-octane conditions, the ignition events for gasoline were always identifiable from the pressure data.

Figures 14–18 show image sequences for HCCI combustion of gasoline for decreasing equivalence ratios. Each of the gasoline sequences show blue emission originating in a localized area in the combustion chamber. As found with the higher equivalence ratios for the indolene and iso-octane fuels, the images obtained at $\phi = 0.65$ showed bright white emission, after blue emission developed across the entire combustion chamber. Similar to the other fuels studied, the white emission was not observed at the leaner conditions. Gasoline exhibited behavior similar to indolene in the relationship between heat release rate and simultaneous volumet-
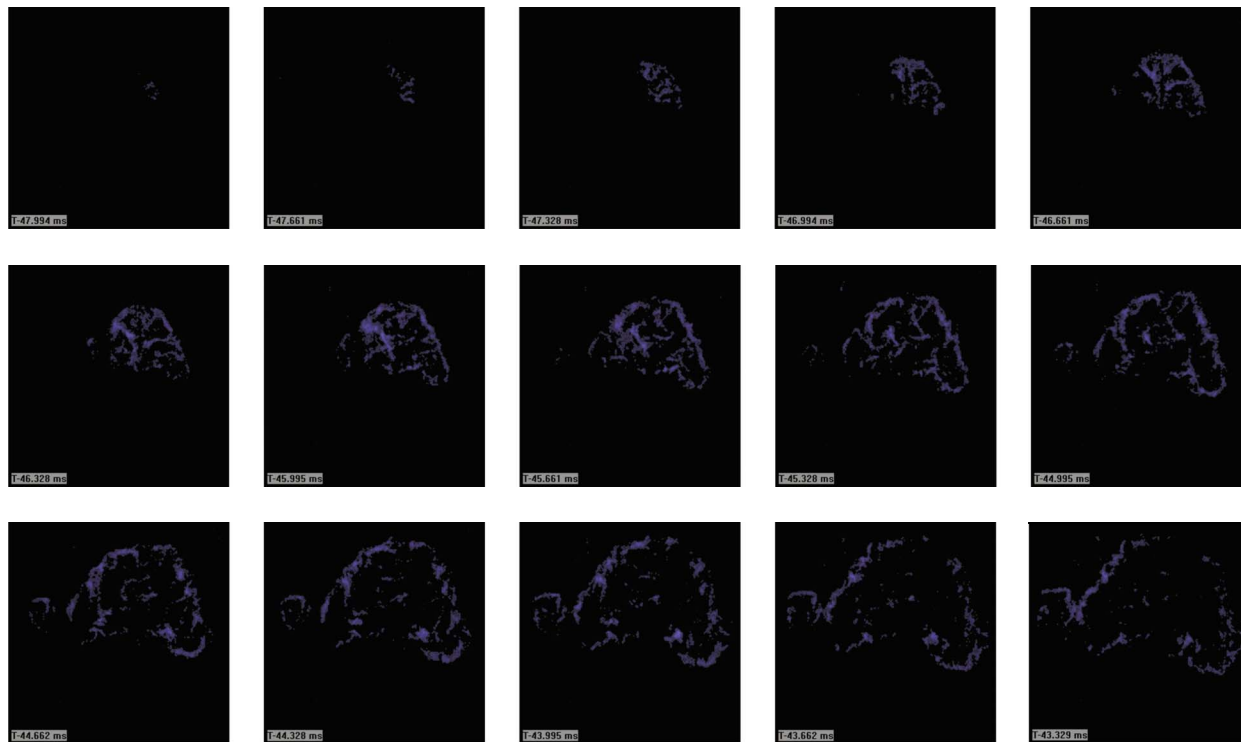
Fig. 12 Image sequence for iso-octane at $\phi = 0.29$

ric blue emission, where higher rates of pressure rise correspond temporally to more intense, volumetric blue emission (see Figs. 13–18).

Discussion

The visible blue emission recorded by the camera is attributed to C_2 and/or CH, which have strong emission bands in the blue (C_2: 473.7 nm, 516.5 nm, 563.5 nm; CH: 431.2 nm [10]). In several flame studies, CH has been used to as a marker of the flame zone (e.g. Refs. [11,12]). Consequently, the blue emission observed here is considered indicative of the combustion reaction front.

Fig. 13 Typical pressure traces versus time for engine conditions with gasoline fuel. The data are superimposed for clarity. The boxed areas coincide with imaging sequences presented in Figs. 14–18.

A separate series of experiments was conducted to determine if the white regions recorded in some imaging sequences were an indication of high-temperature radiation from soot or the result of sensor saturation. For these experiments, the engine was operated in HCCI mode with intake air preheated to approximately 320°C with indolene at an equivalence ratio of $\phi = 0.69$. The engine exhibits strong, consistent HCCI combustion under these conditions. Axial image sequences were then acquired while increasing the frame rate and decreasing the exposure time. The following settings were used:

- 3000 fps, with 309 μs exposure
- 9000 fps, with 100 μs exposure
- 18,000 fps, with 50 μs exposure

The resulting images (Fig. 19) showed only blue emission for the faster frame rates and lower exposure times, indicating that the white regions are due to the sensor saturation from the high-intensity blue emission, not due to the thermal emission from soot. Although such studies of the effects of the camera settings were not conducted for all fuels in this work, the engine operating conditions are sufficiently similar that we attribute the white regions observed in this work (see Figs. 4, 9, and 14) to sensor saturation, not soot.

In this study, gasoline supported the leanest stable HCCI operation and exhibited a gradual transition toward more spatially resolved, slower, weaker ignition behavior as equivalence ratio was decreased. Indolene did not exhibit the same range of lean HCCI operation as gasoline, but followed the same general ignition behavior as mixtures became leaner. Iso-octane did not support a stable transition through leaner mixtures. The ignition imaging for iso-octane at leaner mixtures shows the ignition event to be much more spatially resolved (Figs. 10–12) than either indolene (Figs. 5–7) or gasoline (Figs. 15–18). These differences suggest that neat iso-octane may not accurately predict HCCI lean ignition behavior in a real engine. Future work will include studies of iso-octane/n-heptane mixtures to understand if they more closely follow gasoline and indolene performance.

A study of where the first sign of ignition emission originates in
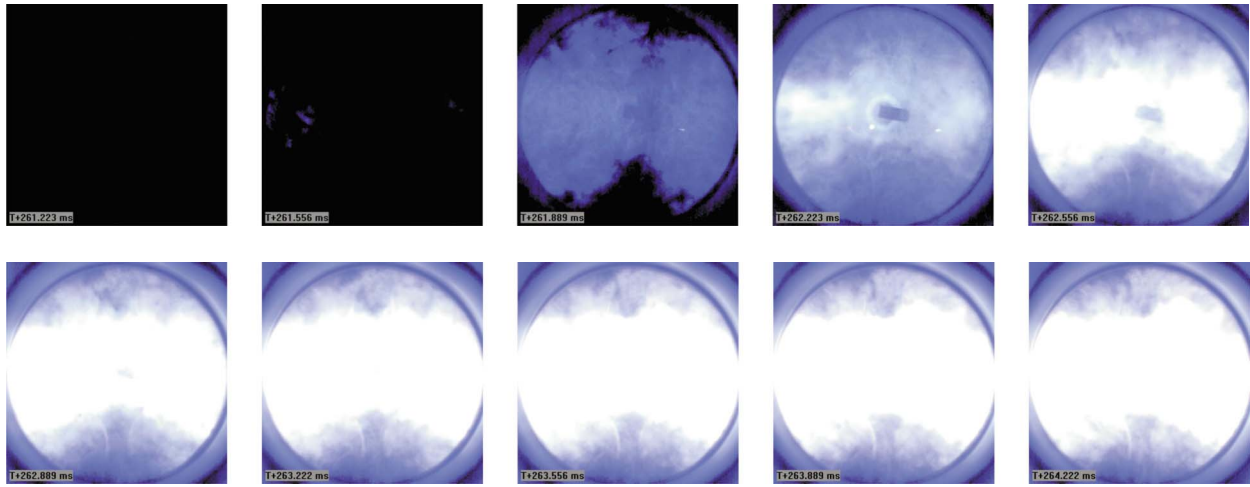
Fig. 14 Image sequence for gasoline at $\phi = 0.65$
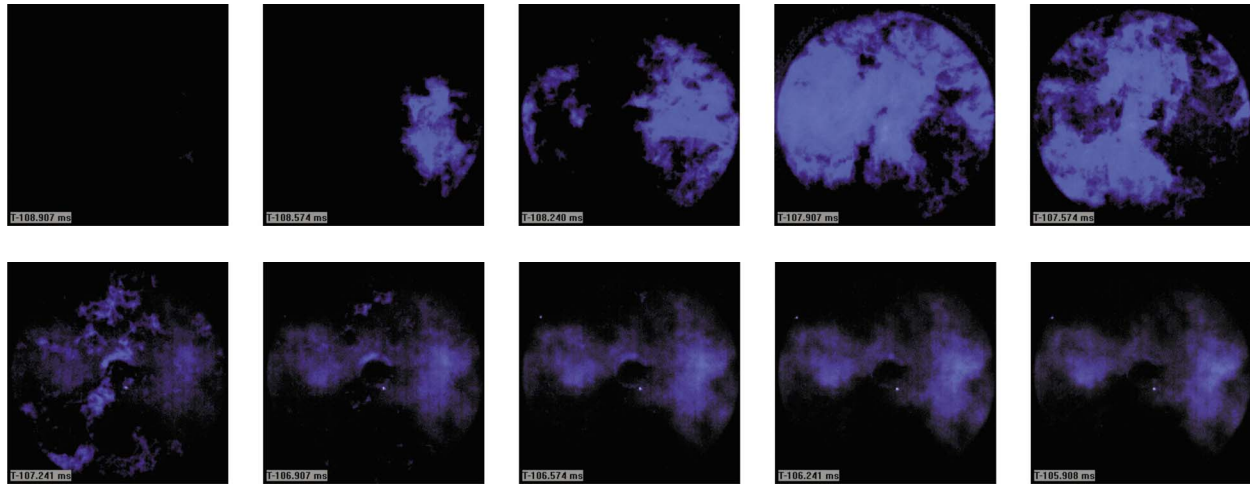
Fig. 15 Image sequence for gasoline at $\phi = 0.52$
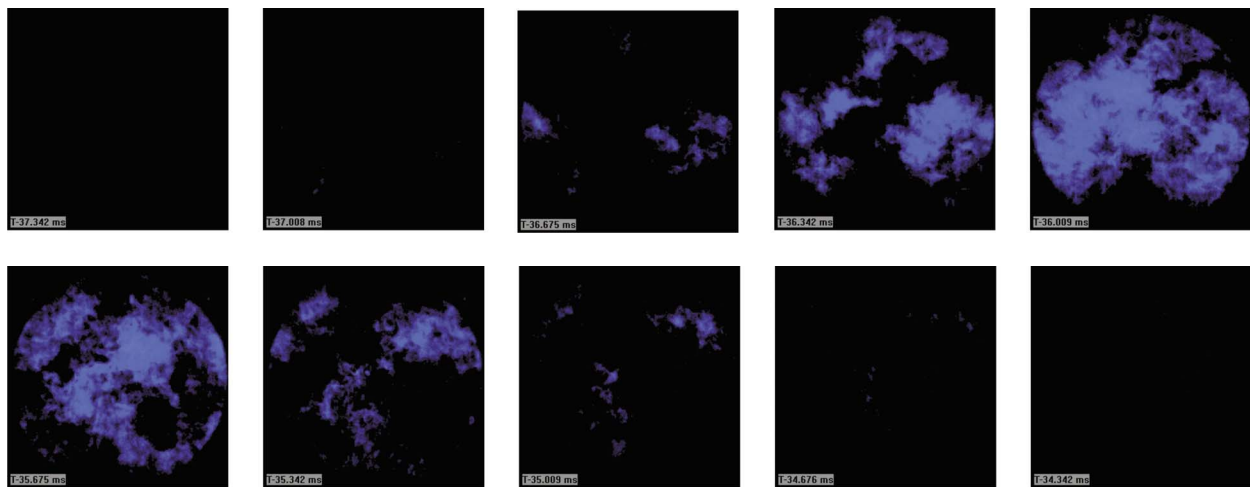
Fig. 16 Image sequence for gasoline at $\phi = 0.45$
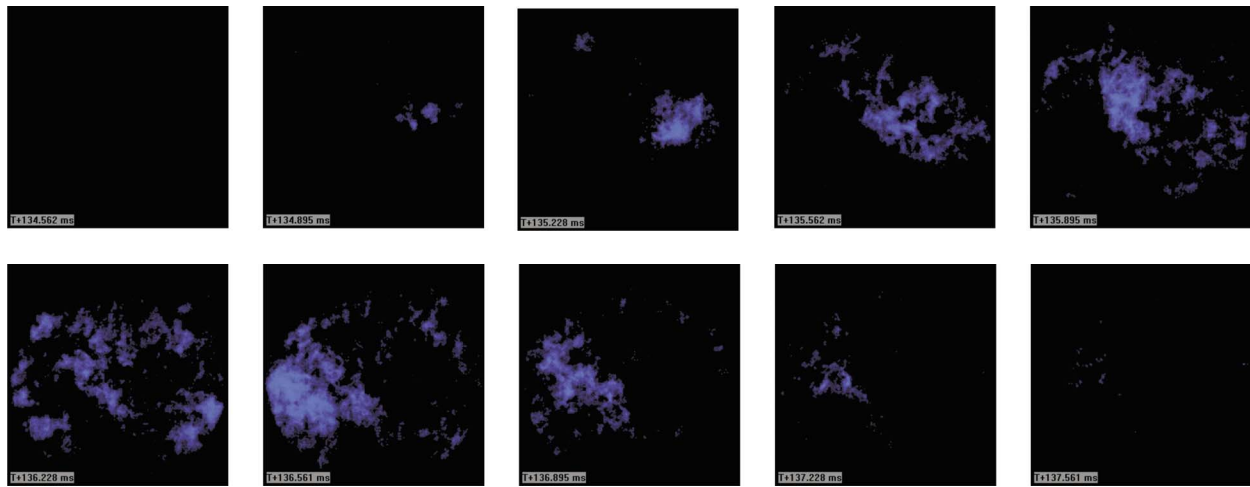
Fig. 17 Image sequence for gasoline at $\phi=0.37$

cylinder was conducted. Image sequences from multiple cycles (a minimum of ten per fuel and equivalence ratio condition) were evaluated in terms of where ignition occurred. Approximately 150 image sequences were considered in total. Plotting these ignition sites revealed a pattern, which existed for all fuels and equivalence ratios studied, where ignition began approximately 50% of the time in a pair of zones located at the edges of the cylinders between the intake and exhaust valves, shown in Fig. 20. The remaining ignition sites appeared randomly distributed. The preferential ignition zones likely indicate the existence of hotter regions within the combustion chamber. While the size, location, and strength of such a temperature gradient would depend on many engine-specific factors, all real engines would exhibit temperature gradients to some extent.

Since the heat release rate is difficult to measure, a net apparent heat release rate is defined from the experimentally measured pressure time histories and the piston displacement profile:

$$\frac{dQ_n}{dt} = \frac{\gamma}{\gamma - 1} p \frac{dV}{dt} + \frac{1}{\gamma - 1} V \frac{dp}{dt} \qquad (1)$$

where Q_n is the net apparent heat release rate, p is the cylinder pressure, V is the cylinder volume, and γ is the specific heat ratio. Equation (1) is taken from Heywood [13] in which $\gamma = 1.35$ was recommended as an appropriate value at the end of the compression stroke, and $\gamma = 1.26-1.3$ was recommended for the burned gas. In this study, $\gamma = 1.35$ was used. Apparent heat release for a moderate HCCI ignition event is shown in Fig. 21. Consistent with observations on HCCI in other imaging literature, peak chemiluminescence is coincident with peak heat release.

Summary and Conclusions

The results of the current work demonstrate that high-speed imaging provides direct time-resolved data on ignition and reaction phenomena important during HCCI operation of a single-cylinder research engine for a range of benchmarking fuels. HCCI combustion was initiated and maintained over a range of lean conditions for the three fuels considered, with equivalence ratios varying from $\phi = 0.69$ to 0.27. Air preheating was required to achieve ignition for the engine geometry and operating conditions considered.
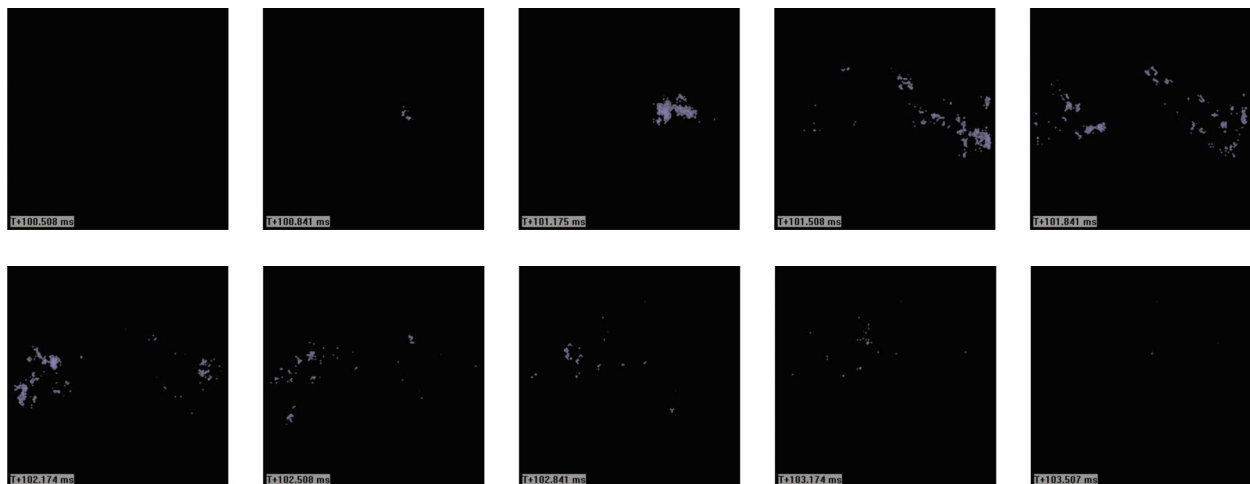
Fig. 18 Image sequence for gasoline at $\phi=0.27$
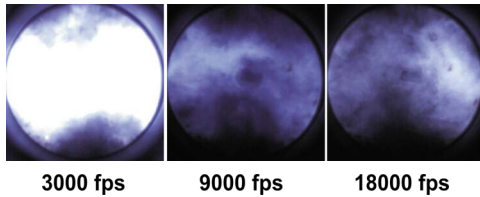
Fig. 19 Images of separate, identical HCCI firing conditions (intake air=320°C, indolene fuel at ϕ=0.69) taken at peak cylinder pressure with camera speeds at 3000 fps, 9000 fps, and 18,000 fps. All images have been color balanced equally for clarity.

The time-resolved imaging and pressure data clearly show that high heat release rates in HCCI combustion correlate to intense blue emission, which occurs simultaneously throughout the volume of the combustion chamber. Lower rates of heat release are characteristic of blue emission that appears at local ignition sites over longer time intervals within the combustion chamber. However, it has been noted in the literature that at conditions close to misfire, there is a weaker relationship between chemiluminescence and heat release rate. The pump gasoline used supported leaner HCCI operation than indolene. Iso-octane showed a dramatic transition into misfire and exhibited many sparse ignition events at low equivalence ratios. Ignition imaging suggests local hot zones result in preferential ignition sites for all of the fuels and equivalence ratios studied.

Fig. 20 Image of cylinder end view showing areas of preferential ignition sites as crosshatch
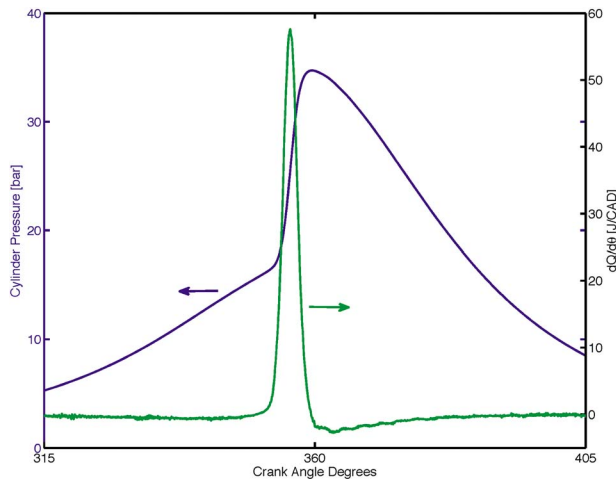
Fig. 21 Cylinder pressure and corresponding heat release rate for HCCI operating conditions of indolene fuel, ϕ=0.57, intake air temperature=318°C. See text for details of the calculation used to determine dQ/dt.

Indolene and gasoline reproduced similar ignition phenomena, whereas iso-octane was markedly different. This is somewhat unexpected as iso-octane is considered a chemical surrogate for gasoline and under HCCI conditions, where kinetics are rate limiting, more similarities in ignition behavior might be expected. Therefore, some caution should be used when considering neat iso-octane for benchmarking HCCI operation. This study also demonstrates the value of ignition imaging when applying HCCI or other low-temperature combustion control strategies, as a means to identify flow field or thermal features, such as nonuniformities or hot spots, which can significantly augment or hinder ignition control and engine performance.

Acknowledgment

Nomenclature

AKI	=	antiknock index ((RON+MON)/2)
atm	=	atmospheres
CAD	=	crank angle degree
fps	=	frames per second
MON	=	motor octane number
RON	=	research octane number
rpm	=	revolutions per minute
TDC	=	top dead center
WOT	=	wide open throttle

Greek Symbols

γ	=	specific heat ratio
ϕ	=	equivalence ratio

Symbols

$\o$	=	diameter

References

[1] Epping, K., Aceves, S., Bechtold, R., and Dec, J., 2002, "The Potential of HCCI Combustion for High Efficiency and Low Emissions," SAE Paper No. 2002-01-1923.

[2] Christensen, M., Einewall, P., and Johansson, B., 1997, "Homogeneous Charge Compression Ignition (HCCI) Using Iso-octane, Ethanol and Natural Gas—A Comparison to Spark Ignition Operation," SAE Paper No. 972874.

[3] He, X., Zigler, B. T., Walton, S. M., Wooldridge, M. S., and Atreya, A., 2006, "A Rapid Compression Facility Study of OH Time Histories During Iso-Octane Ignition," Combust. Flame, **145**, pp. 552–570.

[4] Walton, S. M., He, X., Zigler, B. T., Wooldridge, M. S., and Atreya, A., 2007, "An Experimental Investigation of Iso-Octane Ignition Phenomena," Combust. Flame, **150**, pp. 246–262.

[5] Walton, S. M., He, X., Zigler, B. T., Wooldridge, M. S., and Atreya, A., 2005, "Demonstration of Distinct Ignition Regimes Using High-Speed Digital Imaging of Iso-Octane Mixtures," *Proceedings Fourth Joint Meeting of the U. S. Sections of The Combustion Institute*, Mar. 20–23.

[6] Walton, S. M., He, X., Donovan, M. T., Zigler, B. T., Palmer, T. R., Wooldridge, M. S., and Atreya, A., 2004, "High-Speed Digital Imaging of Iso-Octane Mixtures at Homogeneous Charge Compression Ignition Operating Conditions," *The Central States Meeting of the Combustion Institute*, Mar. 21–23, Paper No. C.1-5, pp. 1–6.

[7] Kaiser, E. W., Yang, J., Culp, T., Xu, N., and Maricq, M. M., 2002, "Homogeneous Charge Compression Ignition Engine-Out Emissions—Does Flame Propagation Occur in Homogeneous Charge Compression Ignition?,"Int. J. Engine Res., **3**, pp. 185–195.

[8] Kaiser, E. W., Maricq, M. M., Xu, N., and Yang, J., "Engine-Out Emissions From a Direct-Injection Spark-Ignition (DISI) Engine," 2005, SAE Paper No. 2005-01-3749.

[9] Sunnaborg, D., 1997, Design Specifications Summary for the Sandia National Laboratories Optical Engine, May.

[10] Gaydon, A. G., 1957, *The Spectroscopy of Flames*, Chapman & Hall, London.

[11] Yoshida, A., Narisawa, M., Tsuji, H., and Hirose, T., 1995, "Chemiluminescence Emission of C_2, CH and OH Radicals from Opposed Jet Burner Flames," JSME Int. J., Ser. B, **38**(2), pp. 222–229.

[12] Walsh, K. T., Long, M. B., Tanoff, M. A., and Smooke, M. D., 1998, "Experimental and Computational Study of CH, CH*, and OH* in an Axisymmetric Laminar Diffusion Flame," *27th Symposium (International) on Combustion*, The Combustion Institute, pp. 615–623.

[13] Heywood, J. B., 1988, *Internal Combustion Engine Fundamentals*, McGraw-Hill, New York.

A Study of the Transition Between Lean Conventional Diesel Combustion and Lean, Premixed, Low-Temperature Diesel Combustion

Stephen Busch
e-mail: sbbusch@gmail.com

Stanislav V. Bohac
e-mail: sbohac@umich.edu

University of Michigan,
1231 Beal Avenue,
Ann Arbor, MI 48109

Dennis N. Assanis
University of Michigan,
2350 Hayward Street,
Ann Arbor, MI 48109
e-mail: assanis@umich.edu

New diesel combustion modes face difficult challenges with respect to engine-out emissions and transient behavior. Transitions between lean conventional diesel combustion and lean, premixed, low-temperature diesel combustion are investigated with an automotive diesel engine. Effects of fuel pressure on transitional cycles are investigated. Cycle-by-cycle heat release analysis is performed and an exhaust mass flow model is used to obtain cycle-averaged NO concentrations. The behavior of combustion progression and NO emissions during the transitions is discussed. Observed cool-flame behavior is identified and explained. [DOI: 10.1115/1.2906177]

Keywords: transient diesel combustion mode switching

Introduction

The EPA expects that by 2015 in the U.S., diesel-powered vehicles will represent 24% of the light truck market and 9% of the car market [1]. Diesel engines are more efficient than gasoline engines. They typically have higher compression ratios for better thermal efficiency; their loads are not controlled by a throttle; they burn lean mixtures with high combustion efficiency; the products of diesel combustion have higher specific heat ratios than for stoichiometric, spark-ignited combustion products and therefore diesels enjoy additional thermal efficiency benefits; and diesel engines are nearly always turbocharged, which further improves efficiency. Increasing corporate average fuel economy standards [2] for light trucks make diesel engines even more attractive to manufacturers.

In order for diesel-powered vehicles to succeed in the US, they will have to pass ever-tightening EPA emission regulations. Shown below are some of the 2007 Tier 2 standards along with the 1994 Tier 1 standards for comparison; light duty vehicles must meet these new limits after 10 years or 120,000 miles of use [3,4].

Vehicle emissions may be reduced in two basic ways: in-cylinder combustion development or exhaust aftertreatment. Although probably necessary, exhaust aftertreatment systems can be expensive and may require complex regeneration strategies [5]. NO_x is particularly difficult to reduce with aftertreatment in diesel engine exhaust because of a lack of reducing agents in the exhaust. Whatever exhaust aftertreatment is in place, its burden will certainly be lessened if the engine-out NO_x and soot emissions are minimized. To this end, low-temperature, premixed compression ignition (PCI) strategies have been developed. In order to achieve low-temperature, "modulated kinetics" combustion in an engine, Kimura et al. flow high levels of EGR in their diesel engine [6]. To ensure that premixing occurs, they verify that all of the fuel is injected before combustion begins. In order to help maintain low temperatures and long ignition delays at higher engine output levels, they decrease the compression ratio, retard the injection tim-

ing, and cool the EGR gas. Also, increased injection pressures create shorter injection durations. High swirl ratios are used to help mixing and reduce both hydrocarbon and soluble organic fraction emissions. Similar operating parameters have been implemented in the General Motors Cooperative Research Laboratory at the University of Michigan [7].

Some literature suggests that the load limits of lean premixed diesel combustion are governed by knocking [8,9], while other literature suggests that excessive soot emissions limit the load range of PCI combustion [10]. Regardless of which problems exist with high-load operation, it has been suggested that diesel engine calibrations utilize PCI operation at low to midloads and conventional diesel combustion at higher loads and engine speeds [9]. This implies that the engine calibration would have to switch between a PCI strategy and a conventional strategy, possibly dozens of times during a driving cycle [11]. This operation is not straightforward and very little has been published on this topic. It is uncertain how characteristics of combustion will change for each cycle during the transition; cycle-by-cycle heat release analysis will provide insight about this combustion progression.

The focus of this study is to examine transitions between lean conventional diesel combustion and low-temperature, lean premixed diesel combustion. Specifically, the effects of such transitions on cycle-by-cycle NO emissions and combustion progression are presented here.

Experimental Development

All experiments are performed at the General Motors Cooperative Research Laboratory (CRL) at the University of Michigan in Ann Arbor. The engine used for this study is a 1.7 l four-cylinder automotive diesel engine. It is equipped with a high pressure Bosch common-rail injection system, four valves per cylinder, a turbocharger with a variable geometry turbine, a poppet-style EGR control valve, and a large EGR cooler. Pistons with larger bowls have replaced the original pistons to reduce the static compression ratio of the engine to 16:1. Cylinder pressure for Cylinder 3 is measured with a Kistler 6041A water-cooled pressure transducer and digitized every half-degree crank angle. The fuel used for this study is low-sulfur Swedish diesel fuel with a cetane number of 55.
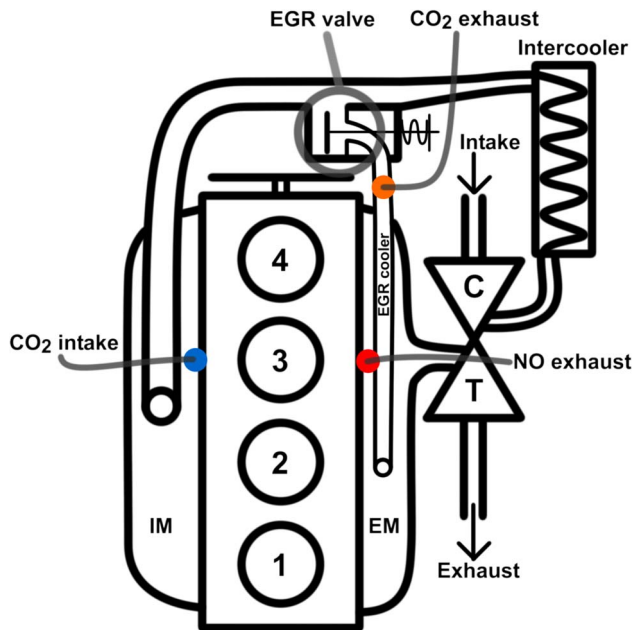
Fig. 1   Schematic of engine and emission measurements

A Cambustion NDIR500 fast-response analyzer is used to simultaneously measure CO_2 concentrations in both the EGR system and in the intake system in between the intake ports for Cylinder 3. Analog voltage outputs from the NDIR500 are digitized on a high-speed basis. Figure 1 schematically shows where these measurements are taken, as well as the location of the exhaust NO measurement. A Cambustion CLD500 is used to measure NO concentrations in Cylinder 3's exhaust port; the analog output signal is also digitized with the high-speed data acquisition system. An AVL CEB II emission analyzer is used to develop and characterize the steady-state operating points of the engine; it provides data not measured by the fast-response emission analyzers (see Table 1).

In order to obtain a representative value for the EGR rate that can rapidly change throughout a transition, the ratio of intake CO_2 concentration to exhaust CO_2 concentration is defined as the EGR rate:

$$\% \text{EGR} = 100 \frac{CO_{2,\text{inlet}}}{CO_{2,\text{exhaust}}} \qquad (1)$$

The mean value of the calculated EGR for the intake stroke of each cycle is taken as the cycle-averaged EGR value for that cycle.

In order to explore the engine's behavior during the transition from lean conventional combustion and lean PCI combustion, two types of transitions are performed: primary and secondary transitions.

Primary Transitions. The primary transitions are intended to establish the "base line" case of quickly switching the engine's calibration from a conventional combustion strategy to a low-temperature, premixed strategy. In order to do this, both the conventional and low-temperature premixed operating conditions are first defined; this involves using the engine control software to set

Table 1   US light-duty vehicle emission standards (g/mi) *NMHC

	NO_x	NMOG	CO	HCHO	PM
Tier 1, diesel (1994)	1.25	0.31*	4.2	. . .	0.1
Tier 2, bin 5 (2007)	0.07	0.09	4.2	0.018	0.01

Table 2   Summary of steady-state operating points

	CONV	PCI
Engine Speed (rpm):	1500	
Fuel flow rate (g/s):	0.541 ± 0.010	
BMEP (kPa):	404 ± 3	400 ± 3
BSFC (g/kWh):	227.5 ± 2.5	229.8 ± 2.5
Main inj. timing (°BTDC):	0.4	4.5
Pilot inj. timing (°BMI):	11	N/A
Rail pressure (bar):	600	900
EGR duty cycle (%):	50	0
VGT duty cycle (%):	50	63
FSN:	1.3 ± 0.2	0.05 ± 0.03
NO conc. (ppm):	75.5 ± 1.5	32.5 ± 1.5
CO conc. (ppm):	965 ± 20	2410 ± 50
THC conc. (ppm C1):	420 ± 40	860 ± 40
EGR (mass-based %):	30.3 ± 0.75	44.2 ± 0.25
Noise (dB):	83 ± 1	89 ± 1

fueling and EGR parameters until the desired operating condition is met (see Table 2 for a summary of each operating condition). The operating conditions are carefully chosen and adjusted so that a calibration change from the conventional calibration to the premixed calibration does not significantly affect the measured overall engine fuel flow rate. Specifically, the target coefficient of variance (COV) for the fuel flow rate during a given transition is 5% for the duration of each transition, but it is often less than 2% or 3% for a given transition. Once the two operating conditions are defined, the engine's calibration is changed as quickly as possible between the two combustion modes as high-speed data are acquired. The process is repeated five times to generate a set of five primary transitions.

Secondary Transitions. After analysis of the primary transitions, it is observed that the fuel pressure does not quickly change from 600 bars to 900 bars. Rather, it makes a slow, controlled, linear change that takes several seconds. Experience with the single-cylinder version of this engine suggests that this is not a hardware phenomenon but a limitation imposed by the engine control unit. Every attempt to alter this fuel pressure ramp rate is made, but all attempts are unsuccessful. This poses a problem, because a modern diesel engine will likely need to perform a much more rapid increase in fuel pressure to make such a transition in a reasonable amount of time. It is out of this problem that the secondary transitions are conceived. Of interest during the transitions are the few cycles immediately following the calibration change; the effect of the fuel pressure on these few cycles needs to be understood. So, the starting fuel pressure is adjusted so that the fuel pressure during these first few transitional cycles is higher than it is for the first few cycles of the primary transitions. For the secondary transitions, three types are tested: 600–900 bar transition (to reevaluate the base line), 750–900 bar transition (intermediate fuel pressure change), and a 900–900 bar transition (constant fuel pressure).

The testing procedure is similar to the primary transitions with one change: As the starting rail pressure is increased, the main injection timing (and consequently the pilot timing) is slightly retarded for the conventional operating points so that the brake mean effective pressure (BMEP) remains near 400 kPa. Multiple secondary transitions of each type are performed in order to establish repeatability.

Analysis

Heat Release. In order to provide insight into the combustion processes that occur during engine transitions, heat release analysis is performed. This analysis provides apparent rate of heat release data, which can be considered as the rate at which the fuel is
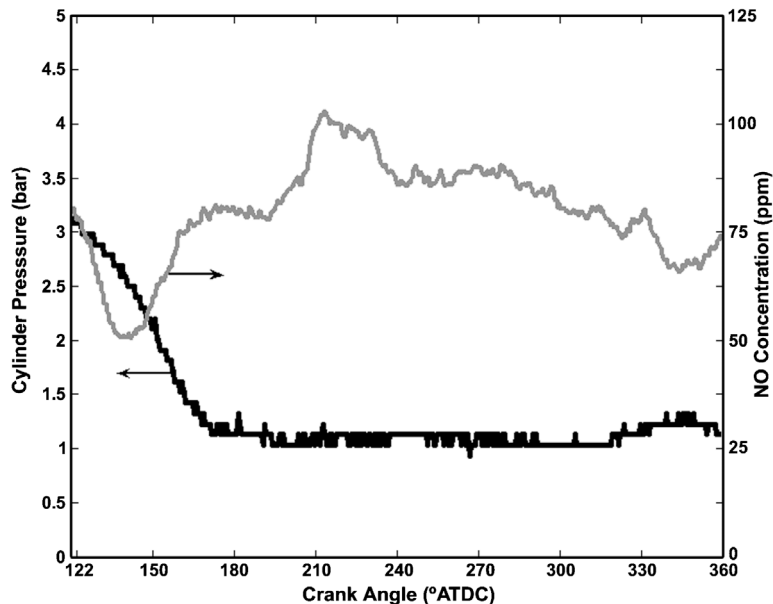
Fig. 2 Example of NO concentration measurement and cylinder pressure

burning. This rate of heat release, when integrated, provides a cumulative heat release curve for each cycle. This cumulative curve provides the locations of various milestones for each cycle (i.e., when 5%, 50%, or 90% of the trapped mass has burned, etc.). The program used for this analysis is called UMHR (University of Michigan Heat Release Program); it is written in FORTRAN. It was originally intended for spark-ignition engines and is a single-zone model, but it has used been previously for analysis of diesel engine cycles [7,12]. More information about this code can be found in Ref. [13].

When reporting various values based on heat release analysis, it is interesting to determine the sensitivity of the analysis to possible errors in the input parameters, especially those measured during the transitions. Of interest are the 5% burn location, which is taken to be the start of combustion, and the 50% burn location, which has important implications on combustion phasing (the relative position in the cycle at which the bulk of combustion occurs) and therefore temperatures in the cylinder during a given cycle. A sensitivity analysis has been performed to determine the effects of errors in the following input parameters: EGR rate, equivalence ratio, and mass of fuel per cycle.

Thirty cycles of heat release data calculated for a transition are compared. The minimum and maximum deviations from the base line case are noted after comparing all of the cycles on a cycle-by-cycle basis, for each changed input parameter and for both burn location values. The error cases that are believed to be least likely (based simply on experience) are disregarded. With combined likely errors in all three input values, the worst-case error in 5% burn location is approximately 1 deg, and for the 50% burn location, it is approximately 1.5 deg. Observed trends in these metrics are not obscured by errors of this magnitude.

Exhaust Mass Flow Model and NO Calculations. Experience from steady-state development of both the conventional combustion and PCI operating conditions suggests that the vast majority of the NO_x in the exhaust exists as NO, so it is assumed that cylinder-out NO_x follows the same trends as does cylinder-out NO. Since the NO concentration measured by the CLD500 is sampled every half degree, there are 1440 different values of NO concentration for each engine cycle. An example is shown in Fig. 2; data are shown from exhaust valve opening (EVO) to the end of the exhaust stroke.

These data must be condensed into a single value for each engine cycle in order to be useful. One means to an end is to simply average the NO concentrations taken between EVO and the end of the exhaust stroke. However, this method does not take into account variations in the flow rate of exhaust gases past the sampling probe as the crank angle changes. For this reason, a model for exhaust mass flow is constructed for every cycle and used to create a weighted average NO concentration for each cycle. This section briefly explains the construction of the model and follows Heywood's analysis [14].

The first part of the model describes the flow through the exhaust valve during the blowdown process, when the flow is assumed to be compressible. Both choked flow and nonchoked flow are modeled. The exhaust system pressure is not directly measured for each cycle; it is taken to be the averaged cylinder pressure measured from 180 deg to 185 deg after top dead center (ATDC). The cylinder pressure data are smoothed with an averaging routine before calculation. Specific heat ratios and gas constants are calculated by the heat release routine and as a first approximation, they are assumed to be constant throughout the exhaust process. Exhaust valve lift profiles are known for the test engine; experimental discharge coefficients are estimated from a paper by Bohac and Landfahrer [15]. Measured discharge coefficients for a small, direct-injected turbodiesel engine (Exhaust Port No. 2 in Ref. [15]) are used to determine the discharge coefficient for a given valve lift. It is assumed that the gas inside the cylinder isentropically expands during the exhaust process and so the stagnation temperature follows the appropriate relationship.

Once the blowdown process is finished, the cylinder pressure is very close to the pressure in the exhaust system. This difference in pressure becomes less important to the exhaust flow. Now, it is assumed that the exhaust gases are not compressible. The volume rate of change of the cylinder is assumed to be equal to the volumetric flow rate through the exhaust valve. This, multiplied by the density (calculated from the ideal-gas law), provides the mass flow rate through the valve. The incompressible displacement model takes effect as soon as the flow rate that is calculated from the compressible flow model becomes less than that calculated for the incompressible flow model.

This analysis ignores the effects of heat transfer, which would serve to decrease temperatures and increase densities and specific
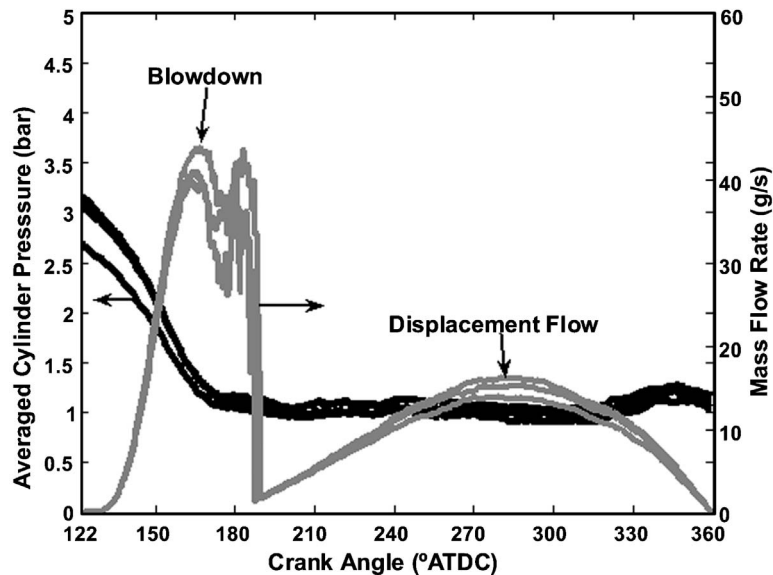
Fig. 3   Examples of exhaust flow model

heat ratios. It also ignores the effects of gas momentum and unsteady flow. Accuracy of cylinder pressure measurements for this portion of the cycle is often poor due to thermal shock effects. Even small errors in pressure can make big differences in flow rates. Every attempt is made to make reasonable assumptions, and the model, although far from perfect, seems to quantitatively agree within reason to Heywood's results. Figure 3 shows several examples of the exhaust flow model.

More important than the absolute scaling of this model are the relative shapes of the compressible and incompressible flows; these serve to weight portions of the NO data different from a simple average. Furthermore, the relative profiles for each combustion event are similar, so the weighting should not significantly change from cycle to cycle.

Once the exhaust flow model is established, it is used to create a mass-weighted NO average for each cycle. It is observed that mass-weighted averaging usually results in NO values that are between 0% and 10% higher than those obtained by unweighted averaging.

Results

Primary Transitions. Figure 4 shows how four of the engine
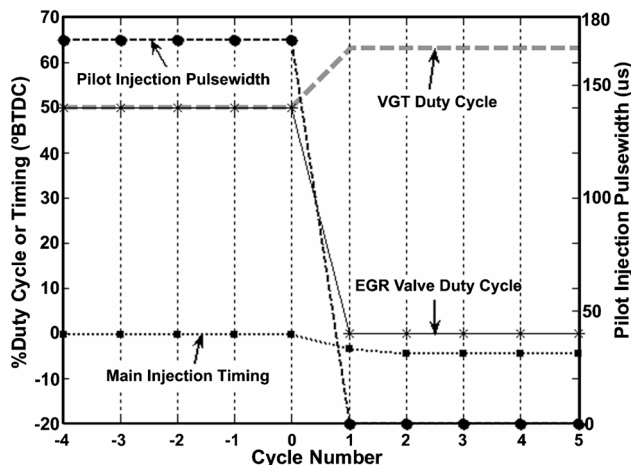
Fig. 4   Engine control parameters during a primary transition

control parameters change during a primary transition. These are pilot injection pulse width variable geometry turbine (VGT) actuator duty cycle, EGR valve duty cycle, and main injection timing.

It is observed that these control parameters are constant for the engine cycles before the transition and then they change to new values for the cycle marked "1." This first cycle is referred to as the "first transition cycle," the second as the "second transition cycle," and so on.

It is known that the VGT vanes and EGR valve do not instantaneously change positions as the pulse-width modulated control signal to them changes. Furthermore, the physical response times of the VGT vanes and the EGR valve are not known. However, the intake manifold pressure and CO_2 concentration, both consequences of adjusting the VGT vanes and the EGR valve, are measured with high temporal resolution, and these strongly affect the nature of the combustion.

Figure 4 shows that for the transition, the VGT duty cycle increases and the EGR valve pulse width decreases to zero; this corresponds to the turbine blades closing down to increase exhaust pressure and the EGR valve opening fully. Both of these changes are made in order to increase the flow of EGR rate to reach that of the PCI operating point. The pilot injection signal decreases to zero as well, because there is no pilot injection with the PCI operating condition. It is assumed that the pilot injection completely ceases and that the main injection timing directly changes to its new value in the first transition cycle.

It is observed that the main injection pulse width decreases, abruptly for the first two transition cycles and then more slowly as the fuel rail pressure increases. The fuel pressure does not abruptly change for the first transition cycles, but then it begins a slow, steady increase to its final value. For this reason, it is believed that the actual amount of fuel delivered to the first few transition cycles is below the average for the whole transition. However, since measurement hardware and/or techniques are not in place to allow a more precise estimation of these fuel delivery deviations, constant fuel flow is still assumed for calculation purposes.

The measured intake manifold pressure only slightly increases (approximately 0.5%) during the transition.

Figure 5 shows concentrations of CO_2 measured by the NDIR500 in the intake manifold and the EGR pipe just before it mixes with the intake air. It also shows the ratio of the two, which is defined as the percent EGR rate. Both the raw CO_2 measure-
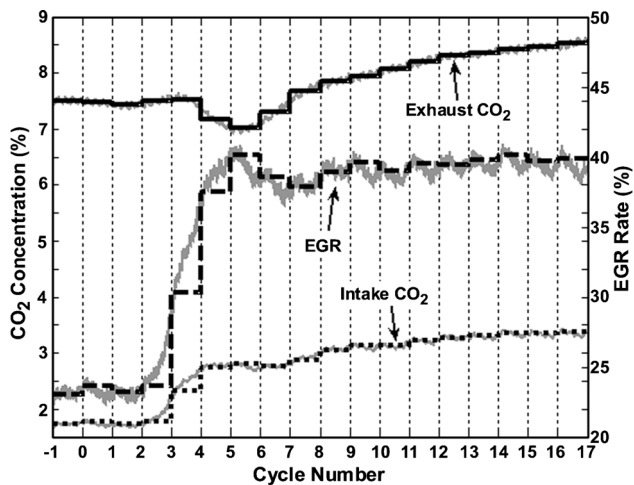
Fig. 5 CO$_2$ concentrations and EGR rate for a primary transition

Fig. 6 NO for a primary transition

ments and the calculated, cycle-averaged values are shown for completeness. The EGR rate and intake CO$_2$ averages are calculated only during the intake stroke of each cycle as this a better representation of the recycled exhaust gas available to each engine cycle. The EGR rate starts just below 23% and does not significantly change during the first two transition cycles. These are shown as Cycles 1 and 2 in Fig. 5. EGR rate dramatically changes during the fourth and fifth transition cycles and by the ninth transition cycle, it has essentially reached its steady-state value of approximately 40%.

The CO$_2$ and EGR behavior is explained as follows: The first rise in the intake CO$_2$ is due to the EGR valve being opened to allow more of the existing recycled exhaust gas to flow in. This causes the CO$_2$ concentration of the intake mixture to dramatically increase. At the same time, the VGT vanes close down so that more exhaust pressure is available to push EGR through the system. Meanwhile, the exhaust from the first few transition cycles takes some time to reach the probe in the EGR system. This is approximately three to four cycles, as determined by a separate test during which fuel injection quantity is quickly switched from zero to a steady-state value. When this exhaust gas does reach the probe (during the fourth transition cycle), the exhaust CO$_2$ concentration slightly decreases. This is attributed to decreased fuel delivery during the first few transition cycles. Then, the CO$_2$ in the exhaust slowly increases. These gradual increases in exhaust CO$_2$ eventually manifest themselves in the intake CO$_2$. More CO$_2$ in the intake leads to higher CO$_2$ concentrations in the exhaust, which feeds back to the intake through the EGR system. In this manner, both intake and exhaust CO$_2$ concentrations tend toward their steady-state values. Transport delay through the EGR system is the primary reason why this behavior is not quicker. Therefore, even though the EGR rate relatively quickly stabilizes, the intake and exhaust CO$_2$ concentrations take longer to reach their steady-state values. This phenomenon has significant implications for the concentration of oxygen in the intake and therefore on combustion and NO emissions.

Mass-weighted, cycle-averaged NO emissions are shown in Fig. 6; they sharply increase for the first two transition cycles and then decrease below the conventional NO concentration for the third transition cycle. Thereafter, concentrations essentially approach the steady-state value of approximately 15–20 ppm.

The data shown thus far are all from the same single primary transition; four other such transitions were also performed and analyzed. The results for the other primary transitions are largely consistent with the transition previously described, except that there is some variation in the magnitudes of the cycle-averaged
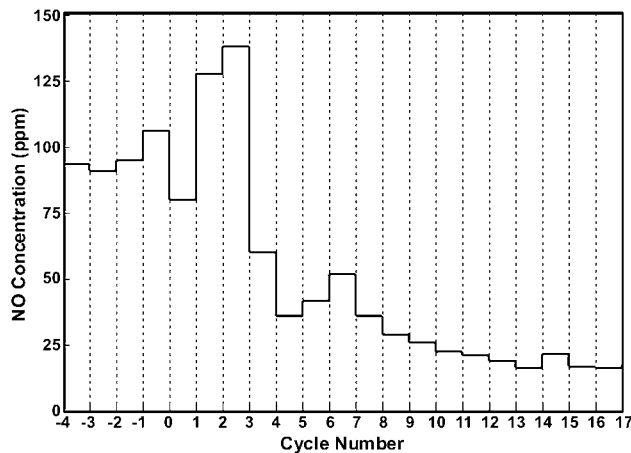
NO values for the first few transition cycles. However, a sharp increase in measured NO is always observed for these first two or three transition cycles before NO decreases to its final steady-state value, a trend that repeats very well.

Figure 7 shows apparent rate of heat release (ROHR) data for Transition Cycles 1, 5, and 17 with three different rail pressures. The first two transition cycles are characterized by extremely high peak rates of heat release and shorter heat release durations (e.g., Cycle 1). After the first two transition cycles, the heat release curves begin to decrease in peak magnitude and the phasing of the peak heat release rate becomes more retarded, as in Cycle 5. Also interesting is the development of the cool-flame region of the heat release curves. This "double hump" has been observed before (for example, Takeda et al. [16], Akagawa et al. [17], Iwabuchi et al. [18], Minato et al. [19], and Kimura et al. [6]) and is attributed to the cool flame associated with premixed diesel combustion (see Ref. [20]). At higher rail pressures, the cool-flame reactions are visible from the first transition cycle as small humps before the main heat release peak, whereas they are not clearly observed for transitions with lower fuel pressure until several cycles have occurred. The location of the cool-flame heat release peaks does not substantially change as the transitions progress. However, the separation between the smaller cool-flame peak and the main heat release peak increases as the transitions progress. This corresponds to increasing ignition delays as the main heat release peaks are retarded relative to the cool-flame peak.

Secondary Transitions. Shown in Fig. 8 are cycle-by-cycle, mass-weighted NO averages as measured during the secondary transitions. Each stair-step line represents the average of several transitions. Specifically,

- The "600 bar" line is the average of three separate transitions that all began with 600 bar of rail pressure.
- The "750 bar" line is the average of three separate transitions that all began with 750 bar of rail pressure.
- The "900 bar" line is the average of two separate transitions that began with 900 bar of rail pressure.

It is observed that the conventional combustion=NO values (Cycles −1 and 0) of Fig. 8 are lower than for the primary transitions. These differences appear to be related to day-to-day variations with the engine. The secondary testing was all performed during the same day, several weeks after the primary transitions. NO values for the three types of secondary transitions begin and end at very nearly the same level; this allows reasonable comparison between different fuel pressure points.

Since the average values for each cycle are shown in Fig. 8, completeness dictates mention of the statistical reliability of the
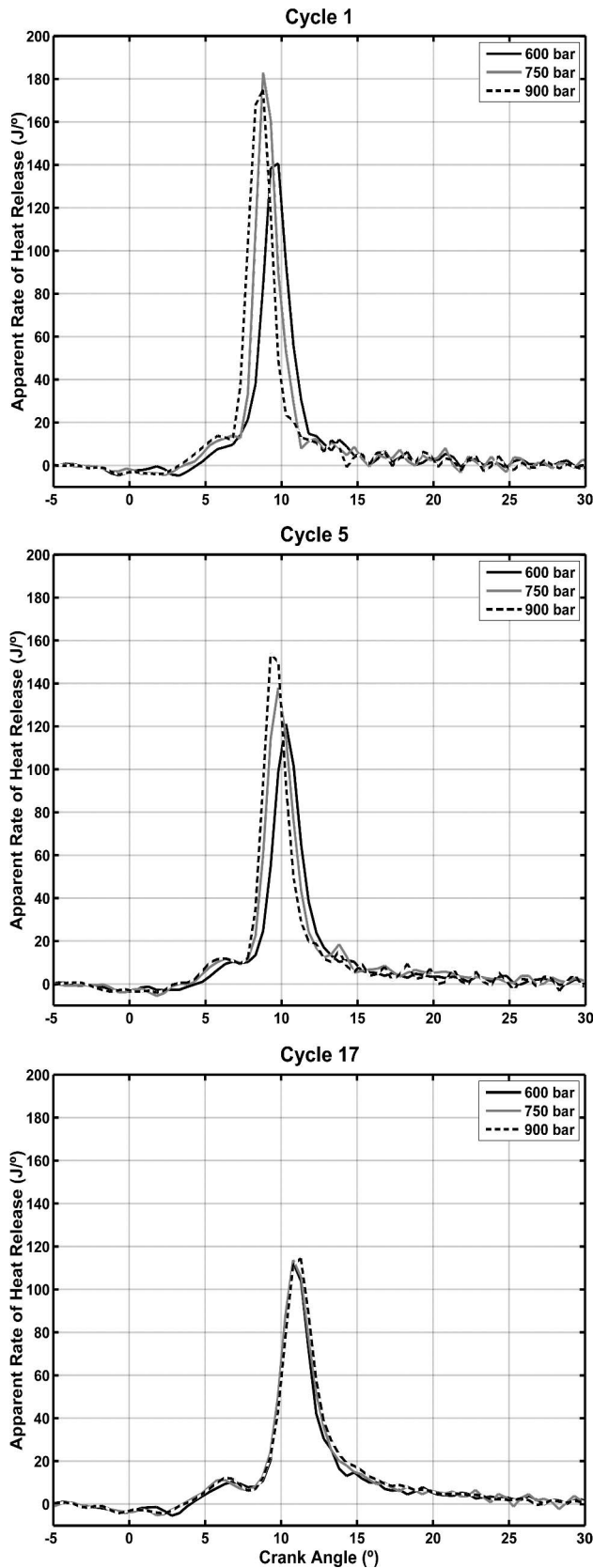
Journal of Engineering for Gas Turbines and Power   SEPTEMBER 2008, Vol. 130 / **052804-5**

Fig. 7 Rates of heat release with three primary transitions with three different starting rail pressures
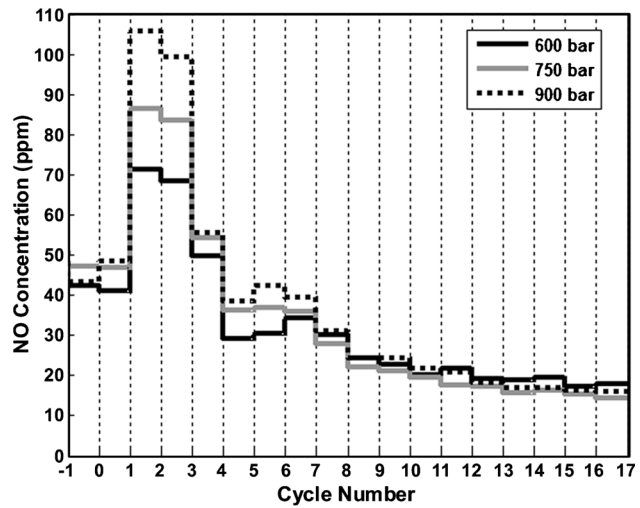

Fig. 8 Averaged NO emission comparison for secondary transitions

NO emissions for the first two transition cycles. This leads to the conclusion that increased fuel rail pressure during the first few transitional cycles does indeed increase the concentration of NO produced from these cycles.

Cycle-by-cycle heat release analysis is performed on one representative transition of each type of secondary transition mentioned above (Fig. 7).

As the rail pressure increases, the peak rate of heat release for the first three transition cycles increases. These peaks also occur earlier in the cycle as the rail pressure increases, which suggests that combustion occurs earlier in the cycle; the combustion phasing is advanced. When the rail pressure starts at 600 bars, it is more difficult to see the cool-flame heat release hump for the first three transition cycles. When the rail pressure during the first few transition cycles is increased to 750 bars and 900 bars, the cool-flame heat release hump is seen more clearly with more separation in crank angle degrees between the cool-flame hump and the main heat release hump from the beginning. In general, increasing the fuel pressure above 600 bars leads to more rapid, violent combustion during the first three transition cycles. The shapes of the three different secondary transition heat release curves are very nearly identical after the tenth transition cycle.

Discussion

Uncertainty in the trapped mass calculation prevents precise calculation of in-cylinder temperatures. Also, the available estimates of ideal-gas bulk cylinder temperatures are not necessarily representative of local cylinder temperatures, especially in the vicinity of the mixture where ignition and combustion occur, but they are the only available calculated temperature and provide insight into the overall cylinder conditions.

Cylinder pressure data from the first two transition cycles show higher peak pressures that occur earlier in the cycle (see Fig. 9). The measured CO_2 concentration in the intake does not substantially change, and there is no evidence to suggest that the air flow rate changes to any appreciable extent during these cycles. Assuming that the mass and mixture molecular weight within the cylinder do not substantially change for these first two cycles, the ideal-gas law dictates that temperatures within the cylinder are considerably higher during these early transition cycles and then probably decrease as peak pressures are lower and occur later, EGR rates increase, and mixture molecular weights increase. This trend has a potentially profound effect on combustion. Estimated cylinder temperatures near top dead center (TDC) and during combustion are highest for the first two transition cycles for rea-

data. When displayed with bars representing one standard deviation, the cycle-averaged NO data still show a clear trend of higher
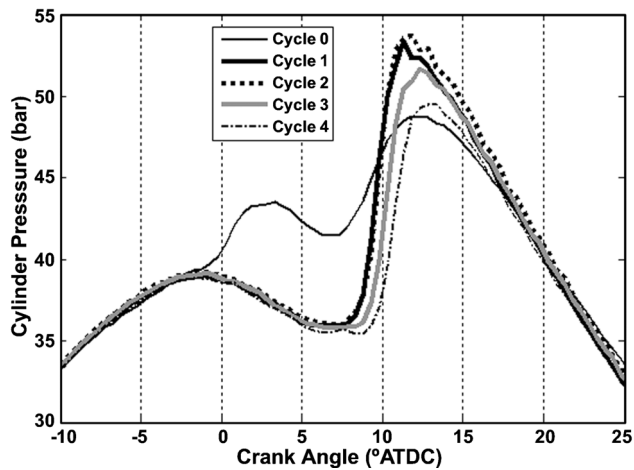
Fig. 9 Cylinder pressure near TDC for a primary transition

sons described above. Since these temperatures are dependent on combustion phasing and mixture properties, real cylinder temperatures do not likely stabilize until the CO_2 concentrations have reached their steady-state values.

Cylinder temperatures have significant implications for the possibility of a separate cool flame. For the first three primary transition cycles, a distinct cool-flame hump is not observed (see Ref. [20] for a thorough explanation of cool-flame reactions). However, heat release does slowly begin for these cycles, which could be the beginnings of cool flames. Localized cylinder temperatures where ignition occurs are unknown, so it is unclear if temperatures are above or below the limits for cool-flame chemistry to occur for any given cycle.

Observations from Fig. 7 indicate that fuel pressure has an effect on the development of cool flames for the secondary transitions. When the rail pressure starts at 750 bars, small heat release humps before the main heat release events are observed in the first three transition cycles, somewhat separate from the main heat release peaks. These appear to be cool flames, which are not so obviously detectable when the rail pressure starts at 600 bars. These same separated cool-flame humps are present when the rail pressure starts at 900 bars, and are likely even more established. Increasing the fuel pressure enhances mixing in the cylinder, and this apparently can determine if a cool flame is observed to be separated from the main heat release event or not.

The first few 900 bar secondary transition cycles are consistently characterized by extremely high rates of heat release, and this is attributed to the lack of additional dilution as the EGR rate has not yet increased. Despite the lack of decreased intake O_2 concentrations, cool flames, along with high peak rates of heat release, are observed for these cycles. These cycles also exhibit high levels of NO, so their combustion cannot be considered to be low-temperature PCI. This then means that the presence of a separated cool flame does not necessarily correspond to low-temperature PCI combustion. The existence of a separated cool flame must mean that some of the adequately mixed reactants have spent sufficient time above 800 K without increasing much above 900–950 K [20]. Thus, the cool-flame reactions have time to progress before the onset of the main heat release.

The rate at which NO forms by the extended Zeldovich mechanism strongly depends on both local temperatures and O_2 concentrations. As the concentration of CO_2 in the intake increases due to increased EGR flow rates, the concentration of O_2 decreases (see Fig. 5). The first two transition cycles do not show significant changes in the intake CO_2 concentration, so it is inferred that the O_2 concentration remains near its relatively high conventional combustion level for these two cycles. These elevated concentrations aid in the creation of NO for the first two transition cycles.

Then, as intake CO_2 levels increase and O_2 levels decrease, the observed NO production decreases. However, Jacobs et al. suggest that the oxygen concentration effect of EGR has a smaller impact on NO formation than does the flame temperature effect of EGR [21], so the discussion is not complete.

For a given mass, volume, and composition, higher pressures tend to increase temperatures within the cylinder. Early combustion phasing leads to higher peak pressures (see Fig. 9). Later transition cycles exhibit later locations for combustion. The combination of early combustion phasing, rapid heat release, and higher adiabatic flame temperatures due to local O_2 concentrations that are closer to stoichiometric is largely responsible for the high pressures and estimated temperatures observed during the first two transition cycles. In later transition cycles, as the combustion phasing retards, peak temperatures and pressures also occur later and are lower in magnitude. The increase in cylinder volume as the piston moves down also contributes to lower temperatures and pressures with later combustion.

It is also important to consider the effects that EGR and charge dilution within the cylinder have on cylinder temperatures. For the first two transition cycles, the intake CO_2 concentration remains relatively stable, and then it increases as more EGR mixes with the intake air (see Fig. 5). The mixture specific heat ratio should increase as these diluents are added, which tends to decrease post-compression temperatures for cycles with higher EGR levels. The mixture heat capacity increases with the presence of triatomic diluents, thereby decreasing flame temperatures and inhibiting NO formation. However, hot EGR decreases the mixture gas constant and preheats the intake air, which could serve to increase temperatures. These competing effects make it difficult to estimate the effects of EGR on density and temperature after compression.

Fuel Rail Pressure. Increased fuel injection pressure should increase the level of mixing within the cylinder; computational results from Minato et al. suggest that increased injection pressures do locally create leaner mixtures [19]. Higher injection pressures increase fuel penetration depth and aid in spray breakup. This allows evaporation and mixing to occur more rapidly, encouraging locally leaner equivalence ratios. The results from the secondary transitions (Fig. 8) do show definite increases in NO emissions from the first two transition cycles as fuel rail pressure increases. It is believed that increasing the rail pressure improves mixing and creates local equivalence ratios that are closer to stoichiometric before combustion. These leaner local equivalence ratios are associated with higher local O_2 concentrations that lead to higher combustion temperatures and therefore increased NO emissions.

Of note are the relative time scales with which intake CO_2 concentrations and the NO emissions rate stabilize; there seems to be a strong link between intake O_2 concentration and the NO produced. This is in agreement with Kook et al. [22] The general combustion characteristics, including NO emissions, largely stabilize by the 15th transition cycle, whereas the exhaust and intake CO_2 concentrations seem not to have completely stabilized by that time. This suggests that there may be a threshold intake O_2 concentration, below which NO emissions are not reduced further.

Conclusions

Transitions between lean conventional diesel combustion and lean, premixed, low-temperature diesel combustion are performed on a high-speed diesel engine. Cycle-by-cycle heat release analysis is performed and an exhaust mass flow model is constructed to provide mass-weighted average NO data.

Cool flames are observed for cycles that produce high and low levels of NO. What is also observed is the change in cool-flame separation as a transition progresses. Higher mixing rates due to increased rail pressure are thought to be responsible for the observed immediate cool-flame separation for secondary transitions.

There appears to be a powerful connection between intake charge dilution and NO emissions for a cycle; this agrees well with the literature. Charge dilution has a profound effect on the severity of combustion, which affects both in-cylinder temperatures and combustion phasing. Intake CO_2 concentration is found to be a much more useful metric than EGR rate for controlling combustion characteristics.

Cycles during which cylinder temperatures are expected to be high and last for a significant time do indeed produce higher levels of NO. There is not a strong observed relationship between premixed burning and NO emissions. Fuel rail pressure and its expected associated mixing improvements are attributed to more severe combustion and as a result higher NO emissions.

Acknowledgment

References

[1] EPA, 2000, "Control of Air Pollution From New Motor Vehicles: Tier 2 Motor Vehicle Emissions Standards and Gasoline Sulfur Control Requirements; Final Rule," Federal Register Vol. 65, No. 28, 40 CFR Parts 80 85, and 86.

[2] U.S. Department of Transportation/NHTSA, 2004, Automotive Fuel Economy Program: Annual Update Calendar Year 2003.

[3] EPA, 1994 "Control of Air Pollution From New Motor Vehicles and New Motor Vehicle Engines: Gaseous and Particulate Emission Regulations for 1994 and Later Model Year Light-Duty Vehicles and Light-Duty Trucks; Final Rule," Federal Register Vol. 59, 40 CFR Part 86.

[4] EPA, 2000, "Control of Air Pollution From New Motor Vehicles: Tier 2 Motor Vehicle Emissions Standards and Gasoline Sulfur Control Requirements; Final Rule," Federal Register Vol. 65, No. 28, 40 CFR Parts 80 85, and 86.

[5] Yu, R., Cole, A., Stroia, B., Huang, S., Howden, K., and Chalk, S., 2002, "Development of Diesel Exhaust Aftertreatment System for Tier II Emissions," Society of Automotive Engineers Transactions, Journal of Fuels and Lubricants, 111(2), pp. 861–875.

[6] Kimura, S., Aoki, O., Kitahara, Y., and Aiyoshizawa, E., 2001, "Ultra-Clean Combustion Technology Combining a Low-Temperature and Premixed Combustion Concept for Meeting Future Emission Standards," Society of Automotive Engineers Transactions, Journal of Fuels and Lubricants , 110(4), pp. 239–248.

[7] Jacobs, T., 2005, "Simultaneous Reduction of Nitric Oxide and Particulate Matter Emissions From a Light-Duty Diesel Engine Using Combustion Development and Diesel Oxidation Catalyst," Ph.D. thesis, University of Michigan, Ann Arbor.

[8] Shimazaki, N., Tsurushima, T., and Nishimura, T., 2003, "Dual Mode Combustion Concept With Premixed Diesel Combustion by Direct Injection Near Top Dead Center," Society of Automotive Engineers Transactions, Journal of Engines, 112(3), pp. 1060–1069.

[9] Okude, K., Mori, K., Shiino, S., and Moriya, T., 2004, "Premixed Compression Ignition (PCI) Combustion for Simultaneous Reduction of NOx and Soot in Diesel Engine," Society of Automotive Engineers Transactions, Journal of Fuels and Lubricants, 113(4), pp. 1002–1013.

[10] Knafl, A., Jacobs, T. J., Bohac, S. V., and Assanis, D. N., 2006, "The Load Limits of Low Temperature Premixed Compression Ignition Diesel Combustion," ISCE 2006, The Second International Symposium on Clean and High-Efficiency Combustion in Engines, Tianjin, China.

[11] Uekusa, T., Nakada, T., Ishikawa, N., Ueda, T., Fujino, R., Brown, D., Paratore, M., and Ryan, D., 2005, "Emission Reduction Study for Meeting New Requirements With Advanced Diesel Engine Technology," Society of Automotive Engineers Transactions, Journal of Fuels and Lubricants, 114(5), pp. 914–926.

[12] Knafl, A., 2007, "Development of Low-Temperature Premixed Diesel Combustion Strategies and Formulations of Suitable Diesel Oxidation Catalysts," Ph.D. thesis, University of Michigan, Ann Arbor.

[13] Depcik, C., Jacobs, T., Hagena, J., and Assanis, D., 2007, "Instructional Use of a Single Zone, Premixed Spark-Ignition Heat Release Simulation," International Journal of Mechanical Engineering Education, 35(1), pp. 1–31.

[14] Heywood, J., 1988, *Internal Combustion Engine Fundamentals*, McGraw-Hill, New York, Chap. 6.

[15] Bohac, S., and Landfahrer, K., 1999, "Effects of Pulsating Flow on Exhaust Port Flow Coefficients," Society of Automotive Engineers Transactions, Journal of Engines, 108(99), pp. 299–309.

[16] Takeda, Y., Keiichi, N., and Keiichi, N., 1996, "Emission Characteristics of Premixed Lean Diesel Combustion with Extremely Early Staged Fuel Injection," Society of Automotive Engineers Transactions, Journal of Fuels and Lubricants, 105(96), pp. 938–947.

[17] Akagawa, H., Miyamoto, T., Harada, A., Sasaki, S., Shimazaki, N., Hashizume, T., and Tsujimura, K., 1999, "Approaches to Solve Problems of the Premixed Lean Diesel Combustion," Society of Automotive Engineers Transactions, Journal of Engines, 108(99), pp. 120–132.

[18] Iwabuchi, Y., Kawai, K., Shoji, T., and Takeda, Y., 1999, "Trial of New Concept Diesel Combustion System—Premixed Compression-Ignited Combustion," Society of Automotive Engineers Transactions, Journal of Engines, 108(99), pp. 142–151.

[19] Minato, A., Tanaka, T., and Nishimura, T., 2005, "Investigation of Premixed Lean Diesel Combustion with Ultra High Pressure Injection," Society of Automotive Engineers Transactions, Journal of Engines, 114(5), pp. 756–764.

[20] Westbrook, C., 2000, "Chemical Kinetics of Hydrocarbon Ignition in Practical Combustion Systems," Proc. Combust. Inst., 28, pp. 1563–1577.

[21] Jacobs, T., Assanis, D., and Filipi, Z., 2003, "The Impact of Exhaust Gas Recirculation on Performance and Emissions of a Heavy-Duty Diesel Engine," Society of Automotive Engineers Paper No. 2003-01-1068.

[22] Kook, S., Bae, C., Miles, P., Choi, D., and Pickett, L., 2005, "The Influence of Charge Dilution and Injection Timing on Low-Temperature Diesel Combustion and Emissions," Society of Automotive Engineers Transactions, Journal of Fuels and Lubricants, 114(5), pp. 1575–1595.

Characteristics of Particulate Emissions of Compression Ignition Engine Fueled With Biodiesel Derived From Soybean

Myung Yoon Kim

Seung Hyun Yoon

Jin Woo Hwang

Graduate School of Hanyang University,
17 Haengdang-Dong, Sungdong-Gu,
Seoul 133-791, Korea

Chang Sik Lee[1]

Professor
Department of Mechanical Engineering,
Hanyang University,
17 Haengdang-Dong, Sungdong-Gu,
Seoul 133-791, Korea
e-mail: cslee@hanyang.ac.kr

An experimental investigation was performed on the effect of engine speed, exhaust gas recirculation (EGR), and boosting intake pressure on the particulate size distribution and exhaust gas emissions in a compression ignition engine fueled with biodiesel derived from soybean. The results obtained by biodiesel fuel were compared to those obtained by petroleum diesel fuel with a sulfur content of 16.3 ppm. A scanning mobility particulate sizer was used for size distribution analysis, and it measured mobility equivalent particulate diameter in the range of 10.4–392.4 nm. In addition to the size distribution of the particulates, exhaust emissions, such as oxides of nitrogen (NO_x), hydrocarbon, and carbon monoxide emissions, and combustion characteristics under different engine operating parameters were investigated. The engine operating parameters in terms of engine speed, EGR, and intake pressure were varied to investigate their individual impacts on the combustion and exhaust emission characteristics. As the engine speed was increased for both fuels, the larger size particulates, which dominantly contribute particulate mass, were increased; however, total numbers of particulate were reduced. Compared to diesel fuel, the combustion of biodiesel fuel reduced particulate concentration of relatively larger size where most of the particulate mass is found. Moreover, dramatically lower hydrocarbon and carbon monoxide emissions were found in the biodiesel-fueled engine. However, the NO_x emission of the biodiesel-fueled diesel engine shows slightly higher concentration compared to diesel fuel at the same injection timing. EGR significantly increased the larger size particulates, which have diameter near the maximum measurable range of the instrument; however, the total number of particulates was found not to significantly increase with increasing EGR rate for both fuels. Boosting intake pressure shifted the particulate size distribution to smaller particulate diameter and effective reduction of larger size particulate was found for richer operating conditions.
[DOI: 10.1115/1.2906215]

Keywords: biodiesel, particulate size distribution, combustion characteristics, exhaust emission, injection rate

1 Introduction

Biodiesel is an attractive fuel as a substitute for petroleum diesel because of its renewable character and reduction potential of greenhouse emissions. Many kinds of resources including soybean, rapeseed, palm, and used frying oil have been suggested as feedstocks for biodiesel. It can be made from the conversion of triglyceride to esters via an etherification process [1]. In contrast to the combustion of fossil fuel, biodiesel provides reduction of lifecycle CO_2 emissions because carbon is biologically cycled when plants convert CO_2 to carbon based compounds through the photosynthesis process. Moreover, the rising petroleum cost improves the price competitiveness of biodiesel fuel.

Biodiesel fuel has many advantages for an alternative fuel for compression ignition (CI) engine. Modest reduction of particulate matter emission has been reported for biodiesel fuel since it includes oxygen content in its molecular structure but virtually no sulfur and aromatic contents. In addition, the use of biodiesel causes some reduction in hydrocarbon (HC) and carbon monoxide (CO) emissions [2–4]. Due to the oxygen content, the combustion

of biodiesel fuel produces lower solid particle emissions as compared to the petroleum-based diesel fuel [5]. The absence of sulfur prohibits SO_x emissions and prevents sulfur poisoning of after treatment system. However, the higher viscosity deteriorates spray atomization; moreover, the high freezing point of the fuel may result in cold starting problems when operating at low ambient temperatures.

Most previous research has reported that NO_x emission of biodiesel is slightly increased by using biodiesel fuel [2,3,6]. When the biodiesel fuel is used for mechanical injection systems, its higher bulk modulus significantly shortens injection delay; moreover, the higher cetane number shortens ignition delay. As a result, biodiesel ignites faster than diesel fuel [7,8]. This can explain the higher NO_x emission of biodiesel. Furthermore, the higher adiabatic flame temperature due to the more double-bonded molecules of biodiesel fuel is suggested as another factor for increasing NO_x emission by Ban-Weiss et al. [9].

Considerably lower solid soot particle emissions with higher soluble organic fraction (SOF) were found in the combustion of biodiesel fuel [10]. In addition, a lower content of polycyclic aromatic compounds (PACs) in the particle emissions of biodiesel fuel reduces the number of mutations [10,11]. There are serious concerns about the negative effects of submicrometer airborne particles on the human body and the climate. Therefore, recent reports regarding the correlation of diesel particulates with health

---
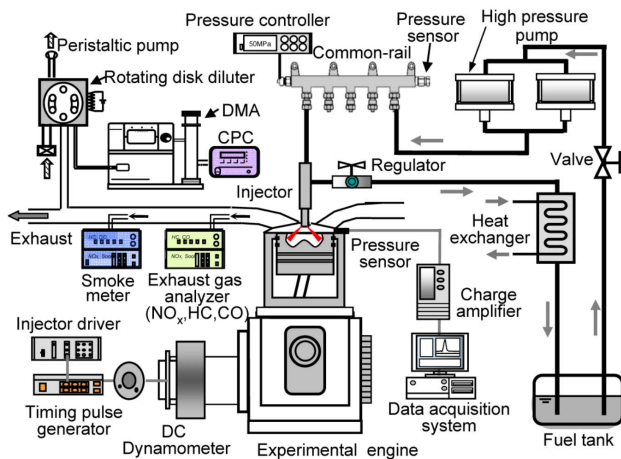
Fig. 1 Schematic of experimental apparatus

Table 2 Properties of test fuels

Property	Biodiesel	Diesel
Ester content (wt %)	97.4	—
Flash point (°C)	168	54
Viscosity at 40°C (mm²/s)	4.022	2.835
Sulfur content (wt ppm)	∼2	16.3
Ash (wt %)	0.002	0.001
Density at 15°C (kg/m³)	884	828
Cloud point (°C)	−1	0
Pour point (°C)	−2	−25

effects and environmental degradation have prompted regulatory agencies to set stricter emission regulations for diesel engines [12]. The particulate size and number distribution are closely related to the engine operating conditions, such as exhaust gas recirculation (EGR) [6], engine speed, engine load [13,14], injection timing [14,15], and intake pressure. Much research has investigated the effect of engine operating parameters on the particulate emission characters using commercial type multi-cylinder engines. However, in that case, it is hard to isolate each operating parameter, such as intake pressure, exhaust pressure, intake temperature, etc., for various operating conditions. Therefore, little information is available on the influence of various distinct operating parameters of CI engines fueled with neat biodiesel on the particulate emissions.

In this work, an experimental investigation was performed on the effect of engine speed, EGR, and boosting intake pressure on the distributions of particulate size and composition of exhaust emissions from a CI engine fueled with biodiesel derived from soybean. The results were compared to those obtained by petroleum-based diesel fuel.

2 Experimental Apparatus and Procedure

2.1 Experimental Engine and Control System. All experiments were conducted on a single cylinder direct injection diesel engine equipped with a common-rail electric controlled fuel injection system capable of injection pressure up to 150 MPa. To make it possible to pressurize various kinds of fuel, an air-driven high-pressure pump system was used (Fig. 1). The pressurized fuel in the common rail was injected through an electrically controlled injector. Specifications of the test engine are listed in Table 1.

The engine speed and torque were controlled using a dc dynamometer with a maximum brake power of 55 kW. The cylinder

Table 1 Specifications of test engine

Type	Single cylinder direct injection diesel engine
Bore × stroke (mm)	75 × 84.5
Compression ratio	17.8:1
Displacement volume (cc)	373.3
Piston type	Reentrant
Injection system	Bosch common rail
Valve system	DOHC 4valves
Number of nozzle holes	6
Nozzle hole diameter (mm)	0.128
Included spray angle (deg)	156

pressure was measured using a piezoelectric pressure sensor (6052B2, Kistler) coupled with a charge amplifier (5011B, Kistler). The data were monitored and stored using a PC-based data acquisition board (PCI-MIO-16E-1, National instrument) and a combustion analysis program. The concentrations of exhaust emission were measured using a NOₓ, HC, and CO analyzer, respectively. For measuring particulate matter concentration in the exhaust gas, a smoke meter (415S, AVL) was used.

The determination of particle number and size distribution was conducted by a scanning mobility particle sizer (Model 3936, TSI). The mobility equivalent diameter range of 10.4–392.4 nm was measured in this work. Dilution was performed by a rotating disk diluter (MD19-2E, Matter Engineering) to lower particle concentration to a value within the measurement range of the scanning mobility particulate sizes (SMPS). By using the dilution system, sampled raw gas was diluted to a dilution ratio of 500:1. The diluted gas was heated to a temperature of 120°C to avoid the condensation of the volatile components of sample raw gas.

2.2 Test Fuels and Experimental Procedure. In this work, the effect of neat biodiesel derived from soybean oil was investigated and the result was compared to the petroleum diesel fuel with a sulfur content of 16.3 ppm. The detailed properties of test fuels are provided in Table 2.

The injection rate profile was measured using an injection rate measurement system based on the design described by Bosch [16,17]. The instrument measures the pressure increase produced by the mass of fuel injected into the instrument. The pressure was measured using a piezoresistive type absolute pressure sensor (4045A50, Kistler) and the data were stored using a data acquisition board (PCI-MIO-16E-1, National instrument) with a maximum sampling rate of 1 megasample/s and an analysis program made by LABVIEW (National instrument). The pressure signal can be converted into the rate of injection because the pressure increase is proportional to the rate of injection. The injection back pressure was maintained constant at 4 MPa for all test conditions to simulate the in-cylinder pressure condition near the top dead center of the combustion chamber where the injection event takes place. The injection profiles were ensemble averaged over 200 injection events.

Most of the engine tests were conducted under an injection mass of 8 mg. At that condition, the equivalence ratio is 0.33 for diesel fuel and it corresponds to a medium engine load condition. The injection timing was defined as the timing when the injection current was applied to the injector. The injection timing was varied between 4 deg and 6 deg BTDC. The injector used for this work has an injection delay of ∼0.29 ms at 50 MPa of injection pressure and ∼0.26 ms at 100 MPa of injection pressure for diesel injection. To investigate the effect of engine speed on the particulate matter and exhaust emissions, the engine speed was varied from 1000 rpm to 2000 rpm in step with 500 rpm. Also, the effect of 30% of EGR and boosting intake pressure of 30 kPa under an injection pressure of 100 MPa on the particulate size distribution was investigated. The detailed experimental conditions are listed in Table 3.

Start of energizing (deg BTDC)	2–6
Injection pressure, P_{inj} (MPa)	50, 100
Mass of fuel (mg/cycle)	8, 12
Engine speed (rpm)	1000, 1500, 2000
EGR rate (%)	0, 30
Air induction rate (kg/h at 1500 rpm)	16.2–16.4
Coolant temperature (°C)	70
Oil temperature (°C)	70
Boost pressure (kPa)	0, 30

3 Results and Discussion

3.1 Injection Rate. The injection profiles and energizing current with an energizing width of 700 μs are shown in Fig. 2. Although the same current pulse width was applied to the injector, slightly different injection rates were indicated. Biodiesel fuel showed slightly shorter injection delay and higher maximum injection rate by 2.79% compared to those obtained by diesel fuel. The higher bulk modulus of biodiesel may cause faster injection of the fuel [8]. The higher maximum injection rate of biodiesel is expected because biodiesel has higher density, as shown in Table 2. However, considering the density and peak of injection rate for both fuels, the peak of volumetric injection rate for biodiesel was lower by 3.72% than for diesel fuel. It can be said that the higher viscosity of biodiesel increased friction in the nozzle of the injector; accordingly, the peak of volumetric injection rate was lowered.

3.2 Combustion Characteristics and Particulate Size Distribution of Biodiesel and Diesel Fuel. The combustion pressure and rate of heat release of biodiesel and diesel fuel under a constant operating condition are shown in Fig. 3. Biodiesel indicates faster ignition and lower premixed spike compared to diesel fuel. As mentioned previously, the higher cetane number of biodiesel shortens ignition delay. In spite of the constant mass of injection for both fuels, the smaller heating value of biodiesel reduced maximum combustion pressure; accordingly, the lower engine power can be expected for biodiesel fuel.

The particulate size distributions emitted from biodiesel and
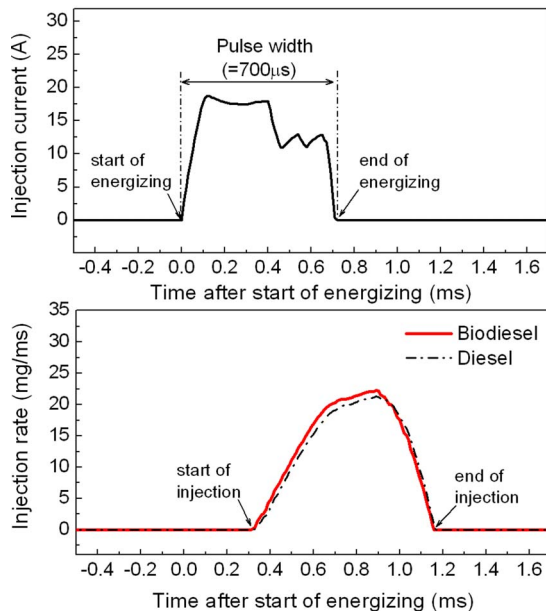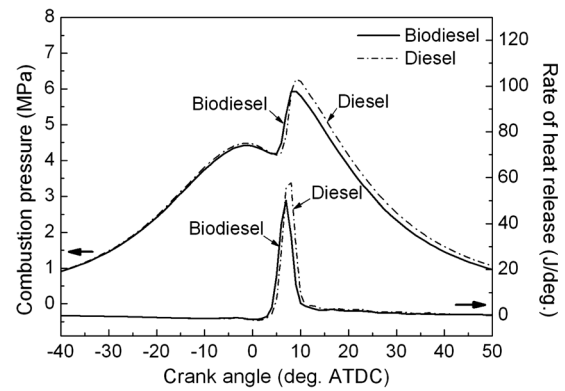
Fig. 3 Combustion characteristics of biodiesel and diesel fuel (m_{fuel}=8 mg, τ_{inj}=6 deg BTDC, P_{inj}=50 MPa, 1500 rpm)

diesel fuel under the same operating conditions are shown in Fig. 4. The measurement of particulate size distribution was conducted after a long time period for engine stabilization and the result was drawn by single measurement of each test condition. The use of biodiesel fuel shifted the particulate size concentration toward smaller particulate diameter, and the larger size particulates, which strongly contribute to the volume and weight of particulates, were remarkably decreased. Previous research has reported that biodiesel decreases the carbon particulate emissions and increases the SOF [18]. However, the volatile condensates (HC and sulfuric acid) have small size, generally less than 50 nm, and the concentration of small size particulates are sensitive to measuring methods and environmental conditions, such as dilution ratio and temperature, relative humidity, and residence time [19,20]. This is because the nucleation mode particles, which have particle diameter smaller than 40–50 nm, are mostly composed of volatile condensates, such as HC and sulfuric acid. Under the operation conditions for this work, biodiesel produced a lower concentration of nucleation particulates.

3.3 Effect of Engine Speed. The effect of engine speed on the combustion pressure and rate of heat release is shown in Fig. 5. The results obtained under different engine speeds of 1000 rpm and 2000 rpm are compared for biodiesel and diesel fuel. As the engine speed was increased, ignition delays of both fuels were prolonged. Consequently, the combustion events were delayed beyond TDC and premixed spikes were lowered. As shown in the results of rate of heat release for an engine speed of 2000 rpm, late combustion regions were continued to the expansion stroke

Fig. 2 Injection rate profiles for a constant current pulse width of 700 μs and an injection pressure of 50 MPa
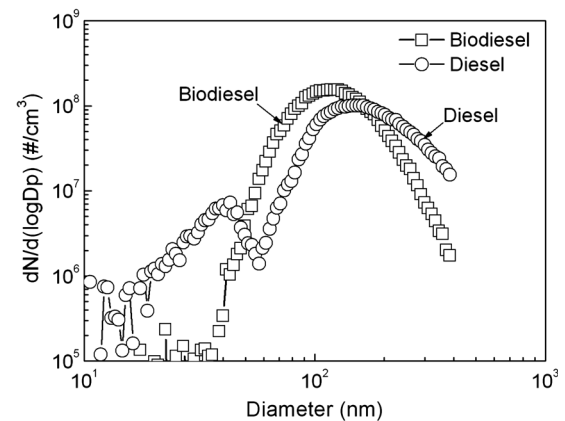
Fig. 4 Particulate size distributions emitted from biodiesel and diesel fuel (m_{fuel}=8 mg, τ_{inj}=6 deg BTDC, P_{inj}=50 MPa, 1500 rpm)
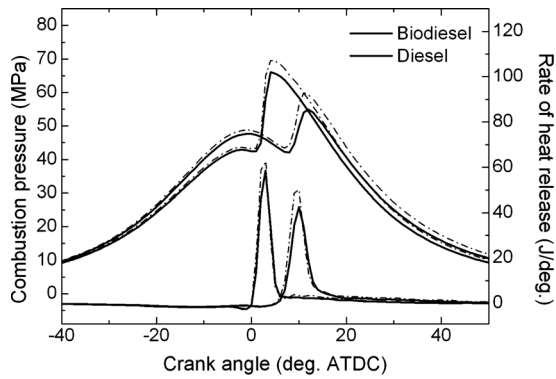
Fig. 5 Effect of engine speed on the combustion pressure and rate of heat release of biodiesel and diesel fuel (m_{fuel}=8 mg, τ_{inj}=6 deg BTDC, P_{inj}=50 MPa)

due to the increased engine speed.

Particulate matters are formed in the locally rich regions of the inhomogeneous combustion in the combustion chamber. Subsequently, it burns at the boundary of diffusive flame due to the high temperature and available oxygen at the region [20]. Therefore, high engine speed can originate the lack of oxidation time for the particulates. Moreover, the delayed combustion event at high engine speed would reduce the reaction rate for oxidation of the particulates produced during the combustion event. Accordingly, increasing engine speed increases particulate emissions and higher smoke emissions are expected at the high engine speed under the same engine load conditions. Figures 6(a) and 6(b) show the particulate size distributions and total particulate number and volume of biodiesel and diesel fuel for engine speeds of 1000 rpm and 2000 rpm, respectively. At an engine speed of 1000 rpm, a significant shift of particulate size to smaller particulate diameter was found when using biodiesel fuel compared to the result at 2000 rpm. This may be explained by the fact that the oxygen content in biodiesel fuel plays a more important role at the lower engine speed condition where available time for oxidation of particulates is enough. The peak concentration of nucleation mode particulate for diesel fuel was reduced by increasing engine speed. For both fuels, increasing engine speed noticeably shifted the particulate size distribution to larger, and as a result, the total volume of the particulates was significantly increased by increasing engine speed, as shown in Fig. 6(b). However, the close correlation between the total particulate number and the engine speed was not found.

The effects of engine speed on the NO_x, HC, and CO emissions for biodiesel and diesel fuel are shown in Fig. 7. The lowest NO_x emission was found at an engine speed of 2000 rpm because the combustion takes place beyond TDC where the charge temperature is rapidly decreased due to the retarded ignition timing, as shown in Fig. 5. As the engine speed decreased, the ignition of the mixture is advanced to the earlier side; moreover, the mixture is exposed for a longer period to the high-temperature burned gas where NO_x is actively formed due to the lower piston movement. As a result, the higher NO_x emission at the lower engine speed can be explained. Biodiesel fuel exhibits slightly higher NO_x emission compared to diesel fuel for all engine speeds. The higher NO_x emissions of biodiesel fuel are reported by many researchers and it can be explained by faster ignition [7,8] and higher adiabatic flame temperature of the combustion of the fuel [9]. Through all engine speeds, significantly lower HC and CO emissions were seen for biodiesel fuel. The lower CO emissions for biodiesel fuel can be explained due to the oxygen in the ester bindings that allows more CO to be oxidized to CO_2. Also, the result showed higher interrelation between engine speeds with CO emission than with HC emission for both fuels.
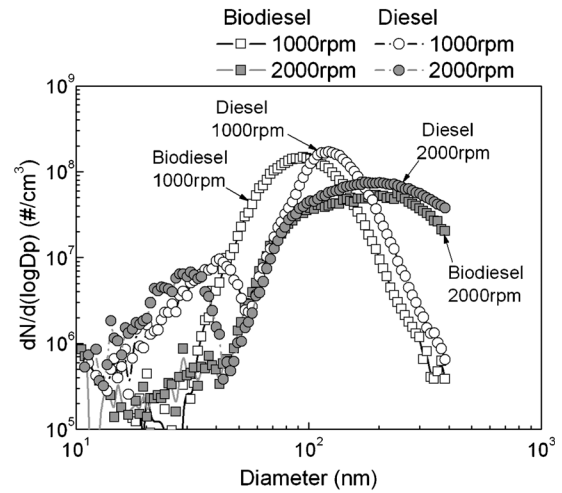
(a)
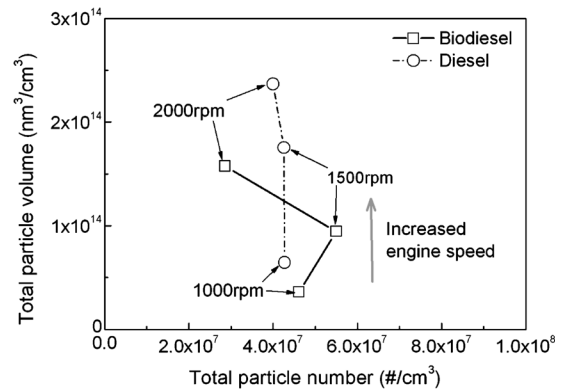
(b)

Fig. 6 Effect of engine speed on the particulate size distribution and total particulate number and volume emitted (m_{fuel}=8 mg, τ_{inj}=6 deg BTDC, P_{inj}=50 MPa): (a) particulate size distribution; (b) total particulate number and volume
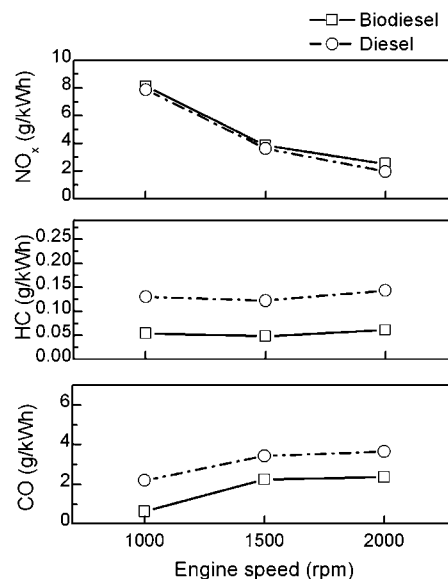
Fig. 7 Effect of engine speed on the CO, HC, NO_x, and soot emissions (m_{fuel}=8 mg, τ_{inj}=6 deg BTDC, P_{inj}=50 MPa)
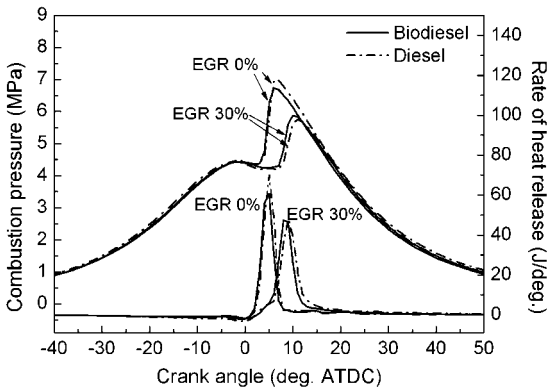
Fig. 8 Effect of EGR on the combustion characteristics of biodiesel and diesel fuel (m_{fuel}=8 mg, τ_{inj}=6 deg BTDC, P_{inj}=100 MPa)

3.4 Effect of EGR. EGR is an effective and simple means to control NO_x emissions by lowering combustion temperature and reducing oxygen concentrations in the intake air [21]. However, the application of EGR has brought about an increase in particulate matters resulting from the lowered oxygen concentration in the flame [22]. The combustion characteristics of both fuels under different EGR rates of 0% and 30% are compared in Fig. 7. The injection pressure and injection timing were kept at 100 MPa and 6 deg BTDC, respectively. It can be seen that 30% of EGR significantly extends the ignition delay period and reduces the peak heat release rate of premixed combustion by lowering the reaction rate. By comparing the effect of EGR on the combustion characteristics of both fuels (Fig. 8), biodiesel fuel showed less sensitivity to EGR on the combustion characteristics. This can be explained by the lower stoichiometric air-fuel ratio of biodiesel fuel. This means that biodiesel fuel requires less air to combust completely due to the lower air-fuel ratio of the fuel. Therefore, the exhaust gas of biodiesel contains more oxygen when the same mass of fuel with diesel is burned. As a result, the fuel-air mixture of biodiesel under the same EGR condition has higher oxygen concentration compared to the petroleum-based diesel fuel.

Desantes et al. [14] reported an increase in the accumulation mode particulates with a rise in the count mean diameter (CMD) value of the distributions with an increasing EGR. The number concentrations of particulates under different EGR rates for both fuels are shown in Fig. 9. It can be seen that 30% of EGR did not
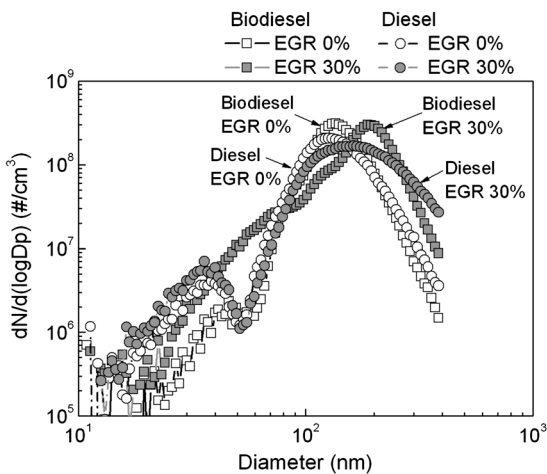
Fig. 9 Effect of EGR on the particulate size distribution for biodiesel and diesel fuel (m_{fuel}=8 mg, τ_{inj}=6 deg BTDC, P_{inj}=100 MPa)
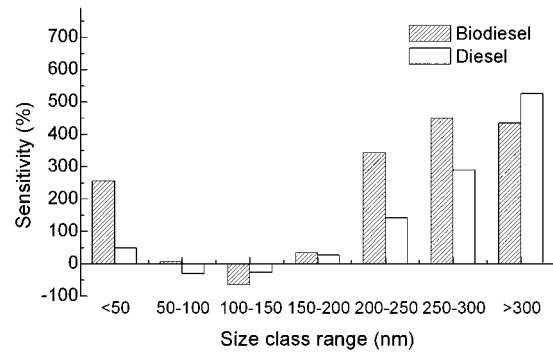
Fig. 10 Sensitivity of particulate size classes to 30% of EGR (m_{fuel}=8 mg, τ_{inj}=6 deg BTDC, P_{inj}=100 MPa)

significantly increase the total number of particulates; however, it shifted the accumulation mode particulates to a large particulate size. As a result, EGR increased the concentration of nucleation mode particulates. A noticeable increase in the concentration of particulates at the largest measurable range of the SMPS was indicated for both fuels.

The sensitivities of each of the size classes to EGR for both fuels are shown in Fig. 10. The percentage variations were calculated on a number of particulate basis. Minus value of sensitivity to EGR was found at a size class range between 100 nm and 150 nm for both fuels. This means that the total particulate number at the range was reduced owing to the EGR. For both fuels, particulate sizes below 50 nm and above 200 nm were significantly increased by the application of EGR. Significant increase in particulate number density was found at a diameter range above 300 nm for diesel fuel compared to biodiesel, and it may cause serious impact on the particulate mass concentration.

3.5 Effect of Supercharging. The effect of supercharging (boost pressure of 30 kPa) on the particulate size distributions of biodiesel at an injection pressure of 100 MPa for different fuel injection masses is shown in Fig. 11. For both cases, boosting intake pressure shifted particulate distribution to a smaller size and this would reduce smoke emission from the engine. However, the concentrations of nucleation mode particulates were increased by boosting intake pressure. Comparing both mass of fuel injection, boosting intake pressure reduced the concentration of larger size particulate at increased mass of fuel injection, as shown in Fig. 11(b). This can indicate that the increased air induction by increasing boost pressure effectively reduced the fuel rich region in the flame at the richer stoichiometric condition. However, the peak of particulate concentration was increased for the richer fuel-air condition.

4 Conclusions

The effect of biodiesel derived from soybean and operating parameters on the particulate size distribution, combustion characteristics, and exhaust emissions were investigated in a single cylinder diesel engine. The main conclusions from this work are summarized as follows.

1. Injection rate of biodiesel indicated shorter injection rate and higher maximum injection rate by 2.79% compared to those obtained from petroleum-based diesel fuel.
2. Biodiesel indicated faster ignition, lower premixed spike, and lower peak of combustion pressure compared to diesel fuel due to the higher cetane number and less heating value of biodiesel when the same mass of fuel was injected.
3. For both fuels, increasing engine speed significantly shifted the particulate size distribution to the larger side; as a result, the total volume of the particulates was significantly in-
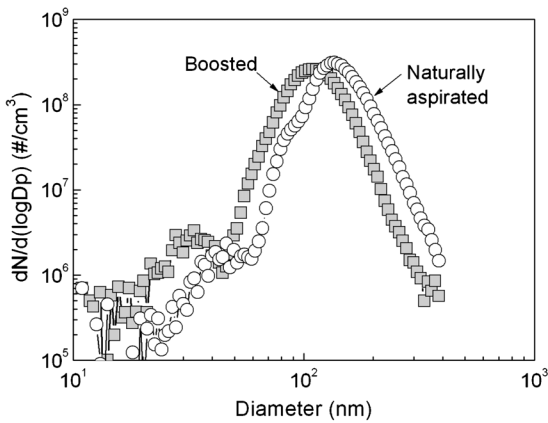
(a)
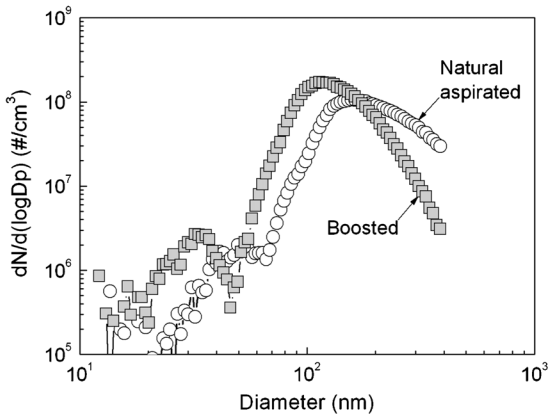
(b)

Fig. 11 Effect of supercharging on the particulate size distribution for biodiesel fuel (P_{inj}=100 MPa, τ_{inj}=4 deg BTDC): (a) m_{fuel}=8 mg/cycle; (b) m_{fuel}=12 mg/cycle

creased by increasing engine speed. However, the close correlation between total particulate number and engine speed was not found.

4. The use of biodiesel fuel shifted the particulate size concentration to the side of smaller particulate diameter, and the larger size particulates, which strongly contribute to the volume and weight of particulates, were remarkably decreased. At the same time, biodiesel produced lower concentrations of nucleation mode particulates.

5. The effect of EGR did not significantly increase the total number of particulates; however, it shifted the accumulation mode particulates to large particulate size. As a result, a noticeable increase in the concentration of particulates at the largest measurable range of the SMPS was indicated for both fuels. Significant increase in particulate number density was found at a diameter range above 300 nm for diesel fuel compared to biodiesel, and it may cause serious impact on the particulate mass concentration.

6. Boosting intake pressure significantly shifted particulate distribution to a smaller size. However, the concentration of nucleation mode particulate was increased by increasing intake pressure.

Acknowledgment

Nomenclature

Acronyms and Abbreviations
BTDC = before top dead center
CO_2 = carbon dioxide
m = mass of injection
P = pressure
TDC = top dead center

Greek
τ = timing

Subscript
inj = injection

References

[1] Graboski, M. S., and McCormick, R. L., 1998, "Combustion of Fat and Vegetable Oil Derived Fuels in Diesel Engines," Prog. Energy Combust. Sci., **24**, pp. 125–164.

[2] Choi, C. Y., and Reitz, R. D., 1999, "An Experimental Study on the Effect of Oxygenated Fuel Blends and Multiple Injection Strategies on DI Diesel Engine Emissions," Fuel, **78**, pp. 1303–1317.

[3] McCormick, R. L., Tennant, C. J., Hayes, R. R., Black, S., Ireland, J., McDaniel, T., Williams, A., Frailey, M., and Sharp, C. A., 2005, "Regulated Emissions From Biodiesel Tested in Heavy-Duty Engines Meeting 2004 Emission Standards," SAE Paper No. 2005-01-2200.

[4] Lee, C. S., Park, S. W., and Kwon, S. I., 2005, "An Experimental Study on the Atomization and Combustion Characteristics of Biodiesel-Blended Fuels," Energy Fuels, **19**, pp. 2201–2208.

[5] Jung, H., Kittelson, D. B., and Zachariah, M. R., 2005, "Characteristics of SME Biodiesel-Fueled Diesel Particle Emissions and the Kinetics of Oxidation," Environ. Sci. Technol., **40**, pp. 4949–4955.

[6] Tsolakis, A., 2006, "Effect of Particle Size Distribution from the Diesel Engine Operating on RME-Biodiesel With EGR," Energy Fuels, **20**, pp. 1418–1424.

[7] Szybist, J. P., Boehman, A. L., Taylor, J. D., and McCormick, R. L., 2005, "Evaluation of Formation Strategies to Eliminate the Biodiesel NO_x Effect," Fuel Process. Technol., **85**, pp. 1109–1126.

[8] Szybist, J. P., Kirby, S. R., and Boehman, A. L., 2005, "NOx Emissions of Alternative Diesel Fuels: A Comparative Analysis of Biodiesel and FT Diesel," Energy Fuels, **19**, pp. 1484–1492.

[9] Ban-Weiss, G. A., Chen, J. Y., Buchholz, B. A., and Dibble, R. W., 2007, "A Numerical Investigation Into the Anomalous Slight NO_x Increase When Burning Biodiesel; A New (old) Theory," Fuel Process. Technol., **88**, pp. 659–667.

[10] Krahl, J., Munack, A., Schröder, O., Stein, H., and Brünger, J., 2003, "Influence of Biodiesel and Different Designed Diesel Fuel on the Exhaust Gas Emission and Health Effects," SAE Paper No. 2003-01-3199.

[11] Bagley, S. T., Gratz, L. D., Johnson, J. H., and McDonald, J. F., 1998, "Effect of an Oxidation Catalytic Converter and a Biodiesel Fuel on the Chemical, Mutagenic, and Particle Size Characteristics of Emissions From a Diesel Engine," Environ. Sci. Technol., **32**, pp. 1183–1191.

[12] Kweon, C., Foster, D. E., Schauer, J. J., and Okada, S., 2002, "Detailed Chemical Composition and Particle Size Assessment of Diesel Engine Exhaust," SAE Paper No. 2002-01-2670.

[13] Virtanen, A. K. K., Ristmäki, J. M., Vaaraslathi, K. M., and Keskinen, J., 2004, "Effect of Engine Load on Diesel Soot Particles," Environ. Sci. Technol., **38**, pp. 2551–2556.

[14] Desantes, J. M., Bermúdez, V., García, J. M., and Fuentes, E., 2005, "Effects of Current Engine Strategies on the Exhaust Aerosol Particle Size Distribution From a Heavy-Duty Diesel Engine," J. Aerosol Sci., **36**, pp. 1251–1276.

[15] Lapuerta, M., Martos, F. J., and Herreros, J. M., 2007, "Effect of Engine Operating Conditions on the Size of Primary Particles Composing Diesel Soot Agglomerates," J. Aerosol Sci., **38**, pp. 455–466.

[16] Bosch, W., 1966, "The Fuel Rate Indicator: A New Measuring Instrument for Display of the Characteristics of Individual Injection," SAE Paper No. 660749.

[17] Kim, M. Y., Bang, S. H., and Lee, C. H., 2007, "Experimental Investigation of Spray and Combustion Characteristics of Dimethyl Ether in a Common-Rail Diesel Engine," Energy Fuels, **21**, pp. 793–800.

[18] Sharp, C. A., Howell, S. A., and Jobe, J., 2000, "The Effect of Biodiesel Fuels on Transient Emissions From Modern Diesel Engine—Part I: Regulated Emissions and Performance," SAE Paper No. 2000-01-1967.

[19] Casati, R., Scheer, V., Vogt, R., and Benter, T., 2007, "Measurement of Nucleation and Soot Mode Particle Emission From a Diesel Passenger Car in Real World and Laboratory In Situ Dilution," Atmos. Environ., **41**, pp. 2125–2135.

[20] Dec, J. E., 1997, "A Conceptual Model of DI Diesel Combustion Based on Laser-Sheet Imaging," SAE Paper No. 970873.

[21] Kim, M. Y., Kim, D. S., and Lee, C. S., 2003, "Effect of Residual Gas Fraction on the Combustion Characteristics of Butane-Air Mixtures in the Constant-Volume Chamber," Energy Fuels, **17**, pp. 755–761.

[22] Zheng, M., Reader, C. T., and Hawley, J. G., 2004, "Diesel Engine Exhaust Gas Recirculation-A Review on Advanced and Novel Concept," Energy Convers. Manage., **45**, pp. 883–900.

Modeling the Effects of Variable Intake Valve Timing on Diesel HCCI Combustion at Varying Load, Speed, and Boost Pressures

C. L. Genzale

Engine Research Center,
Department of Mechanical Engineering,
University of Wisconsin—Madison,
1500 Engineering Drive,
Madison, WI 53705
e-mail: genzale@wisc.edu

S.-C. Kong

Department of Mechanical Engineering,
Iowa State University,
3028 Black Engineering Building,
Ames, IA 50011

R. D. Reitz

Engine Research Center,
Department of Mechanical Engineering,
University of Wisconsin—Madison,
1500 Engineering Drive,
Madison, WI 53705

Homogeneous charge compression ignition (HCCI) operated engines have the potential to provide the efficiency of a typical diesel engine, with very low NO_x and particulate matter emissions. However, one of the main challenges with this type of operation in diesel engines is that it can be difficult to control the combustion phasing, especially at high loads. In diesel HCCI engines, the premixed fuel-air charge tends to ignite well before top dead center, especially as load is increased, and a method of delaying the ignition is necessary. The development of variable valve timing (VVT) technology may offer an important advantage in the ability to control diesel HCCI combustion. VVT technology can allow for late intake valve closure (IVC) times, effectively changing the compression ratio of the engine. This can decrease compression temperatures and delay ignition, thus allowing the possibility to employ HCCI operation at higher loads. Furthermore, fully flexible valve trains may offer the potential for dynamic combustion phasing control over a wide range of operating conditions. A multidimensional computational fluid dynamics model is used to evaluate combustion event phasing as both IVC times and operating conditions are varied. The use of detailed chemical kinetics, based on a reduced n-heptane mechanism, provides ignition and combustion predictions and includes low-temperature chemistry. The use of IVC delay is demonstrated to offer effective control of diesel HCCI combustion phasing over varying loads, engine speeds, and boost pressures. Additionally, as fueling levels are increased, charge mixture properties are observed to have a significant effect on combustion phasing. While increased fueling rates are generally seen to advance combustion phasing, the reduction of specific heat ratio in higher equivalence ratio mixtures can also cause noticeably slower temperature rise rates, affecting ignition timing and combustion phasing. Variable intake valve timing may offer a promising and flexible control mechanism for the phasing of diesel HCCI combustion. Over a large range of boost pressures, loads, and engine speeds, the use of delayed IVC is shown to sufficiently delay combustion in order to obtain optimal combustion phasing and increased work output, thus pointing towards the possibility of expanding the current HCCI operating range into higher load points.
[DOI: 10.1115/1.2938270]

Keywords: homogeneous charge compression ignition, variable valve timing, diesel engine, computational fluid dynamics

Introduction

Diesel engine manufacturers in the United States face a new set of emissions standards for 2007–2010 that will require a 90% reduction of particulate matter (PM) and emissions of nitrogen oxides (NO_x) from the previous level [1]. In addition to emission regulation pressures, there is also a growing need for improved fuel economy. Since homogeneous charge compression ignition (HCCI) operated engines can provide the fuel efficiency of a typical diesel engine with very low emissions of PM and NO_x, much diesel engine research has begun to focus on this technology.

One of the most significant challenges facing diesel HCCI en-gine operation is the need for a robust method of controlling the combustion event. Since diesel fuel has significant cool-flame chemistry, rapid autoignition occurs once compression tempera-tures exceed about 800 K [2]. This can lead to overly advanced combustion phasing and poor indicated mean effective pressure (IMEP). As a result of this phenomenon, HCCI operation is typi-cally limited to low loads and its emission benefits cannot be realized over the entire operating range.

In-cylinder temperature control has been one of the most widely used methods for combustion phasing control. Previous research has explored many ways of controlling in-cylinder tem-peratures for the control of diesel HCCI combustion, including the use of decreased intake temperatures and exhaust gas residual (EGR) [3], variable compression ratio [4], and water injection [5]. With the advent of fully flexible valve trains, a new mechanism has become available, which can offer a highly dynamic and ef-fective method for controlling in-cylinder temperature histories.

While the use of variable valve timing (VVT) for the control of gasoline HCCI combustion is well established in literature (e.g.,

Table 1 Engine specifications and operating condition

Bore × stroke (mm)	137.2 × 165.1
Displacement (L)	2.44
Compression ratio	16:1
Engine speed (rpm)	821
% of maximum load	25
Global equivalence ratio	0.20
EGR	0%
Intake charge motion	Quiescent
Intake temperature (K)	298
Intake pressure (kPa)	102.5
Coolant temperature (°C)	76
Simulated temperature at IVC (K)	364
Simulated pressure at IVC (kPa)	111.9
IVC (CA ATDC)	−143
EVO (CA ATDC)	130
Fuel	*n*-heptane

Fig. 1 Axisymmetric computational grid of piston bowl at top dead center

Refs. [6–8]), the effects of VVT on diesel HCCI combustion have not been as thoroughly explored. This is especially relevant since these fuels display vastly different ignition qualities and therefore require unique approaches to combustion phasing control. In diesel HCCI combustion, the major difficulty to overcome is the tendency towards overly advanced ignition. Ignition tends to occur well before top dead center (TDC) and some method is required to delay the ignition. This is opposite to the fundamental difficulty of gasoline HCCI, which is overly retarded ignition. Due to these unique combustion control issues, it is clear that a different variable valve strategy will be required for diesel HCCI.

The strategy explored here is that of delaying the intake valve closure (IVC) time. By closing the intake valve late in the compression stroke, the effective compression ratio can be decreased, the temperature history adjusted downward, and the start of combustion delayed. Also, by controlling the combustion phasing, thermal efficiency can be maximized.

The goal of this research was to establish a benchmarking study in the use of VVT for combustion phasing control in diesel HCCI engines, particularly for the extension of HCCI operating ranges into higher load regimes. A computational parametric study over a range of loads, boost pressures, and engine speeds is performed to explore the effectiveness of late IVC (LIVC) in controlling the onset of ignition. In parallel, the influence of air-fuel charge characteristics on combustion phasing and duration is examined.

Engine Operating Condition and Computational Model

The present investigation is based on a previous experimental study using a CAT 3400 Series single-cylinder diesel engine, operating under a fully premixed HCCI operating condition [9]. Table 1 summarizes the engine geometry and operating condition. The engine is a 2.44 L displacement heavy-duty diesel single-cylinder research engine with a 137.2 mm bore and a 165.1 mm stroke. The intake geometry produces a quiescent charge motion (no swirl).

Under the operating condition outlined in Table 1, an extremely early injection timing of −250 crank angles after TDC (−250 CA ATDC) was used with a low intake temperature (298 K) to allow for long mixing times prior to combustion, a common strategy for HCCI combustion (see, e.g., Refs. [10,11]). Also, due to its high volatility, *n*-heptane was used as a fuel to further promote the formation of a homogeneous charge. While low NO$_x$ and PM emission were demonstrated in the experiments, the achievable load was limited to 25% of the maximum of that engine, primarily due to a lack of combustion phasing control. Accordingly, the current study explores the extension of this experimental operating condition into higher load regimes via combustion phasing control with LIVC.

A multidimensional computational fluid dynamics (CFD) model
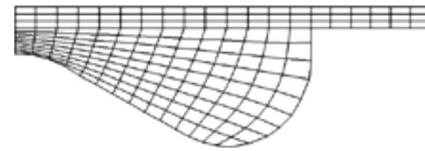
was used to perform the simulations in this investigation. The CFD code used is a version of KIVA-3V [12] with improvements in various physical and chemistry models developed at the Engine Research Center, University of Wisconsin-Madison. Major model improvements have been made to the spray atomization and drop wall impingement models (not used in the current study), wall heat transfer, piston-ring crevice flow, and soot formation and oxidation models (see, e.g., Refs. [13–15]). Turbulence was modeled with the re-normalized group (RNG) *k*-ε model. A reduced reaction mechanism for *n*-heptane [16], with 30 species and 65 reactions, was used for solving the chemistry by integrating the CHEMKIN chemistry solver [17] into the KIVA-3V code. In coupling the CHEMKIN solver with KIVA, each cell in the computational domain was treated as a well-stirred reactor, which neglects turbulence effects on reaction rates, while the species transport was calculated on the computational grid. Findings by Aceves et al. [18] support these model-based assumptions, which show that HCCI is kinetics dominated and that turbulent mixing has a little effect on combustion rates.

Computations were conducted on a two-dimensional (2D) axisymmetric model of the combustion chamber and piston bowl, shown in Fig. 1. The computational grid has a cell size of 3 × 3 mm² at the piston bowl wall and a total of approximately 1900 cells with the piston at the bottom dead center (BDC). As discussed in more detail below, the fuel-air charge is considered to be homogeneously mixed at the start of each simulation. Since the premixing process of the fuel and air is eliminated from the problem, the mesh density has a little effect on the charge preparation process during the compression stroke, allowing for the rather coarse computational mesh used. Furthermore, with the assumption of axial symmetry, the problem is reduced to a 2D grid. These spatial reductions allowed for the inclusion of detailed chemistry calculations while still maintaining fast computational times of less than an hour. The use of a detailed chemistry mechanism in this work was especially important since *n*-heptane displays two-stage ignition chemistry, which has a significant effect on combustion phasing [19]. The ability to capture low-temperature chemistry in computational models is often not found in more simplified models. Indeed, the findings of Aceves et al. [18], showing HCCI to be kinetics dominated, highlight the importance of resolving proper combustion chemistry when modeling HCCI regimes. Furthermore, the reduced *n*-heptane mechanism used in this work was extensively validated against shock-tube and engine measurements at fuel-lean and low-temperature conditions [16], which are typical of HCCI operating conditions.

The model includes several idealized assumptions and boundary conditions that warrant further discussion. First, the model assumes a fully vaporized *n*-heptane and air mixture at IVC. This assumption eliminates the complication of mixing effects in the interpretation of the results and is also likely to be consistent with the physical conditions present in the experimental data [9]. Second, the amount of fuel initialized in the computational domain is kept constant as the IVC time is changed and this results in mixtures that become progressively richer with LIVC times. By maintaining the fueling level, a constant-load condition is simulated. Also, if direct injection of fuel was employed, the injection would likely occur just after IVC and mixtures would become similarly progressively richer as the fresh gas volume available for mixing with the injected fuel quantity decreased with LIVC times. Third,
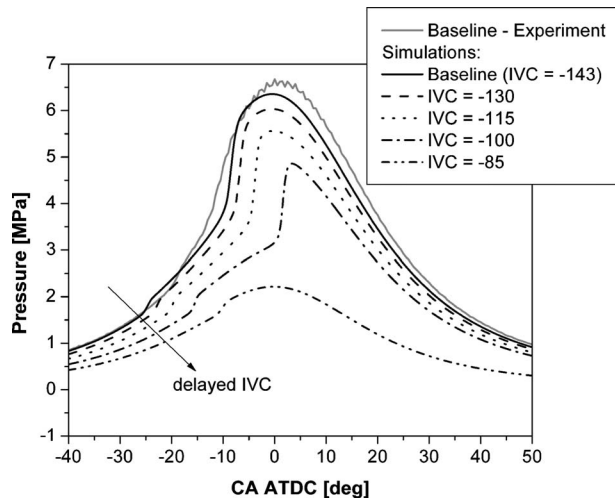
Fig. 2 Effect of late IVC timing on cylinder pressure at base line operating condition (821 rpm, m_{fuel}=31.2 mg, T_{in}=298 K, and P_{in}=102.5 kPa)

Fig. 3 Effect of late IVC timing on heat release rate at base line operating condition (821 rpm, m_{fuel}=31.2 mg, T_{in}=298 K, and P_{in}=102.5 kPa)

it is assumed that regardless of what time the intake valve closes, the pressure and temperature conditions will be the same at IVC. By beginning all of the simulations from the same pressure and temperature environment, it is more straightforward to interpret the effects of the other changes that are made in this study (IVC, boost pressure, and fueling rate), which are the primary interest. It is acknowledged that this assumption neglects effects such as fuel evaporative cooling, compression heating, and wall heat-transfer effects that might occur with changing IVC timing. However, in a real engine, there would be some flexibility to optimize the intake pressure and temperature with the turbocharger and intake cooling systems. Furthermore, the competing effects of increased evaporative cooling and increased compression heating or wall heat transfer with LIVC times would tend to reduce the impact of these individual effects. In summary, while some of the assumptions used to set the boundary conditions in this investigation are somewhat simplified, the current study is focused on understanding the ability to alter the charge history from IVC through combustion, and as such, secondary effects prior to this period are not considered in this work. Additionally, the removal of these secondary effects from the consideration of the problem allows for a more direct interpretation of the effects of load, speed, and boost pressure on the combustion phasing.

Results and Discussion

The computational model was first used to evaluate the potential effectiveness of LIVC times in shifting the combustion phasing of the base line operating condition (Table 1) towards the TDC. The changing of IVC times in the model was accomplished by simply changing the crank angle where the simulation was started. As previously discussed, the temperature and pressure at the start of each computation were kept the same for all of the cases and the simulated injected fuel mass was also kept constant.

Simulated pressure traces for the light-load condition of Table 1, with IVC times ranging from −143 CA ATDC to −85 CA ATDC, are shown in Fig. 2. The experimentally measured cylinder pressure, for the base line operating condition (IVC=−143 CA ATDC), is shown for comparison with the model predictions. The model-predicted cylinder pressure at the base line operating condition is reasonably well matched with the experimental measurement. The start of rapid pressure rise occurs about 3 crank angle degrees (CAD) later in the model predictions than in the measurements and the peak pressure is slightly underpredicted.

As IVC is delayed, Fig. 2 shows that ignition is delayed and the pressure rise is shifted towards the TDC. This results in less nega-
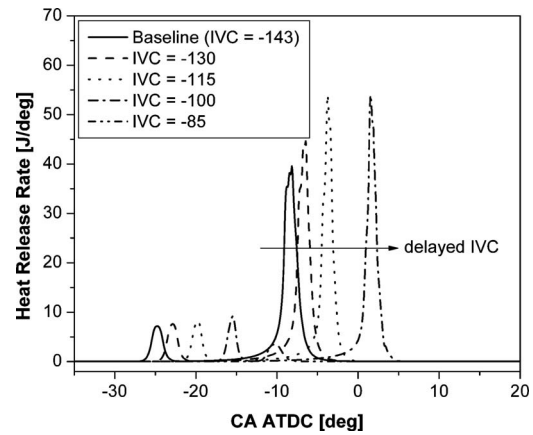
tive work and improved thermal efficiency. The heat release rates for the same range of IVC times are shown in Fig. 3. Again, the delay of IVC can be seen to produce a significant shift of both the cool-flame chemistry and the main combustion event towards the TDC. It is clear that a high level of control may be gained over the combustion phasing by altering the thermal history of the fuel-air charge with LIVC strategies.

Effect of Increasing Load. For HCCI to become a viable operating mode in future engines, combustion control at high loads also needs to be achieved. To evaluate the effectiveness of LIVC times at higher loads, the simulated fueling rates were increased to double and triple the injected mass of the base line operating condition (Table 1). A plot of the resulting 50% accumulated heat release (AHR) points for a range of IVC times with a varying fuel injected quantity is shown in Fig. 4. The phasing of the 50% AHR point is used as a measure of the combustion phasing, where a maximum thermal efficiency would be achieved with a 50% AHR near 0 CA ATDC (TDC).

Figure 4 shows that for all three fueling cases, delayed IVC times are effective at retarding the 50% AHR to near the TDC for optimal combustion phasing. At the base line fueling level of 31.2 mg, the simulations suggest that an IVC timing near −100 CA ATDC will produce a 50% AHR point near the TDC. As the amount of fuel injected is increased from the base line to 62.4 mg, the 50% AHR point is advanced, but by delaying the IVC additional 10 CAD to occur around −90 CA ATDC, the 50% AHR point can again be moved to near the TDC. When the injected fuel
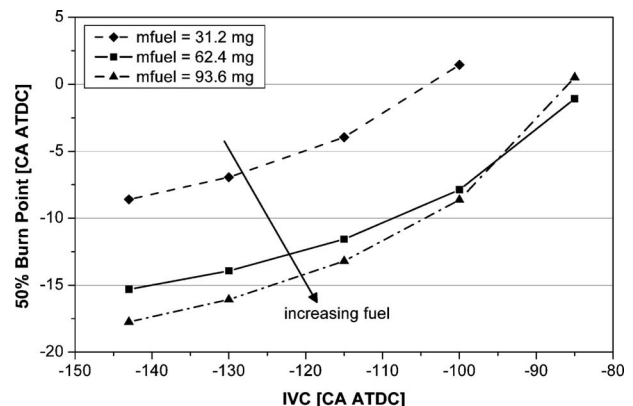

Fig. 4 Effect of late IVC timing on 50% AHR points at varying fueling rates (821 rpm, T_{in}=298 K, and P_{in}=102.5 kPa)

Table 2 Combustion phasing details: Effect of late IVC timing at different fueling rates

Fuel injected	IVC (CA ATDC)	Global equivalence ratio	10% AHR (CA ATDC)	50% AHR (CA ATDC)	10–90% AHR (CAD)	IMEP (bar)
m_{fuel}=31.2 mg	−143	0.20	−24.2	−8.6	16.9	2.57
	−130	0.21	−22.4	−6.9	16.5	2.64
	−115	0.24	−19.3	−4.0	16.3	2.73
	−100	0.27	−15.1	1.5	17.5	2.82
m_{fuel}=62.4 mg	−143	0.40	−23.0	−15.3	7.8	3.91
	−130	0.43	−21.0	−13.9	7.2	3.94
	−115	0.47	−17.8	−11.6	6.3	4.07
	−100	0.55	−13.0	−7.9	5.2	4.22
	−85	0.67	−5.2	−1.1	4.2	4.35
m_{fuel}=93.6 mg	−143	0.60	−21.4	−17.7	3.7	5.18
	−130	0.64	−19.2	−16.1	3.2	5.42
	−115	0.71	−15.6	−13.2	2.5	5.75
	−100	0.82	−10.1	−8.6	1.5	6.08
	−85	1.00	−0.2	0.5	0.7	6.25

is increased to 93.6 mg, the 50% AHR point is again advanced, but not to the same degree. Also, at an IVC time of −90 CA ATDC, the 50% AHR point for the highest fueling case becomes even less advanced and actually occurs later than the 62.4 mg fueling case with the same IVC timing. To understand why this occurs, and to gain more insight about the abilities of LIVC times at higher loads, it is helpful to analyze the combustion phasing details, which are outlined in Table 2.

The timings of three significant portions of the total heat release are outlined in Table 2. First, the time at which 10% of the total fuel energy has been released (10% AHR point) is used as an indicator of the second stage ignition timing. Second, as discussed previously, the time at which 50% of the total fuel energy has been released (50% AHR point) is used as a measure of the combustion phasing, where a 50% AHR point near the TDC is desired for optimal thermal efficiency. Last, the time in CAD for the energy release to occur between the 10% AHR point and the 90% AHR point is used as a measure of the total combustion duration. The analysis of these significant points in the fuel energy release can highlight important variations in the combustion history occurring with the simulated LIVC strategy.

While the 50% AHR points were generally seen to be advanced by increased fueling in Fig. 4, Table 2 shows that, by contrast, the 10% AHR points are delayed as the injected fuel amount is increased for a given IVC time. For example, with an IVC time of −143 CA ATDC, the 10% heat release point is retarded from −24.2 CA ATDC to −23 CA ATDC, and to −21.4 CA ATDC as the fuel injection quantity is increased from 31.2 mg to 62.4 mg and 93.6 mg. As the injected fuel quantity is increased, the specific heat ratio of the fuel-air charge decreases, resulting in decreased compression temperatures and a delayed ignition time.

Table 2 also reveals that the 10–90% AHR, or combustion duration, is dramatically shortened as the fuel injected quantity or equivalence ratio is increased. By contrast, longer combustion durations occur with lower equivalence ratio mixtures, which is a result of reduced adiabatic flame temperatures in these mixtures. The variation of combustion duration with changes in equivalence ratio has a dominant effect over the observed changes in ignition timing and this leads to a general trend of advanced 50% AHR points as the fueling rate increases. However, the gradual decrease in the advancement of the 50% AHR points with increasing fueling is likely due to an increasing impact of the delayed ignition times that arise from the reduced specific heat of the fuel-air charge. Indeed, Kelly-Zion and Dec [19] have shown that the oxidation chemistry of two-stage fuels such as *n*-heptane are affected by these types of competing dependencies on mixture

equivalence ratios. Specifically, they demonstrated that the effect of decreased specific heats in higher equivalence ratio fuel-air mixture causes decreased compression temperatures, and thus increased ignition delays. However, they also found that the time between the first and second-stage combustion is decreased with increased equivalence ratio. This is consistent with a reduction in combustion duration (10–90% AHR) with increasing equivalence ratios, as observed in Table 2.

Looking closer at the heat release points for the 93.6 mg fueling case in Table 2, further insight can be gained about the impact of higher equivalence ratio mixtures on 50% AHR phasing. As discussed previously, the mixtures resulting from this injected fuel quantity produce delayed ignition points, but dramatically shortened the combustion duration. This produces a competition of effects as the delayed ignition time pushes the 50% AHR point towards the TDC while the shortened combustion duration tends to advance the 50% AHR point. For example, as the fueling rate is increased from 62.4 mg to 93.6 mg, with a fixed IVC time of −100 CA ATDC, the decreased specific heat ratio of the 93.6 mg mixture causes a delay in the 10% AHR point of about 3 CAD, compared to that of the 62.4 mg mixture. Recall that since the temperature and pressure boundary conditions are kept constant between the simulations, the compression history will be replicated between these cases since the IVC timing is the same. However, the higher global equivalence ratio of the mixture resulting from a 93.6 mg injection results in a faster combustion reaction and a 50% AHR point which is about 0.5 CAD advanced from the 62.4 mg fueling case. By contrast, with a fixed IVC time of −85 CA ATDC, the 50% AHR point of the 93.6 mg fueling case displays a delay of about 1.5 CAD in the 50% AHR point with respect to the 62.4 mg case. This occurs even though the combustion duration has been reduced by 3.5 CAD relative to the 62.4 mg case. In the higher fueling case, the decreased specific heat ratio of the charge mixture results in a more significantly delayed ignition. Ignition is delayed by an additional 5 CAD, by comparison, leading to the observed relative delay in the 50% AHR point.

Finally, it can be seen that as IVC time is delayed for each fueling case, a higher IMEP is obtained. Since the fueling rate is kept constant as the IVC time is delayed, the increase in IMEP is a result of the shift in the 50% AHR point towards the TDC and an improvement in thermal efficiency. These results indicate that, theoretically, the IMEP can be more than doubled while maintaining an optimally phased HCCI mode by employing a LIVC time near −85 CA ATDC with a fuel injection of 93.6 mg. Note that the
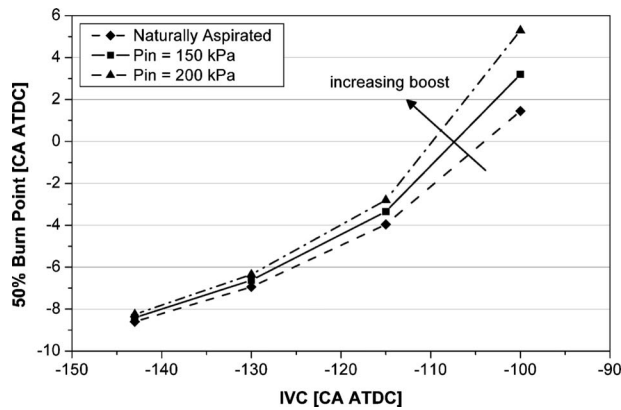
Fig. 5 Effect of late IVC timing on 50% AHR points at varying boost pressures (821 rpm, $m_{fuel}=31.2$ mg, and $T_{in}=298$ K)

combustion duration at this condition becomes rapid (less than 1 CAD) and will result in a severe pressure rise that may not be physically realizable in an actual engine. However, these simulated results occur under a strict set of idealized operating conditions and operation in a real engine is likely to include thermal gradients and air-fuel stratification, which are not included in these simulations. Indeed, thermal and air-fuel stratification has been demonstrated to occur naturally in HCCI operated engines and further offers control of pressure rise rates for high load HCCI operation [20,21]. With the inclusion of a pressure rise control strategy, the potential for optimal phasing of high load HCCI with LIVC is clearly illustrated.

Effect of Increasing Boost. In addition to evaluating the effectiveness of LIVC times at various load ranges, the effect of adding boost on LIVC air-fuel mixture histories was also evaluated. For this portion of the study, the injected fuel quantity was held to the base line value of 31.2 mg and boost was added in two increments (150 kPa and 200 kPa). The IVC times were varied for each boost level and the resulting 50% AHR points are shown in Fig. 5.

Figure 5 shows that increasing boost from the base line naturally aspirated level of 102.5–200 kPa has a little effect on the phasing of the 50% AHR point. An IVC time around −110 CA ATDC would produce a 50% AHR point near the TDC (0 CA ATDC) for all three boost conditions simulated here. However, there is a noticeable spreading of the 50% AHR curves as the IVC is delayed from the base line timing of −143 CA ATDC to −100 CA ATDC. To understand both the lack of significant impact on the combustion phasing and the spreading of the 50% AHR curves

at LIVC times under boosted conditions, it is helpful to examine the combustion phasing details of these results, as outlined in Table 3.

For the set of data presented in Table 3, it should again be noticed that equivalence ratio increases as the IVC time is retarded in each boost case. As boost is increased, however, the global equivalence ratios decrease since the fuel injection quantity is kept constant. It has already been established by the previous set of results that the specific heat capacity of the mixtures plays a large role in altering the thermal history and ignition timing while global equivalence ratios have a large effect on combustion duration, and it is important to keep these effects in mind as this set of data is analyzed below.

Examining the 10% AHR points at each boost level, it can be seen that the used of delayed IVC times causes a retarded 10% AHR point, consistent with previous results. However, as the boost level is increased for a fixed IVC time, the 10% heat release point becomes slightly advanced. This advanced ignition could be due to two factors. As discussed earlier, higher equivalence ratio mixtures with a reduced specific heat ratio were shown to retard ignition. Since the global equivalence ratio decreases with added boost in these simulations, and the resulting specific heat ratio of the mixture increases, it follows from the previous results that lowering the equivalence ratio could result in advanced ignition. Also, since HCCI combustion is known to be kinetically controlled and the global reaction rate is directly proportional to pressure, the higher boost pressures could be contributing to faster ignition reactions, and consequently producing advanced ignition times.

Looking at the 10–90% AHR duration for a given IVC time, it is clear that the combustion duration is increased dramatically as boost is increased. This results from a decrease in global equivalence ratios, which as discussed previously, causes reduced combustion temperatures and slower reaction rates. However, note that the duration between the 10% AHR point and the 50% AHR point is not as significantly impacted as boost levels are increased. This duration is only increased by about 1 CAD with an increase in boost pressure from 102.5 kPa to 150 kPa, while the 10–90% AHR duration increases by about 9 CAD. Prior to the 50% AHR point, rising compression stroke temperatures help us maintain heat release reactions under these low equivalence ratio conditions. After the TDC, piston expansion results in falling temperatures and significantly increased combustion completion times. Indeed, for the 200 kPa case, where the equivalence ratios approach 0.10, the reaction rates become so slow after the TDC that the fuel oxidation process is incomplete in the time available for piston expansion.

Accordingly, the almost negligible shift in 50% AHR points

Table 3 Combustion phasing details: Effect of late IVC timing at different boost levels

Intake pressure	IVC (CA ATDC)	m_{fuel} (mg)	Global equivalence ratio	10% AHR (CA ATDC)	50% AHR (CA ATDC)	10–90% AHR (CAD)	IMEP (bar)
$P_{in}=$ 102.5 kPa	−143	31.2	0.20	−24.2	−8.6	16.9	2.57
	−130		0.21	−22.4	−6.9	16.5	2.64
	−115		0.24	−19.3	−4.0	16.3	2.73
	−100		0.27	−15.1	1.5	17.5	2.82
$P_{in}=$ 150 kPa	−143	31.2	0.14	−25.3	−8.4	26.1	2.34
	−130		0.15	−23.5	−6.6	25.1	2.43
	−115		0.16	−20.5	−3.4	23.9	2.55
	−100		0.19	−16.4	3.2	26.3	2.63
$P_{in}=$ 200 kPa	−143	31.2	0.10	−25.9	−8.3	Incomplete	1.94
	−130		0.11	−24.1	−6.4	Incomplete	2.03
	−115		0.12	−21.2	−2.8	Incomplete	2.15
	−100		0.14	−17.2	5.3	Incomplete	2.13

Journal of Engineering for Gas Turbines and Power
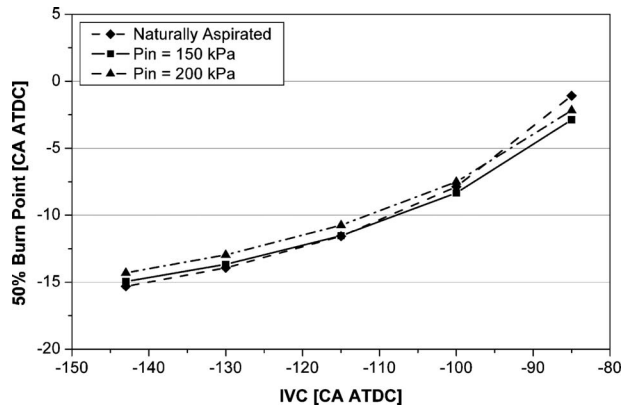
SEPTEMBER 2008, Vol. 130 / **052806-5**

Fig. 6 Effect of late IVC timing on 50% AHR points at higher load with varying boost pressures (821 rpm, $m_{fuel}=62.4$ mg, and $T_{in}=298$ K)

fuel injected quantity of 62.4 mg. Again, the IVC times were varied for each boost level and the resulting 50% AHR points are shown in Fig. 6.

The set of curves shown in Fig. 6 are largely similar to those obtained previously at the lower fueling rate (Fig. 5). Figure 6 shows that increasing boost from the base line level of 102.5 kPa (naturally aspirated) to a level of 200 kPa again shows a little effect on the phasing of the 50% AHR point. With this larger fuel injection quantity, the simulations indicate that a LIVC time of approximately −85 CA ATDC would be necessary to produce a 50% AHR point near the TDC, compared to −100 CA ATDC for the previously discussed lower fueling rate cases. Also, note that the 50% AHR curves are advanced in comparison to those of the lower fueling rate in Fig. 5, consistent with previous observations on the effect of increasing global equivalence ratios. Finally, the naturally aspirated 50% AHR curve shows an increased sensitivity to IVC timing, similar to the trend observed in the high fueling case (93.6 mg) of Fig. 4. Again, to better understand these trends, it is helpful to examine the combustion phasing details, as presented in Table 4.

The trends in the heat release points show many similarities to the 31.2 mg fueling cases previously presented. Similar to the previous results, as boost level is increased for a given IVC time, the 10% AHR point becomes slightly advanced. Also, the 10–90% AHR duration for a given IVC time is increased as boost is increased. As observed previously, the competing effects of advanced ignition and increased combustion duration balance, resulting in a nearly negligible shift in 50% burn points for a given IVC time with increasing boost.

While Fig. 6 indicates that the combustion phasing is not largely affected by boost at this higher fuel rate, the mixtures, which result from this fueling rate, have a significant impact on the parameters, which dominate the combustion process. Examining the 10–90% heat release durations in Tables 3 and 4, the most striking difference between these cases is that the combustion durations are over twice as long in the 31.2 mg fueling cases than for the 62.4 mg fueling cases. Since global equivalence ratios are higher with the 62.4 mg injected quantity, reaction rates are faster and the combustion durations are significantly shorter. At the lower fueling rate, increased boost pressure caused decreased global equivalence ratios and the resulting slow combustion rates were observed to dominate the timing of the 50% AHR point as the phasing neared the TDC. By contrast, at this higher fueling

with increasing boost, as shown in Fig. 5, can be understood from the ignition timing and combustion duration details just discussed. The slightly advanced ignition, caused by the increasing boost level, is balanced by the slight increase in combustion duration prior to the 50% AHR point, produced by decreased global equivalence ratios. The more pronounced spread of the 50% AHR curves at LIVC times in Fig. 5 is likely an effect of the phasing of the 50% AHR point. As the 50% AHR point approaches the TDC, there is less of a compression effect to assist heat release rates and the slow combustion, which results from low global equivalence ratios, begins to dominate. This effect becomes especially prominent for the cases with IVC timings of −100 CA ATDC, where the 50% AHR points occurs after the TDC. Indeed, Fig. 5 shows that these cases resulted in the highest variance of 50% AHR; illustrating a more significant delay in 50% AHR phasing as boost is increased and global equivalence ratios decrease.

Effect of Boost at Higher Loads. The previous discussion of results revealed that combustion phasing is largely insensitive to boost levels. Therefore, it follows that boost might be used at higher loads with a similar range of IVC times in order to improve IMEP and further expand the HCCI load range. To evaluate this possibility, the previous set of boost levels was applied to a higher

Table 4 Combustion phasing details: Effect of late IVC timing at higher load with different boost levels

| Pressure at IVC	IVC (CA ATDC)	m_{fuel} (mg)	Global equivalence ratio	10% AHR (CA ATDC)	50% AHR (CA ATDC)	10–90% AHR (CAD)	IMEP (bar)
$P_{ivc}=$ 102.5 kPa	−143	62.4	0.40	−23.0	−15.3	7.8	3.91
	−130		0.43	−21.0	−13.9	7.2	3.94
	−115		0.47	−17.8	−11.6	6.3	4.07
	−100		0.55	−13.0	−7.9	5.2	4.22
	−85		0.67	−5.2	−1.1	4.2	4.35
$P_{ivc}=$ 150 kPa	−143	62.4	0.27	−24.7	−15.0	10.2	4.72
	−130		0.29	−22.8	−13.7	9.5	4.74
	−115		0.32	−19.8	−11.5	8.5	4.65
	−100		0.37	−15.4	−8.3	7.3	4.55
	−85		0.45	−8.8	−2.9	6.2	4.59
$P_{ivc}=$ 200 kPa	−143	62.4	0.20	−25.7	−14.3	12.9	4.81
	−130		0.22	−23.8	−13.0	12.1	4.94
	−115		0.24	−20.8	−10.8	10.9	5.09
	−100		0.28	−16.7	−7.5	9.7	5.29
	−85		0.34	−10.5	−2.2	8.7	5.13
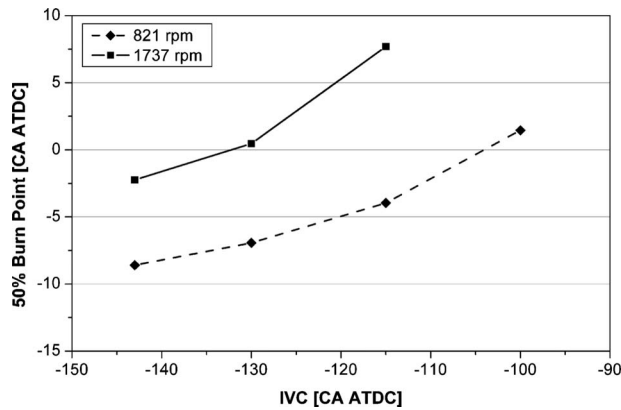
Fig. 7 Effect of late IVC timing on 50% AHR points at high and low engine speeds (m_{fuel}=31.2 mg, P_{in}=102.5 kPa, and T_{in}=298 K)

rate, combustion reaction rates do not appear to have a significant impact on the resulting 50% AHR phasing since combustion durations are relatively short. The increased specific heat ratio of these mixtures are also observed to play a more dominant role in the phasing, particularly in the naturally aspirated case (P_{in}=102.5 kPa). Specifically, the delay that occurs in the 10% AHR point, as the IVC time is changed from −143 CA ATDC to −85 CA ATDC, is the largest of the three boost cases in Table 4. Since the initial temperatures are held constant between these cases and the compression histories are matched for matched IVC timings, the greater sensitivity of ignition timing to IVC timing must result from an altered thermal history of the mixture via the specific heat ratio. Finally, since ignition timing is the controlling parameter in the combustion phasing at this higher fueling level, the greater ignition delay in the naturally aspirated case with a −85 CA ATDC IVC timing results in a greater delay of the 50% AHR point. This phenomenon leads to the observed bend in the naturally aspirated 50% AHR curve of Fig. 6.

Another important observation of the data in Table 4 is that the IMEP can be further increased by the addition of boost at this higher fueling level. For optimal combustion phasing near the TDC, with an IVC timing of −85 CA ATDC, the addition of boost pressure to 200 kPa results in an increase in IMEP from 4.35 bars (naturally aspirated) to 5.13 bars. These simulation results suggest that through the use of LIVC, the combustion phasing can be properly controlled under both higher fueling rates and boost, producing approximately twice the IMEP predicted by the base line case.

Effect of Speed. Increased engine speeds at high loads also affect the ability to control combustion phasing and extend diesel HCCI operating ranges. The last section of this investigation explores the interaction of engine speed and LIVC times on diesel HCCI combustion phasing. For this portion of the study, naturally aspirated intake conditions and a fuel injected quantity of 31.2 mg were applied to high and low engine speeds. The IVC times were varied for each engine speed and the resulting 50% AHR points are shown in Fig. 7.

Figure 7 shows that for a fixed fueling level, the 50% AHR points are retarded (in CA space) at a higher engine speed. This shift in the 50% AHR curve might be expected since the simulations are based on a homogenous fuel-air mixture, which causes the combustion process to be primarily kinetically controlled. However, the highly premixed nature of HCCI combustion is also expected to be largely kinetically controlled and should display a similar response to increased engine speeds. This indicates, for the case illustrated here, that optimal combustion phasing will require less IVC delay at higher engine speeds. This result is especially useful for operation under high fueling rates, where later IVC

times (from −100 ATDC to −85 ATDC) were required to obtain a 50% AHR point near the TDC. The tendency of the higher fueling rate cases to have overly advanced phasing can be offset by the delay of the 50% AHR point with higher engine speed. Furthermore, the reduced requirement for LIVC times would allow longer mixing times of the fuel-air charge for injections occurring after IVC. This is especially important to maximize homogeneity of fuel-air mixtures so that successful HCCI combustion can be realized. Thus, increased engine speed can assist in delaying combustion phasing, reducing LIVC delay times and making it easier to obtain diesel HCCI combustion under high load operation.

Summary and Conclusions

This work investigated the potential use of variable intake valve timing for the control of diesel HCCI combustion. An idealized model was constructed in order to understand the fundamental elements affecting the combustion phasing. The results indicate the following.

1. The use of LIVC times was found to be effective for retarding the combustion event and preventing premature combustion. Also, a higher IMEP can be obtained due to the ability to properly phase the combustion.
2. The use of LIVC times enabled the 50% burn point to be centered at the TDC for a wide range of loads, boost pressures, and engine speeds.
3. Combustion phasing was largely insensitive to boost pressures. As a result, boost could be added at higher fueling rate operating conditions to further increase IMEP, without requiring changes in the IVC times.
4. Changes in equivalence ratio and the resulting changes in mixture specific heat capacity can significantly contribute to combustion event timing:

   - Low equivalence ratio mixtures caused reduced combustion temperatures, slower combustion rates, and increased combustion durations. As combustion durations lengthen, this effect begins to dominate phasing of the 50% AHR point near the TDC.
   - High equivalence ratio mixtures caused rapid combustion. Due to this rapid combustion duration, ignition timing became the primary controller of combustion phasing at high fueling rates.
   - For a fixed IVC pressure, temperature, and compression history (constant IVC time), higher equivalence ratio mixtures caused an increase in the specific heat ratio and lead to a retarded ignition timing.

References

[1] United States Environmental Protection Agency, www.epa.gov.
[2] Kelly-Zion, P., and Dec, J., 2000, "A Computational Study of the Effect of Fuel-Type on Ignition Time in HCCI Engines," Proceedings of the 28th International Symposium on Combustion, Part 1, pp. 1187–1194.
[3] Akagawa, H., Miyamoto, T., Harada, A., Sasaki, S., Shimazaki, N., Hashizume, T., and Tsujimura, K., 1999, "Approaches to Solve Problems of the Premixed Lean Diesel Combustion," SAE Paper No. 1999-01-0183.
[4] Haraldsson, G., Tunestal, P., Johannson, B., and Hyvonen, J., 2002, "HCCI Combustion Phasing in a Multi Cylinder Engine Using Variable Compression Ratio," SAE Paper No. 2002-01-2858.
[5] Kaneko, N., Ando, H., Ogawa, H., and Miyamoto, N., 2002, "Expansion of the Operating Range With In-Cylinder Water Injection in a Premixed Charge Compression Ignition Engine," SAE Paper No. 2002-01-1743.
[6] Law, D., Kemp, D., Allen, J., Kirkpatrick, G., and Copland, T., 2000, "Controlled Combustion in an IC-Engine With a Fully Variable Valve Train," SAE Paper No. 2000-01-0251.
[7] Angstrom, H.-E., Eriksson, B., and Wikander, J., 2003, "Integrated Simulation and Engine Test of Closed Loop HCCI Control by Aid of Variable Valve Timings," SAE Paper No. 2003-01-0748.

[8] Milovanovic, N., Chen, R., and Turner, J., 2004, "Influence of the Variable Valve Timing Strategy on the Control of a Homogeneous Charge Compression (HCCI) Engine," SAE Paper No. 2004-01-1899.

[9] Hruby, E. J., 2003, "An Experimental Investigation of a Homogeneous Charge Compression Ignition Engine Using Low Pressure Injection and Diesel Fuel," MS thesis, University of Wisconsin—Madison, Madison, WI.

[10] Takeda, Y., Keiichi, N., and Keiichi, N., 1996, "Emission Characteristics of Premixed Lean Diesel Combustion With Extremely Early Staged Fuel Injection," SAE Paper No. 961163.

[11] Walter, B., and Gatellier, B., 2002, "Development of the High Power NADI Concept Using Dual Mode Diesel Combustion to Achieve Zero NOx and Particulate Emissions," SAE Paper No. 2002-01-1744.

[12] Amsden, A. A., 1997, "KIVA-3V: A Block-Structured KIVA Program for Engines With Vertical or Canted Valves," Los Alamos National Laboratory Report No. LA-13313-MS.

[13] Han, Z., Uludogan, A., Hampson, G. J., and Reitz, R. D., 1996, "Mechanism of Soot and NOx Emission Reduction Using Multiple-Injection in a Diesel Engine," SAE Paper No. 960633.

[14] Patterson, M. A., and Reitz, R. D., 1998, "Modeling the Effects of Fuel Spray Characteristics on Diesel Engine Combustion and Emissions," SAE Paper No. 980131.

[15] Kong, S. C., Rutland, C. J., and Reitz, R. D., 2002, "Development of an Integrated Spray and Combustion Model for Diesel Simulations," *Thermo- and Fluid-Dynamic Processes in Diesel Engines*, J. H. Whitelaw, F. Payri, and J. M. Desantes, eds., Springer, New York, Chap. 6, pp. 319–334.

[16] Patel, A., Kong, S.-C., and Reitz, R., 2004, "Development and Validation of a Reduced Reaction Mechanism for HCCI Engine Simulations," SAE Paper No. 2004-01-0558.

[17] Kee, R. J., Rupley, F. M., and Miller, J. A., 1989, "CHEMKIN-II: A FORTRAN Chemical Kinetics Package for the Analyses of Gas Phase Chemical Kinetics," Sandia National Laboratories Report No. SAND 89-8009.

[18] Aceves, S. M., Flowers, D. L., Martinez-Frias, J., Espinosa-Loza, F., Christensen, M., Johansson, B., and Hessel, R., 2005, "Analysis of the Effect of Geometry Generated Turbulence on HCCI Combustion by Multi-Zone Modeling," SAE Paper No. 2005-01-2134.

[19] Kelly-Zion, P. L., and Dec, J. E., 2000, "A Computational Study of the Effect of Fuel Type on Ignition Time in Homogeneous Charge Compression Ignition Engines," Proc. Combust. Inst., **28**, pp. 1187–1194.

[20] Dec, J. E., Hwang, W., and Sjoberg, M., 2006, "An Investigation of Thermal Stratification in HCCI Engines Using Chemiluminescence Imaging," SAE Paper No. 2006-01-1518.

[21] Sjoberg, M., and Dec, J. E., 2006, "Smoothing HCCI Heat-Release Rates Using Partial Fuel Stratification With Two-Stage Ignition Fuels," SAE Paper No. 2006-01-0629.

Characterization of Particulate Matter Emissions From a Four-Stroke, Lean-Burn, Natural Gas Engine

Kris Quillen

Maren Bennett

Engines and Energy Conversion Laboratory,
Colorado State University,
430 North College Avenue,
Fort Collins, CO 80524

John Volckens
Environmental and Radiological Health Sciences,
Colorado State University,
1681 Campus Delivery,
Fort Collins, CO 80523

Rudolf H. Stanglmaier
Entwicklung,
Märkishes Werk GmbH,
Haus Heide 21,
58553 Halver, Deutschland

Regulatory agencies are becoming increasingly concerned with particulate emissions as the health and environmental effects are becoming better understood. While much research has been performed on diesel engines, little is known about particulate matter (PM) emissions from natural gas internal combustion engines. In this project, tests were conducted on a Waukesha VGF F18 natural gas engine running at full load. PM_{10} combustion emissions were collected on teflon and quartz filters and a scanning mobility particle sizer was used to determine the particle size distribution. Tests were performed at 4–7% exhaust oxygen (O_2) levels. Overall, it was found that a large number of small particles were emitted from this engine. The total mass based PM emissions were found to be 0.0148 gm/bkW h, which is slightly greater than the Tier-4 nonroad particulate emission standard. Particle distributions revealed that the geometric mean diameter of the natural gas particles was approximately 30 nm and did not change with air to fuel ratio. Particulate concentrations were found to decrease at leaner engine operating conditions. Results showed a strong correlation between the NO_x and particle concentrations, while an inverse correlation between CO and particle concentrations was revealed. [DOI: 10.1115/1.2906218]

Introduction

The health and environmental impacts of particulate matter (PM) emissions are influenced by both the particle size and particle concentration. Hence, characterizing the PM emissions from all sources is necessary to help our understanding of the effects of PM on global warming and respiratory disease. Detailed information on PM emissions from engines also helps direct research to reduce the emissions of harmful constituents and decrease particle number and mass emissions.

Some types of PM are believed to have the ability to scatter incoming radiation either directly or through cloud formation, modifying our natural radiation balance. While buildup of carbon dioxide (CO_2) in the stratosphere can increase the overall temperature, this scattering effect from PM may actually cool the earth. This cooling process is referred to as the "whitehouse" effect and is estimated to offset 20–100% of the heating due to the greenhouse effect [1]. On the other hand, black carbon, or elemental carbon (EC), is thought to increase warming trends due to their tendency to absorb solar radiation. A large uncertainty is present for both effects, increasing the need for more precise size distributions and speciation profiles from all sources to aid in more accurate models. Climate forcing by anthropogenic aerosols is believed to be the largest source of uncertainty in future climate change models [2]. As researchers develop more complex air quality models, specific data on the size distribution of common sources, such as natural gas engines, are needed.

The effects of inhaled particles on human health are largely dependent on particle size. The human respiratory system can be divided into three main sections: the head and nose airways, the tracheobronchial region, and the alveolar region. Particle deposition, mainly occurring through impaction, settling, and diffusion, is strongly dependent on particle size. A substantial drop in deposition around 100–1000 nm can be seen due to lack of an efficient mechanism for collecting particles of this size. Although the mass median diameter for combustion aerosols falls within this range, combustion aerosols still present a major inhalation health hazard.

While total deposition in the 100–1000 nm size range is low, most of these particles deposit in the alveolar or deep lung region. Due to gas exchange of oxygen and CO_2 that occurs in this region, there is no protective mucus layer to trap and remove particles. Once entrained in the alveolar region, insoluble particles may remain in the lungs for months or years. Soluble particles can dissolve into lung tissue or move into the bloodstream.

PM emissions are currently regulated for diesel engines and many other sources, but PM emissions from natural gas engines have not been discussed much. However, this could change as diesel PM levels drop and natural gas PM emissions become comparable to Tier-4 and -5 diesel emission levels.

Some fundamental research has already been done to characterize particulate emissions from natural gas combustion sources.

Hildemann et al. found that natural gas home appliances produced extremely low PM emissions, ranging from 23 ng/kJ to 72 ng/kJ of burned fuel [3].

Schauer et al. estimated that natural gas combustion is the 15th leading cause of fine aerosol organic carbon in Los Angeles, CA. Meat cooking ranked first and diesel vehicles ranked fifth directly behind noncatalyst gasoline vehicles [4].

Ristovski et al. found that measures adopted to reduce gaseous emissions in natural gas engines have resulted in the mass reduction of particulate emissions but have increased the particle count, especially below 100 nm. The typical range of the count median diameter (CMD) measured was between 20 m and 60 nm (nucleation mode) with a maximum of around 140 nm (accumulation mode). The particle concentrations were between 2×10^4 cm^{-3} and 1×10^7 cm^{-3}, the upper end of which is on the same order as a PM from diesel engines [5].

Table 1 Basic engine parameters

Parameter	Value	Unit
Engine type	Natural gas, SI	—
Bore × stroke	0.152 × 0.165	m^2
Number of cylinders	6	—
Displacement	18	l
Engine load	298	kW
Engine BMEP	1108	kPa
Engine speed	1800	rpm

Particulate Measurements

PM emissions were measured on a Waukesha VGF F18 in-line six cylinder natural gas engine used for stationary power generation. This engine is rated at 298 kW at 1800 rpm and was equipped with extensive instrumentation. Table 1 shows the main engine parameters.

PM Measurement Equipment. Flow in the sample probe should be isokinetic to obtain a representative particle sample from the exhaust. Isokinetic flow is present when the velocity of gas entering the probe is equal to the velocity of gas in the bulk stream and the probe is aligned with the flow. Therefore, a circular duct of size D_0 with a flow rate of Q_0 along with a sample probe of diameter D_s and a flow rate of Q_s will ensure that measurement velocity is isokinetic (Eq. (1)) [1].

$$\frac{Q_s}{Q_0} = \left(\frac{D_s}{D_0}\right)^2 \tag{1}$$

After determining an acceptable range of sample probe diameters, stainless steel tubing with an inner diameter of 3.86 mm was selected for construction of the sample probe. The tip of the probe was placed in the exhaust pipe approximately 75 cm above the turbo and centered in the pipe, as shown in Fig. 1.

Other factors that could affect sample probe efficiency are the probe placement and angle. The sample probe location was a concern due to possible variations in particle concentration across the diameter of the exhaust pipe. However, the turbine should serve to mix the exhaust gas and disrupt any variations in PM concentration across the diameter of the exhaust pipe. The angle of the sample probe may also introduce error. However, the error associated with a 15 deg misalignment is, at most, 3.4% for large particles and zero for small particles [1]. Therefore, the probe alignment was maintained within this angle.

Internal combustion processes are never ideal. When carbonaceous fuel is burned in an engine, some unburned or partially burned carbon is released at high temperature. This material cools first in the exhaust system and then by atmospheric mixing, resulting in the formation of PM, which is accompanied by volatile
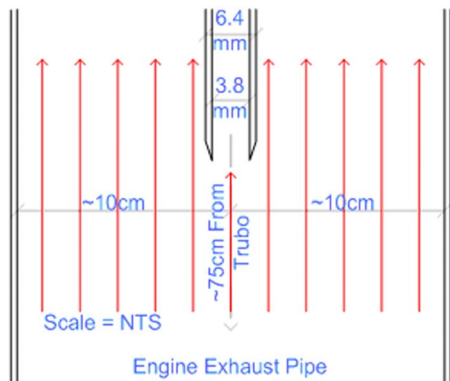
Fig. 1 Particulate sample probe placement
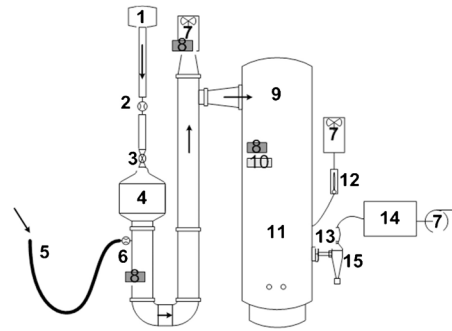
Fig. 2 Dilution tunnel. 1: HEPA filter; 2: turbine flow meter; 3: ball valve; 4: activated charcoal filter; 5: exhaust sample line (heated, flexible); 6: venturi flow meter; 7: pump; 8: thermocouple; 9: residence chamber; 10: humidity sensor; 11: SMPS and cascade impactor sampling ports; 12: rotometer; 13: filter pack; 14: mass flow controller; and 15: PM$_{10}$ cyclone.

and semivolatile gas-phase compounds. PM formation is complicated and depends on several factors, including time, temperature, and concentration of precursor molecules. Direct sampling from the tailpipe at elevated exhaust temperatures will underestimate true particle concentrations since many organics precursors that are destined to enter the particle phase remain as gases upon sampling. Therefore, to simulate real-world conditions, a dilution tunnel allows the exhaust time to cool, mix with ambient air, and reach equilibrium before sampling takes place. A modified version of the Hildemann dilution tunnel [6], shown in Fig. 2, was used in the study described here. This design provides a dilution ratio of approximately 100:1 (air:exhaust) and a sample residence time of roughly 75 s.

A scanning mobility particle sizer (SMPS) was used to measure particle concentrations as a function of size based on electrical mobility. The SMPS system used in this research includes a differential mobility analyzer (DMA) and a condensation particle counter (CPC) developed by Grimm Technologies (Grimm Inc., Douglasville, GA).

Data can be extracted from the SMPS in a variety of formats. Most useful for this study are the raw particle counts, which can be exported into an EXCEL file. Each bin, corresponding to a mobility diameter size range, contains the number of particles counted by the CPC. Data are then normalized to the width of the measurement bin for balanced comparison.

The SMPS system has several limitations owing to the Boltzmann charge distribution rendered on sampled particles. Because the DMA separates particles by electrical mobility rather than directly by diameter, some particles may be misclassified. As an example, a 400 nm particle with a +2 charge has the same electrical mobility as a 200 nm particle with a +1 charge. Prediction of the charge density on a particle becomes difficult as particle size and width of the Boltzmann charge distribution increase [1]. The DMA uses a complicated algorithm referred to as the transfer function to account for the possibility of multiple charges on particles. The transfer function works well for particles below 200 nm but is unable to accurately differentiate between particles larger than 1000 nm.

PM Measurement Procedure. The test engine is a stock production engine, except that it has been equipped with a "low friction" ring pack as described elsewhere [7]. The oil consumption of this engine, however, was unchanged from the stock ring pack. A commercial SAE 40W lubricating oil, as recommended by the manufacturer, was used. The engine, which can operate between ~4% and 7.25% exhaust O_2, was tested at four exhaust oxygen concentration levels selected in random order: 5%, 7%, 6%, and 4%.

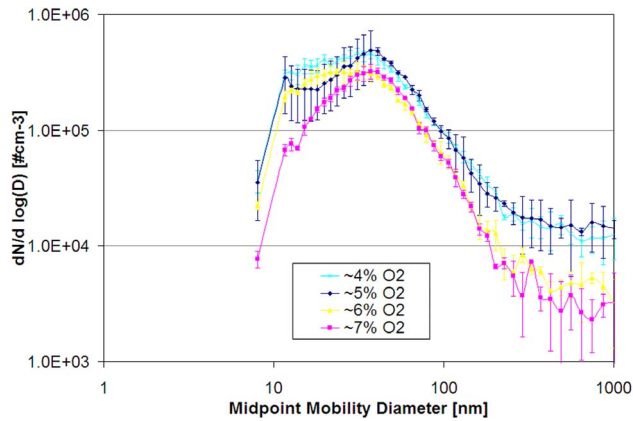Once the engine operating conditions were achieved and al-

Fig. 3 Particle size distribution

Fig. 4 Total PM count versus exhaust O$_2$

lowed to stabilize for some time, two PM$_{10}$ cyclones and two filter packs were connected to the residence chamber (Fig. 2). These filters collected PM$_{10}$ throughout the entire testing period for all O$_2$ exhaust percentages. A teflon filter was used to estimate PM$_{10}$ mass concentration. Two quartz filters were used to collect PM for future analysis of organic carbon/elemental carbon (OC/EC). The quartz filters were not used in the current analysis, but will provide a base line for future testing regarding the effects of oil burning in the cylinder. Pump power was incrementally increased to pull at a constant 28.3 ALPM, measured by a calibrated mass flow meter. The dilution ration was adjusted to roughly a 100:1 ratio through manual control of dilution air flow. An excess air pump was then used to hold the residence time near 75 s.

The SMPS was set to take three 5 minute scans at each engine operating condition. The standard set of engine parameters was recorded (gaseous emissions, temperatures, general engine pressures, and in-cylinder pressures). The dilution tunnel parameters (dilution flow, exhaust flow, temperatures, pressures, and residence time) were also recorded.

Results and Discussion

At the conclusion of the test program, the teflon filter was weighed and found to have collected approximately 0.066 ± 0.018 mg of PM for the entire duration of the tests, corresponding to approximately 0.0148 ± 0.0031 g/bkW h. For comparison, the Tier-4 diesel nonroad emission standards were set at 0.013 g/bkW h [8]. Only a single "overall test PM mass" measurement was performed because a long test time is required to accumulate sufficient PM mass on the teflon filter. Nonetheless, this provides a reference PM mass emission value for this engine.

Particle distribution averages and standard deviations for each test condition were calculated and these results are shown in Fig. 3.

The results of the size distribution clearly show a reduction in the total number concentration as the exhaust O$_2$ increases from 4 to 7%. The decrease in the particulate concentration may be due to the increased availability of oxygen, allowing the particles to oxidize more completely. The distribution modes occur at approximately the same location, ~35 nm, for all exhaust oxygen levels.

Large particle counts above ~300 nm are thought to be primarily a result of oil combustion. The larger particles are of interest due to their ability to increase the total PM mass with only a slight increase in particle count. The total number concentrations and the concentrations above 300 nm were calculated for all of the different test conditions. The total concentration and the concentration above 300 nm were found to decrease as exhaust O$_2$ increased, as shown in Fig. 4.

The effects shown above do not take into consideration the total number of particles exiting the engine but rather the concentration
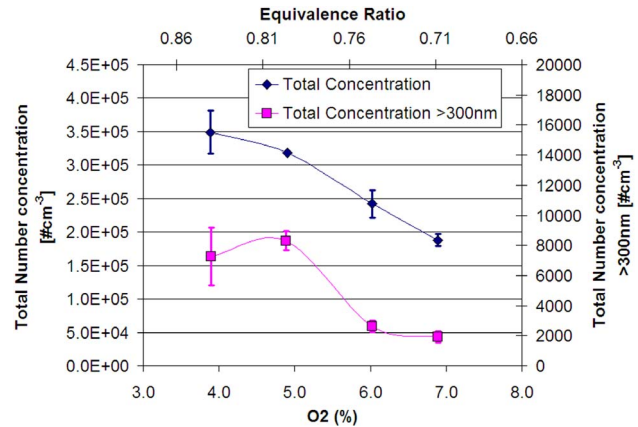
of the particles in the dilution exhaust gas. The exhaust gas contained a larger percentage of oxygen in the leaner tests due to an increased air flow into the engine. Therefore, the total concentrations should be lower for the same particulate output. However, the engine air flow varied by ~16% and the concentrations varied by ~57%. The brake specific total particulate emissions were calculated in order to verify that the effects of the increased air flow through the engine were not obscuring the trends. The brake specific total particulate count is plotted in Fig. 5.

The geometric mean diameter (GMD) was calculated from the particle measurements and found to be approximately 35 nm for all of the test cases. However, the geometric standard deviations (GSDs) were shown to decrease with increasing exhaust O$_2$ (Fig. 6). A decrease in the GSD indicates a narrowing of the particle size distribution with increasing O$_2$, whereas the GMD remained relatively constant. Once again, the reduced particle concentrations at leaner conditions may be a result of the increased oxygen available to oxidize the particles.

Finally, a comparison of the regulated gaseous emissions to the particulate concentrations was made. The NO$_x$ and CO were plotted versus the total particulate concentrations. The NO$_x$ and the CO emissions were found to have reasonably linear correlations to the particle count as the exhaust O$_2$ varied. Brake specific NO$_x$ and PM count were found to decrease as the exhaust O$_2$ levels increased (leaner operating). Conversely, CO increased with decreasing exhaust O$_2$ levels. These results are shown in Fig. 7.

This result is somewhat surprising from the perspective of diesel engine emission management. In diesel engines, almost anything that reduces NO$_x$ emissions will cause PM levels to increase, forming the so-called "NO$_x$-PM trade-off" curve.
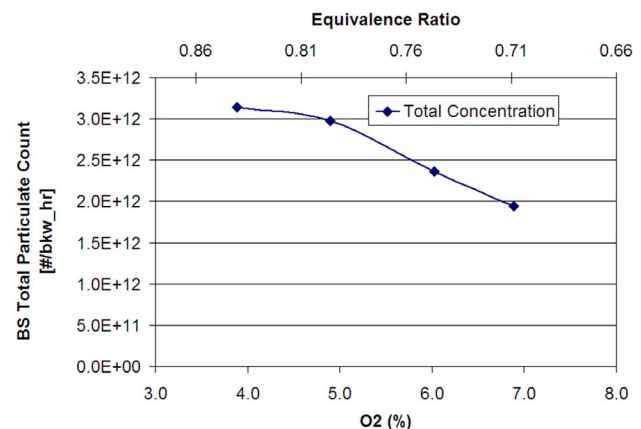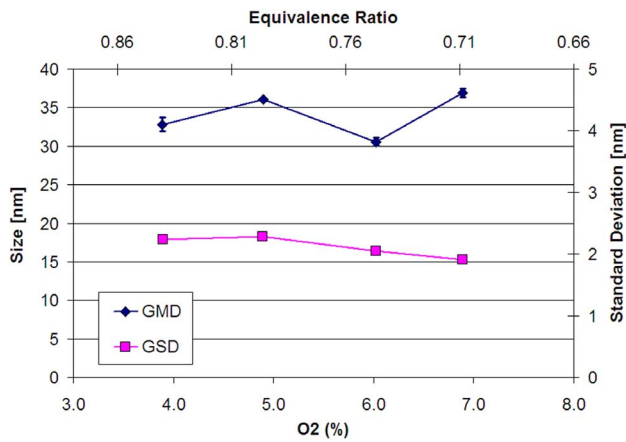

Fig. 5 Brake specific total particulate count

Fig. 6   GMD and GSD versus exhaust O₂

However, these results suggest that the current trend of operating natural gas engines at higher exhaust O_2 levels (leaner) will be beneficial for NO_x and PM emissions.

The combustion stability of this engine was examined by plotting the COV of indicated mean effective pressure (IMEP) as a function of exhaust O_2 concentration, as shown in Fig. 8. This plot reveals that the combustion stability starts to degrade at about 7% exhaust O_2, particularly for Cylinder No. 6. However, this deterioration in the combustion stability did not adversely affect the NO_x and PM emissions, as discussed above.
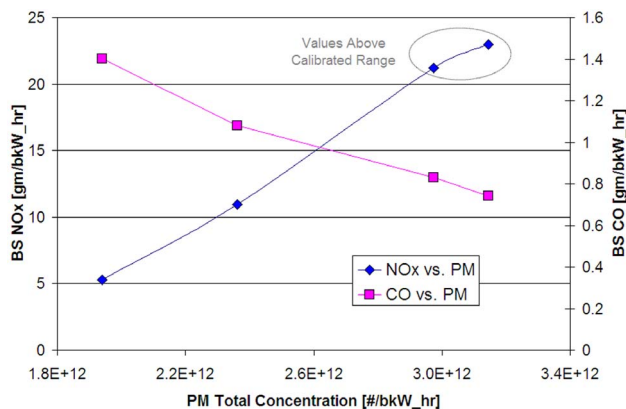
Fig. 7   PM-NOₓ and PM-CO trade-off
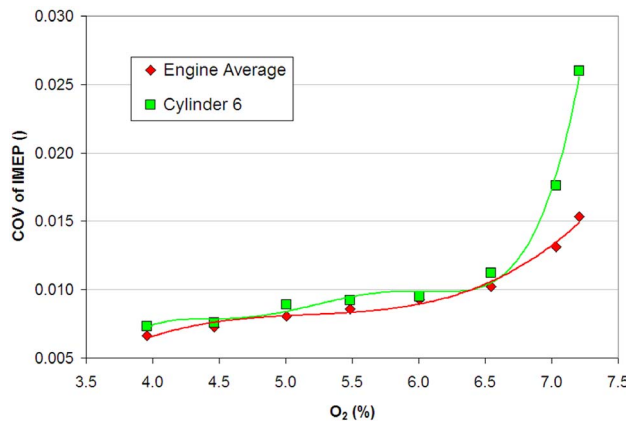
Fig. 8   COV of IMEP of Cylinder 6 and the average for all cylinders

Summary and Conclusions

PM emission size and concentration were measured on a natural gas engine. The total concentrations experimentally found were within the ranges found in published literature [3,9]. The size and distributions found within the range of measured values were expected.

The average PM mass emission rate was 0.0148 gm/bkW h, which is slightly greater than the Tier-4 nonroad diesel particulate emission standard.

The particle size distribution measurements revealed that the GMD of the natural gas particles was approximately 30 nm. Roughly 40% of these particles, once inhaled, will deposit in the alveolar region of the lungs where the health effects are expected to be the greatest [1]. In comparison, typical diesel engines produce particles with a CMD of approximately 100 nm [10] and are only approximately 15% likely to deposit in the alveolar of the lungs [1]. Although the particles created by natural gas engine are fewer in number and smaller, they have a greater chance of depositing deeper in the lungs and are a potential health problem.

The particulate concentrations were found to decrease at leaner engine operating conditions, but the particle size distribution was relatively constant.

A strong correlation between the NO_x and particle concentrations was found. That is, engine operating conditions that produced less NO_x also produced less PM. This is highly advantageous because low particulate emissions and low NO_x emissions are desired and leaner engine operation appears to be a promising strategy for reducing both.

Nomenclature

ALPM = actual liters per minute
bkW = brake kilowatt
CO = carbon monoxide
COV = coefficient of variance (standard deviation /average)
CSU = Colorado State University
D = diameter
kJ = kilojoule
kPa = kilopascal
kW = kilowatt
m = meter
nm = nanometer
ng = nanogram
NO_x = nitric oxide and nitrogen dioxide
O_2 = oxygen
Q = flow rate
rpm = rotations per minute
SI = spark ignition

References

[1] Hinds, W. C., 1999, *Aerosol Technology: Properties, Behavior, and Measurements of Airborne Particles*, 2nd ed., John Wiley & Sons, Inc., New York.
[2] Hansen, J., Sato, M., Ruedy, R., Lacis, A., and Oinas, V., 2000, "Global Warming in the Twenty-First Century: An Alternative Scenario," Proc. Natl. Acad. Sci. U.S.A., **97**, pp. 9875–9880.
[3] Hildemann, L. M., Cass, G. R., and Markowski, G. R., 1991, "Chemical Composition of Emissions From Urban Sources of Fine Organic Aerosol," Environ. Sci. Technol., **25**(4), pp. 744–759.
[4] Schauer, J. J., Rogger, W. F., Hildemann, L. M., Mazurek, M. A., Cass, G. R., and Simoneit, B. R. T., 1996, "Source Apportionment of Airborne Particulate Matter Using Organic Compounds as Tracers," Atmos. Environ., **30**(22), pp. 3837–3855.
[5] Ristovski, Z., Morawska, L., Thomas, S., Hitchins, J., Greenaway, C., and Gilbert, D., 1999, "Submicron Particle Emissions From Compressed Natural Gas Engines," J. Aerosol Sci., **30**(1), pp. S529–S530.
[6] Hildemann, L. M., Cass, G. R., and Markowski, G. R., 1989, "A Dilution Stack Sampler for Collection of Organic Aerosol Emissions: Design, Characterization and Field Tests," Aerosol Sci. Technol., **10**, pp. 193–204.
[7] Quillen, K., Stanglmaier, R. H., Moughon, L., Takata, R., Wong, V., Reinbold, E., and Donahue, R., 2006, "Friction Reduction by Piston Ring Pack Modification of a Lean-Burn 4-Stroke Natural Gas Engine: Experimental Results,"

Proceedings of the ICES2006, Paper Nos. ASME-ICES 2006 and ICES2006–1327.

[8] 2004, Final Regulatory Analysis: Control of Emissions From Nonroad Diesel Engines, Assessment and Standards Division Office of Transportation and Air Quality U.S. Environmental Protection Agency, Paper No. EPA420-R-04–007.

[9] Ristovski, Z. D., Morawska, L., Hitchins, J., Thomas, S., Greenaway, C., and Gilbert, D., 2000, "Particle Emissions From Compressed Natural Gas Engines," J. Aerosol Sci., **31**(4), pp. 403–413.

[10] Burtscher, H., 2005, "Physical Characterization of Particulate Emissions From Diesel Engines: A Review," J. Aerosol Sci., **36**, pp. 896–932.

A Comparison Between Combustion Phase Indicators for Optimal Spark Timing

Emiliano Pipitone
Dipartimento di Meccanica,
University of Palermo,
Vialle delle Scienze,
Palermo 90128, Italy
e-mail: pipitone@dima.unipa.it

The closed-loop control of internal combustion engine spark timing may be accomplished by means of a combustion phase indicator, i.e., a parameter, derived from in-cylinder pressure analysis, whose variation is mainly referable to combustion phase shift and assumes a fixed reference value under optimal spark timing operation. The aim of the present work is a comparison between different combustion phase indicators, focusing on the performance attainable by a feedback spark timing control, which uses the indicator as pilot variable. An extensive experimental investigation has been carried out, verifying the relationship between indicators' optimal values and the main engine running parameters: engine speed, load, and mixture strength. Moreover, assessment on the effect of the most common pressure measurement problems (which are mainly related to pressure referencing, sampling resolution, top dead center determination, and cycle-by-cycle variations) on the indicators' values and on the performance attainable by the spark timing control is included. The results of the comparison point out two indicators as the most suitable: the location of pressure peak and the location of maximum heat release rate. The latter, not available in literature, has been introduced by the author as an alternative to the 50% of mass fraction burned. [DOI: 10.1115/1.2939012]

Introduction

Modern spark ignition engines must meet both rising fuel cost and CO_2 reduction policy by increasing as much as possible energy conversion efficiency; as is known, one of the key parameters for engine performance is spark advance, which is normally controlled in open loop by means of tables stored in the ECU. These tables are drawn up during the ECU calibration process, trying to obtain the maximum output (maximum brake torque, MBT) on the engine test bed for different speed and load conditions; some other tables account for spark advance change due to variation in air and coolant temperature, and absolute pressure. The ECU calibration becomes therefore a time consuming phase, which, however, does not guarantee to obtain always the best performances for the whole engine life: The stored tables, in fact, cannot consider all the possible operative conditions, and, moreover, optimal spark timing can also strongly depend on air humidity, engine wear, and fuel properties [1,2]; for these reasons, a closed-loop control on spark advance, capable to maximize the engine output for every engine operative condition, is preferable; it can also be employed to realize a cost effective calibration process, quickly reaching the best spark timing value. Many techniques are proposed in literature for spark advance feedback control, and most of them make use of the in-cylinder pressure history to obtain the feedback variable. Sometimes, the cylinder pressure is reconstructed by means of analysis performed on another variable, for example, engine speed fluctuation or block vibration, but as far as the spark timing control is concerned, the cylinder pressure analysis remains a fundamental step. The most of these techniques rest on a single parameter derived from in-cylinder pressure, which almost assumes a fixed value under MBT timing: Such parameters are called combustion phase indicators, since their variation is mainly referable to combustion phase shift. The work here presented aims at making a comparison between five combustion phase indicators, to evaluate their qualities and weakness as pilot variables for MBT spark timing control.

Combustion Phase Indicators

This section gives a general outline of the five combustion phase indicators here taken into consideration:

(1) location of pressure peak (LPP)
(2) location of maximum pressure rise (LMPR)
(3) location of 50% of mass fraction burned (MFB50)
(4) location of maximum heat release rate (LMHR)
(5) value of relative pressure ratio 10 crank angle degree ATDC (PRM10)

Location of Pressure Peak (LPP). According to this criterion, spark advance is set to its best value when the pressure peak is found to be 14–16 crank angle degrees (CAD) after top dead center (ATDC), apart from engine speed and load, and from other variables. This is one of the most encountered combustion phase indicators in literature [1,3–7], and requires pressure sampling at least for 30 deg ATDC (see Fig. 1). The set point value is 14–16 crank angle degrees ATDC, and, as for all the other indicators, has been determined empirically and has not yet been theoretically explained.

Location of Maximum Pressure Rise (LMPR). Cook et al. in 1947 [8] showed that under optimal spark advance, the maximum pressure rise occurs about 3 deg ATDC. Rarely encountered in literature among the combustion phase indicators, its evaluation requires pressure sampling in the interval ±20 deg around top dead center (TDC).

Location of 50% of Mass Fraction Burned (MFB50). It is well known to internal combustion engine researchers that in-cylinder pressure allows the evaluation of the fuel MFB [9–14]: This can be accomplished following the procedure proposed by Rassweiler and Withrow, simple yet reliable, or by means of thermodynamic analysis, which instead requires to know wall heat transfer law. According to this criterion, spark timing is set to the best value when MFB reaches 50% about 9 deg ATDC [15,16].
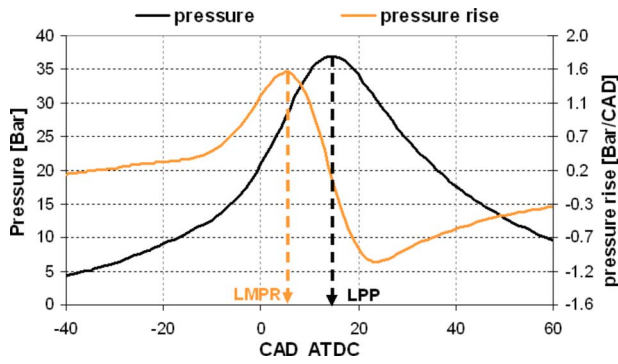
Fig. 1 In-cylinder pressure and its derivative, 2500 rpm—IMEP 6 bar (LPP and LMPR are shown)

Fig. 3 PR as function of CAD: the indicator PRM10 is the ratio between A (PR10) and B (PR55)

Compared to LPP and LMPR, this indicator requires a greater amount of calculus and data to sample: In-cylinder pressure must be acquired during almost the whole compression and expansion strokes. Moreover, unlike LPP and LMPR, absolute pressure values are needed for a correct MFB50 evaluation.

Location of Maximum Heat Release Rate (LMHR). This parameter has not been found in literature among the combustion phase indicators; Pipitone and Beccari, who introduced this indicator in a previous work [17], considered it a valid alternative to MFB50, since it presents similar features, with a lower sensitivity to pressure measurement errors. If the MFB is expressed by the Wiebe function,

$$MFB = 1 - e^{-aX^{(m+1)}} \quad (1)$$

where X represents the fractional combustion angle, and a and m are constants, the position X_{MHR} at which the MHR rate occurs can be evaluated setting the second derivative to zero; this gives

$$X_{MHR} = a^{-1/(m+1)} m^{1/(m+1)} (m+1)^{-1/(m+1)} \quad (2)$$

Now, setting $X=X_{MHR}$ into Eq. (1), the MFB at the MHR rate moment MFB_{MHR} is found as follows:

$$MFB_{MHR} = 1 - e^{-m/(m+1)} \quad (3)$$

As can be seen, it exclusively depends on the constant m, which both literature and experimental results showed to be about 2; this gives $MFB_{MHR}=0.49$.

It is so explained the reason why LMHR and MFB50 share nearly the same values (see Fig. 2).

The author of the present work introduced the parameter LMHR for a comparison with MFB50: its evaluation does not require any extra calculus effort, since MFB is normally obtained by integration, and it is less prone to errors due to bad pressure

referencing or measurement. Naturally, its set point value should be near to that of MFB50, i.e., about 9 deg ATDC with optimal spark timing.

Value of Relative Pressure Ratio 10 Crank Angle Degree ATDC (PRM10). Also this indicator was proposed [18] as an alternative to the MFB50; Matekunas et al., in fact, defined it as

$$PRM10 = \frac{PR(10) - 1}{PR(55) - 1} \quad (4)$$

being $PR(\theta)$ the pressure ratio between the measured *fired pressure* and the evaluated *motored pressure* θ deg ATDC (generally PR values stay between 1 and 4, see Fig. 3).

Under MBT spark timing, the relative pressure ratio PRM10 should assume the value 0.55, quite similar to MFB50, which should reach its 50% around 9 deg ATDC. The ratio between *measured* and *motored pressure* (the latter calculated using a polytropic law) in effect follows the concept proposed by Rassweiler and Withrow, i.e., the heat released by combustion is closely related to the pressure rise besides the compression effect. The advantage in the use of the PRM10 instead of MFB50 theoretically relies on the easier calculation and fewer data to sample: four points should be enough, two taken during compression stroke for polytropic index evaluation and the other two taken 10 and 55 CAD ATDC. As a matter of fact, measurement noise and signal referencing (absolute pressure values are needed) may require the pressure sampling for a great part of the compression stroke to correctly evaluate the expansion polytropic coefficient [19,20]. Moreover, since the expansion polytropic index is often different from the compression one, both of them should be used: This requires a complete pressure sampling during expansion stroke, and makes PRM almost equal to MFB. Unlike all the other indicators, PRM10 is a dimensionless number between 0 and 1, and decreases with a forward shifting of the combustion.

It could be argued that the indicated mean effective pressure (IMEP) could be the most valid parameter for optimal spark timing control, since it represents the total amount of energy received by the piston during a whole cycle. The author compared the spark timing control achievable using IMEP rather than torque (which means BMEP) and found great differences, as showed in Fig. 4 and Table 1. It can be clearly seen that the maximum IMEP spark advance may be quite different from the MBT spark timing. This is due to mechanical efficiency, which can vary strongly with IMEP and has a great influence on the real engine output, that is, BMEP. Using the experimental data collected for this work, the performance differences due to IMEP driven spark timing have been calculated for each operative condition: The maximum differences in terms of spark advance and performance loss are reported in Table 1.
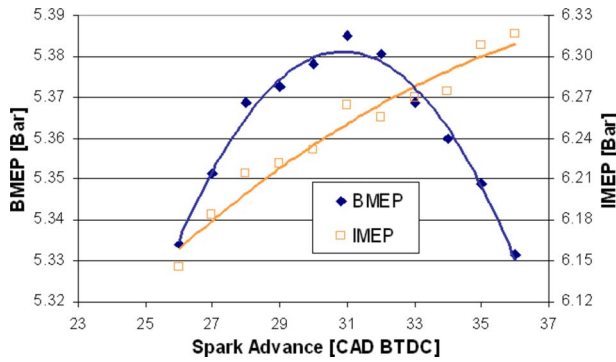

Fig. 2 MFB and heat release rate, 2500 rpm, 6 bar BMEP (MFB50 and LMHR are shown)

Fig. 4 BMEP and IMEP as a function of spark advance 3500 rpm, $\lambda = 0.95$

Fig. 5 Percentage efficiency loss due to bad spark advance setting (1500 to 3500 rpm, 3 bar and 6 bar BMEP)

Experimental Investigation

The comparison between the five combustion phase indicators required the acquisition of pressure cycles with varying spark advance for different operative conditions, so as to evaluate their capacity to pilot the spark advance control and to assess any possible relationship between indicators and the fundamental engine parameters. The experimental tests have been carried out on an internal combustion engine test bench using a Renault four cylinder in-line 1598 cm³ 16 V multipoint spark ignition engine connected to a Schenck eddy current dynamometer managed by means of a Borghi & Saveri control module DCU2000. The engine was equipped with an AVL GU13Z-24 piezoelectric pressure transducer, flush mounted in the combustion chamber by means of its spark plug adaptor ZF42, and a 360 pulse per revolution optical encoder was used to clock the analog acquisition with a resolution of 1 crank angle degree. The data were collected through a National Instrument 6062 DAQ card, a 12 bit resolution data acquisition board with 500 kHz maximum sampling frequency, using the LABVIEW software.

As mentioned before, absolute pressure values are necessary for a correct evaluation of MFB and PRM10 (LMHR, as shown further, is almost insensitive to pressure bias errors); this required the use of a referencing procedure of the uncooled pressure transducer signal. The two most suitable referencing techniques are [19,20] the manifold absolute pressure (MAP) based and the polytropic index based. The first method assumes that mean in-cylinder pressure around the inlet stroke BDC is equal to manifold absolute pressure: this requires the use of a MAP sensor, which is commonly integrated in modern spark ignition engine management system. The second method instead forces the compression polytropic index to a fixed value, which should lie between 1.28 and 1.32. In the tests performed, in-cylinder pressure was referenced by means of the manifold absolute pressure measured by a piezoresistive sensor; assessment on the influence of the referencing technique is, however, reported below.

To remove unwanted noise from the pressure signal, a fourth order Butterworth low-pass filter with zero phase shift (this is an essential prerequisite) and cutting frequency set to 1/9 of the sampling frequency was used, while cycle-by-cycle variations, which strongly affect indicators' measurement, were overcome computing an averaged pressure cycle obtained from a matrix of 50 consecutive pressure cycles recorded at fixed spark advance, engine
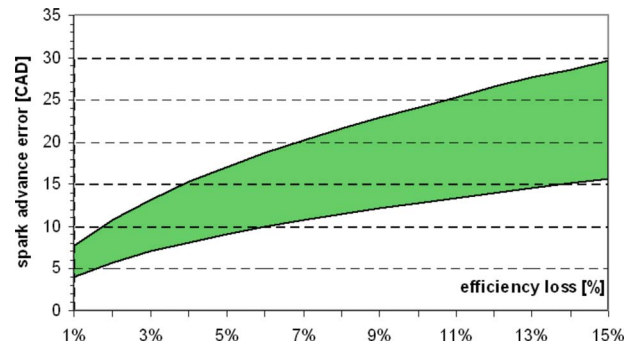
speed, load, and air-to-fuel ratio (A/F). Spark timing was then varied around the MBT value by means of a Walbro TDD computer controlled ECU for every engine operative condition. The tests were performed with engine speed ranging from 1500 rpm to 3500 rpm, while engine loads were kept to about 3 bar and 6 bar BMEP, so as to evaluate load dependences without causing knocking to occur. Moreover, to check for any mixture strength dependence, the engine was fed with different A/F ratios, setting lambda to 0.88, 0.95, 1.00, 1.05, and 1.10.

The test performed permitted first of all a better understanding of the efficiency loss due to a bad spark timing management: the graph in Fig. 5, traced by means of all the experimental data acquired, shows that a 1% loss can be caused by a spark advance error of 4 deg, while a 10 deg error can cause up to a 6% loss. These results can help us to assess the allowable spark advance error with respect to optimal value: accepting, for example, a 0.2% loss in torque, extrapolation from the lower bound in Fig. 5 shows that spark advance should remain in the range of ±1.8 deg from the optimal value.

The typical result of one complete spark sweep test with constant speed, load, and A/F ratio is represented in Fig. 6: here, engine torque and combustion phase indicators are plotted against spark advance. Two immediate simple observations can be drawn: engine torque exhibits a square-law dependence on spark advance (a good second order polynomial regression was confirmed by every test), while all the indicators change linearly with spark advance (a narrow linear correlation was found for every operative conditions), which is a desirable feature for the pilot variable of a feedback control. Table 2 resumes both the mean slope and the mean intercept values found for each indicator, together with their coefficient of variation (COV) (i.e., ratio between standard deviation and mean value). As is shown, MFB50 and LMHR revealed to be more sensitive to spark advance change than LMPR
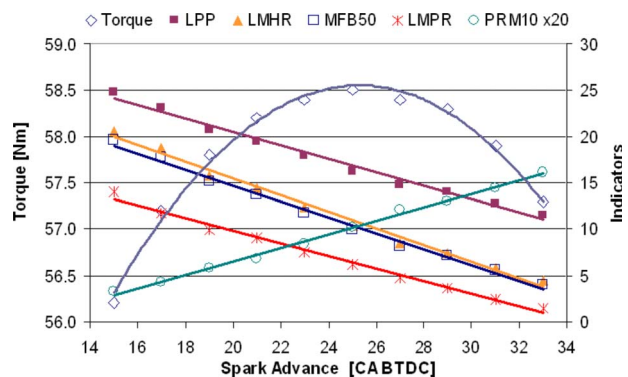
Table 1 Performance loss due to maximum IMEP spark timing

Maximum differences	
Spark advance	25 deg
BMEP loss	0.87 bar
BMEP % loss	16.8%

Fig. 6 Engine torque and combustion phase indicators as a function of spark timing (1500 rpm, $\lambda = 1.1$)

SEPTEMBER 2008, Vol. 130 / **052808-3**

Downloaded 02 Jun 2010 to 171.66.16.107. Redistribution subject to ASME license or copyright; see http://www.asme.org/terms/Terms_Use.cfm

Table 2 Indicators' slope and intercept (mean values)

	Slope		Intercept	
	Mean	COV (%)	Mean	COV (%)
LMPR	−0.662	21.3	23.14	13.4
LPP	−0.725	15.6	35.87	7.5
PRM10	0.0387	21.7	−0.535	26.0
MFB50	−0.905	11.4	34.51	11.3
LMHR	−0.920	12.4	35.26	11.2

and LPP. Naturally, from the point of view of a feedback control, a higher sensitiveness of the pilot variable to the controlled variable is desirable, so as to obtain a fast response. It is worthwhile to mention that the linear regression coefficients in Table 2 are mean values evaluated over all the tests, with a certain dispersion, as pointed out by the COV. However, even considering every single test, the above mentioned relation between the slope coefficients remains true. These linear regression coefficients can also be used to model the indicators' behavior as function of spark advance in the feedback controller development. As mentioned above, the PRM10 is the only indicator that exhibits a positive slope with respect to spark advance. The spark advance for MBT (for example, 25 CAD BTDC in Fig. 6) was then assessed to find the corresponding optimal value for each of the indicators. This procedure was followed for every operative condition, thus obtaining indicators' mean optimal values and their variation range (i.e., the difference between the maximum and the minimum value encountered): In Table 3, the overall results are resumed together with those obtained with stoichiometric mixture.

The ideal pilot variable of a feedback spark timing control system should depend exclusively on spark advance; for this reason, the author verified any possible correlation between each indicator optimal value and the most important running parameters, such as engine speed, load, and mixture strength. The graphs in Fig. 7 show the measured optimal values for each of the indicators with varying engine speed, two load conditions, and stoichiometric mixture: As can be seen, and confirmed by closer examinations, engine speed has a certain influence on every indicator in the higher load case, while for the lower load case a clear relationship with engine speed can be found only for LMPR and PRM10; the latter, moreover, is the only one that showed a quadratic dependence.

Assessment on the effect of engine load shows a feeble influence on the indicators' optimal values; the indicator, which exhibits the highest dependence from engine load, is LMPR, as after all is pointed out by the graphs of Fig. 7: Here, a sort of separation occurs between the medium and the low load points. A negligible influence was found on the other indicators, which can be then considered independent of engine load.

The data recorded at different A/F permitted also to evaluate the influence of mixture strength on the combustion phase indicators: As pointed out by the left graphs in Fig. 8, all of them showed a certain dependence on A/F at low engine speed and medium load;

as can be seen, in these operative conditions, all the angle based indicators (LPP, LMPR, MFB50, and LMHR) increase with increasing A/F up to stoichiometric mixture, then start decreasing. The PRM10, instead, due to its definition (see Eq. (4)), showed a reverse behavior. At the lower loads or higher engine speed, the dependence on mixture composition almost disappear, as shown in the right graphs of Fig. 8. It must be noted, however, that mixture composition changes have a negligible effect on the indicators' set point values, as attested by the results in Table 3: In fact, the variation ranges and the optimal values obtained at stoichiometric mixture do not differ significantly from those obtained considering also the test performed with different A/F values. Therefore, mixture strength can be considered to have no importance for a feedback spark timing control driven by combustion phase indicators.

Some differences arise from the comparison of the range of variation of Table 3: LPP values moved in a 3.6 deg wide band, i.e., remained in the range of ±1.8 deg from the mean optimal value of 14.7; MFB50, LMHR, and LMPR instead were characterized by a wider dispersion around the mean optimal value (about ±2.5 deg). Such a simple comparison cannot be made with PRM10, since it is not expressed in degrees. The real effect of the dispersion range, however, should be evaluated on the basis of the spark advance errors it induce or rather on the efficiency loss it can cause. In fact, if spark advance is controlled so as to set the indicator's value to its set point while for a particular operative condition the best combustion phase requires instead to set the indicator's value at the edge of the variation range, there will be a certain spark advance error with respect to optimal condition, which, in turn, will cause a loss in engine efficiency. To quantify this maximum combustion efficiency loss, the author calculated the spark advance errors using the narrow linear correlations found between each indicator and the spark timing for all the operative conditions tested, supposing to run the engine with maximum indicator's error, while the quadratic correlation between spark timing and torque permitted to calculate the efficiency loss related to each spark advance error: It was then found (see Fig. 9) that LMPR could cause a loss of about 5%, with a spark advance error of more than 8 deg with respect to the MBT condition. PRM10 resulted to cause a lower maximum efficiency loss (around 1.5%), with a spark advance error of 5 deg, while LPP, MFB50, and LMHR proved the best performances with a maximum spark advance error of 4 deg and an efficiency loss of about 1% in the worst condition.

Naturally, the difference between the indicator's optimal value and reference value is maximum only in a few cases, while in all the other cases the indicator's optimal values lie in between the variation band; therefore, for each of the operative condition tested, the efficiency loss due to the spark timing error that a feedback control would cause when driven by indicators' set point values has also been calculated. The results, represented in Fig. 10, show that LMPR would cause the highest spark timing error (up to 8 deg) with an efficiency loss of 1.1%, while the use of the other indicators would allow remaining in the range of 3.5 deg from optimal spark timing, causing a torque loss always under 0.3%.

Table 3 Indicators', optimal values and dispersion range

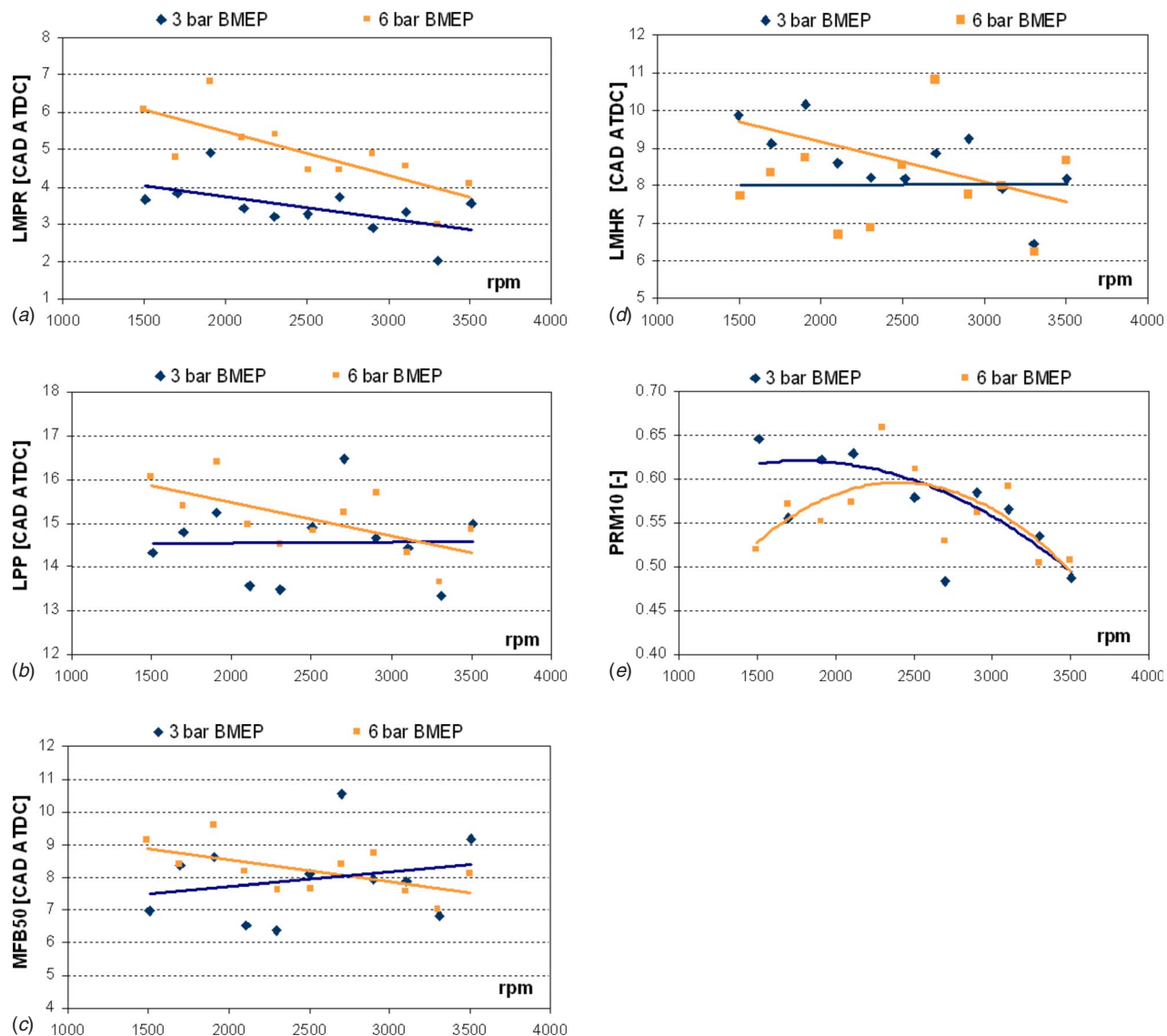|	LMPR	LPP	PRM10	MFB50	LMHR
	Stoichiometric mixture values				
Optimal value	4.1	14.7	0.58	8.0	8.2
Variation range	±2.4	±1.7	±0.11	±2.3	±2.3
	Global values				
Optimal value	4.0	14.7	0.58	7.9	8.2
Variation range	±2.6	±1.8	±0.12	±2.5	±2.5

Fig. 7   Indicators versus engine speed (stoichiometric mixture, 3 bar and 6 bar BMEP)

As regards the LMHR, the results presented up to this point (Tables 2 and 3, figures from 7–10) revealed that this parameter can be considered a good combustion phase indicator for MBT spark timing control, since it is characterized by a set point value, which is almost independent of engine speed and load, and exhibits the same behavior of MFB50 with respect to mixture strength; moreover, its variation range is equal to those found for MFB50 and LMPR. It has been proposed as an alternative to MFB50 and proved to have comparable characteristics and performances: The close resemblance between MFB50 and LMHR is further shown in Fig. 11: Here, LMHR values are reported against MFB50 for every operative condition tested.

Measurement Problems and Evaluation Errors

All the five combustion phase indicators here taken into consideration derive from in-cylinder pressure analysis. Therefore, their evaluation and, hence, the performance attainable by the spark timing control could present some inaccuracy due to pressure measurement problems, which are mainly related to sensor performances, pressure referencing, pressure sampling resolution, TDC determination, and cycle-by-cycle variations. As regards the pressure sensor, for example, it is well known that the output signal of a piezoelectric transducer can carry a bias error, due to

thermal sensitivity shift (long term drift) or to deformation stresses; this may lead to an erroneous evaluation of the indicator [19,20] and consequently to poor spark timing control.

Obviously, the indicators merely based on the phase of the pressure signal, i.e., LPP and LMPR, are free from this problem; the other three indicators, instead, revealed a different sensitivity to pressure bias error: Figure 12(a) shows the highest induced evaluation errors found on LMHR, MFB50, and PRM10; as can be seen, a bias error on pressure values has a stronger impact on MFB50 (nearly 2 deg) than on LMHR (less than 0.5). The effective comparison between the three indicators must be, however, made only on the base of the induced spark advance error: Fig. 12(b) shows that PRM10 caused up to 8 deg deviations from optimal spark timing, while LMHR maintained the best performance with spark timing errors lower than 1 deg. Therefore, the use of PRM10 can seriously damage the control performance, while LMHR demonstrated to be almost insensitive to pressure bias errors.

When absolute pressure values are needed, a referencing procedure on sensor signal output is often required. As previously mentioned, during the tests, the inlet manifold technique was used, which is mainly recommended when low engine speeds are investigated. According to this method, in-cylinder pressure, when
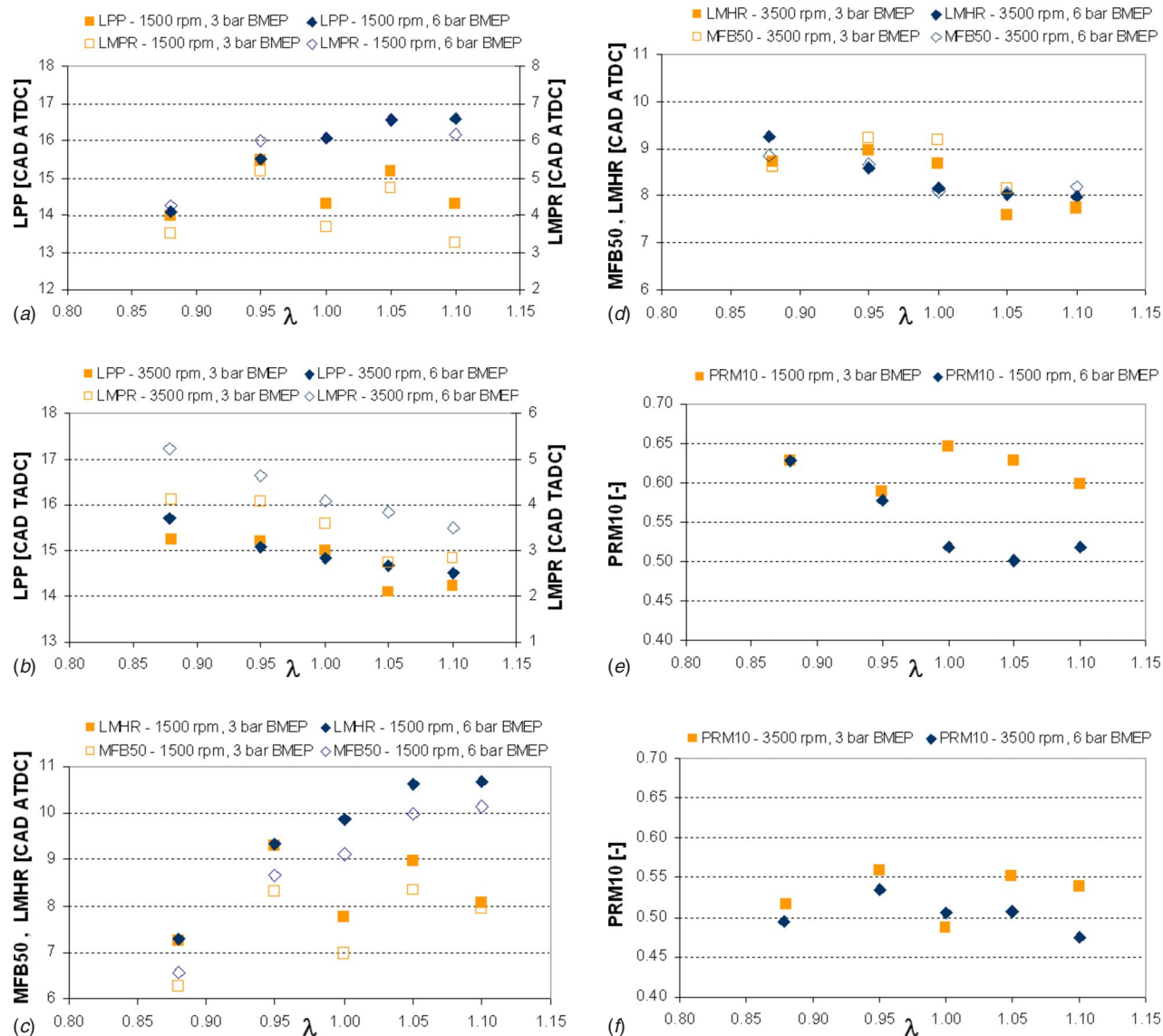
Fig. 8 Indicators versus mixture strength

piston is at intake BDC, should equal manifold absolute pressure. Generally, disturbance on sensor signal compels to use a mean in-cylinder pressure value computed at least over a 10 deg arc, which theoretically should have a symmetrical position with respect to the BDC; inertia effects of fluid flow may cause the BDC pressure to be different from manifold pressure, requiring so the forward shifting of the referencing arc: The magnitude of this shift depends naturally on engine speed and intake duct design, and this fact introduces an uncertainty on the pressure correction procedure. In Fig. 13, the maximum and mean variation in referencing pressure are represented versus the starting position of the referencing arc: As can be seen, a 20 deg shift of the arc can cause a 7 kPa pressure correction variation. When the engine is used at a high speed, above all if it is endowed with tuned intake systems, the polytropic index technique should be preferred, since inertia effect may change considerably in-cylinder pressure on the first part of the compression stroke. As an example, Fig. 14 shows, for each engine speed considered, the maximum difference in pressure correction that occurred using the two techniques on the pressure cycles recorded. It represents an uncertainty in the pressure acquisition chain that, at relatively high engine speed, can reach 20 kPa, which is anything but negligible, as remarked by the graphs in Fig. 12.

Considering that none of the two referencing methods can guarantee an absolute reliability, the difference in pressure correction obtained by the two techniques over all the operative conditions tested and with varying polytropic index was also investigated: As a result, Fig. 15 shows that this difference reached 26 kPa when using a polytropic index equal to 1.28, and 19 kPa with 1.33, which, as can be observed, is the index that best matches with the MAP based method; these polytropic index values are not exactly valid for every engine: Hence, the high differences found in pressure referencing may imply remarkable indicators' evaluation errors (as stated in Fig. 12); therefore, if a referencing procedure must be adopted, the use of indicators immune to pressure correction errors, such as LPP or LMPR, or not much affected, such as LMHR, should be preferred.

Concerning pressure sampling resolution, it is clear that the higher it is, the more precise will be the reconstruction of pressure cycle and consequently the calculation of combustion phase indicators. Actual engines, however, are not equipped with high resolution timing devices, such as encoders; usually a ring gear is employed together with an inductive or Hall effect sensor, which generates a wave form whose frequency gives the engine speed; the generated wave forms can also be used to trigger signal acquisition, but its resolution depends on the number of teeth on the
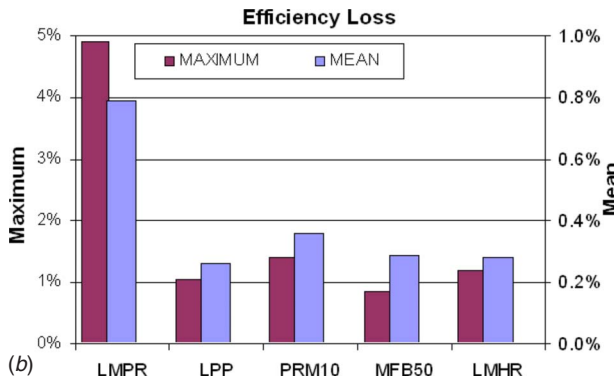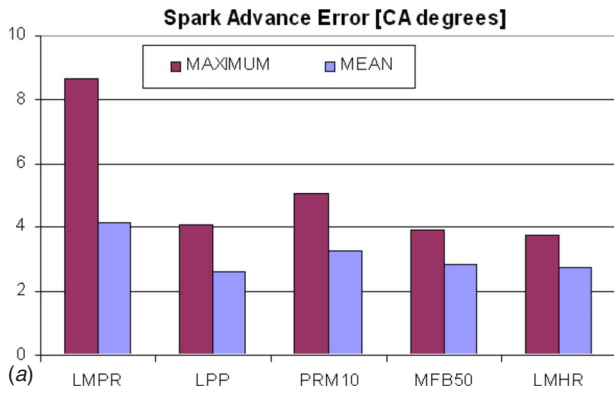
Fig. 9 (*a*) Spark advance error and (*b*) performance loss with indicators' value on the edge of the variation range
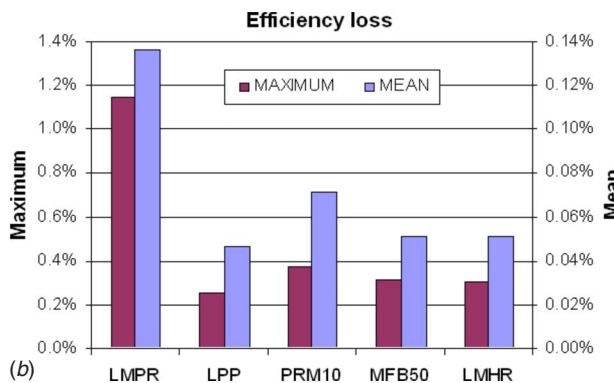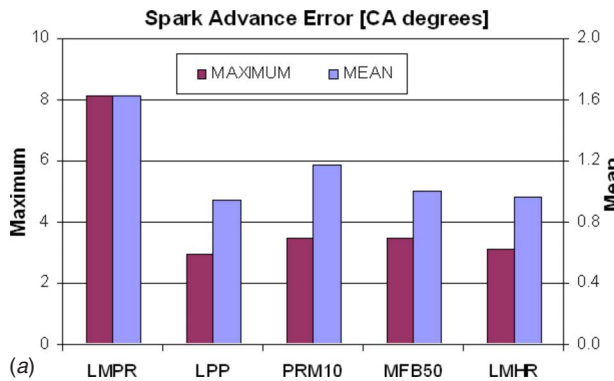
Fig. 10 (*a*) Spark advance error and (*b*) performance loss with optimal spark advance control
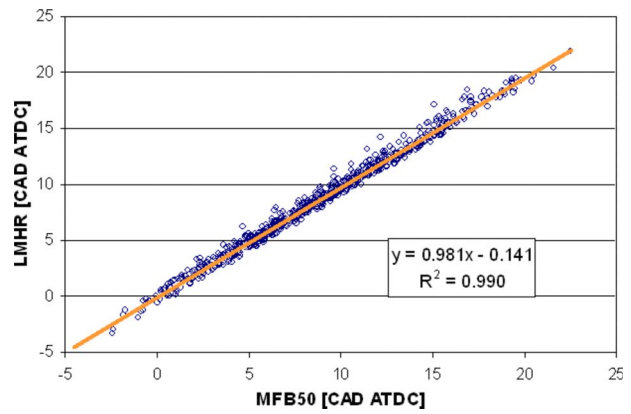

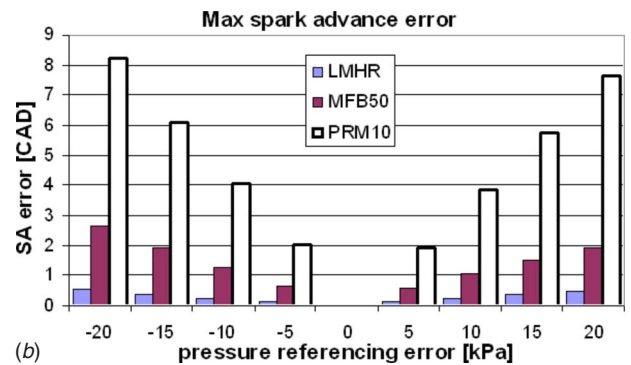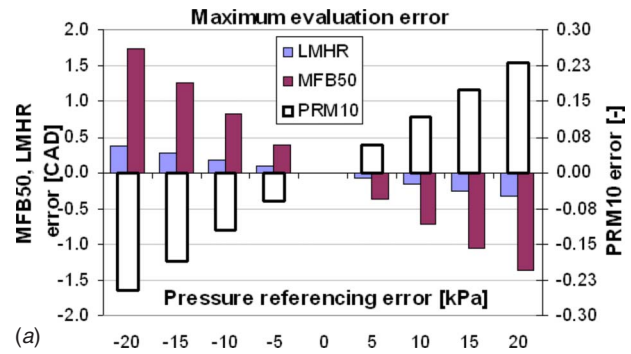Fig. 11 LMHR versus MFB50 (all operative conditions)

Fig. 12 (*a*) Maximum indicators' evaluation error and (*b*) maximum spark advance errors for bad pressure referencing
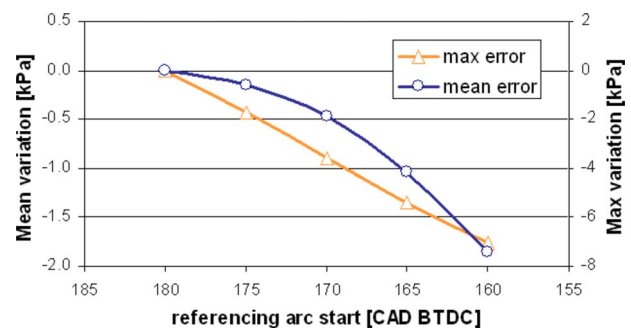

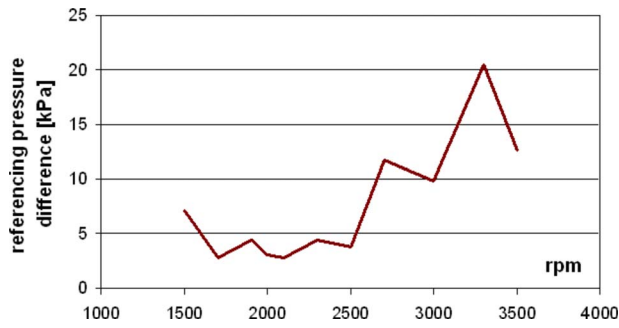Fig. 13 Mean and maximum pressure referencing variation versus start of the referencing arc

Journal of Engineering for Gas Turbines and Power

Fig. 14 Maximum pressure correction difference between "MAP" and *k*=1.32 referencing methods

(a)

(b)
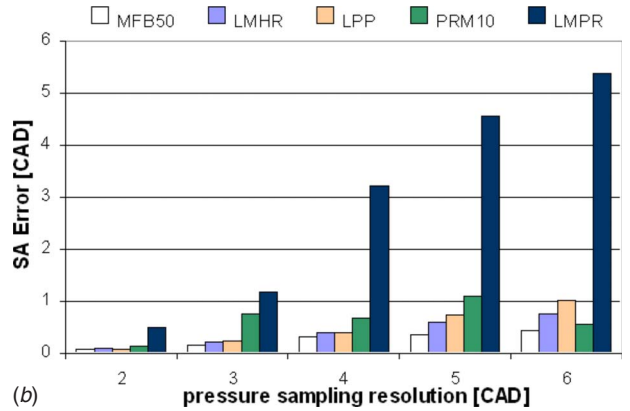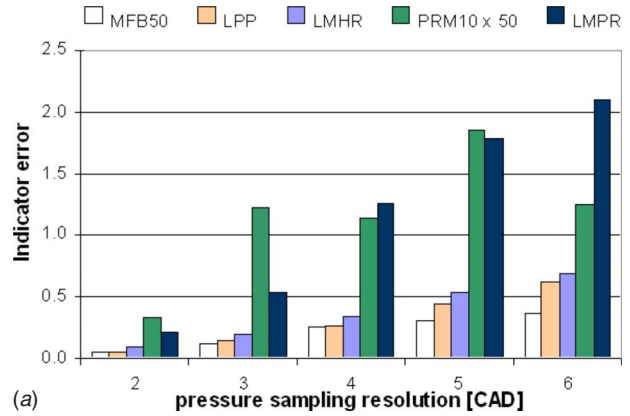
Fig. 16 (*a*) Indicators' maximum evaluation errors and (*b*) spark advance maximum errors with varying sampling resolution

ring gear: Normally these are 60, which means that the wave-forms' period is 6 deg and therefore a maximum resolution of 3 deg (the distance between the positive and negative peaks of the wave form signal) can be achieved with the actual systems. It was then checked how pressure sampling resolution affects both combustion phase indicators' evaluation and the attainable spark advance control. Down sampling the recorded pressure cycles, it was possible to compare the indicators' values obtained using different sampling resolutions (from 2 deg to 6 deg) with those obtained with maximum resolution (1 deg). The results are resumed in the graphs in Fig. 16: It can be seen that the only indicator that suffers for a low sampling resolution is LMPR, showing a maximum evaluation error of 2 deg (which is nearly its variation range) together with a spark advance error of 5 deg. All the other indicators proved to well tolerate coarse sampling resolution, with spark timing errors always within 1 deg.

Another source of error in the evaluation of combustion phase indicators is represented by inaccurate TDC determination, which can be avoided only with the use of TDC position sensor (which guarantees a 0.1 deg precision) or by means of thermodynamic methods, based on engine motored pressure acquisition and analysis [21–23], whose accuracy may be lower.

In both cases, the procedure should be applied for every single engine, which could not be practicable for mass production. The importance of TDC determination is well known in terms of IMEP calculation: As can be seen in Fig. 17, the tests performed revealed an 8% IMEP evaluation error as a consequence of a wrong TDC determination of just 1 deg. The assessment of the influence of TDC position error on the combustion phase indicators' evaluation was carried out altering the phase of the pressure cycles recorded: The results shown in the left part of Fig. 18 point out that MFB50 and LMHR undergo an evaluation error higher than LPP and LMPR, which, obviously, change linearly with the TDC error.

As concern the induced spark advance error with respect to the MBT values, LMPR proved again the worst performances (10 deg error with respect to a 3 deg TDC error), while MFB50, LMHR, and LPP shown almost the same lower spark advance deviation (6–7 deg); the best result was achieved by PRM10, whose induced spark advance error followed almost linearly the TDC error.

The last, but not the least, trouble in pressure measurement is related to cycle-by-cycle variations: As is known, in fact, in-cylinder pressure during the combustion phase is highly variable from one cycle to the next (see, for example, Fig. 19) due to differences in start of combustion and flame propagation speed. This high variability can seriously endanger the stability of a feed-back spark timing control, as a result of the wide variations induced on the combustion phase indicators' values; for example,
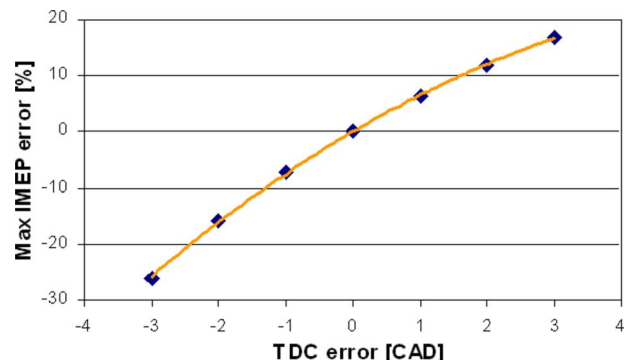

Fig. 15 Pressure correction difference between "MAP" and *k* referencing methods for different polytropic indices

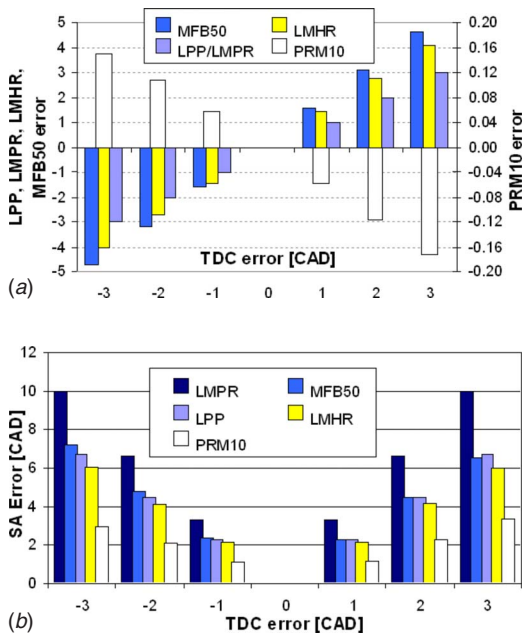Fig. 17 IMEP evaluation error with wrong TDC reference

Fig. 18 (*a*) Indicators' maximum evaluation errors and (*b*) spark advance maximum deviation from MBT value as a function of TDC error

Fig. 20 shows the progress of LPP, PRM10, and MFB50 evaluated over 250 consecutive cycles with constant engine speed, load, spark timing, and A/F: As also resumed in Table 4, it can be noted that all the three indicators move in a wide variation band, whose amplitude is higher than the characteristic dispersion range of Table 3, thus obtaining a relative variation of 2.7 for PRM10 and
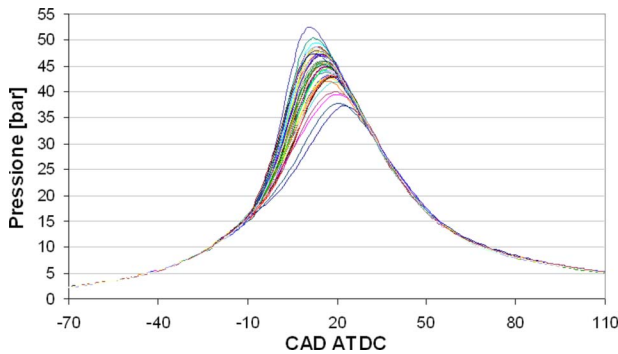
Fig. 19 In-cylinder pressure cycle-by-cycle variation: 50 consecutive cycles with constant speed, load, A/F and spark timing
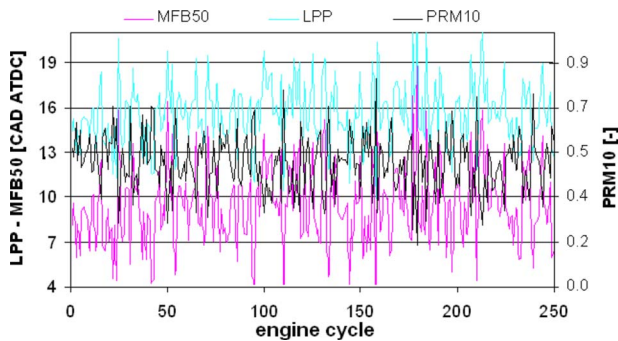
Fig. 20 Indicators cycle-by-cycle variation (3500 rpm 4.8 bar IMEP, MBT SA, $\lambda = 1$)

Table 4 Indicators and consequent SA variation

	LPP	PRM10	MFB50
Variation range	±6.8	±0.33	±9.2
Rel. variation	3.7	2.7	3.6
SA variation	±9.4	±8.4	±10.1

approximately 3.6 for LPP and MFB50. Quite similar results can be obtained by the other two indicators, LMPR and LMHR.

This wide oscillation range could drive the spark timing control system (whose task is to keep indicator value to its set point) to strong, and maybe dangerous, spark advance oscillation, which can be easily evaluated using the slope coefficient of Table 2, as resumed in Table 4. To avoid spark advance oscillations as high as 20 deg (±10.1), it is safer to evaluate indicators on the base of a mean pressure cycle, computed over a certain number of pressure cycles, sufficient for a stable estimation of indicators' value. Naturally, this number of engine cycles must be as low as possible, since a high value would slow down the spark timing controller, which instead must preserve a fast response so as to follow the transient operations, which characterize the application of internal combustion engine to vehicle propulsion.

The number of engine cycles for the calculation of the mean pressure cycle can be established once the allowable indicators' fluctuation has been fixed, and this, in turn, depends on the maximum allowable spark advance oscillation around the MBT value; if a mean 0.2% efficiency loss is tolerated, the lower bound of Fig. 5 gives a maximum spark advance oscillation within the range of ±1.8 deg; by means of the slope coefficient in Table 2, the allowable indicators' range of oscillation have been calculated (see Table 5).

For the assessment of the minimum number of pressure cycles for a stable evaluation of the indicators' value, pressure matrices of 250 consecutive cycles have been recorded with engine speeds of 1800 rpm, 2500 rpm, and 3200 rpm, and two different loads: ~4 bar and 8 bar IMEPs; moreover, to test highly unstable operative conditions, a lean mixture ($\lambda = 1.1$) was adopted, together with a retarded spark advance (MBT-10), thus running the engine with IMEP COV ranging from 1% to 5%.

For each of the operative conditions tested, the minimum number of engine cycles, which bring each indicator's range of oscillation under the respective limits fixed in Table 5, has been calculated: As an example, Fig. 21 shows the range of variations of LMHR, LPP, and PRM10 with respect to the number of engine cycles used for the mean pressure cycle calculation; the broken lines represent the limits of Table 5. As can be seen, in this operative condition, all three of the indicators cross their limit line within less than 25 engine cycles. The overall results, shown in Fig. 22, revealed that the evaluation of the indicators rarely requires more than 25 engine cycles; LMPR presented the highest instability, while PRM10 proved to be the most stable of the indicators; moreover, once again, LMHR performed quite similar to MFB50. The mean values of these results are summarized in Table 6. However, it must be pointed out that the results of Fig. 22 and Table 6 closely depend on the limits in Table 5, and hence on the allowable spark timing variation.

Table 5 Allowable indicators, range of variation for a maximum spark timing error of 1.8 deg from MBT value (0.2% efficiency loss)

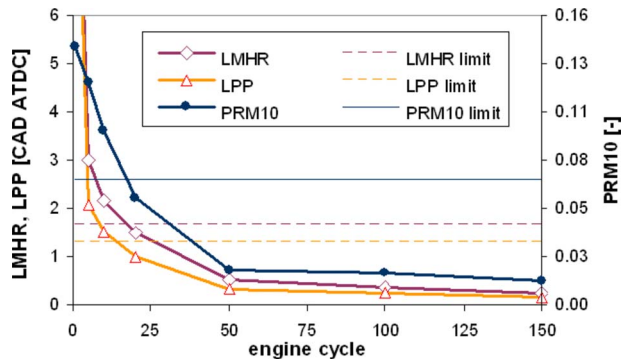| LMPR	LPP	PRM10	MFB50	LMHR
±1.19	±1.31	±0.070	±1.63	±1.66

Fig. 21 Indicators' range of variation versus number of engine cycles for the mean pressure cycle calculation (3200 rpm, 3.78 bar IMEP, COV IMEP 4.9%)

Conclusions

An experimental investigation has been carried out to compare five combustion phase indicators derived from in-cylinder pressure analysis (LMPR, LPP, PRM10, MFB50, and LMHR) as pilot variables for optimal spark timing. One of the indicators (LMHR) was introduced by the author as an alternative to the MFB50, since less prone to pressure measurement error.

The dependence of the indicators' optimal values on the principal engine working parameters has been assessed: LMPR and PRM10 proved to be influenced by engine speed apart from load, while the other indicators manifested a relationship with engine

Fig. 22 Minimum number of engine cycles for stable indicators' evaluation as a function of IMEP COV

Table 6 Mean value of the minimum number of engine cycles for stable indicator evaluation

LMPR	LPP	PRM10	MFB50	LMHR
15	11	9	14	14

speed only for the higher loads. A deeper assessment on the effect of engine speed should be carried on for the application to high speed engine (series production motorcycle engine can reach 12,000 rpm). LMPR was also found to manifest a certain dependence on engine load, while the other indicators proved to be almost insensitive; mixture strength instead was found to influence all the indicators at low engine speed and high loads, even if this influence is of scarce importance, when compared to each indicator's characteristic variation range, i.e., the difference between the maximum and the minimum optimal values. The comparison of these variation ranges revealed the first significant differences among the indicators: It was found, in fact, that the use of LMPR as a pilot variable for best spark timing can cause remarkable engine efficiency losses, while the best performances were obtained by LPP, MFB50, and LMHR. Since all the five combustion phase indicators taken into consideration derive from in-cylinder pressure analysis, the comparison included the indicators' evaluation errors, and the induced spark advance deviation from optimum, due to the most common problems in combustion chamber pressure measurement: pressure referencing, sampling resolution, TDC determination, and cycle-by-cycle variations. All these problems may induce errors on the evaluation of indicators' values, whose sum may seriously prejudice the spark timing control performances: Hence, the indicator to be used must be carefully chosen.

Pressure referencing error was found to affect the control attainable by the use of PRM10 or MFB50, while LMHR revealed to have a negligible sensitivity; LPP and LMPR instead, being based on the phase only of the pressure signal, are immune to pressure bias error. LMPR was also found to be both the only indicator to suffer for low pressure sampling resolution, and the most sensible to wrong TDC determination; in this case, LPP, LMHR, and MFB50 performed almost equally producing non-negligible deviation from optimal spark advance, while PRM10 obtained the best results, causing low spark advance errors.

Internal combustion engine cycle-by-cycle variations induce wide fluctuations on indicators' value, which, in turn, can cause a high instability in the spark timing control; it is then necessary to evaluate the indicators on the base of a mean pressure cycle. All the indicators revealed to require less than 20 engine cycles for a stable measure, being LPP and PRM10 faster than LMPR, MFB50, and LMHR.

The overall results of the comparison, which are also summarized in Table 7, point out that among the combustion phase indicators, the most suitable for MBT spark timing control is the LPP, which not only is fast and easy to calculate, but also resulted scarcely influenced by common pressure measurement errors.

If an indicator related to MFB is preferred, then LMHR should be used. The comparative tests demonstrated, in fact, that LMHR can be considered a good combustion phase indicator for MBT spark timing control, since it is characterized by a set point value, which is almost independent of engine speed and load, and exhibits the same behavior of MFB50 with respect to mixture strength; moreover, its variation range is equal to those found for MFB50

Table 7 Performance comparison between indicators (++ very good, + good, − bad, and −− very bad)

	LMPR	LPP	PRM10	MFB50	LMHR
Calculus and sampling effort	+	++	−	−	−
Engine speed dependence	−	+	−	+	+
Engine load dependence	−	++	++	++	++
Mixture strength dependence	+	+	+	+	+
Efficiency loss related to variation range	−−	+	+	+	+
Sensitivity to bias (or referencing) errors	++	++	−−	−	+
Sensitivity to pressure sampling resolution	−−	+	+	+	+
Sensitivity to wrong TDC determination	−−	−	+	−	−
Sensitivity to cycle-by-cycle variation	+	++	++	+	+

and LMPR, allowing a high efficiency spark timing control. It represents a valid alternative above all for its lower sensitivity to pressure bias or referencing errors, which make unnecessary the pressure measurement accuracy required by MFB50 and PRM10, thus allowing us to use cost effective pressure transducers. The cost of pressure transducers is at present the only drawback in the onboard use of combustion phase indicators; their use can be overcome if in-cylinder pressure is obtained by means of analysis performed on other quantities, such as ionization current, engine block vibration, or engine speed, whose measure is neither problematic nor expensive.

Acknowledgment

Nomenclature

λ = air excess index = $(A/F)/(A/F)_{stoichiometric}$
A/F = air to fuel ration
ATDC = after top dead center
BDC = bottom dead center
BMEP = brake mean effective pressure
BTDC = before top dead center
CA = crank angle
CAD = crank angle degree
COV = coefficient of variation (=standard deviation/mean value)
ECU = electronic control unit
IMEP = indicated mean effective pressure
LMHR = location of maximum heat release rate
LMPR = location of maximum pressure rise
LPP = location of pressure peak
MAP = manifold absolute pressure
MBT = maximum brake torque
MFB = mass fraction burnt
MFB50 = location of 50% of mass fraction burnt
MHR = maximum heat release rate
PR = pressure ratio
PRM = pressure ratio management
PRM10 = pressure ratio management value 10 crank angle degrees ATDC
SA = spark advance
TDC = top dead center

References

[1] Pestana, G. W., 1989, "Engine Control Methods Using Combustion Pressure Feedback," SAE Paper No. 890758.
[2] Plint, M., and Martyr, A., 1999, *Engine Testing—Theory and Practice*, 2nd ed., Butterworth & Heinemann, Oxford.
[3] Kawamura, Y., Shinshi, M., Sato, H., Takahashi, N., and Iriyama, M., 1988, "MBT Control Through Individual Cylinder Pressure Detection," SAE Paper No. 881779.
[4] Powell, J. D., 1993, "Engine Control Using Cylinder Pressure: Past, Present and Future," ASME J. Dyn. Syst., Meas., Control, **115**, pp. 343–350.
[5] Muller, R., Hart, M., Truscott, A., Noble, A., Krotz, G., Eickhoff, M., Cavalloni, C., and Gnielka, M., 2000, "Combustion Pressure Based Engine Management System," SAE Paper No. 2000-01-0928.
[6] Yoon, P., Park, S., Sunwoo, M., Ohm, I., and Yoon, K. J., 2000, "Closed-Loop Control of Spark Advance and Air-Fuel Ratio in, SI Engines Using Cylinder Pressure," SAE Paper No. 2000-01-0933.
[7] Eriksson, L., 1999, "Spark Advance Modeling and Control," Dssertation N° 580, Linköping University, www.vehicular.isy.liu.se.
[8] Cook, H. A., Heinicke, O. H., and Haynie, W. H., 1947, "Spark-Timing Control Based on Correlation of Maximum-Economy Spark Timing, Flame-Front Travel, and Cylinder Pressure Rise," NACA Technical Note 1217.
[9] Rassweiler, G. M., and Withrow, L., 1980, "Motion Pictures of Engine Flames Correlated With Pressure Cards," SAE Paper No. 800131.
[10] Amann, C. A., 1985, "Cylinder Pressure Measurement and Its Use in Engine Research," SAE Paper No. 852067.
[11] Stone, C. R., and Green-Armytage, D. I., 1987, "Comparison of Methods for the Calculation of Mass Fraction Burnt From Engine Pressure-Time Diagrams," Proc. Inst. Mech. Eng., Part D (J. Automob. Eng.), **201**(D1), pp. 61–67.
[12] Shayler, P. J., Wiseman, M. W., and Ma, T., 1990, "Improving the Determination of Mass Fraction Burnt," SAE Paper No. 900351.
[13] Brunt, M. F., Rai, H., and Emtage, A. L., 1998, "The Calculation of Heat Release From Engine Pressure Data," SAE Paper No. 981052.
[14] Ball, J. K., Raine, R. R., and Stone, C. R., 1998, "Combustion Analysis and Cycle-By-Cycle Variations in Spark Ignition Engine Combustion: Part 1 and 2," Proc. Inst. Mech. Eng., Part D (J. Automob. Eng.), **212**, pp. 381–389 (Part 1) and pp. 507–523 (Part 2).
[15] Bargende, M., 1995, "Most Optimal Location of 50% Mass Fraction Burned and Automatic Knock Detection Components for Automatic Optimization of SI-Engine Calibrations," Motortech. Z., **56**, pp. 632–638.
[16] Leonhardt, S., Muller, N., and Isermann, R., 1999, "Methods for Engine Supervision and Control Based on Cylinder Pressure Information," IEEE/ASME Trans. Mechatron., **4**(3), pp. 235–245.
[17] Pipitone, E., and Beccari, A., 2004, "Proportional Integral Spark Timing Control by Means of In-Cylinder Pressure Analysis," FISITA 2004-World Automotive Congress, Barcelona, Spain, May 3–27.
[18] Matekunas, F. A., Battiston, P. A., Chang, C. F., Sellnau, M. C., and Lancaster, D. R., 2000, "Cylinder-Pressure-Based Engine Control Using Pressure-Ratiomanagement and Low-Cost Non-Intrusive Cylinder Pressure Sensor," SAE Paper No. 2000-01-0932.
[19] Randolph, A. L., 1990, "Methods of Processing Cylinder-Pressure Transducer Signals to Maximize Data Accuracy," SAE Paper No. 900170.
[20] Brunt, M. F. J., and Pond, C. R., 1997, "Evaluation of Techniques for Absolute Cylinder Pressure Correction," SAE Paper No. 970036.
[21] Nilsson, Y., and Eriksson, L., 2004, "Determining TDC Position Using Symmetry and Other Methods," SAE Paper No. 2004-01-1458.
[22] Stas, M. J., 1996, "Thermodynamic Determination of T.D.C. in Piston Combustion Engines," SAE Paper No. 960610.
[23] Pipitone, E., Beccari, A., and Beccari, S., 2007, "The Experimental Validation of a New Thermodynamic Method for TDC Determination," SAE Paper No. 2007-24-052.

Results From an Engine Cycle Simulation of Compression Ratio and Expansion Ratio Effects on Engine Performance

Jerald A. Caton

Department of Mechanical Engineering,
Texas A&M University,
College Station, TX 77843-3123
e-mail: jcaton@tamu.edu

This investigation quantified the effects of compression ratio (CR) and expansion ratio (ER) on performance, efficiency, and second law parameters for an automotive, spark-ignition engine. The well known increase in engine performance for increasing CR and ER is demonstrated. These increases for brake engine performance are modest for CRs greater than about 10 for the conditions studied. The results demonstrated that the increasing friction and heat losses for the higher CRs are of the same order as the thermodynamic gains. Also, the results included the destruction of availability during combustion. For a part load condition, the availability destroyed decreased from about 23% to 21% for CRs of 4 and 10, respectively. In addition, this study examined cases with greater ERs than CRs. The overall cycle for these cases is often called an "Atkinson" cycle. For most cases, the thermal efficiency first increased as ER increased, attained a maximum efficiency, and then decreased. The decrease in efficiency after the maximum value was due to the increased heat losses, increased friction, and ineffective exhaust processes (due to the reduced cylinder pressure at the time of exhaust valve opening). For part load cases, the higher ER provided only modest gains due to the increased pumping losses associated with the constant load requirement. For the wide open throttle cases, however, the higher ERs provided significant gains. For example, for a compression ratio of 10, expansion ratios of 10 and 30 provided brake thermal efficiencies of about 34% and 43%, respectively. Although the net thermodynamic gains are significant, large ERs such as 30 may not be practical in most applications. [DOI: 10.1115/1.2939013]

Introduction

The importance of compression ratio (CR) and expansion ratio (ER) for conventional, reciprocating, internal combustion engines has been recognized from the very beginning of engine development. A large literature exists for both experimental and analytical results as functions of CR and, to a lesser extent, of ER. Increases of the CR and ER are known to increase the thermodynamic advantages, but these gains are often limited by knock. The current work is a detailed study of the effects of CR and ER on engine performance from both a first law and second law perspective.

An important feature of the current work is to examine the effects of the ER independent of the CR. This arrangement will be described in more detail below, but, in general, this is often called an Atkinson cycle. The actual mechanism will not be the focus, but rather, the benefits of such arrangements from a thermodynamic viewpoint. A wide range of conditions will be examined including part load and full load operations.

The following sections of this paper will include a brief review of previous work, a description of the cycle simulation, a description of the engine and operating conditions, and a presentation of the results. The results will be divided into three sections: (1) CR effects, (2) ER effects for part throttle, and (3) ER effects for wide open throttle (WOT). Finally, the paper will end with a summary and conclusions.

Brief Review of Previous Research

Investigations of engine performance as a function of CR has a long history. An early, classical paper by Caris and Nelson [1] is often cited with respect to the importance of CR for spark-ignited engines. By using special fuels and fuel additives, spark knocking was avoided even for the highest CRs tested. They demonstrated maximum performance for a specific CR, and for greater CRs the performance remained constant or decreased slightly. Another useful reference is the work by Muranaka et al. [2]. They reported experimental results and provided explanations for the improvement in performance for increases in CR. They found that the items that limit the improvement of thermal efficiency as CR increases were increased heat transfer and incomplete or slow burning. They stated that the effect of CR changes on combustion duration was minor.

For a conventional, four-stroke cycle, spark-ignited engine, the compression and expansion strokes are equal. The gases at the end of a conventional expansion proccess, however, possess the potential to produce more work if allowed to expand to a greater volume. By the use of special linkages, the ER could be greater than the CR, and thereby, provide the potential for greater overall thermodynamic gains. This concept, originally patented [3] in the mid-1880s by James Atkinson, a British engineer, is known as the Atkinson cycle or (in a generic sense) an overexpanded cycle.

Another concept that is closely related is often called the Miller cycle [4], and involves using either early or late intake valve closing to reduce the effective CR relative to the ER. This concept has been relatively successful and exists in a number of commercial engines (e.g., Ref. [5]). Although the Atkinson and Miller cycles are related, they possess unique features. For example, the Miller cycle with late intake valve closing will move gases into the intake system during the initial period of the compression stroke. Also, some studies have shown that certain timings of the

intake valve closing cause poor combustion [6]. The Atkinson cycle, on the other hand, can independently optimize valve events. The Atkinson cycle, however, will require a more complex mechanism and incur additional frictional losses.

Previous studies of the Atkinson and Miller cycles are numerous (e.g., Refs. [7–10]). Most of these studies are based on the Miller cycle; only a few are based on mechanical features, which provide a longer expansion stroke relative to the compression stroke (e.g., Ref. [11]).

Engine Cycle Simulation Description

The cycle simulation used in this work has been described in detail elsewhere [12–14]. This simulation is largely based on thermodynamic formulations and is a complete representation of the four-stroke cycle including the intake, compression, combustion, expansion, and exhaust processes. The simulation uses detailed thermodynamic gas properties including equilibrium composition for the burned gases. The cylinder heat transfer is adopted from the correlation by Woschni [15], and the combustion process is based on a mass fraction burn relation from Wiebe [16]. The major assumptions and approximations used in the development are listed elsewhere [14]. Although no experimental data are cited in the current paper, previous work [17,18] has demonstrated the success of these types of simulations for duplicating experimental results.

Energy Equations. As a result of the thermodynamic analysis, governing differential equations are obtained for the gas temperatures, the cylinder pressure, the volumes, and the masses. The instantaneous cylinder conditions (temperatures, pressure, volumes, masses, and thermodynamic properties) as a function of crank angle are obtained by the simultaneous numerical integration of the various differential equations.

The required input information, and the boundary conditions for the inlet (temperature and pressure) and for the exhaust (pressure) are specified. To begin a particular engine cycle calculation, several parameters are not known. The initial amount of exhaust gases (residual), and the initial cylinder gas temperature and pressure must be assumed. The complete calculation is repeated until the final values agree with the initial values. Depending on the initial values and the specified tolerance, this procedure usually finds convergence within about three complete cycles.

The engine friction includes the mechanical friction and the pumping friction. The mechanical friction, in turn, includes the rubbing friction (such as from the crank, pistons, and valve train) and the work associated with the auxiliaries (such as oil and water pump, and alternator). Algorithms for each of these items were published by Sandoval and Heywood [19], and these are used here exactly as presented.

Availability Parameters. The available energy (or exergy) of the fuel and the cylinder gases is described by a number of parameters. Full details are available elsewhere [13,14]. Once the thermodynamic properties are known for a given set of conditions, the determination of availability is fairly straightforward. Availability is not a conserved property, and hence, may be destroyed by irreversibilities such as heat transfer through a finite temperature difference, combustion, friction, or mixing processes. The irreversibilities are determined via availability balances for each process [13,14].

Engine and Operating Conditions

The selected engine for this study was an automotive, V-8 configuration with a bore and stroke of 101.6 mm and 88.4 mm, respectively. This engine has been used in a series of previous studies (e.g., Refs. [12–14,17]). Table 1 lists the engine specifications as used in the present work. For the Wiebe combustion parameters, the following values were used as recommended by Heywood [18]: $m=2.0$ and $a=5.0$.

Table 1 Engine specifications

Item	Value
No. of cylinders	8
Bore (mm)	101.6
Stroke (mm)	88.4
Crank rad/Con rod ratio	0.305
Compression ratio	various
Inlet valves:	
Diameter (mm)	50.8
Max lift (mm)	10.0
Opens (°CA aTDC)	357
Closes (°CA aTDC)	−136
Exhaust valves:	
Diameter (mm)	39.6
Max lift (mm)	10.0
Opens (°CA aTDC)	116
Closes (°CA aTDC)	371
Valve overlap (deg)	14°
Heat transfer multiplier	1.33

Results and Discussion

This study was divided into two major parts: (1) a study of the effects of CR (with an equal ER) and (2) a study of the effects of the ER (where the CR was smaller and constant).

Study Constraints. The following results are based on a set of assumptions and approximations, which did not consider all features. For example, combustion stability, cycle-to-cycle variations, or other combustion issues are not included. In addition, knock, preignition, or other abnormal combustion phenomena are not considered. In addition, mechanical friction was based on conventional engines (further comments on friction are described below). Due to these assumptions and approximations, some of the following results may be optimistic. The following results are for an engine speed of 1400 rpm, an equivalence ratio of 1.0, and MBT (maximum brake torque) timing.

Compression Ratio. Figure 1 shows the indicated thermal efficiencies as functions of compression ratio for ideal "Otto" cycles and for two simulation cases (part load and WOT). The ideal Otto cycle efficiency results are based on the simple relation:

$$\eta = 1 - r^{(1-k)} \tag{1}$$

where r is the compression ratio and k is the ratio of specific heats. The ratio of the specific heats, k, was selected to be either 1.4 (cold) or 1.3 (hot). These values span the typical range expected for most operating conditions. Recall that the ideal Otto cycle efficiency is derived for adiabatic processes with instantaneous heat addition at TDC, with no mechanical or fluid friction, and no flows. The other two curves in this figure represent the net indicated thermal efficiencies from the simulation for the part load (bmep=325 kPa) and WOT cases. In general, the thermal efficiency increases with increases of CR. The greatest increases are for the initial CR increases up to about 10. The thermal efficiency continues to increase for further increases in CR, but the gains are less and less. Relative to the simulation results, the ideal results are roughly 50% too high. A major part of the difference between the ideal and simulation results is the assumption of adiabatic processes for the ideal calculations. In addition, the lack of flow processes, the instantaneous heat addition, and the constant property assumption contribute to the overprediction of thermal efficiency.

The relative importance of cylinder heat transfer is examined next. The cylinder heat transfer is related to the surface area (A_{surf}), the heat transfer coefficient (h_{heat}), and the temperature difference between the gas and the cylinder walls (ΔT)
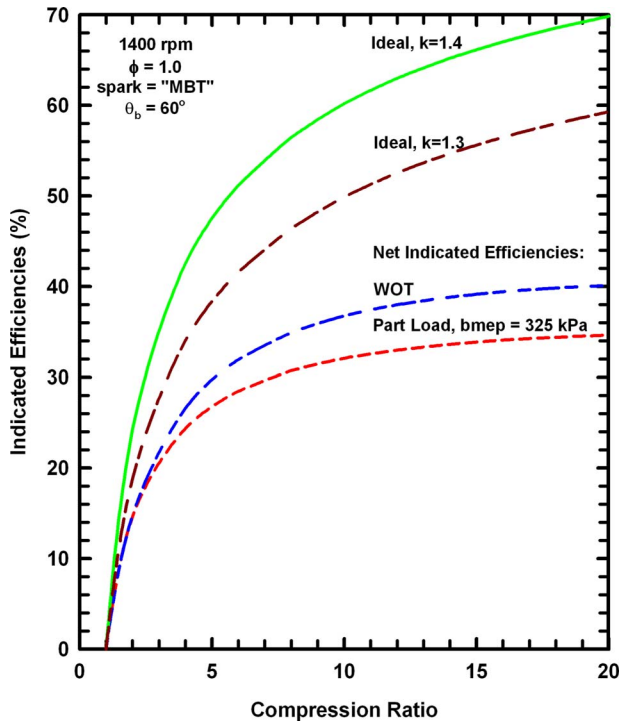
Fig. 1 Indicated thermal efficiencies as functions of CR for two ideal "Otto" cycles, for a part load (bmep=325 kPa) case and for a WOT case

Fig. 2 Relative energy values as functions of CR for the part load case

$$\dot{Q} \alpha A_{surf} h_{heat} \Delta T \qquad (2)$$

The surface area decreases slightly for increasing CR, and the temperature difference first increases and then decreases for increasing CRs (but these are modest changes) [14]. The heat transfer coefficient increases with increasing CR. For an increase of CR from 6 to 20, the peak heat transfer coefficient almost triples in value. The net result of these items is a slight increase in the heat transfer as CR increases. As compression ratio increases, the thermal efficiency and the heat transfer increase, and this results in a decrease in the net exhaust energy.

Figure 2 shows the distribution of the fuel energy between work, heat transfer, and exhaust as functions of CR for the part load case. Brake and indicated work increase as CR increases. Also shown is the slight increase in friction work due to the increase in CR. The heat transfer fraction increases and the net exhaust energy fraction decreases as CR increases. Finally, at the top of the figure, a small amount (0.7%) of the fuel energy is unburned.

In contrast to Fig. 2, Fig. 3 shows the distribution of the relative availability as a function of CR for the same part load case. The following is a description of these results from the bottom to the top of the figure. Again, the indicated work increases as CR increases, and this is similar to Fig. 2. The next item is the availability moved with the heat transfer, which increases as CR increases, as described above. The net availability that leaves with the exhaust gases decreases as CR increases. The availability destroyed during the combustion process only slightly decreases as CR increases (this is examined more fully below). The availability destroyed as the incoming fuel-air mixture mixes with the residual gases decreases as CR increases. This is largely a result of the high residual fractions associated with the lower CR cases. Finally, at the top is the availability associated with the unburned fuel.

Figure 4 shows the availability destroyed during the combustion process as functions of CR for the part load and WOT cases. The availability destroyed decreases from about 23% to about
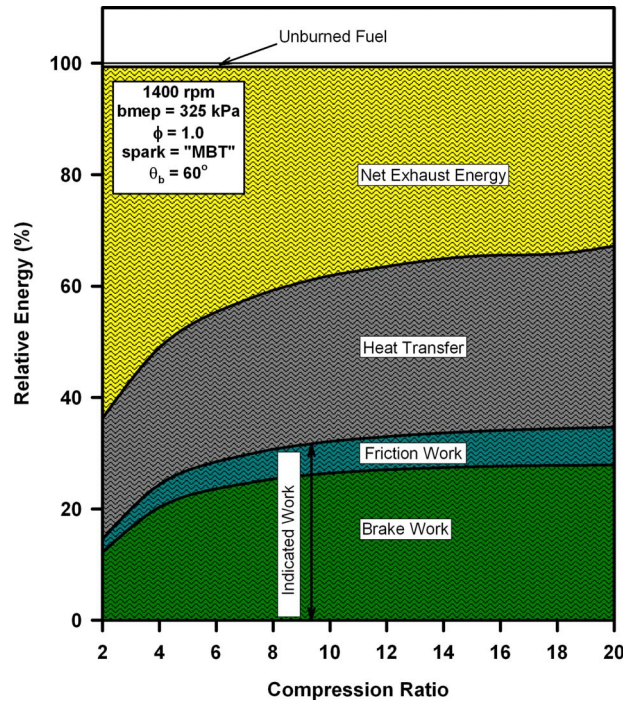
21% for the part load case as the compression ratio increases from 4 to 10. For increases of CR from 10 to 20, the availability destroyed is nearly constant. The WOT case results in slightly less availability destroyed for the higher CRs. The results in Fig. 4 are largely a result of temperature and pressure changes. The average gas temperature during the combustion process increases for CR increases from 2 to 8 [14]. This is, at least, a part of the reason for the decrease in the availability destruction for this range of CR.
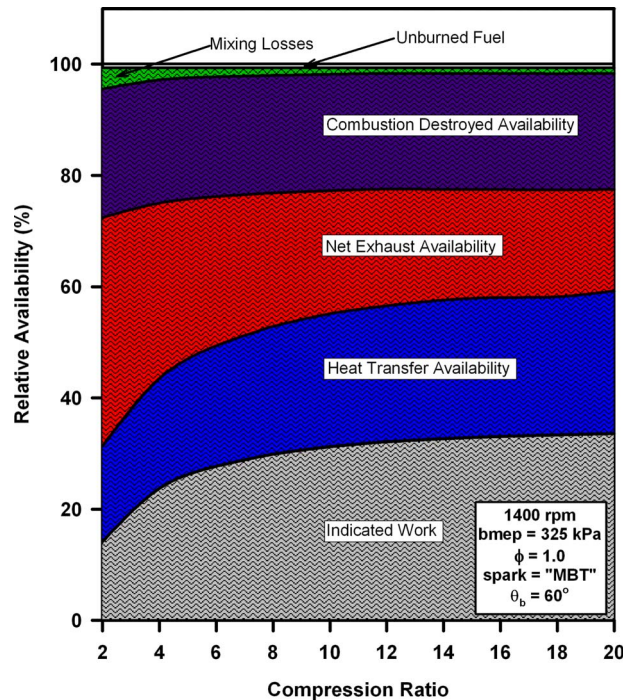

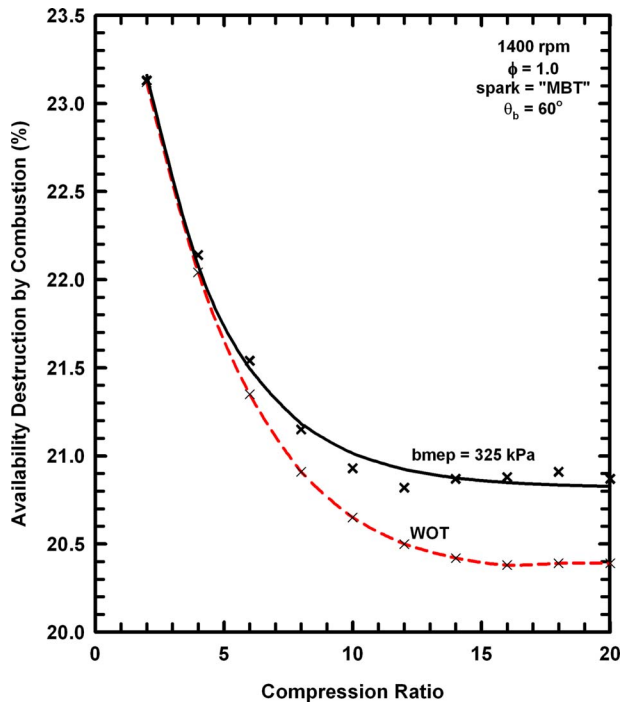**Fig. 3 Relative availability values as functions of CR for the part load case**

Fig. 4 Availability destroyed during the combustion process as functions of CR for the part load and WOT cases

For the CR range of 8–20, the temperature decrease is offset by the pressure increases, such that the destruction of availability decreases slightly.

These results were for CRs up to 20. Higher CRs were briefly examined. The trends were maintained for a CR of 40, and no particular advantage was observed. The trend to lower combustion temperatures continued. For example, for a CR of 40 for the part load case, the average gas temperature during combustion was 1550 K, and the availability destroyed during the combustion process was 21.4%.

Expansion Ratio: Part Load. In the above, a conventional engine was examined, which had the same CR and ER. Since the ER is expected to be more important than the CR in terms of thermodynamic work production, an Atkinson cycle was examined next. To study the Atkinson cycle, a number of approaches may be considered. The current study has adopted the following set of assumptions and approximations.

- The piston motion will be assumed to be approximated by two superimposed motions based on the classic "slider-crank" mechanism.
- The clearance volume will be based on the CR and the stroke dimension (S_{comp}) of the standard engine.
- By selecting an ER and using the clearance volume from above, the expansion stroke (S_{exp}) can be determined.
- The transition between the compression and expansion strokes will be at 0.0°CA (TDC during combustion) and 360°aTDC.
- The engine mechanical friction will be based on the standard engine using the CR. The slight increase of friction due to the longer expansion stroke will be neglected. (The effect of other friction assumptions are considered at the end of the results section.)
- The engine performance parameters (such as bmep) will be based on the standard engine configuration using the compression stroke to determine the displaced volume.
- As mentioned above, items such as knock, preignition,

roughness, and cyclic variability are ignored for this preliminary study.

First, some of the required variables will be defined. The CR follows the normal definition:

$$CR = \frac{V_{comp}}{V_{cl}} \tag{3}$$

where V_{comp} is the total cylinder volume based on the compression stroke length (S_{comp}) and V_{cl} is the clearance volume. The ER is

$$ER = \frac{V_{exp}}{V_{cl}} \tag{4}$$

where V_{exp} is the total cylinder volume based on the expansion stroke length (S_{exp}). The "displaced" volumes are

$$V_{disp,compression} = \frac{\pi B^2}{4} S_{comp} \tag{5}$$

$$V_{disp,expansion} = \frac{\pi B^2}{4} S_{expansion} \tag{6}$$

The first example of results for the Atkinson cycle is based on a CR of 15 and an ER of 20. Figure 5 shows the instantaneous cylinder volume as a function of crank angle for this configuration, and for reference, also shows the cylinder volume for the conventional case where the CR and ER are the same (and equal to 15). To the right of the figure is a schematic of the cylinder arrangement with the two stroke dimensions indicated. The cylinder volume decreases during the compression stroke from intake valve close (IVC) to TDC (0.0°CA), and then increases to a maximum volume during the expansion stroke from TDC to 180°aTDC. Although two expressions were used for the volume computation, the transition appears smooth on this scale.

Figure 6 shows the computed brake thermal efficiency as functions of ER for three CR (6, 10, and 15) for the base case part load engine conditions. For these computations, the bmep was constant (=325 kPa)—so as the brake efficiency increased, the inlet pressure was reduced. For each CR case, as the expansion ratio increases, the thermal efficiency first increases, reaches a maximum, and then decreases. The ER for the highest efficiency appears to be equal to about the CR plus three. The use of this ER provides a thermal efficiency increase of about 1% (e.g., from 24% to 25%). These results are examined more fully in the following.

First, the case with a CR of 15 and an ER of 20 will be examined. This case represents the highest efficiencies of the cases examined. The longer expansion stroke results in a maximum cylinder volume of about 0.973 dm³, while the conventional case has a maximum cylinder volume of 0.717 dm³. The inlet pressure is slightly lower for the overexpanded case, and this results in generally lower pressures throughout most of the cycle. The overexpanded case has slightly higher temperatures for most of the cycle.

Figure 7 shows the intake and exhaust flow rates as functions of crank angles for the two cases. The most significant difference is the lower flow rates during the blowdown portion of the exhaust flow for the overexpanded cases. This is because of the greater expansion, which results in a lower cylinder pressure at the time of exhaust valve opening (EVO). This is compensated by the greater flow rates during the exhaust displacement phase of the exhaust process. The effect of the exhaust valve open time is examined below.

The next item to discuss is the results in Fig. 6, which indicated that for each CR a specific ER provided the maximum efficiency. This will be examined for the case with a CR of 6.0. The relative heat transfer increases as the ER increases, largely due to the increase of surface area as the ER increases. The relative energy leaving in the exhaust first decreases, and then increases slightly for the ERs greater than about 12. This is a net result of the energy
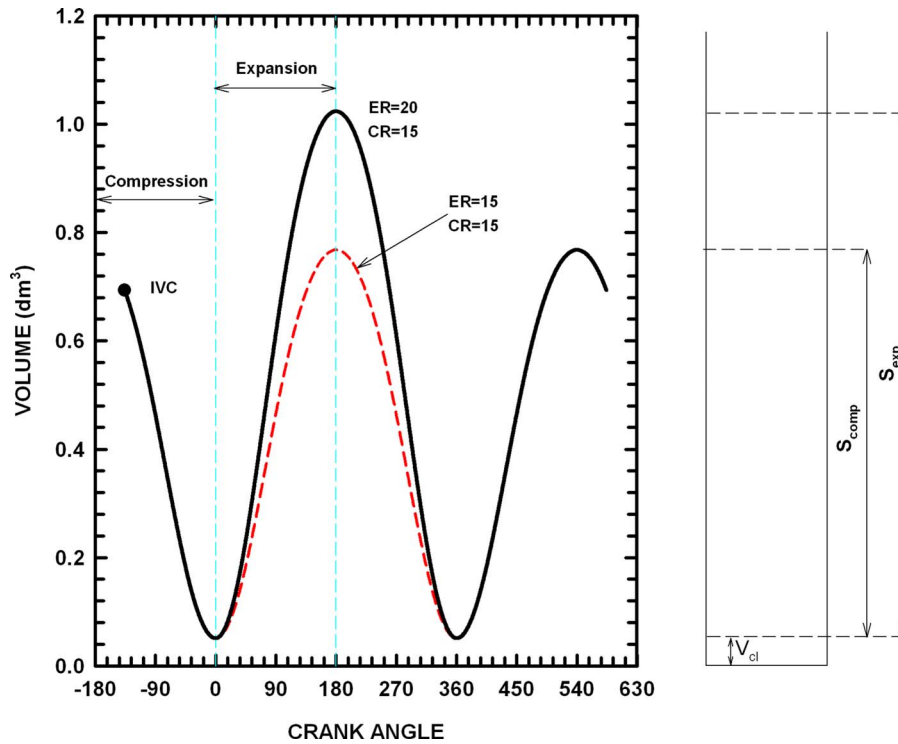
Fig. 5 Cylinder volume as a function of crank angle for a CR of 15 and for ERs of 15 (dashed lines) and 20 (solid lines). Schematic of engine cylinder shown on the right side.

delivered as work and transferred out of the system via heat transfer. For the higher ERs, the work decreases faster as the heat transfer increases, and this results in a net increase in the exhaust energy.

The cases, which will be examined in some detail, are for ER of

8 (near maximum efficiency) and 10 (both for a CR of 6). The question is why does the thermal efficiency begin to decrease even as the ER increases from 8 to 10. Due to the longer expansion stroke, when the exhaust valve opens the cylinder pressure is lower for the case with the higher ER of 10. One of the most significant differences is the much lower flow rates during the
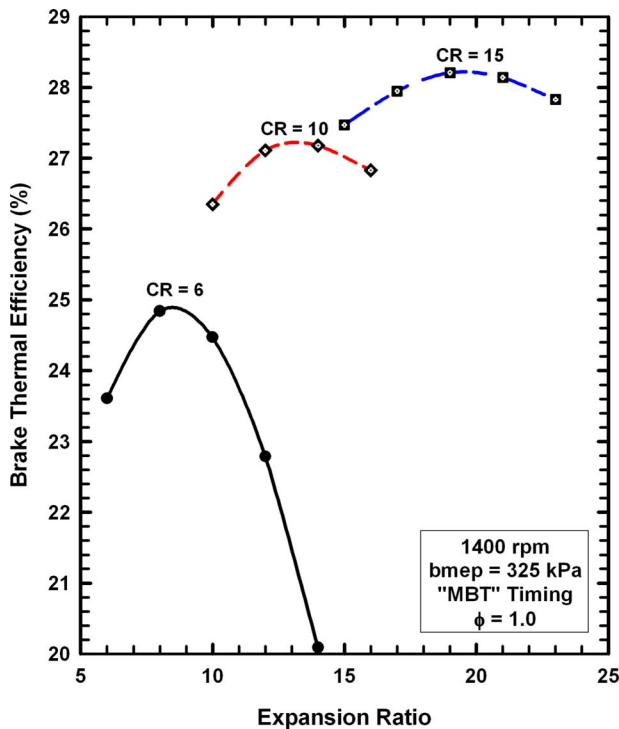
Fig. 6 Brake thermal efficiency as functions of the ER for the base case for three CRs
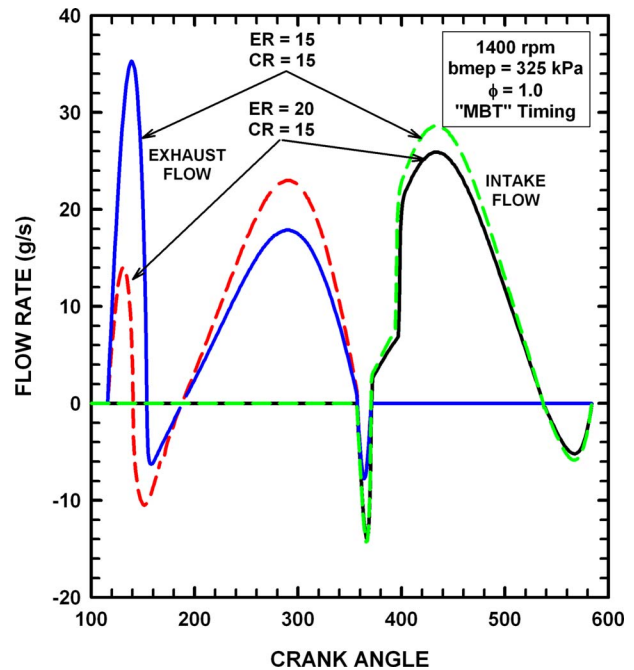
Fig. 7 Exhaust and intake flow rates as functions of crank angle for the base case for a CR of 15 and for ERs of 15 (dashed lines) and 20 (solid lines)

Journal of Engineering for Gas Turbines and Power
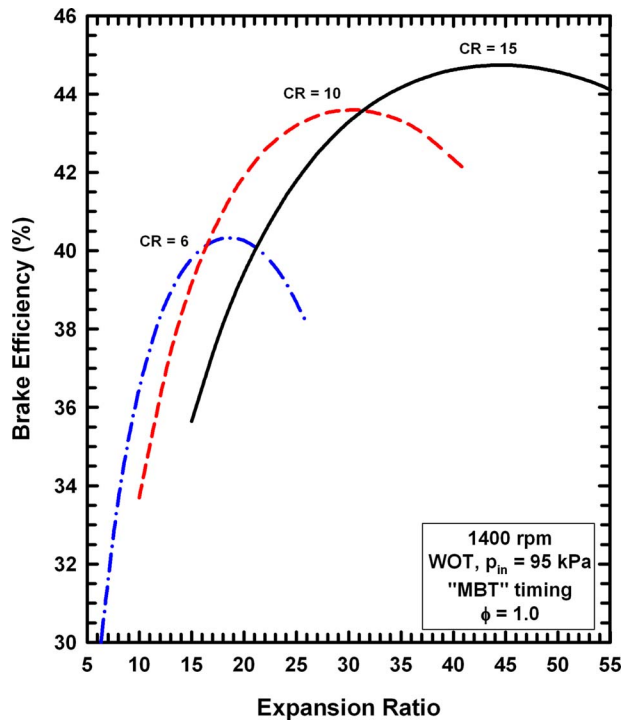
Fig. 8 Brake thermal efficiency as a function of ER for CRs of 6, 10, and 15 for an engine speed of 1400 rpm and an inlet manifold pressure of 95 kPa (WOT)
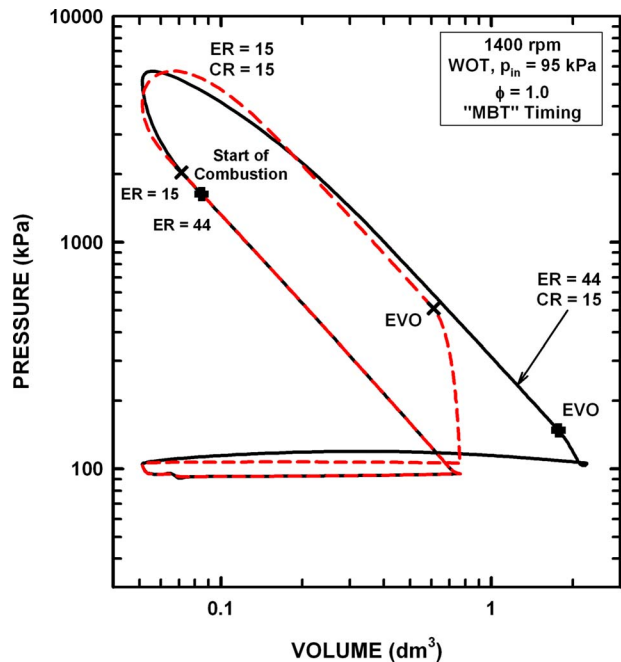

Fig. 9 Log of cylinder pressure as a function of log of cylinder volume for a CR of 15 and ERs of 15 and 44 for an engine speed of 1400 rpm and an inlet manifold pressure of 95 kPa (WOT)

blowdown portion for the case with an ER of 10. In fact, for ERs higher than 10, due to the low cylinder pressures, the initial blowdown is back into the cylinder (rather than out of the cylinder). The lack of an effective exhaust blowdown for higher ERs is one of the reasons that the higher ERs result in decreasing efficiencies.

Since the timing of the EVO may be important, this was examined as well. For the case with a CR of 6 and an ER of 10, two EVO timings were examined: an early opening at 96°aTDC and a late opening at 146°aTDC. The cylinder pressures and thermal efficiencies were nearly the same for these changes of the EVO.

Finally, the destruction of availability during the combustion process as a function of ER was examined. For the case with a CR of 6, the percentage of availability destroyed was nearly constant, and ranged between 21.74% and 21.79% for ERs between 6 and 14. One of the major reasons for this negligible difference is the modest changes of the combustion gas temperatures as the expansion ratio increased.

Expansion Ratio: WOT. In addition to the above results for a part load condition, results were obtained for the use of greater ERs for the case of WOT. Figure 8 shows the brake thermal efficiency as functions of the ER for three CRs (6, 10, and 15). For each CR, the thermal efficiency first increases, reaches a maximum, and then decreases. The ER for the highest thermal efficiency is about 19, 29, and 44 for the CRs of 6, 10, and 15, respectively. The use of these ERs resulted in an increase in the thermal efficiency of about 10%. For example, for a CR of 6, the brake thermal efficiency increased from about 30% to slightly over 40% as the ER increases from 6 to about 19. Compared to the previous part load cases, the WOT cases result in much greater improvements with greater values of ERs. The following will discuss some aspects of these results.

Figure 9 shows the log of the cylinder pressure as a function of the log of the cylinder volume for the WOT case with the highest brake thermal efficiency (of the cases examined), which was for a CR of 15 and an ER of 44 (solid line). For comparison, the results for the WOT case for a CR of 15 and an ER of 15 (standard

engine configuration) are included (dashed line). The pressures during the compression stroke are the same for both configurations, but the pressures during the expansion are different, and of course, for the overexpanded configuration, the expansion proceeds to a much greater volume. The additional area within the pressure-volume diagram associated with the overexpanded configuration is indicative of the additional work (power) obtained with the greater expansion. The pressures for the exhaust stroke are generally higher for the overexpanded configuration, but the pressures during the intake stroke are nearly the same.

Figure 10 shows the mass flows as functions of crank angle for the two cases. For the standard configuration, the blowdown portion of the exhaust flow is significant whereas for the overexpanded case, the blowdown portion is much less significant. For the overexpanded case, the majority of the exhaust flow occurs during the displacement portion of the exhaust flow. In addition, for the overexpanded case, the backflow after the blowdown is much more significant. For ERs greater than about 44 (not shown), the exhaust process is compromised, and when the exhaust valve first opens, the flow is back into the cylinder. The intake flows are nearly the same for both configurations.

For completeness, the availability destroyed due to combustion was determined for the WOT cases, and was found to increase slightly (from about 20.2% to 21.0%) as the ER increases from 15 to 55 for a CR of 15. This slight increase is due to the lower combustion temperatures associated with the higher expansion cases. Since the work output increases for the higher ERs, the gas temperatures decrease, which is a major cause of availability destruction during the combustion process [13,14].

One final consideration was the mechanical friction. For an overexpanded configuration, the mechanical friction would be expected to be higher due to the additional mechanism and the longer stroke. This can not be quantified without some knowledge of the specific design and experimental information. To explore this issue, some estimates were completed. By assuming that the friction was due to an engine configuration possessing the ER for both the compression and expansion strokes (a higher estimate for the friction component), the maximum thermal efficiency decreased by about 2% (i.e., from 45% to 43%). In addition, the
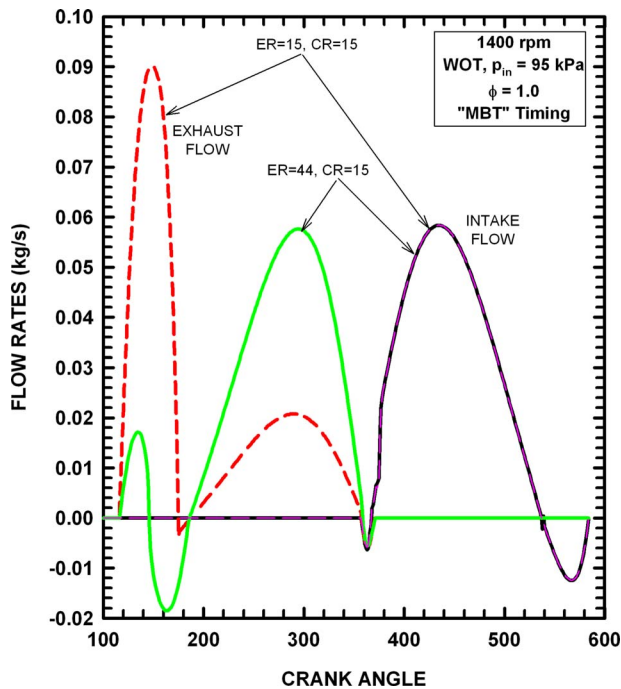
Fig. 10 Mass flow rates as a function of crank angle for a CR of 15 and two ERs (15 and 44) for an engine speed of 1400 rpm and an inlet manifold pressure of 95 kPa (WOT)

optimum ER for the higher friction case decreased. Again, a more detailed consideration of friction would be needed for a particular mechanism.

Summary and Conclusions

This paper has presented results for the effects of CR and ER on performance, efficiency, and second law parameters for an automotive, spark-ignition engine. The cases with greater ERs than CRs are often called Atkinson cycles. For these cases, the ER was assumed independent of the CR. The results of this study may be summarized as follows.

- Indicated and brake performance increase for increases in CR. These gains are most significant up to a CR of about 10.
- For the highest CRs (>10), gains of brake performance and efficiency with further CR increases are modest for the conditions studied. The results demonstrated that the increasing friction and heat losses for the higher CRs are of the same order as the thermodynamic gains.
- For the part load condition, the availability destroyed due to the combustion process decreased from about 23% for a CR of 4 to about 21% for a CR of 10.
- The study included ERs up to four times the CR. For most cases, the thermal efficiency first increased as ER increased, then attained a maximum efficiency, and then decreased. The decrease in efficiency after the maximum value was shown to be due to increased heat losses, increased friction, and ineffective exhaust processes (due to the reduced cylinder pressure at the time of EVO).
- For the part load cases, the higher expansion ratio provided only modest gains due to increased pumping losses associated with the constant load requirement.

- For the WOT cases, however, the higher ERs provided significant gains. For example, for a CR of 10, ERs of 10 and 30 provided brake thermal efficiencies of about 34% and 43%, respectively. Although the net thermodynamic gains are significant, large ERs such as 30 may not be practical for most applications.
- For the WOT cases, for a CR of 15, the availability destroyed due to the combustion process increased slightly from about 20.2% to 21.0% as the ER increased from 15 to 55.

Acknowledgment

References

[1] Caris, D. F., and Nelson, E. E., 1959, "A New Look at High Compression Engines," SAE Trans., **67**, pp. 112–124.
[2] Muranaka, S., Takagi, Y., and Ishida, T., 1987, "Factors Limiting the Improvement in Thermal Efficiency of S. I. Engine at Higher Compression Ratio," SAE Paper No. 870548.
[3] Atkinson, J., 1887, "Gas Engine," U.S. Patent No. 367,496.
[4] Miller, R. H., 1947 "Supercharging and Internal Cooling for High Output," SAE Trans., **69**, pp. 453–464.
[5] Goto, T., Hatamura, K., Takizawa, S., Hayama, N., Abe, H., and Kanesaka, H., 1994, "Development of V6 Miller Cycle Gasoline Engine," SAE Paper No. 940198.
[6] Hara, S., Nakajima, Y., and Nagumo, S., 1985, "Effects of Intake-Valve Closing Timing on Spark-Ignition Engine Combustion," SAE Paper No. 850074.
[7] Boggs, D. L., Hilbert, H. S., and Schechter, M. M., 1995, "The Otto–Atkinson Cycle Engine—Fuel Economy and Emissions Results and Hardware Design," SAE Paper No. 950089.
[8] Chen, L., Lin, J., Sun, F., and Wu, C., 1998, "Efficiency of an Atkinson Engine at Maximum Power Density," Energy Convers. Manage., **39**(3/4), pp. 337–341.
[9] Shiga, S., Hirooka, Y., Miyashita, Y., Yagi, S., MacHacon, H. T. C., Karasawa, T., and Nakamura, H., 2001, "Effect of Over-Expansion Cycle in a Spark-Ignition Engine Using Late-Closing of Intake Valve and Its Thermodynamic Consideration of the Mechanism," International Journal of Automotive Technology, **2**(1), pp. 1–7.
[10] Wu, C., Puzinauskas, P. V., and Tsai, J. S., 2003, "Performance Analysis and Optimization of a Supercharged Miller Cycle Otto Engine," Appl. Therm. Eng., **23**, pp. 511–521.
[11] Raynes, S. H., 1998, "An Atkinson Cycle Engine for Low Pollution," *Proceedings of Combustion Engines and Hybrid Vehicles*, Apr., 28, Institute of Mechanical Engineers, London, Paper No. C529.
[12] Caton, J. A., 2001, "A Multiple-Zone Cycle Simulation for Spark-Ignition Engines: Thermodynamic Details," *Large-Bore Engines, Fuel Effects, Homogeneous Charge Compression Ignition, Engine Performance and Simulation*, Vol., 2, V. W. Wong, ed., ASME, New York, ICE-Vol. 37-2, New York, pp. 41–58.
[13] Caton, J. A., 2003, "A Cycle Simulation Including the Second Law of Thermodynamics for a Spark-Ignition Engine: Implications of the Use of Multiple-Zones for Combustion," SAE Trans., **111–3**, pp. 281–299.
[14] Caton, J. A., 2007, "The Effects of Compression Ratio and Expansion Ratio on Engine Performance Including the Second Law of Thermodynamics: Results From a Cycle Simulation," *Proceedings of the 2007 Fall Conference of the ASME Internal Combustion Engine Division*, Charleston, SC, Oct. 14–17.
[15] Woschni, G., 1968, "A Universally Applicable Equation for the Instantaneous Heat Transfer Coefficient in the Internal Combustion Engine," SAE Trans., **76**, pp. 3065–3083.
[16] Wiebe, J. J., 1970, "Brennverlauf und Kreisprozess von Verbrennungsmotoren," VEB-Verlag Technik Berlin.
[17] Heywood, J. B., Higgins, J. M., Watts, P. A., and Tabaczynski, R. J., 1979, "Development and Use of a Cycle Simulation to Predict SI Engine Efficiency and NO$_x$ Emissions," SAE Paper No. 790291.
[18] Heywood, J. B., 1988, *Internal Combustion Engine Fundamentals*, McGraw-Hill, New York.
[19] Sandoval, D., and Heywood, J. B., 2003, "An Improved Friction Model for Spark-Ignition Engines," SAE Paper No. 2003-01-0725.

A Numerical Study on the Effect of CO Addition on Flame Temperature and NO Formation in Counterflow CH₄/Air Diffusion Flames

Hongsheng Guo[1]
e-mail: hongsheng.guo@nrc-cnrc.gc.ca

W. Stuart Neill

Institute for Chemical Process and Environmental
Technology,
National Research Council of Canada,
1200 Montreal Road,
Ottawa, ON, K1A 0R6, Canada

A numerical study was carried out to understand the effect of CO enrichment on flame temperature and NO formation in counterflow CH₄/air diffusion flames. The results indicate that when CO is added to the fuel, both flame temperature and NO formation rate are changed due to the variations in adiabatic flame temperature, fuel Lewis number, and chemical reaction. At a low strain rate, the addition of carbon monoxide causes a monotonic decrease in flame temperature and peak NO concentration. However, NO emission index first slightly increases, and then decreases. At a moderate strain rate, the addition of CO has negligible effect on flame temperature and leads to a slight increase in both peak NO concentration and NO emission index, until the fraction of carbon monoxide reaches about 0.7. Then, with a further increase in the fraction of added carbon monoxide, all three quantities quickly decrease. At a high strain rate, the addition of carbon monoxide causes increase in flame temperature and NO formation rate, until a critical carbon monoxide fraction is reached. After the critical fraction, the further addition of carbon monoxide leads to decrease in both flame temperature and NO formation rate. [DOI: 10.1115/1.2906222]

Keywords: diffusion flame, NOₓ, fuel enrichment, carbon monoxide

1 Introduction

Fuel enrichment is a promising concept for reducing fuel consumption and pollutant emission from combustion systems. Usually, hydrogen is selected as the additive for fuel enrichment combustion. Many studies have been conducted for some fundamental concepts of fuel enrichment combustion [1–4].

However, not enough attention has been paid to the effect of fuel enrichment on NOₓ formation in diffusion flames. Naha and Aggarwal [5] investigated the effect of hydrogen addition on NOₓ formation in strained nonpremixed methane and *n*-heptane flames at a fixed strain rate (100 s⁻¹). It was found that the addition of hydrogen has a minor effect on NOₓ formation in methane (CH₄) flames and reduces the formation of NOₓ in *n*-heptane flames. Our previous study [6] on the effect of hydrogen enrichment on NO

formation in CH₄/air diffusion flames at various strain rates showed that the addition of a small amount of hydrogen has negligible effect on NO formation at low to moderate strain rates, but significantly increases NO formation at a high strain rate.

Although hydrogen has been shown to be an effective additive for fuel enrichment technology, it is only an energy carrier. It has to be generated from other fuels or water. A widely used method to obtain hydrogen is reforming hydrocarbon fuels. However, the reformate gas contains not only hydrogen but also carbon monoxide (CO) and some other minor components. If CO and other components contained in reformate gas do not have any negative side effects, or even helps in terms of improving combustion efficiency and reducing pollutant emission, we can directly use reformate gas as the additive in fuel enrichment combustion technology. Therefore, it is of interest to understand the effect of CO enrichment on combustion performance and pollutant emission.

In this paper, a detailed numerical study on the effect of CO addition on the formation of NO in CH₄/air diffusion flames with various strain rates was conducted. The fraction of CO changed from 0 to 0.9. The investigated strain rate covered a wide range.

2 Numerical Model

As in our previous investigation [6], an axisymmetric laminar counterflow flame configuration was employed, with fuel stream issuing from one nozzle and air from another. The simulations assumed the stagnation point flow approximation. The governing equations can be found elsewhere [7]. The calculations were carried out with a code revised from that of Kee et al. [8]. Upwind and center difference schemes were, respectively, used for the convective and diffusion terms in all the governing equations. Adaptive refinement of meshes was done to obtain grid independent results. Radiation heat loss was accounted for by an optically thin model [1].

The potential boundary conditions were used for freestream. The chemical reaction mechanism used is GRI-MECH 3.0 [9]. The thermal and transport properties were obtained by using the database of GRI-MECH 3.0 and the algorithms given in Refs. [10,11]. The pressure and the fresh mixture temperature were 1 atm and 298 K, respectively.

3 Results and Discussion

In all the studied flames, the fuel stream consists of CH₄ and CO. The fraction of CO is defined as $\alpha_{CO} = V_{CO}/(V_{CO} + V_{CH_4})$, with V_{CO} and V_{CH_4} being, respectively, the volume flow rates of CO and CH₄. The fraction of CO in this study covers a range from 0.0 to 0.9 for completeness.

3.1 Flame Temperature. Figure 1 shows the variation of peak flame temperature as the fraction of CO in fuel stream increases at three typical strain rates, a low ($a=10$ s⁻¹), a moderate ($a=100$ s⁻¹), and a high ($a=300$ s⁻¹) one. Since the adiabatic equilibrium flame temperature (called adiabatic temperature hereafter) of CO is higher than that of CH₄ at stoichiometric condition, it was expected that the addition of CO to CH₄ would increase the peak flame temperature. However, the simulation results in Fig. 1 do not support this. Moreover, it is noted that the variation trend of peak flame temperature differs when strain rate is changed.

At $a=10$ s⁻¹, the addition of CO causes a monotonic decrease in peak flame temperature. At $a=100$ s⁻¹ or 300 s⁻¹, the peak temperature is almost constant or slightly increases and then decreases, as α_{CO} increases. These phenomena are due to the combined effects of adiabatic temperature, fuel Lewis number, chemical reaction, and residence time.

If the Lewis number is defined as the ratio of thermal diffusion rate to mass diffusion rate, the peak flame temperature of a diffusion flame will be increased or decreased when the Lewis number is less or greater than unity. The Lewis number of fuel is slightly

[1]Corresponding author.
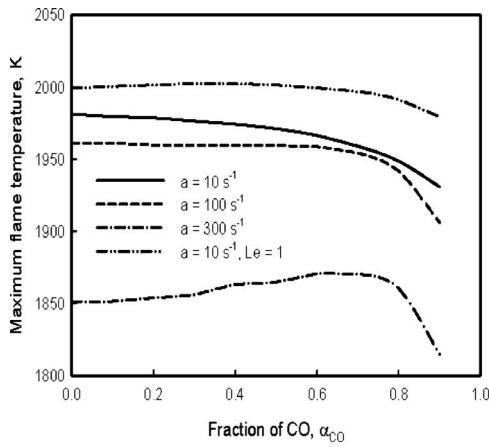
Fig. 1 Variation of peak flame temperature

Fig. 2 Variation of peak NO mole fraction

less than unity for pure CH_4 diffusion flame. When CO is added, the fuel becomes a mixture. The Lewis number of CO is slightly greater than unity, leading to the slightly greater fuel Lewis number in CO enriched mixture than in pure CH_4. The increase in fuel Lewis number tends to decrease the peak flame temperature, which is one reason for the decrease in peak flame temperature at $a=10$ s^{-1} when α_{CO} is small. The almost constant and slight increase in maximum flame temperature at $a=100$ s^{-1} and 300 s^{-1} will be explained later.

To confirm the effect of the fuel Lewis number, extra calculations were carried out at a strain rate of 10 s^{-1} with the Lewis numbers artificially set as unity for all species. The maximum flame temperatures from these extra calculations are also shown in Fig. 1. It is found that being qualitatively consistent with the variation trend of adiabatic temperature, the peak flame temperature slightly increases as α_{CO} is increased from zero to about 0.4. Therefore, the fuel Lewis number is a key factor causing the monotonic decrease in peak flame temperature at a low strain rate. However, with further increasing α_{CO}, similar to normal calculations, the peak flame temperature also starts to decrease. This is because the addition of CO causes variation not only in the fuel Lewis number but also in chemical reactions.

The primary oxidation reaction of CO is OH+CO=H+CO_2. When CO is added to CH_4, the rate of this reaction is increased, and thus more OH is needed. Meanwhile, the main chain branching reaction H+O_2=OH+O is also intensified because more H is formed by the previous one. The net variations of radical OH and combustion intensity depend on the balance between the two reactions when CO is added. At $a=10$ s^{-1}, when α_{CO} becomes bigger, chemical effect causes the flame temperature to decrease, since a large amount of OH is needed to complete the reaction OH+CO=H+CO_2, which results in the reduction in OH concentration and combustion intensity.

With strain rate being increased to a moderate or high value, when a small amount of CO is added, the maximum flame temperature does not change (at $a=100$ s^{-1}) or slightly increases (at $a=300$ s^{-1}). It is because the residence time in these flames is not long enough to complete the combustion of CH_4. With the addition of a small amount of CO to CH_4, the combustion intensity is enhanced due to the reactions OH+CO=H+CO_2 and H+O_2 =OH+O. This enhancement of combustion intensity does not happen at a low strain rate, since the residence time is long enough to complete the combustion of CH_4. However, when α_{CO} is increased to a larger value, the flame temperature also starts to decrease, owing to the consumption of OH by the reaction OH +CO=H+CO_2. This is similar to what is observed in flames of low strain rate.
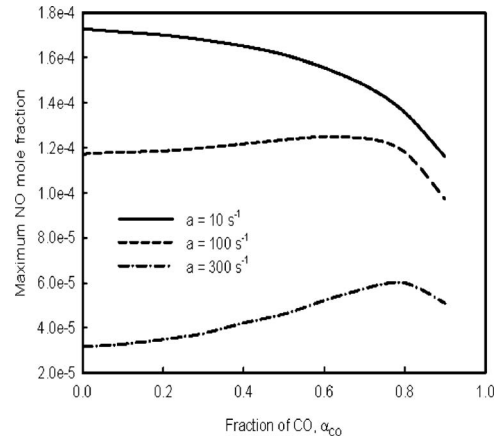
Therefore, the variation of flame temperature is caused by the combination of the effects of adiabatic temperature, fuel Lewis number, chemical reaction, and residence time.

3.2 NO Formation. Figures 2 and 3 show the variations of maximum NO mole fraction and NO emission index, defined as the ratio of total formed NO to total heat release, as α_{CO} changes.

At $a=10$ s^{-1}, the maximum NO concentration monotonically decreases with increasing α_{CO}. However, when the strain rate is increased to a moderate or high value, the maximum NO concentration first increases and then decreases. Being different, at all three strain rates, NO emission index varies in a qualitatively similar way, i.e., first increases to a critical value and then decreases, as α_{CO} is increased. However, the increase rate of NO emission index is smaller at lower strain rates. The critical CO fraction, at which NO emission index reaches its maximum, changes at different strain rates. To explain these phenomena, we first analyze the mechanism of NO formation.

Figure 4 shows the pathway of NO formation for pure CH_4 flame at $a=10$ s^{-1}. The thickness of each line represents the magnitude of the rate and the arrow indicates the direction of the reaction. The paths with rates less than 1.0×10^{-8} mole/(cm^2 s) have been neglected. It is observed that most NO is formed by the reactions HNO (+H,OH)$\rightarrow$NO and N(+OH)$\rightarrow$NO. Apparently, the reactions HNO (+H,OH)$\rightarrow$NO belong to the prompt route, since species HNO is from the paths resulting from the reaction of molecular nitrogen with radical CH. Although the reaction N(+OH)$\rightarrow$NO, which was attributed to the thermal NO formation

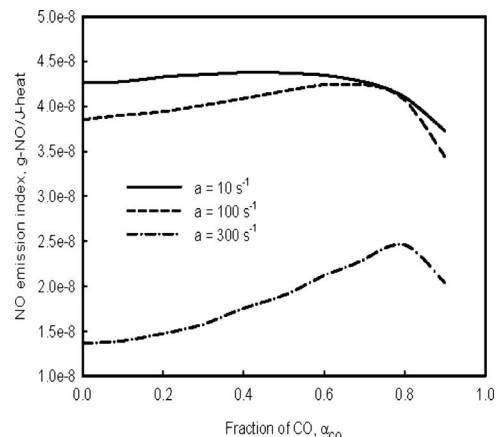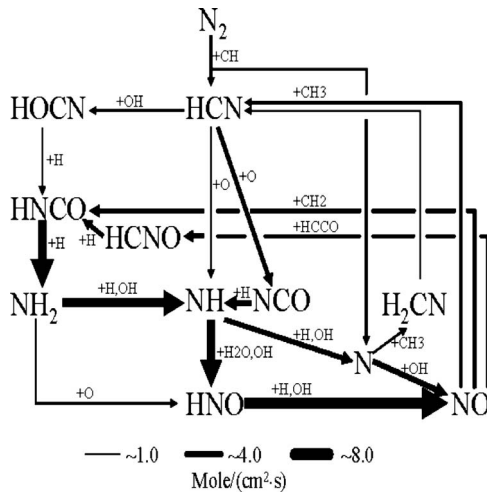**Fig. 3 Variation of NO emission index**

Fig. 4 NO formation pathway in CH$_4$/air at a strain rate of 10 s^{-1}

Fig. 6 Variation of peak CH concentration

route in many references, significantly contributes to NO formation, it is noted that atomic nitrogen participating in this reaction comes from the paths N$_2$(+CH)$\rightarrow$HCN$\rightarrow$NCO$\rightarrow$NH$\rightarrow$N, N$_2$(+CH)$\rightarrow$HCN$\rightarrow$NH$\rightarrow$N and N$_2$(+CH)$\rightarrow$N. Therefore, the formation of atomic nitrogen is initiated by the reaction of molecular nitrogen with radical CH, which is the typical prompt route nitrogen conversion. Consequently, we conclude that prompt route dominates the formation of NO in a pure CH$_4$ diffusion flame.

In addition to the formation, NO is also consumed by reactions with some hydrocarbon radicals, such as CH$_2$, CH$_3$, and HCCO. The consumption of NO is usually called reburning. Figure 5 displays the distribution of NO formation rate for the pure CH$_4$ flame at $a=10$ s^{-1}. It is found that NO is formed on the left side of stagnation plane (near the peak temperature region) and consumed later when transported to stagnation plane. Although not displayed, our results show that other flames have qualitatively similar phenomenon until the fraction of CO is increased to greater than about 0.8, i.e., prompt route dominates NO formation in most of our studied flames.

Now, we can explain the phenomena in Figs. 2 and 3. At $a=10$ s^{-1}, the monotonic decrease in peak NO concentration is because the reduction in flame temperature (as shown in Fig. 1) reduces the formation rate of NO when CO is added. It should be pointed out that although prompt route dominates NO formation, temperature variation still modifies the rates of most reactions. However, the addition of CO moves the primary reaction zone
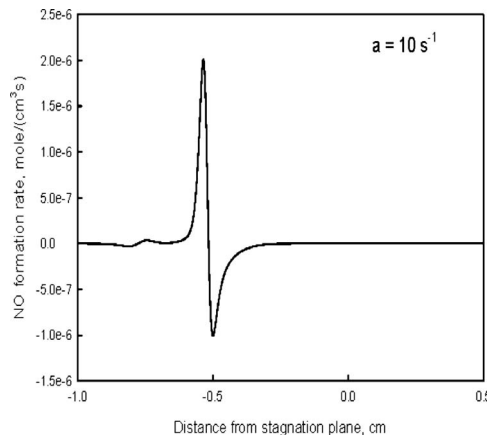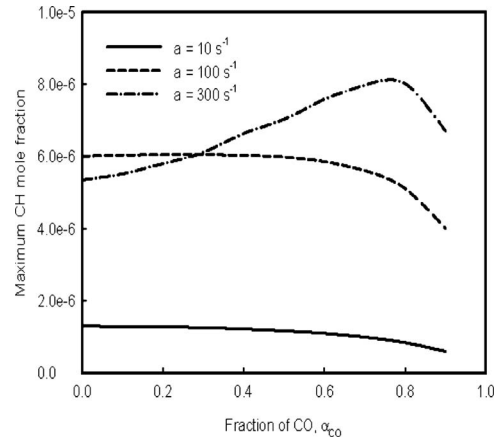
toward the stagnation plane, which also leads to the reduction in the NO reburning rate. When a small amount of CO is added, the reduction in total NO formation (positive rate in Fig. 5) near the peak flame region is less than that of the NO reburning (negative in Fig. 5), resulting in the slight increase in NO emission index. With further increasing the fraction of CO, the significant reduction in NO formation rate results in the decrease in both peak NO concentration and NO emission index.

When the strain rate is increased to a moderate or high value, a small amount of CO addition enhances the combustion intensity of CH$_4$, as mentioned before. This leads to CH radical concentration increase, as shown in Fig. 6. The increase in CH concentration and constant (at $a=100$ s^{-1}) or increase (at $a=300$ s^{-1}) in flame temperature cause the rise in both maximum NO concentration and NO emission index as a small amount of CO is added. This is the reason that both the maximum NO concentration and NO emission index increase when a small amount of CO is added. As noted from Figs. 2, 3, and 6, the rise rate increases with increasing strain rate. It is because the enhancement in combustion intensity is more significant at a high strain rate. With further increasing the fraction of added CO, the situation becomes similar to that at a strain rate of 10 s^{-1}, i.e., both the maximum NO concentration and NO emission index start to decrease.

Therefore, the addition of CO to CH$_4$ may modify the emission characteristics of NO. The effect changes at different strain rates. Overall, we find that the effect of CO addition on NO formation is minor at low to moderate strain rates. Although the addition of CO causes relatively significant increase in NO formation at high strain rate flames, the absolute NO emission level is low for these flames.

4 Conclusions

A numerical study on the effect of CO enrichment on flame temperature and NO formation in counterflow CH$_4$/air diffusion flames has been conducted. The results indicate that the addition of CO to CH$_4$ modifies both flame temperature and NO emission due to the variations in adiabatic flame temperature, fuel Lewis number, and chemical reaction. For a low strain rate flame, the addition of CO causes a monotonic decrease in flame temperature and peak NO mole fraction. However, NO emission index first slightly increases, and then decreases. When the strain rate is increased to a moderate or high value, the addition of a small amount of CO either does not change peak flame temperature too much or slightly increases it. Both peak NO concentration and NO emission index increase when a small amount of CO is added at a moderate or high strain rate. For all the cases studied, both peak flame temperature and NO emission rate start to decrease when additional CO is added.

Fig. 5 Distribution of NO formation rate

References

[1] Guo, H., Smallwood, G. J., Liu, F., Ju, Y., and Gülder, Ö. L., 2005, "The Effect of Hydrogen Addition on Flammability Limit and NO_x Emission in Ultra Lean Counterflow CH_4/Air Premixed Flames," Proc. Combust. Inst., **30**, pp. 303–311.

[2] Guo, H., Smallwood, G. J., and Gülder, Ö. L., 2007, "The Effect of Reformate Gas Enrichment on Extinction Limits and NO_x Formation in Counterflow CH_4/Air Premixed Flames," Proc. Combust. Inst., **31**, pp. 1197–1204.

[3] Guo, H., Liu, F., Smallwood, G. J., and Gülder, Ö. L., 2006, "A Numerical Study on the Influence of Hydrogen Addition on Soot Formation in a Laminar Ethylene-Air Diffusion Flame," Combust. Flame, **145**, pp. 324–338.

[4] Fotache, G. G., Kreutz, T. G., and Law, C. K., 1997, "Ignition of Hydrogen-Enriched Methane by Heated Air," Combust. Flame, **110**, pp. 429–440.

[5] Naha, S., and Aggarwal, S. K., 2004, "Fuel Effects on NO_x Emissions in Partially Premixed Flames," Combust. Flame, **139**, pp. 90–105.

[6] Guo, H., Neill, W. S., and Smallwood, G. J., 2006, "A Numerical Investigation of NOx Formation in Counterflow CH_4/H_2/Air Diffusion Flames," ASME Paper No. IMECE2006–14458.

[7] Giovangigli, V., and Smooke, M. D., 1987, "Extinction of Strained Premixed Laminar Flames With Complex Chemistry," Combust. Sci. Technol., **53**, pp. 23–49.

[8] Kee, R. J., Grcar, J. F., Smooke, M. D., and Miller, J. A., 1985, "A Fortran Program for Modelling Steady Laminar One-Dimensional Premixed Flames," Sandia National Laboratories, Report No. SAND85-8240.

[9] Smith, G. P., Golden, D. M., Frenklach, M., Moriarty, N. W., Eiteneer, B., Goldenberg, M., Bowman, C. T., Hanson, R. K., Song, S., Gardiner, Jr. W. C., Lissianski, V. V., and Qin, Z., http://www.me.berkeley.edu/gri_mech/

[10] Kee., R. J., Warnatz, J., and Miller, J. A., 1983, "A Fortran Computer Code Package for the Evaluation of Gas-Phase Viscosities, Conductivities, and Diffusion Coefficients," Sandia National Laboratories, Report No. SAND 83-8209.

[11] Kee., R. J., Miller, J. A., and Jefferson, T. H., 1980, "A General-Purpose, Problem-Independent, Transportable, Fortran Chemical Kinetics Code Package," Sandia National Laboratories, Report No. SAND 80-8003.

A Numerical Study on the Effect of Water Addition on NO Formation in Counterflow CH_4/Air Premixed Flames

Hongsheng Guo[1]
e-mail: hongsheng.guo@nrc-cnrc.gc.ca

W. Stuart Neill

Gregory J. Smallwood

Institute for Chemical Process and Environmental Technology,
National Research Council Canada,
1200 Montreal Road,
Ottawa, Ontario K1A 0R6, Canada

The effect of water addition on NO formation in counterflow CH_4/air premixed flames was investigated by numerical simulation. Detailed chemistry and complex thermal and transport properties were employed. The results show that the addition of water to a flame suppresses the formation of NO primarily due to flame temperature drop. Among a lean, a stoichiometric, and a rich premixed flame, the effectiveness of water addition is most significant for the stoichiometric flame and least for the rich flame. The addition of water also reduces the formation of NO in a flame because of the chemical effect. Compared to the stoichiometric flame, the chemical effect is intensified in the lean and rich flames. [DOI: 10.1115/1.2432890]

Keywords: premixed flame, water addition, numerical simulation, NO_x

1 Introduction

Li and Williams [1] indicated that the addition of water suppresses NO_x formation through both the thermal and chemical effects in two-stage methane/air flames. Zhao et al. [2], Park et al. [3], and Hwang et al. [4] showed that although the concentration of OH is increased, the formation of NO is decreased, when steam is added to a diffusion flame. Bhargava et al. [5] illustrated that the addition of moisture to air stream also brings a significant reduction in NO_x emission in premixed flames. However, only lean premixed flames were studied, and a perfectly stirred reactor network code was employed for the simulation. Therefore, it is of interest to further investigate the effect of water addition on NO_x formation in premixed flames over a wide equivalence ratio range by a more detailed flame model.

The purpose of this technical brief is to numerically investigate the effect of water addition on the formation of NO in counterflow CH_4/air premixed flames, with equivalence ratio varying from lean to rich.

2 Numerical Model and Result Discussion

The flame configuration studied was an axisymmetric laminar counterflow premixed flame [6]. The calculation method can be found elsewhere [7]. The chemical reaction mechanism used was GRI-Mech 3.0 [8]. The pressure and the fresh mixture temperature were, respectively, 1 atm and 300 K. The simulations were conducted for three typical premixed flames: a stoichiometric flame ($\phi=1.0$), a lean flame ($\phi=0.7$), and a rich ($\phi=1.3$) flame. Stretch rate was 45 s^{-1} for all the flames studied.

The fraction of added water changed from 0% to 20%. The definition of the water fraction is $\alpha_{H2O}=V_{H2O}/(V_{H2O}+V_{CH4})$, with V_{H2O} and V_{CH4} being, respectively, the volume flow rates of water and fuel. The added water was assumed to be steam with the same temperature as CH_4/air mixture. In the presentation of results, NO emission index (EI_{NO}) is defined as the ratio of the formed NO to the consumed fuel, and the normalized NO emission index (β_{NO}) is the ratio of NO emission index from a flame with water addition to that from a flame without water addition.

Figure 1 shows the drop of the maximum temperature, when water is added. It is illustrated that the temperature drop is greatest for the rich flame and smallest for the lean flame. The flame temperature drop can cause the reduction of NO formation in a flame. We call this thermal effect. In addition, there may be some variation in chemical reaction rates owing to the addition of water, which also changes the formation of NO in a flame. This is referred to as the chemical effect.

To identify the relative importance of the thermal and chemical effects, an extra calculation was carried out for each flame. In this extra calculation, the added water was replaced by an artificial inert species (XH_2O). The artificial species has the same thermal and transport properties as water, but does not participate in any chemical reaction. Therefore, the addition of XH_2O suppresses NO formation only through the thermal effect. As a result, the difference between the results from the normal and the extra simulations is caused by the chemical effect. The disparity between the results from the flame without water or XH_2O addition and the flame with XH_2O addition is attributed to the thermal effect.

Figure 2 illustrates the effect of water addition on the normalized NO emission indices of the three studied flames. It shows that although the addition of water suppresses NO formation in all the flames, the effectiveness varies. It is most efficient for the stoichiometric flame ($\phi=1.0$) and least efficient for the rich flame ($\phi=1.3$). This differs from the flame temperature variation, as in Fig. 1. In addition, Fig. 2 also reveals that the addition of water causes the reduction of NO in a premixed flame through both the thermal and chemical effects. Although the chemical effect is much smaller than the thermal effect for all the three flames, it is relatively enhanced in the lean and rich flames.

Figure 3 illustrates the integrated NO formation and destruction rates from the most significant reactions. The number of each reaction is based on the order of it in GRI-Mech 3.0 [8]. Among these reactions, R186, R187, and R189 are the three related to NO_2. The net contribution of these three reactions to NO formation is negligible. For rest of the reactions, the dominant ones for the three flames vary. Reactions R178 ($N+NO=N_2+O$) and R180 ($N+OH=NO+H$) are the two most significant for the stoichiometric flame, while the dominant ones become R179 ($N+O_2=NO+O$), R208 ($NNH+O=NH+NO$), and R214 ($HNO+H=H_2+NO$) for the lean flame. For the rich flame, the most important reactions are R180 and R214.

NO can be formed by four routes, i.e., the thermal, the prompt, the N_2O, and the NNH intermediate routes. It is clear that R178 and R208 belong to the thermal and NNH intermediate routes [7,9], respectively. Although R179 and R180 were defined as reactions belonging to the thermal route in many references, it should be noted that the atomic nitrogen participating in these two reactions might come from other routes. Reaction R214 is caused by HNO that may come from the prompt route and the NNH or N_2O intermediate route. Therefore, to figure out which route
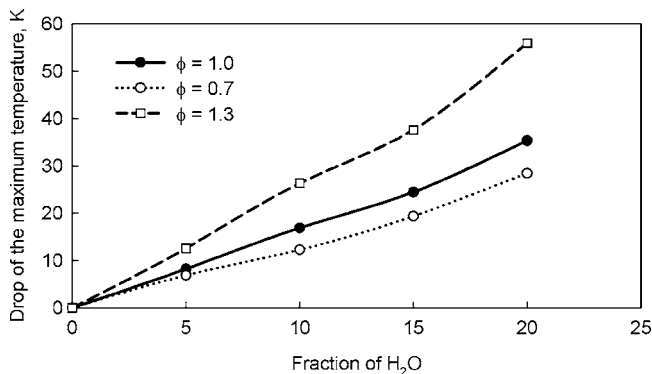

Fig. 1 Variation of the maximum flame temperature drop

dominates NO formation in a flame, we should further examine the rate of molecular nitrogen conversion to atomic nitrogen and species containing nitrogen element.

Figure 4 displays the integrated consumption rate of molecular nitrogen by different routes in the three flames. It is observed that in the stoichiometric flame, the thermal route dominates the con-
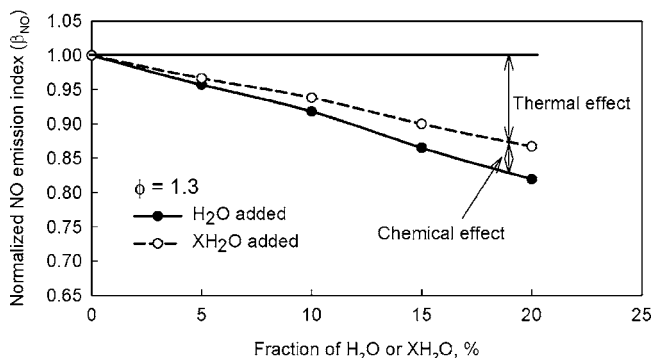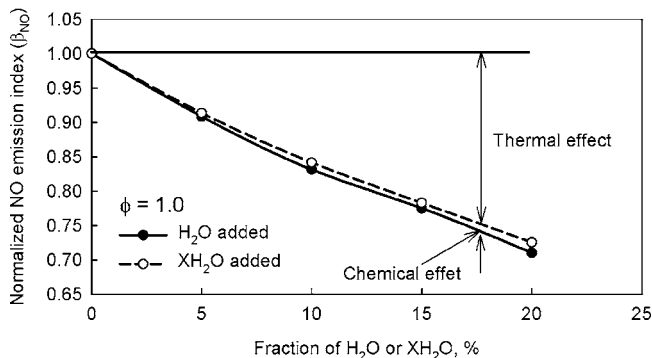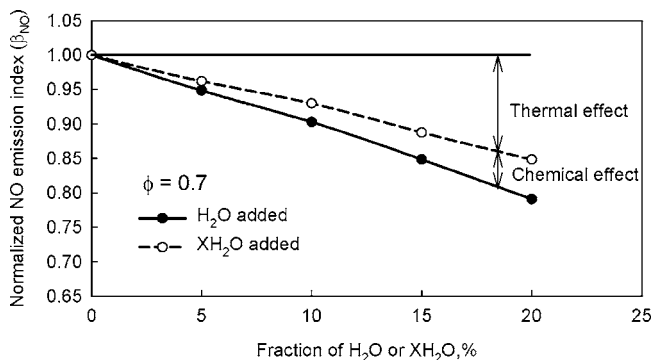

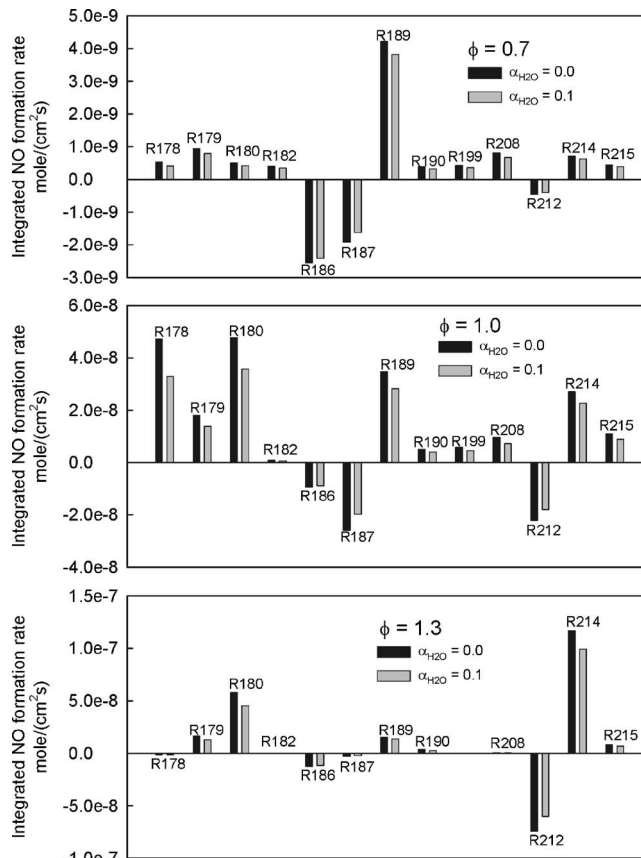**Fig. 2 Variation of normalized NO emission index**

Fig. 3 Total NO formation and destruction rates

version of molecular nitrogen. Although the thermal and prompt routes also contribute to the conversion of molecular nitrogen, the NNH and N_2O intermediate routes do the most in the lean flame. In the rich flame, almost all the molecular nitrogen conversion is through the prompt route. A pathway analysis shows that the most significant molecular nitrogen consumption reaction in the prompt route is R240 ($CH+N_2=HCN+N$). Therefore, we conclude that the thermal route dominates NO formation in the stoichiometric flame, while the NNH and N_2O intermediate routes contribute the most NO in the lean premixed flame. In the rich flame, NO is mainly formed by the prompt route.

Since the thermal route forms NO in the high-temperature post-flame region, it is most sensitive to the variation in flame temperature. On the other hand, the prompt route usually forms NO in a very narrow low-temperature layer of flame front. Therefore, it is less sensitive to the variation of temperature. The NNH and N_2O intermediate routes dominate the formation of NO in the lean flame, but the thermal route also contributes some. Consequently, the effect of water addition on NO formation is most significant for the stoichiometric flame (mainly due to the thermal effect), and least for the rich flame, although the temperature drop in the rich flame is the greatest.

Now we examine how the addition of water causes the chemical effect on NO formation by comparing the results from the normal (H_2O addition) and the extra (XH_2O addition) simulations. The calculations first indicate that no recognizable difference can be observed in the maximum flame temperature for a flame between the results from the normal and extra simulations. However, the chemical effect of water addition does modify the concentrations of radicals OH, H, and O that affect the formation of NO, as shown in Fig. 5. For each flame, the maximum OH mole fraction from the simulation with H_2O addition is higher than that from the simulation with XH_2O addition, implying that the chemical effect
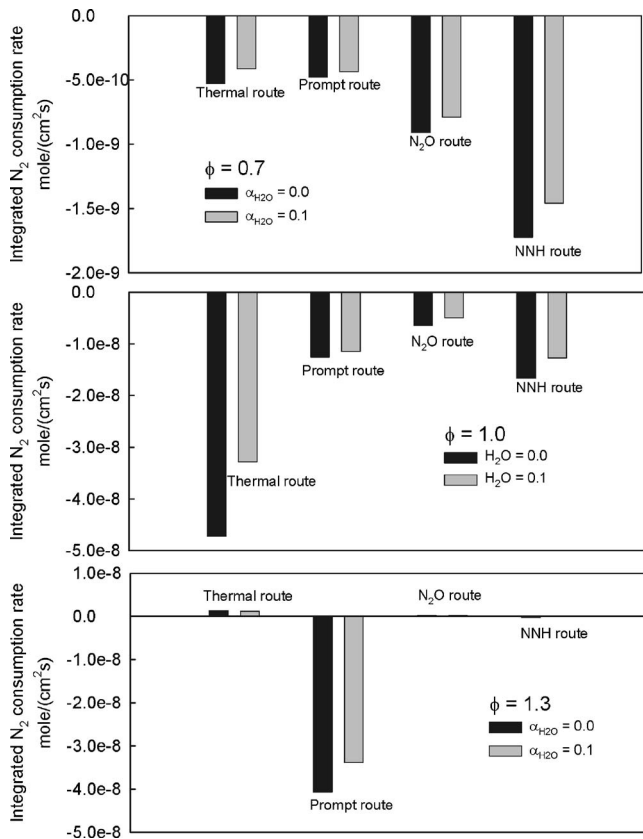
Fig. 4 Total molecular nitrogen consumption rate from different routes

Fig. 5 Chemical effect of water addition on radicals OH, O, and H

of water addition actually enhances the production of OH. Reversely, the chemical effect of water addition reduces the concentrations of radicals O and H.

The formation of NO by the thermal route is through R178, R179, and R180. The chemical effect of water addition leads to negligible variation in flame temperature and increased OH concentration but decreased O concentration. Therefore, it has a very small net effect on NO formation from the thermal route, leading us to conclude that the chemical effect of water addition on NO formation in the stoichiometric flame is very small.

In the NNH and N_2O intermediate routes, the molecular nitrogen is first converted to NNH and N_2O. The formed NNH and N_2O are subsequently converted to NO. H and O radicals play significant roles in these conversion processes. Therefore, the chemical effect of water addition in the NNH and N_2O intermediate routes is bigger than in the thermal route, which leads us to conclude that the chemical effect of water addition in the lean flame is enhanced.

Molecular nitrogen is first converted to N atom and species containing nitrogen elements mainly by R240 in the prompt route. Then the N atom and HCN are converted to NO. The conversion rates of these reaction sequences are also closely related to O and H radicals. Besides, the chemical effect of water addition reduces the concentration of CH radical, as shown in Fig. 6 for the rich flame, which suppresses the initial conversion of molecular nitrogen by R240. As a result, the chemical effect of water addition on NO formation in the rich flame is also relatively bigger than in the stoichiometric flame.

3 Conclusions

This paper reports a numerical study on NO formation in counterflow CH_4/air premixed flames. The main conclusions are: (1)
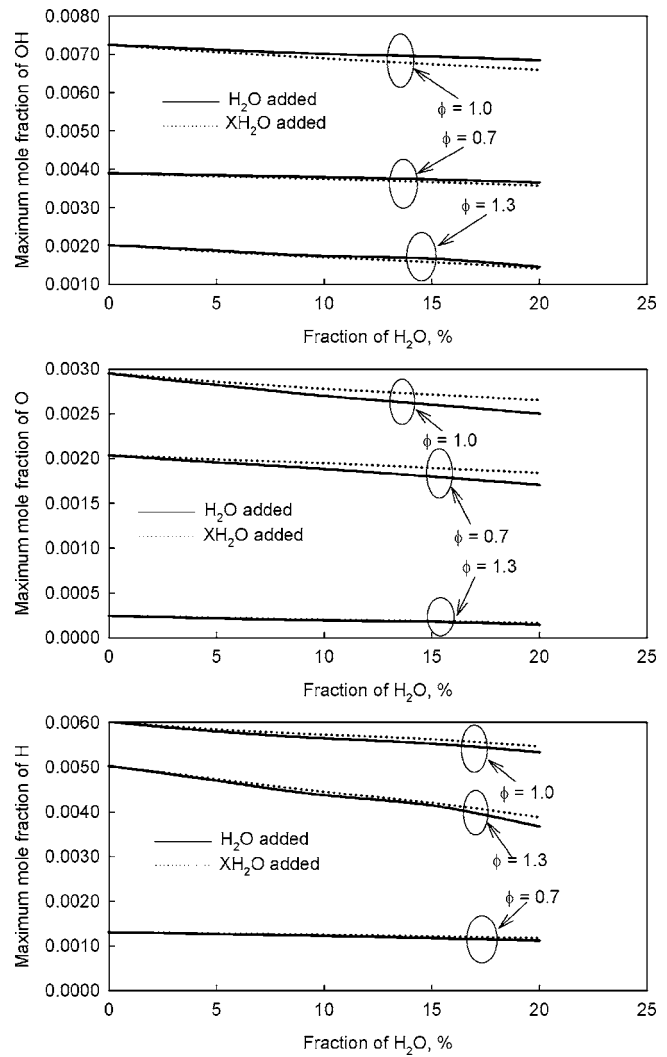
The addition of water to a flame suppresses the formation of NO primarily due to temperature drop. (2) The effectiveness of water addition for NO suppression is most significant for the stoichiometric flame and least for the rich flame. (3) The addition of water also reduces the formation of NO in a flame due to the chemical effect. (4) Compared to in the stoichiometric flame, the chemical effect is intensified in the lean and rich flames.
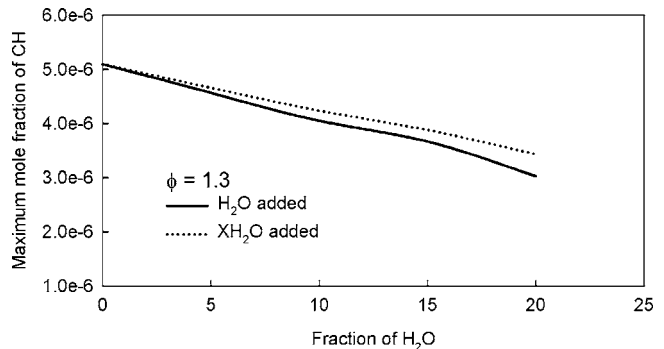

Fig. 6 Chemical effect of water addition on radical CH in the rich flame

References

[1] Li, S. C., and Williams, F. A., 1999, "NO_x Formation in Two-Stage Methane-Air Flames," Combust. Flame, **118**, pp. 399–414.

[2] Zhao, D., Yamashita, H., Kitagawa, K., Arai, N., and Furuhata, T., 2002, "Behavior and Effect on NO_x Formation of OH Radical in Methane-Air Diffusion Flame with Steam Addition," Combust. Flame, **130**, pp. 352–360.

[3] Park, J., Kim, S. C., Keel, S. I., Noh, D. S., Oh, C. B., and Chung, D., 2004, "Effect of Steam Addition on Flame Structure and NO Formation in H2–O2–N2 Diffusion Flame," Int. J. Energy Res., **28**, pp. 1075–1088.

[4] Hwang, D. J., Choi, J. W., Park, J., Keel, S. I., Ch, C. B., and Noh, D. S., 2004, "Numerical Study on Flame Structure and NO Formation in $CH_4-O_2-N_2$ Counterflow Diffusion Flame Diluted with H_2O," Int. J. Energy Res., **28**, pp. 1255–1267.

[5] Bhargava, A., Colket, M., Sowa, W., Casleton, K., and Maloney, D., 2000, "An Experimental and Modeling Study of Humid Air Premixed Flames," J. Eng. Gas Turbines Power, **122**, pp. 405–411.

[6] Guo, H., Ju, Y., Maruta, K., Niioka, K., and Liu, F., 1997, "Radiation Extinction Limit of Counterflow Premixed Lean Methane-Air Flames," Combust. Flame, **109**, pp. 639–646.

[7] Guo, H., Smallwood, G. J., Liu, F., Ju, Y., and Gülder, Ö. L., 2005, "The Effect of Hydrogen Addition on Flammability Limit and NO_x Emission in Ultra-Lean Counterflow CH4/Air Premixed Flames," Proc. Combust. Inst., **30**, pp. 303–311.

[8] Gregory, P., Smith, D. M., Golden, M., et al. http://www.me.berkeley.edu/gri_mech/.

[9] Rørtveit, G. J., Hustad, J. E., Li, S., and Williams, F. A., 2002, "Effects of Diluents on NO_x Formation in Hydrogen Counterflow Flames," Combust. Flame, **130**, pp. 48–61.

Modal Parameter Extraction of a Turboset From High Speed Balance Data

Anoop K. Dhingra[1]
e-mail: dhingra@uwm.edu

Juan I. Hidalgo[2]

Mechanical Engineering Department,
University of Wisconsin,
Milwaukee, WI 53201

Turbosets used in power generation industry are frequently placed on flexible foundations, which significantly influence the overall dynamics. Establishment of structural models that capture the rotor and foundation effects reliably using finite element modeling or modal analysis is difficult because of model complexity and/or costs involved. This paper presents a method to extract modal parameter information of a turboset using frequency response function data recorded during high speed balancing. The main advantage of the present method over the others is the low cost and small effort involved, so that it is of practical use in an industrial setting. A real life example dealing with parameter extraction for a large generator rotor is presented to demonstrate its implementation. [DOI: 10.1115/1.2938275]

1 Introduction

Finite element (FE) modeling has become a dominant technique in the power generation industry for analysis and design of complex rotating systems. However, when it comes to accurately representing the dynamic behavior of large systems such as turbosets to the point at which fault detection can be made based on model predictions, FE modeling may not always yield accurate results. This happens mainly due to the large number of unknown turboset parameters, and assumptions that are made during modeling. In this regard, it will be useful to have a method of reconciliation between the FE model and real machine behavior to be able to perform fault analysis and troubleshooting using a FE model of the turboset. The objective of this work is to create a system identification tool that can be used later in a model reconciliation technique while meeting the time and cost constraints of an industrial setting.

High speed balance is a critical step during turboset's maintenance, and balance data are usually readily available or can be obtained with relative ease. The early work of Diana et al. [1] used shaft and support vibration to create a modal model of a rotor system. Smart et al. [2] estimated foundation parameters using unbalance response during run-up or run-down of a turbogenerator. This work emphasizes the advantage of using unbalance response in the case of large turbosets and the difficulties in implementation of any kind of test equipment on a real machine. Later, Edwards et al. [3] extended this work to produce experimental results in a rotor test ring. The only drawback of this approach is that it needs as many measurement points as balancing planes, a situation that is rather unusual in practice.

Rouch et al. [4] introduced the use of frequency response functions (FRF) in combination with FE model of rotor foundation

systems to improve the model accuracy. Redmond [5] presented a similar approach and stressed the technical difficulties encountered during implementation of the FRF-FE method. Vazquez et al. [6] presented a method that employs polynomial transfer functions extracted from FRFs to model rotor supports. This approach has the advantage that the space required to store the matrices is much smaller than in the case of FRFs.

The above works indicate that FRFs and polynomial transfer functions can be successfully utilized for system identification and modal parameter extraction. Even though a lot of effort has been put in model reconciliation and parameter identification of rotating equipment, lack of real life case studies suggest that there are still a lot of implementation issues that need to be resolved before model reconciliation can became a standard technique for industry. This paper presents a method to extract modal parameter information from high speed balance data of turbosets using FRFs and polynomial transfer functions. The main advantage of the present method over existing approaches is that balance data are usually readily available or can be obtained with relatively small effort, so that it can be easily used in an industrial setting. An example dealing with a 100 ton generator rotor is presented to demonstrate its implementation.

2 Background

The FRFs are obtained by dividing vibration amplitude due to exciting force at each measurement point or frequency. The displacement is measured at the bearing location in the *x-y* plane, perpendicular to the machine's *z* axis of rotation, while the force is applied at (balance) planes used during balancing. The exciting force is synchronous with the machine with a magnitude proportional to the square of machine's rotational speed. In order to obtain the FRFs for a particular force, two test runs are performed on the rotor: the first one with no trial weight and the second with the selected trial weight. Subtracting the two results, it is possible to know the FRFs produced just by the trial weight, neglecting the inherent rotor unbalance. This procedure, making two runs with and without a trial weight, constitutes the foundation of high speed balance, so no extra effort is required from an industrial perspective.

Each FRF $g_{i,j}(\omega)$ establishes a relationship between the applied force at location j (balance plane) and the displacement produced at location i (generally bearing locations) as $g_{ij}(\omega) = u_i(\omega)/f_j(\omega)$. Since bearing vibration data are normally recorded in industry, the FRF is extracted at these locations, but it can be extracted at any location for which data are available.

A mathematical representation of a rotor bearing foundation system can be written as

$$[M][\ddot{u}] + [C][\dot{u}] + [K][u] = [F] \tag{1}$$

The equation can be rearranged such that we collect all the degree of freedom (DOF) of interest for which the FRF is extracted into one vector u_s and the remaining DOF into another vector u_r. Applying dynamic condensation to reduce the system and expressing it in terms of DOF of interest, the equations in condensed form are given as $u_s = [G_{(s)}] f_s$, where $G_{(s)}$ is

$$G_{(s)} = [[m_{ss}s^2 + c_{ss}s + k_{ss}] \cdots - [m_{sr}s^2 + c_{sr}s + k_{sr}]$$
$$\times [m_{rs}s^2 + c_{rs}s + k_{rs}][m_{rr}s^2 + c_{rr}s + k_{rr}]^{-1}]^{-1} \tag{2}$$

In Eq. (2), $G_{(s)}$ is the transfer function matrix that relates the DOF of interest (journal displacement) and applied forces (by trial weights) on the rotor. It is convenient to rewrite this matrix in terms of each DOF of interest as follows:

$$G_{(s)} = \begin{bmatrix} g_{ii}(s) & g_{ij}(s) \\ g_{ji}(s) & g_{jj}(s) \end{bmatrix} \tag{3}$$

Copyright © 2008 by ASME

Here, i and j, respectively, refer to the DOFs where the measurement is taken and the force is applied so that $u_i = g_{ij}(s)f_j$. The relationship between FRFs and transfer functions is now clear.

3 Calculating Polynomial Transfer Functions From FRFs

The problem of extracting polynomial transfer functions from FRF data is one of fitting a ratio of two polynomials to the FRF data. In order to do so, an error function is defined and then minimized. This method was originally developed by Sanathanan and Koerner and later modified by Gähler and Herzon [7]. The original development is expanded herein to couple the system equations, and be able to solve the problem for MIMO systems while keeping the same denominator polynomial coefficients.

Since $g(s)$ is a polynomial transfer function to be fitted to the FRF data in the frequency domain, s can be replaced with $j\omega$ yielding

$$g_{ij}(j\omega) = \frac{p_m(j\omega)^m + p_{m-1}(j\omega)^{m-1} + \cdots + p_0}{q_n(j\omega)^n + q_{n-1}(j\omega)^{n-1} + \cdots + q_0} = \frac{P(j\omega)}{Q(j\omega)} \quad (4)$$

The error function can now be constructed as

$$\varepsilon_k = g(j\omega_k) - \frac{P(j\omega_k)}{Q(j\omega_k)} \quad (5)$$

In Eq. (5), k refers to each frequency point. To overcome the difficulty of minimizing an error function that requires a polynomial ratio to be fitted, an iterative approach of the form

$$\varepsilon_k'' = \frac{\varepsilon_k Q(j\omega_k)_L}{Q(j\omega_k)_{L-1}} = \frac{g(j\omega_k)Q(j\omega_k)_L - P(j\omega_k)_L}{Q(j\omega_k)_{L-1}} \quad (6)$$

is adopted. In this equation, subscript L refers to the iteration step. The error function ε_k'' is minimized over the entire frequency domain as

$$\sum_{k=1}^{n} |\varepsilon_k''|^2 = \sum_{k=1}^{n} W_{k,L}|g(j\omega_k)Q(j\omega_k)_L - P(j\omega_k)_L|^2 \quad (7)$$

where the weighting factor $W_{k,L}$ is given as

$$W_{k,L} = \left| \frac{1}{Q(j\omega_k)_{L-1}} \right|^2 \quad (8)$$

The problem outlined above is a typical weighted least mean square problem. The solution to this problem is well known and can be found in the work of Åström and Wittenmark [8]. Defining a matrix $\Phi(k)$ made of $\varphi^T(k)$, the solution is

$$\theta = (\Phi^T W \Phi)^{-1} \Phi^T W Y \quad (9)$$

where θ is a vector containing the coefficients q_{n-1} to q_0 and p_m to p_0 of the polynomials Q and P. It may be noted that q_n is set equal to 1, and $\Phi(k)$ is constructed as $\Phi = [\varphi_1^T, \varphi_2^T, \ldots, \varphi_k^T]^T$ where

$$\varphi_1^T = [g(j\omega_1) \quad g(j\omega_1)\omega_1 \quad g(j\omega_1)\omega_2^2 \quad \cdots \quad g(j\omega_1)\omega_k^n]$$

$$\varphi_2^T = [g(j\omega_2) \quad g(j\omega_2)\omega_1 \quad g(j\omega_2)\omega_2^2 \quad \cdots \quad g(j\omega_2)\omega_k^n] \quad (10)$$

$$\varphi_k^T = [g(j\omega_k) \quad g(j\omega_k)\omega_1 \quad g(j\omega_k)\omega_2^2 \quad \cdots \quad g(j\omega_k)\omega_k^n]$$

$$Y = [g(j\omega_1)\omega_k^{n+1}, g(j\omega_2)\omega_k^{n+1}, \ldots, g(j\omega_k)\omega_k^{n+1}]^T \quad (11)$$

In Eq. (9), W is a diagonal matrix with $\sqrt{W_{k,L}}$ as elements of its diagonal and $W_{k,L}$ is evaluated at each frequency point and iteration step. This system is solved in a recursive manner by updating $W_{k,L}$ at each iteration L until the convergence criteria is met. It is thus possible to find θ, and therefore P and Q.

In the case of a MIMO system, such as a rotor under an unbalance excitation force, there are at least two bearings in the system and the vibration data are normally acquired in two independent directions at each bearing, resulting in at least four outputs for

each excitation force. The problem of extracting polynomial transfer functions is slightly more complicated in this case because we have to solve the problem in a global manner to ensure that the denominator polynomial Q is the same for all the transfer functions.

Following the same approach as that for a SISO system and recalling Eq. (9), θ now consists of the coefficients of Q, P_1, P_2, P_3, etc., and Φ can be written as

$$\Phi = \begin{bmatrix} \Theta_1 & \Theta_2 & \cdots & 0 \\ \Theta_1 & \Theta_2 & 0 & \Theta_d \\ \Theta_1 & 0 & \cdots & \Theta_d \end{bmatrix} \quad (12)$$

where Θ is assembled as

$$\Theta_1 = \begin{bmatrix} \varphi_1^T \\ \vdots \\ \varphi_k^T \end{bmatrix}\Bigg|_{g_1}, \quad \Theta_2 = \begin{bmatrix} \varphi_1^T \\ \vdots \\ \varphi_k^T \end{bmatrix}\Bigg|_{g_2}, \quad \Theta_d = \begin{bmatrix} \varphi_1^T \\ \vdots \\ \varphi_k^T \end{bmatrix}\Bigg|_{g_d} \quad (13)$$

In Eq. (13), g_d refers to each FRF measured for each independent DOF d, and φ is given as

$$\varphi_1^T = [g_d(j\omega_1) \quad g_d(j\omega_1)\omega_1 \quad g_d(j\omega_1)\omega_2^2 \quad \cdots \quad g_d(j\omega_1)\omega_k^n]$$

$$\varphi_2^T = [g_d(j\omega_2) \quad g_d(j\omega_2)\omega_1 \quad g_d(j\omega_2)\omega_2^2 \quad \cdots \quad g_d(j\omega_2)\omega_k^n] \quad (14)$$

$$\varphi_k^T = [g_d(j\omega_k) \quad g_d(j\omega_k)\omega_1 \quad g_d(j\omega_k)\omega_2^2 \quad \cdots \quad g_d(j\omega_k)\omega_k^n]$$

with Y given as

$$Y = [g_1(j\omega_1)\omega_k^{n+1}, g_1(j\omega_2)\omega_k^{n+1}, \ldots, g_d(j\omega_k)\omega_k^{n+1}]^T \quad (15)$$

For the MIMO case, the weighting factor W looks like

$$W = \begin{bmatrix} W_1 & 0 & 0 \\ 0 & \ddots & 0 \\ 0 & 0 & W_d \end{bmatrix}, \quad W_d = \text{diag} \left| \sqrt{\frac{1}{Q(j\omega_k)}} \right|^2_{L-1} \quad (16)$$

The rest of the estimation process remains the same as for a SISO system.

4 Experimental Setup

The rotor retention pit is an underground reinforced concrete structure. It is a high speed, high-energy facility designed to spin rotors up to their operating speed (1800 rpm or 3600 rpm) or allowable overspeed test (up to 4320 rpm) as well as contain a rotor burst. A 5000 Hp motor is used to drive the rotors, and precautions are taken to isolate the rotor from vibrations transmitted through the driving unit.

Each bearing pedestal is equipped with two noncontacting proximity probes mounted on the face of the bearing shell, 45 deg either side of the vertical centerline. These probes are used for measurement of relative shaft vibration; they are monitored and used for balancing. The probes are normally mounted on the side of the bearing that faces the rotor body. An axial position probe is mounted to observe position of the rotor during runs. A seismic velocity probe is also mounted on each bearing pedestal. These probes provide pedestal vibration data and are used to determine absolute shaft vibration along with outputs from shaft proximity probes.

5 Modal Parameter Identification for a Generator Rotor

An example dealing with numerical estimation of the polynomial transfer function extracted from the FRF of a large generator rotor, while being balanced, is presented. The test rotor used is shown in Fig. 1. This 200,000 lb rotor with 18 in. journal diameter operates at 1800 rpm. Since the rotor operates close to its second critical speed, balancing the second mode is of primary
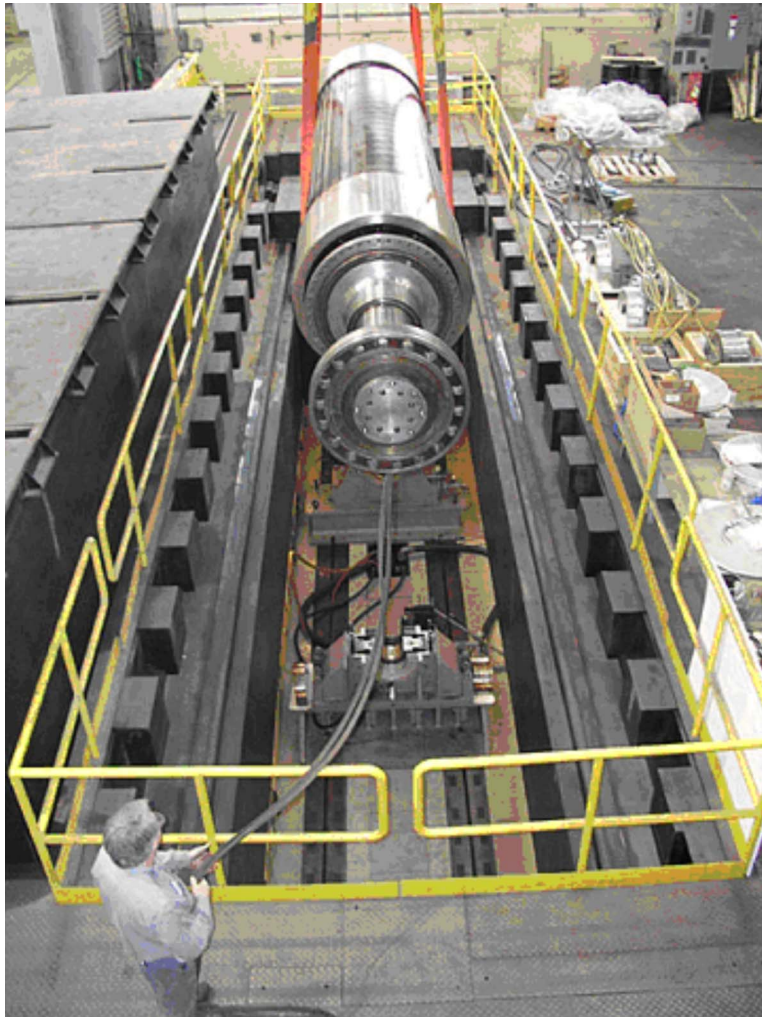
Fig. 1   The generator rotor being lowered into balancing pit

concern. Figure 2 shows the rotor FE model with Elements 26 and 27 denoting the pedestal or foundation while the springs represent the bearing and foundation stiffness and damping characteristics. The bearing stiffness and damping properties vary with speed.

The trial weight used is designed to balance the rotor's second mode and therefore suppresses (or excites) primarily this second mode. Even though the primary intention is to find a polynomial transfer function that correctly represents the second critical speed, the first critical speed will be identified as well but this result may not be as accurate.

The FRF was constructed with a resolution of 20 rpm in the range between 100 rpm and 1800 rpm using two different balancing runs, with a weight correction included in the second run. Then, by subtracting these two runs, the response due to balance correction can be obtained. This has to be done on absolute vibration readings. Therefore, the vector summation of the proximity probes (mounted on the bearing and measuring shaft vibration relative to the bearing) and the seismic probe readings (mounted in the bearing housing and measuring absolute vibration of the bearing) was done before subtracting the results of the two runs.

After the FRF is constructed, the next step is to fit polynomial transfer functions to these FRFs. The fit is done in the region between 600 rpm and 1800 rpm because below 600 rpm the bearings use high pressure oil to lift the rotor to prevent wear thereby changing the dynamic properties of the rotor system. Since the FRF is constructed with a resolution of 20 rpm, there are 60 measurements per FRF ($n_\omega=60$). For this example, the orders chosen for the three polynomials are P_1 and P_2 of order 2 and Q of order 4 (since we are trying to capture at least two natural frequencies). The selection of the polynomial order has to be done in accordance with the accuracy needed. In general, it is recommended
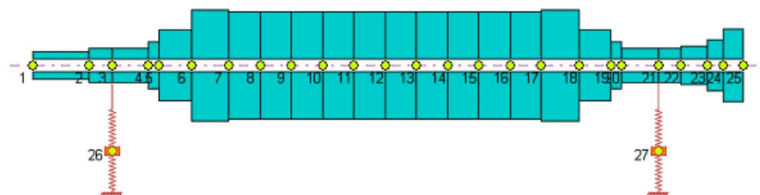

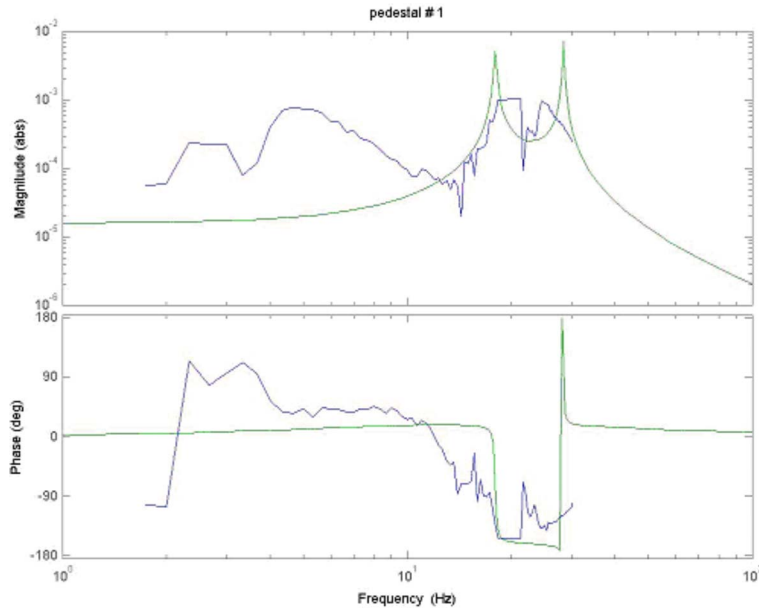**Fig. 2   FE model of the generator rotor**

Journal of Engineering for Gas Turbines and Power   SEPTEMBER 2008, Vol. 130 / **054503-3**

Fig. 3 Transfer function fitted to the FRFs of the system at Bearing 1 measurement location

that the order of the denominator polynomial Q be twice the maximum number of frequencies to be extracted. Figure 3 shows the FRFs for measurement location at Bearing 1 as well as the bode diagram of the corresponding transfer functions superimposed. Once the transfer function parameters converge, the resulting transfer functions are given as

$$G_1(\omega) = \frac{-0.7090(j\omega)^2 + 46.6380(j\omega) + 6473.60}{(j\omega)^4 + 2.7182(j\omega)^3 + 44,539(j\omega)^2 + 62,861(j\omega) + 405,460,000}$$

$$G_2(\omega) = \frac{-1.4108(j\omega)^2 - 120.84(j\omega) + 19,482}{(j\omega)^4 + 2.7182(j\omega)^3 + 44,539(j\omega)^2 + 62,861(j\omega) + 405,460,000}$$

(17)

or in modal notation after partial fraction expansion as

$$G_1(\omega) = \frac{1.9819 \times 10^{-5}}{(\omega^2 + 2(0.0035)178.26\omega + 178.26^2)} + \frac{1.456 \times 10^{-5}}{(\omega^2 + 2(0.0066)112.95\omega + 112.95^2)}$$

$$G_2(\omega) = \frac{9.9970 \times 10^{-5}}{(\omega^2 + 2(0.0035)178.26\omega + 178.26^2)} + \frac{8.6209 \times 10^{-5}}{(\omega^2 + 2(0.0066)112.95\omega + 112.95^2)}$$

(18)

The extracted natural frequencies of the system are 178.26 rad/s (1702 rpm) and 112.95 rad/s (1078 rpm) and the damping coefficients 0.35% and 0.66%. The observed natural frequencies during balancing are 1700 rpm and 1000 rpm, which are in good agreement with the extracted data. The extracted damping coefficients appear to be low because damping of the order of 1%–3% is expected for these bearings. Note that if we choose q_0 to be 1 instead of q_n, then the transfer function is very sensitive to low frequencies close to the origin and insensitive to high frequencies which, in this case, are of interest.

The errors in estimated modal parameters include errors due to experimental response measurements, errors in bearing model, and errors in the rotor model. In this work, it is assumed that a good dynamic rotor model is available and no errors due to rotor modeling are present. The measurement noise, which affects both inputs and outputs, was modeled using experimental resolution associated with various transducers. The bearing stiffness and

damping coefficients had maximum uncertainties of the orders of 6% and 10%, respectively. Per ANSI/ASME Standard on Measurement of uncertainty, the coefficient of variation (standard deviation/mean) for extracted frequencies is approximately 0.1.

6 Discussion of Results

A method to obtain FRFs and polynomial transfer functions for a turboset from high speed balance data is presented. The proposed approach yields the transfer functions as well as overcomes the numerical difficulties related to convergence and ill conditioning of the least squares problem. For practical reasons, constructing FRFs from balancing data is very convenient for large turboset units, which have vibration instrumentation already installed on the machine and the implementation of an external force, such as the one produced by a shaker, is impractical and costly compared

to the introduction of an unbalance weight. In many cases, balancing data are already available from previous balancing operation and need not to be obtained.

The practical utility of this method is very promising, as it requires very little effort and yields very good practical results (error of the order of 5% or less for natural frequencies) and allows FE reconciliation techniques to be easily implemented in an industrial environment. The disagreement in the amount of damping present is not a cause of concern in a balancing operation because the focus during a high speed balance in an industrial setting is on knowing where resonance occurs, rather than knowing what the attenuation factor is.

Finally, it may be noted that journal bearings and pedestal dynamics in the balancing pit may be substantially different than rotor's permanently installed location. An in situ balancing with rotor in its permanently installed location will generally produce better results in terms of vibration but balancing in a balance pit generally produces a better balance because the compounding field installation factors are not present.

Nomenclature

f_j = force applied at DOF j

g_{ij} = transfer function between displacement at DOF i and applied force at DOF j

MIMO = multiple input multiple output system

$[M],[C],[K]$ = mass, damping, and stiffness matrices of rotor bearing foundation system

p_i = coefficients of the numerator polynomial fitted to FRF data

q_i = coefficients of the denominator polynomial fitted to FRF data

SISO = single input single output system

u_i = displacement at DOF i

ω_k = kth specific value of forcing frequency

References

[1] Diana, G., Cheli, F., and Vaina, A., 1988, "A Method to Identify the Foundation Modal Parameters Through Measurement of Rotor Vibrations," IMechE Conference Publications, C300/88.

[2] Smart, M., Friswell, M. I., Lees, A. W., and Prells, U., 1998, "Estimation of Turbogenerator Foundation Parameters," Proc. Inst. Mech. Eng., Part C: J. Mech. Eng. Sci., **212**(C8), pp. 653–665.

[3] Edwards, S., Lees, A. W., and Friswell, M. I., 2000, "Experimental Identification of Excitation and Support Parameters of a Flexible Rotor-Bearing-Foundation System From a Single Run-Down," J. Sound Vib., **232**(5), pp. 963–992.

[4] Rouch, K. E., McMains, T. H., and Stephenson, R. W., 1989, "Modeling of Rotor-Foundation System Using Frequency Response Functions in a Finite Element Approach," *ASME Design Technical Conference 12th Biennial Conference on Mechanical Vibration and Noise*, Montreal, Canada, pp. 157–166.

[5] Redmond, I., 1995, "Practical Rotordynamics Modeling Using Combined Measured and Theoretical Data," *Proceeding of the 13th International Modal Analysis Conference*, Nashville TN, Society for Experimental Mechanics, Bethel CT, pp. 377–386.

[6] Vázquez, J. A., Barrett, L. E., and Flack, R. D., 2002, "Flexible Bearing Support Using Experimental Data," ASME J. Eng. Gas Turbines Power, **124** pp. 369–374.

[7] Gähler, C., and Herzon, R., 1994, "Identification of Magnetic Bearings Systems," *Proceedings of the Fourth International Symposium on Magnetic Bearings*, ETH Zurich, University Press, Swiss Federal Technical University, Zurich, Switzerland, pp. 293–298.

[8] Åström, K. J., and Wittenmark, B., 2001, *Adaptive Control*, Parson Education, Singapore.

Optimization of the Flow in the Catalytic Converter of Internal Combustion Engines by Means of Screens

Eduardo M. R. Arantes

Departamento de Engenharia Mecânica,
Pontifícia Universidade Católica de Minas Gerais,
Avenida Dom José Gaspar,
500 Belo Horizonte,
30535-610 Minas Gerais, Brazil
e-mail: emuriloarantes@ig.com.br

Marcello A. F. Medeiros

Departamento de Engenharia de Materiais,
Aeronáutica e Automobilística,
Escola de Engenharia de São Carlos,
Universidade de São Paulo,
Avenida Trabalhador Sancarlense,
400 São Carlos,
13566-590 São Paulo, Brazil
e-mail: marcello@sc.usp.br

The flow in the automotive catalytic converter is, in general, not uniform. This significantly affects cost, service life, and performance, in particular, during cold startup. The current paper reports on a device that provided a large improvement in flow uniformity. The device is to be placed in the converter inlet diffuser and is constructed out of ordinary screens. It is cheap and easy to install. Moreover, the device does not present most of the undesired effects, such as increase in pressure drop and time to light off, often observed in other devices developed for the same purpose.
[DOI: 10.1115/1.2770492]

1 Introduction

Despite the research devoted to the automotive catalytic converter, there are aspects of the systems which still need to be improved [1,2]. One of such aspects is the exhaust gas distribution in the converter [3–5]. Often, the converter consists of a ceramic honeycomb structure wash coated with a porous layer impregnated with the catalytic substance. A nonuniform distribution of the exhaust gases among the cells of the honeycomb brings a series of problems. The current work presents the results of an experimental investigation of a device that provided a significant improvement in the flow distribution of a typical catalytic converter. The device is built from ordinary screens.

As the converter is designed to provide a minimum residence time, the flow uniformity reduces the length of the converter, which reduces cost. It also extends the converter service life by uniformly consuming the expensive substances that take part in the chemical reactions. Associated with the flow maldistribution, there is also a temperature maldistribution. They both contribute to a longer time to light off, which affects the efficiency during the cold startup. This temperature nonuniformity also promotes thermal stresses that may crack the ceramic material [3–5]. Lastly, the

flow nonuniformity increases the already large pressure drop in the converter, which often reduces engine performance.

The reason for the flow maldistribution in the converter is related to its design. The flow is directed from the exhaust duct to the honeycomb via an inlet diffuser. Due to space restrictions, often the diffuser angle is so wide that its high pressure recovery promotes the separation of the boundary layer that develops on the diffuser wall. As a consequence, the resulting flow is not evenly distributed over the frontal area of the honeycomb, but concentrates along its central part.

Boundary layer separation is an important aerodynamic phenomenon. It affects airplane performance and is dealt with in very many different ways in aeronautical research and development. One specific example where this phenomenon must be properly controlled is in the design of wind tunnels. These tunnels are experimental facilities consisting essentially of a duct where air is driven through in a controllable fashion. In this controlled air flow, airplane models can be tested under conditions that simulated flight. In these tunnels, the existence of wide-angle diffusers is commonplace but, in spite of that, a uniform flow must be produced as it is necessary for the usefulness of the experiment. In view of these, a number of techniques have been investigated to inhibit boundary layer separation in diffusers.

Some of these techniques, such as the use of vanes and splitter plates, are quite obvious and have already been tested in catalytic converters [6]. However, often they are very complicated to install and not very efficient. In the context of the catalytic converter, there are yet other undesirable effects, as, for example, the large amount of heat that they extract from the exhaust gases during the cold startup and the large backpressure that they produce [3,7].

From the various methods developed, one, which involves the use of screens, has become the standard technique in the design of wide-angle diffusers for wind tunnels. The current work presents the results of an experimental investigation into the use of screens to improve flow uniformity in the catalytic converter. To the knowledge of the authors, this has not yet been carried out. Although from the start of the work there was great confidence that the method would also work in the current application, there were a few differences with respect to wind tunnel applications that could affect the performance of the system. These differences were mainly the size of the duct and the fact that in the catalytic converter, there is a long honeycomb downstream of the diffuser. In view of this, a device was designed and tested. The results confirmed the expectations and are presented here in some detail. The analysis also included screen configurations that were simpler than those that led to optimum performance, but that could be more cost effective.

2 Experimental Setup and Procedure

The severe restrictions on pollutant emissions sometimes call for the use of more than one catalytic converter. The current investigation is focused on the so called underbody catalytic converter, but it is expected that, under some circumstances, the results would also be useful for closed-coupled converter.

Diffuser performance is affected by both the diffuser angle and the area ratio, which is the relation between the outlet and the inlet area. When the included angle is above 10 deg, the diffuser is normally referred to as a wide-angle diffuser. The included angle is that between the opposite walls of the diffuser. For such diffusers, boundary layer separation can be avoided only by some means of separation control. The inlet diffuser of catalytic converter used in the current study had an included angle of 47 deg and an area ratio of about 4. Its inlet diameter was 45 mm and its length was 48 mm. It is by no means among the widest angle diffusers used by the automotive industry in catalysts, but is well within the wide-angle class. The honeycomb dimensions corresponded to those utilized in ordinary 1000 cm^3 engines produced by the Brazilian automotive industry. It was 20 cm in length and 10 cm in diameter. The honeycomb cells were 1×1 mm^2. Some-

times, catalytic converters have an elliptical cross section, a curved inlet pipe, or a not fully developed inflow. These aspects affect the flow in the converter. However, in order to reduce the number of parameters involved, none of them were here analyzed. The tests used a cylindrical converter, connected to a straight pipe so long that the flow could be considered a fully developed turbulent pipe flow at the diffuser entrance. Nevertheless, the optimizing device to be described here can, in principle, be adjusted to cope with those perhaps more severe conditions. Similar adjustments have been successfully done for wide-angle diffusers of wind tunnels.

Despite the fact that, owing to the valve motion, the flow in the exhaust system of vehicles is pulsating, most studies of catalytic converter have considered steady flow. This is partially because it is more difficult to conduct either experiments or computations for pulsating flows, but, for the underbody converter, this is, in general, regarded as an acceptable simplifying assumption [8–10]. In view of these, the current work also investigated only steady flow. This simplification may not be acceptable for close-coupled converters [2].

The experiments did not use the actual exhaust gases from the engine, but, instead, room air was employed (about 25°C in temperature and 1.01 bars in pressure). This had many obvious advantages and is appropriate as long as dynamic similarity is maintained. The velocity in the exhaust system is relatively high, but the flow can be regarded as incompressible, in particular, in view that the temperatures involved are high, which increases the speed of sound. Dynamic similarity is then warranted by ensuring the same Reynolds number. Applying this condition to the current experiment resulted that the test volume flow was about five times lower than the actual exhaust flow. The rotational speed range of 2000–5000 rpm for a 1000 cm³ engine corresponded to test volume flows in the range of about 0.007–0.02 m³/s. The system used, with the converter in place, provided a maximum volume flow of around 0.027 m³/s.

A gate valve was fixed to the vacuum cleaner and connected, via a flexible rose, to a 3 m long polymer pipe. In order to promote flow uniformity in the pipe, a screen was placed in the connection between the rose and the pipe. A metal rod was attached to the pipe to prevent bending. The pipe internal diameter, 45 mm, was chosen to match the inlet of the converter diffuser. The converter was connected to the exit of the pipe. The downstream nozzle of the converter was removed, but the honeycomb was maintained in place.

The measurements of the streamwise velocity profiles were carried out at the exit section of the honeycomb with a Pitot tube connected to an inclined manometer. The Pitot tube was shape as a "L," with dimensions 5 cm and 20 cm. The total pressure hole was 1 mm in diameter. This provided an accuracy of ±0.25 Pa. The Pitot tube was positioned with an estimated accuracy of 0.5 mm. Measurements inside the diffuser with the honeycomb in place would require a Pitot-static tube. The standard Pitot-static tubes are also L shaped and would not fit adequately inside the diffuser. Even the smallest Pitot tube would restrict the measurements to a region well upstream of the diffuser exit and would not give a good indication of the flow in the honeycomb. Also, the flow in the diffuser is very complex, in particular, when no screens are used, and would lead to severe inaccuracy in the Pitot-tube readings. Moreover, even a small Pitot tube inside the diffuser would almost certainly interfere with the flow. In fact, reliable measurements inside the diffuser would require other measuring techniques and are not often reported in the literature. Such measurements would almost certainly bring further interesting information, but they fall outside the objective of the current paper. Since the honeycomb is composed of longitudinal cells, which are not interconnected, the flow at the exit is essentially identical to that of the honeycomb inlet. Therefore, it provides

enough information to verify the device performance. A large number of experimental studies of this problem also relied on measurements at the honeycomb exit.

The volume flow was adjusted using the gate valve and was measured with a calibrated Pitot-static tube placed inside the pipe at 270 mm from the pipe outlet. The Pitot static tube was connected to a digital manometer. Care was taken that the Pitot-static tube did not affect the velocity profiles in the diffuser inlet. Prior to the tests, the dynamic pressure measured at the centerline of the pipe was calibrated against volume flow measurements made by integration of two dimensional velocity profiles measured at the pipe exit, without the diffuser in place. At this position, the flow was much more axisymmetric than at the exit of the honeycomb. An almost perfect quadratic relation between the dynamic pressure and the volume flow was obtained, providing confidence on the procedure. The apparatus could adjust and maintain a volume flow rate accurate to within an estimated 2% for the higher flow rates, but degraded to about 10% at the lowest flow rate studied. Flow temperature was monitored with a thermopair placed close to the pipe entrance and remained almost constant from test to test. Therefore, dynamic similarity could be warranted by ensuring a constant flow rate.

Prior to the tests, it was deemed necessary to verify flow quality. This was carried out by removing the converter and taking measurements of the streamwise velocity profiles at the pipe exit for flow rates in the range of those to be used in the experiment. They compared well with the seventh-root law [11].

Ideally, wide-angle diffusers promote large pressure recoveries due to the increase of the flow area and subsequent reduction of flow velocity. The resulting positive pressure gradient also acts on the flow close to the diffuser wall, the so called boundary layer. The low momentum of the fluid in this region is insufficient to overcome the force associated with the positive pressure gradient of a wide-angle diffuser. The process leads to reverse flow in the region close to the wall and boundary layer separation. In this scenario, the forward flow is concentrated only in the center of the diffuser. The effective flow area is drastically reduced and the pressure recovery is significantly diminished. One way to interpret the effect of the screen in the diffuser is as follows. The screen contributes a pressure drop in the diffuser. If this is matched to the positive pressure gradient of the diffuser, an almost zero pressure gradient can be obtained. Boundary layer separation, and hence reverse flow, is reduced or even prevented and the flow in the diffuser becomes more uniform. Apart from the improved flow uniformity, a wide-angle diffuser with an appropriate set of screens sometimes yields a pressure recovery that is higher than what would be achieved by the same diffuser without screens. This is important as low pressure recoveries in the diffuser represent large head loss in the exhaust system and may reduce engine performance.

Mehta [12] compiled the data from wide-angle diffusers used in wind tunnels throughout the world and, based on these results, prepared graphics that enable one to select the screens for a given diffuser geometry. The graphics give the minimum value of ΣK that would prevent flow separation in the diffuser. ΣK is related to the total head loss provided by a set of screens. Mehta [12] also provides empirical relations that enable the calculation of K for a given screen and Reynolds number [11].

The experimental model had four slots where screens could be placed. The first slot was 5 cm from the inlet. The other three screen positions were separated from each other by about 10 cm. They were named P05, P15, P25, and P35 and spanned the total length of the diffuser.

A selection of four different flat screens was used in the investigation. According to Mehta [12], K is either constant or decreases with Reynolds number. On the other hand, both the literature and the results given here show that the nonuniformity increases with Reynolds number. As a consequence, the most demanding situation both in terms of flow uniformity and K param-

Table 1 Characteristics of the screens tested

Screen BWG	Wire diameter (mm)	Screen mesh length (mm)	Open area ratio β	K
18/32	0.23	1.18	0.70	0.58
26/30	0.30	0.67	0.47	2.28
28/32	0.23	0.67	0.56	1.33
30/32	0.23	0.61	0.53	1.59

eter corresponded to the highest Reynolds number flow condition. Therefore, the selection of the screens was based on this case. Table 1 gives the characteristics of the screens used.

Preliminary tests showed that very close to the honeycomb exit, at about 10 mm from it, the velocity profiles were not smooth. At 30 mm, they looked much better. The problem was attributed to a nonuniformity of the flow associated with the exit of the individual cells of the honeycomb, but this was not investigated any further. The velocity profiles were then obtained at 30 mm from the honeycomb.

The repeatability of the experiment was also investigated. It was found that it could be reproduced to within the experimental uncertainty. An asymmetry was noticed in the profile, which could be traced to misalignment between the diffuser and the honeycomb. Rotating the converter reduced the problem. Finally, a two dimensional velocity profile on a plane perpendicular to the flow was taken, which showed that the flow was reasonably axisymmetric. This allowed that the analysis could be carried out using velocity profiles along one diameter of the honeycomb.

3 Results

Initially, the velocity profile at the honeycomb exit was measured without the use of screens for a number of flow rates, Fig. 1. The flow rates were 7.6 l/s, 12.8 l/s, 14.3 l/s, and 17.5 l/s, which roughly corresponded to engine operation at 2000 rpm, 3000 rpm, 4000 rpm, and 5000 rpm. The maximum flow rate that the experimental rig could provide, about 27 l/s, was also tested. Hereinafter, the flow rates used are referred to by using the engine rotation, with the maximum flow rate case being called >5000 rpm. As expected, the flow was very nonuniform, in particular, at higher velocities. The maximum speed occurred at the
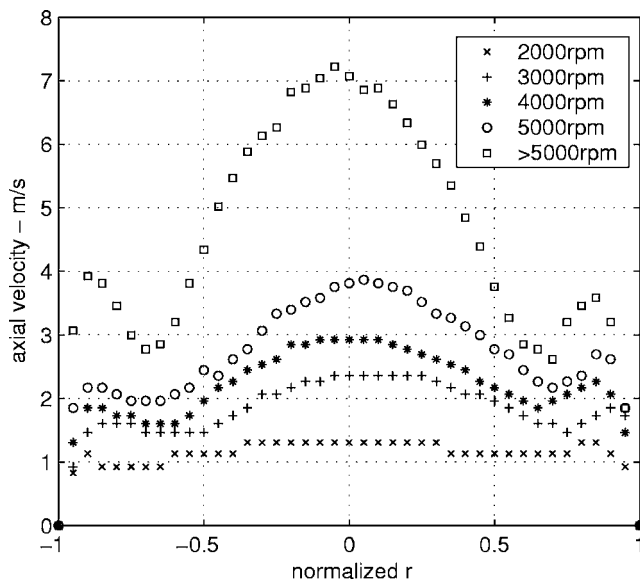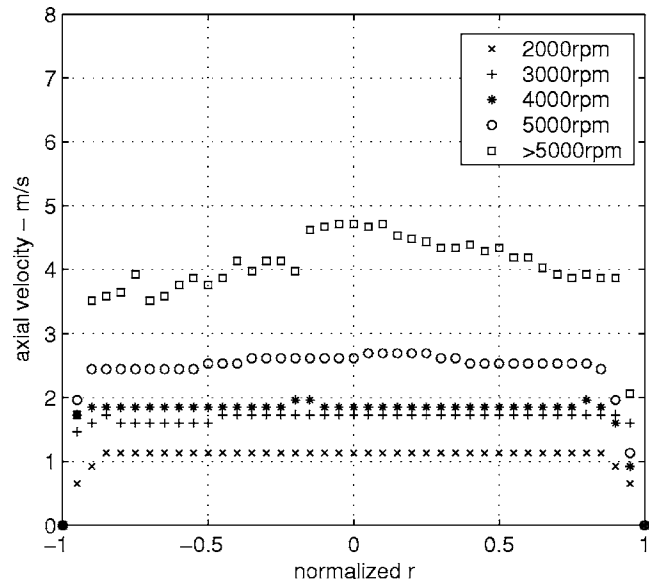
Fig. 2 Velocity profiles at the honeycomb exit for various flow rates with the use of one screen in the inlet diffuser

center, but local maxima were also found at the edges. Apparently, these local maxima have not been reported previously. Their origin was not deeply investigated here, but the result was very repeatable and there was a pattern linking the various curves. It is believed that they are not a result of experimental error. For instance, they are not due to leaking between the honeycomb and the metal casing as they were tightly adjusted. In any case, as is shown below, the screens were also able to reduce these maxima.

It is perhaps important to note that the flow rates given were not estimated from integrating the velocity profiles in Fig. 1. Such estimates result in significant variations with respect to the flow rates given from the calibrated Pitot-static tube. An indication of these variations can be obtained from estimating the flow rates by integration of the left- and right-hand sides of the profiles of Fig. 1. Although the profiles look reasonably symmetric, these estimates result in differences that can reach ±8%. Therefore, differences of about 10% between the flow rates estimated from these velocity profiles and that of the calibrated Pitot-static tube are not unexpected. Differences between such estimates for measurements with and without the screens may be expected to be at least of the same order. Since the Pitot-static tube was not directly affected by the screens and was calibrated against flow rates obtained from velocity profiles at the pipe exit, which were two dimensional and more symmetric, it was considered more reliable.

As proposed by Bressler et al., the standard deviation of the velocity along the profile provides a measure of flow uniformity. A coefficient was defined as

$$\gamma = 1 - \frac{1}{n} \sum_{i=1}^{n} \frac{\sqrt{(u_i - \bar{u})^2}}{\bar{u}} \qquad (1)$$

where $\bar{u}$ is the velocity averaged over the profile. $\gamma = 1$ indicates a uniform profile, and lower values indicate less uniformity. The values of γ for the rotational speeds from 2000 rpm to >5000 rpm were, respectively, 0.84, 0.78, 0.76, 0.74, and 0.66.

For the current diffuser, Mehta [12] indicates $\Sigma K = 2.6$ and the use of two or three screens. The ΣK should not exceed the required value by a significant amount as it could lead to divergence of the flow. Indeed, from the selection of screens used, the value of $\Sigma K = 2.6$ is only achievable with the use of more than one screen, but, from a manufacturer's point of view, it may be very important to check what can be achieved with a single screen. Therefore, this analysis was carried out first. Figure 2 gives the
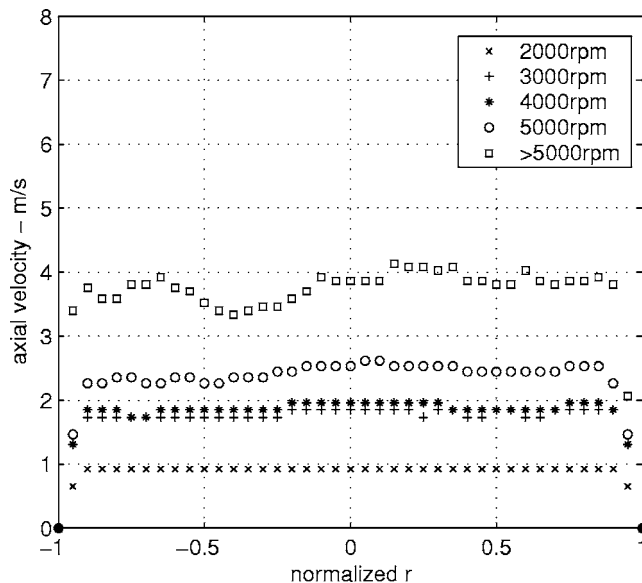
Fig. 1 Velocity profiles at the honeycomb exit for various flow rates without the use of screens

Fig. 3 Velocity profiles at the honeycomb exit for various flow rates with the use of two screens in the inlet diffuser

Fig. 4 Diffuser inlet pressure as a function of flow rate for different screen combinations

results obtained with the use of screen 26/30 at position P05. The values of K stayed in the range of 2.1–2.6, depending on the flow speed. In general, these were below the value of 2.6 required for the current diffuser. For speeds from 2000 rpm to >5000 rpm, γ were found to be, respectively, 0.86, 0.90, 0.88, 0.864, and 0.84. Comparison of Figs. 1 and 2, and of the values of γ, reveals a significant improvement in the flow uniformity.

Another aspect that might be of interest to manufacturers is the sensitivity of the results to the position of the screen. According to Mehta, for straight-walled diffusers, like the current one, the best screen positioning is where the diffuser wall changes angle, that is, at the inlet or outlet. The analysis was performed for 5000 rpm. For positions closer to the inlet of the diffuser, say, P05 and P15, the flow quality was not sensitive to screen positioning [11]. The values of γ were very close to each other, namely, 0.864 and 0.866, respectively. The uniformity degraded for screens closer to the diffuser exit, giving $\gamma=0.856$ and 0.844.

To achieve ΣK above 2.6, at least two screens were needed. Tests were then carried out with screen 30/32 at position P05 and screen 18/32 at position P15, except for the case when the speed was higher than 5000 rpm, which used two screens of the type 28/32. This yielded ΣK in the range of 2.4 to 3.2 for rpm from 2000 to >5000. Results are shown in Fig. 3. For speeds from 2000 rpm to >5000 rpm, γ were, respectively, 0.882, 0.884, 0.878, 0.870, and 0.86. In comparison with the use of a single screen, a little improvement was obtained, in particular, for the higher rpm. However, it might not justify the extra cost of installing a second screen. The use of three screens was also tested but no measurable improvement was obtained. For example, for the >5000 case, γ raised from 0.860 to 0.865, clearly within the experimental uncertainty.

Analysis of the effect of the device on the pressure drop of the catalyst is also important and was carried out within the current study. The honeycomb exhausted directly to the atmosphere. Therefore, measuring the pressure upstream of the diffuser provided a good indication of the effect of the screen on the head loss. Figure 4 gives the variation of the diffuser inlet pressure against the flow rate for different combinations of screens. The use of screens did not add a significant head loss to the system. For the combination using two screens, which appeared to be the optimum for the current catalyst, the head loss was virtually unaffect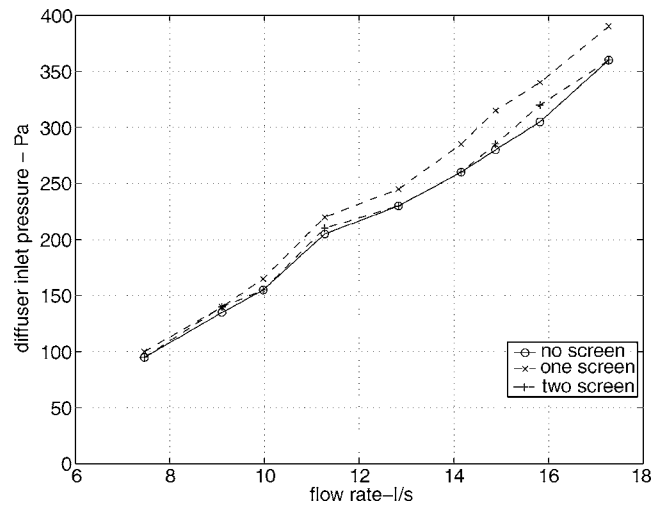ed. This is an indication of the bad performance of this diffuser without screens in terms of pressure recovery. The improved flow provided such an increase in the effective pressure recovery of the diffuser that it compensated for the head loss introduced by the screen.

4 Conclusion and Discussion

The experimental results confirmed previous works in that the flow in the catalytic converter is very nonuniform, in particular, for higher flow speeds. The expectation that the use of screens would improve the uniformity of the flow in the catalytic converter was also confirmed by the experiments. The improvement was seen not only from the velocity profiles shown but also from the coefficient γ, which is a measure of flow uniformity. In extreme cases, the uniformity measured by this coefficient increased by 30%.

The results suggested that the use of one single screen may be enough for most applications, but in extreme conditions, the use of more screens may provide further improvement. The results also indicated that the flow quality is not very sensitive to the position of the screen, as long as it stays in the first portion of the diffusers. The device is both cheap and easy to install.

The investigation also included analysis of the engine backpressure provided by the converter. The use of screen did not increase the backpressure significantly. In particular, with the use of two screens, no measurable difference was found from the case without screens.

Questions may be raised as to the effect on the device performance of temperature variation and chemical reactions, which take place in the real application. These should have little effect other than a variation of the Reynolds number. They occur downstream of the diffuser inlet and in pipe flow, there is usually very little upstream effect on the velocity profiles. Durability issues of the screens are also of concern in view of the humidity and extremely high temperature in the catalyst diffuser. Stainless steel screens are currently being successfully tested for durability and performance under real conditions. Unfortunately, details of these results are classified and are not available for publications.

References

[1] Pontikakis, G. N., Konstantas, G. S., and Stamatelos, A. M., 2004, "Three-

Way Catalytic Converter Modeling as a Modern Engineering Design Tool," Trans. ASME: J. Eng. Gas Turbines Power, **126**(4), pp. 906–923.

[2] Tsinoglou, D. N., and Koltsakis, G. C., 2005, "Influence of Pulsating Flow on Close-Coupled Catalyst Performance," Trans. ASME: J. Eng. Gas Turbines Power, **127**(3), pp. 676–682.

[3] Howitt, J. S., and Sekella, T. C., 1974, "Flow Effects in Monolithic Honeycomb Automotive Catalytic Converters," SAE Technical Report No. 740244.

[4] Wendland, D. W., and Matthes, W. R., 1986, "Visualization of Automotive Catalytic Converter Internal Flows," SAE Technical Report No. 861554.

[5] Guojiang, W., and Song, T., 2005, "CFD Simulation of the Effect of Upstream Flow Distribution on the Light-Off Performance of a Catalytic Converter," Energy Convers. Manage., **46**, pp. 2010–2031.

[6] Bella, G., Rocco, V., and Maggiore, M., 1991, "A Study of Inlet Flow Distribution on Catalytic Conversion Efficiency," Trans. ASME: J. Eng. Gas Turbines Power, **13**(113), pp. 419–426.

[7] Day, J. P., and Socha, L. S.Jr., 1991, "The Design of Automotive Converter for Improved Pressure Drop and Conversion Efficiency," SAE Technical Report No. 910371.

[8] Bressler, H., Rammoser, D., Neumaier, H., and Terres, F., 1996, "Experimental and Predictive Investigation of a Close Coupled Catalytic Converter With Pulsating Flow," SAE Technical Report No. 960564.

[9] Zhao, F. Q., 1997, "Transient Flow Characteristics Inside the Catalytic Converter of a Firing Gasoline Engine," SAE Technical Report No. 971014.

[10] Jeong, S. J., and Kim, W. S., 2001, "A Three-Dimensional Numerical Study of the Effect of Pulsating Flow on Conversion Efficiency Inside a Catalytic Converter," Proc. Inst. Mech. Eng., Part D (J. Automob. Eng.), **215**, pp. 45–61.

[11] Arantes, E. M. R., and Medeiros, M. A. F., 2004, "Optimization of the Flow in the Catalytic Converter of Internal Combustion Engines by Means of Screens," Tenth Brazilian Congress of Thermal Engineering and Sciences, Rio de Janeiro, Brazil.

[12] Mehta, R. D., 1977, "Aerodynamic Design of Blower Tunnels With Wide-Angle Diffusers," Prog. Aerosp. Sci., **18**, pp. 59–120.

Experimental Blowout Limits and Computational Flow Field of Axial Single and Multijet Flames

Khaled M. Shebl

Faculty of Engineering (Mattaria),
Mechanical Power Engineering Department,
Helwan University,
Masaken Helmiat Al-zitoun,
P.O. Box 11718,
Cairo, Egypt

Measurements of the lean blowout equivalence ratio ($\Phi_{overall,b}$) along with the numerical simulations of flame structure and dynamics of the flow field for coaxial burner configurations are reported. The burner comprises central mixture (air + liquefied petroleum gas) issuing either through six holes distributed radially each of 2 mm diameter or through a circular single port of area equal to the total areas of the six holes. A bluff-body stabilizer is attached to provide recirculation of the coaxial air surrounding the central flame. The study covers the effect of the central injection configuration with emphasis on the multijet on the overall lean equivalence ratio at which flame is extinguished. The dynamics of the flow field for the multiflame configurations were identified and compared with the single flame, using the generalized finite-rate chemistry model of FLUENT 6.2 with the detailed chemical reaction mechanism defined by GRI-MECH 3.0 and other mechanisms for the higher carbon species. The computed flow field of the multijet flame provides an extra intermediate vortex in addition to the two counter-rotating vortices observed for cases of the single central stream configuration. Such a vortex is believed to enhance the stability characteristics for all the test flames in the form of reduced experimental $\Phi_{overall,b}$-values.
[DOI: 10.1115/1.2938276]

1 Introduction

The criteria of flame stabilization of the simple jet diffusion flames have attracted the interest of many investigators. A good overview of the phenomena of lift-off and blowout of such flames can be found in Refs. [1–6]. Three different theories have been proposed to explain the stabilization mechanism and the criteria for establishing the lift-off height of such flames. The first theory assumes a premixed mixture to be placed under the lifted flame base, the second [5,7] suggests that the flame extinction occurred when the local strain rates in fluid exceed the extinction rate for a laminar diffusion flamelet, while the third theory [5,7–9] postulated the blowout conditions when the time available for backmixing by large-scale flow structures of hot products with fresh mixture is less than a critical chemical time required for ignition.

The flame blowout limits of such jet diffusion flames situated in a quiescent atmosphere are found to be narrow and the interpretation of these limitations relies on one of the above theories. It is well known that one can improve the fuel-air mixing rate and the flame blowout limits above those associated with simple jet flames by introducing internal flow recirculation [10–13] coaxially with the jet flame. Recirculation can be introduced either by employing swirl or a central bluff body. The use of swirl in improving the lean blowout stability limits was studied in Refs. [10,14], where swirl creates a jet-vortex interaction, and the recir-

culation vortex reduces the fuel jet velocity on the centerline, strongly stabilizing the lifted flame. The presence of the bluff-body flame holder in the coaxial airstream as a tool for improving the stability limits of the jet flame has yet received significant attention because of their relevance to many engineering applications [15,16]. Previous studies on this field [e.g., Refs. [16,17] are focused on the flame structure modeling of axial *single jet* (stream) flame surrounded by a recirculated coaxial air. To the end of the author's knowledge, none of these investigations were focused on studying the parameters affecting flame stabilization of axial *multijet* flames placed in recirculated coflowing air. The present investigation covers not only the stabilization mechanism of multijet flames of the geometries considered but also a comparative study of the flame stability between both the single- and multijet configurations. The bluff-body burner studied here provides an interesting model problem for industrial flows because of its simple and well-defined initial and boundary conditions, as well as its ability to stabilize flames with complex recirculating zones.

In this technical brief, the effects of the inner mixture injection configurations on the overall lean blowout equivalence ratio were studied and compared experimentally for both central single- and multijet flames. Furthermore, the stabilizer near the zone flow field for each configuration, the velocity field, and the temperature contours were studied computationally using the generalized finite-rate chemistry model of FLUENT 6.2 with the detailed chemical reaction mechanism defined by GRI-MECH 3.0. Both the experimental and computational results were exploited to gain better understanding of the stabilization mechanism of the test flames.

2 Experiments

2.1 Experimental Apparatus. Experiments were performed at atmospheric pressure using the axisymmetric, coaxial burner configuration shown in Fig. 1. The central mixture (air + liquefied petroleum gas (LPG)) is supplied axially either through a central tube with a single hole of 4.9 mm diameter or through six holes each of diameter equals 2 mm (with a total area equivalent to the single-hole area). The coflowing (coaxial) air passes over any of five bluff-body flame holders with included angles of 60 deg, 90 deg closed and open base for both included angles, and 180 deg (disk) mounted horizontally on the central tube with its apex pointing upstream. Each bluff-body flame holder has a diameter of 55 mm. The holders examined are placed inside a burner pipe of 82 mm diameter such that the stabilizer lee, the edge of the central axial tube, and the burner pipe are situated in the same vertical plane. The burner is confined in a combustor of 152.4 mm diameter surrounded by a cooling jacket. The inner airflow rate is supplied via a 5 kW reciprocating air compressor and measured by a calibrated rotameter. The inner fuel, which is supplied from a standard gas cylinders, together with the outer air (from a 5 kW air blower) flow rates were measured by a calibrated orifice plates.

2.2 Experimental Program and Procedure. The experimental program is divided into two main sections under the conditions shown in Table 1. These are concerned with investigating the effect of the following parameters on the stability of the inner single- or multijet flames;

(i) stabilizer shape and
(ii) inner mixture injection configuration

At each experiment and for the determined outer and inner air flow rates, the inner (central) fuel flow rate is reduced until the flame extinction is observed visually. At such a condition, the overall lean blowout equivalence ratio supplied to the burner ($\Phi_{overall,b}$) is identified. It should be stated that all the blowout experiments have been done for confined flames, i.e., when the burner is placed inside the combustor, to prevent the effect of the ambient air on the values of $\Phi_{overall,b}$.
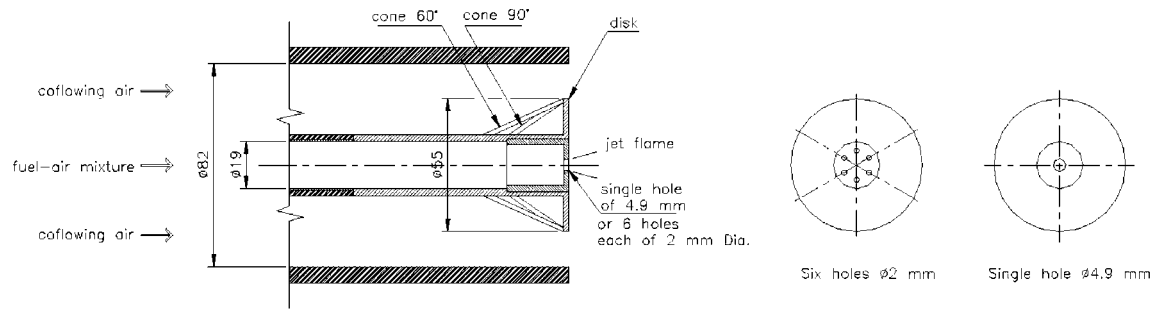
Fig. 1 Schematic of the burner (the combustor tube of 152.4 mm diameter does not appear in the figure)

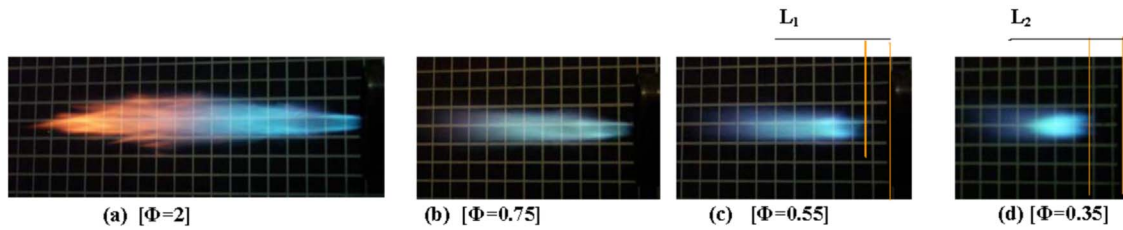(a) [Φ=2]   (b) [Φ=0.75]   (c) [Φ=0.55]   (d) [Φ=0.35]

Plate (1) Side view of consecutive flame photos showing the extinction procedure of the single jet flame as a response to increasing the central-jet velocity (disk-stabilizer).

3 Flame Calculations

3.1 Numerical Simulations.
Numerical simulations of the problem have been carried out to help better understand the stabilization mechanisms for the test flames. These simulations have been done using the generalized finite-rate chemistry model [18] of FLUENT 6.2. The generalized finite-rate chemistry formulation used in the present study is suitable for a wide range of applications including laminar or turbulent reaction systems, and combustion systems with premixed, nonpremixed, or partially premixed flames. The GRI-MECH 3.0 detailed chemical reaction mechanism, consisting of 325 elementary reactions involving 53 species, was used as the first part of the mechanism describes the reaction chemistry of CH_4. The second part of the mechanism was taken from Ref. [19] and involves the reactions of C2–C4 hydrocarbon fuels considered herein. The reaction rates that appear as source terms in the species transport equations are computed based on Arrhenius rate expressions, from the eddy-dissipation model [20]. The K-ε model [21] was used as the turbulence model. The segregated solver has been used for sequentially (i.e., segregated from one another) solving the modeled continuity, momentum, energy, and species equations.

Validation of the present simulation results has been proved by comparing the mean axial velocity profiles (V; m/s) calculated from the model (as an important parameter for the current flame configuration) with both the experimental data of Dally et al. [15] and computational results of a new strategy for the large-eddy simulation (LES) grid generation (recursive filter-refinement-based LES) obtained by Raman and Pitsch [22]. It was found that the present simulation was in reasonable agreement with both the experimental data and the LES simulation at all the axial locations.

4 Results and Discussion

### 4.1 Dynamics of the Flow Field

4.1.1 Flame Appearance and Dynamics of the Flow Field for Single Central-Jet Configuration. For the case of the disk-stabilizer configuration (as an example for all cases), the single jet flame extinction procedure as a response to increasing the central-jet velocity is shown in Plate 1. The flame is originally slender and relatively long. When the central-jet exit velocity is relatively low (24 m/s), flame ignition begins at a short quenching distance downstream from the tube mouth and a lengthy rich flame is observed (see Plate 1(a)). If this velocity exceeds 30 m/s, the flame shortens and the yellow tail disappears and the flame base detaches abruptly and moves to a certain position (≈ 4 mm) away

Table 1   Detailed experimental program

Set	Description	Geometrical parameters	U_i (m/s)	m_i (kg/h)	$U_{o,a}$ (m/s)	$m_{o,a}$ (kg/h)
			Flow parameters			
1	Stabilizer shape	Disk Cone 90 deg open base Cone 90 deg closed base Cone 60 deg open base Cone 90 deg closed base	From 23.8 to 42.3	From 1.94 to 3.45	4.8	60.48
2	Injection method	Multijet Singlejet	From 23.8 to 42.3	From 1.94 to 3.45	4.8	60.48
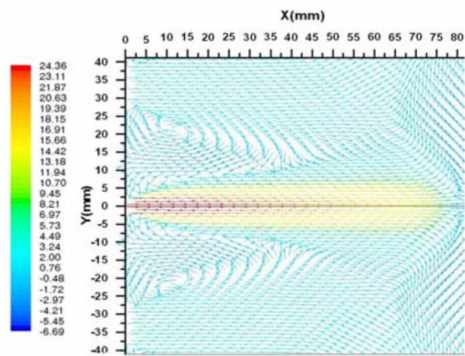
(a)
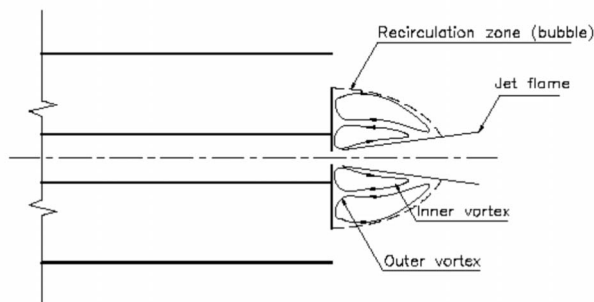
(b)

Fig. 2 Two dimensional near stabilizer flow field for the single jet flame: (*a*). computed mean axial and radial velocity vectors (*U*$_i$=24 m/s, *U*$_{o,a}$=4.8 m/s) and (*b*) schematic of the proposed flow field

Fig. 3 Two dimensional contour plots of the computed static temperature (°K) for the single jet flame

from the burner tip (distance L_1 in Plate 1(c)). Further increase in velocity would shorten the flame further and increase the lift-off height as shown in Plate 1(d), distance L_2 (≈ 6 mm) just before the extinction condition.

For better understanding of the above mentioned flame extinction procedure, it was decided to discuss the detailed flow field characteristics of the stabilizer near the zone, in the form of the calculated mean axial velocity vectors. This appears in Fig. 2(*a*), which shows the time-averaged axial velocity vector plots of the flow field near the disk stabilizer with $U_i=24$ m/s and $U_{o,a}$ =4.8 m/s. It is clear that the coaxial air converges toward the centerline downstream of the bluff body and forms a wake region, which extends approximately one bluff-body diameter downstream the stabilizer edge. A toroidal recirculating flow region is formed within the wake region by the interaction of the outer coaxial air with the central-jet flow. The structure of this recirculation region has been found by Roquemore et al. [23] to vary significantly with the relative flow rates of the inner and coaxial streams. For the central-jet dominated flow (present flames), two counter-rotating vortices appeared in the recirculation zone behind the stabilizer of Fig. 2(*a*) (these vortices appeared schematically in Fig. 2(*b*)). Inner vortex rotated in the counterclockwise direction, located adjacent to the central jet, and driven primarily by the central jet. An outer vortex close to the coaxial air side rotated in the clockwise direction. It should be stated here that due to the sudden expansion of the gases as they flow inside the combustor (confinement), Fig. 2(*a*) would exhibit some vortices (verified by the negative velocities) located at the downstream locations outside the recirculation zone.

In view of the above described flow field characteristics of the stabilizer near the zone, it seems easier to discuss the reasons for the flame extinction as a result of increasing the jet momentum
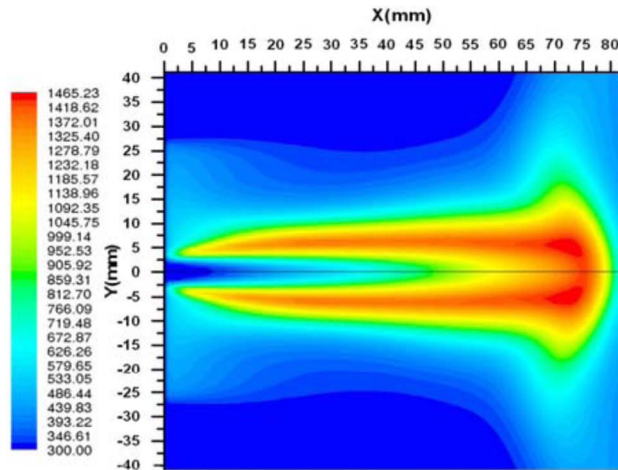
relative to the coflow. When the jet momentum relative to the coflow is increased, the jet expands and shifts the core of the inner vortex downstream until it loses its recirculating pattern and becomes part of the jet. At the same time, the outer vortex becomes shorter and smaller. As these vortices transfer enthalpy from the primary reaction zone (which is located at the end of the two vortices, see the zone of the maximum temperature in Fig. 3) to the incoming jet mixture and the coflow, so the heat required for ignition of the fresh mixture will reduced as their sizes reduced. Furthermore, increasing the jet velocity (momentum) will result in rapid mixing between the hot reaction products and the unburned jet fluid, and this time might be less than the critical chemical time required for ignition [5]. These effects will consequently lead to extinction and might also be applied to discuss the flame behavior shown in Plate 1.

4.1.2 Dynamics of the Flow Field for Multijet Flames. In this section, the discussion of the flow field characteristics will take place when the inner single jet is replaced by a multijet configuration. As mentioned above, the total area of the multijet (six holes) is equivalent to the single-hole area. The multijet flame configuration was modeled as two dimensional problem. This two dimensional species transport model is appropriate for such geometry where it is proved by Dally et al. [15] and Raman and Pitsch [22] that is capable of capturing the flow field, particularly in the near field of the stabilizer lee where the local extinction is negligible. The computed axial velocity vector of the multijet configuration is shown in Fig. 4(*a*) and their proposed schematic flow field is shown in Fig. 4(*b*). Figure 4 exhibits similar flow field characteristics to that observed for the single jet (shown in Fig. 2) with an additionally intermediate vortex that is formed in the interspacing between the jets. This vortex would transfer additional enthalpy from the main reaction zone, identified by the zone of the maximum flame temperature in Fig. 5, to the incoming multijet and coaxial air. Thus, there is an additional source of enthalpy transfer created by such intermediate vortices, which is proved to play a significant role in enhancing the stability characteristics of such flame configuration (it will appear in Sec. 4.2).

4.2 Effect of the Inner Mixture Injection Configuration on the Experimental $\Phi_{overall,b}$. Figure 6 shows the effect of increasing the inner bulk axial velocity on $\Phi_{overall,b}$, for all stabilizers, at different injection methods of the central mixture, namely, single jet and multijet. It should be stated that the total area of the mixture exit is kept the same for either the single or the multijet cases. The general trend for all stabilizers considered, shown in Fig. 6, exhibits lower $\Phi_{overall,b}$ for the multijet than the single jet case.
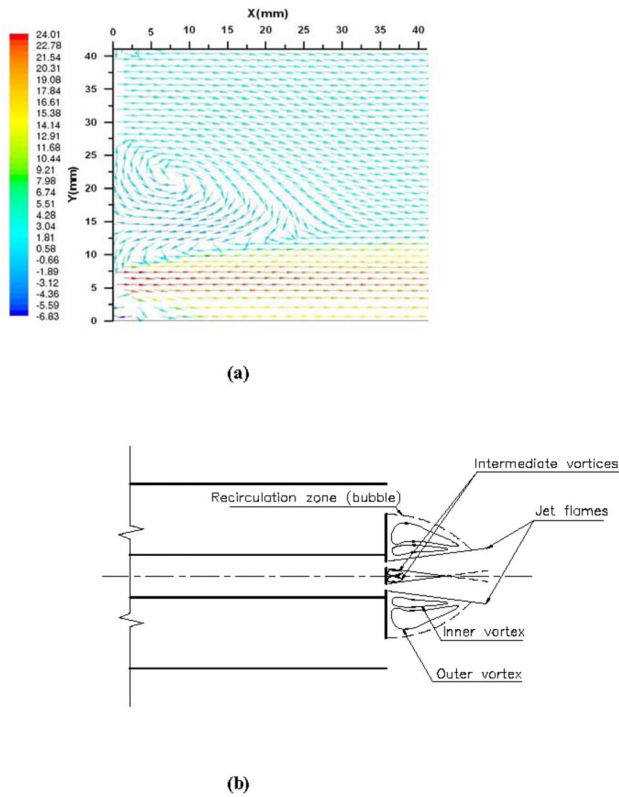
Fig. 4 Two dimensional near stabilizer flow field for the multi-jet flames: (a) computed mean axial velocity vectors (U_i =24 m/s, $U_{o,a}$=4.8 m/s) and (b) schematic of the proposed flow field

Fig. 6 Effect of inner mixture injection configurations on $\Phi_{overall,b}$ at different inner bulk axial velocities

The diminished levels of $\Phi_{overall,b}$ for the multijet case are attributed to the combined recirculation effect of both the intermediate vortices, formed in the interspacing between the jets, together with the main recirculation zone (inner and outer vortices) formed in the lee of the bluff-body stabilizer, see Fig. 4(b). This is expected to increase the rate of both heat transfer and recirculated mass from the recirculation zones to the incoming jets and consequently improves the flame stability.
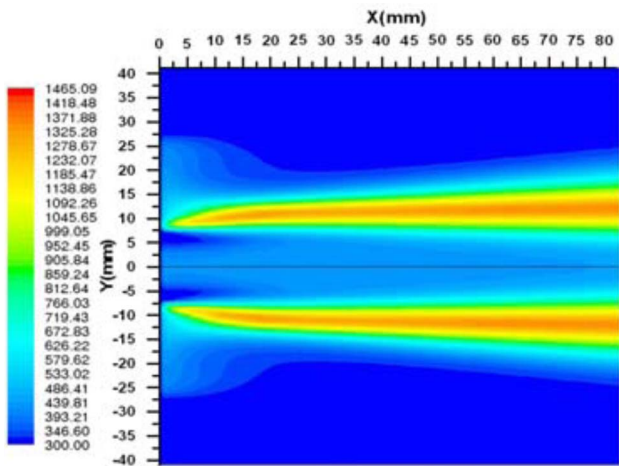

Fig. 5 Two dimensional contour plots of the computed static temperature (°K) for the multijet flames

5 Conclusions
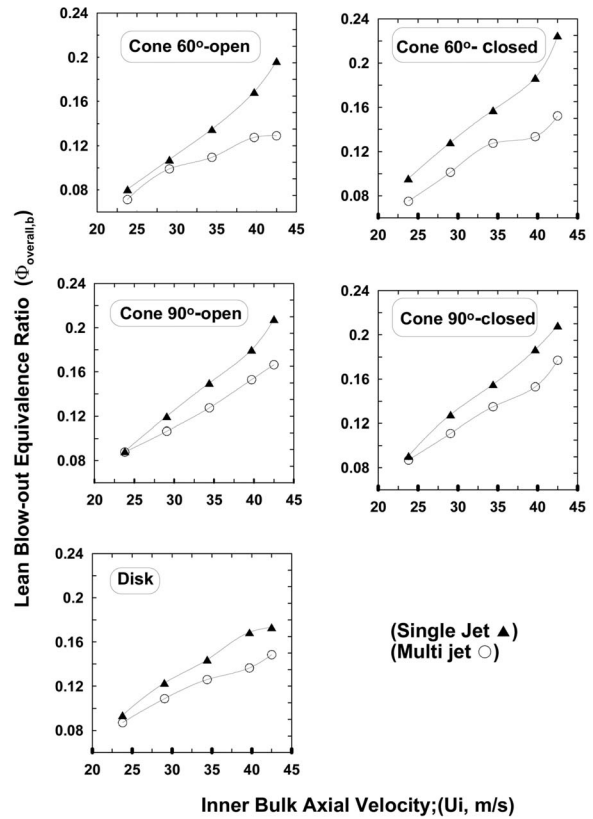
An axial jet flame surrounded by a bluff-body recirculated co-axial air has been used to determine the effect of the central mixture configuration on the overall lean equivalence ratio at which the flame extinguished [24–27].

The major conclusions of the study are as follows.

(1) The stabilizer near the field for both configurations considered in this study has been identified using the generalized finite-rate chemistry model of FLUENT 6.2. The resulted flow field for the single central stream configuration provides two counter-rotating vortices, while additional intermediate vortex is found for the multijet flames.

(2) Multijet flames are more stable than similar single jet flames. In both configurations, the recirculation zones outside the jet provide better stability than the corresponding cases with no bluff body. The multijet flame is further stabilized due to the combined recirculation effects of the additional vortex formed in the interspacing between the jets together with the inner and outer vortices formed in the lee of the bluff-body stabilizer.

Nomenclature

D = outer pipe inner diameter (mm)
D_s = stabilizer diameter (mm)
m = air mass flow rate (kg/h)
U = mean velocity normal to the exit flow area (bulk axial velocity) (m/s)
V = mean axial velocity component (m/s) ($U=V$ at $X=0$)

X = axial location in the downstream direction (X =0; at the stabilizer lee)

Y = radial location (Y=0; at the bluff-body axis)

Greek Symbols

$\Phi_{\text{overall},b}$ = overall lean blowout equivalence ratio

Φ = equivalence ratio

Subscripts

a = air

b = blowout

i = inner

o = outer

References

[1] Eickhoff, H., Lenze, B., Leuckel, W., and Driscoll, J. F., 1984, "Experimental Investigation on the Mechanism of Jet Diffusion Flames," *20th Symposium (International) on Combustion*, The Combustion Institute, pp. 311–318.

[2] Kaplan, C. R., Oran, E. S., and Baek, S. W., 1994, "Stabilization Mechanism of Lifted Jet Diffusion Flames," *25th Symposium(International) on Combustion*, The Combustion Institute, pp. 1183–1189.

[3] Takahashi, F., Mizomoto, M., Ikai, S., and Futaki, N., 1984, "Lifting Mechanism of Free Jet Diffusion Flames," *20th Symposium (International) on Combustion*, The Combustion Institute, pp. 295–302.

[4] Takahashi, F., and Schmoll, W. J., 1990, "Lifting Criteria of Jet Diffusion Flames," *23rd Symposium (International) on Combustion*, The Combustion Institute, pp. 677–683.

[5] Broadwell, J. E., Dahm, W. J. A., and Mungal, M. G., 1984, "Blowout of Turbulent Diffusion Flames," *20th Symposium (International) on Combustion*, The Combustion Institute, pp 303–310.

[6] Pitts, W. M., 1989, "Importance of Isothermal Mixing Processes to the Understanding of Lift-Off and Blowout of Turbulent Jet Diffusion Flames," Combust. Flame, **76**, pp. 197–212.

[7] Vanquickenborne, L., and Van Tiggelen, A., 1966, "The Stabilization Mechanism of Lifted Diffusion Flames," Combust. Flame, **10**, pp. 59–69.

[8] Peters, N., 1983, "Local Quenching Due to Flame Stretch and Non-Premixed Combustion," Combust. Sci. Technol., **30**, pp. 1–17.

[9] Janicka, J., and Peters, N., 1982, "Prediction of Turbulent Jet Diffusion Flame Lift-Off Using a PDF Transport Equation," *19th Symposium (International) on Combustion*, The Combustion Institute, p. 367.

[10] Chen, R. H., and Driscoll, J. F., 1988, "The Role of Recirculating Vortex in Improving Fuel-Air Mixing Within Swirling Flames," *22nd Symposium (International) on Combustion*, The Combustion Institute, pp. 531–540.

[11] Tangirala, V., Chen, R. H., and Driscoll, J. F., 1986, "Effect of Heat Release and Swirl on the Recirculation Within Swirl-Stabilized Flames," Combust. Sci. Technol., **51**, pp. 75–95.

[12] Driscoll, J. F., Chen, R. H., and Tangirala, V., 1987, "The Role of Recirculation in Improving Internal Mixing and Stability of Flames," AIAA J., **87**, pp. 306–325.

[13] Beer, J. M., and Chigier, N. A., 1972, *Combustion Aerodynamics*, Wiley, New York.

[14] Douglas, F., Chen, R. H., and Driscoll, J. F., 1990, "Enhancement of Flame Blowout Limits by the Use of Swirl," Combust. Flame, **80**, pp. 183–195.

[15] Dally, B. B., Masri, A. R., Barlow, R. S., and Fiechtner, G. J., 1998, "Instantaneous and Mean Compositional Structure of Bluff-Body Stabilized Nonpremixed Flames," Combust. Flame, **114**, pp. 119–148.

[16] Muradoglu, M., Liu, K., and Pope, S. B., 2003, "PDF Modeling of Bluff-Body Stabilized Turbulent Flame," Combust. Flame, **132**, pp. 115–137.

[17] Kim, S. H., and Huh, K. Y., 2002, "Use of Conditional Moment Closure Model to Predict NO Formation in a Turbulent CH_4/H_2 Flame Over a Bluff-Body," Combust. Flame, **130**, pp. 94–111.

[18] Gran, I. R., and Magnussen, B. F., 1996, "A Numerical Study of a Bluff-Body Stabilized Diffusion Flame; Part 2: Influence of Combustion Modeling and Finite Rate Chemistry," Combust. Sci. Technol., **119**, pp. 171–190.

[19] Qin, Z., Lissianski, V. V., Yang, H., Gardiner, W. C., Davis, S. G., and Wang, H., 2000, Proc. Combust. Inst., **28**, pp. 1663–1669.

[20] Magnussen, B. F., and Hjertager, B. H., 1976 "On Mathematical Models of Turbulent Combustion with Special Emphasis on Soot Formation and Combustion," *16th Symposium (International) on Combustion*, The Combustion Institute.

[21] Spalding, D. B., 1970, "Mixing and Chemical Reaction in Steady Confined Turbulent Flames," *13th Symposium (International) on Combustion*, The Combustion Institute.

[22] Raman, V., and Pitsch, H., 2005, "Large-Eddy Simulation of a Bluff-Body-Stabilized Non-Premixed Flame Using a Recursive Filter-Refinement Procedure," Combust. Sci. Technol., **142**, pp. 329–347.

[23] Roquemore, W. M., Bradley, R. P., Stutrud, J. S., Reeves, C. M., and Krishnamurthy, L., 1980, "Preliminary Evaluation of a Combustor for Use in Modeling and Diagnostics Development," ASME Paper No. 80-GT-93.

[24] Al-Feky, S. M. S., 1988, "An Investigation in the Factors Affecting Flame Stabilization Behind a Conical Bluff-Body," MS thesis, Helwan University, Cairo, Egypt.

[25] Baxter, M. R., and Lefebvre, A. H., 1992, "Weak Extinction Limits of Large-Scale Flame Holder," ASME J. Eng. Gas Turbines Power, **114**, pp. 776–782.

[26] Hillemanns, R., Lenze, B., and Leuckel, W., 1986, *21st Symposium (International) on Combustion*, The Combustion Institute, p. 1445.

[27] Tangirala, V., and Driscoll, J. F., 1988, "Temperature Within Non-Premixed Flames: Effect of Rapid Mixing Due to Swirl," Combust. Sci. Technol., **60**(1–3), pp. 143–162.